Proceedings of the International RILEM Conference

Materials, Systems and Structures in Civil Engineering 2016
Segment on

Service Life of Cement-Based Materials and Structures

Vol. 1

Edited by
Miguel Azenha, Ivan Gabrijel, Dirk Schlicke, Terje Kanstad
and Ole Mejlhede Jensen

Proceedings
PRO 109

cost
EUROPEAN COOPERATION
IN SCIENCE AND TECHNOLOGY

rilem

International RILEM Conference on

Materials, Systems and Structures in Civil Engineering 2016

segment on

Service Life of Cement-Based Materials and Structures

Vol. 1

International RILEM Conference on Materials, Systems and Structures in Civil Engineering
Conference segment on Service Life of Cement-Based Materials and Structures
22-24 August 2016, Technical University of Denmark, Lyngby, Denmark

Published by RILEM Publications S.A.R.L.
4 avenue du Recteur Poincaré 75016 Paris - France
Tel : + 33 1 42 24 64 46 Fax : + 33 9 70 29 51 20
http://www.rilem.net E-mail: dg@rilem.net
 ISBN Vol. 1: 978-2-35158-170-4
Vol. 2: 978-2-35158-171-4 Vol. 1&2: 978-2-35158-172-8 e-ISBN : 978-2-35158-173-5
Printed by Praxis – Nyt Teknisk Forlag, Ny Vestergade 17, 1471 København K, Denmark
Photo 1st cover page: Øresund Bridge seen from below the deck. Credit: Antony McAulay (Adobe Stock, boutik.pt)

RILEM, The International Union of Laboratories and Experts in Construction Materials, Systems and Structures, is a non profit-making, non-governmental technical association whose vocation is to contribute to progress in the construction sciences, techniques and industries, essentially by means of the communication it fosters between research and practice. RILEM's activity therefore aims at developing the knowledge of properties of materials and performance of structures, at defining the means for their assessment in laboratory and service conditions and at unifying measurement and testing methods used with this objective.

RILEM was founded in 1947, and has a membership of over 900 in some 70 countries. It forms an institutional framework for co-operation by experts to:

- optimise and harmonise test methods for measuring properties and performance of building and civil engineering materials and structures under laboratory and service environments,
- prepare technical recommendations for testing methods,
- prepare state-of-the-art reports to identify further research needs,
- collaborate with national or international associations in realising these objectives.

RILEM members include the leading building research and testing laboratories around the world, industrial research, manufacturing and contracting interests, as well as a significant number of individual members from industry and universities. RILEM's focus is on construction materials and their use in building and civil engineering structures, covering all phases of the building process from manufacture to use and recycling of materials.

RILEM meets these objectives through the work of its technical committees. Symposia, workshops and seminars are organised to facilitate the exchange of information and dissemination of knowledge. RILEM's primary output consists of technical recommendations. RILEM also publishes the journal *Materials and Structures* which provides a further avenue for reporting the work of its committees. Many other publications, in the form of reports, monographs, symposia and workshop proceedings are produced.

International RILEM Conference on Materials, Systems and Structures in Civil Engineering
Conference segment on Service Life of Cement-Based Materials and Structures
22-24 August 2016, Technical University of Denmark, Lyngby, Denmark

International RILEM Conference on

Materials, Systems and Structures in Civil Engineering 2016

Segment on
Service Life of Cement-Based Materials and Structures
Vol. 1

Lyngby, Denmark

August 22-24, 2016

Edited by
Miguel Azenha, Ivan Gabrijel, Dirk Schlicke, Terje Kanstad and
Ole Mejlhede Jensen

RILEM Publications S.A.R.L.

Sponsors:

CITY OF COPENHAGEN

Knud Højgaards Foundation

Larsen & Nielsen foundation

Ingeborg og Leo Dannis Legat for Videnskabelig Forskning

Hosted by:

Technical University of Denmark

Department of Civil Engineering

DANISH
TECHNOLOGICAL
INSTITUTE

International Organization by:

- Miguel Azenha (University of Minho, Portugal)
- Ole Mejlhede Jensen (Technical University of Denmark)
- Dirk Schlicke (Graz University of Technology, Austria)
- Terje Kanstad (Norwegian University of Science and Technology)

Scientific Committee:

Ivan Gabrijel (chair)	Croatia
Miguel Azenha	Portugal
Farid Benboudjema	France
Violeta Bokan Bosiljkov	Slovenia
Matthieu Briffaut	France
Laurie Buffo-Lacarrière	France
Paulo Cachim	Portugal
Robby Caspeele	Belgium
Özlem Cizer	Belgium
Cyrille Dunant	Switzerland
Rui Faria	Portugal
Erez Gal	Israel
Dariusz Gawin	Poland
Max Hendriks	Norway
Wibke Hermerschmidt	Germany
Ole Mejlhede Jensen	Denmark
Terje Kanstad	Norway
Agnieszka Knoppik-Wróbel	Poland
Katalin Kopecskó	Hungary
Tang Luping	Sweden
Enrico Masoero	United Kingdom
Theodore Matikas	Greece
Sreejith Nanukuttan	United Kingdom
Ivan Paric	Germany
Bernhard Pichler	Austria
Vlastimir Radonjanin	Serbia
Emmanuel Rozière	France
Aljoša Šajna	Slovenia
Dirk Schlicke	Austria
Wolfram Schmidt	Germany
Marijana Serdar	Croatia
Vít Šmilauer	Czech Republic
Tayfun Altuğ Söylev	Turkey
Stéphanie Staquet	Belgium
François Toutlemonde	France
Gregor Trtnik	Slovenia
Neven Ukrainczyk	Germany
Jörg F. Unger	Germany
Mateusz Wyrzykowski	Switzerland
Guang Ye	Netherlands
Yibing Zuo	Netherlands

RILEM Publications

The following list presents the latest offer of RILEM Publications, sorted by series. Each publication is available in printed version and/or in online version.

RILEM PROCEEDINGS (PRO)

PRO 94 (online version): HPFRCC-7 - 7th RILEM conference on High performance fiber reinforced cement composites, e-ISBN: 978-2-35158-146-9, *Eds. H.W. Reinhardt, G.J. Parra-Montesinos, H. Garrecht*
PRO 95: International RILEM Conference on Application of superabsorbent polymers and other new admixtures in concrete construction, ISBN: 978-2-35158-147-6; e-ISBN: 978-2-35158-148-3, *Eds. Viktor Mechtcherine, Christof Schroefl*
PRO 96 (online version): XIII DBMC: XIII International Conference on Durability of Building Materials and Components, e-ISBN: 978-2-35158-149-0, *Eds. M. Quattrone, V.M. John*
PRO 97: SHCC3 – 3rd International RILEM Conference on Strain Hardening Cementitious Composites, ISBN: 978-2-35158-150-6; e-ISBN: 978-2-35158-151-3, *Eds. E. Schlangen, M.G. Sierra Beltran, M. Lukovic, G. Ye*
PRO 98: FERRO-11 – 11th International Symposium on Ferrocement and 3rd ICTRC - International Conference on Textile Reinforced Concrete, ISBN: 978-2-35158-152-0;
e-ISBN: 978-2-35158-153-7, *Ed. W. Brameshuber*
PRO 99 (online version): ICBBM 2015 - 1st International Conference on Bio-Based Building Materials, e-ISBN: 978-2-35158-154-4, *Eds. S. Amziane, M. Sonebi*
PRO 100: SCC16 - RILEM Self-Consolidating Concrete Conference**,** ISBN: 978-2-35158-156-8; e-ISBN: 978-2-35158-157-5
PRO 101 (online version): III Progress of Recycling in the Built Environment, e-ISBN: 978-2-35158-158-2, *Eds I. Martins, C. Ulsen and S. C. Angulo*
PRO 102 (online version): RILEM Conference on Microorganisms-Cementitious Materials Interactions, e-ISBN: 978-2-35158-160-5, *Eds. Alexandra Bertron, Henk Jonkers, Virginie Wiktor*

In relation to the International RILEM Conference on Materials, Systems and Structures in Civil Engineering, MSSCE 2016 which the present proceedings belongs to, the following RILEM proceedings will be issued:

PRO 108: Innovation of Teaching in Materials and Structures
PRO 109 (two volumes): Service life of Cement-Based Materials and Structures
PRO 110: Historical Masonry
PRO 111: Electrochemistry in Civil Engineering
PRO 112: Moisture in Materials and Structures
PRO 113: Concrete with Supplementary Cementitious materials
PRO 114: Frost Action in Concrete
PRO 155: Fresh Concrete

RILEM REPORTS (REP)

Report 45: Repair Mortars for Historic Masonry - State-of-the-Art Report of RILEM Technical Committee TC 203-RHM, e-ISBN: 978-2-35158-163-6, *Ed. Paul Maurenbrecher and Caspar Groot*

International RILEM Conference on Materials, Systems and Structures in Civil Engineering
Conference segment on Service Life of Cement-Based Materials and Structures
22-24 August 2016, Technical University of Denmark, Lyngby, Denmark

Contents

		Page
	Preface Miguel Azenha, Ivan Gabrijel, Dirk Schlicke, Terje Kanstad and Ole Mejlhede Jensen	XIII Vol 1
	Welcome Ole Mejlhede Jensen	XV Vol 1
1	**Volume stability of alkali activated Portland cement concretes with alkali-susceptible aggregates** Pavel Krivenko	1 Vol 1
2	**Impact of slag content in alkali-activated slag cement on porosity of concrete** Pavel Krivenko, Oles Lastivka, Igor Rudenko, Sergei Lakusta	11 Vol 1
3	**Nanoscale simulations of cement formation and structural evolution: A new kinetic approach** Enrico Masoero, Igor Shvab	21 Vol 1
4	**Condition assessment of reinforced concrete elements exposed to carbonation** Samindi Samarakoon, Jan Sælensminde, Cecilie Myklebust Helle	29 Vol 1
5	**Control of early age cracking in a massive tunnel structure based on experimental investigations and numerical simulations** Wibke Hermerschmidt, Martin Laube, Alex-W. Gutsch, Hartmann Alberts, Robert Teuber, Eckart Thoms	39 Vol 1
6	**Computational prediction of restraint-induced macrocrack patterns in concrete walls** Agnieszka Knoppik-Wróbel, Dirk Schlicke	49 Vol 1
7	**Some examples on shrinkage restraint effects on concrete and concrete structures** Farid Benboudjema	59 Vol 1
8	**Service life design and assessment for concrete structures in HZM sea link project for 120 years** Kefei Li, Dongdong Zhang, Quanwang Li	69 Vol 1
9	**VERCORS mockup – first experimental results and synthesis of the benchmark** Benoît Masson, Manuel Corbin	79 Vol 1
10	**Experimental study of corrosion-induced degradation of reinforced concrete elements** Olfa Loukil, Lucas Adelaide, Véronique Bouteiller, Marc Quiertant, Thierry Chaussadent, Frédéric Raguenau, Xavier Bourbon, Laurent Trenty	95 Vol 1
11	**Evaluation of concrete's resistance to physical sulfate salt attack** Semion Zhutovsky, R. Douglas Hooton	105 Vol 1
12	**The importance of multiphysics and multiscale modelling of concrete to understand its complex macroscopic properties** Jörg F. Unger, Vitaliy Kindrachuk, Volker Hirthammer, Thomas Titscher, Christoph Pohl	115 Vol 1
13	**Residual concrete strength after sustained load: Experimental results and modelling approach** Zainab Kammouna, Matthieu Briffaut, Yann Malecot	125 Vol 1

14 **Remaining service life of railway prestressed concrete sleepers** 135 Vol 1
Sakdirat Kaewunruen, Shintaro Minoura, Tsutomu Watanabe, Alex M Remennikov

15 **Numerical simulation since early ages of the RG8 beam test from concrack benchmark by means of a 3D fibre frame model** 145 Vol 1
Maria D. Crespo, Denise Ferreira, Jesus Miguel Bairan, Antonio Mari

16 **Predicting chloride induced depassiviation and minimum concrete cover with different binders** 155 Vol 1
Ingemar Löfgren, Tang Luping, Oskar Esping, Anders Lindvall

17 **Coupling limit states of corrosion initiation and corrosion induced crack opening – sensitivity analysis of model parameters** 165 Vol 1
Miguel Ferreira, Edgar Bohner, Olli Saarela

18 **Bio-based pH-responsive superabsorbent polymers for self-healing cracks in concrete** 177 Vol 1
Arn Mignon, Dries Devisscher, Jolien Vermeulen, Peter Dubruel, Sandra Van Vlierberghe, Nele De Belie

19 **Comparison of measured and prescribed k-values for the equivalent performance of fly ash concrete** 187 Vol 1
T. Altuğ Söylev

20 **Carbon nanoparticles cement-based materials for service life monitoring** 195 Vol 1
André O. Monteiro, Paulo B. Cachim, Pedro M. F. J. Costa

21 **Can a reliable prediction of cement paste transport properties be made using microstructure models?** 203 Vol 1
Ravi A. Patel, Janez Perko, Diederik Jacques, Geert De Schutter, Guang Ye, Klaas Van Breugel

22 **Measuring the influence of temperature on electrical properties of concrete** 211 Vol 1
Alex Coyle, Robert Spragg, Armen Amirkhanian, Jason Weiss

23 **Modelling of chloride transport in unsaturated concrete: Study of electrocapillary effect** 221 Vol 1
Phu Tho Nguyen, Ouali Amiri

24 **Influence of fibre reinforcement on the initiation of corrosion-induced cracks** 231 Vol 1
Carlos G. Berrocal, Ignasi Fernandez, Karin Lundgren, Ingemar Löfgren

25 **Water release process of superabsorbent polymers in cement paste at early age** 241 Vol 1
Yujiang Wang, Ming Li, Qian Tian

26 **Hardening induced stresses in very thick concrete members – insights from comprehensive FE-studies** 249 Vol 1
Peter Joachim Heinrich, Dirk Schlicke

27 **Benchmarking of complex systems: Application to cement based materials** 259 Vol 1
Janez Perko, Diederik Jacques, Ravi A. Patel, Joan Govaerts

28 **A new analytical approach in modelling of cracking of RC members** 269 Vol 1
Gintaris Kaklauskas, Regimantas Ramanauskas

29 **Experimental investigation on strain distribution in reinforcement of RC specimens under tension loading** 279 Vol 1
Gintaris Kaklauskas, Mantas Juknys, Ronaldas Jakubovskis, Eugenijus Gudonis, Regimantas Ramanauskas, Viktor Gribniak, Aleksandr Sokolov

30 **Numerical modelling of fracture of macro-polymer fiber reinforced concrete** 287 Vol 1
Marcos G. Alberti, Alejandro Enfedaque, Jaime C. Galvez, Encarnación Reyes

31 **Bender-extender elements for characterization of cement paste at early ages** 297 Vol 1
José Granja, Miguel Azenha

32 **Developing an engineering approach for migrating from prescriptive to performance-based specification for concrete** 307 Vol 1
Sreejith Nanukuttan, P. A. Muhammed Basheer, W. John McCarter, Tang Luping

33 **Properties of concrete recycling clay-rich dredging sediments as a novel supplementary cementitious material** 317 Vol 1
Céline Van Bunderen, Ruben Snellings, Liesbeth Horckmans, Joris Dockx, Jos Vandekeybus, Koenraad Van Balen, Lucie Vandewalle, Özlem Cizer

34 **Experimental and numerical analysis of drying shrinkage on cement-based materials** 325 Vol 1
Marie Malbois, Adrien Socie, Aveline Darquennes, Caroline De Sa, Farid Benboudjema

35 **Study on the effects of deformed steel fibres on strengthening and toughening of ultra-high performance concrete** 335 Vol 1
Gai-Fei Peng, Xu-Jing Niu, Yi-Lin Zhao, Yi-Gang Li

36 **Couplings between creep and damage: Role of the fracture criterion** 345 Vol 1
Cyrille Dunant, Adrien Hilaire

37 **Service life prediction of a cementitious coating system based on chloride-induced corrosion** 355 Vol 1
Hua Dong, Guang Ye

38 **Usability of basalt fibres in fibre reinforced cementitious composites** 365 Vol 1
Zehra Canan Girgin

39 **Use of ultrasonic p- and s-waves transmission velocity for the early age behaviour of eco-concrete** 377 Vol 1
Jérôme Carette, Stéphanie Staquet

40 **Concrete drying: effects of boundary conditions and specimen shape** 385 Vol 1
Jérôme Carette, Farid Benboudjema, Georges Nahas, Kamilia Abahri, Aveline Darquennes, Rachid Bennacer

41 **Mitigation of early age shrinkage of UHPFRC by using spent equilibrium catalyst** 395 Vol 1
Ana Mafalda Matos, Sandra Nunes, Carla Costa

Author index 405 Vol 1

Preface XIII Vol 2
Miguel Azenha, Ivan Gabrijel, Dirk Schlicke, Terje Kanstad and Ole Mejlhede Jensen

Welcome XV Vol 2
Ole Mejlhede Jensen

42 **Effect of recycled aggregate concrete on early age behavior** 407 Vol 2
Ahmed Z. Bendimerad, Brice Delsaute, Emmanuel Roziere, Stéphanie Staquet, Ahmed Loukili

43 **Mechanical activation of supplementary cementitious materials in order to use as hydraulic binder** 415 Vol 2
Gábor Mucsi, Ákos Debreczeni, Viktor Török

44 **Modelling of ageing of low-pH concretes** 425 Vol 2
Laurie Buffo-Lacarrière, Youssef El Bitouri, Alain Sellier, Xavier Bourbon

45 **Chloride penetration coefficient and freeze-thaw durability of waste metakaolin containing high strength self-compacting concrete** 435 Vol 2
Girts Bumanis, Diana Bajare

46 **An investigation on usability of basalt fibre in cement-based composites** 443 Vol 2
Şükrü Özkan, Emre Sancak, Fuat Demir

47 **Effects of curing temperature on chloride migration and electrical resistivity of concrete** 453 Vol 2
Utkan Corbacioglu, Egemen Kesler, T. Alper Yıkıcı, Yilmaz Akkaya

48 **Contemp – a virtual thermo-mechanical simulator for hydrating reinforced concrete blocks with extension to service life** 463 Vol 2
Vít Šmilauer, Luis Baquerizo, Thomas Matschei, Petr Havlásek, Wilson Ricardo Leal da Silva, Karolina Hájková

49 **Mechanical properties of ultra high performance fibre reinforced concrete** 473 Vol 2
Radoslav Sovják

50 **Discrete modeling of surface cracking of drying concretes at different ages: Application to TU1404 RRT concrete** 483 Vol 2
Arnaud Delaplace, Clément Vert, Eric Brouard

51 **Impact of biogenic self-healing additive on performance of cement-based mortar** 493 Vol 2
Ali Amiri, Zeynep Basaran Bundur

52 **Non-destructive evaluation of eco-friendly cementituous materials by ultrasound** 503 Vol 2
Markus Krüger, Rok Bregar, Gheorghe Alexandru David, Joachim Juhart

53 **Waste ceramics as partial cement and aggregate replacements in self-compacting concrete** 513 Vol 2
Paul Archbold, John Flattery

54 **Comparative analysis of compressive strength and volume change for determination of sulfate resistance of RAC** 523 Vol 2
Vesna Bulatović, Vlastimir Radonjanin, Mirjana Malešev, Miroslava Radeka, Ivan Lukić

55 **Sensitivity analysis for prediction of corrosion initiation by carbonation** 533 Vol 2
Van Loc Ta, Stéphanie Bonnet, Tristan Senga Kiesse, Anne Ventura

56 **Chloride diffusion and binding in hardened cement paste from microscale analyses** 543 Vol 2
Pietro Carrara, Laura De Lorenzis

57 **Non-destructive evaluation of strength development in concrete** 553 Vol 2
Ivan Gabrijel, Dubravka Bjegović, Josip Kujek

58 **Crack width control – verification of the deformation compatibility vs. covering the cracking force** 563 Vol 2
Dirk Schlicke, Nguyen Viet Tue

59 **CEMRS: Fast and efficient modelling platform for the simulation of cementitious systems** 573 Vol 2
Shiju Joseph, Shashank Bishnoi, Koen Van Balen, Özlem Cizer

60 **Chloride ion diffusion in concrete under tensile load** 579 Vol 2
Ling Wang, Yan Yao, Zhendi Wang, Yin Cao, Juan Li

61 **Basic and drying shrinkage of infrastructure concretes with variable fly ash content** 589 Vol 2
Anja E. Klausen, Gunrid Kjellmark, Terje Kanstad

62 **Avoiding overfitting in inverse modeling of chloride migration in concrete** 599 Vol 2
Sreejith V. Nanukuttan, Neven Ukrainczyk, Des J. Robinson, Eduardus A.B. Koenders

63 **Plastic shrinkage cracking in self-compacting concrete: A parametric study** 609 Vol 2
Faez Sayahi, Mats Emborg, Hans Hedlund, Ingemar Löfgren

64 **Definition of damage distribution due to internal expansive reactions in long term concrete structures** 621 Vol 2
Esperanza Menéndez, Ricardo García-Rovés, Sergio Ruiz, José de Frutos

65 **A risk-based model for determining allowable admixed chloride limits in concrete** 631 Vol 2
Mahmoud Shakouri, David Trejo, Paolo Gardoni

66 **Influence of restrained shrinkage in RC builduing slabs: A case study** 641 Vol 2
Carlos Sousa, Emanuel Felisberto, Rui Faria

67 **Extended round robin testing program of COST action TU1404 – lessons learned from the initial experimental phase** 651 Vol 2
Marijana Serdar, Stéphanie Staquet, Dirk Schlicke, Emmanuel Rozière, Gregor Trtnik, Sree Nanukuttan, Miguel Azenha

68 **Short-term creep of cement paste: Experiments and multiscale modeling** 665 Vol 2
Markus Königsberger, Muhammad Irfan-ul-Hassan, Christian Hellmich, Bernhard Pichler

69 **Experimental and numerical investigation of drying effets on concrete's mechanical properties** 675 Vol 2
François Soleilhet, Farid Benboudjema, Fabrice Gatuingt, Xavier Jourdain

70 **On utilisation of elliptical rings for assessing cracking tendency of concrete and other cement-based materials** 685 Vol 2
Xiangming Zhou, Wei Dong, Gediminas Kastiukas

71 **Modelling of transport of chloride ions in concrete under compressive load** 695 Vol 2
Yin Cao, Yan Yao, Ling Wang, Zhendi Wang

72 **Multidepth corrosion monitoring system evaluation and application** 705 Vol 2
Dalibor Sekulic, Ivan Gabrijel

73 **Modeling of early age concrete creep using rheological modeling approaches** 715 Vol 2
Wibke Hermerschmidt, Farid Benboudjema

74 **Size effect on the drying shrinkage** 725 Vol 2
Aveline Darquennes, Mariana Vasylchenko, Farid Benboudjema

75 **Aging tests for performance of photocatalytic cement based materials** 735 Vol 2
František Peterka, Michaela Jakubičková, Tereza Sázavská, Elia Boonen

76 **Quantification the filling of microcracks due to autogenous self-healing in cement paste** 745 Vol 2
Jiayi Chen, Xian Liu, Guang Ye

77 **Ultrasonic assessment in curing process of cbm using experimental monitoring tests and microstructural simulation tools** 755 Vol 2
José Vicente Fuente, Jorge Gosalbez, Sofía Aparicio, Margarita González, José J. Anaya

78 **Finite element models capable to give detailed information about cracks spacing and opening in concrete structures in service life conditions** 765 Vol 2
Pierre Rossi, Jean-Louis Tailhan

79 **Effect of granulated blast furnace slag on the durability of self compacting concrete in hot environment** 777 Vol 2
Said Kenai, Walid Yahiaoui, Belkacem Menadi

80 **Evaluation of the LDPM elastic and fracture parameters by up-scaling procedure** 789 Vol 2
G. Sherzer, Peng Gao, Guang Ye, Erez Gal

Author Index 799 Vol 2

Preface

The conference "Materials, Systems and Structures in Civil Engineering – MSSCE 2016" is part of the RILEM week 2016, which consists of a series of parallel and consecutive conference and doctoral course segments on different topics as well as technical and administrative meetings in several scientific organizations. The event is hosted by the Department of Civil Engineering at the Technical University of Denmark and the Danish Technological Institute and it is held at the Lyngby campus of the Technical University of Denmark 15-29 August 2016.

This volume contains the proceedings of the MSSCE 2016 conference segment on "Service Life of Cement-Based Materials and Structures", which is organized by COST Action TU1404 (www.tu1404.eu). This COST Action is entitled: "Towards the next generation of standards for service life of cement-based materials and structures", dedicated to assist deepening knowledge regarding the service life behaviour of cement-based materials and structures. The main purpose of this Action is to bring together relevant stakeholders (experimental and numerical researchers, standardization offices, manufacturers, designers, contractors, owners and authorities) in order to reflect today's state of knowledge in new guidelines/recommendations, introduce new products and technologies to the market, and promote international and inter-speciality exchange of new information, creating avenues for new developments. The COST Action is basically divided in three main workgroups targeted to this purpose:

WG1 – Testing of cement-based materials and RRT+
WG 2 – Modelling and benchmarking
WG 3 – Recommendations and products

The activities of TU1404 started in November 2014 with a kick-off meeting in Brussels. Since then, three major meetings have taken place, as to promote networking and scientific discussions among participants: April 2015 in Ljubljana, Slovenia; September 2015 in Vienna, Austria; March 2016 in Zagreb, Croatia.

Also, two important instruments of the Action are now under way: the Extended Round Robin Testing Program (RRT^+), and the numerical benchmarking. The RRT^+ is currently involving 43 laboratories and has involved shipment of more than 100 tons of raw materials. An initial phase of testing has been finished already, and laboratories are shifting focus to the main experiments of this extended program. The numerical benchmarking program has also begun and will soon interact with the RRT^+ program and even extend beyond it.

The present conference segment deals with a wide breadth of topics related to the service life of concrete, comprising aspects related to the 3 Workgroups mentioned above. The conference segment is attended by 80 presenters from university, industry and practice representing more than 30 different countries. All contributions have been peer reviewed.

It should be mentioned, that these proceedings do not contain all the papers that have been submitted in the scope of COST TU1404 in MSSCE2016. Due to scheduling and organization issues, as well as affinity with topics of other segments, some of the papers were moved. A separate set of electronic proceedings shall be prepared to include all papers related to COST TU1404, and will be made available in the website of the Action (www.tu1404.eu).

Miguel Azenha Ivan Gabrijel Dirk Schlicke Terje Kanstad Ole Mejlhede Jensen

August 2016, Lyngby, Denmark

Acknowledgements

This publication is based upon work from COST Action TU1404 'Towards the next generation of standards for service life of cement-based materials and structures', supported by COST (European Cooperation in Science and Technology).

COST (European Cooperation in Science and Technology) is a pan-European intergovernmental framework. Its mission is to enable break-through scientific and technological developments leading to new concepts and products and thereby contribute to strengthening Europe's research and innovation capacities. It allows researchers, engineers and scholars to jointly develop their own ideas and take new initiatives across all fields of science and technology, while promoting multi- and interdisciplinary approaches. COST aims at fostering a better integration of less research intensive countries to the knowledge hubs of the European Research Area. The COST Association, an International not-for-profit Association under Belgian Law, integrates all management, governing and administrative functions necessary for the operation of the framework. The COST Association has currently 36 Member Countries.

COST is supported
by the EU Framework
Programme Horizon 2020

Welcome

Were you aware that a part of your daily language is likely to be in Danish? A thousand years ago the Danish word "*Vindue*" came along with the Vikings to England. Several hundred years later it reached North America, and from there – just two to three decades ago – almost every person in the world learned to understand and pronounce this word: "*Windows*", which etymologically means "an eye to the wind".

As a child your career as construction professional may have started with *LEGO*, and before you went to bed, your mother told you the unforgettable fairytales of *H.C.Andersen*. You may have grown up with the delicious taste of *Lurpak* butter on your bread, and though you might find it strange that "God plays dice with the Universe", hopefully your school teacher told you that on this topic Einstein was flat out wrong and *Niels Bohr* was right. Right now you may prefer to be sitting in the sun with a chilled *Carlsberg* beer in your hand, enjoying the iconic view of the *Sydney Opera House*. All of it is Danish made, and many things around you at home, if not made in Denmark, were probably brought to you by *Maersk*, the world's largest shipping company, the modern Danish Viking fleet.

Though Denmark is one of the world's smallest countries, yet it stands – along with your country – among the greatest. On top of a thousand years of outreach from Denmark, your visit to the Danes is most welcome. On your approach to Copenhagen airport you had a view to *wind turbines* harvesting green energy, you saw record breaking *bridges*, and perhaps you got a glimpse of the island Ven where the nobleman *Tycho Brahe* literally speaking changed our view of the world through perfection of astronomical observations with his naked eye. In Copenhagen you may appreciate a walk in the fairytale amusement park *TIVOLI*, and in the Copenhagen harbour you may have a rendezvous with a *Little Mermaid*.

Of all things in Denmark you will surely enjoy the conference and doctoral courses *Materials, Systems and Structures in Civil Engineering, MSSCE 2016* which are held in conjunction with the *70th annual RILEM week*. On this occasion RILEM celebrates its 70 years birthday and thus maintains generations of experience. However, new activities and the in-built diversity keep RILEM fresh and dynamic like a teenager.

The event takes place in northern Copenhagen, Lyngby, at the campus of the Technical University of Denmark, 15-29 August 2016. MSSCE 2016 aims at extending the borders of the RILEM week by including doctoral courses, by involving a palette of RILEM topics in the conference and workshop activities, and by collaborating with other scientific organizations. The insight and outlook provided by this event make it RILEM's technical and educational activity window.

It is a pleasure to share with you what is unique to RILEM and Denmark!

Ole Mejlhede Jensen, Technical University of Denmark
Honorary president of RILEM 2016, Chairman of MSSCE 2016

International RILEM Conference on Materials, Systems and Structures in Civil Engineering
Conference segment on Service Life of Cement-Based Materials and Structures
22-24 August 2016, Technical University of Denmark, Lyngby, Denmark

VOLUME STABILITY OF ALKALI ACTIVATED PORTLAND CEMENT CONCRETES WITH ALKALI-SUSCEPTIBLE AGGREGATES

Pavel Krivenko [(1)]

(1) Kyiv National University of Construction and Architecture, Scientific Research Institute for Binders and Materials, Ukraine

Abstract
The paper presents the results of study on the influence of metakaolin additive on volume stability and strength characteristics of alkali activated portland cement concrete with alkali-susceptible aggregates with basalt as example. The structure- forming processes in an interfacial transition zone of the concrete "alkali activated portland cement – cast basalt bar" have been studied. The results of study allowed to reveal a positive effect arising from corrosion of the alkali- susceptible basalt bar in case of modification of the alkali- activated portland cement by a metakaolin additive. These conclusions are supported by data on interaction of structure forming processes in the interfacial transition zone and physico-mechanical characteristics of the concrete made with the alkali- susceptible aggregate (cast bar from basalt rock). A mechanism of AAR in case of alkali- susceptible aggregates in alkali- activated portland cement concretes modified by active Al_2O_3 – containing additive (metakaolin) has been described and discussed in details.

1. Introduction

The fact that aggregates for concrete containing amorphous silica in the form of opal can enter into reaction with the alkalis (Na_2O, K_2O) contained in the cement was first discovered and studied by STANTON [1]. As a result of this reaction a concrete expands in volume, cracks appear in it and its load carrying ability declines.

The results of experimental studies held by many researchers [2–5] allowed to formulate basic fundamentals of the mechanism of alkali- aggregate reaction (AAR):

- a cement itself, concrete additives and external aggressive environment are a source of alkalis;

- allowable contents of alkalis in portland cement (calculated on Na_2O–equivalent (Na_2O + 0.658 K_2O) is restricted by a value ≤ 0.60%. In case of blended cements this value may reach 2%;
- the expansion process is accompanied by osmotic pressure, which is created by a viscous-flow (plastic) gel of the alkali metal silicate formed as a result of reaction. The gel acts as a semi-permeable membrane, through which ions of OH^-, K^+, Na^- can penetrate in a direction of a surface of the reaction- susceptible aggregate. First of all, the alkali metal silicate fills in the surrounding pore space, and only after a pressure of expansion occurs;
- an important role in the above described process is played by a free $Ca(OH)_2$, present in the cement stone, which, first of all, enhances semi-permeable properties of the membrane, secondly, enables the formation of additional quantities of alkali as a result of exchange reactions between $Ca(OH)_2$ and alkali metal salts, which can be introduced into the concrete within various additives (plasticizers, accelerators of hardening, anti-freeze additives, etc.)[5];
- minimization of the expansion effect is reached through an introduction into the cement composition of various active mineral additives of sedimentary and volcanic origin (limestone with small amounts of amorphous silica, zeolites, perlite, tuff, pumice, etc.), as well as of man-made origin (fuel ashes, metallurgical slags, amorphous silica, etc.).

An effect of these additives is based, first of all, on their high reactivity with regard to alkali metal hydroxides. This promotes a homogeneous distribution of the reaction products in a concrete, thus preventing a harmful attack of alkalis of coarse alkali-susceptible aggregate. Secondly, pozzolana additives bind free Ca^{2+}- ions. This results in the decrease of CaO/SiO_2–ratio and stable binding of Na^+ and K^+ within the C-S-H–phases.

The described views on the mechanism of AAR were accepted by scientists for many years as basic prerequisites for developing recommendations as to prevention of hazardous consequences of this reaction and did not allow to substantiate the application of new cements (alkali activated ash- and slag cements, geocements, geopolymers, etc.), within which the contents of alkalis are considerably higher than those of traditional cements.

Nevertheless, known in the art are attempts to explain corrosion processes in case of alkali-susceptible aggregates in the presence of alkalis not only from the point of view of quantitative contents of alkalis and free $Ca(OH)_2$. So, MALEK and ROY [6] studied a role of Al_2O_3, being dissolved from a feldsparthoid stone and established that with increase in Al_2O_3/SiO_2 the AAR transforms from a destructive into constructive one. Later, the results of works reported in [7–11] showed that a possibility of formation in the interfacial transition zone of the alkaline or mixed alkaline – alkaline earth aluminosilicate hydrates depends not only upon aggregate type, but composition of the aluminosilicate component of the alkali activated cement. A conclusion was drawn that by regulation of the Al_2O_3 -content within the aluminosilicate component of the cement by introduction of the active Al_2O_3-containing additives it became possible to prevent destructive consequences of the AAR in concretes even with high content of alkalis in the cements under study. This may be applicable in equal extent to the alkali activated portland cement.

Purpose of the study were comparative tests of volume stability and to reveal specific features of corrosion processes in case of alkali- susceptible aggregates taking place in the concretes made from traditional portland cement and alkali activated portland cement and to study a possibility to prevent destructive processes in concretes made from cements with the increased contents of alkalis due to introduction into the cement composition of Al_2O_3-containing additive – metakaolin.

2. Raw materials and testing technique

Used in the studies as aluminosilicate component of the alkali activated portland cement was a strength class 42,5 ordinary portland cement. A specific surface of the portland cement was under control with the help of a Blaine apparatus and varied within the range of 320…350 m^2/kg.

In testing compressive strength, a basalt rock (fraction ≤ 2.50 mm) was used as aggregate. A glassy bar from cast basalt was used to simulate an interfacial transition zone and to study it. A ratio between the cement and aggregate was taken as 1:3.

Used as alkaline activator in the cement was sodium soluble glass (SG) in a form of solution with silicate modulus Ms=2.87 and p=1300 kg/m^3.

A metakaolin was used as an active mineral additive. A quantity of the metakaolin additive in the cement was 15% by mass. A specific surface of the metakaolin was of around 1860 m^2/kg. Chemical composition of raw materials is given in Table 1.

Table 1: Chemical composition of raw materials.

Raw material	Oxide content, % by mass									
	SiO_2	Al_2O_3	Fe_2O_3	MnO	CaO	MgO	K_2O	Na_2O	SO_3	LOI
Basalt (natural rock)	50.20	14.00	6.34	0.24	8.35	6.60	0.71	2.27	0.08	0.55
cast basalt (from melt)	50.00	15.30	6.23	0.30	9.21	5.58	0.77	2.18	0.15	–
portland cement	21.80	5.30	4.90	–	65.90	11.10	0.22		0.99	0.20
metakaolin	55.10	35.40	4.27	–	3.01	0.92	–	–	0.28	0.07

The interfacial transition zone was studied with the help of a scanning electron microscopy. Thin sections were cut from the specimens “cement-aggregate” – 1:2 to study an interfacial transition zone. Above, elemental distribution in the interfacial transition zone and its microhardness were studied.

The study of hydration products in the interfacial transition zone between the alkali-susceptible aggregate and the cement stone was done with the use of X-ray analysis. One more model of the interfacial transition zone (the specimens containing a mix of ground basalt powder and the cement taken in a ratio 1:1 mixed with the soluble glass) was used in the study. Curing conditions – 360 days of continuous treatment at t= 38±3 ºC and RH= 100%.

Determination of strength was done on beam specimens 25×25×255 mm (cement: aggregate= 1:2 by mass). Two days after the specimens were taken from the molds and placed for further hardening at t = 38 ºC and RH ≈100% into thermostats.

Linear deformations were measured using a digital strain gauge to an accuracy of up to 0.01 mm. Basic measurement was taken 2 days after the molding immediately after the specimens were taken from the molds. Curing conditions – the same as used in the determination of strength.

3. Results and discussion

3.1 Volume stability and strength.

The results of changes in strength characteristics and deformations of the specimens are given in Table 2.

Table 2: Strength and deformations of the specimens made from portland cement.

Nos	Composition	Compressive/flexural strength, MPa, after, days					Deformations: shrinkage (–) /expansion (+), mm/m, after, days				
		28	90	180	270	360	28	90	180	270	360
1	portland cement + H_2O	72.30 7.30	74.30 10.30	74.00 10.00	75.30 8.90	73.00 8.10	–0.41	–0.18	–0.02	+0.06	+0.14
2	portland cement + H_2O + MK	67.00 6.40	64.20 7.10	66.80 7.00	67.70 6.80	67.00 6.90	–0.16	–0.10	–0.06	–0.02	+0.10
3	portland cement + SG	80.30 7.10	109.70 6.70	133.30 6.30	132.80 6.20	130.30 6.00	–0.20	+0.09	+0.21	+0.28	+0.30
4	portland cement + SG + MK	104.40 6.30	119.80 7.20	127.20 7.50	130.70 7.40	131.00 7.60	–0.19	–0.10	–0.08	–0.03	–0.01

Remarks:

1. SG − soluble glass with Ms = 2.87 and ρ = 1300 kg/m^3.
2. MK – metakaolin in a quantity of 15% of the total cement mass.

As is clearly seen from the results given in Table 2, values of the expansion deformation of the specimens tend to decrease with introduction into the cement composition of active Al_2O_3 within the metakaolin.

It is clearly seen that with increase in quantity of active Al_2O_3 even with the increased contents of Na_2O in the mixtures the specimens maintained their volume stability (Table 3).

The specimens without metakaolin additive (Compositions 2 and 4) after one year of storage have the highest values of expansion compared to those with metakaolin additive. Above, as a result of expansion the first specimens showed a tendency to continuous decline of strength characteristics (Compositions 1 and 3), whereas the specimens 2 and 4 showed a tendency to constantly increase of strength characteristics.

Table 3**:** Characterization of cement compositions.

Nos	Cement compositions	Na_2O – content %, by mass	Al_2O_3 / SiO_2
1	portland cement + H_2O	0.60	0.242
2	portland cement+MK +H_2O	0.51	0.366
3	portland cement + SG	1.70	0.210
4	portland cement+MK+ SG	1.61	0.325

3.2 Interfacial transition zone

The presence of active Al_2O_3 intensifies structure formation processes in the interfacial transition zone "cement stone – aggregate". This is confirmed by the results of studies of physico-mechanical characteristics of the interfacial transition zones and visual observation of changes in it state on the model system "cement–basalt bar".

Microphotos of the interfacial transition zones show flow of destructive processes in case of portland cement without metakaolin additive (Fig 1).

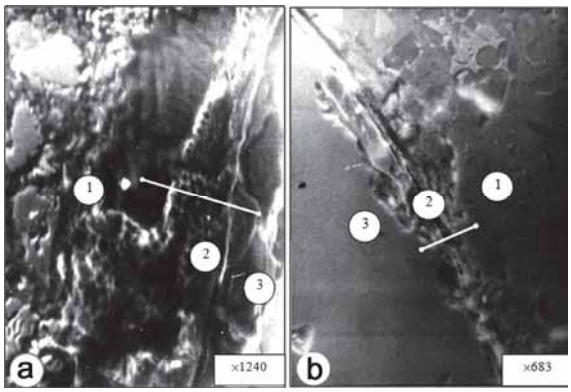

Figure 1: Microphotos of the interfacial transition zone of the model system "cement stone – basalt bar": 1 – cement stone; 2 – interfacial transition zone; 3 – basalt bar.
a – cement composition: "portland cement + water"; b – cement composition: "portland cement + soluble glass (M_s = 2.87; ρ = 1300 kg/m^3)"

It is clearly seen that the interfacial boundary has lost its geometry and clearness as compared to its primary state, the edges of basalt are "eaten" (eroded), and the interfacial transition zone is rather wide and filled with products of corrosion of whitish colour. Microcracks stretching in the direction perpendicular to basalt aggregate and which are evidently caused by the increasing pressure in the interfacial transition zone are clearly visualized in the body of cement stone. The metakaolin additive somewhat changes picture for better (Fig. 2). No microcracks are seen. The products of corrosion are present but in lower quantities and edges of the basalt aggregate are more clear and not so heavily eroded ("eaten") by corrosion, as in the first case.

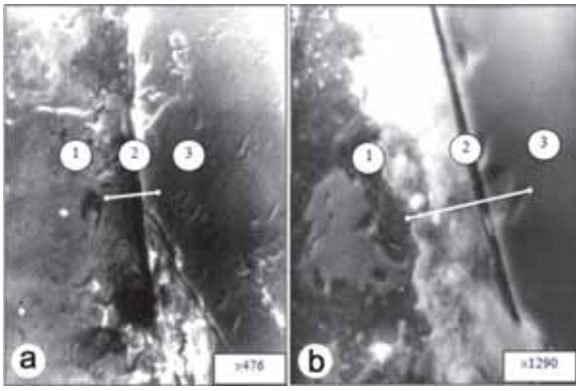

Figure 2: Microphotos and elemental distribution in the interfacial transition zone of the model system "cement stone – basalt bar": 1 – cement stone; 2 – interfacial transition zone; 3 – basalt bar.
a – cement composition: "portland cement + metakaolin + water"; b – cement composition: "portland cement + metakaolin + soluble glass (Ms=2.87; ρ = 1300 kg/m^3)"

4. Structure formation processes in the interfacial transition zone.

In compliance with the data of X-ray analysis, a phase composition of the hydrated dispersions in the interfacial transition zone of the concrete made with the cement composition 1 (Table 2) is represented briefly (Fig. 3, Curve 2), by the following reaction products: C_6S_3H (d = 0.335; 0.284; 0.246; 0.237; 0.225; 0.180 nm), C_2SH (d =0.284; 0.270; 0.246; 0.190; 0.180 nm), C_3S_2H (d = 0.560; 0.284; 0.184 nm), $Ca(OH)_2$ (d = 0.487; 0.311; 0.261; 0.193; 0.180 nm), $CaCO_3$ (d = 0.303; 0.229; 0.210; 0.193; 0.188 nm). Weak lines of the phase corresponding to the C_2AH_4 type (d = 0.717; 0.376; 0.266; 0.258; 0.246 nm) were identified. An X-ray amorphous phase of the calcium silicate gel, which can be formed in the interfacial transition zone and to weaken it, was not identified in the X-ray pattern. However, judging by the elemental distribution in the interfacial transition zone and with account of a relatively high value of expansion (+0.44 mm/m), this possibility may exist and is supported to a great extent by the increased contents of Ca and Si in the interfacial transition zone. As it is seen from the microphotos, the interfacial transition zone is not clear, thus supporting this assumption.

The use of the alkali activated portland cement (Table 2, Composition 3) results in changes in the diffraction picture of the model of the interfacial transition zone (Fig. 3, Curve 5). So, the hydration of the cements deepens, what is seen from the reduction of intensity of the initial diffraction lines. A re-distribution of the phase formation in the direction of synthesis of the more low-basic calcium silicate hydrates CSH(I) (d = 0.283; 0.270; 0.247; 0.179 nm), tobermorite (d = 0.560; 0.307; 0.299; 0.283; 0.227; 0.208; 0.183 nm) types takes place. The lines corresponding to $Ca(OH)_2$ are completely absent. This allowed to make a conclusion

about synthesis of sodium and mixed sodium- calcium aluminosilicate hydrates, what is confirmed by the analysis of the X-ray patterns (Fig. 3). The lines corresponding to $Na_2O{\cdot}Al_2O_3{\cdot}4SiO_2{\cdot}2H_2O$ (d = 0.560; 0.343; 0.293; 0.252; 0.174 nm), $2Na_2O{\cdot}2CaO{\cdot}5Al_2O_3{\cdot}10SiO_2{\cdot}10H_2O$ (d = 0.654; 0.467; 0.353; 0.283; 0.270 nm) are clearly identified in Curve 5. The expansion of the interfacial transition zone due to formation of the above mentioned hydration products is clearly seen in the microphotos, thus, with account of physico- mechanical characteristics, testifying about a constructive corrosion of the basalt bar in the interfacial transition zone "cement stone – basalt bar". Introduction of the metakaolin additive to pure portland cement (without alkaline activation) (Table 2, Composition 2) does not affect essentially a diffraction picture (Fig. 3, Curve 4). However, as it is clearly seen from, a content of Ca and, hence, of the hydroxide-ions tends to decline essentially in the interfacial transition zone, thus reducing considerably risk of flow of corrosion processes in the interfacial transition zone associated with destructive processes.

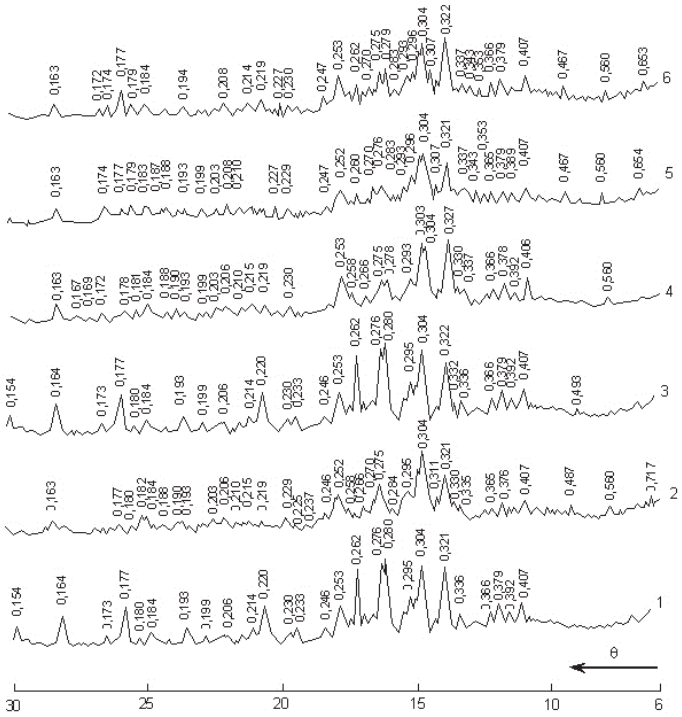

Figure 3: X-ray patterns of the interfacial transition zone of the model system "cement stone – basalt": 1 – initial system "portland cement + basalt"; 2 – "portland cement + basalt + water"; 3 – initial system "portland cement + metakaolin + basalt"; 4 – "portland cement + metakaolin + basalt + water"; 5 – "portland cement + basalt + soluble glass"; 6 – "portland cement + metakaolin + basalt + soluble glass"

This correlates well with a sharpness of the interfacial transition zone in the microphoto (Fig. 2a), as well as with the data given in [11], according to which the presence of active alumina in portland cement stone reduces considerably a concentration of alkalis in its pore space. The presence of alkalis does not exclude transformation of clay minerals of the interfacial transition zone into more stable minerals of the zeolite type [12, 13].

The introduction of the metakaolin into the alkali activated portland cement (Table 2, Composition 4) is found to suppress almost completely corrosion of the basalt bar. The line of contact in the microphotos is sharp and clear (Fig. 3). Zeolite-like hydration products of the $Na_2O{\cdot}Al_2O_3{\cdot}4SiO_2{\cdot}2H_2O$ (d = 0.569; 0.343; 0.293; 0.251; 0.174 nm), $Na_2O{\cdot}Al_2O_3{\cdot}3SiO_2{\cdot}2H_2O$ (d = 0.653; 0.587; 0.436; 0.286; 0.219 nm), $2Na_2O{\cdot}2CaO{\cdot}5Al_2O_3{\cdot}10SiO_2{\cdot}10H_2O$ (d = 0.654; 0.467; 0.353; 0.285; 0.269 nm) types are clearly identified in the X-ray patterns (Fig. 3, Curve 6), what is confirmed by the increase of contents of $Al^{3+}$and Na^+ and decrease in the Ca^{2+} content in the interfacial transition zone.

5. Mechanism of AAR prevention in the presence of metakaolin

A mechanism of AAR in concrete is described in details in [14, 15]. The AAR in concrete takes place in case of alkali susceptible aggregates and when concrete works in high humidity service conditions. However, deterioration of concrete as a result of corrosion induced by AAR takes place only in cases when quantities of alkali in concrete exceed limit values. Alkalis can be formed both in the process of cement hydration according to the following scheme: $Na_2SO_4+Ca(OH)_2+2H_2O \rightarrow CaSO_4{\cdot}2H_2O+2NaOH(Na^+,OH^-)$, and can be brought in from outside (for example, by alkaline activation of portland cement): $Na_2O{\cdot}nSiO_2{\cdot}mH_2O+Ca(OH)_2 \rightarrow CaO{\cdot}nSiO_2{\cdot}mH_2O+2NaOH$.

An alkali metal hydroxide enters into reaction with alkali susceptible silicon dioxide (SiO_2) with the formation of silicic acid gel, which, by adsorbing water and calcium, will create expanding pressure, resulting in deterioration of concrete ($2NaOH+nSiO_2+mH_2O \rightarrow Na_2O{\cdot}nSiO_2{\cdot}mH_2O$).

In the presence of $Ca(OH)_2$, an alkali metal silicate gel can form C-S-H– phase and this is accompanied by further release of greater and greater quantities of alkali metal hydroxide: $Na_2O{\cdot}nSiO_2{\cdot}mH_2O+Ca(OH)_2+ mH_2O \rightarrow CaO{\cdot}SiO_2{\cdot}mH_2O$(stands for C-S-H)$+2NaOH$.

Some portions of alkalis are bound by C-S-H– phases; with decrease of Ca/Si ratio an ability of C-S-H – phase to binding alkalis increases [16]. With addition of metakaolin to cement composition an interaction mechanism will change. This can be attributed, first of all, to its (metakaolin) ability to bind the formed gel of $Na_2O{\cdot}nSiO_2{\cdot}mH_2O$ and free alkali metal hydroxide (NaOH) with the formation, as was shown by the studies, of alkaline aluminosilicate hydrates: $Al_2O_3{\cdot}2SiO_2+2NaOH+mH_2O \rightarrow Na_2O{\cdot}Al_2O_3{\cdot}2SiO_2{\cdot}mH_2O$; $Al_2O_3{\cdot}2SiO_2+ Na_2O{\cdot}nSiO_2{\cdot}mH_2O \rightarrow Na_2O\ Al_2O_3{\cdot}(n+2)SiO_2{\cdot}mH_2O$.

Moreover, C-A-S-H– phases can be formed in a cement stone in the presence of $Al_2O_3{\cdot}2SiO_2$. These phases are able to bind greater quantities of alkalis compared to C-S-H– phases [17]

according to the following reaction: $CaO \cdot nSiO_2 \cdot mH_2O + Al_2O_3 \cdot 2SiO_2 + 2NaOH + kSiO_2 \rightarrow CaO\ Na_2O \cdot Al_2O_3 \cdot (n+2+k)SiO_2\ (m+1)H_2O$ (C-N-A-S-H) – phase with the formation of stable in volume zeolite-like compounds. That is why a Al_2O_3/SiO_2 ratio can serve as additional criterion for prediction of AAR. Above all, metakaolin additive is, similar to silica fume, a pozzolanic additive, allowing to bind large quantities of portlandite by low basic C-S-H–phases.

Thus, as a result of binding the corrosion products into stable phases that do not swell the metakaolin additive can provide volume stability of the alkali activated portland cements and concretes with alkali susceptible aggregates. A schematic representation of mechanism of AAR and measures on its prevention is represented in Fig.4.

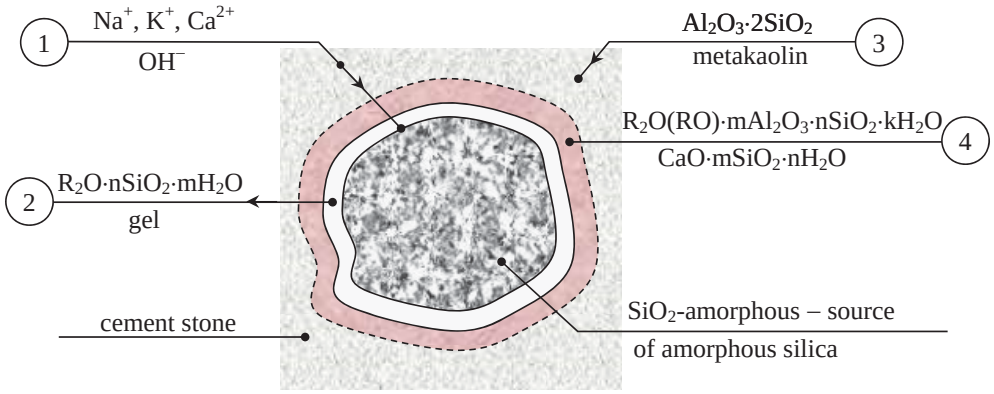

Figure 4: Reaction “alkali −susceptible silica – metakaolin”.

6. Conclusions

The results of the study suggested to show efficiency of introduction of active alumina in the form of metakaolin into cements with the increased contents of alkali, thus allowing to regulate structure formation processes in the interfacial transition zone “cement stone − alkali susceptible aggregate” in the direction of formation of the alkaline or mixed alkaline-alkaline earth aluminosilicate hydration products. Formation of the latter results in the reduction of expansion deformations until allowable values or even completely avoiding them.

Acknowledgments
The author would like to acknowledge the contribution of the COST Action TU1404. http://www.tu1404.eu/

References

[1] Stanton, T.E., Expansion of concrete through reaction between cement and aggregate. In: Proc.Amer.Soc.Eng. – 66 (1940). 1781−1811
[2] Bredsdorf, P., Idorn, G.; Kjaer, A.; Plum, N. and Poulsen, E., Chemical reaction involving aggregate. In: Proc. IV Inter.Sym.Chem.Cem. –II (1960), 749−783
[3] Forschungsinstitut der Zementindustrie, Zusammensetzung und Eigenschaften von Betonzuschlagstoffen. VDZ. Taetigkeitsbericht (1969/1971), 88−100
[4] Moskvin, V.M.; Royak, G.S., Corrosion of Concrete under Action of Alkalis of Cement on Silica of Aggregate. Moscow (1962)
[5] Stark, J.; Wicht, B: Dauerhaftigkeit von Beton. Bau Praxic Birkhaeuser Verlag, (2001). – S.288–330
[6] Malek, R.I.A., Roy, D.M., Effect of Slag Cements and Aggregate Type on Alkali−Aggregate Reaction and its Mechanism. In: Proc.6 Inter. Confer. Alkalis in Concrete, Research and Practice, Denmark (1983), 223−230
[7] Krivenko P.V., et al, Structure-forming Processes in the Interfacial Transition Zone "Slag Alkaline Cement – Aggregate". In: Journal Tsement (Cement), Leningrad, 11−12 (1991), 64−70
[8] Krivenko P.V., Ilyin V.P., Zgardan E.P., Durability of Slag Alkaline Concrete with Aggregates Susceptible to Alkali−silica Reaction. In: Proc. Beijing Int. Symp. Cement and Concrete. Oct. 27−30 (1998)
[9] Krivenko, P.V. et al, Durability of Alkaline Portland Cement Concretes made with Alkali-Reactive Aggregates. In: Proceed. ACI International Conference on Durability of Concrete. Sydney, Australia-22 (1997)
[10] Krivenko, P.V. et al, A Role of Metakaolin Additive on Structure Formation in the Interfacial Transition Zone "Cement−Alkali-susceptible Aggregate". In: Proc. Inter. Symp. "Non−traditional Cements", Brno, June, 14−16 (2005), 83−95
[11] Krivenko, Pavel, et al., Mechanism of preventing the alkali–aggregate reaction in alkali activated cement concretes. In: Journal: Cement and Concrete Composites, 45 (2014), 157-165.
[12] Olginskyy, A.G.; Cherniavskyy, V.L., The Influence of Environment on Adoption of the Contact Zone of Aggregates and a Cement Stone in Concrete. In: Journal Beton i zhelezobeton (Concrete and Reinforced Concrete), (2001), 4, 5−8
[13] Ramlochan, T.; Thomas M.; Gruber K.: The Influence of Metakaolin on ASR in Concrete. In: Journal: Cement and Concrete Research, 30 (2000)3, 339−344
[14] Stark, J. Alkali-Kieselsäure-Reaktion Stark Jochen Schriftenreihe des FA. Finger-Institutes für Baustoffkunde, Bauhaus-Universität Weimar, Weimar, 2008
[15] Syr, M., Pouhet, R. Resistance to alkali-aggregate reaction (AAR) of alkali-activated cement-based binders. Handbook of Alkali-activated Cements, Mortars and Concretes, Edit. Pacheco-Torgal, F. et al, ELSEIVER (2015) 373-396
[16] Hong, S-Y, Glasser F.P. Alkali sorption by C-S-H and C-A-S-H gels, Part II: Role of Alumina Cement and Concrete Research, 29 (1999) No 12, 1893-1903.
[17] Hong, S-Y, Glasser F.P. Alkali sorption by C-S-H and C-A-S-H gels, Part II: Role of Alumina Cement and Concrete Research, 32 (2002) No 7, 1101-1111

International RILEM Conference on Materials, Systems and Structures in Civil Engineering
Conference segment on Service Life of Cement-Based Materials and Structures
22-24 August 2016, Technical University of Denmark, Lyngby, Denmark

IMPACT OF SLAG CONTENT IN ALKALI-ACTIVATED SLAG CEMENT ON POROSITY OF CONCRETE

Pavel Krivenko[(1)], Oles' Lastivka[(1)], Igor Rudenko[(1)], Sergei Lakusta[(1)]

(1) Kyiv National University of Construction and Architecture, Scientific Research Institute for Binders and Materials, Ukraine

Abstract
The paper covers results of studies on porosity, freeze/thaw resistance of alkali-activated slag cement (AAC) concrete depending upon composition of AAC and chemical admixtures. Freeze-thaw resistance was assessed by a number of cycles of alternate freezing/thawing in aqueous solution of NaCl at t= - (50 ± 5) °C until 5% loss of compressive strength. This strength loss can be attributed to accumulation of deteriorations caused by cyclic volume deformations occurred in concrete structure in the process of ice formation. With increase of slag content in AAC from 50 to 100% and corresponding increase of alkaline component content a volume of open capillary pores tended to decrease with formation of more quantities of micro- and conditionally closed pores. Effect of polyethers as admixtures was greater, whereas, effect of polyesters was "suppressed". Change of alkaline component from sodium carbonate to sodium silicate in AAC resulted in increase of concrete porosity. With reduction of volume of open capillary pores the volumes of ice formed in the AAC concrete tended to decrease, similar to stresses which could cause changes in the AAC concrete structure, thus "spoiling" its freeze/thaw resistance.

1. Introduction

A need in alternative types of cements is explained by the fact that portland cement is characterized by high consumption of natural resources and energy, accompanied by carbon dioxide emissions [1].

The use of ground granulated blast furnace slag allows for not only reducing energy consumption in cement production. Blast furnace cement has several advantages over portland cement: high resistance in soft and sulfate waters, high heat resistance, low heat of hydration (low heat cement) and shrinkage [2, 3]. However, concretes made from the cements with high slag contents (blast furnace cement) are characterized by low early strength and are

sensitive to attacks of freeze/thaw resistance, especially under exposure of de-icing salt solutions.

One of the ways to avoid these disadvantages is to add to traditional blast furnace cement the alkali metal compounds in order to produce alkali-activated slag cement (further, AAC) the hydration products of which provide high strength and density of the resulted cement stone and to minimize contents of portland cement clinker in the cements [4, 5, 6].

A key factor of physical nature which determines performance properties and durability of concrete is its porosity. However, if strength of concrete depends on a total porosity, freeze/thaw resistance and durability are determined chiefly by a capillary porosity. The reason for these phenomenons is the effect of capillary pores, which is caused by dependence of a freezing point from pore size [7].

In general, the incorporation of alkali metal compounds into the blast furnace cement shifts of ratio between macro- and micro-porosities towards the formation of micro- and conditionally closed pores, resulting in higher freeze/thaw resistance of concrete [8]. In this case, in order to make concrete technology simpler, and to obtain better performance properties, the use of plasticizers is a necessity. However, plasticizers that are traditionally used in making portland cement concretes are not suitable for the alkali-activated cement concretes because in the alkali-activated cement matrix they behave in a different way and an alkaline medium causes degradation of traditional plasticizers [9, 10, 11].

The results of study held on various plasticizers in the AAC concretes are reported in [12]. These results can be explored for a choice of chemical nature of main active substance of plasticizers to be suitable for the AAC concretes depending upon slag contents and, accordingly, contents of alkaline component.

The purpose of this study was to reveal an impact of slag contents in the AAC on water absorption, open capillary porosity and conditionally closed porosity of the plasticized AAC concrete as a function of its freeze/thaw resistance.

2. Raw materials and testing techniques

The alkali activated cements varying in slag contents between 50 and 100% as per national standard of Ukraine were used [13].

Ground granulated blast furnace slag (further, slag) and portland cement clinker (further, clinker) were used as aluminosilicate components of the AACs, their chemical compositions are shown in Table 1. The comparative low content of glass phase in slag (56%) was in accordance with [13] and can be explained by high basicity modulus of slag (M_b = 1.1)

Table 1: Chemical composition of AACs components.

Component	Oxides, % by mass								LOI
	SiO_2	Al_2O_3	Fe_2O_3	MnO	MgO	CaO	Na_2O	SO_3	
clinker	21.30	5.70	4.62	-	1.20	65.90	0.30	0.86	0.12
slag	39.00	5.90	0.30	0.50	5.82	46.94	-	1.54	-

Soda ash (Na_2CO_3) and sodium metasilicate pentahydrate ($Na_2SiO_3 \cdot 5H_2O$) were used as alkaline components. In the production of the AACs under "all- in- one" technology (alkaline components in the form of solids) it is required to use sodium lignosulfonates (further, LST) in order to provide the required setting times and strength. In order to intensify a grinding process and to prevent sorption of moisture from air and preserve properties of the AAC an admixture of ethyl hydro-siloxane polymer was also used.

The AAC compositions are shown in Table 2. Fineness of the AACs (measured as specific surface by Blaine) was 4500 cm^2/g. The contents of alkali metal compounds (alkaline activators) were taken over 100% of the aluminosilicate components in accordance with [13]. In order to change a consistency of the AAC concrete mixtures from class S1 (that of the reference composition) to class S4 at ambient temperature of 20±2 ºC, complex admixtures (further, CA) based on LST in combination with corresponding plasticizing admixtures (taken in quantities of 1.5% by the AAC) were used.

The plasticizing admixtures varied in nature of main active substances: 1 – surfactant based on polyacrylate esters, Type PA (traditional superplasticizer "Dynamon SR 2", Mapei); 2 - surfactant based on polyethers (polyethylene glycol "PEG-400", JSC "Barva"); 3 - surfactant based on sodium gluconate ("Mapetard SD 2000", Mapei), which is traditionally used as a retarder.

Table 2: Compositions of the AAC.

# of composition	Basic composition
1	50% slag, 50% clinker, 2% Na_2CO_3, 1% LST
2	50% slag, 50% clinker, 3% $Na_2SiO_3 \cdot 5H_2O$, 1% LST
3	69% slag, 31% clinker, 2,5% Na_2CO_3, 1% LST
4	69% slag, 31% clinker, 3,5% $Na_2SiO_3 \cdot 5H_2O$, 1% LST
5	88% slag, 12% clinker, 3% Na_2CO_3, 1% LST
6	100% slag, 4.7% Na_2CO_3, 0.8% LST

In these studies in order to determine the influence of variables (cement composition and nature of main active substance of admixtures) on capillary porosity and freeze/thaw resistance of the AAC concrete, one cement composition was chosen. The standard composition of the AAC concrete was taken in accordance with [14], kg/m^3: cement - 350; silica sand - 740; granite gravel: 330 (5/10) and 780 (10/20).

Water absorption and porosity of the AAC concretes were studied in accordance with methodology of the national standard of Ukraine [15]. According to this method, the concrete cubes (100 mm) after 28 days were dried up to a constant weight at t= 105±10 °C. Then, the

specimens were saturated with water until a constant weight would be obtained at t= 20±2 °C. The values of porosity were calculated from the values of average density and water absorption of the concrete specimens.

Freeze/thaw resistance was studied in accordance with third test method prescribed by the national standard of Ukraine [16]. According to this accelerated method, the concrete cubes (100 mm) were saturated with a 5% solution of NaCl at t= 18±2 °C and after that were subjected to freezing at t= -50 °C. Thawing was done in a 5% solution of NaCl. A class of concrete in freeze/thaw resistance was designated as a number of alternate freezing and thawing at which a mean compressive strength decreased by no more than 5%. The freeze/thaw resistance of concrete was assessed by the correspondence between permissible number of freezing-thawing cycles on the used accelerated method and on first (basic) method prescribed in mentioned standard.

3. Research results

As a result of the study a conclusion was drawn that changes in slag contents, type and content of alkaline component affected porosity and consequently freeze/thaw resistance of the AAC concrete depending on the nature of main active substance of plasticizer.

The use of polyester - based CA in the AAC concretes containing 50% of slag and 2% of soda ash (composition #1) lead to slight increase in water absorption and open capillary porosity of the AAC concretes (Fig. 1; Fig. 2) to 3.7% and 8.8%, respectively, compared to those of the reference composition: water absorption of 3.4% and volume of open capillary pores of 8.1%.

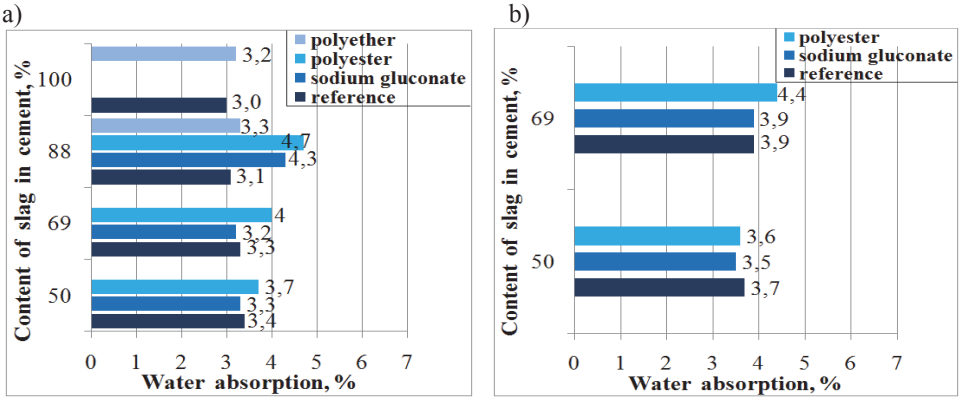

Figure 1: Water absorption of the AAC concretes vs. type of surfactants as ingredient of CA and slag contents in the AACs, % (see Table 2): a) #1, #3, #5, #6; b) #2, #4.

With increase in slag contents in the AACs up to 88% the effectiveness of modification of the AAC concretes by this CA tended to significantly decrease and was accompanied by decline

in properties, i.e. higher water absorption (up to 4.7%) and volume of open capillary pores (up to 11%).

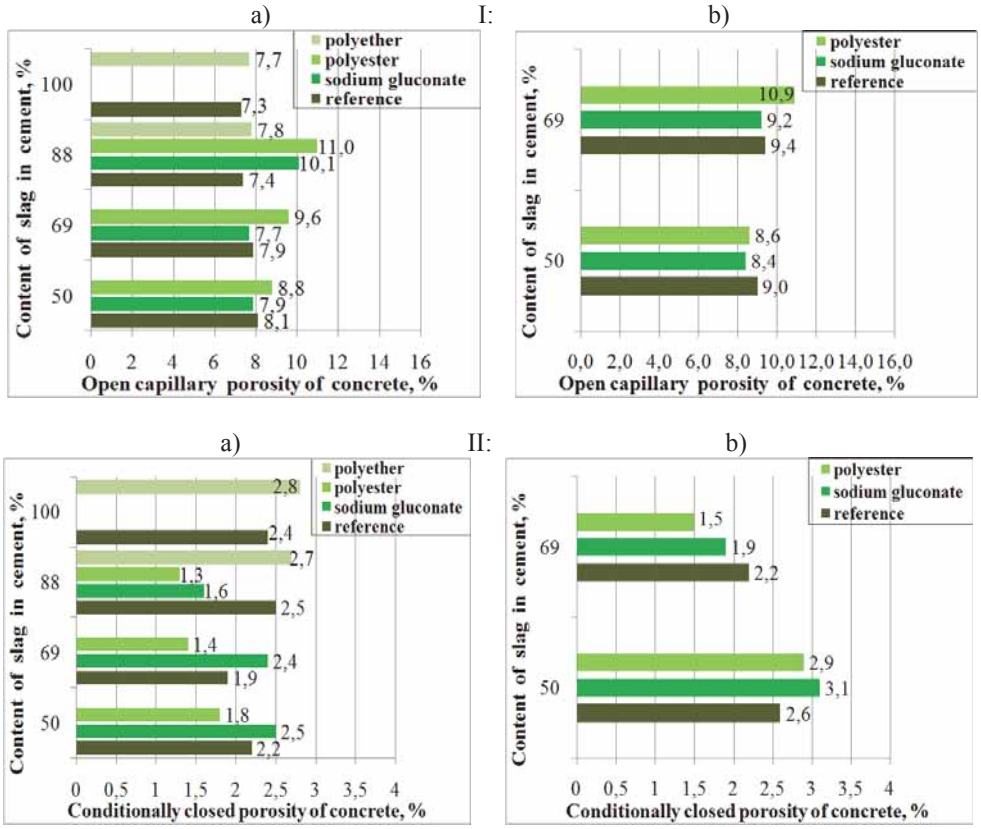

Figure 2: Volume of open capillary pores (I) and conditionally closed pores (II) of the AAC concrete vs. type of surfactant as ingredient of CA and slag contents in the AACs, % (see Table 2): a) #1, #3,#5, #6; b) #2, #4.

Substitution of anionic part of alkaline component from carbonate to silicate resulted in the higher values of water absorption and porosity of both reference and modified AAC concretes. For example, when used AAC with slag content of 50% (composition #1) water absorption and volume of open capillary pores was 3.4% and 8.1% respectively. When soda ash was changed with sodium silicate pentahydrate (composition #2) the water absorption and the volume of open capillary pores of concrete increased to 3.7% and 9.0% respectively.

At the same time, there was observed a general tendency to reduction of volume of the open capillary pores of the reference AAC concretes with increase in slag contents and, accordingly, with increase in the required alkaline component contents of the AACs (Fig. 2). This fact can be attributed to changes taking place in pore structure towards the formation of

micro- and conditionally closed pores which determine the formation of more dense and impermeable concrete structure with simultaneous increase of its performance properties.

Modification of the AAC concretes by addition of polyester-based admixtures in case of the AAC compositions #1 and #3 (50% of the slag) provided class F200 in freeze/thaw resistance (Fig. 4), i.e. highest class for the most demanding concrete structures in unheated buildings undergoing alternate freezing-thawing and operating at ambient temperature t = -20...-40 ° C (exposure class XF4). However, with increase in slag contents up to 69% the efficiency of modification by this admixture tended to decrease: the volume of capillary pores increased (up to 9.6%) and freeze/thaw resistance declined (class F150).

Therefore efficiency of the admixture Type 1 as ingredient of CA in the AAC concretes depends on the AAC composition. At slag contents up to 50% and with corresponding concentration of alkaline component the CA provided changes in consistency of the AAC concrete mixtures from S1 to S4 class with maintaining physical properties of the AAC concretes nearly at the level of the reference composition and without decline of freeze/thaw resistance. However, the increase in slag contents up to 88% in the AACs resulted in decrease in efficiency of the mentioned CA: deterioration of pore structure and decline of freeze/thaw resistance.

The use of polyethylene glycol as ingredient of CA in case of the AACs containing 88% of slag did not significantly affect pore structure of the resulted concrete (Fig. 1, Fig. 2). Water absorption increased from 3.1% to 3.3% and porosity from 7.4% to 7.8%, respectively, as compared to those of the reference composition. This helped to obtain a dense structure of the plasticized AAC. The admixture of this type as ingredient of CA with the AAC composition #5 (88% of slag) provided class F 200 freeze/thaw resistance for the AAC concrete (Table 3). With increase in slag contents in the AAC up to 100%, structure indexes of the AAC concretes did not significantly change: water absorption increased from 3.0% (of the reference composition) to 3.2%; the quantity of open capillary and conditionally closed pores increased from 7.3% to 7.7% and from 2.4% to 2.8%, respectively. This allowed obtaining the modified AAC concretes containing 100% of slag (composition #6) with class F200 in freeze/thaw resistance (Table 3) due to additionally generated artificial air pore volume.

Substitution of soda ash by sodium metasilicate pentahydrate as alkaline component of the AACs leads to the higher values of water absorption and open capillary porosity of the modified AAC concretes. With slag contents of 50% in the AACs water absorption tended to increase from 3.3% (composition #1) to 3.5% (composition #2); the volume of open capillary pores tended to increase from 7.9% to 8.4%, respectively. A similar trend was observed with the increase in slag contents in the AAC up to 69%: water absorption of the modified AAC concrete was 3.2%, with sodium metasilicate pentahydrate in the AAC cement (composition #4) – 3.9%, volume of open capillary pores of the modified AAC concrete was 7.7%, with sodium metasilicate pentahydrate in the AAC (composition #4) – 9.2%.

Thus, in contrast to the polyester-based CA the effect from the polyether-based CA on plasticizing and formation of the concrete pore space increased proportionally to the growth in slag contents and, correspondingly, in alkaline component content in AAC.

Application of sodium gluconate as ingredient of CA positively affected formation of pore structure of the modified AAC concretes (Fig. 1, Fig. 2). Addition of admixture of this type to the AAC concretes in case of the AACs with 50...69% of slag allowed obtaining values of water absorption close to those of the reference composition. However, modification of the AAC concretes by this admixture with simultaneous increase in slag contents up to 88% gave a significant increase in water absorption of the AAC concretes (4.3%) compared to the reference composition (3.1%).

A similar trend was observed for changes in porosity of the AAC concretes plasticized by sodium gluconate as ingredient of CA. With 50% of slag in the AAC the volume of open capillary pores in the AAC concrete was 8.1% (reference) and 7.9% with the admixture. With increase in slag contents up to 69% the volume of these pores tended to decrease. However, the addition of this type of admixture to the AAC concretes with 88% of slag in the AAC deteriorated pore structure and volume of the open capillary pores increased up to 10.1%.

The sodium gluconate-based CA added to the plasticized AAC concretes provides them a compliance with a class F200 in freeze/thaw resistance in case of the AAC with 50…69% of the slag (Table 3). However, even with 88% of slag in the AAC the freeze/thaw resistance of the plasticized AAC concrete tended to decrease to class F150 and loss of strength after 5 cycles of alternate freezing/thawing cycles exceeded 5%.

Table 3: Freeze/thaw resistance of the AAC concretes.

Cement composition (see Table 2)	Type of admixture	Loss of strength after number of freezing/thawing cycles by third (accelerated) method, %			Number of cycles by first (basic) method	Class in freeze/thaw resistance
		3	4	5		
#1	polyester	1.4	4.4	4.9*	200	F200
	sodium gluconate	0.6	2.4	4.2*	200	F200
#2	polyester	0.9	3.1	5.0*	200	F200
	sodium gluconate	1.0	2.6	4.4*	200	F200
#3	polyester	1.6	4.9*	8.1	150	F150
	sodium gluconate	1.1	3.2	4.7*	200	F200
#4	polyester	1.9	5.0*	9.9	150	F150
	sodium gluconate	0.8	2.9	5.0*	150	F150
#5	polyether	1.0	2.8	4.9*	200	F200
	sodium gluconate	1.5	4.9*	7.9	150	F150
#6	polyether	0.9	2.3	4.7*	200	F200

* - permissible value

The relationship between porosity (P) and freeze/thaw resistance (F) of the plasticized AAC concretes is shown in Fig. 3 and Fig. 4. The curves F = *f* (slag content) and P = *f* (slag content) reflect the greater volume of open capillary pores and, respectively, decline of freeze/thaw resistance of the modified AAC concretes.

Freeze/thaw resistance of the modified AAC concrete (Table 3) was found to be dependent on type of porosity. Increase in volume of the open capillary pores and respective reduction in conditionally in volume of closed pores resulted in the lower freeze/thaw resistance (Fig. 3, Fig. 4).

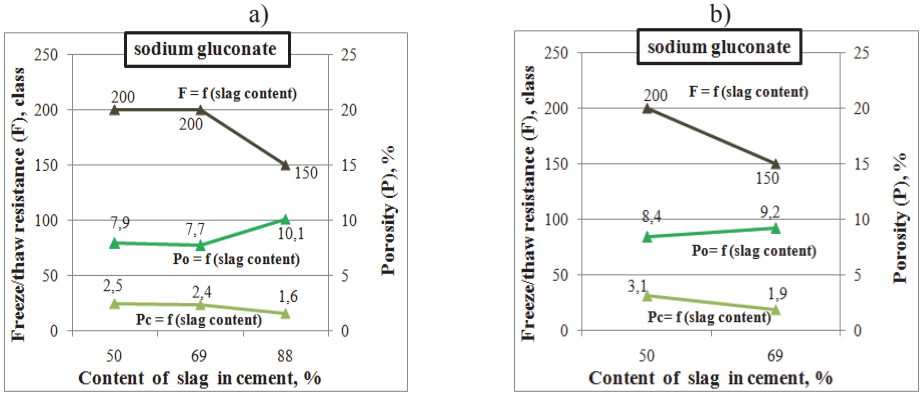

Figure 3: Open capillary porosity (P_o), conditionally closed porosity (P_c) and freeze/thaw resistance (F) of the AAC concretes plasticized by sodium gluconate vs. slag contents in the AAC (see Table 2): a) #1, #3, #5; b) #2, #4.

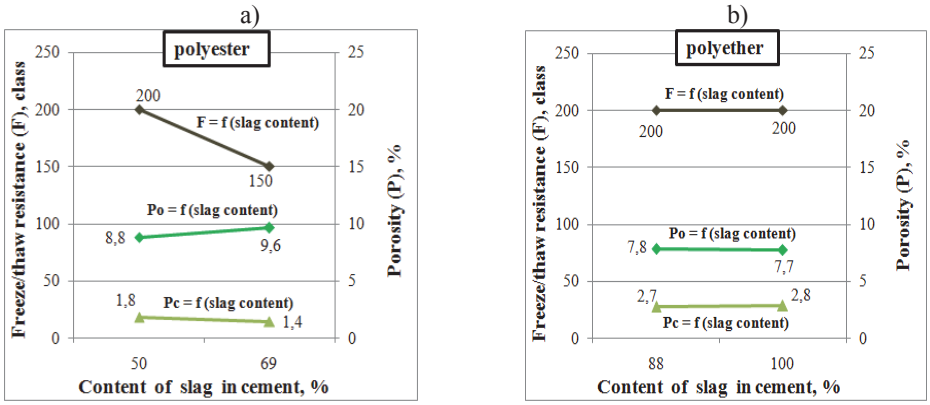

Figure 4: Open capillary porosity (P_o), conditionally closed porosity (P_c) and freeze/thaw resistance (F) of the AAC concretes vs. main active substance of plasticizing admixture as ingredient of CA and slag contents in the AAC (see Table 2): a) #1, #3; b) #5, #6.

Thus, it can be concluded about multifactor influence of AACs composition on the porosity and, consequently, on the freeze/thaw resistance of AAC concretes.

Increase in slag content from 50% to 100% and corresponding maintenance in content of alkaline component in AACs cause reduction of water absorption of AAC concrete. At the same time the volume of open capillary pores decreases and thus the volume of conditionally

closed pores in AAC concrete rises. This is due to fact that the hydrated AACs contain higher volume of gel pores compared than portland cement [17]. Accordingly, with increase in the content of alkaline component in AACs formation of gel with conditionally closed pores occurs with greater speed. This phenomenon determines formation of a more dense and impermeable structure of AAC concretes accompanied with higher freeze/thaw resistance.

In addition, it is possible to control the porosity and accordingly freeze/thaw resistance of AAC concretes by addition of placticizing admixtures with various nature of main active ingredient, which must be selected depending on composition of AACs. In case of the AACs with 50...69% of slag the maximum efficiency has sodium gluconate, i.e. salt of carbonic acid and alkali, and at 88...100% of slag in AACs the polyether as polyethylene glycol is effective. At the same time, polyacrylate esters, which are traditionally used in concretes based on portland cement, can be ineffective in AAC concretes due to destruction of their molecular structure in hydration medium of AACs.

4. Conclusions

Regularities of formation of pore structure of the AAC concretes were found to depend on slag contents and type of alkaline component of AACs. The possibility of obtaining AAC concretes with high freeze/thaw resistance from the concrete mixes with high slumps was shown. In general, the increase in slag contents in the AACs associated with higher contents of the alkaline component resulted in the lower volumes of open pores and higher volumes of conditionally closed pores. This phenomenon can be attributed to volumetric loss of ice resulted in the higher freeze/thaw resistance of the AAC concretes. Change of anionic part of the alkaline component from carbonate to silicate improved water absorption and porosity of the reference and plasticized AAC concretes.

The polyester-based admixtures were found to be effective in the AACs only to some extent. With increase in contents of slag and alkaline component the application of admixtures based on polyethers and alkaline salts of carboxylic acids in the presence of sodium lignosulfonate was found to result in the formation of artificial pore structure of the plasticized AAC concretes. This phenomenon was found to create additional air space allowing water to expand during freezing and therefore the weakening of concrete structures under cyclic freezing and thawing was lower.

Acknowledgments

The authors would like to acknowledge the contribution of the COST Action TU1404. http://www.tu1404.eu/

References

[1] Dhir, R.K., Cement: a question of responsible use, Proceed. Int. Conference held at the University of Dundee, 5–7 July, Scotland, UK (2005), 1-12
[2] Usherov-Marshak, O., Herhychni, Z., Malomepshy, Ya., Blastfurnace cement and concrete, Kolorit, Ukraine (2004)
[3] Runova, R.F. et al, Construction materials of new generation and technologies of their implementation in construction, UVK "EksOb", Ukraine (2008)
[4] Gelevera, A.G., Munzer, K., Alkaline portland and slag portland cements, Proceed. 1-st Int. conf. on alkaline cements and concretes, Vipol Stock company, Ukraine (1994), 173-180
[5] Krivenko, P.V. et al, Features of Alkali-Activated Slag Portland Cement, Proceed. 1-st Int. Conf. on the Chemistry of Construction Materials, October 7-9, Berlin, Germany (2013), 453-456
[6] Glukhovsky, V.D. et al, Fine Alkali-Activated Slag Cement Concretes, Vysscha Shkola Publishing, Ukraine (1981)
[7] Stark, J. Wicht, B., Dauerhaftigkeit von Beton, Weimar: Hochschule für Architektur u. Bauwesen, Weimar, Schriften 100 (1995)
[8] Krivenko, P., Petropavlovskii, O., Mokhort, N., Pushkar, V., Influence of alkali activation on the structure formation and properties of blastfurnace cements, Proceed. 3-rd Int. Symposium “Non-traditional cement&concrete”, Brno (2008), 410-424
[9] Palacios, M., Puertas, F., Effect of superplasticizer and shrinkage-reducing admixtures on alkali-activated slag pastes and mortars, Cement and Concrete Research 35 (2005), 1358 – 1367
[10] Puertas, F. et al, Effect of superplasticisers on the behaviour and properties of alkaline cements, Adv. Cem. Res. 15 (1) (2003), 23 – 28
[11] Krivenko, P.V. et al, Constructive properties of the concretes made with alkali-activated cements of new generation, First Int. Conf. on Advances of Chemically-activated Materials, May 9-12, Jinan, Shandong, China (2010), 139 – 146
[12] Krivenko, P.V. et al, Plasticizing alkaline cements: state-of-the-art and solutions, Proceed. the 14-th Int. Congress on the Chemistry of Cement, 13-16 October, Beijing, China (2015).
[13] National standard of Ukraine DSTU B V.2.7-181:2009 Alkaline cements. Specification
[14] National standard of Ukraine DSTU B V.2.7-171:2008 (EN 934-2:2001. NEQ). Admixtures for concretes and mortars. General specification (that meets EN 934-2:2001 “Admixtures for concrete. mortar and grout – Part 2: Concrete admixtures – Definitions. requirements. Conformity, marking and labelling”)
[15] National standard of Ukraine DSTU B. V.2.7-170:2008 Building materials. Concretes. Methods for determining of average density, humidity, water absorption, porosity and water resistance
[16] National standard of Ukraine DSTU B V.2.7-47-96 Building materials. Concretes. Method for determination of freeze/thaw resistance
[17] Krivenko, P.V., Alkali-activated alumosilicates: past, present and future, Proceed. the 4-th Meeting on Chemistry and Life, Brno University of Technology, Brno (2008), 1-5

International RILEM Conference on Materials, Systems and Structures in Civil Engineering
Conference segment on Service Life of Cement-Based Materials and Structures
22-24 August 2016, Technical University of Denmark, Lyngby, Denmark

NANOSCALE SIMULATIONS OF CEMENT FORMATION AND STRUCTURAL EVOLUTION: A NEW KINETIC APPROACH

Enrico Masoero [(1)], Igor Shvab [(1)]

(1) Newcastle University, Newcastle upon Tyne, United Kingdom

Abstract
The formation and degradation of cementitious materials are largely controlled by the nanostructural evolution of hydration products. Modelling such evolution across multiple length and time scales is a great challenge. Here we present a new kinetic approach to simulate the nucleation, dissolution, and aggregation of cement hydrates nanoparticles. The approach is based on a Kinetic Monte Carlo algorithm in which the rates of the transitions are obtained via a new coarse-graining procedure. The rates account for free energy changes due to both mechanical interactions and chemical reactions. The methodology is able to address the long timescale of cement formation and captures various possible mechanisms of nucleation and growth of the hydrates. By coupling chemistry, mechanics, and long timescales, this work is a first step towards simulating cement hydration and degradation.

1. Introduction

The hardened cement paste is the glue of concrete. It forms upon chemical reaction between dry cement powder and water [1]. This hydration process leads to the precipitation from ionic solution of several hydrated phases (HP). The HP progressively fills the space and induces the liquid-to-solid transition known as setting. In ordinary cement pastes, the main HP is calcium-silicate-hydrate (C—S—H) and at least 50% of the total hydration reaction takes place during the first 24 hours after mixing dry cement with water. Setting typically occurs during this stage, which is known as “early hydration” [2].

There is a considerable scientific and technological interest in controlling the early hydration and setting of the cement paste. In the last decades, this led to a number of models and simulation approaches whose target is to predict the early hydration based on the chemistry and mix design proportions of the paste. These models consider length scales above the μm and use a combination of thermodynamics and chemical kinetics in order to reproduce the

microstructural evolution of the paste [3-8]. Their results can fit well the rate of early hydration from isothermal calorimetry experiments. These models however have the limitation of considering the HP as homogenous domains, without information on the underlying texture at sub/micrometre length scales (except for user-defined parameters that sometimes are employed to mimic the anisotrpic formation of needles and foils [9]). Missing the sub-micrometre texture is a particularly limiting for the C—S—H hydration product, whose network of mesopores with size 1-50 nm dictates largely the macroscopic response to humidity cycles and creep [10-14].

Simulating the formation of HP at the sub-micrometre level is a challenging task. In the last decade, several authors have shown that aggregating nano-units of 1-10 nm lead to model structures of the cement HP that display many of the experimentally measured structural features and mechanical properties [15-23]. Some of these models have also attempted to describe the process of HP formation by precipitation from solution. However, the timescale of cement hydration is of the order of 24 hours while nanoparticle simulations are limited to dynamic processes in the timescale of nano-to-micro seconds or, on the other extreme, to equilibrium studies in the infinite-time limit. To overcome this limitation, the simulations to date have either introduced constraints on the mechanisms of particle aggregation, or applied ad-hoc nonlinear mapping between simulation steps and time [17, 19-21]. None of the simulations to date can predict the mechanisms of HP nanoparticle formation and aggregation directly from the chemistry of the aqueous solution.

In this work, we propose a new approach to simulate the formation of cement HP at the mesoscale of 1-to-500 nm. Our approach is based on Kinetic Monte Carlo (KMC) simulations of nanoparticle insertion and deletion. The rates of insertion and deletion are calculated using a new coarse graining scheme that considers both Classical Nucleation Theory (CNT) and crystal growth theory. First results show that the rates can address the long timescale of cement hydration and consider the interplay between chemical driving force and mechanical interactions between the nanoparticles.

2. Methodology

The simulations of HP formation start with an orthogonal box that is empty except for a 30 nm thick layer that represents the surface of a cement grain (see Figure 1). The cement layer is discretized using 10 nm spherical particles that are fixed, i.e. not displaced nor removed during the simulations. It is implicitly assumed that the box is filled with aqueous ionic solution, whose supersaturation β with respect to HP formation is known.

After a certain number of KMC steps, a certain number of HP spherical particles will have formed in the box (see Figure 1). The next KMC step computes first the rates of all possible particle deletions and then the rates of all possible particle insertions. The insertion is tricky because there are infinite possible positions for a new particle. In order to manage this, we create many trial HP particles and allow them to move a bit in order to find a local minimum of interaction energy with the other existing particles (HP and layer; no interactions between two trial particles, because they do not exist yet; see Figure 1).

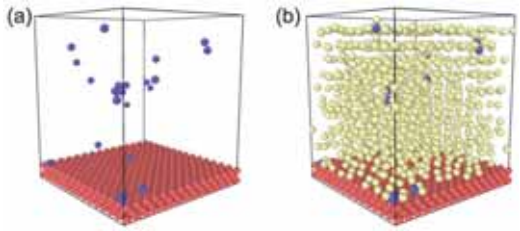

Figure 1: (a) Layer of particles representing a cement grain surface, in red, and hydration phase HP particles formed near it, in blue. (b) Same configuration showing also the trial particle for KMC insertion in yellow.

The rate of particle insertion is coarse grained from the molecular scale following the classical theories of Classical Nucleation Theory (CNT) and crystal growth [24]:

$$R^{in} = C_{cn}\frac{V_{box}}{M}\left\{\frac{1}{Z}e^{\left(\frac{\Delta G_{CNT}}{k_B T}\right)} + \frac{1}{a^2 r_0^* \beta}\int_{R_{nucl}}^{R_{part}} e^{\left[\left(\frac{\gamma\Delta\Omega_{1rx}+\Delta U_{1rx}}{k_B T}\right)\right]}dR\right\}^{-1} \quad (1)$$

Details on the derivation of Eq. 1 and on the corresponding equation for the deletion rate R^{del} are given in ref. [25] (notice that the chemical conditions considered for the simulations in this paper will be such that the number of dissolution events will be negligible alongside their effect on the rate, so the results that we will show will be reproducible even without implementing a deletion step at all). In Eq. 1, C_{cn} is the concentration of possible particle nucleation sites in solution (e.g. the concentration of ions), V_{box} is the volume of the simulation box, and M is the number of trial particles assumed as uniformly distributed in V_{box}. In the curly bracket, the first term is the characteristic time to form a critical nucleus as per CNT, while the second integral term is the time to grow the radius of the critical nucleus by single-molecule growth reactions until reaching the wanted particle size R_{part} (here diameter = 10 nm, thus R_{part} = 5 nm). Z is the Zeldovich factor, expressing the probability that a critical nucleus will indeed start growing rather than dissolving back. ΔG_{CNT} is the difference in free energy between critical nucleus and solution. For spherical particles:

$$\Delta G_{CNT} = \frac{4}{3}\pi R_{nucl}^3 k_B T \ln(-\beta) + 4\pi R_{nucl}^2 \gamma + \Delta U_{nucl} \quad (2)$$

R_{nucl} is the radius of the critical nucleus, given by the condition $d\Delta G_{CNT} / dR = 0$, k_B is the Boltzmann constant, T is the temperature in Kelvin degrees, and γ is the interfacial energy between cement HP and water. ΔU_{nucl} is the change in total interaction energy in the system in case the critical nucleus appears; its relationship to the nucleus size depends on the type of interaction potential employed. Here we use a pairwise interaction potential $U_{ij}(r)$ that depends only on the distance r between the particles and has been shown to capture well the mechanical properties of cement HP at the 500 nm mesoscale [13, 18, 23]:

$$U_{ij}(r) = 4\epsilon(R^3)\left[\left(\frac{2R}{r}\right)^{28} - \left(\frac{2R}{r}\right)^{14}\right] \quad (3)$$

$\varepsilon(R)$ is the energy strength, which is assumed to scale as the volume of the particle. A different hypothesis on the scaling of ε is discussed in ref. [25], in relation to the prediction of the rate of early cement hydration.

Going back to Equation 1, a is the linear size of a molecule of cement HP (here we assume a = 0.645 nm, thus a^3 = 0.267 nm^3, as for C—S—H [26]). r_0^* is a kinetic constant (rate per unit surface) that contains the activity coefficient of the activated complex and the standard free energy barrier of the C—S—H formation reaction [24]. $\Delta\Omega_{1rx}$ and ΔU_{1rx} are the change of particle surface and interaction energy caused by one molecular reaction of HP product forming on the surface of a growing nanoparticle. Each molecular reaction changes the particle volume by a^3 and consequently the radius R; both $\Delta\Omega_{1rx}$ and ΔU_{1rx} therefore depend on the current R. The rate of particle deletion can be obtained in a very similar manner as R^{in} and contains neither the supersaturation term β nor the sampling-related prefactor before the curly brackets. Deletion will be considered in the simulation but the rate expression is omitted here for brevity and because we will only consider values of beta that are sufficiently high for deletion to be negligible.

To simulate the formation of cement HP, we consider γ = 86.7 mJ/m^2 [26]. The interpretation of experiments based on CNT indicates that the size of the critical nucleus in cement hydrates is as small as one single molecule [27]. This means that the CNT term in Equation 1 is small compared to the crystal growth term (the integral one) and we will neglect it. For cement hydration, both C_{cn} and r_0^* are unknown, hence the two will be combined and treated as a single effective parameters that is used to fit the right timescale (actually, if one decides to identify C_{cn} with the concentration of calcium or silicon ions in solution, then literature data could be used to set a value for it, e.g. [28]). It is important to notice that differently from the existing simulations, the only scaling of time here is linear. This means that any nonlinearity in the rate can only be a true reflection of the formation mechanism and is not imposed ad-hoc.

The particles of cement hydrates that we insert during the simulations are monodisperse even though just after insertion, a small random change of the diameter by 5% is imposed to avoid crystallization. It is known in the cement literature that realistic details of the heterogeneities at the sub-micrometer scale can only be captured using polydiperse nanoparticles [16, 23], and there are experiments that suggest that anisotropic shapes of the particles are more realistic [29]. However, spherical and monodisperse particles are sufficient to discuss the qualitative kinetics of collective precipitation-aggregation mechanisms, as shown in the literature [19] and in line with the objective of this work.

As a final note for this section, it is interesting to note that the coarse grained rate expression in Equation 1 combines some terms that are related to the chemical kinetics of the process (e.g. r_0^*) with other terms that are related to the thermodynamics. Among the latters, there are terms that are related to the chemistry of the system (e.g. β) and terms that are related to the

mechanical interactions between particles (e.g. ΔU_{Irx}). The proposed scheme therefore combines chemistry and mechanics over the large timescales of chemical kinetics.

3. Results

The KMC approach presented here has been used to study the effect of the interaction potential and initial system configuration on the mechanism of growth-by-aggregation of the cement HP. Here we are interested only in the qualitative trends of rates as a function of time, and how these relate to the mechanisms of precipitation that are triggered. Converting the qualitative results into quantitative rates would require a model calibration to define the r_0^* terms in Equation 1; this is left to another manuscript currently under review [21] The results for three scenarios are shown in Figure 2:

a) very large ε in Equation 2, taken from ref. [18] where it was shown that such a large ε captures well the mechanics of the C—S—H; in this first case the interaction between cement surface particles and cement HP particles is taken to be as strong as the interaction between two HP particles;
b) same as the previous scenario, but this time the ε between cement surface and HP particles is smaller than the that between two HP particles (25% of it to be precise) except for a small region in the middle of the cement surface where a full 100% of the HP-HP interaction is maintained; this small region serves as a preferential site for nucleation of the mesoscale HP domain;
c) a 3 orders of magnitude smaller ε, taken from atomic force microscopy experiments [30].

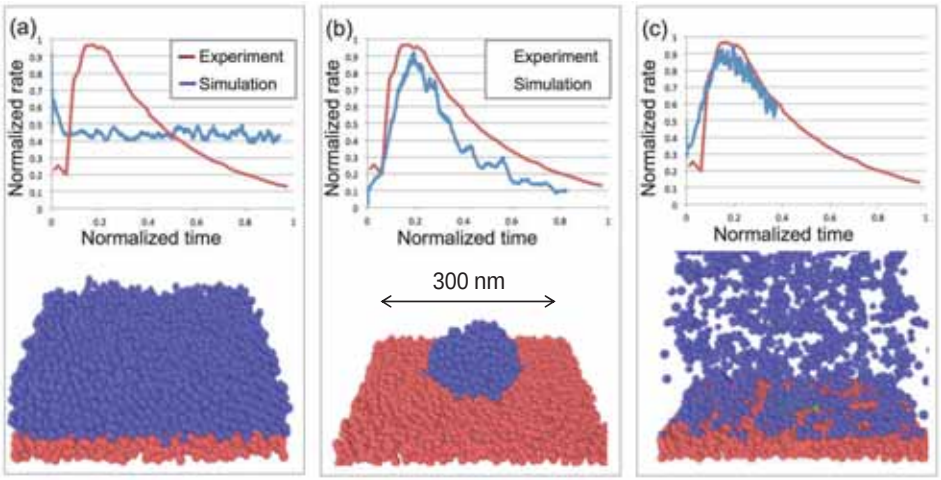

Figure 2: Results from our simulations with different initial conditions (a) strong interactions between nanoparticles and homogeneous cement surface; (b) strong interaction and surface with one preferential site for HP particle formation; (c) weak interactions.

The snapshots in Figure 2 show that the first scenario leads to a layered growth of the HP domain, formed by aggregated nanoparticles. For this scenario we kept β constant in time and very large, in order to avoid particle deletion. The layered growth results into a constant rate, very different from what is expected during early hydration (see simulation and experimental values in Figure). Notice that the size of the HP domain simulated here is in the same order as that observed experimentally during early hydration, i.e. ~500 nm, so it makes sense to aim for a rate curve that is similar to the one measured experimentally from calorimetry).

The second scenario, with the favourable nucleation site, gives a much better result, with a roughly hemispherical domain growing radially. The increasing surface of the hemispherical domain is at the origin of the acceleration in the rate curve. Indeed, in the KMC algorithm the total rate is the sum of all particle insertion rates, and an increasing surface of the HP domain implies that more trial nuclei can find a favourable spot that leads to a high rate. When the HP domain crosses the periodic boundary on the cement surface, the lateral impingement causes the rate peak, similar to the calorimetry experiments. The continuous decrease of rate after the peak is due to the fact that, for this simulation, we took a supersaturation β that decreases with time, as known for the cement solution and as quantified in ref. [31].

Finally, the third scenario with much weaker strength of the interactions causes the mechanisms of HP formation to change from heterogeneous on the cement surface to homogeneous in the bulk. This also leads to a rate curve that agrees qualitatively with the experiments. In this case however the peak occurs when the space gets filled, which implies a quantitative dependence of the area under the rate curve (number of HP particles inserted) and the amount of water in the cement mix (viz. the size of the simulation box perpendicular to the cement surface). Such dependence would contradict the experiments [8], but the problem can be avoided assuming that the homogeneous nucleation is limited to a small region near the surface of the cement grain, as proposed in ref. [20]. This constraint might indeed originate from a gradient of supersaturation in the simulation box, sustained by a diffusive process of the ions in solution, which move from the cement surface toward the bulk solution. To explore this possibility, future work should couple the simulations presented here with the type or reaction-transport simulations mentioned in the introduction of this manuscript [7,8].

4. Conclusion

We have presented a new approach to simulate the precipitation of nanoparticle of cement hydrates from aqueous solution and their aggregation to form mesoscale domains. The approach is based on new coarse-grained expressions for the rate of particle insertion and deletion, which are derived from the theories of classical nucleation and crystal growth. The rate expression involve one kinetic parameter r_0^* which has physical meaning but is often hard to measure. r_0^* determines a linear scaling of time, which means that even if it is not quantified, all the nonlinearities in the rate of HP formation obtained from the simulations are still a true reflection of the predicted mesoscale mechanism only. Another important feature of our coarse-grained rates is that they combine chemistry and the mechanical interactions between nanoparticles, creating new opportunities to study technologically important phenomena where chemistry and mechanics play together, e.g. crystallization pressure and

dissolution-induced creep. Finally, simulation results show that our approach can predict various mesoscale mechanisms of HP formation and clarify how these affect the hydration rate. Overall, this is a first step in developing nanoscale simulations that can contribute to the challenge of understanding and controlling the formation, setting, and chemo-mechanical degradation of concrete.

Acknowledgements

The authors thank the TU1404 COST Action "Towards the next generation of standards for service life of cement-based materials and structures", for supporting the presentation of this work at the MSSCE 2016 Conference.

References

[1] Taylor, H. F. W., Cement chemistry, Thomas Telford (1997)
[2] Bullard, J. W. et al, Mechanisms of cement hydration, Cem Concr Res 41 (2011), 1208-1223
[3] Van Breugel, K., Numerical simulation of hydration and microstructural development in hardening cement-based materials:(II) applications. Cem Concr Res 25 (1995), 522-530.
[4] Bentz, D. P. CEMHYD3D: A three-dimensional cement hydration and microstructure development modelling package. Version 2.0, National Institute of Standards and Technology Interagency Report 7232 (2000).
[5] Bishnoi, S., and Scrivener, K. L., μic: A new platform for modelling the hydration of cements. Cem Concr Res 39 (2009), 266-274.
[6] Bullard, J.W., et al., A parallel reaction-transport model applied to cement hydration and microstructure development. Model. Simul Mater Sci Eng 18 (2010), 025007.
[7] Thomas, J. J., et al, Modeling and simulation of cement hydration kinetics and microstructure development, Cem Concr Res 41 (2011), 1257-1278.
[8] Masoero, E., Thomas, J. J., and Jennings, H. M., A Reaction Zone Hypothesis for the Effects of Particle Size and Water□to□Cement Ratio on the Early Hydration Kinetics of C3S, J Am Ceram Soc 97 (2014), 967-975
[9] Bishnoi, S., Geometric limitations of nucleation and growth models: Revisiting the impingement assumption. Cem Concr Res 46 (2013), 30-40
[10] Manzano, H., et al, Shear deformations in calcium silicate hydrates. Soft Matter 9 (2013), 7333-7341
[11] Jennings, H., et al, Water isotherms, shrinkage and creep of cement paste: hypotheses, models and experiments, Mechanics and Physics of Creep, Shrinkage, and Durability of Concrete (2013), 134-141
[12] Pinson, M. B., et al, Hysteresis from Multiscale Porosity: Modeling Water Sorption and Shrinkage in Cement Paste, Phys Rev Appl 3 (2015), 064009
[13] Masoero, E., et al, Kinetic simulation of the logarithmic creep of cement, Mechanics and Physics of Creep, Shrinkage, and Durability of Concrete: A Tribute to Zdenk P. Bazant, (2013), 166-173.
[14] Bažant, Z. P., et al, Interaction of Concrete Creep, Shrinkage and Swelling with Water, Hydration, and Damage: Nano-Macro-Chemo, In 10th International Conference on

Mechanics and Physics of Creep, Shrinkage, and Durability of Concrete and Concrete Structures (2015)
[15] Gonzalez-Teresa, R., et al, Structural models of randomly packed Tobermorite-like spherical particles: A simple computational approach, Materiales de construccion 60 (2010), 7-15
[16] Masoero, E., et al, Nanostructure and nanomechanics of cement: polydisperse colloidal packing, Phys Rev Lett 109 (2012), 155503
[17] González-Teresa, R., et al, Nanoscale texture development of CSH gel: A computational model for nucleation and growth, Appl Phys Lett 103 (2013), 234105
[18] Masoero, E., et al, Nano-scale mechanics of colloidal C–S–H gels, Soft Matter 10 (2014), 491-499
[19] Ioannidou, K., et al, Controlling local packing and growth in calcium–silicate–hydrate gels, Soft Matter 10 (2014), 1121-1133
[20] Del Gado, E., et al, A soft matter in construction–Statistical physics approach to formation and mechanics of C–S–H gels in cement, Europ. Phys. J. Special Topics 223 (2014), 2285-2295
[21] Etzold, M. A., McDonald, P. J., and Routh, A. F., Growth of sheets in 3D confinements—a model for the C–S–H meso structure, Cem Concr Res 63 (2014), 137-142
[22] Yu, Z., and Lau, D., Nano-and mesoscale modeling of cement matrix, Nanoscale Res Lett 10 (2015), 1-6
[23] Ioannidou, K., et al, Mesoscale texture of cement hydrates, Proc Natl Acad Sci 113 (2016), 2029-2034
[24] Lasaga, A. C., Kinetic theory in the earth sciences, Princeton University Press (2014)
[25] Shvab, I., and Masoero, E., Kinetic simulations of nanoparticle precipitation: the early hydration of cement (under review)
[26] Bullard, J. W., A determination of hydration mechanisms for tricalcium silicate using a kinetic cellular automaton model, J Am Ceram Soc 91 (2008), 2088-2097
[27] Garrault-Gauffinet, S., and Nonat, A., Experimental investigation of calcium silicate hydrate (CSH) nucleation, J Crystal Growth 200 (1999), 565-574
[28] Lothenbach, B. and Winnefeld, F., Thermodynamic modelling of the hydration of Portland cement. Cem Concr Res 36 (2006), 209-226.
[29] Chiang, W.S., Fratini, E., Baglioni, P., Liu, D. and Chen, S.H., Microstructure determination of calcium-silicate-hydrate globules by small-angle neutron scattering. The J Phys Chem C 116 (2012), 5055-5061.
[30] Plassard, C., et al, Nanoscale experimental investigation of particle interactions at the origin of the cohesion of cement, Langmuir 21 (2005), 7263-7270
[31] Bullard, J.W., Scherer, G.W. and Thomas, J.J., Time dependent driving forces and the kinetics of tricalcium silicate hydration. Cem Concr Res 74 (2015), 26-34

International RILEM Conference on Materials, Systems and Structures in Civil Engineering
Conference segment on Service Life of Cement-Based Materials and Structures
22-24 August 2016, Technical University of Denmark, Lyngby, Denmark

CONDITION ASSESSMENT OF REINFORCED CONCRETE ELEMENTS EXPOSED TO CARBONATION

Samindi Samarakoon [(1)], Jan Sælensminde [(2)], Cecilie Myklebust Helle [(1)]

(1) University of Stavanger, Stavanger, Norway
(2) Betec AS, Bergen, Norway

Abstract
Onshore reinforced concrete structures are vulnerable to deterioration due to carbonation. Condition assessment is a vital task, which helps to determine the reliability of structural elements over the remaining service life. This study assesses the condition of reinforced concrete structural elements (i.e. consoles) which are 53 years into their service life. The reinforced concrete consoles, exhibiting no visible signs of corrosion, were chosen to measure carbonation depths. In addition, non-destructive testing method: half-cell potential measurements were taken over the surfaces of the consoles. A full-probabilistic service life prediction model was used to calculate the expected service life, and a comparison was made based on the actual carbonation depth measurements.

1. Introduction

Condition assessment of the existing reinforced concrete structures is an important task in the planning of maintenance and modification activities. Reinforcement corrosion can be considered as one of the potential mechanisms which affect the durability of reinforced concrete structures. There are many reasons for the corrosion of steel reinforcement, with carbonation and chloride-induced corrosion being dominant mechanisms among them. Therefore, it is important to choose the dominant phenomenon based on the exposure condition of the structure. Hence, in this study, the diffusion of CO_2 is considered as the dominant transport mechanism for the corrosion in steel reinforcement of residential buildings.

Deterministic and probabilistic models have been developed for service life design, to predict the time to initiate corrosion and the time to propagate corrosion. However, the probability based models can help to make more realistic decisions than deterministic models. Therefore, in this study, the full probability based model given in fib_bulletin_34 [1] is used to calculate

the probability of corrosion initiation. In addition, there are various proactive and reactive approaches developed for controlling the condition of reinforced concrete structures, such as measuring carbonation depths, using non-destructive testing methods (i.e. Half-Cell Potential (HCP) measurements), visual inspection, etc. In this, study, potential mapping has been carried out over the surface of three consoles, and carbonation depths were measured at selected locations. Moreover, this manuscript discusses a case study of three reinforced concrete consoles in a residential building. In addition, it determines the probability of corrosion initiation using the DuraCrete [2, 3] model and compares it with HCP data. Moreover, the measured carbonation depths are compared with calculated average carbonation depths.

2. Modelling of reinforcement corrosion due to carbonation

Carbonation is a chemical process, in which the carbon dioxide in air diffuses into the concrete, dissolves in the pore solution, and reacts with calcium hydroxide, forming insoluble calcium carbonate and water. This results in a reduced pH-value of the concrete, which is one reason for initiating the corrosion of steel reinforcement. The level of damage due to the corrosion of embedded steel in a concrete structure over time can be described using Tuutti's model [4]. Essentially, the model categorizes the service life of a structure into the corrosion initiation period and the corrosion propagation period. This manuscript focuses on the corrosion initiation phase.

Many researchers have used Fick's second law to model the carbonation to the un-cracked concrete, considering diffusion as the dominant transport mechanism. In this paper, the DuraCrete [2, 3] model, derived using Fick's second law, is adopted to include environmental and material parameters, as given in Eq. (1).

$$X_c(t) = \sqrt{2 * k_e * k_c * \left(k_t * R_{ACC,0}^{-1} + \varepsilon_t\right) * C_s} * \sqrt{t} * \mathrm{w(t)} \quad (1)$$

$X_c(t)$: carbonation depth (mm)
k_e: environmental function (-)
k_c: execution parameter (-)
k_t: regression parameter (-)
$R_{ACC,0}^{-1}$: inverse effective carbonation resistance ($(mm^2/year)/(kg/m^3)$)
ε_t: error term ($(mm^2/year)/(kg/m^3)$)
C_s: CO_2 concentration of the ambient environment (kg/m^3)
w(t): weather function (-), where $w(t)=(t_0/t)^w$, where t_0: time of reference (years), w: weather exponent (-)
t: time (years)

Time to initiate corrosion (T_i), when $X_c(t)= X_{cover}$ (concrete cover) is given in Eq. (2).

$$T_i = \left\lfloor \frac{{X_{cover}}^2}{2*k_e*k_c*\left(k_t*R_{ACC,0}^{-1}+\varepsilon_t\right)*C_s*{t_o}^{2w}} \right\rfloor^{\frac{1}{1-2w}} \quad (2)$$

3. Reliability concepts to model the corrosion initiation due to carbonation

The safety margin (M) or limit state function for corrosion initiation can be defined as Eq. (3), where 't' is the exposure period, 'X' is random variables.

$$M = G(X, t) = T_i - t \quad (3)$$

Assuming that a system fails when corrosion initiation takes place, the probability of corrosion initiation (P_f) is evaluated by integrating $G(X, t) \leq 0$ over the failure domain, considering the statistical distribution of each random variable. Eq. (4) shows how to estimate 'P_f' using the joint density function $fx(x_i)$ with random variables [5].

$$P_f = \int_{M\leq 0} fx(x_i)dx_i = \int_{M\leq 0} I(x_i)fx(x_i)dx_i = E[I(x_i)] \quad (4)$$

In addition, Monte Carlo simulation can be used to calculate 'P_f' by simulating the limit state function for a range of sampling. In this approach, the mean value of $I(x_i)$ can be an estimator for the probability of corrosion initiation as given in Eq. (5).

$$E[I(x_i)] = \frac{1}{N}\sum_{i=1}^{N} I(X_i) \quad (5)$$

where $I(x_i) = \begin{Bmatrix} 1 \rightarrow M \leq 0 \\ 0 \rightarrow M > 0 \end{Bmatrix}$

In estimating 'P_f', it is vital to identify the basic set of random variables, of which uncertainties have to be considered. Then, the randomness of all the variables is modelled, recognizing the probability distributions of the variables. These probability distributions can be defined by physical observations, statistical studies, laboratory analysis, and expert opinion [5, 6, 7].

4. Case study: condition assessment of reinforced concrete consoles

4.1 Statistical quantification of random variables and prediction of corrosion initiation

Three consoles, with almost no visible corrosion damage, were chosen to be tested 53 years into their service life. They are located on the fourth floor in a residential building in Bergen, Norway (about 2-3 km away from sea and 50 m above sea level); one of the consoles is shown in Figure 1. While assessing the present condition of the consoles, it is necessary to collect existing data. The existing data includes general information about the structure, material properties and exposure condition, documentation of former inspections/monitoring

and documentation of former maintenance and repair. In the absence of information about the actual cement type and water/cement ratio, cement type CEM I R and w/c 0.5 are chosen for this analysis. The probability distributions for the random variables ($R_{-1ACC,}$, ε_t, RH_{real}, $C_{s,atm}$, b_c, b_w, X_{cover}) for Eq. (2) were chosen, taking into consideration the actual exposure condition, as given in Tab. 1. Based on the exposure condition to rain, the probability of corrosion initiation has been found for two cases: sheltered from rain and partially exposed to rain, as shown in Figure 1.

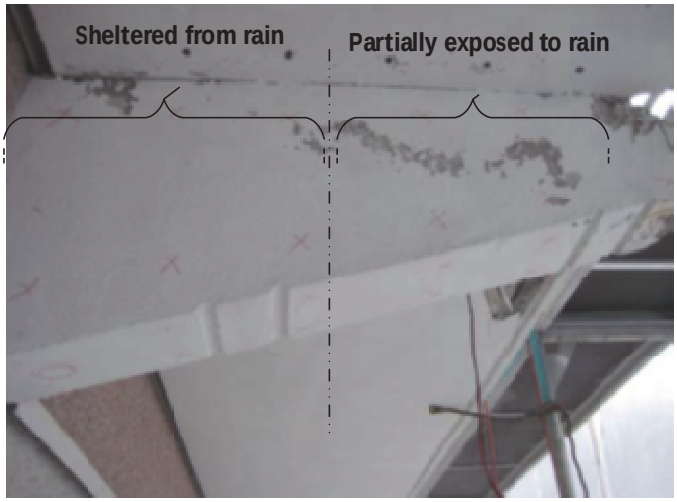

Figure 1: Reinforced concrete Console 1 in the building

Table 1: Statistical characteristics of variables

Parameter		Distribution	Mean	Standard deviation	Reference
$R^{-1}_{ACC,}(10^{-11}*mm^2/s/kg/m^3)$		Normal	6.8(w/c=0.50 and CEM I R)	2.5	*fib* Bulletin 34[1]
ε_t ($mm^2/s/kg/m^3$)		Normal	315.5	48	*fib* Bulletin 34[1]
k_t		Normal	1.25	0.35	*fib* Bulletin 34[1]
$ke=\left(\frac{(1-(RH_{real})^{fe})}{(1-(RH_{ref})^{fe})}\right)^{ge}$	RH_{real}	WBmax(w=1)	0.825	0.032	*From weather station*
	RH_{ref}	Constant	0.65	-	
	f_e	Constant	2.5	-	*fib* Bulletin 34[1]
	g_e	Constant	5.0	-	
$C_s=C_{s,atm}+C_{s,em}(kg/m^3)$	$C_{s,atm}$	Normal	0.0008	0.0001	*fib* Bulletin 34[1]
	$C_{s,em}$	-	0		
k_c	b_c	Normal	-0.567	0.02	*fib* Bulletin 34[1]
	t_c (days)	Constant	1	-	
W(t) Exposed to rain	t_0(years)	Constant	0.0767	-	*fib* Bulletin 34[1]
	ToW	Constant	0.010	-	
	b_w	Normal	0.446	0.163	*fib* Bulletin 34[1]
Sheltered from rain	W(t)	Constant	1		
X_{cover}(mm)		Normal	25	8	

Monte Carlo simulation was used to simulate the limit state function and to calculate the probability of corrosion initiation using Eqs. (4) and (5) for the statistical characteristics of random variables given in Tab. 1. In this study, 10^6 simulations were performed using Matlab software to calculate the probability of corrosion initiation. The probability of corrosion initiation versus time (years) was plotted, as shown in Figure 2.

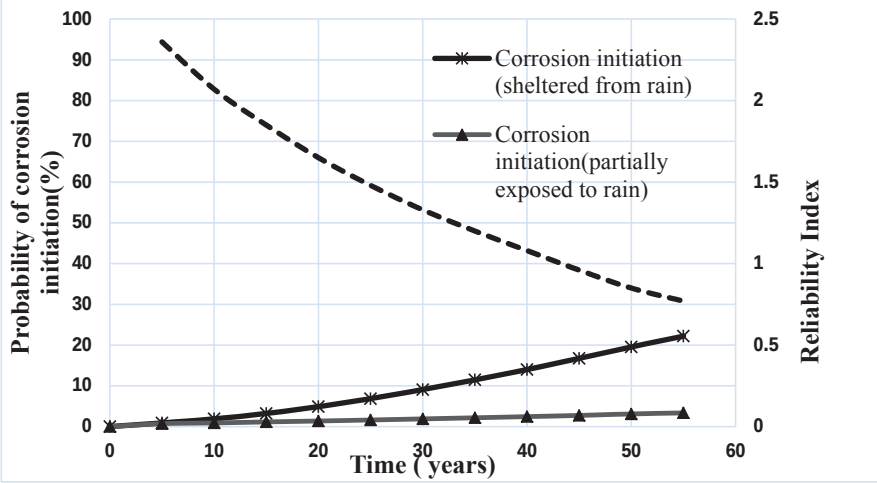

Figure 2: Probability of corrosion initiation versus time

4.2 Determination of carbonation depths on-site

Initially, the location of the reinforcement was identified, and 10 holes were chiselled into the concrete, as marked in Figure 3. The phenolphthalein test was carried out on site to measure carbonation depths. Tab. 2 shows the mean carbonation depths measured at test locations in each console, as indicated in Figure 3. The test locations ((a) to (j)) are chosen, about 22 cm from the closet edge. Test locations (a) to (e) are considered as sheltered from rain, whereas locations (f) to (j) are considered as partially exposed to rain.

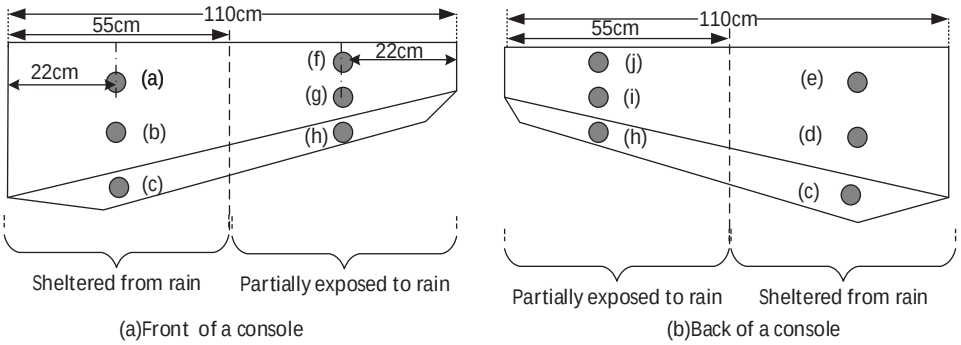

Figure 3: Sampling point of a console

Table 2: Mean carbonation depth at locations given in Figure 2

	Mean carbonation depth at locations shown in Figure 3									
	Sheltered from rain					**Partially exposed to rain**				
Location	**(a)**	**(b)**	**(c)**	**(d)**	**(e)**	**(f)**	**(g)**	**(h)**	**(i)**	**(j)**
Console 1 (mm)	7	7	6	10	7	2	4	6	7	4
Console 2 (mm)	5	7	8	5	7	3	3	4	5	4
Console 3 (mm)	6	8	10	5	7	3	5	8	6	4

4.3 Half-cell potential (HCP) mapping

Half-cell potential mapping (HCP) is a non-destructive method, which is widely used for monitoring steel corrosion in concrete structures. However, there are no specific guidelines available in the literature to interpret HCP measurements due to carbonation. According to ASTM (1991) Standard [8], the results from a potential mapping process can be interpreted as shown in Tab. 3, which is based on the findings from laboratory testing (partial immersion in chloride solution) and outdoor exposure of various reinforced concretes structures above ground level. The standard states that criterion given in Tab. 3 should not be utilized if concrete is carbonated to the level of the embedded steel, unless either experience or destructive examination of some areas, or both, suggest their applicability. Considering measured carbonation depths (i.e. destructive examination) in Tab. 2, it can be seen that concrete is not carbonated to the level of embedded steel. This is because the average concrete cover to the reinforcement (25 mm) is deeper than the measured carbonated depths. Considering that fact, Tab. 3 was used to evaluate HCP values due to carbonation. At 53 years of service life, the three consoles had 36 HCP measurements taken at 200 mm intervals over each of their surfaces, using Cu/CuSO4 as reference electrode. Figure 4 shows the HCP measurement over the surface of Console 2 as an example.

Table 3: Interpretation of half-cell potential values as per ASTM C876 [8]

Half-cell potential (mV) relative to $Cu/CuSO_4$ reference electrode (HCP)	**percentage chance of active corrosion**
<-350	> 90%
-300 to -200	50%
>-200	Less than 10%

5. Comparison of calculated values with field measurements

5.1 Comparison of measured and calculated carbonation depths

Considering the mean value of each random variable in Eq. (1) and Tab. 2, the mean value of the carbonation depths vs time have been plotted as given in Figure 4 for the area sheltered from rain and the area partially exposed to rain. It can be seen that, at 53 years, the calculated mean value of the carbonation depth is 18 mm for the area sheltered from rain, which is higher than the measured average carbonation depth (X1=7 mm). For the locations in the area which is partially exposed to rain, the calculated mean carbonation depth is 8.7 mm, which is also higher than the measured carbonation depth (X2=4.5 mm, as shown in Figure 5). However, both measured and calculated carbonation depths are below the mean value of

cover thickness, which indicates that corrosion has not initiated yet, despite the building being 53 years of age.

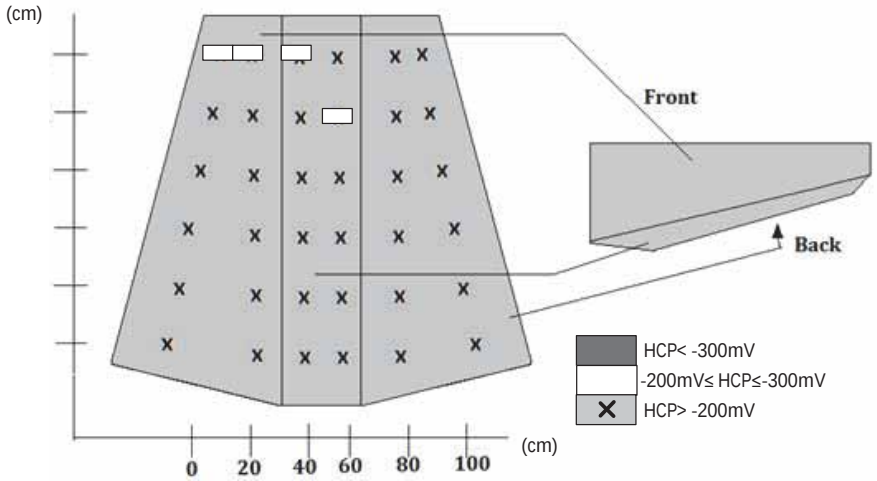

Figure 4: HCP measurement over Console 2

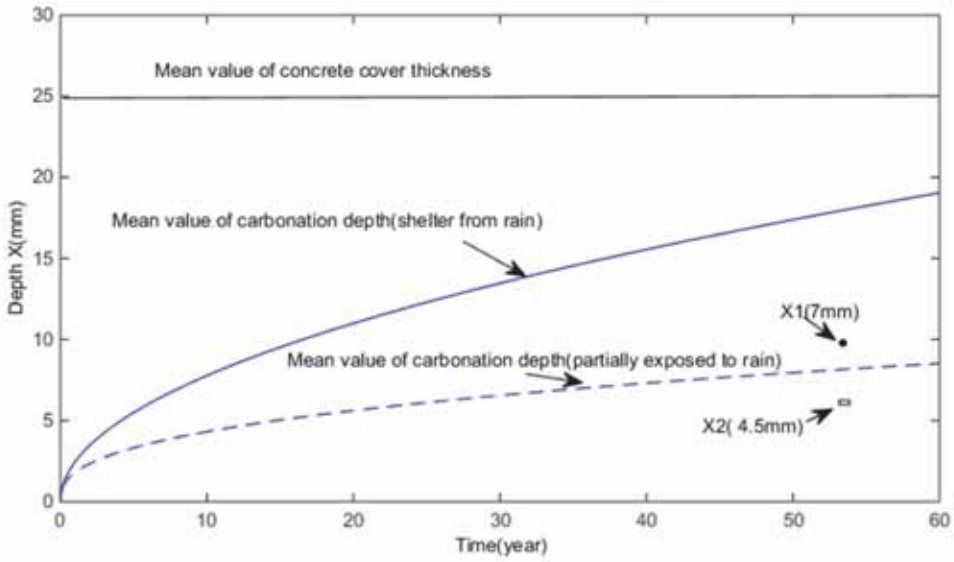

Figure 5: Carbonation depth versus time

5.2 Comparison of estimated probability of corrosion initiation with field investigations
Considering Tab. 3, the overall weighted probability of corrosion initiation for each console is estimated, and the results are given in Tab. 4. According to Tab. 4, it can be seen that the steel reinforcements in each console have overall less chance (about 10% - 19%) of corrosion initiation. In addition, it can be seen that the area which is considered as partially exposed to rain has 10% to 19% chance of corrosion initiation. However the area which is considered to be sheltered from rain has10% chance of corrosion initiation. In this case, HCP mapping gives unrealistic results. In addition, the estimated probability of corrosion initiation at the age of 53 years, given in Figure 2, is 22.5% for the area sheltered from rain and 4% for the area exposed to rain. The field investigated corrosion initiation probabilities are lower than those for the area sheltered from rain and higher than those of the area with partial exposure to rain.

Table 4: Summary of HCP measurement over consoles

		Frequency of occurrence of HCP value					
		Console 1		**Console 2**		**Console 3**	
Half-cell potential (mV) (Re. Cu/CuSO4 reference electrode)	**Percentage chance of corrosion initiation**	**(a)**	**(b)**	**(a)**	**(b)**	**(a)**	**(b)**
<-300	90%	0	0	0	0	0	0
-200 to -300	50%	0	0	0	4	0	2
>-200	10%	18	18	18	14	18	16
Overall weighted probability of corrosion initiation		10%	10%	10%	19%	10%	14 %

(Note: (a) area sheltered from rain and (b) area partially exposed to rain)

6. Discussion and conclusion

Carbonation can be considered as the dominant mechanism for the corrosion of reinforcement in residential buildings. Hence, the carbonation depths were measured in three consoles of no visible corrosion in a 53-year-old residential building, considering exposure to rain and shelter from rain. It could be seen that the measured average carbonation depth at the side sheltered from rain was 7 mm (X1) and that of the side partially exposed to rain was 4.5 mm (X2). Considering the mean values of random variables, the calculated mean carbonation depth is 18 mm for the side sheltered from the rain and 8.7 mm for the side partially exposed to rain. It could be seen that the calculated mean carbonation depths are higher than the measured carbonation depths. Moreover, painting of the surface may hinder the carbonation process, resulting in lower measured carbonation depths than expected. Furthermore, the probability of corrosion initiation was estimated using Monte Carlo simulation; results were 22.5% at 53 years for the area sheltered from rain. The HCP measurement at 53 years shows that the percentage chance of corrosion initiation for the same area is 10-19%, which is lower than the estimated probability of corrosion initiation. This implies that the estimated probability of corrosion initiation provides a good safety margin in designing the concrete cover.

References

[1] Fib_bulletin_34, Model code for service life design, ISBN 978-2-88394-074-1 (2006)
[2] DuraCrete, Modeling of degradation, BRITE–EURAM-Project BE95-1347/R4-5 (1998)
[3] DuraCrete, Statistical quantification of the variables in the limit state functions, BRITE–EURAM-Project BE95-1347/R9 (2000)
[4] Tuutti, K., Corrosion of steel in concrete. Stockholm, Sweden: Swedish Cement and Concrete Research Institute (1982)
[5] Fib_bulletin_59, Condition control and assessment of reinforced concrete structures exposed to corrosive environments (carbonation/chlorides): State of the art, ISBN 978-2-88394-099-4 (2011)
[6] Samarakoon, S. M. S. M. K. and Sælensminde, J., Condition assessment of reinforced concrete structures subject to chloride ingress: A case study of updating the model prediction considering inspection data, Cement Concr Compos 60 (2015), 92–98
[7] Malioka, V., Condition indicators for the assessment of local and spatial deterioration of concrete structures, PhD thesis, Swiss Federal Institute of Technology, Zurich, (2009)
[8] ASTM C876, Standard test method for half-cell potentials of uncoated reinforcing steel in concrete, 03(02) (1991), 434-9

International RILEM Conference on Materials, Systems and Structures in Civil Engineering
Conference segment on Service Life of Cement-Based Materials and Structures
22-24 August 2016, Technical University of Denmark, Lyngby, Denmark

CONTROL OF EARLY AGE CRACKING IN A MASSIVE TUNNEL STRUCTURE BASED ON EXPERIMENTAL INVESTIGATIONS AND NUMERICAL SIMULATIONS

Wibke Hermerschmidt [(1)], Martin Laube [(2)], Alex-W. Gutsch [(2)], Hartmann Alberts [(2)], Robert Teuber [(2)], Eckart Thoms [(3)]

(1) Technische Universität Braunschweig, iBMB, Germany
(2) MPA Braunschweig, Germany
(3) Senate Department for Urban Development and the Environment, Berlin, Germany

Abstract
In massive tunnel structures, early age cracking can lead to a loss of serviceability of the structure due to leakage. Therefore, a realistic calculation of the temperature and stress development caused by heat of hydration is necessary to ensure an economic design. This paper presents an application example for the control of early age cracking in a massive tunnel structure. Experimental investigations are carried out to characterize the thermomechanical behaviour of the concrete at early ages. This includes the testing of the adiabatic heat release, the development of the mechanical short term properties (compressive strength, tensile strength and Young's modulus) and the autogenous shrinkage. The experimental results are used to perform numerical simulations of the temperature and stress development in the tunnel structure. In addition, the temperatures and strains in the structure are metrologically monitored to validate the simulation results.

1. Introduction

In massive concrete structures, the temperature development caused by heat of hydration in combination with restraint of the structure can cause cracking at early ages. To avoid cracking or limit the crack width with reinforcement, a realistic calculation of the temperature and stress development is needed. For such a calculation, several factors affecting the material and the structural behaviour have to be taken into account. These factors have been studied extensively in the last decades to improve the description of the material properties since early ages, e.g. [1-4]. Several different modelling approaches and numerical tools for the description of the thermo-chemo-mechanical behaviour of concrete structures have been derived from these studies, e.g. [5-10]. Numerical models that account for all the influencing factors provide a realistic description of the structural behaviour but are at the same time computationally expensive and need an advanced theoretical knowledge from the user to

produce reliable results. Therefore, in engineering practice it is more common to use simplified modelling strategies due to their easier inclusion into the planning process.
The present paper describes the application of such a simplified modelling strategy for the control of early age cracking in a massive tunnel structure. In the course of the extension of a highway in Berlin, a part of this highway is built as a tunnel with four lanes in each direction. The tunnel is constructed as cut-and-cover tunnel, where the excavation is supported with slurry walls and an underwater concrete slab founded on piles. The cross section of the tunnel is shown in fig. 1. The tunnel is built in independent segments with a length of 10 m. Each segment is constructed in three stages: First, the foundation slab is cast, followed by the middle wall. The outer walls and the top slab are cast together in the third stage.

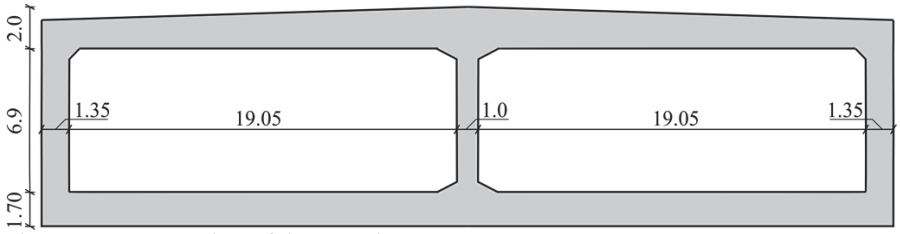

Figure 1: Cross section of the tunnel structure

As the tunnel is exposed to groundwater, special attention has to be paid to the water tightness of the structure. Due to the large thickness of the walls and slabs there is a high risk of cracking due to restraint stresses caused by heat of hydration and shrinkage. To avoid leakage of the structure, the evolution of restraint stresses has to be taken into account for the design of the reinforcement.
Hence, a comprehensive experimental program has been carried out to obtain an accurate description of the concrete's material behaviour at early ages. This includes the testing of the adiabatic heat release, the evolution of the compressive strength, the tensile strength and the Young's modulus and the autogenous shrinkage.
The experimental results act as input parameters for the subsequently performed numerical simulations. Staggered temperature-stress simulations with three dimensional finite element models were performed. With the results of the numerical simulations, the cracking risk due to restraint stresses can be estimated and an economic design of the reinforcement needed for crack width control can be ensured.

2. Material properties

2.1 Concrete mix design

A concrete of strength class C35/45 is used for the tunnel construction. Table 1 shows the mixture for 1 m³ fresh concrete. For reasons of fire protection, an amount of 2 kg/m³ polypropylene (PP) fibres is added to the mix. These fibres reduce the risk of explosive concrete spalling due to fire impact, because they melt at about 170°C and increase the gas permeability of the concrete [11]. In this relatively small dosage applied here, PP-fibres do not influence the properties of the hardened concrete, but the fresh state properties. The

addition of PP-fibres leads to a higher water demand and increases the risk of bleeding. Thus, a special mix design is required. A high content of fly ash is added to ensure the stability of the paste. A low heat slag cement (CEM III/A 32.5 N-LH/NA) is chosen to keep the heat evolution as low as possible and thus to reduce restraint stresses at early ages.

Table 1: Concrete mix

Cement CEM III/A 32,5 N-LH/NA	[kg/m³]	340
Fly ash	[kg/m³]	135
Gravel 0/16	[kg/m³]	1617
Water	[kg/m³]	182
Superplasticizer	[kg/m³]	2,7
PP-fibres	[kg/m³]	2,0
w/c-ratio (k_{FA} = 0,4)	[-]	0,46

2.2 Heat of hydration

The heat of hydration of the concrete was measured using an adiabatic calorimeter. The results are shown in fig. 2. The low heat slag cement in combination with the high amount of fly ash leads to a moderate heat release.

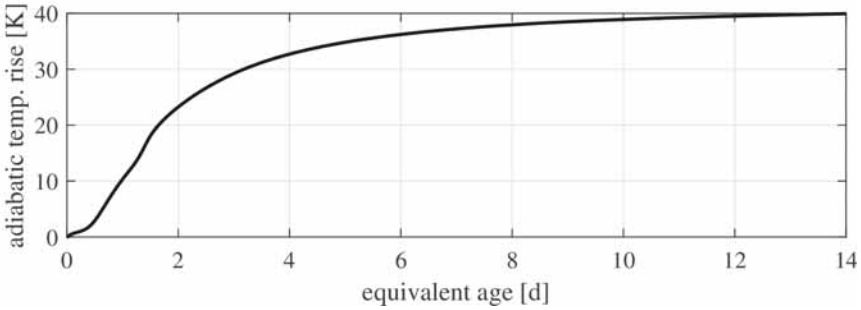

Fig. 2: Heat of hydration

To take into account the effect of temperature on the reaction rate, a maturity approach based on the Arrhenius formula is used [12]. The real concrete age t is transformed into the equivalent age t_{eq} using the relation

$$t_{eq} = \int_0^t \exp\left(\frac{E_A}{R} \cdot \left(\frac{1}{293\ \mathrm{K}} - \frac{1}{273\ \mathrm{K} + T(\tau)}\right)\right) \mathrm{d}\tau, \quad (1)$$

in which E_A is the activation energy and R is the ideal gas constant (R = 8,314 J/(mol K)). The activation energy mainly depends on the cement type. A constant value of E_A = 40 kJ/mol is assumed for the calculations. The equivalent age t_{eq} defines the time that is needed at 20°C to reach the same hydration degree as under the given temperature history $T(\tau)$.

2.3 Mechanical short term properties

The compressive strength, the tensile strength and the Young's modulus in tension have been tested at ages of 1, 2, 3, 4, 7, 14 and 28 days. The compressive tests were performed on cubes with an edge length of 150 mm. The tensile strength and the Young's modulus in tension have been tested on cylindrical specimens (d = 80 mm, h = 300 mm) in direct tensile tests. Fig. 3 shows the test results.

The combination of slag cement and fly ash leads to a relatively slow evolution of the compressive strength which still shows a significant increase for ages greater than 14 d. The tensile strength and the Young's modulus evolve quicker and reach their final value earlier.

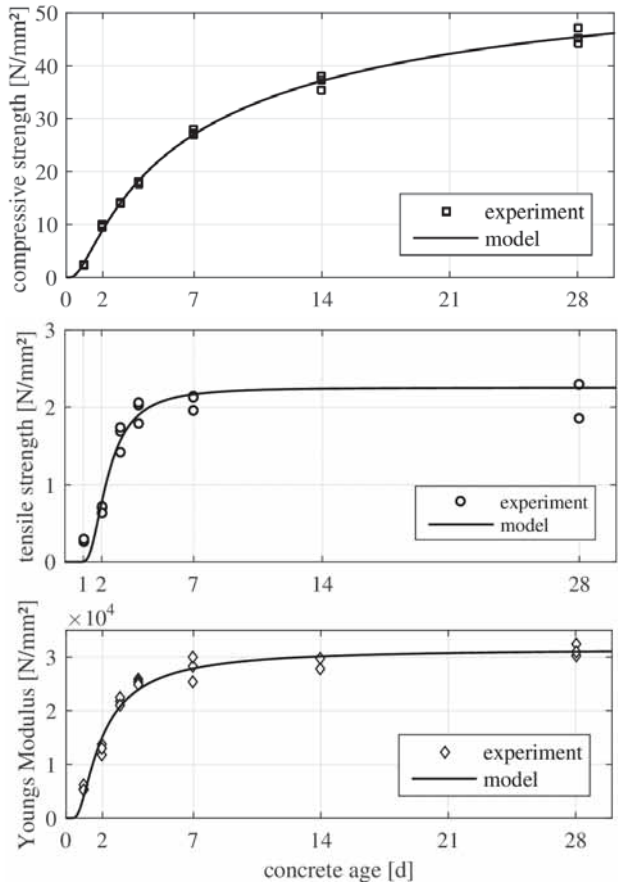

Fig 3: Evolution of compressive strength, tensile strength and Young's modulus

The calculation of restraint stresses requires a continuous description of the evolution of the mechanical properties. Therefore the exponential function

$$f(t_{eq}) = f_\infty \cdot \exp\left(A \cdot \left(\frac{t_{eq}}{t_k}\right)^B\right) \quad (2)$$

is fitted to the experimental results, see fig. 2. The corresponding model parameters are listed in table 2.

Table 2: Model parameters for the description of mechanical short term properties

	f_∞ [N/mm²]	A [-]	B [-]	t_k [d]
compressive strength	64.9	-3.1	-0.65	1.0
tensile strength	2.25	-6.7	-2.64	1.0
Young's modulus	31500	-2.0	-1.42	1.0

2.4 Autogenous shrinkage

The autogenous shrinkage has been tested on horizontal specimens with a cross section of 100 mm x 60 mm and a length of 1000 mm. The specimens can move totally free on a layer of neoprene and are sealed with PE-foil and a metallic mould against moisture loss. The shrinkage strain is measured at the ends of the specimens with a highly sensitive LVDT.
The strain evolution shows an intense swelling in the first 1.5 days followed by a continuous shrinkage, see figure 4. The swelling at the beginning compensates a part of the subsequent shrinkage, but for the evolution of stresses the shrinkage becomes more important, because the Young's modulus is significantly higher in this phase.

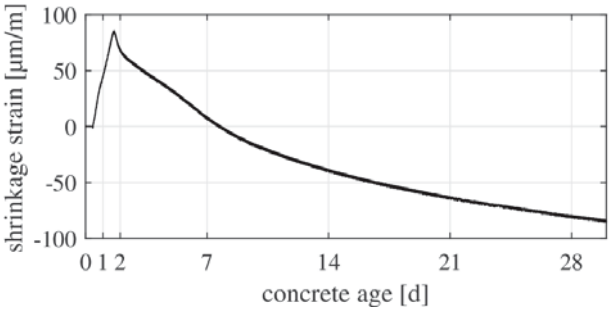

Figure 4: Autogenous shrinkage

2.5 Viscoelasticity

Early age concrete shows an intense viscoelastic behaviour that decreases continuously with the progression of the hydration process [2,13,14]. The viscoelastic behaviour greatly influences the evolution of stresses in restrained construction parts. Because no experimental results are available for the concrete used here, assumptions were made to take into account the viscoelastic behaviour for the calculation of stresses. The data from [14] was used as a reference because it describes the creep behaviour of a concrete with the same cement type and a similar strength evolution. The double power law (DPL) [15] is used to define the creep coefficient:

$$\varphi(t, t_l) = \varphi_1 \cdot {t_l}^{-m} \cdot (t - t_l)^n \quad (3)$$

In this equation, t is the concrete age and t_l the concrete age at loading. φ_1, m and n are model parameters that define the magnitude and the shape of the creep curves. The assumed values of φ_1, m and n are listed in table 3.

Table 3: Parameters for DPL

φ_1	m	n
0.37	0.10	0.17

3. Numerical simulations

3.1 Finite element model and calculation procedure

The temperature and stress evolution in the tunnel structure has been analysed using the finite element software TNO Diana. The calculations were carried out as staggered analyses, which means that the temperatures are calculated first and act as loading in the subsequent structural analysis. For the thermal analysis the measured hydration heat from fig. 2 was implemented as heat source. The heat exchange with the surrounding air has been modelled with convective boundary elements that take into account the formwork or other surface treatments through an adaption of the film coefficient. For the ambient temperature, the following scenario was assumed: The concrete casting is performed during mild winter weather (10°C). The fresh concrete is assumed to have a constant temperature of 20°C. After five days of curing, a sudden start of winter occurs and the ambient temperature decreases linearly to -7°C. This scenario can be treated as worst case scenario, because the cooling down of the air leads to an additional contraction of the concrete that increases the magnitude of restraint stresses.

To take into account the phased construction, separate models were used to perform the temperature and stress calculations. In each model, the experimentally determined material properties of the early age concrete were implemented directly into the simulation. The material properties of the previously cast segments were assumed to be constant and equal to the values at 28 days, because the intervals between the construction phases are relatively long.

The simulations do not take into account cracking even if the calculated stress exceeds the tensile strength. This simplification is accepted because a description of the strain-softening behaviour needs complex experiments and its implementation into numerical simulations is computationally expensive. Thus, the stress evolution calculated after the exceeding of the tensile strength is not realistic because cracking leads to a redistribution of the stresses. Nevertheless the calculated stress distributions can be used to identify zones with a high risk of cracking, which was shown in a comparative study in [16].

Because of the symmetry, only a quarter of the total system has to be modelled for the finite element analyses. Fig. 5 shows the finite element mesh for the construction phases of the middle wall and the outer walls together with the ceiling slab. All construction parts are assumed to be monolithically connected. The nodes at the lower surface of the underwater concrete slab are assumed to be fixed in each direction.

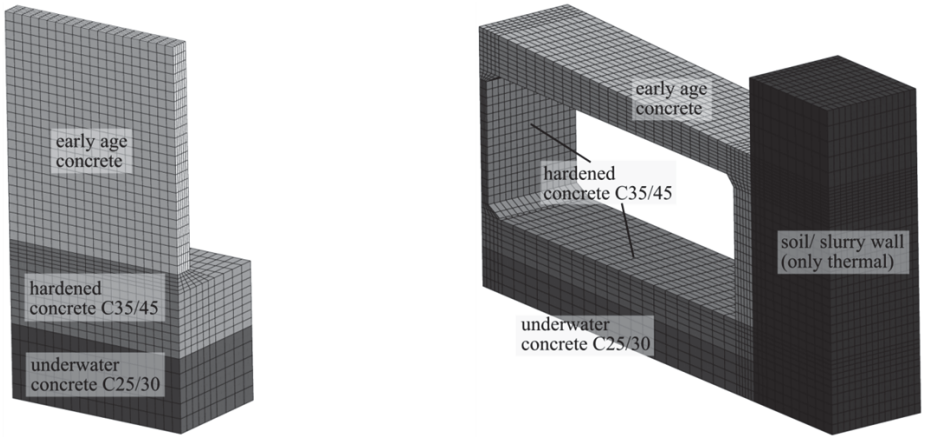

Figure 5: Finite element mesh for the casting of the middle wall (left) and the casting of the outer walls and the ceiling slab (right)

3.2 Temperature evolution

Fig. 6 shows the temperature distribution for the two investigated construction phases at the time when the maximum temperature is reached. The maximum temperature in the middle wall occurs 2 days after casting and reaches a value of 44.2°C. In the outer walls, the maximum temperature is 49.0°C which occurs at an age of 2 days and 6 hours. The maximum overall temperature occurs in the ceiling slab directly above the middle wall, because this part of the construction has the largest thickness. A maximum value of 57°C after 2 days and 20 hours was calculated for the ceiling slab.

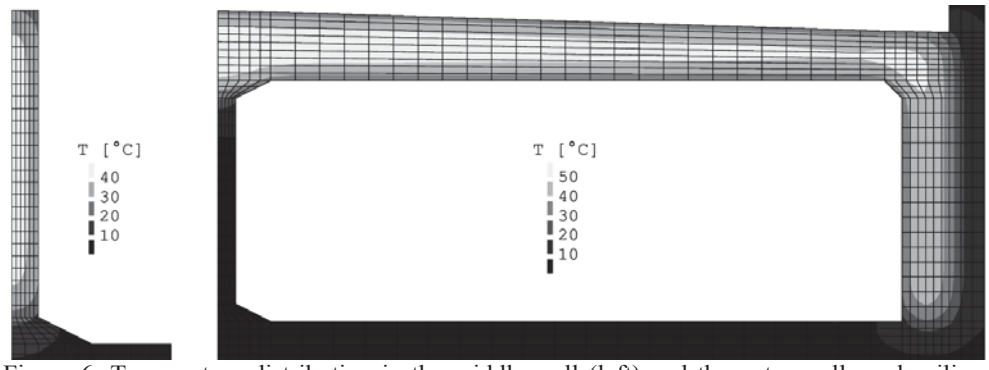

Figure 6: Temperature distribution in the middle wall (left) and the outer walls and ceiling slab (right) at the time when the maximum temperature is reached.

3.3 Stress evolution

The restraint of the thermal deformations by already hardened parts of the construction leads to the formation of compressive stresses in the warming phase and tensile stresses in the cooling phase. In addition, the temperature gradients between the core and the surface lead to

eigenstresses in the cross sections. The largest values of tensile stresses that may cause cracking are thus expected during or after the cooling down of the structure.
Fig. 7 shows the distribution of stresses in the longitudinal direction in the middle wall at an age of 28 days.

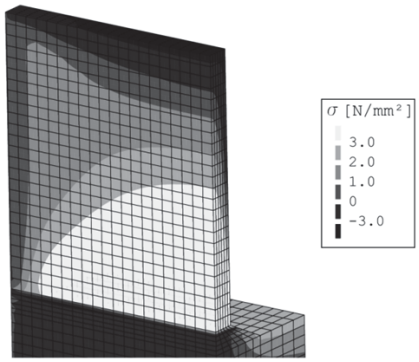

Figure 7: Stress distribution (longitudinal direction) in the middle wall 28 days after casting

Due to the restraint by the already hardened slab, the highest tensile stresses occur in the symmetry plane near to the joint. The large contraction caused by the cooling down and the shrinkage of the concrete leads to the excess of the tensile strength in big parts of the wall. From the results of the stress calculation, it has to be assumed that vertical cracks from the joint between slab and wall up to more than half of the height of the wall will occur.
A similar stress distribution can be observed in the outer walls, see fig. 8. The ceiling slab is restrained both in longitudinal and transverse direction. The highest tensile stresses in longitudinal direction occur directly above the walls, because these areas correspond to the areas with the maximum temperature and are at the same time highly restrained due to the monolithical connection with the walls. The part between the walls shows a lower tensile stress level that does not exceed the tensile strength. In the transverse direction, high tensile stresses that exceed the tensile strength occur nearly in the whole ceiling slab. These stresses are mainly caused by the rigid connections between the slab and the outer walls.

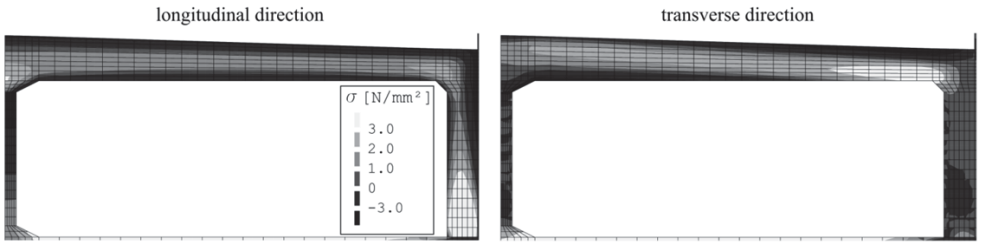

Figure 8: Stress distribution in the outer walls and ceiling slab 28 days after casting

The results of the stress simulations reveal that all parts of the tunnel construction are subjected to a high risk of cracking due to restraint. To limit the crack width and ensure the serviceability of the structure, the resulting stresses must be taken into account for the design

of the reinforcement. The design of the minimum reinforcement according to the German version of Eurocode 2 [17] is mainly affected by the tensile strength at the time of cracking that may be derived from the calculated stress evolutions. In the parts of the structure where no cracking has to be expected, the minimum reinforcement can be reduced related to the calculated stress level.
To ensure the correctness of the numerical investigations and the reinforcement design, monitoring measures for the temperature and strain evolution in the most critical parts will be installed in the construction phase.

4. Conclusions

In this paper, an application example for the control of early age cracking in a massive tunnel structure based on experimental investigations and numerical simulations was presented.
An experimental program was carried out to characterise the material behaviour of the concrete at early ages. This included the testing of the heat of hydration, the evolution of the compressive strength, tensile strength and Young's modulus and the autogenous shrinkage. For reasons of fire protection, a special concrete mix with PP-fibres was used. The high fly ash content in combination with a low heat slag cement lead to a relatively slow evolution of the mechanical properties and a long lasting growth of the compressive strength. The concrete showed a significant autogenous shrinkage that was compensated partly by a swelling at the beginning of the reaction.
The experimental results were used as input parameters for numerical simulations of the temperature and stress evolution in the tunnel structure. The results of the thermal analyses show that the maximum temperature inside the concrete structure goes up to 57°C for the assumed boundary conditions. The restrained contraction of the structure due to the intense cooling down and the simultaneous shrinkage of the concrete lead to high tensile stresses and consequently to a high risk of cracking.
To ensure the water tightness of the structure these stresses must be taken into account during the design of the reinforcement. Because the boundary conditions have been assumed for the worst case scenario, a high amount of reinforcement is necessary for crack width control. To ensure an economic design, further simulations will be carried out to check if a reduction of the reinforcement is possible when the construction process is optimised. This will include investigations on the influence of the climate during construction and the sequence of construction phases. Additionally, the temperature and strain evolution will be metrologically monitored during construction to check the reliability of the numerical results.

References

[1] De Schutter, G., Taerwe, L.: Degree of hydration based description of mechanical properties of early-age concrete. Materials and Structures 29 (1996), 335-344
[2] Gutsch, A.-W.: Properties of early-age concrete – experiments and modeling. Materials and Structures 35 (2002), 76-79.
[3] Schindler, A.K.: Effect of temperature on hydration of cementitious materials. ACI Materials Journal 101 (2004), 72-81.

[4] Lackner, R., Mang, H.A.: Chemoplastic material model for the simulation of early-age cracking: from the constitutive law to numerical analyses of massive concrete structures. Cement and Concrete Composites 26 (2004), 551-562
[5] Faria, R., Azenha, M., Figueiras, J.A.: Modelling of concrete at early ages: application to an externally restrained slab. Cement and Concrete Composites 28 (2006), 572-585.
[6] Briffaut M., Benboudjema F., Torrenti J.-M., Nahas G.: Effects of early-age thermal behaviour on damage risks in massive concrete structures. European Journal of Environmental and Civil Engineering 16 (2012), 589-605
[7] Buffo-Lacarrière L., Sellier A., Kolani B.: Application of thermo-hydro-chemo-mechanical model for early age behaviour of concrete to experimental massive reinforced structures with strain–restraining system. European Journal of Environmental and Civil Engineering 18 (2014), 814-827
[8] Gutsch, A.-W., Laube, M., Nothnagel, R.: Crack control in a massive reinforced concrete foundation slab as concrete sandwich element for a water basin. Proceeding of the 8th International Conference on Creep, Shrinkage and Durability Mechanics of Concrete and Concrete Structures (CONCREEP 8), Ise-Shima (2008), 647-654
[9] Gutsch, A.-W., Laube, M.: Crack control for the massive structures of the new central railway station in Berlin, Germany. Proceedings of the International Workshop on Control of Cracking in Early Age Concrete, Sendai (2000), 377-384
[10] Krauß, M., Rostásy, F. S., Budelmann, H.: Probabilistic concept for the validation of the effectiveness of countermeasures against early age cracking in massive concrete structures. Proceedings - Workshop Crack Risk Assessment of Hardening Concrete Structures, Trondheim (2005), 34-43
[11] Zeiml, M., Leithner, D., Lackner, R., Mang, H. A.: How do polypropylene fibers improve the spalling behavior of in-situ concrete? Cement and Concrete Research 36 (2006), 929-942
[12] Carino, N. J.: The maturity method: theory and application. Cement, Concrete and Aggregates 6 (1984), 61-73
[13] Gutsch, A.-W.: Creep and relaxation of early-age concrete. Creep, Shrinkage and Durability Mechanics of Concrete and other Quasi-Brittle Materials, Proceedings of the 6th International Conference CONCREEP-6@MIT, Cambridge (2001), 619-624
[14] Hermerschmidt, W., Budelmann, H.: Creep of early age concrete under variable stress, Proceedings of the 10th International Conference on Mechanics and Physics of Creep, Shrinkage, and Durability of Concrete and Concrete Structures (CONCREEP 10), Vienna (2015), 929-937
[15] Bažant, Z.P., Osman, E.: Double power law for basic creep of concrete. Materials and Structures 9 (1976), 3-11
[16] Honorio, T., Bary, B., Benboudjema, F.: Factors affecting the thermo-chemo-mechanical behaviour of massive concrete structures at early-age. Materials and Structures 48 (2015), 1-19.
[17] Eurocode 2: Design of concrete structures – Part 1-1: General rules and rules for buildings; German version EN 1992-1-1:2004 + AC:2010

International RILEM Conference on Materials, Systems and Structures in Civil Engineering
Conference segment on Service Life of Cement-Based Materials and Structures
22-24 August 2016, Technical University of Denmark, Lyngby, Denmark

COMPUTATIONAL PREDICTION OF RESTRAINT-INDUCED MACROCRACK PATTERNS IN CONCRETE WALLS

Agnieszka Knoppik-Wróbel [(1)], Dirk Schlicke [(2)]

(1) Silesian University of Technology, Gliwice, Poland
(2) Graz University of Technology, Graz, Austria

Abstract
Two independent approaches to predict the restraint-induced macrocrack patterns in walls have been recently proposed by the authors [1, 2]. The model of *Knoppik-Wróbel and Klemczak* [1] is fully numerical whereas the approach of *Schlicke and Tue* [2] is a simplified engineering model on the basis of analytical considerations. Both approaches are macroscopic solutions aiming at a robust prediction of macrocrack patterns with respect to its main driving forces. Both accept a certain level of simplification to ensure a broad applicability, however, their reliability was verified by satisfying results of recalculations of practical observations, as presented e.g. in [4, 6].This contribution presents both approaches and compares the results of each for a given example. Besides computational aspects, mechanical background of the restraint-induced cracking is outlined with special regard to relevant material properties, geometry and restraint situations.

1. Fundamentals on hardening-induced macrocrack formation in walls on foundations

1.1 Driving forces

Concrete is a material which gains its strength and stiffness due to cement hydration. In concrete elements with significant dimensions this leads to remarkable temperature histories, beginning with self-heating due to the heat release of the highly exothermal hydration and limited conductivity of concrete. Subsequently, the hydration reaction rate decreases and the element cools down to the ambient temperature level. In case of walls on foundations, the accompanying temperature deformations are restrained by the rigid connection between both components, which leads in the warming phase to compression in the wall. By cooling down, the imposed compressive stresses are decreased again. However, since also the concrete stiffness evolves strongly at the same time, compressive stresses due to warming are significantly smaller than tensile stresses due to cooling down. Autogenous shrinkage, decreasing viscoelasticity of aging concrete and the difference between concrete temperature

at setting and ambient temperature level increase these tensile stresses additionally. The final resultants of these stresses are a tensile force and a positive bending moment in the cross section of the wall (N_W, M_W) which are superimposed by negative bending moment over the combined cross section of the wall and foundation due to activation of self-weight (M_g). Fig. 1 illustrates this context schematically.

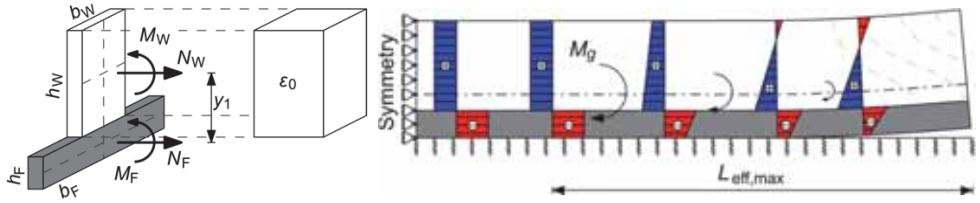

Figure 1. Hardening-induced stress resultants in a wall on a foundation

Besides, transient influences on the temperature and moisture field of the cross section cause internal restraint. Temperature and drying differ significantly between the surface and the interior of the wall, but the accompanying deformations are fully restrained in the uncracked state since the cross section remains plane, which leads to self-balanced stresses or the so-called *Eigenstresses*. For better understanding, Fig. 2 shows the described parts of a hardening-induced stress distribution.

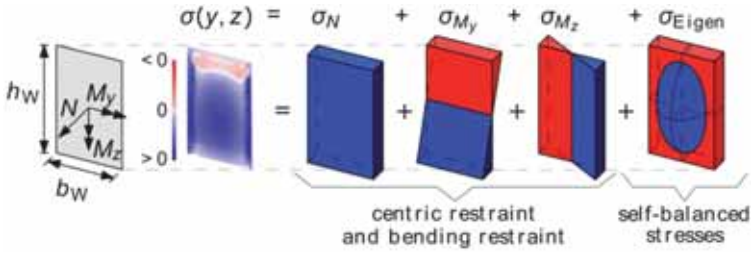

Figure 2. Hardening-induced stress resultants in a wall on a foundation

1.2 Crack formation process

From macroscopic point of view, crack formation starts if the present tensile strength is exceeded in a single material point ($\sigma(y,z) > f_{ct}(y,z)$). As long as Eigenstresses are predominant in this stage, only microcracking – respectively small, locally restricted cracks – occur. However, this type of cracking comes along with softening of the cross-section and beneficial compressive Eigenstresses decrease. In the worst case, only stresses due to stress resultants remain. If these stresses reach the tensile strength of the cross-section, macrocracking is to be expected ($\sigma_N + \sigma_{My} + \sigma_{Mz} > f_{ctm}$). Figure 4 in [3] illustrates this context.

The risk of macrocracking is usually reduced by Eigenstresses, however, as soon as microcracking occurs, the risk of macrocracking increases. This effect is intensified by further Eigenstresses over the width, which are not illustrated in Fig. 2 for clearness reasons.

With respect to the final stress distribution without Eigenstresses as shown in Fig. 1 (right), the formation of macrocracks starts theoretically in the bottom part of the wall. But in these

parts the stiffness of the foundation will reduce the crack width considerably. Only if the macrocrack proceeds over the height of the wall, they become visible. For an efficient design it is very desirable to know whether these macrocracks will stop at a certain height or proceed over the whole wall as well as what is the distance to the next macrocrack. Thus, significant factors influencing these aspects are discussed in the following section.

1.3 Relevant influences on the final macrocrack pattern

The material, technological and environmental conditions determine mostly the magnitude of strains and strain rate, and as such define whether the cracks form or not. The final pattern of cracks depends mostly on geometry, dimensions and restraint conditions.
In general, the maximum tensile stresses in a base-restrained element occur in the plane of symmetry in length direction. This is also where first cracks are formed and where they reach the greatest heights. For the same material, technological and environmental conditions the height of this crack would depend solely on the restraint situation dependent on the *EA* and *EI* as well as *L*/*H* ratios.
Depending on the cracking potential of hardening concrete and geometrical characteristics of the wall, further primary cracks can successively develop in the wall. In shorter walls, these cracks reach lower heights due to a smaller effective *L*/*H* ratio. The cracks are usually vertical in the central part of the wall and slanted near the edges where the rotational restraint becomes more significant. Horizontal cracks can be formed at the joint if shear stresses at the joint exceed the bond strength. A comprehensive description of cracking pattern in walls on foundations is presented in chapter 2 of [4].

1.4 Modelling

The modelling of hardening-induced macrocrack patterns of walls on foundations is a complex matter. The major challenge is to combine complex time- and stress-dependent material behaviour with crack formation on structural level. Only a modest number of contributions exist, whereby the fundamental work by *Rostasy and Henning* [5] is certainly to be seen as one of the most important ones. Next to this, the authors of this paper proposed two approaches independently of each other. Other pertinent proposals are not known.

2. Numerical prediction of hardening-induced macrocrack formation in walls

2.1 Model used

The model used was based on the proposal of *Knoppik-Wróbel and Klemczak* [1]. Calculations were performed with a computer implementation of this phenomenological model that allows for thermo–mechanical analysis of walls on foundation taking into account the effect of hydration heat, temperature development, ageing, creep, soil–structure interaction and behaviour of concrete after damage.
The analysis was performed in two steps. In the first step non-linear and non-stationary thermal fields were determined in concrete elements and subsoil, respectively:

$$c_b \rho \dot{T} = \mathrm{div}(\lambda \, \mathrm{grad}\, T) + q_v(t, T) \quad (1)$$

$$c_b \rho \dot{T} = \mathrm{div}(\lambda \, \mathrm{grad}\, T) \quad (2)$$

where T is temperature, K; c_b is specific heat, kJ/(kg·K); ρ is density, kg/m^3; λ is thermal conductivity, W/(m·K) and $q_v(t,T)$ is the rate of hydration heat generated per unit volume of concrete, W/m^3. The function of hydration heat time-development was described with the approximation function of equivalent age, t_e:

$$Q(t,T) = Q_{tot} e^{[-a_1 t_e{}^{a_2}]} \tag{3}$$

where Q_{tot} is the total amount of hydration heat, J/g, and a_1, a_2 are calibration coefficients dependent on the type of cement. 3rd type boundary conditions were used. The aim of this study was to investigate mechanical behaviour of the wall, thus physical analysis was limited to thermal analysis. The authors are, however, aware that other influences such as autogenous and drying shrinkage as well as coupling of these phenomena are not less important.
The imposed thermal strains were treated as volumetric strains and they were calculated based on the changes of temperature:

$$\mathrm{d}\boldsymbol{\varepsilon}_n = [\mathrm{d}\varepsilon_{n,x} \quad \mathrm{d}\varepsilon_{n,y} \quad \mathrm{d}\varepsilon_{n,z} \quad 0 \quad 0 \quad 0] \tag{4}$$

$$\mathrm{d}\varepsilon_{n,x} = \mathrm{d}\varepsilon_{n,y} = \mathrm{d}\varepsilon_{n,z} = \alpha_T \, \Delta T \tag{5}$$

where α_T is the coefficient of thermal expansion, 1/K.
Viscoelasto–viscoplastic material model with the modified 3-parameter Willam–Warnke failure criterion (MWW3) was used for hardening concrete following *Klemczak* [7] and elasto–plastic material model with the modified Drucker–Prager failure criterion was used for soil (see [4]). Detailed formulations of these models are given in [1] and [4]. The possibility of crack occurrence was defined with the damage intensity factor (*DIF*):

$$0 \le DIF = \frac{\tau_{\mathrm{oct}}}{\tau_{\mathrm{oct}}^f} \le 1 \tag{6}$$

Graphical interpretation of *DIF* is shown in Fig. 3. When *DIF* = 1, it is equivalent to formation of a crack in the direction perpendicular to the direction of the principal tensile stress. Smeared cracking pattern was used. When failure is reached, material exhibits softening behaviour. In the model, deviatoric and volumetric softening was applied with hardening and softening laws adopted following *Majewski* [8].

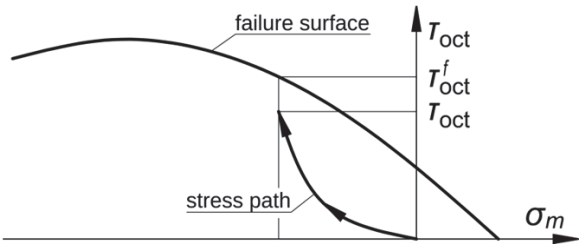

Figure 3. Graphical interpretation of damage intensity factor (*DIF*)

2.2 Reference case and limitations of the model

For the reference case, a wall on foundation was chosen with the dimensions as specified in Fig. 4. Material, environmental and technological data used are given in Tab. 1. The wall was concreted 3 weeks after the foundation. The structure was kept in formwork during the whole analysis. The initial temperature of concrete was T_i = 25°C and the ambient temperature was T_a = 20°C. The initial temperature of soil was equal to the ambient temperature. Final geometry of the wall and input data were chosen after extensive parametric study.

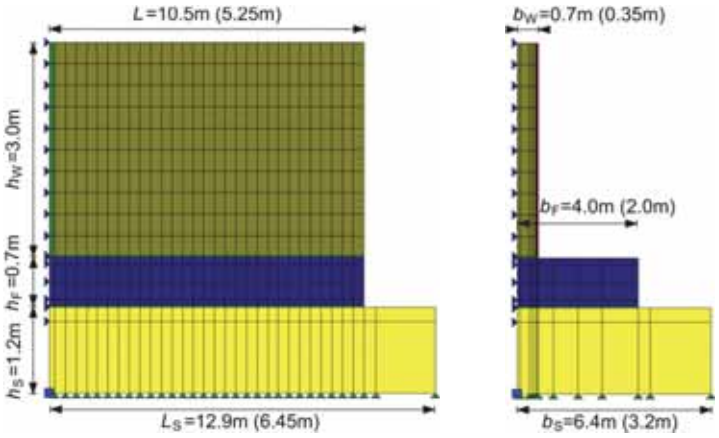

a) longitudinal view *yz* plane, $x = 0$ b) transverse view *xy* plane, $z = 0$

Figure 4. Analysed wall on foundation: geometry and FE mesh for ¼ of wall. Reference case

Table 1: Parameters used in the study.

THERMAL PROPERTIES		
parameter	**unit**	**value**
Thermal conductivity, λ	W/(m·K)	2.6
Specific heat, c_b	kJ/(kg·K)	1.0
Density, ρ	kg/m^3	2500
Amount of cement, C_c	kg/m^3	340
Total heat of hydration, Q_{tot}	J/g	400
Coefficients a_1 and a_2	-	470, -0.1
Coefficient of heat exchange, α_p	W/(m^2·K)	4.0
Thermal expansion coefficient, α_T	1/K	10^{-6}
MECHANICAL PROPERTIES		
parameter	**unit**	**value**
Final value of compressive strength, $f_{c,28}$	MPa	38
Final value of tensile strength, $f_{t,28}$	MPa	2.9
Final value of modulus of elasticity, $E_{c,28}$	MPa	33
Coefficient *s* for cement	-	0.25
Coefficient *n* for tensile strength	-	0.6
Coefficient *n* for modulus of elasticity	-	0.4

During the parameter study some limitations of the model were encountered which needed to be addressed. The following issues should be mentioned:

Finite Element mesh. To capture the most important phenomena, the mesh was densified in the areas of expected damage intensification, i.e. at the joints between the subsequent elements (soil – foundation – wall) and over the width of the wall. Especially a small element size in the core of the wall was needed to realistically simulate the decrease of Eigenstresses during the cracking process. In this regard the model is mesh-dependent, so the same size of finite elements was used in all the analysed models to allow for comparison among them.

Group control of elements. In the model, mechanical properties of hardening concrete (strength, elastic modulus) vary in time according to the assumed ageing functions but, because of computational limitations, the aging of each element could not be simulated independently. To still achieve representative results, groups of elements with comparable aging were defined and mechanical properties assigned according to the mean values of the equivalent age. With respect to the very smooth cooling phase (the wall was continuously kept in the formwork for the whole time), it was adequate to divide the wall only into 4 groups: groups for surface elements (to the depth of 5 cm) and core elements. The elements at the axis of symmetry at the length were also assigned to 2 separate groups to avoid numerical problems at the beginning of cracking. Besides, two additional groups of contact elements were introduced: between the soil and the foundation and between the foundation and the wall. The groups of elements are marked with different colours in Fig. 4.

Cracking. The model assumes smeared cracking, whereby a set of finite elements in which *DIF* reached 1 in tension was considered as cracks. The first crack was always induced in the plane of symmetry by a reduced tensile strength of $0.95 \cdot f_{t,28}$, which ensured the worst-case scenario to happen.

Softening behaviour. If the actual stress state of an element reaches the failure surface, *DIF* reaches the value of 1 and concrete exhibits softening behaviour in this element according to the assumed softening law. Although this softening behaviour can be observed in the results of this study, the extent of this effect seems, from the authors' point of view, to be underestimated. Thus, verification and recalibration of the softening function is required before further investigations.

2.3 Results

Figures 5 and 6 show development of cracks indicated by damage intensity factor (*DIF*) in the reference wall (of 10.5 m length). Areas of expected cracks are marked in red. Figure 5 shows a map of *DIF* right before the primary crack starts to develop in the axis of symmetry of the wall. It can be observed that some locally restricted damage has already developed in the interior of the wall which complies with the before explained influence of Eigenstresses.

Directly after the state of Fig. 5 a primary crack forms in the axis of symmetry between 16 and 18 days. The final state is shown in Fig. 6 and it can be seen that this crack goes through the whole thickness of the wall. The softening behaviour which can be observed in the vicinity of this crack starts directly at the beginning of formation of this crack at 16 days. Moreover, the crack develops from the interior towards the surface of the wall as the wall is kept in the formwork, so any pre-damage on the surface due to temperature shock after early stripping was avoided. The crack reaches on average ~50 % of the height of the wall. As it should be expected from the length-to-height ratio of the wall (L/H = 3.5), the crack does not

reach whole height and no further primary cracks are formed. Besides, a horizontally running damage intensity concentration can be observed near the edge of the wall due to shear.

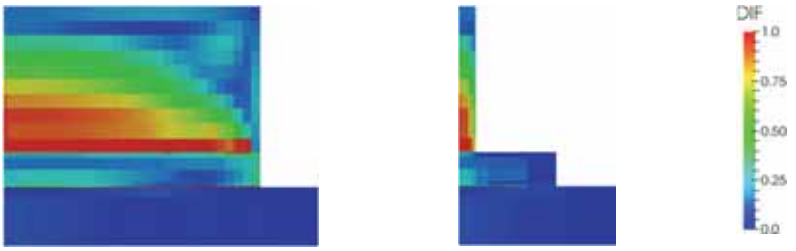

a) *yz*, $x = 0$ (interior) b) *xy*, $z = 0$ (axis of symmetry)

Figure 5. Map of *DIF* in the $L = 10.5$ m wall at the age of wall $t = 15.5$ days

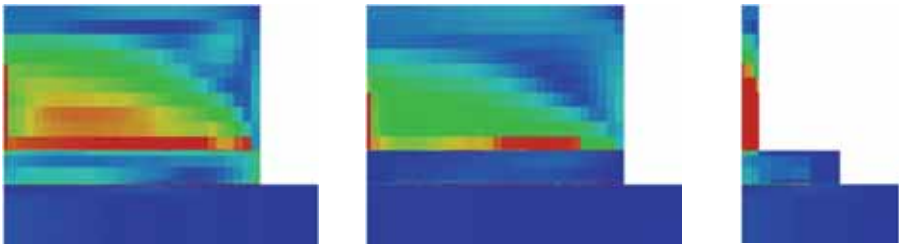

a) *yz*, $x = 0$ (interior) b) *yz*, $x = 0.5\ b_W$ (surface) b) *xy*, $z = 0$

Figure 6. Final map of *DIF* in the $L = 10.5$ m wall at the age of wall $t = 18$ days

Figures 7 to 9 present analogical simulation of damage development in a long wall with the length of 21 m ($L/H = 7$, so twice of the reference case). In Fig. 7 it can be seen again that when the first primary crack develops, softening occurs in its vicinity. It must be noted that the crack in the long wall starts to develop sooner than in the short wall, at the age of wall of 4.5 days. The crack progresses at the thickness of the wall and at its height. It gets its final shape at the age of 8.7 days when it reaches whole height of the wall, which was to be expected for the higher *L*/*H*.

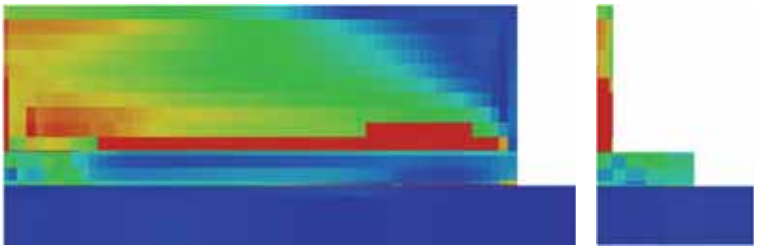

a) *yz*, $x = 0$ (interior) b) *xy*, $z = 0$

Figure 7. Map of *DIF* in the $L = 21$ m wall at the age of wall $t = 5$ days

Figure 8 shows the *DIF* map at the age of 12 days. Intensive damage was indicated in the interior of the wall which represents microcracks due to Eigenstresses. Besides, a fully-

developed separating crack is visible at the surface in the symmetry axis which "splits" the wall in two halves. After the first primary crack, the remaining half of the wall still has an L/H of 3.5 so ongoing cooling forms another primary crack at the age of 12.7 days (Fig. 9).

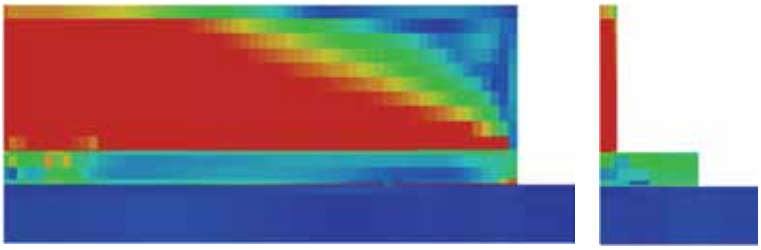

a) *yz*, x = 0 (interior) b) *xy*, z = 0

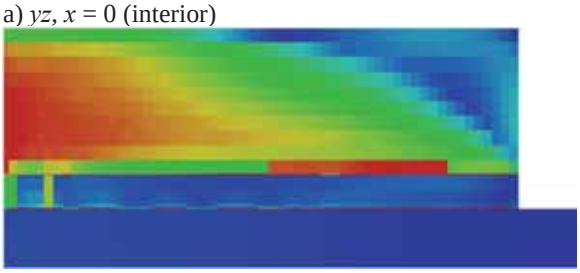

c) *yz*, x = 0.5 b_W (surface)

Figure 8. Map of *DIF* in the L = 21 m wall at the age of wall t = 12 days

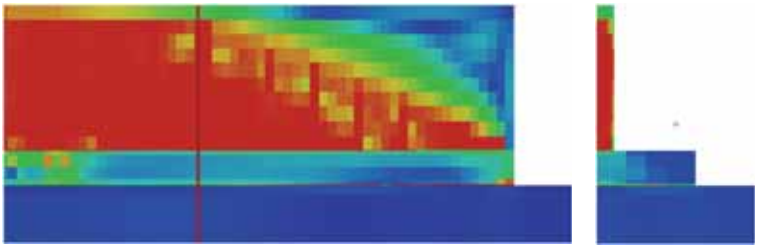

a) *yz*, x = 0 (interior) b) *xy*, z = 4 m

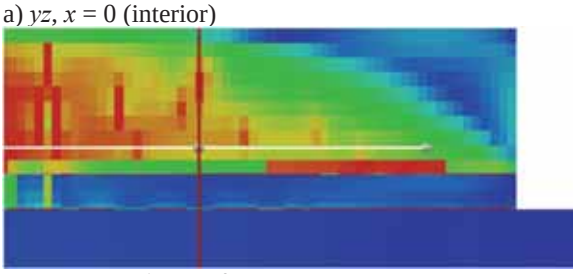

c) *yz*, x = 0.5 b_W (surface)

Figure 9. Final map of *DIF* in the L = 21 m wall

The distance from the axis of symmetry to this crack amounts ~4 m, which is ~1.3·h_W. Softening is observed in the vicinity of this crack, too. In contrast to the corresponding wall of

L/H = 3.5, this crack reaches on average ~80 % of the height of the wall. This difference may result from the fact that the crack is formed earlier, so the strength of the concrete is lower.

3. Analytical prediction of hardening-induced macrocrack formation in walls

The analytical approach to determine the macrocrack pattern of walls on foundations was comprehensively explained by *Schlicke and Tue* in [2]. The basic idea is to relate the distance between primary cracks to the length needed to build up the restraint stresses again. From the theoretical point of view, this length strongly correlates with the height which the primary crack reaches. Thus, the stress at the top of the macrocrack σ_R will be determined according to the remaining concrete area above the top of the crack h_R to compare the resulting curve with the present tensile strength f_{ct}. In all cases where $\sigma_R(h_R)$ falls below the tensile strength, a stop of the cracking will be assumed at this height; in any other case a continuous crack over the wall height will be assumed.

If the crack height is known, the distance between the geometrically set primary cracks will be assumed to have a size of $l_{cr} = 1.2 \cdot h_{cr}$. The application of this approach for the numerically studied systems is shown in Fig. 10. The considered stress resultants were determined fully analytically on the basis of an equivalent deformation impact ε_0 taking into account the temperature field changes due to hydration heat release uniformly distributed in the cross section, stiffness evolution and viscoelasticity for the given material parameters in Tab. 1. Details on the approach used are given by *Schlicke* in [9].

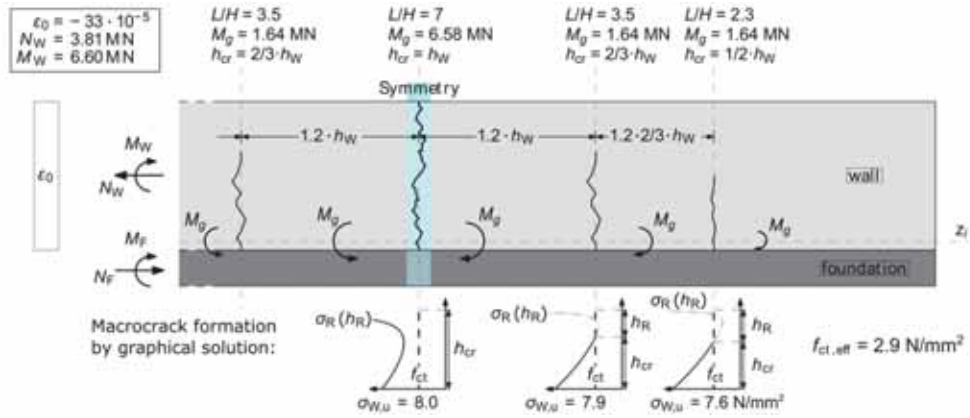

Figure 10. Analytically determined primary crack patterns of the numerically studied cases

4. Discussion and conclusions

The paper presents a comparative study on early-age cracking process with two independent methods recently proposed by the authors [1, 2]. Although the proposed models accept a certain level of simplification, the comparative study gives an acceptable agreement. Both

solutions indicate a separating crack over the whole height in the symmetry axis of the wall with $L/H = 7$ as well as a further stopping crack in the distance of $l_{cr}=(1.25\pm0.05)\cdot h_W$ with a height of ~2/3 h_W. A questionable continuation of the analytical approach would indicate another stopping crack at $L/H = 2.3$ with a height of $1/2\,h_W$, but this is unlikely due to the weaknesses of the remaining wall length.

From the authors' point of view the achieved consistency between the numerical and analytical approach confirms the appropriateness of the included simplifications. In detail this refers to the role of Eigenstresses, which are remarkably reduced when any microcracking occurs, so that the process of macrocrack formation is driven predominantly by the stress resultants of the uncracked state AND the conceptual model to derive the distance between the primary cracks from the height reached by the previous crack is adequate. Of course, reinforcement will decrease this distance slightly and cracks which just reached full separation without reinforcement might be stopped somewhat before.

Apart from the comparison between the two models, the insight into the structural behaviour of a wall on a foundation is very valuable for deformation based design concepts as presented by *Schlicke and Tue* in [3] or *Knoppik-Wróbel* in [4].

References

[1] Knoppik-Wróbel, A. and Klemczak B., Degree of restraint concept in analysis of early-age stresses in concrete walls, Engineering Structures 102 (2015), 369-386, DOI: 10.1016/j.engstruct.2015.08.025
[2] Schlicke, D. and Tue, N. V., Minimum reinforcement for crack width control in restrained concrete members considering the deformation compatibility, Structural Concrete 16 (2015), 221-232, DOI: 10.1002/suco.201400058
[3] Schlicke, D. and Tue, N. V., Crack width control – verification of the deformation compatibility vs. covering the cracking force, Proceedings of MSSCE2016/Service Life Segment, Lyngby, Denmark (2016)
[4] Knoppik-Wróbel, A., Analysis of early-age thermal–shrinkage stresses in reinforced concrete walls, PhD thesis, Silesian University of Technology (2015) DOI: 10.13140/RG.2.1.2970.8407
[5] Rostasy, F. S. and Henning, W., Zwang und Rissbildung in Wänden auf Fundamenten, Heft 407. Deutscher Ausschuss für Stahlbeton (1990)
[6] Schlicke, D., Tue, N. V., Klausen, A., Kanstad, T. and Bjøntegaard, Ø., Structural analysis and crack assessment of restrained concrete walls – 3D FEM-simulation and crack assessment, Proceedings of the 1st Concrete Innovation Conference, Oslo, Norway (2014)
[7] Klemczak, B., Adapting of the William–Warnke failure criteria for young concrete, Archives of Civil Engineering 53(2) (2007), 323-339
[8] Majewski, S., MWW3 – elasto–plastic model for concrete, Archives of Civil Engineering 50(1) (2004), 11-43
[9] Schlicke, D., Mindestbewehrung für zwangbeanspruchten Beton, PhD thesis, Graz University of Technology (2014)
http://lamp.tugraz.at/~karl/verlagspdf/buch_schlicke_25052016.pdf

International RILEM Conference on Materials, Systems and Structures in Civil Engineering
Conference segment on Service Life of Cement-Based Materials and Structures
22-24 August 2016, Technical University of Denmark, Lyngby, Denmark

SOME EXAMPLES ON SHRINKAGE RESTRAINT EFFECTS ON CONCRETE AND CONCRETE STRUCTURES

Farid Benboudjema[(1)]

(1) LMT-Cachan/ENS-Cachan/CNRS/Université Paris Saclay

Abstract
Although concrete is the most widely-used materials in construction in the world, its delayed behavior (shrinkage and creep) is still poorly understood. Shrinkage has negative impacts on concrete structures: cracking, prestress loss etc. Shrinkage (autogeneous, drying and thermal) restraint occurs at different scales. At the mesoscopic scale, shrinkage of cement paste is restrained by aggregates: debonding at cement paste/aggregate interface and inter-granular cracks may occur. At the macroscopic scale, gradients of temperature and relative humidity, restraint by adjacent elements (previously cast slabs, concrete lift etc.) and by reinforcement may induce also debonding and cracking. Effects are various. A decrease of stiffness and load bearing capacity occurs. Penetration of aggressive species (carbonation, chloride etc.) is promoted due to the increase of transport properties (permeation and diffusivity). Finally, if a tightness is required and ensured only by concrete (nuclear reactor containment, tunnel lining, dams, wastewater treatment plant, etc.), it can be compromised. Some examples will be presented through experiments and numerical simulations, and will concern early-age and long term behavior, at different scales. A focus will be addressed on some issues still unresolved.

1. Introduction

At early-age in massive concrete structures, cracking may occur during hardening. Indeed, hydration is an exothermic chemical reaction (temperature in concrete may overcome 60°C [1-3]. Therefore, if autogenous and thermal strains are restrained (self restraint, construction joints), compressive stresses and then tensile stresses rise, which may reach the concrete strength and induce cracking in a real structure. For instance, Ithuralde [3] observed several crossing cracks (opening up to 0.5 mm) in a 1.2m width concrete wall (representative of French nuclear power plant containment), cast on a concrete slab. At long term, since drying is not uniform, gradient of drying shrinkage induces tensile stresses at the surface equilibrated

by compressive stresses in the core. For structures like tanks or nuclear containment vessels, this cracking may significantly increase concrete permeability and reduce tightness. For other massive structures (bridges, tunnels…), the serviceability may be reduced due to the penetration of aggressive species (such as carbon dioxide, sulfate and chloride ions).

Cracking highly depends on creep (essentially basic creep in massive structures). However, the question whether creep strains are the same in compression (such tests are "classical") and in tension (difficult to perform) is not fully resolved. This literature review highlights the fact that there is no consensus in scientific community regarding basic creep in tension. Moreover, at early age, concrete structures can reach 60°C and thus, an important effect of this temperature evolution is expected on the concrete behaviour and especially on the basic creep strains rate.

The behaviour of heterogeneous materials, as cement-based materials (concrete, mortar) depends on the behaviour of each phase of this material (cement paste and aggregates mainly), which can be very different depending on the loading. Tensile stresses are thus induced in the cement paste surrounding aggregates. They are also counterbalanced by compressive stresses in the aggregates (self-equilibrated state of stresses again), leading to debonding at the cement paste/aggregate interfaces and to the growth of intergranular cracks. To accurately predict the mechanical consequences of induced cracking, it is required to develop of a powerful numerical tool to account for the influence of drying loadings on the mechanical response. Indeed, several features should be considered, such as, drying, drying shrinkage, basic and drying creep (which relaxes inducing stresses), cracking in tension.

The first part will be devoted to modelling at macroscopic scale. Influence of boundary conditions and basic creep strains at early age (age effect and temperature effect), including coupling between cracking and creep, and dissymmetric effect in compression/tension. This study is based on the RG8 experiment (CEOS national project, [4]) and on a concrete mix which is representative of a nuclear power plant which are used for numerical simulations. Effectf of drying on the behavior of reinforced concrete structures will be also studied.

In the second part, restraint of shrinkage by aggregates will be investigated. Numerical simulations are compared to experimental results using digital images correlations on controlled heterogeneous specimens from a cylindrical aggregates obtained by coring and a cement paste cast around. Digital images correlation allows for extracting cracking patterns as crack openings and displacement field (after post processing), which is more exhaustive than the use of global data from local sensors (drying shrinkage for instance). The numerical simulations show the great and positive impact of creep strains, which must be taken into account. If creep is not taken into account, cracking is overestimated largely (which may induce a large decrease of mechanical properties) after drying, which is not consistent with experimental data.

2. Macroscopic scale

The influence of the delayed strains is numerically quantified on the studied concrete structures. The total concrete strain is calculated according to:

$$\varepsilon = \varepsilon_{elas} + \varepsilon_{ds} + \varepsilon_{au} + \varepsilon_{th} + \varepsilon_{bc} + \varepsilon_{dc} + \varepsilon_{ttc} \quad (1)$$

Where ε_{elas}; ε_{sh}; ε_{au}; ε_{th}; ε_{bc}; ε_{dc}; ε_{ttc} are the respective elastic, drying shrinkage, autogeneous shrinkage, thermal strain, basic creep, drying creep strain and thermal transient creep. Classical models for drying, hydration and temperature predictions are used.
The damage model proposed by Mazars [5] has been slightly modified [6]. In this model, a scalar mechanical damage variable is associated to the mechanical degradation process of concrete induced by the development of microcracks. The relationship, between apparent stress $\boldsymbol{\sigma}$, effective stress $\tilde{\boldsymbol{\sigma}}$, damage D (depending also on tensile strength f_t), elastic stiffness tensor $\mathbf{E}$ and the previously defined elastic strain, reads:

$$\sigma = (1 - D)\tilde{\sigma} \text{ and } \dot{\tilde{\sigma}} = E\dot{\varepsilon}_{elas} \quad (2)$$

According to the softening behavior, an energetic regularization [7] prevents of mesh dependency. All the main constitutive relationships can be found in [2] and [10].

2.1. Early-age behaviour

2.1.1 Influence of thermal boundary conditions

Investigating the maximal temperature reached at early age can be a good way to study the massive structure sensibility to cracking (due to restrained thermal and autogeneous shrinkage) and delayed ettringite formation (DEF). Besides, the early age cracking can be a consequence of a high temperature gradient between the core and the surface of an element. Both effects have been studied for a massive wall (thickness: 1.2m; height: 2m; length: 20m, see Figure 1) and with the assumption that the wind direction is parallel to the wall.

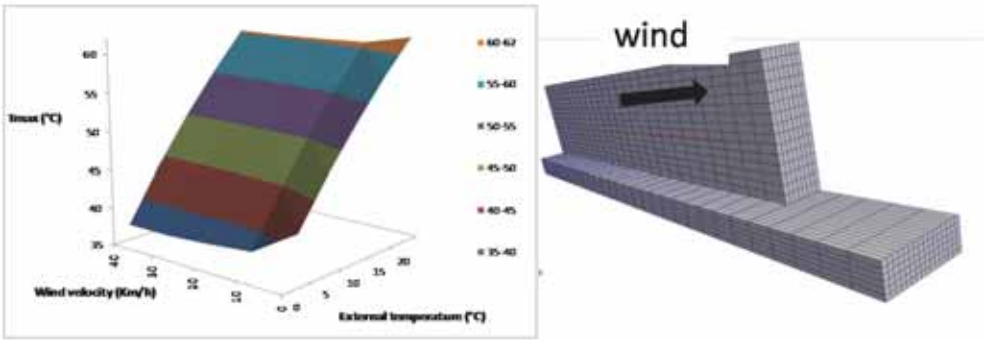

Figure 1: Maximal temperature Tmax reached in a massive wall (thickness 1.2m) with respect to wind velocity and external temperature.

In this study, only the external conditions (wind velocity and external temperature) are sources of variability but for an application to a real case, materials properties variability must

also be taken into account (total heat release, concrete thermal conductivity,… [8]). Besides, the initial concrete temperature has a significant effect on the maximal temperature but to avoid this third parameter, we used a relationship between the external temperature T_{ext} and the initial concrete one T_{ini}, proposed by Torrenti and Buffo-Laccarrière [8].

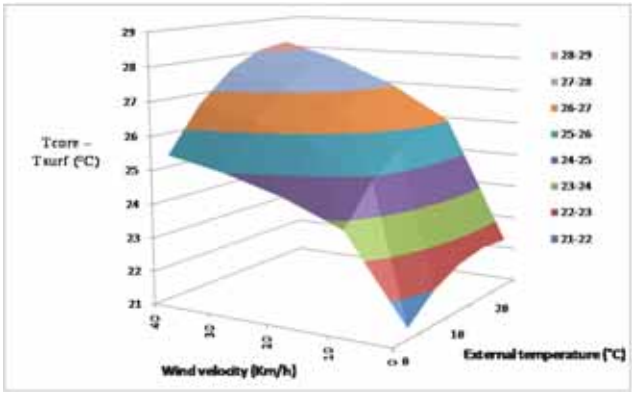

Figure 2: Temperature difference between the core and the surface in a massive wall (thickness 1.2m) with respect to the wind velocity and of the external temperature.

The results of this study are resumed on figure 1 and 2. One can see on the figure 2 a slight effect of wind velocity on maximal temperature. This can be explained by the fact that, as the thermal concrete conductivity is rather low, the thermal exchange conditions at the core are close to adiabatic ones. On the contrary, the evolution of the maximal temperature due to the external temperature is quasi-linear. This can be explained by the fact that the initial temperature is assumed to be a linear function of the external temperature. On contrary to the previous results, the wind velocity has a high effect on "temperature gradient" (Figure 2), whereas the external temperature has a slight one. This indicates that with regards to these two phenomena, there are no optimal casting conditions (autogenous and drying shrinkage are not considered).

2.1.2 Dissymmetry of creep: effect on stresses

There is no consensus on the tensile creep of concrete at early-age and at long term. In most cases, only compressive creep tests are performed, since they are easier to perform. Besides, stresses (compression/tension) may change during service life of concrete structures. In order to show the impact of this dissymmetrical behavior, material parameters were identified on experimental results for creep of Briffaut et al. [9] (see the results in Figure 3 at left). Then, numerical simulations were performed on a 1.2 m thick concrete structure [3]. The results shown in Figure 3 (right) highlight a difference which is greater than the difference between the results obtained with and without the taking into account or not of creep (after 10 days). However, the difference occurs only after 4 days.

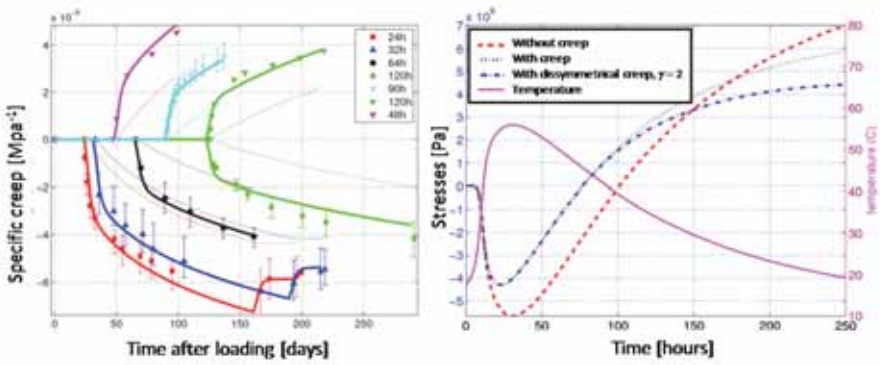

Figure 3: Comparison between simulated (thick lines) and experimental evolutions of strains (left). Stress and temperature evolutions versus time in a 1.2 m thick massive wall [3] (right).

2.1.3 Simulation of RG8 specimen: influence of creep and creep/cracking coupling

Numerical simulations are performed on a large beam specimen realized for ConCrack international Benchmark (for Control of Cracking in Reinforced Concrete Structures, [4]). After casting, the structure is thermally isolated and protected from drying during 48 hours. Then, the isolation and the formwork are removed and the structure is kept during two months outside. During all the test, longitudinal strains of the structure are globally restrained by two metallic struts.

Numerical simulations on an active thermal ring test [9] and on RG8 beam [4] show that the coupling between creep and cracking should be taken into account in order to retrieve experimental simulations (i.e. the occurrence of 1 crack at least). Indeed, as displayed in Figure 4 and Table 1, no cracking is predicted with an approach where creep is not coupled with damage (3 cracks appear during the experiment at different times). Taking into account creep reduces drastically the crack opening. However, it should be emphasized that only 2 (considering the symmetry) cracks occur, as 3 cracks (the first one in the center of the specimen) have been reporting during the experiments.

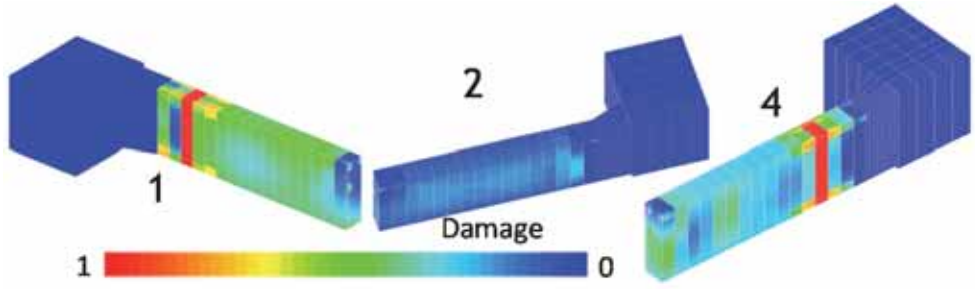

Figure 4: Damage field on the RG8 beam for different creep approach: 1 = without creep, 2 = Creep without coupling with cracking, 3&4 = creep coupled with cracking for 2 different meshes (3 is not displayed but it is very similar to 4).

Table 1: Predicted crack opening for different models

Model	Without creep (1)	Creep without coupling with cracking (2)	Creep coupled with cracking, mesh 1 (3)	Creep coupled with cracking, mesh 2 (4)
Crack opening [μm]	359	0	158	152

2.2. Effect of drying at long term

The effect of drying shrinkage is illustrated on a RC-tie specimen (w/c = 0.48, section of 10x10 cm², 1 m long reinforced with a steel bar of 12 mm diameter, see [10]). Ninety days of drying are taken into account (only a quarter is meshed). Figure 5 shows the damage and axial stress fields after 90 days. Along the interface, it can be observed a slight concrete degradation (*D* around 0.3) due to the strain incompatibility between concrete and the couple rebar-interface. However, considering a uniform drying shrinkage strain, the rebar restraint induces significant tensile quasi-uniform axial stresses in the specimen. The axial stresses are equal to about 0.75 MPa (=1/4 *of* the tensile strength). The mechanical response of the tension test will be therefore influenced by the ‘‘initial’’ state of stress in the specimen.

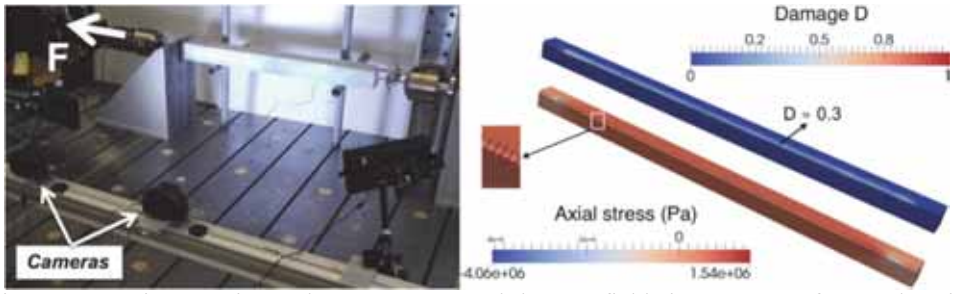

Figure 5: RC tie: experimental set-up; stress and damage fields in concrete, after 90 days in drying conditions (quarter of structure) – the steel rebar and the interface are not represented.

The tension test is then numerically carried out. The mechanical response is plotted in Figure 6. The response is greatly impacted by the drying shrinkage strain in the specimens. The first cracking force decreases by about 30%, in accordance with the initial internal stresses before loading. The first crack establishes the course of the further crack initiations. It is also observed a slight loss of initial stiffness if drying. That is explained by concrete degradation at the steel–concrete interface before loading (Fig. 5).

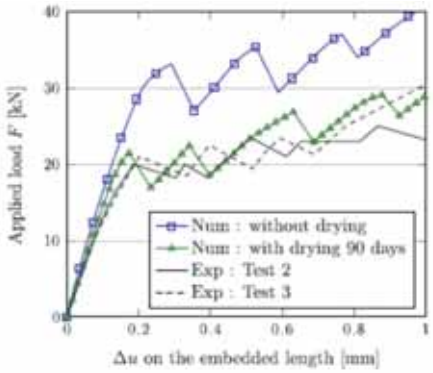

Figure 6: Numerical tension test on RC ties, with or without considering drying (among 90 days).

Finally, the presented results show the importance of considering the delayed strains in structural analysis. It mainly controls the first crack initiation along the specimen. However, the restraint phenomenon is reinforcement-ratio dependent. A specific analysis must be therefore conducted for each specific structure.

3. Mesoscopic scale

3.1. Description of the test

A cement paste with a water to cement ratio of 0.57 containing different contents of sandstone cylindrical aggregates (with different diameters) is used as a ‘‘model’’ material mix [11]. The specimen are demoulded and protected from drying by a plastic foil recovered by an adhesive aluminium layer. The impermeability of the system has been checked by measuring its weight evolution.

Thin layers of these mesostructures (10 mm width) are cut from each block of mesostructure ($100 \times 100 \times 50$ mm^3) after 28 days of hydration. The aggregates position is determined precisely so as to be able to mesh easily these mesostructures for the numerical simulations. Three thin layer mesostructures constituted of cement paste only are also cast so as to assess cement paste behaviour during drying without interaction with aggregates effects (and check that drying shrinkage gradient does not lead to cracking. The tests were carried out at 25°C and 45 % of relative humidity.

A monitoring of the displacement field for the different mesostructures has been performed using a digital camera (CANON EOS 350D), at the rate of one shot every 10 min during the 48 first drying hours, on one of the drying surfaces. The evolution of the displacement field on the observed surface is determined by Digital Image Correlation (DIC) using the Correli-Q4-LMT software developed in our laboratory (Besnard and Hild, [12]). The observed surface is previously recovered by a spraying paint so as to obtain a random texture in order to increase the correlation technique performance.

3.2. Numerical simulations

The simulation of the mesostructure "1D28" (one aggregate of 28 mm is located in the middle of the specimen) is performed. Different scenarios have been considered:

- FE (Finite Element) boundary conditions: only rigid body motion are prevented, by eliminating 2 translations and 1 rotation (2D);
- DIC (Digital Image Correlation) boundary conditions: experimental displacements (U_x and U_y) are imposed in the four edges. Note that one has to project the displacements from the DIC to the generated mesh by the finite element code.

Another numerical simulation has been added,, where creep has not been taken into account. The results are summarized in Figure 7. It should be noted that only the numerical simulations with the DIC boundary conditions and with the take into account of creep has converged.

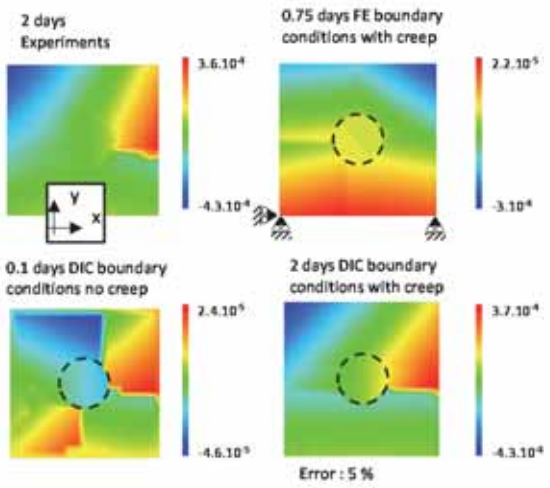

Figure 7: Evolution of vertical displacement for the mesostructure 1D28: comparison between experiments and numerical simulations.

The difference between experimental and numerical displacements corresponds to the square difference of both horizontal and vertical displacements in the whole surface:

$$error = \frac{1}{\overline{U}^2} \int_V \left[\left(U_x^{DIC} - U_x^{FE} \right)^2 + \left(U_y^{DIC} - U_y^{FE} \right)^2 \right] dV \tag{3}$$

where

$$\overline{U}^2 = \int_V \left[\left(U_x^{FE} \right)^2 + \left(U_y^{FE} \right)^2 \right] dV \tag{4}$$

U_x^{FE} and U_y^{FE} are horizontal and vertical displacements predicted by finite element calculations, U_x^{DIC} and U_y^{DIC} are the experimental displacements determined by DIC.

The numerical simulations show that the take into account of creep and the use of DIC boundary conditions give an error of about 5 %. One major horizontal crack at the right side as the experimental result is obtained. But, another one is also visible at the left, which is not so visible in experiments. In the case where creep is not taken into account, several significant cracks are predicted very rapidly leading to no convergence. In the case where only rigid body motions are prevented, the calculation also does not converge, but the cracking pattern is also very different from experiments, as expected. Therefore, in this case, it is very important to impose experimental boundary conditions in order to make a relevant comparison with experiments. But it is not sufficient; a relevant model (including creep) should be also used.

4. Conclusion and perspectives

With the sake of durability, the modeling of reinforced concrete structures is more and more focused on their cracking behavior. Specific attention is devoted to the influence of the concrete delayed strains on the mechanical response of structures. The restraint of shrinkage shows a significant effect on the cracking behavior. It has to be taken into account in order to accurately design reinforced concrete structures.

In the first part, numerical simulations were performed on different concrete structures (RG8 beam, a massive wall, a RC tie) to analyze the effect of creep including the dissymmetry compression/tension and the coupling with cracking, the effect of thermal boundary conditions including the effect of wind and the reinforcement. They show:

- The coupling between creep and cracking allows partially for retrieving experimental results on the ring test and the RG8 beam experiment;
- At early-age, there is a sign change of stresses (compression followed by tension) in restrained massive structures. Taking into account dissymmetrical creep in tension and compression leads to results which are noticeably different from results obtained with considering equal creep in tension and compression;
- Wind has a negligible effect on reached maximal temperature, but a significant effect on temperature gradient;
- Initial state of stress caused by shrinkage restraint should be taken into account in order to assess the mechanical behavior of RC structures

In the second part, investigation of the prediction of drying in a “model” heterogeneous material has been undertaken, constituted of cylindrical aggregates surrounded by cement paste. Drying shrinkage is restrained by the aggregates, which leads to cracking perpendicular to the aggregate and debonding. Digital Image Correlation has been used in order to get access to the displacements fields. Numerical simulations show that convergence is easily obtained for the studied mesostructure, and that the cracking pattern is much more in accordance between experiments and simulations. It has been also showed that a relevant model should also be used: indeed, when creep is not taken into account, divergence occurs rapidly, and too much damage is predicted.

References

[1] Cook, W. D., Miao, B., Aïtcin, P. C. and Mitchell, D., 'Thermal stresses in large high-strength concrete columns', ACI materials journal 89 (1992) 61-68.
[2] Benboudjema, F. and Torrenti, J.-M., 'Early-age behaviour of concrete nuclear containments', Nuclear Engineering and Design 238 (2008) 2495-2506.
[3] Ithurralde, G., 'The permeability observed by the prescriber', in the 'Colloque Béton à hautes performances', Ecole Normale Supérieure, Cachan, 1989. (in french)
[4] ConCrack: International Benchmark for Control of Cracking in R.C. Structures, in 'www.concrack.org', 2011.
[5] Mazars J., 1986. A description of micro and macroscale damage of concrete. Engineering Fracture Mechanics 25:729–737
[6] Feenstra PH. Computational aspects of biaxial stress in plain and reinforced concrete. PhD thesis. TU Delft; 1993.
[7] Hillerborg A, Modéer M, Petersson P-E. 1976. Analysis of crack formation and crack growth in concrete by means of fracture mechanics and finite elements. Cem Concr Res 6(6):773–81.
[8] Torrenti, J.M. and Buffo-Lacarrière, L., 'On the variability of temperature fields in massive concrete structures at early age', in '2nd International Symposium on Service Life Design for Infrastructures', Proceedings of an International Conference, Delft, 2010 893-900.
[9] Briffaut, M., Benboudjema, F., Torrenti, J.-M. and Nahas, G., 'Numerical analysis of the thermal active restrained shrinkage ring test to study the early age behavior of massive concrete structures', *Engineering Structures*, 33(4) (2011) 1390-1401.
[10] Michou A., Hilaire A., Benboudjema F., Nahas G., Wyniecki P., Berthaud Y., Reinforcement-concrete bond behavior: experimentation in drying conditions and meso-scale modeling, Engineering Structures, 2015, 101 (15), 2015, p. 570–582.
[11] Lagier F., Jourdain X., De Sa C., Benboudjema F., Colliat J.B., Numerical strategies for prediction of drying cracks in heterogeneous materials: comparison upon experimental results, Engineering Structures, 33 (3), 2011, p. 920 – 931.
[12] Besnard, G., Hild, F., Roux, S., 2006. Finite-element displacement fields analysis from digital images: Application to Portevin-Le Châtelier bands. *Exp. Mech.* 46: 789-804.

International RILEM Conference on Materials, Systems and Structures in Civil Engineering
Conference segment on Service Life of Cement-Based Materials and Structures
22-24 August 2016, Technical University of Denmark, Lyngby, Denmark

SERVICE LIFE DESIGN AND ASSESSMENT FOR CONCRETE STRUCTURES IN HZM SEA LINK PROJECT FOR 120 YEARS

Kefei Li [(1)], Dongdong Zhang [(1)], Quanwang Li [(1)]

(1) Civil Engineering Department, Tsinghua University, Beijing, China

Abstract

The ongoing mega project of Hong Kong – Zhuhai-Macau (HZM) sea link project consists of sea bridges of 28.8km, an immersed tube tunnel of 6.8 km and two offshore artificial islands. One of the major challenges of this project is to ensure a service life of 120 years for the concrete structures in a rather aggressive marine environment. This paper gives a comprehensive presentation on the durability design and the durability assessment for the concrete elements and structures in the project. For the durability design, the general philosophy and approaches are given for the concrete elements, and model-based design is conducted for the carbonation-induced and chloride induced corrosion of steel rebars. The durability requirements are obtained from this model-based design process. During the construction phase, the durability requirements are represented by quality control parameters, and in-situ tests are performed to collect the data for these parameters. On the basis of the statistical properties of these parameters, the achieved durability extent of concrete elements is evaluated through a systematic durability assessment process. On the basis of the assessment results, a preliminary maintenance planning is formulated for the service life

1. Project introduction

The HZM project links the cities of Zhuhai and Macau on the South-eastern coast of China mainland and the city of Hong Kong (HK) across the water region of Ling'ding Ocean. The total length of project is near 36km, consisting of sea bridges of 28.8 km, two offshore artificial islands and an immerged tube tunnel of 6.8 km. The traffic capacity is 6 lanes in dual direction with a design speed of 100km/h. The design working life of the whole project is 120 years [1]. The preliminary study of project began from 2008 to 2010, the detailed study phase started from 2010 and construction works are expected to end in 2017. The general view of HZM project is illustrated in Figure 1.

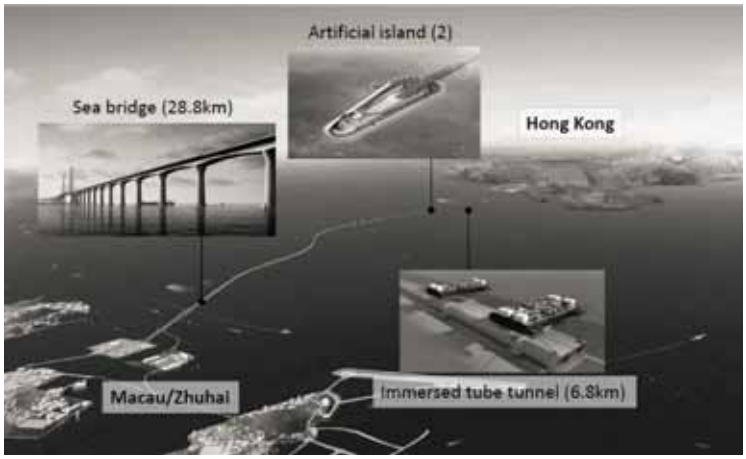

Figure 1: General view of HZM sea link project

The sea bridges consist of four navigable spans and non-navigable spans of 28.8km. The structure for the three navigable spans is cable-stayed bridge while the Hong Kong side span adopts continuous beam structure. These spans are connected by 110m non-navigable spans of continuous beam with steel box-girder. Except for the pylons and auxiliary piers in the navigable spans, all the piers and the bearing-platforms of sea bridges are prefabricated in segments and assembled in place. The immerged tube tunnel is made of concrete, consisting of four in-place segments (112.5m each) and 27 prefabricated segments (180m each). The cross section of the tunnel tube is 38m×11.4m with wall thickness of 1.5m. The prefabricated segments of immersed tunnel are made in factory near the project site and transported to the project site by floating-sinking method. Two artificial islands are constructed serving as the connections between the sea bridges and the immersed tunnels. The area of artificial islands is nearly 200,000 m^2, constructed with the help of cofferdam made from sand-filled steel tubes.

The HZM project is exposed to the subtropical marine monsoon climate. The annual average temperature is between 22.3~23.1ºC. The annual average humidity is between 77%~80% with large seasonal variation. The sea water salinity is 32.9 for eastern part and 25.4 for western part (bottom on sea bed), and lowest salinity is recorded as 8.1 and 10.4 for eastern and western regions. The concentration of Cl^- in sea water is between 10700~17020 mg/L and the sulfate ions (SO_4^{2-}) between 1140~2260 mg/L. The pH values of sea water are between 6.65~8.63. On the basis of hydrology data, the exposure zones are evaluated as: atmospheric zone (>+6.26m), splashing zone (+6.26m~-0.40m), tidal zone (-0.40m~-2.10m) and immerged zone (<-2.10m).

2. Durability design for 120 years

2.1 Design philosophy

For the concrete structures exposed to the marine environments of project site, the possible deterioration mechanisms include: the carbonation-induced corrosion of reinforcement steel

by CO_2 in atmosphere, the chloride-induced corrosion of reinforcement steel by the chloride in sea water, the physical and chemical attack of salts (SO_4^{2-}, Mg^{2+}) in sea water and soils. Moreover, the alkali-aggregate reaction and the delayed-ettringite formation (DEF) should be avoided given the crucial function of concrete elements. The global philosophy of durability design with respect to these deterioration processes is to formulate the requirements on both material and structural levels, combining the material design with the structural design to achieve a working life of 120 years. For the raw materials of structural concretes, the mass ratio of calcium aluminates (C_3A) in cement is controlled to 5%-8%; the SO_3 content is controlled to below 4% of binder; the aggregates are required to be not alkali-reactive and the alkali content of concrete is controlled to 3kg/m^3. By these specifications, the risks of salt attacks and internal expansion reactions are regarded low enough to be acceptable. Accordingly, the carbonation-induced corrosion and chloride-induced corrosion remain as the most critical processes for durability design.

The design working life of whole project is 120 years. Aiming at this target, the durability design at structural level should firstly determine the working lives for structural elements on the basis of their structural importance and technical feasibility. The principal elements adopt the same working life as whole project, 120 years, and the secondary or replaceable elements can adopt shorter lives. For these elements, the maintenance and replacement schemes should be specified in design phase. Durability limits states (DLS) are needed for quantitative durability design [2]. These states are specified as the minimum acceptable performance levels for different durability processes [3]. For carbonation-induced and chloride-induced corrosion processes, two DLS can be defined: (a) corrosion initiation; (b) corrosion to an acceptable extent. In the project, PC elements, principal RC elements and RC elements with high maintenance difficulty should adopt DLS (a) while secondary RC elements can adopt DLS (b).

2.2 Model-based design for chloride ingress

The design model for chloride induced corrosion is adapted from the widely used analytical model of Fick's second law [4,5]. With the DLS specified as the corrosion initiation, i.e. DLS (a), the design equation in partial factor format writes,

$$G_1 = \frac{C_{cr}}{\gamma_c} - \gamma_s C_s \left[1 - \mathrm{erf}\left(\frac{x_d^{nom} - \Delta x_d}{2\sqrt{\left(\gamma_D D_{Cl}^0\right)\cdot\left(\gamma_\eta \eta\right)\cdot t_{SL}}} \right) \right] \geq 0 \qquad (1)$$

Here, $C_{cr,s}$ stand for the threshold chloride concentration for steel corrosion and the concrete surface chloride concentration (%binder) respectively; x_d^{nom} and Δx_d are the concrete cover nominal thickness and its construction error (m); D_{Cl}^0 is the chloride diffusivity of concrete at a given age (m^2/s); η is the ageing factor of concrete chloride diffusivity (-); t_{SL} is the design service life of structural elements; erf is the mathematical error function. The terms, $\gamma_{c,s,D}$, are the partial factors for the corresponding parameters. The ageing factor η describes the gradual decrease of concrete chloride diffusivity with time, □

$$\eta(t_0,t)=D_{\mathrm{Cl}}(t)\Big/D_{\mathrm{Cl}}^{0}=\left(\frac{t_0}{t}\right)^{n}\quad\text{with}\quad\eta(t_0,t>30\text{ years})=\eta(t_0,t=30\text{ years}) \tag{2}$$

Here, the term n is the exponential coefficient for the ageing law and $D_{\mathrm{Cl}}{}^{0}$ the concrete diffusivity at age t_0. Since it is not rational to assume this densification is to develop infinitively, this decrease law is truncated at t = 30 years to ensure the conservative design.

To apply this design model, the characteristic values for the parameters and their corresponding partial factors should be determined for the concrete structures in HZM project. To this purpose, the statistical properties are regressed for the design parameters, C_{cr}, C_s, x_d, $D_{\mathrm{Cl}}{}^{0}$ and n, from the long-term exposure tests on a similar exposure site (Zhanjiang Exposure Station) and structural inspections during the recent 30 years. The detailed statistical properties and the regression details were reported in [6,7]. On the basis of the obtained statistical properties, the partial factors and characteristic values for design parameters are calibrated through a fully probabilistic scheme for a target reliability index of β=1.3 [7].

2.3 Model-based design for carbonation

The carbonation model is an extended form of the widely used square time law for carbonation depth x_c [4,5], and the design equation is expressed in partial factor format as,

$$G_2=x_d-x_c(t_{SL})=x_d-W_t\sqrt{2k_e\left(\frac{h}{\gamma_{RH}}\right)k_c\left(k_tR_{ACC,0}^{-1}\gamma_R+\varepsilon_t\right)\cdot C_{CO2}\cdot t_{SL}}\geq 0 \tag{3}$$

Here, W_t is the weather function expressing the influence of atmospheric precipitation on concrete carbonation process (-); k_e is the environmental factor of humidity with detailed expression in (fib 2006) (-); k_c is the curing factor defining the influence of curing time during concrete hardening (-); $(k_tR_{ACC,0}{}^{-1}+\varepsilon_t)$ is the carbonation resistance of concrete in natural environment; $R_{ACC,0}{}^{-1}$ is the concrete carbonation resistance in accelerated test conditions (20ºC, RH=65%), in (mm^2/year)/(kg/m^3); k_t is the regression parameter between the two resistances; ε_t is the error term; C_{CO2} is the CO_2 concentration in atmosphere (kg/m^3) and t_{SL} is the design life (year). The terms $\gamma_{RH,R}$ are partial factors for relative humidity and concrete carbonation resistance. The equation (3) takes the corrosion initiation as DLS.

The design value of cover thickness x_d refers to $x_d{}^{nom}$-Δx_d. The statistical properties for the parameters needed for partial factor calibration can be found in [5]. Four representative cases are considered: interior surface and exterior surface of concrete elements for service lives of 50 years and 120 years. Compared to interior surface, exterior surfaces have elevated humidity and lower weather function due to rain exposure conditions. For CO_2 concentration, a high concentration of 32.8×10^{-4}, four times of design value, is also retained to consider the possible CO_2 accumulation in the tunnel by automobile exhaust. The characteristic values of concrete cover thickness $x_d{}^{nom}$ and the carbonation resistance $R_{ACC,0}{}^{-1}$ are retained as design parameters.

2.4 Durability requirements

The preliminary concrete proportioning sets the water to binder ratio (w/b) around 0.35 for structural concretes in HZM project, and both fly-ash and slag are used in binder. After model-based design through (1), (2) for chloride ingress and (3) for carbonation, it is found that the thickness and quality of concrete cover is controlled by the chloride ingress process, and the final requirements from model-based approach are given in Table 1.

Table 1: Model-based durability design results for concrete structures in HZM project (design life t_{SL}=50, 120 years, β=1.3)[6].

Element	Exposure	t_{SL} (year)	DLS	$x_{d,}^{nom}$ (mm)	Design value D_{nssd} (10^{-12} m^2/s)		Control value D_{nssm} (10^{-12} m^2/s)	
					28d	56d	28d	56d
Box girder (exterior)	Salt fog	120	(a)	45	3.0	2.0	6.0	4.0
	Splashing	120	(a)	80	3.0	2.0	6.0	4.0
Box girder (interior)	CO_2	120	(a)	35	-	-	-	-
	Salt fog	120	(a)	45	3.0	2.0	6.0	4.0
Pier, Pylon (exterior)	Salt fog	120	(a)	50	3.5	2.2	7.0	4.5
	Splashing	120	(a)	85	3.5	2.2	7.0	4.5
Pier (interior)	CO_2	120	(a)	35	-	-	-	-
	Salt fog	120	(a)	50	3.5	2.2	7.0	4.5
Bearing platforms	Splashing	120	(a)	85	3.5	2.2	7.0	4.5
	Immerged	120	(a)	65	3.5	2.2	7.0	4.5
Bored hole pile	Immerged	120	(a)	65	3.5	2.2	7.0	4.5
RC facilities (artificial islands)	Splashing	50	(a)	60	3.5	2.2	7.0	4.5
	CO_2	50	(a)	20	-	-	-	-
Tunnel tube (exterior)	Splashing	120	(a)	80	3.5	2.2	7.0	4.5
Tunnel tube (interior)	Salt fog	120	(a)	50	3.5	2.2	7.0	4.5
	CO_2	120	(a)	30	-	-	-	-

On the basis of the design results for chloride ingress, the values of required cover thickness and chloride diffusion coefficient are obtained, modulated and given in Table 1 for the main concrete elements. These results provide the basis of durability requirements for RC elements in HZM project. The rapid chloride migration (RCM) test conform to NT Build 492 [8] is used to measure the chloride diffusivity in construction phase. However, the design values from (1) cannot be used directly for the quality control by RCM method because the D_{Cl}^{0} in (1) is the apparent chloride diffusion coefficient regressed from in-situ exposure tests at a given concrete age while RCM measures a short term migration coefficient under an electrical field. The former is a non-steady state diffusion (NSSD) coefficient while the latter is a non-steady state migration (NSSM) coefficient. Thus it is necessary to establish a relationship between the NSSD design value and the NSSM quality control value. To this aim, concrete materials in the Zhanjiang Exposure Station are reconstituted in laboratory, and the NSSM coefficients are measured by RCM method at 28d and 56d. Using the correlation between

these two groups of coefficients, the design values are converted to the corresponding RCM values for quality control in Table 1.

3. Quality control in construction

3.1 Control criteria

The acceptance criteria are set up respectively for the compressive strength and the chloride diffusivity. For the compressive strength, both the average and the minimum values for a given specimen group are controlled. For a group containing 5 or more specimens, the acceptance criterion is expressed as,

$$m_{\mathrm{fcu}} - s_{\mathrm{fcu}} \geq f_{\mathrm{cu,k}},\ f_{\mathrm{cu,min}} \geq f_{\mathrm{cu,k}} - C\sigma_0 \tag{4}$$

Here, m_{fcu},s_{fcu} are respectively the average value and standard deviation of compressive strength of specimens, $f_{\mathrm{cu,k}}$ and $f_{\mathrm{cu,min}}$ are respectively the characteristic value for required compressive strength (strength grade) and the minimum strength of specimens, σ_0 is the assumed standard deviation of compressive strength. The coefficient C depends on the number of specimens: C=0.7 (5-9), 0.9 (10-19), 1.0 (>19). For specimen groups containing 2-4 specimens, the following criteria apply,

$$m_{\mathrm{fcu}} \geq f_{\mathrm{cu,k}} + \sigma_0,\ f_{\mathrm{cu,min}} \geq f_{\mathrm{cu,k}} - 0.5\sigma_0 \tag{5}$$

The acceptance criteria for chloride diffusivity from RCM method are formulated on the similar basis. According to the technical document [9], the following requirements apply to specimen groups containing 5 or more specimens,

$$m_{\mathrm{Cl}} + s_{\mathrm{Cl}} \leq D_{\mathrm{nssm,k}},\ D_{\mathrm{Cl,max}} \leq D_{\mathrm{nssm,k}} + C\sigma_{\mathrm{Cl}} \tag{6}$$

Here, m_{Cl}, s_{Cl} are respectively the average value and standard deviation of chloride diffusivity of specimens, $D_{\mathrm{nssm,k}}$ and $D_{\mathrm{Cl,max}}$ are respectively the characteristic values for required RCM chloride diffusivity and the maximum value of diffusivity, σ_{Cl} is the standard deviation of chloride diffusivity regressed from laboratory specimens with enough number. The coefficient C takes the same value as (4) in terms of specimen number. For specimen groups containing 2-4 specimens, the following criteria apply,

$$m_{\mathrm{Cl}} \leq D_{\mathrm{nssm,k}} - \sigma_{\mathrm{Cl}},\ D_{\mathrm{Cl,max}} \leq D_{\mathrm{nssm,k}} + 0.5\sigma_{\mathrm{Cl}} \tag{7}$$

Note that the design results D_{nssm} in Table 1 should be used as the characteristics value $D_{\mathrm{nssm,k}}$ in (6) and (7).

3.2 Chloride diffusivity

The in-situ data of chloride diffusivity of structural concretes were collected from the on-site laboratories for different concrete elements in different contract bids. The chloride diffusion

coefficients were measured on concrete specimens under standard curing conditions (20°C and RH > 95%) for given ages, 28d and 56d, by RCM method.

For tunnel segments, the target mean values for D_{nssm} are respectively $6.5\times10^{-12}m^2/s$ and $4.5\times10^{-12}m^2/s$ for 28d and 56d. The mean values of measured D_{nssm} are $4.68\times10^{-12}m^2/s$ (28d) and $2.95\times10^{-12}m^2/s$ (56d), much lower than the required values. The variation coefficient of this D_{nssm} is 9.9% (28d) and 8.7% (56d), smaller than the expected level of 20% in design phase, especially for 56d age. For concretes in bridge structures, much lower mean values, compared to the required values, are obtained for both prefabricated and cast-in-place elements. The D_{nssm} dispersion of prefabricated bridge elements is very near 20% for both 28d and 56d ages, but the variance ranges from 4% to 44% for cast-in-place elements. Most diffusivity values conform to the complaince critera (6) and (7).

3.3 Concrete cover thickness

The concrete cover was measured through the common midpoint (CMP) method and the principle of CMP method detects the depth of reinforcement bars through transmitting an electromagnetic wave pulse and receiving the reflected waves from the steel bars by two adjacent antennas. The measurement error of the device used in HZM project is evaluated as around 3mm through the comparison with the measurement on extracted cores from test segments of tunnel. For information, the compliance criteria for the construction errors of concrete cover are within -5mm/+18mm.

For the prefabricated tunnel segments, the required values for thickness are respectively 50mm (intrados) and 70mm (extrados). The measurements show that the mean values are 53.5mm (intrados) and 73.4(extrados) and the construction error, corresponding to the distance between 5% percentile value and mean value, is 5.8mm (intrados) and 6.4mm (extrados), slightly larger than the expected construction tolerance, 5.0mm, for prefabricated elements. For the cast-in-place concrete elements in bridge structures, the design value for concrete cover thickness for bridge decks is 45mm, and the measured mean value attains 50.5mm with only 1.11mm as standard deviation (SD) value; the design thickness for piers, in splashing zones, is 70mm and the measured values have 80.0mm as mean value and 6.74mm as SD value. The design values for bearing platforms, in immerged and splashing zones, are respectively 60mm and 80mm, and their measured values have mean values of 71.0mm and 95.5mm and SD values of 6.85mm and 4.22mm.

4. Durability assessment

4.1 Assessment model

The assessment model for chloride-induced corrosion is also adapted from the analytical model of Fick's second law, similar to the design model in (1). With the corrosion initiation specified as DLS, the assessment equation writes,

$$G = \left(C_{cr} - C_0\right) - \left(C_s - C_0\right)\left[1 - \mathrm{erf}\left(\frac{x_d}{2\sqrt{D_{Cl}^0 \eta\left(t_0, t\right) t}}\right)\right] \geq 0 \tag{8}$$

with C_0 standing for the initial chloride concentration in concrete (%binder). Hereafter, this model is to be used through full probabilistic approach to evaluate the failure probability of durability,

$$p_f(t_{SL}) = \text{prob}\left[G(t_{SL}) < 0\right] \tag{9}$$

The service life is judged to be satisfied or not by comparing the failure probability at t_{SL} with the target failure probability p_{target}. Thus, the assessment model contains six parameters: C_{cr}, C_s, C_0, x_d, D_{Cl}^0 and n(or η). The statistical properties of the parameters $C_{cr,s}$ and ageing exponent n have been investigated in depth on the basis of the long-term exposure tests in design phase [7], and the same statistical properties are retained in durability assessment. For the initial concentration C_0, a rectangle, or uniform, distribution is calibrated for the structural concretes from the chemical analysis of raw materials. For the chloride diffusivity D_{Cl}^0, the collected data are used to update the statistical properties, and the collected data are also used to update the statistical properties of concrete cover thickness.

In the construction phase, different protection measures are adopted, including the silane impregnation on concrete surface, epoxy-coating on steel bars, stainless steel bars, coating on steel surface and cathode protection of steel bars in concrete elements. These measures are adopted to increase the durability safety margin and/or to compensate the possible adverse effect from construction defects. In durability assessment, these measures are taken into account after the following assumptions: (1) the silane impregnation is assumed to delay the accumulation of chloride on concrete surface to its stabilized value by 10 years in the assessment; (2) the epoxy-coatings have no impact on the corrosion initiation of reinforcement steel bars in the durability assessment; (3) the C_{cr} of stainless bars is conservatively taken as 5 times the value of the conventional carbon steel bars; (4) the cathodic protection passivates completely the reinforcement steel once it is put into function, keeping the steel in passivation during its active duration.

4.2 Assessment through full probabilistic approach

The fully probabilistic analysis for the durability assessment of RC/PC elements is realized through Monte-Carlo simulations. A computer-based program is developed especially to perform the probabilistic assessment. In the simulation, six parameters are considered as joint occurrence random variables. For a given exposure age, the Monte-Carlo simulations are performed to calculate the failure probability of (9), and 1,000,000 samplings are used to ensure the solution of "real" probability. Accordingly, the failure probability is solved with time from t=0 to t=120 years. Some assessment results are presented in Figure 2 for bridge elements in splashing and tidal zones.

Globally the concrete elements all achieve reliability index above 2.0 at 120 years. The bridge elements in atmospheric zones have very low failure probability, i.e. $p_f < 10^{-3}$ at 120 years and the corresponding reliability index β>3.0. The silane impregnation is generally adopted as protection measure for elements, the stainless bars are adopted for pylons and the epoxy-coated bars are used respectively for decks and box girders. The bridge elements in splashing/tidal zone, piers and bearing platforms, have satisfactory durability safety margin:

the cast-in-place piers and bearing platforms, using both stainless bars in first reinforcement layer and surface silane impregnation, have quite high reliability index, β>5.0; the prefabricated piers adopt epoxy-coated bars in first reinforcement layer and surface saline impregnation, achieving β=2.32 at 120 years.

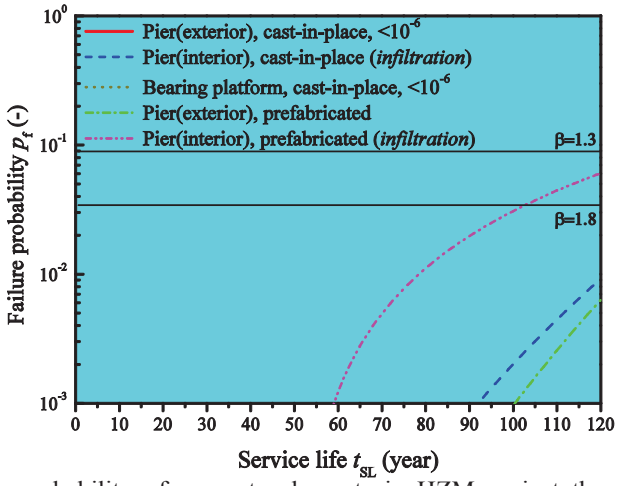

Figure 2: Failure probability of concrete elements in HZM project through Monte-Carlo simulation for bridge elements in splashing and tidal zones.

The bridge elements in immerged zone also have satisfactory durability safety margin: the cast-in-place platforms use stainless bars and surface silane impregnation and the failure probability is very low; the prefabricated platforms use epoxy-coated steel bars instead thus have a reliability index β=2.81 at 120 years; the bored hole piles achieve β=2.42 at 120 years without special protection. For prefabricated tunnel segments, the reliability index is evaluated respectively as β=2.81 (interior) and β=2.13 (exterior) at 120 years.

5. Preliminary maintenance planning

A preventive maintenance strategy is adopted, intervening in the deterioration of concrete elements in early stage. The basic maintenance planning considers mainly two aspects: the durability performance level of elements denoted by failure probability pf or reliability index β_{SL} at 120 years, and the structural importance of elements. The maintenance techniques consist in performing the surface chloride extraction by electrochemical method and applying silane impregnation on the surface of elements periodically. The maintenance period is recommended to be 20-40 years: the intervention period 20 years is recommended for the elements without stainless steel bars and the period of 40 years is attributed to the elements using stainless bars due to their much lower failure probability (<10^{-6}). For tunnel segments, a cathodic protection system has been installed to protect the steel bars against the unexpected durability failure. The activation time is preliminarily set as 100 years, corresponding to the failure probability p_f=1%. It should be noted that this basic maintenance scheme is to interact

with the durability inspection/ monitoring data and the real-time durability assessment during the service life.

6. Summary

This paper introduces the HZM sea link project in construction, covering the durability design, quality control, durability assessment in construction and the maintenance planning of concrete structures in the project. The durability design establishes firstly a general philosophy and divides the requirements onto material and structural levels, and then employs model-based methods to determine the quantitative design parameters for durability. On the basis of the quantitative requirements, the quality control is performed with concrete compressive strength and chloride diffusivity as control parameters. The on-site data were collected for the chloride diffusivity and concrete cover thickness. Using these data, the statistical properties for variables in chloride ingress model are updated, and a comprehensive durability assessment is given through a full probabilistic method. The assessment shows that the durability safety margin is satisfactory, with β_{SL}>2.0 at 120 years. A preventive maintenance planning is recommended for the RC elements.

References

[1] HZMBA, Bidding Documents for General Contracting of Design and Construction of HZM Project Main Works in Artificial Islands and Tunnel, Hong Kong-Zhuhai-Macau Bridge Administration, Zhuhai, China (2010).
[2] ISO, General principles on the design of structure for durability (ISO13823:2008(E)), International Organization for Standardization, Genève, Switzerland (2008).
[3] Li, K.F., Chen, Z.Y. and Lian, H.Z., Concepts and requirements of durability design for concrete structures: An extensive review of CCES01, Mater Struct 41 (2008), 717-731.
[4] DuraCrete, Probabilistic performance based durability design of concrete structures, Modelling of degradation, Document BE95-1347/R4-5, The Netherlands (1998).
[5] fib, Model Code for Service Life Design, fib Bulletin 34, Federation Internationale des Bétons, Lausanne (2006).
[6] Li, K.F., Li, Q.W., Zhou, X.G., and Fan, Z.H., Durability design of Hong Kong-Zhuhai-Macau sea-Link project: Principle and procedure, J Bridge Engrg ASCE 04015001(2015), 1-11.
[7] Li, Q.W., Li, K.F., Zhou, X.G., Zhang, Q.M. and Fan, Z.H., Model-based durability design of concrete structures in Hong Kong- Zhuhai- Macau sea link project, Struct Saf 53(2015), 1-12.
[8] Nordtest, Concrete, Mortar and cement-based repair materials: Chloride migration coefficient from non-steady migration experiments (NT Build 492), Nordtest Method, Nordtest, Espoo, Finland (1999).
[9] HZMBA, Technical Specifications for Quality and Durability of Structural Concrete in HZM Project, Hong Kong-Zhuhai-Macau Bridge Administration, Zhuhai, China (2012).

International RILEM Conference on Materials, Systems and Structures in Civil Engineering
Conference segment on Service Life of Cement-Based Materials and Structures
22-24 August 2016, Technical University of Denmark, Lyngby, Denmark

VERCORS MOCKUP – FIRST EXPERIMENTAL RESULTS AND SYNTHESIS OF THE BENCHMARK

Benoît Masson [(1)], Manuel Corbin [(1)]

(1) EDF SEPTEN, Villeurbanne, FRANCE

Abstract
EDF VERCORS is focusing on the behavior of a large prestressed concrete structure. VERCORS's concrete is studied by numerous researchers of COST project and EDF offers three benchmarks about civil works calculations: early age, aging and severe accident. This paper summarizes the results shown during the workshop (March 2016) following the first benchmark. The next benchmarks are scheduled in 2017 and 2021.

1. Introduction

As part of EDF's continuous effort on the safety and life extension of its Nuclear Power Plants fleet, an experimental mock-up of a reactor containment building at 1/3 scale [Figure 1] has been built at "EDF Lab Les Renardières" near Paris (France).

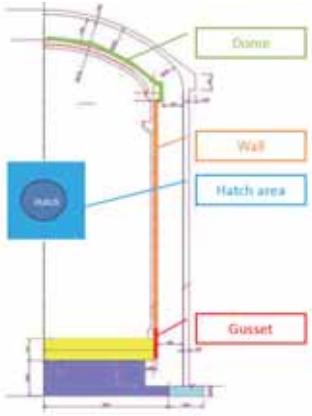

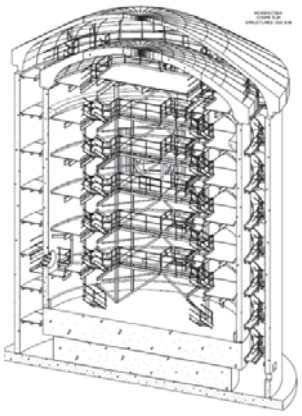

Height from gusset to the top [m]: **20.79**

Internal radius of cylinder [m]: **7.30**

Thickness of cylinder [m]: **0.3**

Free volume inside containment [m^3]: **3160**

Figure 1: VERCORS scheme

Materials of the model have been selected to be as much similar than the ones used for construction of full scale containments as possible, in terms of mechanical and thermal behavior as well. Concrete class is 34/37 MPa. Nevertheless, the concrete mix microstructure cannot be perfectly scaled due to aggregates size.

The prestressing tendons layout is exactly scaled, including any deviations around penetrations: tendons spacing is divided by three, and the ducts diameter is scaled as much as reasonably possible for the contractor (Φ50mm). Every tendon has been cement grouted as in full scale structures, excepted instrumented ones (four vertical and two horizontal) in order to follow the prestress delayed losses, or to simulate tendons breaks. The prestressing tendons are composed of class 1860 MPa strands T15 (nominal cross section S = 139mm²). Each tendon has been tensioned at 1488 MPa at active extremities before anchorage slip, as in full scale structures. The number of strands composing each tendon is governed by the following design principle: the initial compressive state of concrete shall be equal to the one in the full scale containment walls, when tensioning phase is just over. Consequently, at one third scale, tendons section is divided by nine, so that each tendon is made with 4 T15 strands, instead of 37 T15 in the full scale structures.

Steel class 500 MPa has been used for the reinforcement of concrete in the mock-up containment walls. Design principles for the reinforcement are the followings: rebars spacing and diameters are scaled to keep the same ratios ρ (%) as in full-size structures. In typical areas of the cylinder, reinforcement principles are alternatively HB 6/8 @6.7cm in horizontal direction at both inner and outer face, and HB 8/10 @0.75° in vertical direction. In the dome, reinforcement principles are also alternatively HB 8/10 @9.8cm at both faces. Stirrups are made with HB 5. Length of the rebars and the number of overlapping zones are not scaled for practical reasons. Concerning concrete cover, exact scaling is not possible due to the aggregates size.

The mock-up is finely instrumented so that its behavior is monitored from the beginning of the construction. The monitoring system is composed with:

- 1 meteorological station
- for the ambient air measure : 10 thermometers, 10 relative humidity sensors, 1 atmospheric pressure gage, 1 flow meter
- 12 pendulums (4 plumb lines with each 3 tables of aiming at different heights on 4 vertical lines)
- 4 vertical Invar wires
- 336 Embedded strain meters
- 211 Thermometers PT100
- 2 km of optic fiber
- 31 TDR (Time Domain Reflectometry) sensors
- 30 « pulse » sensors (permeability measure)
- 6 dynamometers for instrumented tendons
- 160 strain gauges on rebars

The mock up construction has been completed at the end of 2015 [Figure 2]. All over the

research program, several measurements will be collected every day on each sensor. Hundreds of samples of concrete have been prepared and tested to determine their material behaviors and parameters, including hydration, strengths, fracture energy and elastic properties, drying, shrinkage (autogenous and drying), creep (basic and drying) and permeability.

Figure 2: Picture of the VeRCoRs mock-up [11-12-2015]

The main objectives of the project are to study:

- the behavior at early age,
- the evolution of the leak tightness under the effect of aging (drying effects are about 9 times faster on the mock up because of scale effects),
- the behavior under severe accident conditions for which the thermo-mechanical loading is maintained for several days.

The experimental campaign consists of a daily measurement (four measurements a day) of the whole sensors and in a periodic air pressure test (scheduled every 13 months) of the mock-up. During this test, the containment is pressurized at 5.2 bar absolute (pressurization at 200 mbar/h and plateau at 5.2 bar abs during 24 hours before deflation at 150mbar/h), all sensors are interrogated each hour and the leakage is measured.

EDF proposed in 2015 a first benchmark dedicated to early-age, mechanical and leak tightness behaviors.
Two other benchmarks are planned in the future:

- In 2017, to assess the impact of two successive identical loadings (pressurization tests) on a concrete structure and to take into account the aging, in particular long term creep

and shrinkage.
- In 2021, to predict the behavior under severe accident conditions.

This paper is dedicated to the results of the first workshop where 14 teams (over 46 registred for the benchmark [Figure 3]) have presented their blind results (only a part of the results is presented).

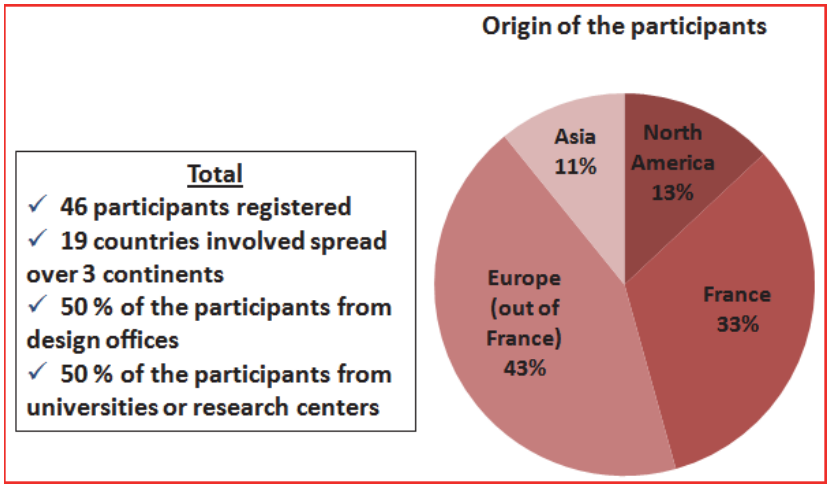

Figure 3: Repartition of the registered participants

2. Benchmark VERCORS 2015

2.1 Theme 1: early age

The topic is the prediction of the gusset behavior at early age, from the pouring to ten month (end of construction of the whole containment). The results expected were temperature evolution, strains, stresses and cracking patterns.

2.1.1 Temperature evolution

For the first phase, 11 participants have proposed a temperature evolution in the gusset [Figure 4]. A short summary of the results is presented in this paper.

We can note that the temperature values were underestimated during the first 50 hours and that the experimental temperature plateau (between 10 and 35 h) was not found [Figure 5]. This can be due to a poor evaluation of the heated air temperature around the gusset. The obtaining of the plateau is directly linked to the duration of the air heating around the gusset. The thermometer providing us with the heated air temperature around the gusset has malfunctioned. Due to this unreliable measurement, new boundary conditions have been proposed by EDF to the participants. Participants were free to use any numerical calibration: the adjustment should only regard the boundary conditions of the gusset during heating. The results were better.

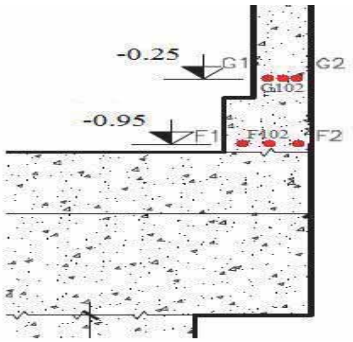

Figure 4: Position in the gusset of the sensors concerned by the theme 1

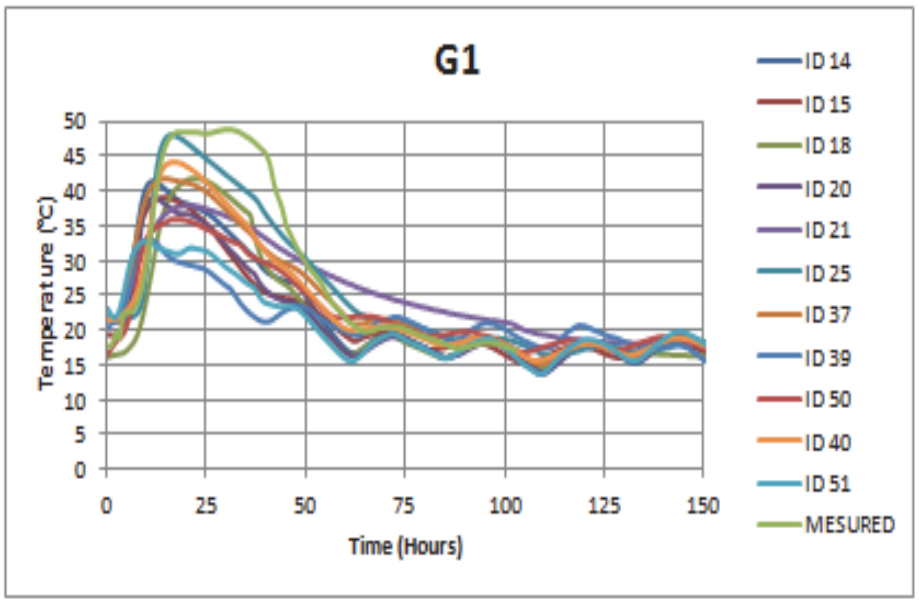

Figure 5: Preliminary results - Temperature given by participants in the gusset (G1 and F1)

2.1.2 Evolution of tangential strains in the gusset

Four teams (Team 25, Team 40, Team 44 and Team 50) have submitted tangential strain values in the gusset.

It shows that almost Teams overestimate the experimental strains for all sensors. The team 50 gives the best results [Figure 6].

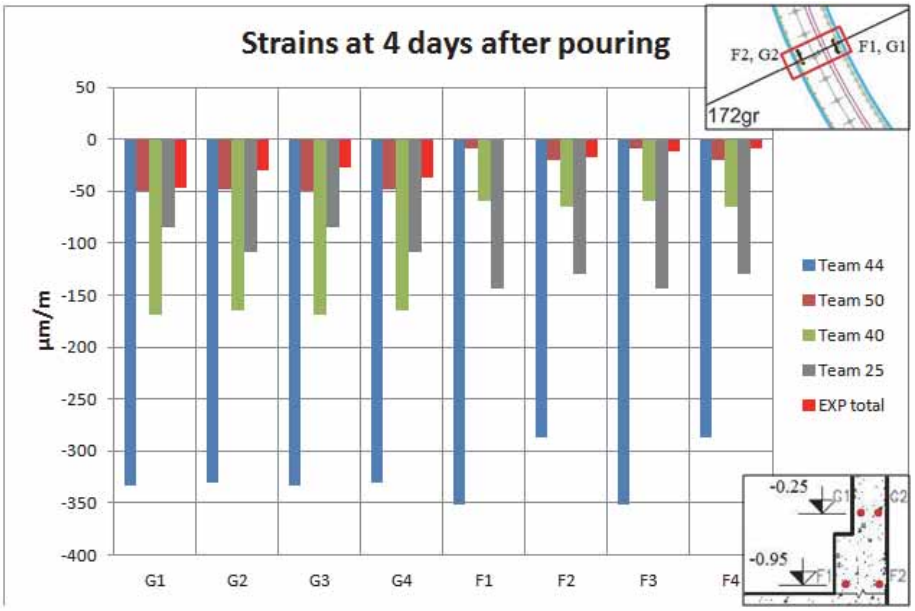

Figure 6: Tangential strains in the gusset at 4 days after pouring

2.1.3 Evolution of stresses in the gusset

5 participants (Team 21, Team 25, Team 40, Team 44 and Team 50) have given stresses values in the gusset, mainly after 4, 12 and 30 days (and 10 months for Teams 21 and 50). No experimental measure is available for the stresses.

Team 40 has provided the evolution of tangential stresses in the gusset during the first days after concreting. It shows that the maximum tensile stresses are obtained almost 2 days after concreting (> 3MPa in G1 and G2). This means that the cracking occurs almost 2 days after the pouring, while the temperature decreases. Team 40 recommends not taking into account stresses values after the cracking for early age calculation but only the stresses evolution between the pouring and the cracking. In fact, stresses values have no physical meaning when cracking occurred.

At four days after pouring [Figure 7], 3 participants (Team 21, Team 25 and Team40) have tensile stresses in the entire gusset (from 0,4 to 2,7 MPa). For these teams, the lower part of the gusset is more tensioned than the upper part.

The 2 other participants have lower tensile stresses and even a compressive stress, especially for Team 44 showing about 3 MPa compressive stress in F1 (and lower compressive stress in G1).

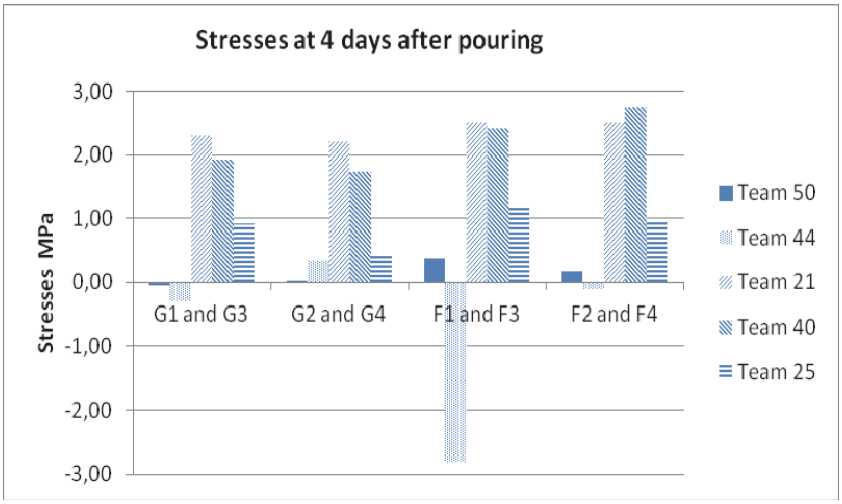

Figure 7: Tangential stresses in the gusset at 4 days after pouring

2.1.4 Cracks in the gusset

The tables [Table 1&2] below give the experimental cracks evolution in the gusset between the concreting of the gusset and the end of construction (before pre-stressing). These cracks were highlighted during visual inspections of the mock-up, 5, 12 days and 8 months after the pouring. All cracks are vertical. The two tables below synthesis the main characteristics of the cracks evolution.

Table 1: Main characteristics of the cracks on the inner face of the gusset

	Intrados			
Time	**total length in mm**	**max opening in mm**	**spacing in mm**	**number of cracks**
t0 + 5 days	4990	0,1	~1200	18
t0 + 12 days	8490	0,2	~1200	22
t0 + 30 days	wall not accessible			
t0 + 8 months	no inspection conducted			

Table 2: Main characteristics of the cracks on the outer face of the gusset

	Extrados			
Time	**total length in mm**	**max opening in mm**	**spacing in mm**	**number of cracks**
t0 + 5 days	6325	<0,1	~1200	17
t0 + 12 days	9940	0,1	~1200	23
t0 + 30 days	wall not accessible			
t0 + 8 months	16000	0,2	~1200	30

Only three participants have submitted some results about cracking in the gusset: Team 50, Team 25 and Team 40. Each team uses a different methodology. Although, comparing results is difficult. Only Team 50 and Team 40 have given some quantitative results about number of cracks, spacing between cracks or openings.

All teams give results after 4 days of concrete pouring. At 4 days after the pouring, the spacing between two cracks is about 0.8-2m (cf. team 40 and 50), while in situ observations show a spacing of 1.2 m. Therefore, the width of the cracks at 4 days is about 0.07-0.1mm, which is similar to what is observed in situ. Given to team 50, the maximum opening of the cracks increases significantly from 0.1 at 4 days to 3.3 mm at 10 months.

2.2 Theme 2: prediction of the behavior of the containment wall

The predictions of the behavior of the containment wall were expected at different steps: before prestressing, after prestressing and at 5.2 bar abs. during the pressurization test. The strains and stresses in 10 points defined in the gusset, the cylindrical wall and the dome, and cracking state evaluation (inner face cracks, outer face cracks and through cracks) were expected.

The experimental data are below [Figure 8] (the results are limited to the cylindrical part in this paper).

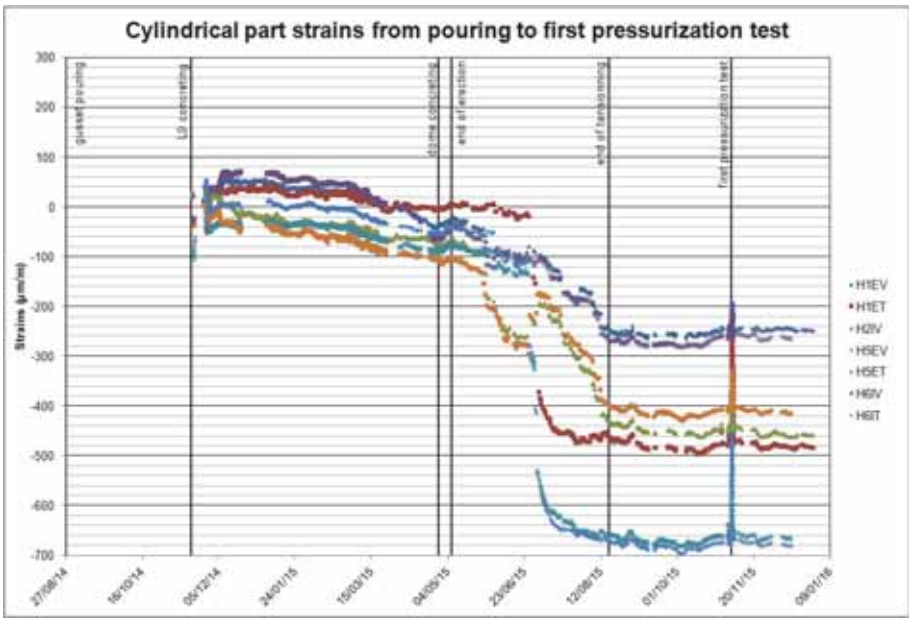

Figure 8: Cylindrical part strains from pouring to first pressurization test

The experimental results showed in this part [Table 3] correspond to the visual inspection made after the first pressurization test. During this inspection, only cracks which had an opening superior to 0.1mm were measured and mapped. The difference of cracking state between these results and those showed in Theme 1 part can be explained by the fact that during early age inspection, all visible cracks (without any criterion on the opening) were measured and by the fact that prestressing can have closed some of the early age cracks.

Table 3: Visual inspection results on cracking; Total length and max opening measured.

	Dome: Outer face	**Dome: Inner face**	**Gusset: Outer face**	**Gusset: Inner face**
Number	38	197	28	0
Total length (m)	13.73	138.07	24.63	/
Max length (m)	1.16	1.66	3.14	/
Average length (m)	0.36	0.70	0.88	/
Max opening (mm)	0.10	0.10	0.10	/

NB: The cracks identified in the dome inner face are located on precast slab forms and don't reflect the dome mechanical behavior.

Nine teams answered Theme 2. Their results are given and compared to experimental results in this part. Teams 70, 50, 37 and 24 began their calculation since the raft concreting. Teams 49, 21, 15 and 14 took the end of containment erection date as starting date. Team 23 took the raft concreting date as starting date, but didn't provide values for strains and stresses at the end of concreting date.

The experimental results represented in this part are *strains corrected from temperature effects*. The teams are divided into two groups:

- Group 1, which includes teams which began their calculation since the raft concreting (Team 70, 50, 37, 24, 23)
- Group 2, which includes teams which began their calculation since the end erection (Team 49, 21, 15, 14)

These 2 groups are separated by a vertical red line on the following graphs.

2.2.1 Strain evolution results

The results are presented for the cylindrical wall strain evolution, in tangential directions. The results are quite the same in vertical direction.

Teams' results are scattered [Figure 9].

In both directions, all teams, except Team 15 for tangential strains, show a more or less high shortening for all captors as experimental results.

Team 15 results for tangential strains show elongation for captors H5 ET and H6 IT and a very low shortening for H1 ET.

Except for Team 14, the right evolution is predicted between the end of the erection and the end of prestressing, and between the end of prestressing and the pressure test. But the amplitudes are not always well reproduced.

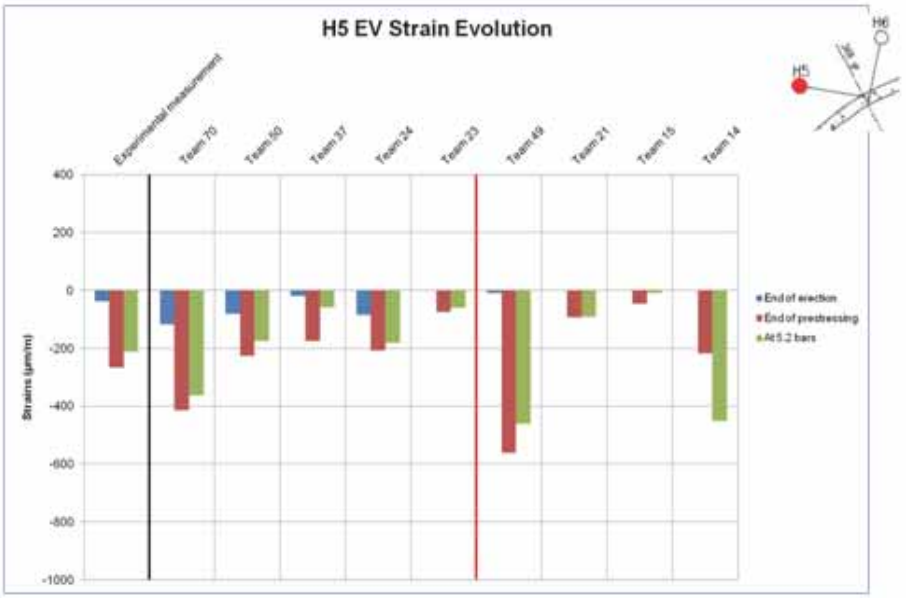

Figure 9: H5 Extrados Vertical strains evolution

2.2.2 Prestressing effects in the cylindrical wall

On the following graph [Figure 10], experimental results are represented by a red horizontal line. The experimental results represented in this part are *strains corrected from temperature effects*. The strains represented in this part correspond to strains between the end of construction and the end of prestressing. As the prestressing begins short after the end of construction, it can be assumed that they correspond to the prestressing effects, but also include some shrinkage and creep effects.

Near the inner surface (figure not presented here), the vertical (not presented here) and the tangential measured strains are greater than near the outer surface. This is also obtained in the simulation for Teams 24, 21 and 14. For Teams 50, 37, 23 and 15, the vertical strains are the same near the outer surface as near the inner surface. In general, in both directions, prestressing effects are underestimated by the teams, except Team 49 which overestimates them. Team 15 results for tangential prestressing effects show elongation for captors H5 ET and H6 IT and a very low shortening for H1 ET. However in many cases, Teams 70 and 14 are closer than the others.

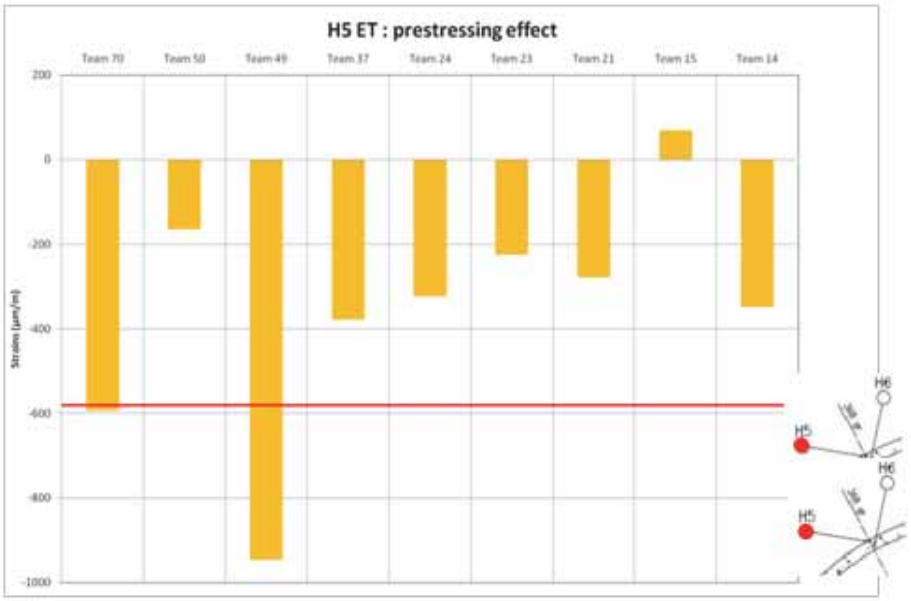

Figure 10: H5 Extrados Tangential prestressing effect

2.2.3 Strains between end of prestressing and 5.2 bar abs. plateau

On the following graph [Figure 11], experimental results are represented by a red horizontal line. The experimental results represented in this part are strains corrected from temperature effects. Experimental results take into account the effects of pressurization, but also creep and shrinkage effects since the end of prestressing.

Experimental results take into account the effects of pressurization, but also creep and shrinkage effects since the end of prestressing. In both directions, experimental results are elongation strains.

In vertical direction, strains are globally well estimated: some teams overestimate elongation a little, others underestimate it a little. In tangential direction, strains are globally well estimated.

2.2.4 Stresses evolution results

For this part, experimental results are not available. Teams' results are scattered. After prestressing, in vertical direction, the results ranged from 3 to 12 MPa of compression taking all captors together. In tangential direction, the results ranged from 5 to 15 MPa of compression taking all captors together. At 5.2 bar abs., the results show that the wall stays in compression. There is a large scattering between results; some teams estimated a compression stress inferior to 1 MPa. Team 15 results are very strange for captor H6 IT in tangential direction and are not represented on the graph: they show that pressurization leads to much more compression (33 MPa) than prestressing.

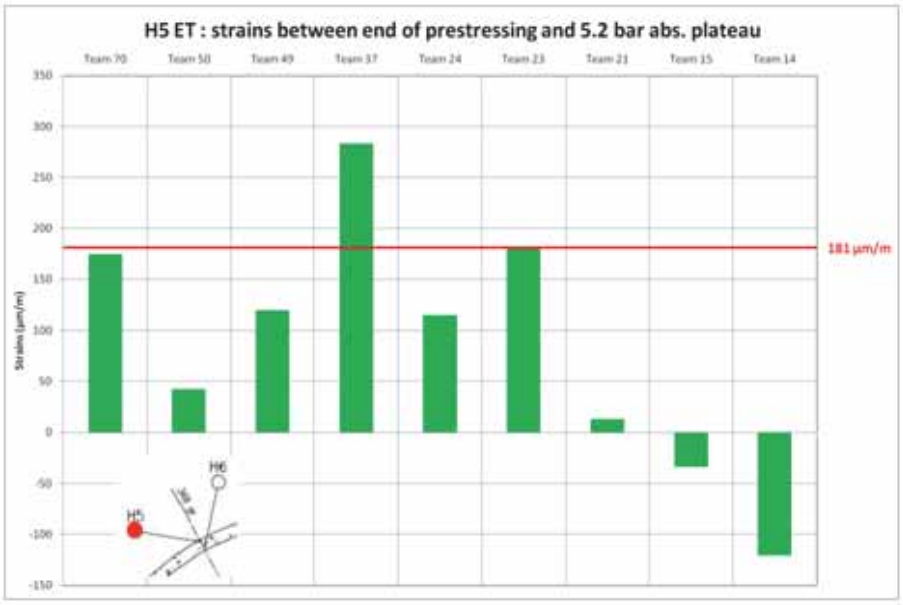

Figure 11: H5 Extrados Tangential strains between end of prestressing and 5.2 bars abs.

2.2.5 Cracking state results

Eight teams answered this topic. All the results are given in the table [Table 4&5] below, even if some of them are partial.

Experimental results correspond to the results of the inspection after first pressurization test. In this inspection, cracks which had an opening inferior to 0.1mm were not mapped.

Table 4: Inner face cracks total length

Inner face cracks – Total length (meter)									
Team	Team 70	Team 50	Team 49	Team 37	Team 23	Team 21	Team 15	Team 14	Experimental results
Gusset	0	1.0	0	19.32	N/A	0.97	4	N/A	0
Hatch area	N/A	1.5	0	0.00	4.6	2.90	8	N/A	0
Cylindrical part	0	1.2	0	6.58	6.0	0.79	28	N/A	0
Dome	0	0.0	0	0.00	0.0	0	8	N/A	138.07 (precast slab forms)

Table 5: Inner face cracks max opening

Inner face cracks - max opening (millimeter)									
Team	Team 70	Team 50	Team 49	Team 37	Team 23	Team 21	Team 15	Team 14	Experimental results
Gusset	0	0.4	0	0.061	N/A	0.12	N/A	0.015	0
Hatch area	N/A	9.0	0	0	0.1	0.17	N/A	0.04	0
Cylindrical part	0	0.4	0	0.052	0.1	0.12	N/A	0.01	0
Dome	0	0	0	0	0	0	N/A	none	0.10

Results (not presented in this paper) are available for outer face and for through cracks.

Experimental results show only cracks > 0.1 mm in dome inner face, dome outer face and gusset outer face. Team results show cracks in hatch area outer face, gusset inner and outer faces and in cylindrical part inner and outer faces. All team results show no cracks in the dome inner face. Experimental results show that it is in this area that there are most cracks, but it is on the precast part of the dome: they don't reflect the dome mechanical behavior.

Team 50 overestimates cracks opening, other teams are close to experimental results.

Team 37 overestimates cracks total length, especially for hatch area outer face, other teams globally underestimate it.

2.3 Theme 3: air leakage during the pressurization test

VeRCoRs mock-up first pressurization test has taken place from November 2nd to November 6th 2015. The global air leakage has been measured at the end of the 5.2 bar abs. plateau. During the pressurization test, at the 5.2 bar abs. plateau, the containment wall has been sprayed in order to locate leakage faults and quantify the flow through these defects.

The theme 3 of this benchmark consists in the prediction of air leakage during the pressurization test, at the end of the 5.2 bar abs. plateau. The air leakage flow is expressed in Nm^3/h (Normo m^3 per hour). The normal volume of a gas (expressed in Nm^3) is the volume it occupies in normal conditions of temperature and pressure: TN = 273.15 K (0°C) and PN = 1013.25 hPa (102 Pa).

The global air leakage is 7.7 Nm^3/h. Only 4.384 Nm^3/h have been measured during the spraying phase of the pressurization test.

Six teams answer to Theme 3. Their global air leakage results are given in the following table [Table 6] with the experimental results:

Table 6: Global air leakage results

	Experimental	Team 14	Team 21	Team 23	Team 37	Team 49	Team 50
Global air leakage (Nm^3/h)	7.7	42.89	434	834	82.7	4.2	13.83

The experimental results show that approximately half of the global air leakage is in the gusset. This result confirms that all the containment wall history, especially at early age, matters in the air leakage study. Indeed, this result seems to show that early age gusset cracks reopen during the pressurization test.

Global air leakage has been overestimated by all teams except by Team 49 which underestimated it. Team 21 and Team 23 results are very high compared to experimental and other Teams results. Only Team 21 has identified the gusset as the major contributor to the global air leakage. Other teams predicted that its contribution would be very low. All teams, except Team 50, identified the cylindrical part as a major contributor to the global air leakage and overestimated its contribution. Dome contribution to air leakage has been globally well estimated, except Teams 49 and 37 which overestimated its contribution. The hatch area contribution to air leakage has been significantly overestimated by Teams 50 and 23. Other teams didn't identify hatch area as a contributor of the global air leakage.

The repartition given in the following graph [Figure 12] is in percentage of the global air leakage.

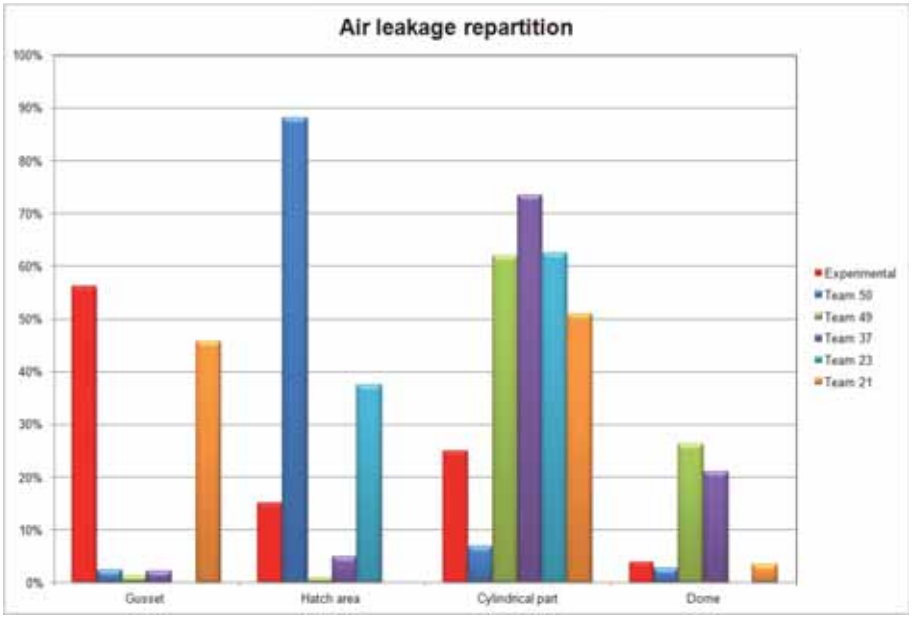

Figure 12: Air leakage repartition (percentage)

3. Conclusions

Following the presentation of the results one can retain, from the first international benchmark on the VeRCoRs mock-up, the good quality of the work done by the participants.

Regarding the theme "gusset at early age" (theme 1), the results provided show that the temperature curves are close to experimental results despite some approximations in the

starting data. This allows us to affirm that the tools and their uses are mastered to reproduce the thermal aspect of concrete hydration reactions. For strains, the results are more scattered. Strains provided by participants are always below the measured deformations. Participants generally found the setting in tension of the gusset, even if the results are relatively scattered. One team manages to predict fairly precisely when cracking occurs at early age. Predictions about the cracking at early age in the gusset are good, but only few participants were able to deliver results on this point. This shows that modeling the concrete behavior at early age is still unconventional for civil engineers.

About modeling the containment behavior since its concreting to its first mechanical loading (theme 2), the results provided are more numerous. These calculations are indeed more common in the profession. Some participants have undertaken comprehensive and complex calculations incorporating all the construction phases of the containment. Some have obtained results very similar to experimental measurements, showing a good understanding of the behavior of the structure. Nevertheless there are sometimes significant differences both between the participants and compared with experimental measurements. The gusset area in particular is complex to model and its behavior remains poorly mastered. To a lesser extent, the dome can also result in more scattered results.

However, interpretation of these results is difficult in some cases because the compared values include several phenomena with sometimes opposing effects (effects due to time / mechanical loadings effects). So, it was not always possible to distinguish the source of a significant deviation with other participants or in comparison to the experience.

For future benchmarks, it will be important to ask results in a very precise way to compare and interpret more thoroughly the results transmitted.

One can also note that the results for cracks are distant from experimental results. In particular one can notice:

- That, ignore the effects associated to early age is a gap in forecasting the state of active cracking during pressurization, particularly in the gusset;

- That, built the determination of cracking on a postprocessing of the stress state based on a linear calculation, can lead to overestimation of active cracking.

Efforts seem necessary to move forward on modeling strategies integrating nonlinearities throughout the whole history of the building

Finally, the prediction of the leakage flow remains a difficult exercise. The results show a factor of 1 to 200 between the lowest flow and the highest. However, this factor is much better than that which was obtained in previous benchmarks on the subject of the leak through a concrete wall.

This shows that this type of calculation becomes more controlled. However it appears clearly that the determination of the cracking state is a major element to forecast leakage. VeRCoRs should be a real way to further improve the air leakage prediction tools.

International RILEM Conference on Materials, Systems and Structures in Civil Engineering
Conference segment on Service Life of Cement-Based Materials and Structures
22-24 August 2016, Technical University of Denmark, Lyngby, Denmark

EXPERIMENTAL STUDY OF CORROSION-INDUCED DEGRADATION OF REINFORCED CONCRETE ELEMENTS

Olaf Loukil[(1)], Lucas Adelaide[(1)], Véronique Bouteiller[(1)], Marc Quiertant[(2)], Thierry Chaussadent[(3)], Frédéric Ragueneau[(4)], Xavier Bourbon[(5)], Laurent Trenty[(5)]

(1) Université Paris-Est, MAST, SDOA, IFSTTAR, France.
(2) Université Paris-Est, MAST, EMMS, IFSTTAR, France.
(3) Université Paris-Est, MAST, CPDM, IFSTTAR, France.
(4) LMT/ENS Cachan/CNRS/Univ. Paris 6/PRES UniverSud, France
(5) ANDRA, Chatenay-Malabry, France

Abstract
Corrosion of steel reinforcement is the main cause of damage for reinforced concrete structures. Iron oxides produced during the corrosion process can induce concrete cracking, loss of adhesion at the steel-concrete interface, loss of reinforcing bar cross-section and even spalling of the concrete cover. In the presented research, the durability problems related to the corrosion of the reinforcement are investigated by combining experimental and numerical studies. However, this paper particularly focuses on the experimental methodology used for the time evolution of damages (steel corrosion products formation and crack patterns) induced by the accelerated corrosion test. The accelerated corrosion tests were carried out by applying a constant current between reinforcement used as an anode and a counter electrode. To control the corrosion process, electrochemical parameters (such as free corrosion potential, polarization resistance, electrical concrete resistance) were measured. The purpose of this paper is to determine the width and length of the cracks and their orientation according to the current density and time.

1. Introduction

Corrosion of steel reinforcement is one of the main causes of deterioration of existing reinforced concrete (RC) structures. The consequences of this phenomenon are degradation of the steel/concrete bond, reduction of the steel rebar cross-section and concrete cover cracking [1]. This last phenomenon results from the production of oxides which occupy a volume two to seven times higher than the parent steel. Actually, when this production is greater than diffusion of iron oxide in the concrete, pressure increases at the interface between the surrounding concrete and the rebar [2] [3] and exerts tensile stresses in the concrete all along the corroding reinforcements. If these stresses exceed concrete tensile strength, the cracking initiates and propagates towards the outer surface leading to the delamination of the concrete

cover [4] [5]. Due to the mechanical deleterious effect of the corrosion phenomenon, it is important to develop non-destructive techniques as well as predictive numerical modelling to assess the corrosion evolution of RC structures. This could help the structure's end users to provide an efficient maintenance policy. The main issue of this paper is to design a specific protocol to generate a "controlled" corrosion evolution versus time in order to bring some experimental evidences on the concrete cover cracking process due to corrosion and to determine relevant input parameters for the numerical modelling.

2. Experimental program

2.1 Materials and specimens

Twelve single-rebar specimens (500x125x100mm^3) were casted with a 600mm long and 20mm diameter steel deformed rebar. The reinforcement was positioned to obtain a 30mm concrete cover at two sides of the beam [Figure 1]. The specimens designed with a not symmetric location of the rebar aim to get closer to reality, to represent the heterogeneity of the mechanical environment of the reinforcement in a structure. A Portland cement and siliceous aggregates were used for the concrete composition with a water to cement ratio of 0.73. This ratio is representative of old reinforced concrete structures. Moreover, it allows the penetration of the chloride ions during the accelerated corrosion test.

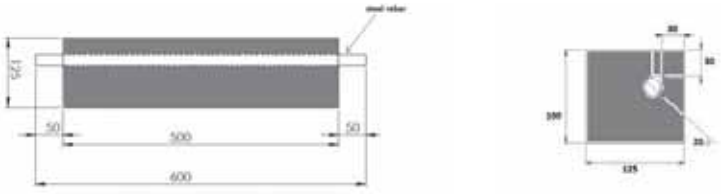

Figure 1. Schematic representation of RC specimens (dimensions in millimeters)

The cement type used for the concrete composition was CEM I 52.5 CP2 NF according to European standards. Concrete was prepared with aggregates having different particle size classes ((0/0.315 mm; 0.315/1 mm; 0.5/1 mm; 1/4 mm; 2/4 mm; 4/8 mm; 8/12 mm; 12.5/20 mm)). Compressive and tensile strengths were measured on concrete cylinders (160mm in diameter, 320mm in height) after 28 days according to NF EN 12390-3 [6] and NF EN 12390-6 [7] standards. The mean compressive strength is 32 MPa ± 2.46, the tensile strength is 2.6 MPa ± 0.08 and the Young's modulus is 35 GPa ± 1.58. The Poisson's ratio is equal to 0.15.

2.2 Accelerated corrosion tests and monitoring system

The set-up used for accelerated corrosion test and the monitoring system are illustrated in [Figure 2]. RC samples were corroded using a power supply (Agilent 6614C, 100V, 0.5A) which delivered an imposed anodic current to the steel rebar. The counter electrode (cathode) consisted in an inert platinum titanium mesh (275mm long, 75mm wide) placed into a PVC tank containing the alkaline electrolyte (1 g/L of NaOH, 4.65 g/L of KOH, 30 g/L of NaCl) which was glued on the top side of the concrete (in the middle of the specimen). All the specimens were connected in series and a current density of 100 µA/cm² of steel (0.0172A for a steel surface area of 172.8 cm²: diameter 20mm and length 275mm) was applied during the

chosen exposure time (7d, 14d, 21d, 28d and 35d). At the end of each considered exposure time, two specimens were disconnected from the electrochemical test set-up. One of the specimens was used for the non-destructive electrochemical characterization and the other one was dedicated to destructive measurements. The accelerated corrosion test was monitored using a data acquisition unit (Keysight 34970A): temperature, delivered constant current, each sample voltage and total voltage were recorded every two hours. Moreover, two cameras were used for the digital image acquisition of the front side of the two specimens subjected to a 35 days accelerated corrosion test.

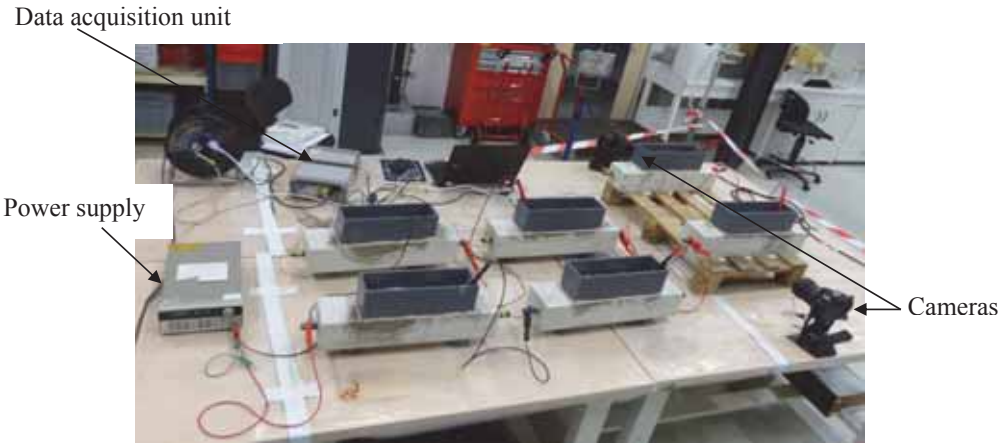

Figure 2. Accelerated corrosion and monitoring system

2.3 Electrochemical characterizations

In order to determine the corrosion state of the rebar before the accelerated test, half-cell potential measurements (E_{corr}) linear polarization resistance measurements (LPR) and impedance spectroscopy (Re) were carried out, using a potentiostat (Bio-Logic, PARSTAT 2263) and the usual electrochemical cell with three electrodes. The working electrode was the steel rebar, the reference electrode was a KCl saturated calomel electrode (SCE, 242 mV / SHE) and the counter electrode was a titanium platinum mesh [Figure 3]. The same electrolyte as for the accelerated corrosion test was used. Then the corrosion current density J_{corr} (µA/cm²) was calculated based on the following equation:

$$J_{corr} = \frac{B}{R_p \ S} \quad (1)$$

with B a constant (26mV), Rp (ohm) the linear polarization resistance and S (cm²) the steel surface (172.78 cm² in this study).

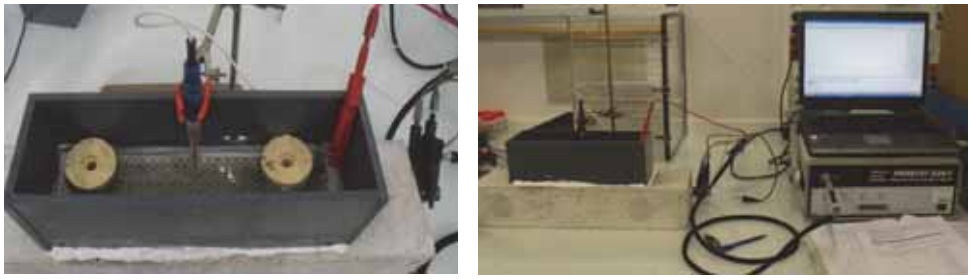

Figure 3. Electrochemical setup

2.4 Observation of corrosion products, of steel/concrete interface and estimation of the crack patterns

Visual observations

After the accelerated corrosion test, the specimens were observed and a special focus was made on the top and the front sides because of their lower concrete cover (30mm). Cracks opening were measured with a crack measuring magnifier (resolution 0.1mm) on these two surfaces. Then the specimens were sliced (125x100x20mm^3), considering corroded areas as illustrated in [Figure 4]. After 24h drying in an oven at 45°C, the slices were photographied and examined in order to characterize the crack pattern (angle and length) [Figure 5]. To determine the angular position, the methodology developed by Sanz-Merino [8] was adopted [Figure 5-a]. To estimate the length of the cracks in each cross-sections, the photographs of the cross-section and a circle graduated every centimeter were superimposed as shown in [Figure 5-b]. Moreover, the corrosion products embedding the rebar and filling the concrete cracks were analyzed. Then from both results an attempt was made to correlate what was seen on the concrete surface in 2Dimensions (by the bridge's owner) and what happened inside the concrete with an aim of 3Dimensions.

Scanning Electron Microscopy observations

The slices were then impregnated with an epoxy resin under vaccum (to prevent decohesion between concrete and steel when the corrosion damage was severe) and then cut into samples which dimensions (2x4.5x4.5cm^3) fitted in the Scanning Electron Microscopy (SEM) observation room. A first goal is to determine the corrosion product thickness and their length circling the perimeter of the rebar. A second objective is to observe the crack pattern and the transfer of the oxides through the cracks.

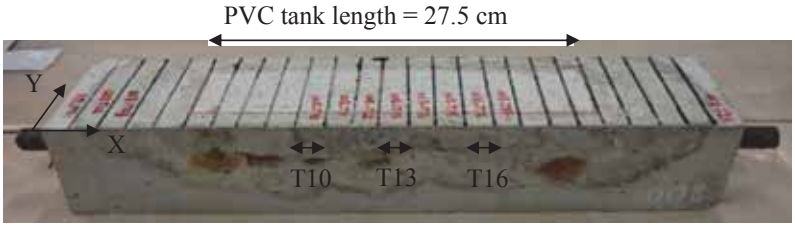

Figure 4. Specimen sawing design (25 slices named Tn° according to the axis. Corrosion test zone is between x=10 and x= 40 cm

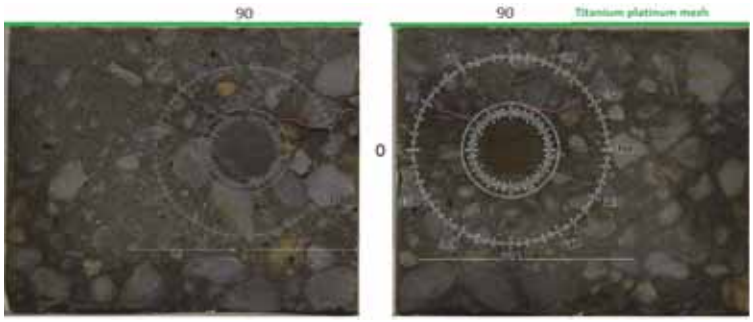

(a)

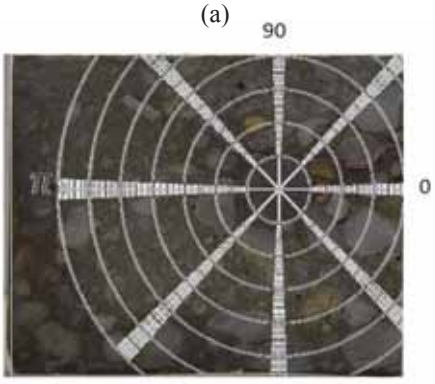

(b)

Figure 5. Determination of the crack angular position (a) and the crack length (b) after the accelerated corrosion test on the two sections of a slice

3. Experimental results

3.1 Voltage evolution during the accelerated corrosion test

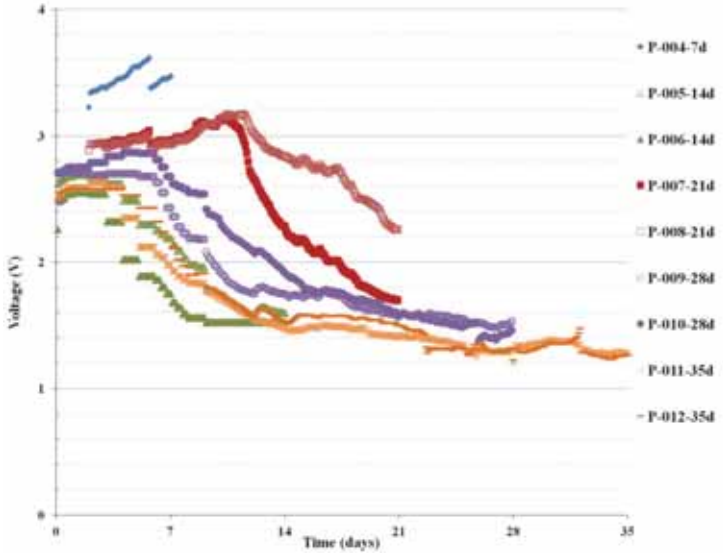

Figure 6. Voltage evolution during the accelerated corrosion test

[Figure 6] shows the voltage evolution for each RC specimen subjected to the accelerated corrosion test versus time. Before the test (time=0), the voltage reflects the electrical resistance of the specimens which are in a close range from 2.5 to 3 V except for P004-7d specimen (3.3V). During the test, three stages are observed. In the first stage, the voltage increase (about 1V) may be explained by the formation of resistive iron oxides (passive layer) [9], [10] around the rebar and also by the diffusion into the concrete and the filling up of the concrete pores by the oxides in the vicinity of the steel. In the second step, the drastic voltage decrease (50% loss) can arise from the concrete cracking and the steel / concrete debonding. The last stage with a constant voltage (1.4V) appears for longer durations, 28d and 35d and is likely representative of a constant impedance of the corrosion layer. These preliminary observations need to be discussed considering the migration of the ionic species under current and particularly the penetration of the chloride ions. Tests are under progress.

3.2 Corrosion rate and crack patterns

[Figure 7] shows the corrosion signs and the cracks observed for the top side and the front side of the two specimens after an accelerated corrosion test of 21 days.

Regarding the top sides, specimen P-007 shows some corrosion product stains and a visible crack roughly along the steel rebar whereas specimen P-008 is not damaged. Regarding the front sides, the opposite behaviour is observed: specimen P-007 only exhibits a single spot of corrosion product while specimen P-008 shows significant corrosion products along the crack

that follows the rebar. An assumption to explain this difference could be that the aggregate as well as the rebar's ribs are not homogeneously distributed and promote this heterogeneity.

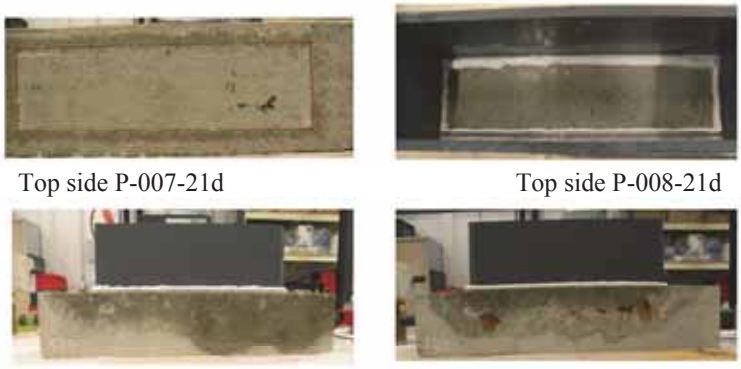

Top side P-007-21d Top side P-008-21d

Front side P-007-21d Front side P-008-21d

Figure 7. Qualitative results of the specimens after an accelerated corrosion of 21 days

[Figure 8] reveals that all corroded specimens for over 14 days have a J_{corr} equal to 10 µA/cm² approximately except the specimen P-004-7d corroded for 7 days. The proposed assumption is that at 7 days chloride ions have not reached the steel/concrete interface yet and consequently, the corrosion is still passive. To give an answer to this question, chloride measurement ingress with $AgNO_3$ will be achieved on each slice. Regarding the crack width, the behaviour of corroded specimens is different. As previously mentioned, all specimens are not cracked on the same side. As already suggested, this difference could be ascribed to the heterogeneity of the concrete (the random distribution of the aggregates into the cement paste). Besides, the crack on the top side is wider than the one on the front side. This observation might be attributed to the close localization of the counter electrode on the top side of the specimen (by comparison with the steel rebar) that permits chloride ions to quickly reach the rebar (modification of the physico-chemical conditions that locally enhances the corrosion process).

[Figure 9] shows the evaluation of the crack patterns (angular position (a), length (b) and width (c)) for each of the 10 cross-sections of the five slices of specimen P-008-21d. The cracks propagate from the steel/concrete interface to the concrete surface.

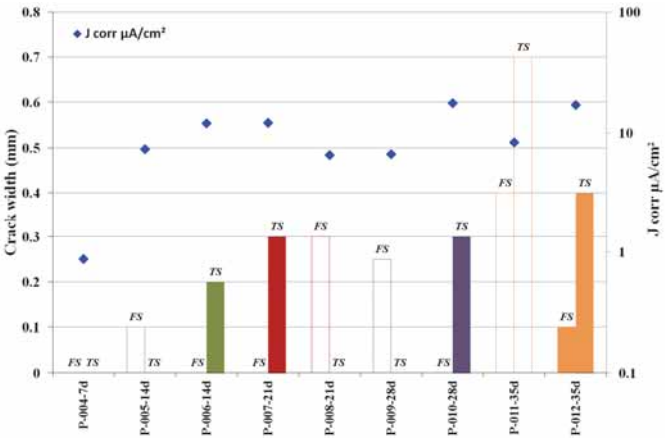

Figure 8. Crack width evolution and J_{corr} *(FS:front side ; TS:top side)*

As shown in [Figure 9-a], two groups of the position of the cracks near the steel surface are observed oriented close to 40° and 120° according to the graduated circle (see [Figure 5-a]). Two mains cracks seem to be displayed. Two sets of crack lengths could be identified, the first one is between 2 and 3cm and the second one is between 1 and 2cm in [Figure 9-b]. The lengths tend to fluctuate because of the distribution of the aggregates which influences the crack path. The graph in [Figure 9-c] corresponds to crack widths and shows the observed general trend. The crack widths are around 0.1 and 0.3mm.

The thickness of corrosion products is measured by Scanning Electron Microscopy and the perimeter represents the length of the shape of the rebar according to the corrosion volume.

The minimum thickness of corrosion products varies from 50 to 57µm and the maximum thickness varies from 257 to 314µm (see Table 1). The highest thickness is located in the upper part of the steel rebar. This 'expected' difference could result from the distance between the counter electrode and the steel surface area. The closer they get, the more the corrosion is forced. The crack width located on the top side is wider than the one located on the front side because the penetration path of the chloride ions to reach the steel surface area is the shortest.

Comparing the internal measurements 'crack orientations' and the widths measured on the sliced samples to the external observations (corrosion products spots on the front side of the samples), the surface observations do not reflect the internal corrosion state at the steel/concrete interface.

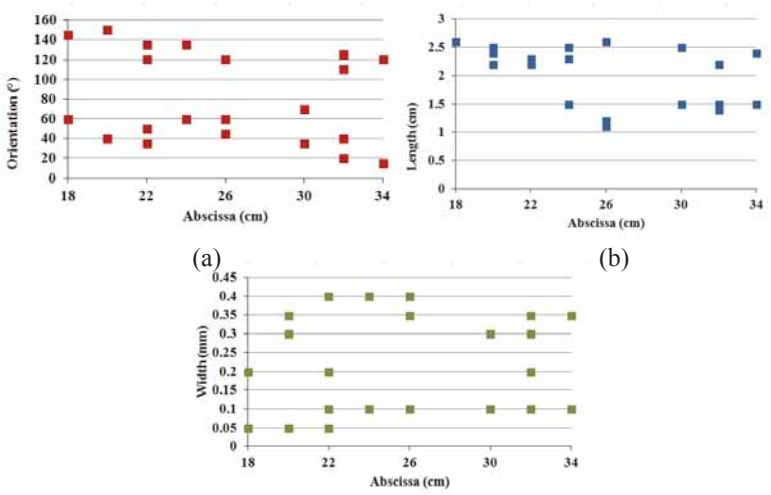

Figure 9. Quantitative results of internal cracks– a) angular position, b) length and c) width

Table 1 : Thickness of the corrosion products layers and corresponding visual distribution of evidences on the front side

Slices	Maximum thickness of the corrosion products layers (µm)	Minimum thickness of the corrosion products layers (µm)	Perimeter of the corrosion products layers Max/Min (µm)
P-008-21d-T10	257	57	2 617 / 5 233
P-008-21d-T13	314	63	5 233 / 5 233
P-008-21d-T16	257	50	5 233 / 10 467

4. Conclusions

In this work, cracks due to the corrosion of the steel reinforcement in concrete specimens have been investigated using an accelerated corrosion test. This work exposes the finalized methodology associated with the experimental program. The following preliminary results can be drawn:

- There are three stages in the corrosion process: during the first stage, the increase of polarization resistance may be explained by the development of resistive iron oxides (passivation layer). The second stage could highlight the loss of the resistance of the set due to respectively the concrete cracking and the decohesion between the steel and concrete surface area. Regarding the third stage, the observed effect may be attributed to the fact that the properties of corrosion layers remain unchanged. Then, the value of the voltage at the end of the test certainly reflects the resistance of both cracked concrete cover and iron oxide layer. After 7 days, an active corrosion is not clearly

observed and this could be explained by the fact that chloride ions have not reached the steel/concrete interface.

- The crack orientation, length and width are coherent for the same specimen corroded for 21 days. This result has to be confirmed after achieving the measurements for the other specimens.
- The corrosion-product spots on the surface of the samples do not reflect the internal corrosion state at the steel/concrete interface of the specimen.

Some of the experimental results such as the thickness and the display of the oxide layer will be used as input data for the numerical modelling. The other experimental results associated to the crack patterns will allow a comparison between the experience and the modelling. To improve the modelling of the corrosion product layer in the numerical simulation, an experimental test is in progress to characterize mechanical properties of these products.

References

[1] Cairns, J. and S. Millard, Reinforcement corrosion and its effect on residual strength of concrete structures, in 8 th International Conference Structural Faults+Repair-99. 1999: London.
[2] weyers, R. and B. Prowell, Corrosion inhibiting repair and rehabilitation treatment process for reinforced concrete structures. Cement and Concrete Composites, 1996: p. 459.
[3] Mehta, P.K. and P.J.M. Monteiro, in Concrete: structures, Properties and Materials. 1997, Indian Concrete institute: India.
[4] Jamali, A., et al., Modeling of corrosion-induced concrete cover cracking: A critical analysis. Construction and Building Materials, 2013. 42: p. 225-237.
[5] Dehoux, A., Propriétés mécaniques des couches de produits de corrosion à l'interface acier / béton. 2012, Université Pierre et Marie Curie.
[6] AFNOR(2001) , N.E.-. Testing hardened concrete. Part 6: Tensile splitting strength of test specimens. 2001.
[7] AFNOR (2003), NF EN 12390-3., Testing hardened concrete. Part 3: Compressive strength of test specimens Andrade C., Alonso C. and Molina F. (1993), “Cover cracking as a function of bar corrosion: part I – experimental test”, Materials and Structures. 26: p. 453-464.
[8] Sanz Merino, B., Experimental and numerical study of cracking of concrete due to corrosion. 2014, Universidad Politecnica de Madrid Escuela Tecnica Superior de Ingeniros de Caminos, Canales y Puertos. p. 254.
[9] Caré, S. and A. Raharinaivo, Influence of impressed current on the initiation of damage in reinforced mortar due to corrosion of embedded steel. Science Direct, 2007. 37: p. 1598-1612.
[10] Poupard, O., Corrosion by chlorides in reinforced concrete: Determination of chloride concentration threshold by impedance spectroscopy. Cement and Concret Reasearch, 2004. 34: p. 991-1000.

International RILEM Conference on Materials, Systems and Structures in Civil Engineering
Conference segment on Service Life of Cement-Based Materials and Structures
22-24 August 2016, Technical University of Denmark, Lyngby, Denmark

EVALUATION OF CONCRETE'S RESISTANCE TO PHYSICAL SULFATE SALT ATTACK

Semion Zhutovsky [(1)], R. Douglas Hooton [(1)]

(1) University of Toronto, Canada

Abstract
Physical sulfate salt attack (PSA) is one of the most severe and rapid deterioration mechanisms that can take place in concrete. Yet there is no standard method for evaluation of concrete resistance to PSA. Testing of concrete's resistance to PSA has two main aspects – exposure conditions and evaluation of deterioration. Evaluation of concrete's resistance to PSA often requires a long time, which is inappropriate for evaluation of concrete mixtures for a construction project. Many studies report sulfate resistance based on subjective visual ratings, which is inadequate as a durability design criterion. The objective of this research is to identify exposure conditions and deterioration evaluation methods suitable for standard testing that can be used for rapid comparison of mixture compositions, durability design, and analysis of life cycle cost. Various methods for assessment of deterioration were applied using selected exposure. It was found that 100 thermal cycles between 5 and 30 °C immersed in 30% sodium sulfate solution were sufficient to assess the resistance of a range of mortar mixtures. The most suitable techniques for evaluation of deterioration rate was mass loss, while fundamental resonance frequency and ultrasonic pulse velocity were found to be unsuitable.

1. Introduction

Physical sulfate salt attack (PSA) is one of the most severe and rapid deterioration mechanisms that can take place in concrete. Salt scaling, salt weathering, or salt hydration are the terms that are often used for PSA [1]. PSA is sometimes confused with chemical sulfate attack [2], [3]. Unlike in sulfate attack of chemical origin, no chemical interaction between sulfate salts and cement minerals is involved in PSA [3]. Sulfate attack of concrete has been the subject of extensive research, though the mechanisms of PSA were often overlooked [4]. A recent Portland Cement Association report on the results of testing concrete resistance to

sulfate attack declares that the PSA damage of concretes can be significantly more extensive than the damage caused by chemical sulfate attack [5].

It has been demonstrated by previous research that water to binder (w/b) ratio is the most important parameter for the resistance to sulfate attack [5]. The current North American standards limit w/b ratio to 0.40 and 0.45 in Canada [6] and USA [7], respectively, for the severe conditions of sulfate exposure. However, the reduction of w/b ratio does not prevent deterioration, though it enhances the resistance to sulfate attack [8]. Supplementary cementitious materials (SCM) are often used to make concrete tolerant for sulfate rich environment. While SCMs improve the resistance to chemical sulfate attack by diluting aluminates in the binder, some literature sources report that they may even increase the susceptibility to PSA [5], [9], [10]. So there is a controversy about the resistance of different binders and mixture designs to PSA.

Currently, there are no standard methods for testing concrete resistance to PSA [2]. Existing standard test methods ASTM C452 [11] and ASTM C1012 [12] were prepared for testing the resistance of binders to chemical sulfate attack. In these standards, the expansion of mortar bars is used as a measure of deterioration, while PSA is typically not associated with expansion. The form PSA damage is usually the gradual surface scaling, much like the damage caused by freezing and thawing [3]. This is because PSA causes damage by means of the cycles of crystallization, dissolution and phase transitions of sulfate salts [13]. Testing of concrete's resistance to PSA has two main aspects – exposure conditions and evaluation of deterioration. Historically, field testing was used for testing sulfate resistance of concretes [5], [9], [8], [14]. Such tests could take from 8 to 40 years. Such long time is inappropriate for evaluation of concrete mixtures for a construction project. Many such studies report sulfate resistance based on visual ratings, which are subjective and inadequate as a design criterion for durability. Thus it is of great interest to identify exposure conditions and deterioration evaluation methods suitable for accelerated standard testing that can be used for rapid comparison of mixture compositions, durability design, and analysis of life cycle cost.

Different accelerated exposure conditions for the testing of PSA resistance of concrete are reported in the literature [13], [15], [16]. Typically, the most significant damage in PSA is caused by phase transitions between sulfate salts: thenardite (Na_2SO_4) and mirabilite ($Na_2SO_4 \cdot 10H_2O$) [13]. To activate this mechanism, either relative humidity (RH) or temperature variations are needed. Thus, PSA testing exposures can be categorized into three groups: wetting and drying cycles, partial submerged samples, and fully submerged samples. In first group, changes in RH are triggered by wetting and drying cycles, inducing the phase changes between mirabilite and thenardite. However, change of RH inside concrete or mortar samples is slow, and significant time is required to reach RH equilibrium inside a sample. For this reason, there will always be a moisture gradient through the sample cross-section, which results in partial conversion of thenardite to mirabilite, and the testing time required to achieve the damage level needed to quantify PSA resistance in a wide range of mixtures is long. In partially submerged samples, the rate of deterioration may be fast, but the damage is localized in the evaporation zone, which makes it difficult to quantify the resistance to PSA. On the other hand, thermal cycling of fully submerged samples seems to be a very promising PSA exposure, because thermal equilibrium can be achieved quickly. When temperature is

reduced, e.g. from 30° C to 5° C, all thenardite absorbed inside the sample will convert to mirabilite. The expansion caused by the crystallization and phase change during such thermal cycles is significant (more than 3 times volume increase [13]) resulting in rapid deterioration. Since the sample is submerged, the whole sample surface is exposed to the deterioration process, so extent of damage is higher and easier to quantify. Folliard and Sandberg achieved complete disintegration of 25 mm concrete cubes with w/cm ratio of 0.5 after only 30 thermal cycles when submerged in 30% sodium sulfate solution. This exposure condition was compared with other different exposures involving drying cycles, partial drying, with and without thermal cycles. While particular damage was seen in all exposures, other exposures didn't cause such fast and extensive damage. Since the thermal cycling between 5 and 30 °C in 30% sodium sulfate solution is reported as the one of the most severe exposures (due to rapid crystallization of mirabilite [13]), this exposure condition was selected for the current research.

In the field studies of sulfate attack, the extent of damage was often assessed using visual rating [8], [9]. However, rating damage based on visual appearance is subjective, semi-quantitative method, which is not suitable for PSA considering the surface scaling nature of degradation. Considering the similarity of degradation mechanism and character of the damage, methods used for assessment of concrete resistance to freezing and thawing, such as mass loss, ultrasonic pulse velocity or fundamental resonance frequency appear to be particularly promising for quantification of extent of damage and rate of deterioration in PSA.

The objective of this research is to identify exposure conditions and deterioration evaluation methods suitable for standard testing that can be used for rapid comparison of mixture compositions, durability design, and analysis of life cycle cost. For this purpose, mortars with various w/cm ratio and different types and contents of supplementary cementitious materials were subjected to the selected exposure conditions. Mortars were preferred over concrete because of higher permeability, which shortens the testing time, and over cement paste because of the presence of interfacial transition zones. High-sulfate resistant cement (ASTM Type V) was used in all mixtures to reduce the possibility of chemical interaction between cement and sodium sulfate. Various methods for assessment of deterioration were applied using selected exposure. It was found that 100 thermal cycles between 5 and 30 °C immersed in 30% sodium sulfate solution were sufficient to assess the resistance of a range of mortar mixtures. The most suitable techniques for evaluation of deterioration rate was mass loss, while fundamental resonance frequency and ultrasonic pulse velocity were found to be unsuitable.

2. Materials and methods

2.1 Materials

High sulfate-resistant cement produced by Lafarge was used in all mixtures in order to reduce the possibility of chemical sulfate attack. SCMs used in this research were Holcim GGBFS, from Ontario, and FA type F from Avon Lake, Ohio, USA. Natural glacial sand of mixed mineralogy from Sunderland Pit, Ontario, Ontario Canada was used in all mortars at a constant rate of 45% by volume.

The effects of w/b ratio, and cement replacement by slag and fly ash - on the resistance of cement mortars to PSA were investigated. Sulfate resistant portland cement (ASTM Type V) mortars with w/cm ratio of 0.35, 0.40, 0.45 and 0.50 were tested. Sulfate resistant cement was used in order to minimize chemical sulfate attack. The effect of SCM on PSA was studied using mortars with w/b ratio of 0.40. The replacement levels of cement by SCM were: 45 and 65% for GGBFS, and 20 and 40% for FA. The mix designs are shown in Table 2. The mass of sand is given in oven dry condition, and additional water was added to compensate for water absorption of 0.6% by mass.

Table 1: Mixture proportions [kg/m^3].

Mixture notation	**w/b**	**SCM content, %**		**Cement**	**Water**	**GGBFS**	**FA**	**Sand**
		Slag	***FA***					
M50	0.50	0	0	663	332	0	0	1182
M45	0.45	0	0	706	318	0	0	1182
M35	0.35	0	0	811	284	0	0	1182
M40	0.40	0	0	755	302	0	0	1182
SG45	0.40	45	0	406	295	332	0	1182
SG65	0.40	65	0	256	292	475	0	1182
FA20	0.40	0	20	594	297	0	148	1182
FA40	0.40	0	40	438	292	0	292	1182

2.2 Methods

For each mixture, three mortar prisms of 51 mm × 51 mm × 266 mm were cast for PSA exposure. The specimens were demolded at the age of 1 day and kept in saturated lime solution until 3 days. After 3 days of age the specimens were removed from the solution and kept in sealed conditions at 23 °C until the start of sulfate exposure at 28 days. This curing regime was selected considering common practice and standard requirements in North America. For sulfate exposures CSA A23.1-14 [6] requires “additional” curing for the highest level of sulfates that corresponds to 7 days of curing, though no wet curing is required. Sealed curing would meet the CSA definition of additional curing. According to this Canadian standard [6] “extended” wet curing of 7 days is only required for extremely severe chloride exposure. Thus the curing conditions used here, wet curing until the age of 3 days and sealed curing until the age of 28days, exceed the “additional” curing requirements of [6] but would likely be inferior to “extended” curing.

Sulfate exposure involved thermally cycling mortar prisms submerged in sodium sulfate solution. Thermal cycles were between 4 ±1 and 32 ±2 °C with maximum cooling and heating rates of 2.5 and 4 °C/h, respectively. The duration of one full thermal cycle was 24 hours. The concentration of sodium sulfate solution was 30% by mass and the solution was replaced

every 5 cycles. The damage caused by PSA was assessed by means of mass loss. The measurements were taken every 10 cycles.

Fundamental transverse, longitudinal, and torsional resonant frequencies of mortar specimens was measured using forced resonance method according to ASTM C215 [17]. Ultrasonic pulse velocity was measured in accordance with ASTM C597 [18] using transducers with the resonant frequency of 54 kHz. Mass loss was measured using scales with the capacity of 3 kg and precision of 10 mg.

3. Results and discussion

The deteriorated mortar samples after 100 thermal cycles are shown in Figure 1. As can be recognized in Figure 1, the nature of damage caused by PSA is surface scaling. It can be seen that tested mixtures exhibited degree of deterioration ranging from very high in mortar with w/b ratio of 0.50 to minor in the mortars with slag. However, besides the size change, it is very hard to rate the degree of deterioration by visual appearance. The surface of all samples was affected by PSA. If significantly larger samples would be used in testing, it would be hard to quantify visually the difference between the resistance to PSA of these mixtures. For this reason, the rate of deterioration due to PSA was also assessed using mass loss, dynamic modulus of elasticity by measured by means of UPV, fundamental transverse frequency and fundamental longitudinal frequency, and modulus of rigidity determined by fundamental torsional frequency. The comparison of the mass loss and the durability factors determined by these methods for mortar with w/b ratio of 0.50 is shown in Figure 2.

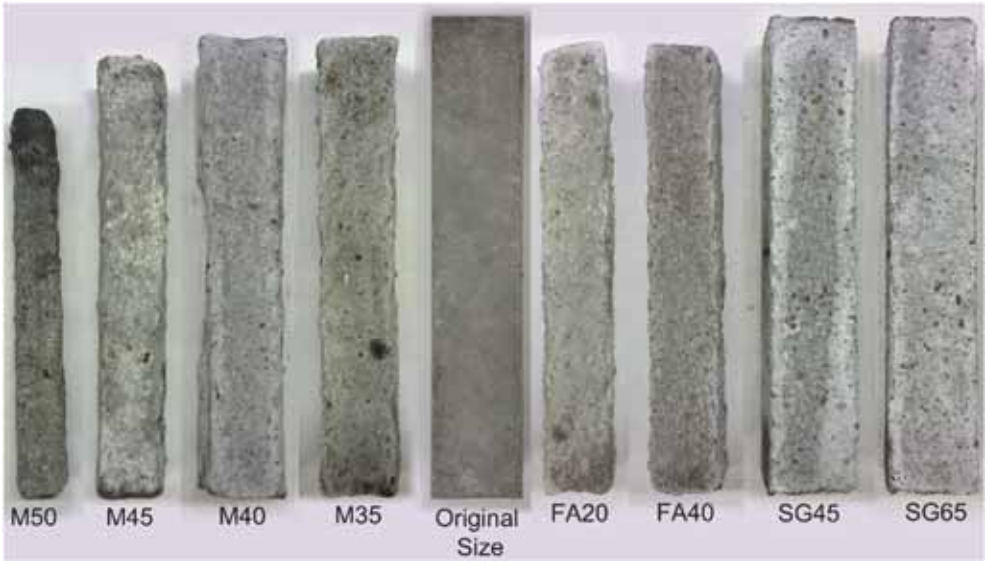

Figure 1: Deteriorated samples after 100 thermal cycles

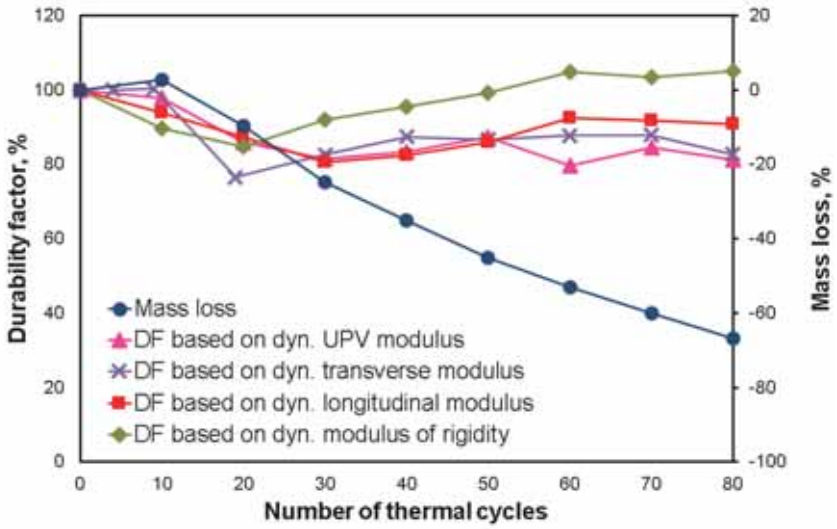

Figure 2: Comparison of different methods for evaluation of deterioration rate for mortar with w/b ratio of 0.50.

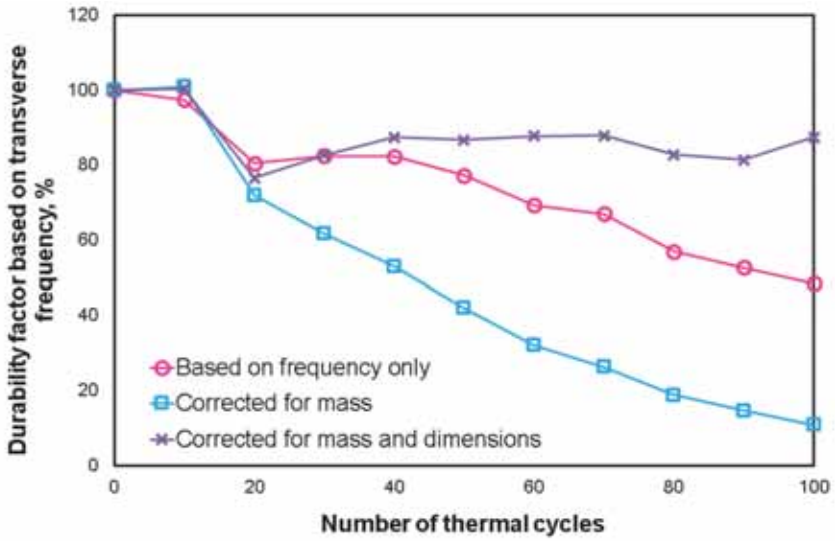

Figure 3: Durability factor based on fundamental transverse frequency

The mortar with w/b ratio of 0.50 was selected to show the differences between various methods used to assess the rate of PSA, because it had the highest degree of damage, although the same tendency was observed in all tested mortar mixtures. It can be seen in Figure 2 that only mass loss reflects the full extent of degradation caused by PSA. It should be noted that

durability factor based on a fundamental frequency may be calculate by different ways. For example, in ASTM C666 [19], durability factor is calculated based on the ratio of the square of the fundamental frequency after and before the detrimental exposure. However, dynamic properties depend not only on the fundamental frequency, but on the mass and dimensions of the tested sample. In case of severe damage, mass loss and dimensional changes may significantly affect the fundamental frequency. In Figure 3, the durability factor is calculated based on the fundamental transverse frequency only, with corrections for mass and with full correction for mass loss and dimensional changes are compared. As can be seen in Figure 3, the reduction of dynamic transverse modulus of elasticity is about 20%, while durability factor based solely on the fundamental frequency reduces by more than 50%. Because of high mass loss, the durability factor with the correction for the mass shows degradation of almost 90%. However, as can be seen in Figures 2 and 3, due to the nature of damage the true elastic properties of the mortar exposed to PSA are not impaired proportionally to the extent of deterioration. Figure 3 shows the values calculated based on fundamental transverse frequency as it is the most widely used method, but the same pattern appears in the other dynamic properties. In addition, due to significant reduction of the cross-section, the dimensional ratio of length to maximum transverse direction is shifted away from the optimum. Thus, it may be concluded that mass loss is the most effective approach to evaluation of the damage in PSA.

The comparison of mortar mass losses during PSA exposure is given in Figure 4. Here the difference in PSA resistance between various mixtures can by quantified more easily than by visual appearance. In addition, it can be recognized that the rate of deterioration during PSA exposure was not constant. The rate of mass loss of mortars as function of thermal cycles number is shown in Figure 5. It can be seen that all mixtures demonstrated a sort of induction period in the beginning of exposure. Most mixtures increased the mass during the first 10 cycles, after which the mass loss started with an increasing rate. After this initial period the rate of mass loss either stabilized or decreased. There may be two reasons for the decrease of the rate of mass loss. First, the size of deteriorating specimens decreased, and the surface available for PSA is reduced as well. Since the nature of the damage causing mass loss is surface scaling, the rate of mass loss depends on the surface area exposed to PSA. Second, the specimens during PSA exposure are submerged in sodium sulfate solution. This may promote hydration, particularly in the mixtures containing SCMs. Most probably, this is the reason for the reduction of the rate of mass loss in the mixtures with fly ash as the later stages of testing. Thus, FA mixtures could benefit from a longer period of moist curing. Further investigation is needed to confirm this hypothesis.

As expected, the reduction of w/b ratio increases the resistance of mortars to PSSA. The difference in PSSA resistance between w/b ratios of 0.50, 0.45 and 0.40 are significant. However, there is not much change in PSA resistance between w/b ratio of 0.40 and 0.35. The possible reasons for this behavior maybe insufficient compaction, since the workability of mortars decreased with w/b ratio since no plasticizing admixture was used. Comparing the resistance of mortars with and without SCMs with the same w/b ratio, it can be seen that GGBFS significantly improved the resistance to PSA, while it was reduced with FA. It is interesting to note that the content of SCMs didn’t have significant impact on the behavior of mortars in PSA.

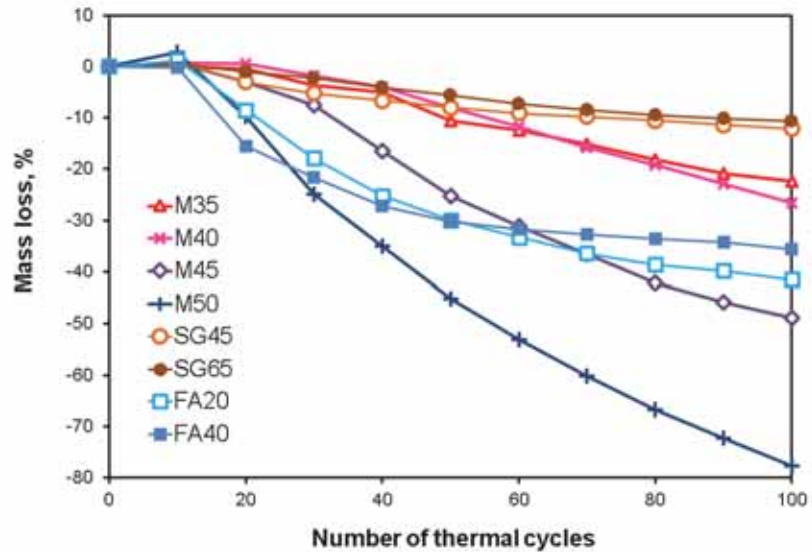

Figure 4: Mass loss of mortars as a function of thermal cycles

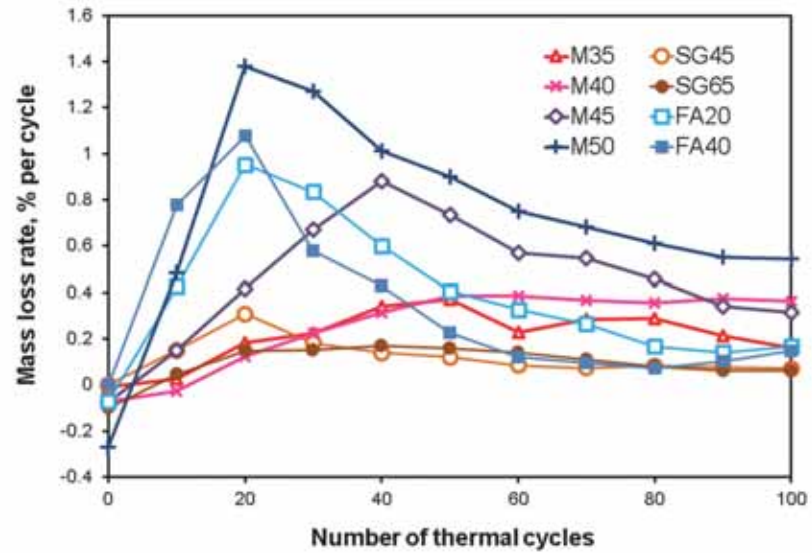

Figure 5: Mass loss rate of mortars as a function of thermal cycles

It can be seen that suggested exposure conditions combined with mass loss measurements are valuable methods for testing the resistance of cementitious materials to PSA. This method demonstrated good sensitivity that enabled precise capture of the differences in rate of deterioration due to PSA in mortar mixes with a wide range of w/b ratios and two different

SCMs. The results of such testing method can be used for comparison of different mixture designs for a construction project. In order to use the results of this type of test method for service life prediction, the performance of suggested concrete mixture can be compared to the performance of a mixture with known performance from field testing.However, it is impossible to mimic all possible real live scenarios of aggressive environmental conditions either by laboratory or by field testing. The best approach is to obtain basic properties using laboratory testing and use them for service life predictions by means of modeling. Further research is needed to extend this testing method to concretes.

4. Conclusions

Based on the presented experimental results the following conclusions can be made:

- The combination of the selected sample size and thermal cycling in 30% sodium sulfate solution produced exposure conditions suitable for testing of the resistance to physical sulfate salt attack for a wide range of mortar mixture designs.
- Mass loss was the most efficient and sensitive method for the evaluation of the extent of damage and rate of deterioration during exposure to physical sulfate salt attack.
- Further research is needed to extend the suggested testing method to concretes.

References

[1] Mehta, P. and Monteiro, P. J. M., Concrete: Microstructure, Properties, and Materials, 3rd ed., McGraw-Hill, (2006).
[2] Hooton, R., Current developments and future needs in standards for cementitious materials, Cem Concr Res 78 (2015), 165-177.
[3] Haynes, H., O'Neill, R. and Mehta, P. K., Concrete deterioration from physical attack by salts, Concr Int 18 (1996), 63-68.
[4] Haynes, H., O'Neill, R., Neff, M. and Mehta, P. K., Salt weathering distress on concrete exposed to sodium sulfate environment, ACI Mat J 105 (2008), 35-43.
[5] Verbeck, G. J., Field and laboratory studies of the sulfate resistance of concrete, in Performance of Concrete. A symposium in Honor of Thorbergur Thorvaldson, ACI and National Research council of Canada, Reprinted as Portland Cement Association Bulletin RX227, (1968).
[6] CSA A23.1-14, Concrete materials and methods of concrete construction, Canadian Standards Association, Toronto, Ontario, Canada, (2014).
[7] ACI 318-14, Building Code Requirements for Structural Concrete and Commentary, American Concrete Institute, (2014).
[8] Stark, D., Performance of Concrete in Sulfate Environments, Portland Cement Association, Skokie, Illinois, USA, (2002).
[9] Stark, D., Durability of concrete in sulfate rich soils, Portland Cement Association, Skokie, Illinois, USA, (1989).
[10] Irassar, E., Di Maio, A. and Batic, O., Sulfate attack on concrete with mineral admixtures, Cem Concr Res 26 (1996), 113-123.

[11] ASTM C452-15, Standard Test Method for Potential Expansion of Portland-Cement Mortars Exposed to Sulfate, American Society for Testing and Materials, USA, (2015).
[12] ASTM C1012-15, Standard Test Method for Length Change of Hydraulic-Cement Mortars Exposed to a Sulfate Solution," American Society for Testing and Materials, USA, (2015).
[13] Folliard, K. and Sandberg, P., Mechanisms of concrete deterioration by sodium sulfate crystallization, in Durability of Concrete, Proceedings Third CANMET - ACI International Conference, ACI SP145, Nice, France, (1994).
[14] McMillan, F., Stanton, T., Tyler, I. and Hansen, W., Long-Time Study of Cement Performance in Concrete, Chapter 5, ACI Special Publication, published in cooperation with the Portland Cement Association, American Concrete Institute, (Reprinted as Portland Cement Association Research Department Bulletin 30, Portland Cement Association, Skokie, IL.), Farmington Hills, MI, (1949).
[15] Haynes, H. and Bassuoni, M., Physical Salt Attack on Concrete, Concr Int. 33 (2011), 38-42.
[16] Bassuoni, M. and Nehdi, M., Durability of self-consolidating concrete to different exposure regimes of sodium sulfate attack" Mat and Struc 42 (2009), 1039-1057.
[17] ASTM C215-08, Standard Test Method for Fundamental Transverse, Longitudinal, and Torsional Resonant Frequencies of Concrete Specimens, American Society for Testing and Materials, USA, (2008).
[18] ASTM C597-09, Standard Test Method for Standard Test Method for Pulse Velocity Through Concrete, American Society for Testing and Materials, USA, (2009).
[19] ASTM C666-15, Standard Test Method for Resistance of Concrete to Rapid Freezing and Thawing, American Society for Testing and Materials, USA, (2015).
[20] Haynes, H., Sulfate Attack on Concrete: Laboratory vs. Field Experience, Concr Int 24 (2002), 64-70.
[21] Yoshida, N., Matsunami, Y., Nagayama, M. and Sakai, E., Salt weathering in residential concrete foundations exposed to sulfate-bearing ground, J of Adv Concr Technol 8 (2010), 121-134.
[22] Liu, Z., Deng, D. and De Schutter, G., Does concrete suffer sulfate salt weathering?, Constr and Build Mat 66 (2014), 692-701.

International RILEM Conference on Materials, Systems and Structures in Civil Engineering
Conference segment on Service Life of Cement-Based Materials and Structures
22-24 August 2016, Technical University of Denmark, Lyngby, Denmark

THE IMPORTANCE OF MULTIPHYSICS AND MULTISCALE MODELLING OF CONCRETE TO UNDERSTAND ITS COMPLEX MACROSCOPIC PROPERTIES

Jörg F. Unger [(1)], Vitaliy Kindrachuk [(1)], Volker Hirthammer [(1)], Thomas Titscher [(1)], Christoph Pohl [(1)]

(1) Federal Institute for Materials and Structures, Berlin, Germany

Abstract
Concrete is a complex material. Its properties evolve over time, especially at early age, and are dependent on environmental conditions, i.e. temperature and moisture conditions, as well as the composition of the material. This leads to a variety of macroscopic phenomena such as hydration/solidification/hardening, creep and shrinkage, thermal strains, damage and inelastic deformations. Most of these phenomena are characterized by specific set of model assumptions and often an additive decomposition of strains into elastic, plastic, shrinkage and creep components is performed. Each of these phenomena are investigated separately and a number of respective independent models have been designed. The interactions are then accounted for by adding appropriate correction factors or additional models for the particular interaction. This paper discusses the importance of reconsider even in the experimental phase the model assumptions required to generalize the experimental data into models used in design codes. It is especially underlined that the complex macroscopic behaviour of concrete is strongly influenced by its multiscale and multiphyscis nature and two examples (shrinkage and fatigue) of interacting phenomena are discussed.

1. Introduction

The understanding and the prediction of the macroscopic behaviour of concrete is very important to ensure a safe design of structural components. In the design phase, it is often very difficult and certainly not appropriate to use complex models with a multiscale and multiphysics approach. The focus is in many cases a safe design for the ultimate limite state. However, a profound understanding of the material behaviour with a realistic modelling of hardening and the interacting phenomena is required to understand the behaviour under service conditions or the evaluation of a structure after extraordinary loading situations. This ranges from the detection of microcracking, crack spacing and crack opening, creep and shrinkage deformations up to the influence of high temperatures or fatigue loading. In this

case, the experimental investigations of interacting phenomena are usually performed with a specific modelling assumption, e.g. a linear decomposition of the strain into elastic, plastic, shrinkage and creep components. Interactions are then taken into account by additional interaction terms.
An example is concrete under combined thermal and mechanical loads, where often an additive decomposition into mechanical and thermal strains is done. The mechanical model is calibrated for constant room temperature, whereas the thermal model is adjusted for zero mechanical load. The (nonlinear) interaction is then characterized by so called load induced thermal strains [1].

Even though this approach seems to be straightforward in general, it has several drawbacks

- these interaction terms have to be calibrated separately and only model the real physics in a homogenized, macroscopic way;
- it is often difficult to design experiments, where only a single parameter is changed and calibrated, and the distribution of this parameter is often not fully homogeneous within the specimen;
- the predictive capacities of models with interaction factors are often limited to the set of training/validation data, since the interaction model is purely phenomenological and does not capture the real physics;
- the consideration of additional inputs requires a recalibration of the model, i.e. the heating of concrete does not only change the temperature, but also induces drying which itself leads to shrinkage phenomena. So depending on whether shrinkage is considered as additional (additive) strain, the interaction term varies;
- the number of parameters for those models is often large and particularly the interaction terms often do not have a clear physical meaning;
- the thermodynamic consistency of the model is sometimes difficult to ensure, e.g. when modelling a series of loading scenarios with a parallel temporal evolution of macroscopic properties such as strength, Young's modulus or fracture energy, which is especially important at early age.

As a consequence, the choice of the right model assumptions is very important, especially when dealing with multi-physics problems. Two models might give very similar results, e.g. a damage or softening plasticity model for monotonic loading. However, both models will give significantly different results for general loading sequences including unloading. A similar example is the modelling of shrinkage in concrete based either on a strain or stress based approach. Pure shrinkage deformations can be modelled appropriately with both approaches, but it will be demonstrated that combined loading (mechanical, thermal, moisture content) might lead to significantly different results.

A second reason for the macroscopic complex behaviour of concrete is the importance of its heterogeneous structure. This comprises very different scales. Some (non exhaustive) examples are

- atomistic models
  - the influence of moisture on macroscopic creep behaviour is often explained by the disjoining pressure due to very thin layers of water;
- microscale models
  - micro-cracks lead to a macroscopic softening with a quasi-brittle post-peak

- mesoscale models
    - particles and cement paste have significantly different properties. This includes the time-dependent hydration of the cement paste compared to the fixed properties of the aggregates, only cement paste is prone viscous deformations and the different properties, e.g. in the simplest case the Young's modulus, lead to a heterogeneous distribution of the quantity of interest, e.g. stresses.

2. Mesoscale generation

In the following, a special focus is given to mesoscale models.

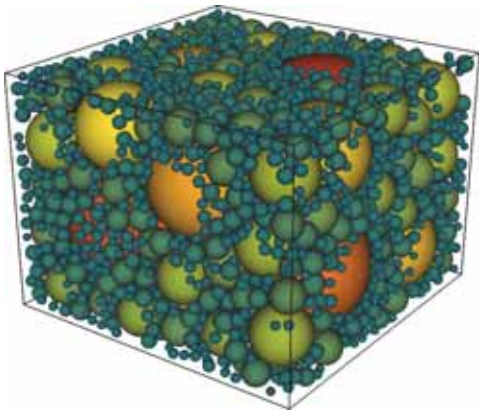

Figure 1 : Mesoscale geometry of a concrete cube with spherical aggregates.

For modelling purposes, the procedure of simulating virtual concrete specimens with a direct discretization of the mesoscale structure can either be performed by scanning real specimens [2] or by sampling "virtual" concrete specimens. In the latter case, the grading curve characterizes the size distribution of the aggregates within the material. In this case, the discretization can be decomposed into a take and a place phase. In the first phase, the particles numbers shapes are generated, whereas in the second step these particles are placed into the specimen with the constraint that overlapping is not allowed. In our current model, an algorithm based on [3] is used. The particles are assumed to be spherical and inserted at random positions within the specimen with a reduced diameter. This requires checks to avoid overlapping, but due to the reduced diameter and the corresponding low particle volume this is computationally not expensive and can be performed with standard checks enhanced with special subboxes to reduced the number of overlapping checks. In the second step, an event-driven molecular dynamics simulation is performed with initial random velocities of the particles and a slow growth of the particle radii up to the envisages size. For detailed information, the reader is refered to [3]. An example of mesoscale geometries created with the enhanced algorithm is given in Figure 1.

3. Multiphysics modelling of shrinkage

Shrinkage in concrete is usually determined experimentally for stress free conditions. For modelling purposes, this experimentally determined shrinkage strain is often subtracted from the macroscopic strain assuming that shrinkage only produces stresses if the macroscopic deformation of the specimen is constrained.

Looking at concrete on a mesoscale level, a heterogeneous material consisting of aggregates and cement paste is present, where only the latter is prone to shrinkage deformations. As a consequence, internal stresses at the particle boundaries occur. Especially at early ages, these

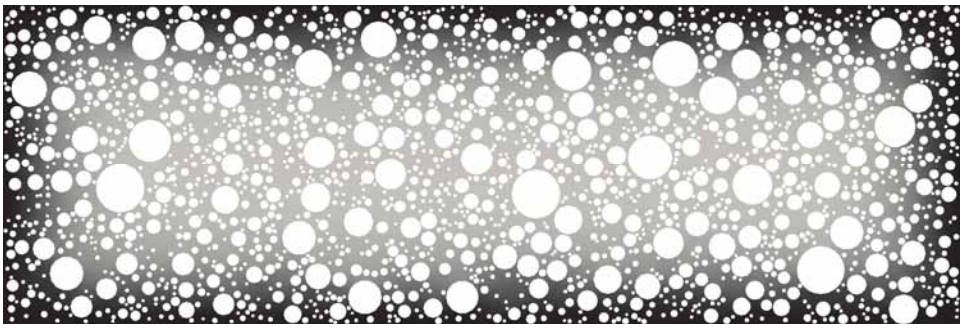

Figure 2 : Distribution of relative humidity after 28 days of drying.

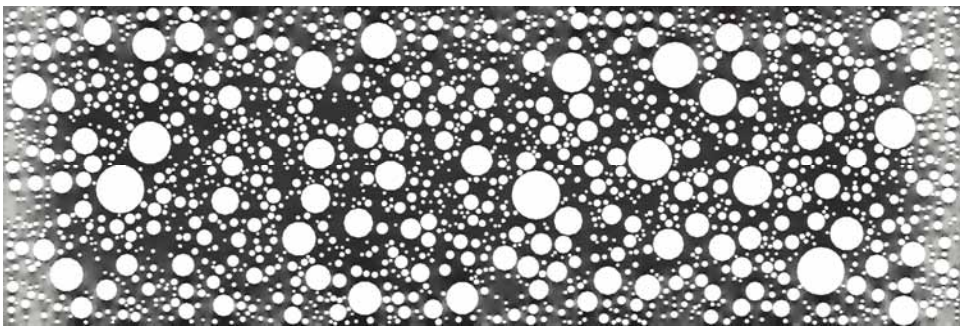

Figure 3 : Ratio between local and macrospic strain in horizontal direction.

stresses are significant and lead to a microcrack evolution and a pre-damage (without any mechanical loads).

In this paper, shrinkage is assumed to be a reversible process related to the moisture content of the material. It is difficult to test this assumption experimentally, since fully rewetting the specimen is not possible. Moreover, the aging effects are always present resulting in additional permanent strains that are sometimes interpreted as permanent shrinkage strains.

A two-phase moisture transport model based on [4] has been implemented. In Figure 2, an exemplary moisture distribution within a concrete specimen (40mm x 160mm) after 28 days of drying is illustrated. A Fullers-curve for the aggregate size distribution with a maximum aggregate size of 16mm was used. The drying process starts once the relative humidity of 95% is reduced to 40%. A large gradient of the moisture distribution is observed with the core of the specimen remaining almost at the initial RH of 95%. Under the assumption of the moisture content being the driving force of shrinkage strains, this leads to a very heterogeneous distribution even for this small specimen as illustrated in Figure 3. Another remark is related to the hydration of the concrete material that is characterizing the development of the material strength. The hydration stops at relative humidities below 80%.

As a consequence, any experimental test that measures the concrete strength (or similar the Young's modulus) as a function of the time or degree of hydration should take this heterogeneous distribution into account. Otherwise, size effects are present and the generalization of the results is very difficult since other effects such as e.g. creep strongly influence the results.

There are many different approaches on how to include the relation between shrinkage and moisture content in the numerical model. The first approach follows a strain based model [5]. Based on the simulation of the moisture distribution and an experimental shrinkage tests, an additional strain component is calculated. Note that when using this approach with a direct discretization of the mesoscale structure, substantial tensile stresses are obtained.

Calibrating a shrinkage model based on weighting the specimen, that is calculating the loss of water in a homogeneous way, might significantly deviate from the real situation, since – as already discussed – the moisture distribution is strongly heterogeneous. Due to the drying

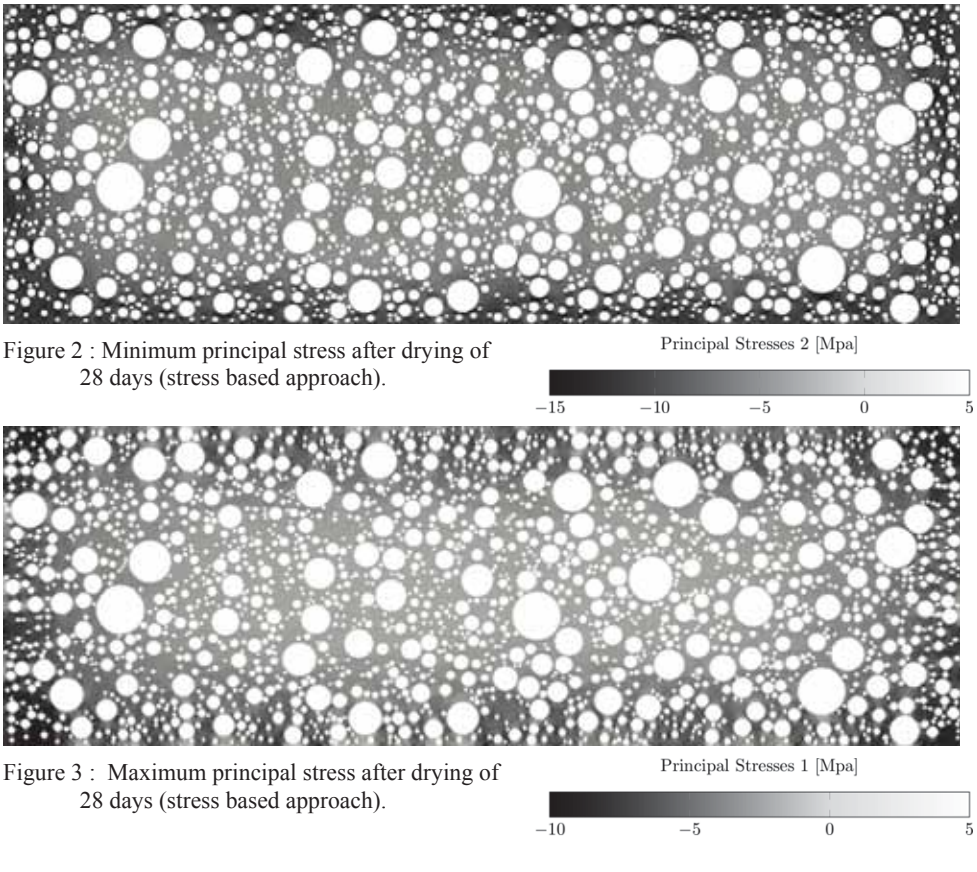

Figure 2 : Minimum principal stress after drying of 28 days (stress based approach).

Figure 3 : Maximum principal stress after drying of 28 days (stress based approach).

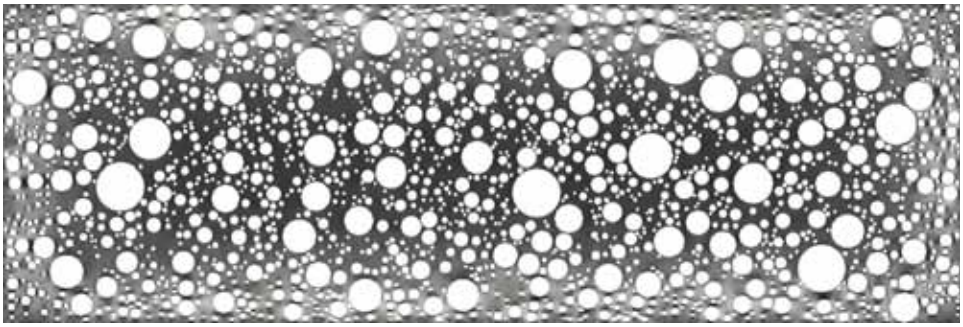

Figure 4 : Minimum principal stress after drying of 28 days (strain based approach).

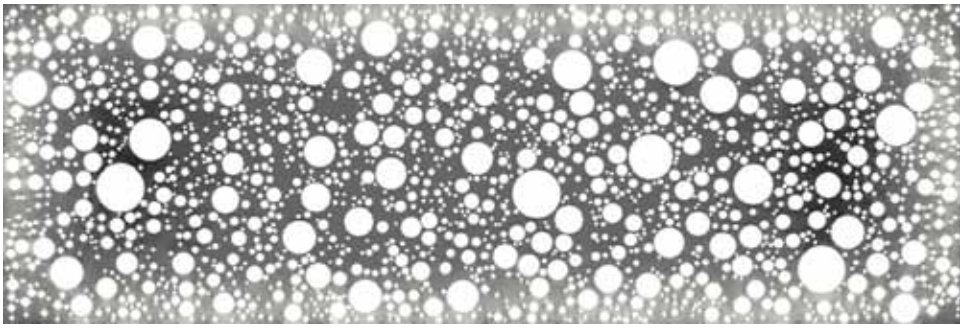

Figure 5 : Maximum principal stress after drying of 28 days (strain based approach).

shrinkage in the outer layer and the almost zero shrinkage strains in the core, tensile stresses in the outer layer build up and the specimen is no longer stress free. This effect is already present for a macroscopic model, but additional restraining stresses build up when considering the mesoscale structure. As a consequence, a calibration of a strain based shrinkage model can only be obtained by a direct modelling of the experimental setup (and not a smeared diagram where weight loss and thus water volume fraction is plotted over macroscopic strains).

Another option to model shrinkage strains is based on the Biot-theory of porous media with an additional stress component resulting from the moisture distribution.

$$\boldsymbol{\sigma}_{\mathrm{cap}} = \eta_{\mathrm{w}} \cdot p_{\mathrm{cap}} \cdot \boldsymbol{I}, \tag{1}$$

where the capillary pressure p_{cap} can be calculated from the local relative humidity using the Kelvin equation as discussed in [6]. The parameter η_{w} comprises the water volume fraction, and $\boldsymbol{I}$ is the identity tensor to link the scalar variables to the hydro-static stress tensor. Shrinkage in this model is then interpreted as a hydrostatic pressure on the solid skeleton. According to [7], an additional contribution is due to surface adsorbed water as well as interlayer water. The latter is neglected in our model, since it does not contribute for relative

humidities above 20%. The results of the simulation are shown in Figure . As discussed before, this only corresponds to the capillary pore water, the effects for surface adsorbed water for 40% RH are in the same order of magnitude, resulting in roughly twice as much global shrinkage strains. For the calculation, a Young's modulus of the matrix material of 30GPa has been used, the particles have a Young's modulus of 60GPa. According to the figure, the strain distribution is strongly heterogeneous along the horizontal direction with a maximum at the two ends and in the vertical direction at the top and bottom. This is due to the core of the sample that is still at a RH of 95% and thus constrains the shrinkage of the outer layer in the central part. Furthermore, the strong influence of the mesostructured is recognized that is assumed to be inert regarding shrinkage.

The corresponding principal stresses are plotted in Figure 2 and Figure 3 for the stress based approach, where a large hydrostatic stress state is obtained. The consideration of mesoscale structure directly creates tensile stresses in some parts of the specimen that are in the order of the material strength. For the strain based approach shown in Figure 4 and Figure 5, the tensile stresses in the matrix are significantly larger.

Both approaches (strain or stress based) result in a very similar distribution of shrinkage deformations. The main difference is that a coupling with a mechanical load does not induce any influence on the strength for a strain based coupling (at least not for specimens that are not restrained while drying), whereas the stress based approach shifts the failure surface in the principal stress space of the mechanical failure surface along the hydrostatic axis. For the additional hydrostatic pressure, shrinkage would be accompanied with an increase of the uniaxial compressive strength, whereas the strain based model predicts a strength independent of the moisture content.

4. Mesoscale modelling of fatigue with a continuum model

Evaluation of fatigue life is usually derived from a linear elastic simulation of the very first cycle in order to comprise the stress level, more precisely the mean stress and the oscilation amplitude. In combination with the experimentally determined Wöhler lines, the safety of the structure is verified. For different loading amplitudes and mean values, a damage accumulation theory such as the Palmgren Miner rule is used. This assumes a linear accumulation of damage for different stress levels. The approach seems to be natural from an engineering point of view, but it inherently has many weak points including both experimental limitations

- the experimental determination of Wöhlerlines is very time consuming, especially for relatively low stresses with a large number of cycles up to final failure. Furthermore, a high number of samples per setup is required to obtain statistically reliable results, since the scatter for fatigue tests is in the order of a factor of 10;
- standard Wöhler lines do not include a mean value of the stress. The additional consideration of the mean stress in the test program is often not feasible. In addition, the real stress in a structure is rarely a uniaxial stress, but a full 3D problem. The extrapolation from 1D to 3D requires additional assumptions,

and model assumption. These include

- the assumption of the linear damage accumulation which is only a rough approximation. It has been shown [8] that first cycling with low amplitudes and a subsequent large amplitude leads to a longer life time compared to linear theory,

whereas first loading with large amplitudes with subsequent lower amplitudes results in a reduced life time. As a consequence, this assumption may or may not be conservative;

- ignorance of the stress redistribution which is attributed to accumulated damage within the fatigue cycles as well as creep deformations that reduce stress concentrations;
- size effects that are well captured to influence the static behaviour of concrete are not taken into account;
- the evaluation of the structural performance with the reduced stiffness and permanent deformations is not possible at intermediate stages;
- a combination with other influences is only possible to macroscopic phenomenological coupling terms that are difficult to calibrate and often lack a clear physical interpretation.

For this purpose, a continuum model for fatigue deterioration of concrete has been developed [9]. This model is based on a viscoplastic formulation in the effective stress space, where isotropic damage is related to the irreversible strains. For details, the reader is referred to the original paper. As can be seen in Figure 6 in [9], the model is able to approximate the general trend of the Wöhler line. A better lifetime prediction in the low cycle regime can be achieved once the reversible strain is assumed to contribute to damage as well. Furthermore, the application to structural problems requires additional regularization procedures such as the gradient enhanced damage model [10]. An generalization of the model is required to extend the model towards applications in fatigue modelling.

The stress $\boldsymbol{\sigma}$ in the new model is given as a function of the elasticity tensor $\boldsymbol{C}$ and the local elastic strain $\boldsymbol{\varepsilon}$

$$\boldsymbol{\sigma} = (1-\omega)\,\boldsymbol{C} : \boldsymbol{\varepsilon}, \tag{2}$$

with an isotropic damage variable ω. Generally, the regularization can be formulated by either expressing the isotropic damage using an integral type nonlocal model, or as a gradient enhanced model using additional nonlocal quantities as unknowns and an additional Helmholtz equation to describe its evolution. The latter approach is proposed here, since the bandwidth of the corresponding stiffness matrices is constant. The evolution equation for the equivalent nonlocal strain is given by

$$\overline{\varepsilon}^{eq} - c\nabla^2\overline{\varepsilon}^{eq} = \varepsilon^{eq}, \tag{3}$$

with additional Neumann boundary condition for the nonlocal quantities. For a discussion on the model see e.g. [11]. The local equivalent strain is given by a modified von Mises criterion according to [12]. In the original formulation by Peerlings, damage occurs once the maximum equivalent strain κ achieves the threshold strain ε_0

$$D = 0 \text{ if } \kappa \leq \varepsilon_{0,} \tag{4}$$

$$D = 1 - \frac{\varepsilon_0}{\kappa}\exp\left(\frac{\varepsilon_0 - \kappa}{e_f}\right) \text{ if } \kappa > \varepsilon_0. \tag{5}$$

An exponential softening is assumed in the present model. The damage variable is now driven by the accumulated strain instead of the accumulated irreversible strain as in the previous

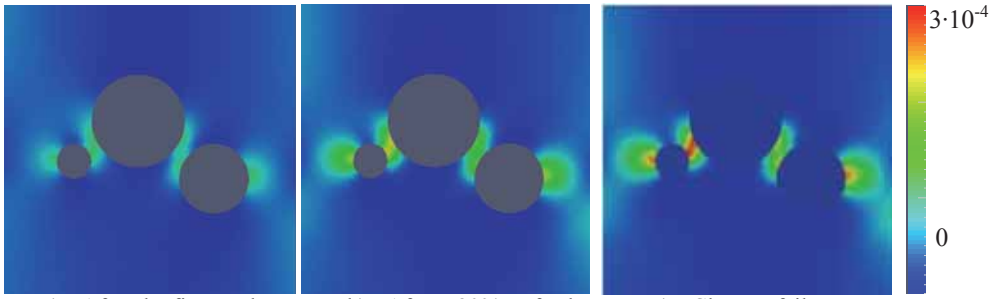

a) After the first cycle b) After 20% of the lifetime c) Close to failure

Figure 6 : Evolution of the nonlocal equivalent strain $\bar{\varepsilon}^{eq}$ at different stages of the lifetime.

model. In order to allow for the cyclic damage accumulation, the evolution equation was reformulated by the initial value problem

$$\dot{D} = \left(\frac{\partial \kappa}{\partial D}\right)^{-1} \left(\frac{\bar{\varepsilon}^{eq}}{\kappa}\right)^{n} \langle \dot{\bar{\varepsilon}}^{eq} \rangle_{+}, \tag{6}$$

where the history variable κ is no longer the maximum equivalent strain in the material point. Using this continuum model to simulate fatigue requires a time discretization that decomposes each cycle into subincrements, e.g. 12 subincrements. For high cycle fatigue with a total number of cycles until failure in the order of 10^6, this exceeds most computational resources, especially when dealing with complex heterogeneous mesoscale models that itself require a fine resolution of the spatial discretization.

For this purpose, a cycle jump method has been implemented. The idea is based on the assumption that the stress within consecutive cycles is quasi-periodic. The increment of the history variables that characterize the evolution of damage is calculated within a single cycle and then extrapolated to the next 10, 100 or 1000 cycles. After the extrapolation step, an equilibrium solution has to be calculated and another cycle is fully integrated to obtain the next jump for the extrapolation. A result of the calculation is shown in Figure 6, where the evolution of the equivalent nonlocal strain is plotted for different stages of the lifetime. A displacement controlled tensile analysis is performed in vertical direction with a mean displacement amplitude corresponding to 10% of the mean displacement. A stress amplitude resulting in the first cycle achieves 45% of the tensile strength (f_t = 3MPa, f_c = 20 MPa, E = 40 GPa, c=18mm², n=1, $e_f = 0.33$, $\varepsilon_0 = 7.5\,10^{-5}$). In this test case, only voids are considered to validate the cycle jump method and the extension of the model to fatigue for heterogeneous models.

The example should only demonstrate that a continuum model for fatigue has to include the influence of the heterogeneous microstructure. It allows to evaluate the damage state and the crack distribution within the specimen/structure at intermediate stages of the lifetime. Furthermore, interactions with other effects such as thermal loads, creep/shrinkage or the influence of the mean stress as well as the full 3D-stress state can be taken into account. It is further to be highlighted that, in this model, the static strength is assumed to be the limiting case of fatigue failure with a failure after a single cycle. As a consequence, standard material test can be used to calibrate the fatigue model with only a few additional tests required to

characterize the cyclic damage accumulation. In addition, a continuum model to simulate fatigue failure can incorporate other effects that where previously discussed, notably shrinkage, creep, thermal strains, order effects or the influence of the mean stress as well as the full three-dimensional stress state.

5. Summary

In this paper, the importance of simulating concrete as a multiphysics and multiscale material have ben highlighted. It is emphasized that most scenarios (including mechanical as well as thermal, hygral loading or the time-dependent solidification/hardening) are not separable and a profound understanding of nonlinear effects requires a full coupling. The advantage is that otherwise phenomenologically determined interaction coeffcients are automatically included in the model as thus simplify the calibration of material parameters and thus the generalization capabilities of the model.

References

[1] Khoury, G.A., Strain of heated concrete during two thermal cycles. Part 3: isolation of strain components and strain model development. Magazine of Concrete Research, 2006. **58**(7): p. 421-435.
[2] Nagai, G., T. Yamada, and A. Wada, Three-dimensional nonlinear finite element analysis of the macroscopic compressive failure of concrete materials based on real digital image. Proc. 8th ICCCBE. 2000, Stanford Univ., California, USA. 449-456.
[3] Titscher, T. and J.F. Unger, Application of molecular dynamics simulations for the generation of dense concrete mesoscale geometries. Computers & Structures, 2015. **158**: p. 274-284.
[4] Johannesson, B. and U. Nyman, A Numerical Approach for Non-Linear Moisture Flow in Porous Materials with Account to Sorption Hysteresis. Transport in Porous Media, 2010. **84**(3): p. 735-754.
[5] Havlasek, P., Creep and shrinkage of concrete subjected to variable environmental conditions, in Faculty of Civil Engineering, Department of Mechanics. 2014, Czech Technical University, Prague.
[6] Coussy, O., et al., The equivalent pore pressure and the swelling and shrinkage of cement-based materials. Materials and Structures, 2004. **37**(265): p. 15-20.
[7] Pinson, M.B., et al., Hysteresis from Multiscale Porosity: Modeling Water Sorption and Shrinkage in Cement Paste. Physical Review Applied, 2015. **3**(6).
[8] Zhang, B., D.V. Phillips, and K. Wu, Further research on fatigue properties of plain concrete. Magazine of Concrete Research, 1997. **49**(180): p. 241-252.
[9] Kindrachuk, V.M., M. Thiele, and J.F. Unger, Constitutive modeling of creep-fatigue interaction for normal strength concrete under compression. International Journal of Fatigue, 2015. **78**: p. 81-94.
[10] Peerlings, R.H.J., Enhanced damage modelling for fracture and fatigue. 1999, Technische Universiteit Eindhoven.
[11] Peerlings, R.H.J., et al., Gradient enhanced damage for quasi-brittle materials. International Journal for Numerical Methods in Engineering, 1996. **39**: p. 3391-3403.
[12] de Vree, J.H.P., W.A.M. Brekelmans, and M.A.J. van Gils, Comparison of nonlocal approaches in continuum damage mechanics. Computers and Structures, 1995. **55**(4): p. 581-588.

International RILEM Conference on Materials, Systems and Structures in Civil Engineering
Conference segment on Service Life of Cement-Based Materials and Structures
22-24 August 2016, Technical University of Denmark, Lyngby, Denmark

RESIDUAL CONCRETE STRENGTH AFTER SUSTAINED LOAD: EXPERIMENTAL RESULTS AND MODELLING APPROACH

Zainab Kammouna [1,2], Matthieu Briffaut [1,2], Yann Malecot [1,2]

(1) Univ. Grenoble Alpes, 3SR, Grenoble, France
(2) CNRS, 3SR, Grenoble, France

Abstract
Rheological models for estimating the creep of concrete generally assume that concrete is an homogeneous material. Therefore, strains incompatibilities between the cement paste and aggregates when the concrete is subjected to a creep loading cannot be taken into account whereas they can generate microcracking. These microcracks may cause a decrease of the elasticity modulus and of the strength of concrete, and an increase in the amount of creep strains under the same loading level. This increase in creep strains can be considered as the source of nonlinearity with the stress level. To study the influence of these microcracks on the mechanical behaviour, compressive creep tests at different loading level (50% and 80% of the strength) and for different age of loading (1 and 3 month) have been performed followed by quasi static test to measure the residual concrete strength. Experimental results highlight different trends with respect to the age of loading. Besides, a viscoelastic-damageable model has been adopted for calculating creep using a mesoscopic meshing approach. The results show that a significant proportion of non-linearity can be explained by the microcracks and that the mesoscopic approach allows to reproduce a strength decrease for hardened concrete.

1. Introduction

The existing models for estimating creep of concrete, based on a rheological model generally assume that concrete is a homogeneous material (see for instance [1-3]). Therefore the incompatible strains between cement paste and aggregates throughout creep loading could not be taken into account. Recently, [4] represents concrete as a composite material which consist of spherical elastic inclusions (aggregate and/ or voids) imbedded in a linear viscoelastic matrix. Nevertheless, the model does not take into account micro-cracks at cement-aggregates interface level which occurs due to incompatible deformations between these two materials.

Experimentally the relation between the stress level and creep is not linear. Microcracks at cement – aggregates interface which is directly related to the stress level could be a reason.

Indeed, creep of concrete is related to the creep of cement paste rather than aggregates. Therefore, these lasts act as an obstacle and a resistance to the global creep. Consequently, tensile stresses arise close to the interface between cement paste and aggregates and lead to micro-cracks in this zone. A decrease of the modulus of elasticity and the strength of concrete and an increase in the amount of creep strain under the same loading level is therefore expected. This creep strain increase is seen as a nonlinearity of the strain with respect to the stress level.

To reproduce this nonlinearity at a macroscopic scale, a coupling between damage and creep was proposed by [5]. Another solution was given by using a rheological law which depends on the stress level. Nevertheless, the tertiary creep could not be achieved when the concrete is considered as a homogenous material without coupling with damage. Recently, mesoscopic mesh has been used to study the failure of concrete beam under flexural load and highlight the presence of microcracking during the sustained load [6].

The aim of this research is to study the influence of micro-cracks due to incompatible strains between cement paste and aggregates, on the creep strains amplitude. Hence, a visco-elastic-damage model [2] is adopted for computing creep using a mesoscopic mesh for representing the greatest size of aggregate (more than 1mm) in the cement paste [7].

After a short presentation of the model and the mesh used in this study, the first part of the paper is devoted to study the creep of concrete in compression. This part allows verifying the ability of this model in estimating the creep of concrete under variant loading levels and mainly for studying the nonlinearity of creep strain with respect to stress level. For studying the probability of cracking prediction in concrete under compressive creep, the experimental results of Roll [8] was adopted.

Experimentally, the effects of creep strain on the residual mechanical properties of concrete like Young's modulus and compressive strength were not clearly mentioned in previous creep studies [6] and [9]. Therefore, the second part of this paper presents the evolution of the concrete compressive strength due to creep loading under two different loading levels (80% and 50%) and two age of loading.

2. Mesoscopic creep test simulation

2.1 Mesoscopic mesh

The algorithm of mesh generation used in this study was developed by [7]. Numerical simulations are performed in two dimensions (plane stresses) on a Representative Elementary Volume (REV) of concrete of 100×100 mm² (Figure 1). In this mesoscopic approach, two phases are considered; cement paste and aggregates. The mesh is not adapted to the exact shape of aggregates, but the properties of the material are projected on a finite element mesh square grid. The model used for aggregates is an elastic damageable model whereas the cement paste strains are described by a visco-elastic damageable model.

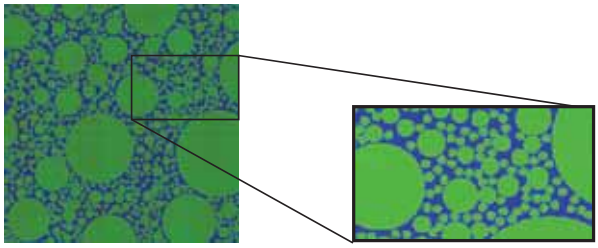

Figure 1: Mesh of the REV

2.2 Mechanical model

The viscoelastic damage model used is described in [2] and [10]. The mechanical behaviour of concrete is modelled by an elastic damage model [11] uncoupled with creep. The advantage of using a mesoscopic approach arises in the possibility of using simplified behavior laws. The mesoscopic damage occurs due to the geometric representation of cement and aggregate which have different material properties.

The relationship between apparent stresses $\boldsymbol{\sigma}$, effective stresses $\tilde{\boldsymbol{\sigma}}$, damage D, elastic stiffness tensor $\mathbf{E}$, total strain ε, elastic strains $\boldsymbol{\varepsilon}_e$, basic creep strains $\boldsymbol{\varepsilon}_{bc}$, total strain $\boldsymbol{\varepsilon}$, is given by:

$$\boldsymbol{\sigma} = (1-D)\tilde{\boldsymbol{\sigma}} = (1-D)\mathbf{E}(\xi)\dot{\boldsymbol{\varepsilon}}_e = (1-D)\mathbf{E}(\xi)(\dot{\boldsymbol{\varepsilon}} - \dot{\boldsymbol{\varepsilon}}_{bc}) \tag{1}$$

The damage criterion defined by [Mazars, 86] reads:

$$f = \varepsilon_{eq} - k_0 \tag{2}$$

Where $\boldsymbol{\varepsilon}_{eq}$ is the equivalent elastic is strain and k_0 is the tensile strain threshold and it is equal to $\frac{f_t}{E}$. The post peak behaviour is calculated as a function of the cracking energy (G_f) and of the element size (h). This regularised technique based on the proposition of Hillerborg (1978) allows to avoid strong mesh dependency.

The basic creep model use two Kelvin Voigt units (KV) (Figure 2)[2]. Creep is defined in the effective stress space, and then damage is added afterwards taking into account only the elastic part.

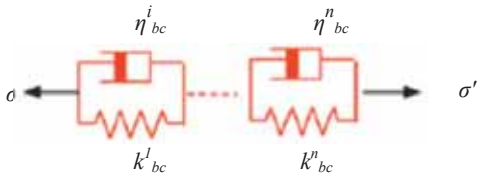

Figure 2: Kelvin-Voigt elements for predicting creep strain [2]

2.3 Compressive test results

The experimental compressive creep results of [8] for four loading levels (25%, 35%, 50% and 65% of the compressive strength) were adopted. The creep law parameters were calibrated for the lowest loading level whereas the mechanical properties were calibrated with ordinary cement paste values [7] and to obtain no damaged element after the instantaneous loading at 25% of the compressive strength.

A comparison between the experimental results and the mesoscopic approach with and without damage are presented in Table 1 and Figure 2. The figure and the table highlight that the simulation of creep evolution with damage are closer to the experimental ones than the simulation curves without damage. Assuming that creep of concrete occurs without damage means that there are no micro-cracks at the interface between cement paste and aggregate. Consequently, there is no additional creep strain that occurs normally due to these micro-cracks. The mesoscopic approach reveals the nonlinearity between the creep strain and the applied load. It could be seen, for example, that for the highest loading level, the percentage of nonlinearity due to the incompatible strains and the associated damage is about 66%. Nevertheless, if an accurate prediction can be obtained with 2D model for tension test, for compressive test, 3D modelling is required.

By comparing the field of damage for two loading levels 25% and 65%, one can remark that the damage amount is higher for 65% than that for 25% as expected. That is related to the tensile stresses that develop at the cement paste - aggregates interface and lead to the cracking development. As the creep strain of cement paste is directly related to the loading level, the damage at the interface between cement paste and aggregates increases.

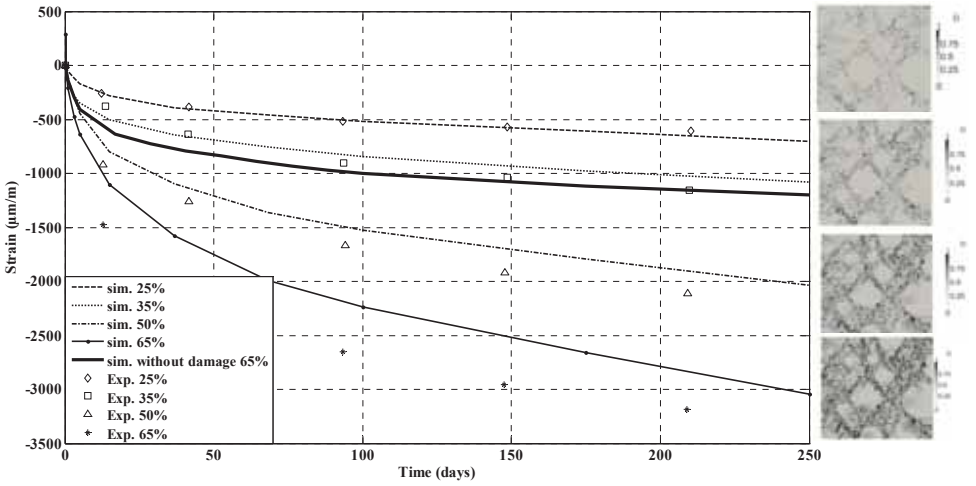

Figure 2: Compressive creep strain evolution: comparison between experimental data and mesoscopic approach with and without damage

Table 1: Comparison of the experimental compressive creep results with those of mesoscopic approach with and without damage (Nonlinearity% = 100 (ε_{wd} - ε_{wod}) / (ε_{exp} - ε_{wod})

Loading level		Exp. Results	Sim. Results		Explained Nonlinearity
MPa	$\sigma / \sigma_{25\%}$	(ε_{exp}) 10^{-6} at 210days	With damage (ε_{wd}) 10^{-6}	Without damage (ε_{wod}) 10^{-6}	%
10.5	1.4	1153	1026	594	77.2
15	2	2108	1719	836	69.4
19.5	2.6	3183	2476	1087	66.3

2.4 Numerical mechanical behaviour after creep loading in compression

Fichant [12] developed two damage models (isotropic model and orthotropic model) to solve problems with more complex loadings. In these models, the damage development is coupled with the cracking energy. When the radial loading is applied, the isotropic model is adequate while for the disproportionate loading, the orthotropic model is adopted. In both models, a coupling could be done with plasticity and unilateral effects.

The damage affects the elastic part of the stress-strain relation behavior [12]:

$$\sigma_{ij} = C_{ijkl}\,\varepsilon_{kl} \tag{3}$$

Where C_{ijkl} is the stiffness of the damaged material whereas σ_{ij} and εkl C_{ijkl} represent the components of the stresses tensors and elastic strain tensor.

The equivalent strain is calculated from the elastic strain ε_e and the damage evolution law is expressed as follows:

$$D' = 1 - \frac{\varepsilon_{d0}}{\varepsilon_{eq}} \exp\left(B_t(\varepsilon_{d0} - \varepsilon_{eq})\right) \text{ when } D' \rangle 0 \tag{4}$$

where ε_{d0} is the threshold in tension. The parameter B_t is calculated as a function of cracking energy G_f and of the element size h with the following equation:

$$B_t = h \cdot f_t / G_f \tag{5}$$

where f_t is the tensile fracture stress of the material. This regularised technique based on the proposition of [13] allows to avoid strong mesh dependency.

In this study, the isotropic model is used without plasticity and unilateral effect. Moreover, damage in compression is also unconsidered. Indeed, at the mesoscale, the rupture is assumed to be only due to extension. The geometric representation of the constituents and the contrast between material properties is assumed the source of complex behavior observed at the macroscopic scale.

Figure 3 represents the constitutive law of compressive behaviour after creep in compressive had taken place. It reveals that the maximum strength and in the Young modulus are lower for the concrete specimens that were under a higher creep loading and all are lower than the one

which were not subjected to creep test. Comparing to the specimens that were not subjected to the creep test, the strength decreasing for creep specimens that were under creep loading could reach 13% while the Young Modulus decreasing is about 25%. The Young modulus decrease is therefore due to both creep strains and previous loading of the structure to a stress level of 25, 35, 50 or 65% and could not be only attributed to only creep.

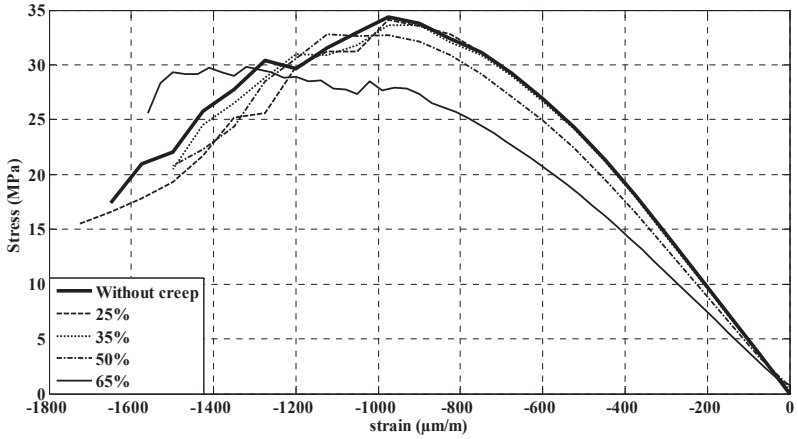

Figure 3: Constitutive law - compressive test before creep and after creep in compression had taken place.

3. Experimental campaign

For performing the compressive basic creep test, concrete cylindrical specimens (diam. 7cm, length 14cm) were used. For two concrete maturity (1 or 3 months; curing under water), two loading levels (stress/strength = 0.5 and 0.8) were applied for two months. The creep device is based on the principle of the roman balance which allows maintaining a constant loading (see figure 4). After the creep test, the residual mechanical properties of concrete were compared to control specimens from the same batch but which had not been submitted to sustain loading. For each strength value, three concrete specimen where tested.

The concrete mix design is close to one that was extensively caracterized in our laboratory under uniaxial and triaxial behaviour and is given in table 2. The low maximal aggregate size (8mm) allows to obtain a representative concrete specimen.

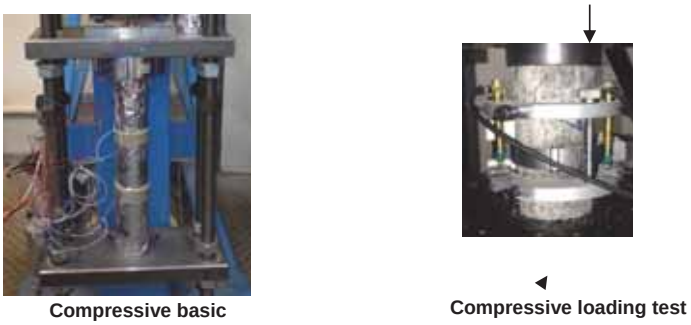

Figure 4: Creep test device and instantaneous compressive test

Table 2: Concrete mix

Constituant	Weigth in Kg for 1m^3
Water	174
Cement (CEM I 52.5)	348
Sand (0 - 1.8mm)	826
Gravel (0.2 – 8mm)	991

3.1 Creep test results

Longitudinal mean strains during the creep test are plotted in figure 5 (measured by two strain gages for two concrete specimens). As expected, higher the stress/strength ratio is higher is the strains. The effect of the concrete maturity between 1 and 3 month remains slight.

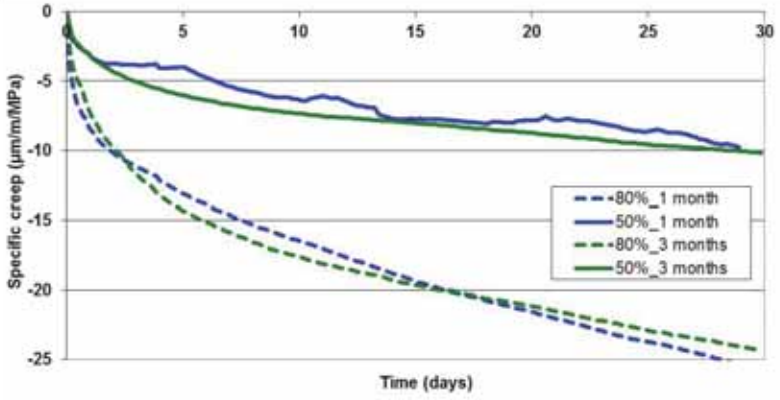

Figure 5: Creep strains evolution for two loading rate (stress/strength = 80% and 50%) and two loading age (1month and 3 month)

Thanks to the strain measurements in two directions (parallel and perpendicular to the loading), an apparent creep Poisson ratio could be calculated. The results for the loading age

equals to 3 months and for two loading level tests, is displayed in the figure 6. One can remark that after a slight increase, theses lasts seem to tend around a value which is close to 0.2.

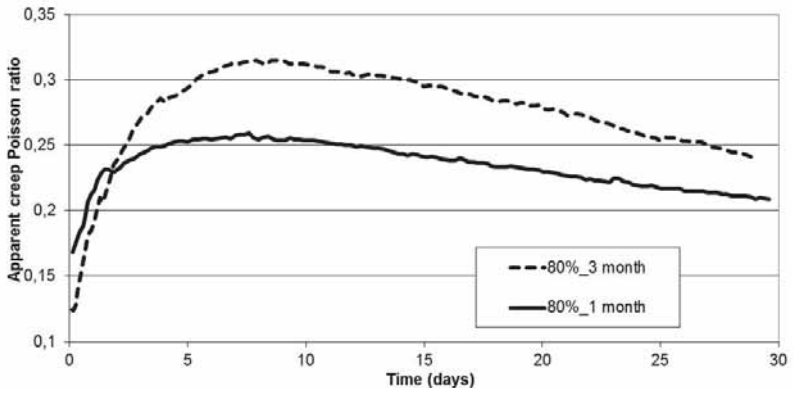

Figure 6: Apprarent creep Poisson ratio evolution for two loading rate (stress/strength = 80% and 50%)

3.2 Mechanical strength after creep loading

From figure 8 which presents the compressive strength evolution due to the creep loading, different trends could be remarked. In the one hand, for the specimens which were loaded at one month after casting, a significant increase in compressive strength is observed for two loading levels, 50% and 80%. On the other hand, for the higher concrete maturity (3 months) a slight decrease is obtained for the both loading levels. It is therefore obvious that at least two phenomena are in competition. The first one is the microcracking at the cement paste/aggregate interface which could explain the strength decrease. The compressive strength increase could be explained by the solidification theory proposed by Bažant [14] or by an increase of the hydration due to microcrack. Indeed, microcracks become new path for water to react with anhydrous cement and create inner hydration product. Another possibility is that creep reduces stress concentrations (especially when dealing with real aggregate shapes) and thus lead to an increase of the maximum strength.

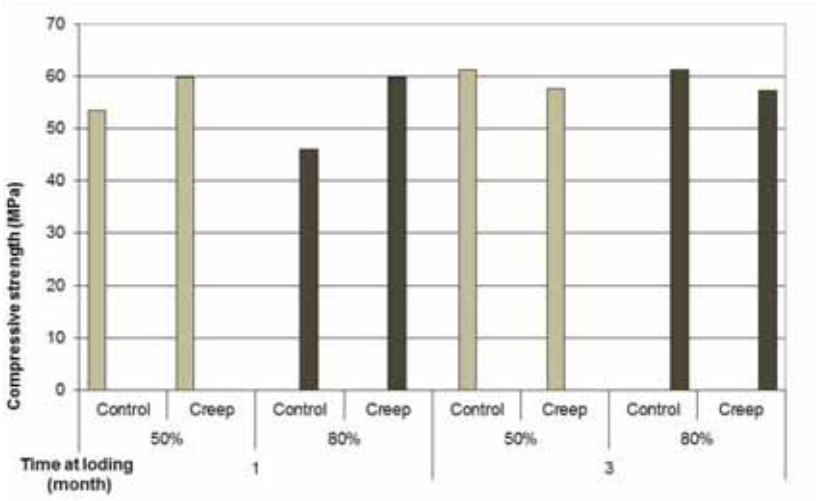

Figure 7: Compressive strength evolution due to creep loading

4. Conclusion

In this study, the numerical part was devoted to study the effect of micro cracks during creep loading type in compression. It is worth noting that the use of a mesoscopic mesh allows retrieving the nonlinearity with respect to loading level without having to introduce coupling between creep and damage. Indeed, although these mesoscopic simulations are based on simple assumptions as the form of aggregates (spherical), the absence of Internal Transition Zone (ITZ) and a 2D plane stress state, its value is noticeable at a loading level of 65%.

In the second part, experimental tests were presented to highlight the effect of creep for different age of loading on the concrete strength. The results show that in function of the concrete maturity, the strength increases due to creep effect for one month age loading while slightly decreases for older concrete (3 months). It is obvious that damage model are not able to reproduce the strength increase even if hydration is taken into account (early age behaviour model are not able to reproduce the concrete properties evolution after one month) and that mesoscopic approach should be coupled with the solidification theory proposed by Bažant to be more realistic.

References

[1] Sellier, A. and Buffo-Lacarrière, L., (2009), "Vers une modélisation simple et unifiée du fluage propre, du retrait et du fluage en dessiccation du béton", Revue Européenne de Génie Civil, Vol. 13, No. 10, pp. 1161-1182.
[2] Benboudjema, F. and Torrenti, J.-M. (2008), "Early-age behaviour of concrete nuclear containments", Nuclear Engineering and Design, Vol. 238, pp. 2495-2506.

[3] Bazant, Z.P. and Panula L., (78-79)"Practical Prediction of Time-Dependent Deformations of Concrete", Materials and Structures, RILEM, Part (1)- Shrinkage and Part (2)-Basic Creep: Vol.11, No.65, Sep.-Oct. 1978, pp. 307-328; Part (3)-Drying Creep and Part (4)-Temperature Effect on Basic Creep: Vol. 11, No.66, 1978, pp. 415-434; Part (5)-Temperature Effect on Drying Creep: Vol.12, No.69, 1979, pp. 169-182.
[4] Thai, M.-Q., Bary B. and He Q.-C., (2014), "A homogenization-enriched viscodamage model for cement-based material creep", Engineering Fracture Mechanics, Vol. 126 (2014), pp.54-72.
[5] Mazzotti C, Savoia M., (2003) "Nonlinear creep damage model for concrete under uniaxial compression". Journal of Engineering Mechanics, ,129(9), 1065–75.
[6] Saliba, J., Grondin F., Matallah M. and Loukili A., (2012), "Relevance of a mesoscopic modelling for the coupling between creep and damage in concrete", Mechanics of Time-Dependent Materials, Vol. 16, No.4.
[7] Nguyen T., Lawrence C., La Borderie, C., Matallah, M. and Nahas, G. (2010), "A mesoscopic model for a better understanding of the transition from diffuse damage to localized damage", European Journal of Environment and Civil Engineering, Vol.14(6-7), pp.751-776.
[8] Roll, F. (1964). "Long time creep-recovery of highly stressed concrete cylinders". ACI Special publication no. 9 - Symposium on creep of concrete, pp. 113–114.
[9] Brooks, J. J. and Neville, A.M. "A comparison of creep, elasticity and strength of concrete in tension and in compression", Magazine of Concrete Research, Vol. 29, No. 100, 1977, pp. 131-141.
[10] Briffaut, M., Benboudjema, F., Torrenti, J.-M. and Nahas, G. (2011), "Numerical analysis of the thermal active restrained shrinkage ring test to study the early age behavior of massive concrete structures", Engineering Structures, vol. 33(4) pp.1390-140.
[11] Mazars, J., (1984), "Application de la mécanique de l'endommagement au comportement non linéaire et à la rupture du béton de structure", PhD thesis ENSET, LMT, in French.
[12] Fichant, S., La Borderie, C., and Pijaudier-Cabot, G. 1999. "Isotropic and anisotropic descriptions of damage in concrete structures", Mechanics of Cohesive-Frictional Material, vol. 4 pp.339–359.
[13] Hillerborg A., Modeer M. and Petersson P. E. (1976), "Analysis of crack formation and crack growth in concrete by means of fracture mechanics and finite elements", Cement and Concrete Research, vol. 6, p. 773-782.
[14] Bažant Z.P., Prasannan S. (1989), Solidification theory for concrete creep I. Formulation, Journal of Engineering Mechanics, vol. 115 (8), p. 1691-1703.

International RILEM Conference on Materials, Systems and Structures in Civil Engineering
Conference segment on Service Life of Cement-Based Materials and Structures
22-24 August 2016, Technical University of Denmark, Lyngby, Denmark

REMAINING SERVICE LIFE OF RAILWAY PRESTRESSED CONCRETE SLEEPERS

Sakdirat Kaewunruen [(1)], Shintaro Minoura [(2)], Tsutomu Watanabe [(2)], and Alex M Remennikov [(3)]

(1) The University of Birmingham, Birmingham, UK
(2) Railway Technical Research Institute, Tokyo, Japan
(3) University of Wollongong, Wollongong, Australia

Abstract
Prestressed concrete sleepers (or railroad ties) are structural members that distribute the wheel loads from the rails to the track support system. Over a period of time, the concrete sleepers age and deteriorate in addition to fully experiencing various types of static and dynamic loading conditions, which are attributable to train operations. Recent studies have established two main limit states for the design consideration of concrete sleepers: ultimate limit states under extreme impact and fatigue limit states under repeated probabilistic impact loads (low and high cycles). It was noted that the prestress level has a significant role in maintaining the high endurance of the sleepers under low to moderate repeated impact loads. Based on extensive field investigations and experimental tests, this paper presents a variation of static and dynamic load condition of railway concrete sleepers in revenue services. It presents the limit states involving in testing and evaluating for the remaining service life of railway prestressed concrete sleepers. Experimental results are also highlighted to demonstrate the deterioration and toughness of the sleepers after services.

1. Introduction

Railway prestressed concrete sleepers have been utilised in railway industry for over 50 years. The railway sleepers (called 'railroad ties') are a main part of railway track structures. A major role is to distribute loads from the rail foot to the underlying ballast bed. Based on the current design approach, the design life span of the concrete sleepers is considered around 50 years [1-3]. Figure 1 shows the typical ballasted railway tracks and their components. There are two main groups of track components: substructure and superstructure. The substructure includes subballast, subgrade, and ground formation, while the superstructure consists of rails, rail pads, fastening systems, railway sleepers (concrete or timber) and ballast (crushed aggregate). Railway track structures often experience the aggressive dynamic loading conditions due to wheel/rail interactions associated with the irregularities in either a wheel or

a rail [4]. The magnitude of the dynamic impact loads per railseat is varying from 200 kN to sometimes more than 750 kN, whilst the design static wheel load per railseat for a 40-tone axle load could be only as much as 110 kN [5-6].

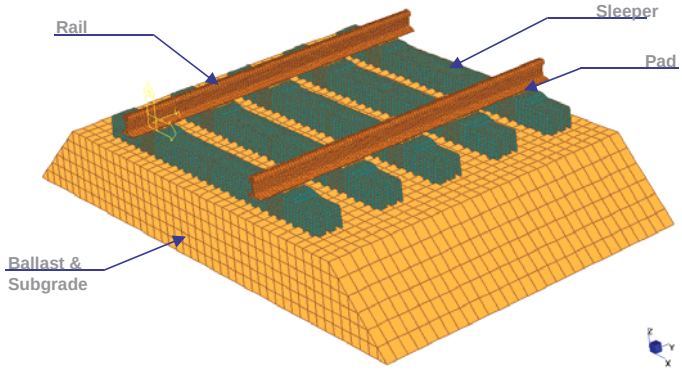

Figure 1: Illustration of typical railway track system and its components (generally sleepers are embedded in ballast)

All static, quasi-static, and impact loads are very important in design and analysis of railway track and its components. The typical dynamic load imposed by running wagons can be treated as a quasi-static load when no irregularity exists. However, when the irregularity appears, dynamic shock loading corresponds to the frequency range from 0 to 2000 Hz due to modern track vehicles passing at any generic operational speed [7-8]. The shape of impact loading varies depending on various possible sources of such loading, e.g. wheel flats, out-of-round wheels, wheel corrugation, short and long wavelength rail corrugation, dipped welds and joints, pitting, and shelling. Wheel/rail irregularities induce high dynamic impact forces along the rails that may greatly exceed the static wheel load. In all cases, the impact forces are significantly dependent on the train speed. These impulses would occur repetitively during the roll. Loss of contact between wheel/rail, so-called "wheel fly", will occur if the irregularity is large enough, or the speed is fast enough. However, the impact force could be simplified as a shock pulse applied right after when the static wheel load is removed during the loss of contact [8]. The typical magnitude of impact loads depends on the causes and the traveling speed of train. The durations of such loads are quite similar, varying between 1 and 10 msec. However, the representative values of the first peak (P_1) of the forces caused by dipped joints should be about 400 kN magnitude with 1 to 5 msec time duration. For the second peak (P_2), the average values are about 80 kN magnitude and 5 to 12 msec time duration. The effect of impact forces depends on the duration. It was found that the longer the duration, the significance the effect [4]. Therefore, it should be taken into account that the typical duration of impact wheel forces varies widely between 1 and 12 msec [4, 9, 10].

A recent study showed that it is highly likely that railway sleepers could be frequently subjected to severe impact loads [11]. In general, the dynamic load characteristics considered in design and analysis include the magnitudes of impact loading and the variety of pulse durations. In general, although the loading and strain rate effects may increase the strength of

materials, the high loading magnitude could devastate the structural members. In structural design and analysis, the public safety must not be compromised so the design loads must be appropriate and associated with the long return periods, which would optimally provide the low probability of occurrence on structures during their design life. For further explanation, a design load that is associated with 50 year return period has the likelihood of occurrence that the design load might happen only once in 50 years regardless of the structural life span. Wheel load is an important factor in design and analysis of railway track and its components. The design load (F^*) for the limit states design concept takes into account both the static (F_s) and dynamic (F_i) wheel loads. There are three main steps in designing the concrete sleepers. First, the design actions or loads are to be determined based on the importance level of the track (e.g. $F^* = 1.2\ F_s + 1.5\ F_i$). Then, the design shear and moment envelopes can be achieved by converting the design load to sleeper responses using advanced railtrack dynamic analysis or the design formulation [12]. Last, the strength and serviceability of the prestressed concrete sleepers can be optimized in accordance with AS3600 Concrete structures (Standards Australia, 2012). An initially proposed limit states design methodology and procedure can be found in details in Remennikov et al. [13].

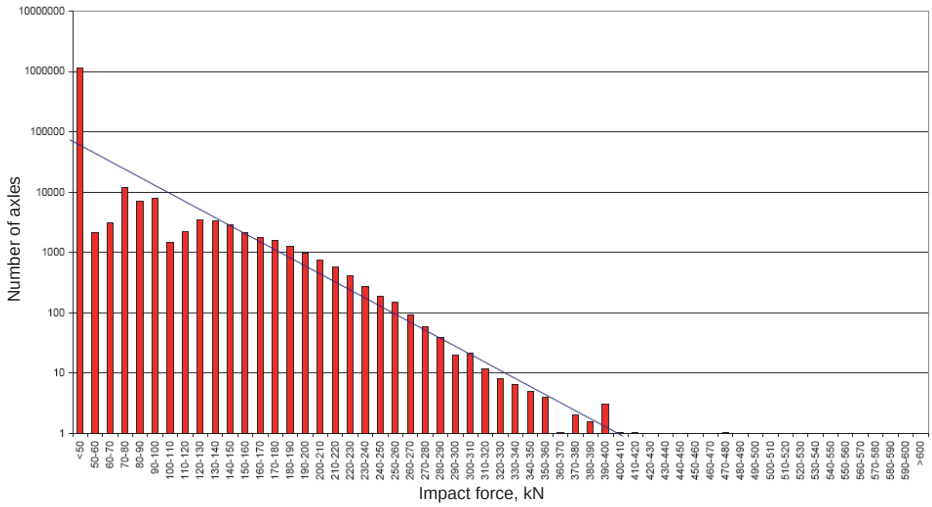

Figure 2: Example of statistical data of actual track loading [15]

Leong [15] showed the statistical data of wheel loading obtained from railway networks in Queensland, Australia. Using probabilistic analysis, the possibility of occurrence related to the magnitude of impact loading on railway sleepers can be predicted. Figure 2 shows a statistical data of actual wheel loading applied on top of the rail obtained from a railway network in North Queensland [15-16]. From Figure 2, the relationships between the impact forces I (kN) and the return periods R (year) can be written as follows:

$$\frac{1}{R} = 10^{-0.010I+4.1} \tag{1}$$

These formulae can be used to determine the impact force factor (k_r), which is based on the return periods and consequences of changing operations, such as speeds or wheel/rail defects [15].

Limit states concept is a more logical entity for use as the design and analysis approach for prestressed concrete sleepers, in a similar manner of Australian Standard AS3600 [3]. It considers both strength and serviceability. Over time, the concrete sleepers experience diverse traffic loads from operational activities, and may have damage and cracks, also resulting in an additional time-dependent loss in prestress level [17-19]. However, previous studies have not thoroughly investigated the deterioration and residual strength of concrete sleepers [20]. This study thus investigates the remaining life of railway prestressed concrete sleepers after a period of service life through a variety of structural testing programs. It experimentally investigates the remaining service life of railway prestressed concrete sleepers considering limit states design concept. The ageing railway concrete sleepers from various operational environments have been investigated. This paper presents the nominal reserve capacity of the old prestressed concrete sleepers from previous experimental investigations aimed at proposing a rational method for evaluating the remaining life of concrete sleepers.

2. Limit states of railway concrete sleepers

According to Leong [15], Australian railway organisations would condemn a sleeper when its ability to hold top of line or gauge is lost. It is also found that this practice is actually adopted in most of railway industries worldwide. Those two failure conditions can be reached by the following actions:

- abrasion at the bottom of the sleeper causing loss of top
- abrasion at the rail seat location causing a loss of top
- severe cracks at the rail seat causing the 'anchor' of the fastening system to move and spread the gauge
- severe cracks at the midspan of the sleeper causing the sleeper to 'flex' and spread the gauge
- severe degradation of the concrete sleeper due to alkali aggregate reaction or some similar degradation of the concrete material.

Since abrasion and alkali aggregate reaction are not structural actions causing failure conditions, only severe cracking leading to sleeper's inability to hold top of line and gauge will be considered as the failure criteria defining a limit state related to the operations of a railway system. A challenge in the development of a limit states design concept for prestressed concrete sleepers is the acceptance levels of the structural performances under design load conditions. Infinite fatigue life of sleepers *cannot* be retained after allowing cracks under impact loads. Therefore, the general principles for reliability for structures, and indicates that limit states can be divided into the following two categories:

1. **ultimate limit states**, which correspond to the maximum load-carrying capacity or, in some cases, to the maximum applicable strain or deformation;
2. **serviceability limit state**, which concerns the normal use and service life (fatigue and deformation).

Leong [15] suggested three limiting conditions would be relevant to the design of railway concrete sleeper:

Ultimate Limit State

A single once-off event such as a severe wheel flat that generates an impulsive load capable of failing a single concrete sleeper. Failure under such a severe event would fit within failure definitions causing severe cracking at the rail seat or at the midspan. The single once-off event will be based on the probabilistic analysis of train load spectrums recorded over several years or for a suitable period (generally at least a year as to obtain the good representative of track forces over its lifetime under various train/track conditions). The load magnitude of the ultimate event for ultimate limit state design of sleepers depends on the significance or importance level of the railway track. It should be noted that in some cases when the load frequency distributions can only be obtained from the long-term track force measurements, the ultimate design loads are usually taken to be the 95 percent fractiles, and hence have a 5 percent probability of being exceeded [19].

Damageability (or Fatigue) Limit State

A time-dependent limit state where a single concrete sleeper accumulates damage progressively over a period of years to a point where it is considered to have reached failure. Such failure could come about from excessive accumulated abrasion or from cracking having grown progressively more severe under repeated loading impact forces over its lifetime. In sleeper design perspective, the lifetime can be specified by the design service life of the sleepers (e.g. 30, 50, or 100 years) or from the expected train/track tonnage (or how many load cycles expected for the track infrastructure, e.g. 10, 50, or 100 million cycles). The loading ranges for the fatigue life prediction vary on the load frequency distribution as shown in Figure 2 (the load frequency data recorded for a year). Using the data in Figure 2 for fatigue life prediction of sleepers is applicable whereas the actual life must be longer than design life. Alternatively, if the sleeper is to be designed for 50 year service life under 28ton axle load, the loading range for the fatigue life consideration can be obtained from Equation 1 plus the wheel load of 140kN, which is up to 540 kN [15]. Using a statistical analysis, the number of axles or cycles of each loading range can be achieved for the cumulative fatigue damage. Based on previous example, it shows likelihood that there is only 1 time that the sleeper experiences the dynamic load of 540 kN over the sleeper design life of 50 years. Once the numbers of cycle in each loading range (e.g. 105-115 kN, 535-545 kN range) are obtained, the cumulative fatigue damage can be calculated using the endurance limits of materials or generic fatigue design codes (e.g. European Code, CEB Model code, etc.). Such damage should not result in any failure condition described earlier.

Serviceability Limit State

This limit state defines a condition where sleeper failure is beginning to impose some restrictions or tolerances on the operational capacity of the track, for example, prestressing losses, sleeper deformations (shortening and camber), track stiffness, etc. The failure of a single sleeper (in track system) is rarely if ever a cause of a speed restriction or a line closure. However, when there is failure of a cluster of sleepers, an operational restriction is usually applied until the problem is rectified. Recently, this serviceability limit state has extensively applied to the methodology for retrofit and replacement of sleepers made of different material properties in the existing aged track systems. For example, the deteriorated timber sleeper tracks have been replaced by new concrete/steel sleepers through a suitable spacing arrangement as to provide a similar track modulus or stiffness to the existing one. This

method is sometimes called 'spot replacement' or 'intersperse method'. It is important to note that a general recommendation (e.g. by Australian Office of Transport Safety Investigations) is to perform concree sleeper installation only '*in-face*' (i.e. the practice of installing the same sleeper type constinuously rather than interspersed with other sleepers in between, also referred to as '*on-face*') [21-22].

By nature, under operatinal services, the bottom face of prestressed concrete sleepers abrades by relative movement with ballast. The on-face method is likely to cause local differential stiffness and localised differential vertical smoothness ('*top*' surface geometry), resulting in a more aggressive dynamic wheel/rail interaction and causing higher level of sleeper's soffit abrasion.

3. Deterioration of concrete sleepers

This relative movement is occurred by dynamic action during train passage and impact force due to the wheel flat and rail irregularities. Abrasion of prestressed concrete sleeper can cause reduction of the loading capacity and the head of the PC steel. In this section, investigation into the abrasion of the bottom face (or called soffit) of aged prestressed concrete sleepers have been carried out in order to determine a relationship between amount of the abrasion and gross passing tonnage and aging of the prestressed concrete sleeper. In addition, effect of abrasion to loading capacity of prestressed concrete sleepers has been investigated by numerical analysis [22-23].

In this collaborative research project, more than 200 sleepers which is called "Type 3 sleeper" specified in Japanese industrial standard (JIS) have been monitored and tested under static and fatigue loading conditions in accordance with JIS standard benchmarking arrangements [24-25]. The amount of abrasion is investigated in two ways, detailed method and simple method. For the detail method, the abrasion of sleeper is measured at 20mm interval in longitudinal and rail directions. For the simple method, the abrasion is measured at 100mm intervals in only longitudinal direction.

Figure 3 shows the results of the detailed and simple methods. For sleeper A, the amount of abrasion is approximately 30mm at the rail position and 10mm at the centre of the sleeper. For sleeper B, the amount of abrasion is over 30mm in some part of the sleeper. From these figures, simple method can generally trace the detailed method. Figure 4a shows the relationships between the maximum amount of abrasion and gross passing tonnage. Amount of abrasions were measured by the simple method. The power approximations curve that guides the envelope of maximum amount of abrasion in each aging and gross passing tonnage is also shown in the figure. From Figure 4, the maximum amount of abrasion is approximately 20mm when gross passing tonnage is 1 billion tons. Furthermore, amount of abrasion exceeds 30mm when gross passing tonnage is 1.2 billion tons. For this sleeper, PC steel bar was exposed and corrosion and fracture were observed. Figure 4b shows the relationships between the maximum amount of abrasion and aging of sleepers. From the figure, maximum amount of abrasions increased with aging and it exceeds 20mm when aging is approximately 30 years.

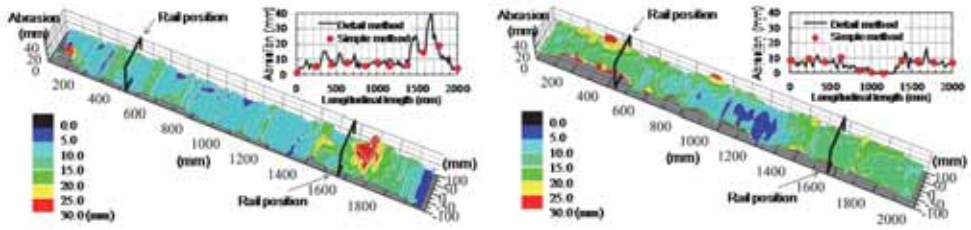

(a) Sleeper A (b) Sleeper B

Figure 3: Abrasion of railway concrete sleepers in high speed rail environment

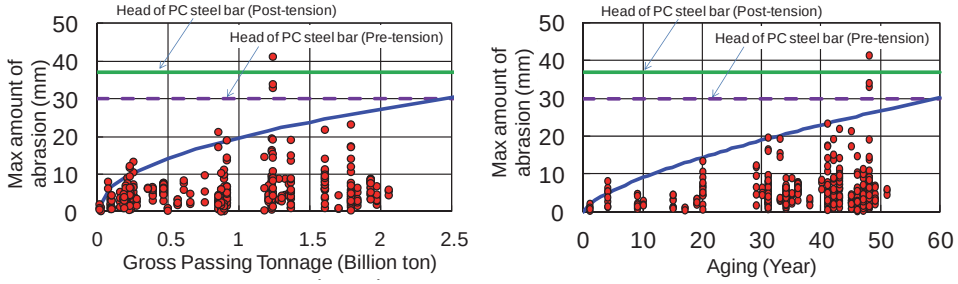

(a) Gross passing tonnage (b) Aging

Figure 4: Maximum amount of abrasion of high speed rail sleepers

In comparison, a heavy haul track section (100m track length with sleeper spacing of 0.6m) had been inspected and about 20 sleepers were extracted for further load tests in accordance with AS1085.14 [11-12]. It is found that similar load effects can be observed in Australian heavy haul environment as shown in Figure 5. However, lesser soffit abrasion can be observed in general.

4. Experimental load rating of concrete sleepers

Figure 6 shows the effect of the amount of abrasion to the loading capacity at rail position (positive bending) and the centre (negative bending) of the high speed rail sleeper. As showed in the figure, effect of abrasion to the loading capacity at the rail position was small. On the other hand, at the centre of the sleeper, loading capacity reduced with the increase of the amount of abrasion. In particular, loading capacity reduced approximately 10% with 10mm of abrasion at the rail position and loading capacity reduced 48% at the centre of the sleeper. At the rail position, even if the bottom surface of the sleeper was abraded, the distance from the compression edge of the concrete to the PC steel bar does not change. However, at the centre of the concrete, the distance from the compression edge of the concrete to the PC steel bar changes with the abrasion of the bottom face.

Figure 5: Abrasion of 30 years old heavy haul sleepers

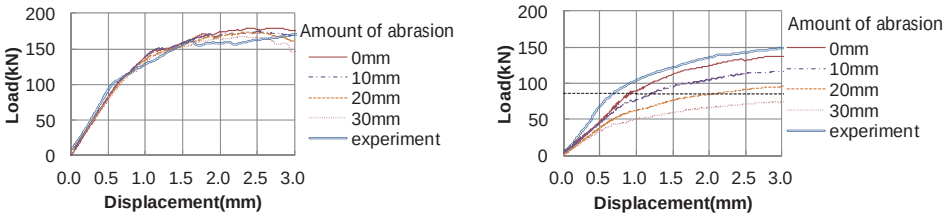

(a) Rail position (positive bending) (b) Center ot the sleeper (negative bending)

Figure 6: Effect of the amount of abrasion to the loading capacity of high speed rail sleepers

In comparison, aged sleepers have been tested under static loading to determine the positive and negative, cracking and ultimate moment capacities at the sleeper centre. The overall experimental program at the University of Wollongong indicated that heavy haul sleepers also suffer from severe abrasion of the concrete cover at the bottom surface and the concrete was damaged adjacent to the rail seat. The load-displacement relationships for both sleepers were similar up to the maximum load capacity. Figure 7 shows the load-displacement relationships for aged sleepers in heavy haul environment. Cracks started when the load reached approximately 150 kN. The crack propagated upward when the loading increased. It is found from Figures 6 and 7 that the tendency of the load carrying capacity of aged sleepers seems to be similar for both high speed and heavy haul rail operations.

4. Conclusions

This paper presents the field investigation of railway sleeper deterioration and the experimental load rating studies arose from the planned expansion of the traffics from both high speed and heavy haul rail operations. There was concern whether the railway concrete sleepers would be capable of sustaining existing operations after its design life, and whether they could be carrying the increased traffic loads. The visual inspection of the concrete sleepers revealed that there were potential problems with durability of the aged sleepers. Concrete spalling of sleepers due to tamping damage, poor construction, and loss of concrete

section due to abrasions were among the problems that could cause the rapid deterioration of strength and serviceability. The results from field observations and static tests of Japanese and Australian concrete sleepers reveal that minor structural cracking was detected in the sleepers under the most adverse loading conditions for all three track supporting conditions. This implies that the in-track sleepers are likely to be capable of resisting extreme loads generated by wheel and rail abnormalities without catastrophic failure under current traffic and even with increased traffic. The confirmation derived from numerical evaluations of fatigue life based on fracture mechanics and cumulative energy absorption will be presented elsewhere in the near future.

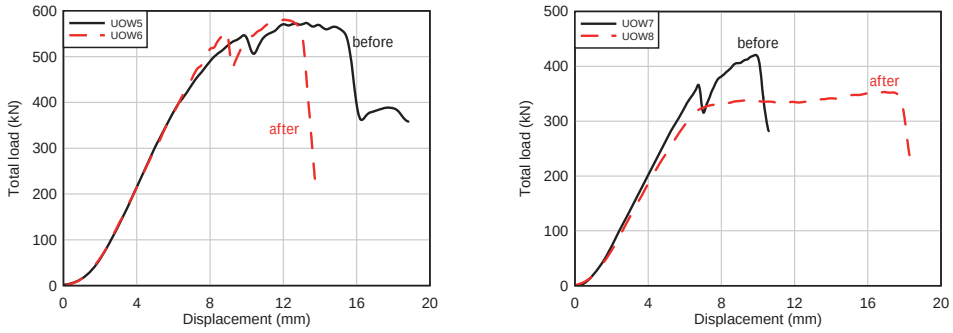

(a) Rail position (positive bending) (b) Center ot the sleeper (negative bending)

Figure 7: Loading capacity of heavy haul rail sleepers (before and after 30-year service)

Acknowledgement
The first author is grateful to Australian Academy of Science (AAS) and Japan Society for the Promotion of Sciences (JSPS) for his JSPS Invitation Fellowship for Research (Long-term), Grant No. JSPS-L15701, at Railway Technical Research Institute (RTRI) and the University of Tokyo, Japan. The authors are sincerely grateful to European Commission for the financial sponsorship of the H2020-MSCA-RISE Project No. 691135 "RISEN: Rail Infrastructure Systems Engineering Network," which enables a global research network that tackles the grand challenge in railway infrastructure resilience and advanced sensing.

References

[1] Standards Australia, 2003. Railway track material - Part 14: Prestressed concrete sleepers. *Australian Standard: AS1085.14-2003.*
[2] Standards Australia, 2001. Railway track material - Part 19: Resilient fastening systems. *Australian Standard: AS1085.19-2001.*
[3] Standards Australia, 2001. Design of Concrete Struct. *Austr. Standards: AS3600-2001.*
[4] Remennikov, A.M. and Kaewunruen, S., 2008. A review on loading conditions for railway track structures due to wheel and rail vertical interactions. *Progress in Struct. Engn. and Materials*, incorporated in *Structural Control and Health Monitoring*, 15(1):207-234.
[5] Kaewunruen, S. and Remennikov, A.M., 2008, Nonlinear transient analysis of railway concrete sleepers in track systems. *Int. J. of Struct. Stability and Dynamics*, 8(3): 505-520.

[6] Kaewunruen, S. and Remennikov, A.M., 2009, "Influence of ballast conditions on flexural responses of railway concrete sleepers in track systems." Concrete In Australia, Journal of Concrete Institute of Australia, 35(4): 57-62.
[7] Kaewunruen, S. and Remennikov, A.M., 2009, "Progressive impact behaviour of prestressed concrete sleepers" Engineering Structures, 31(10): 2460-2473.
[8] Kaewunruen, S. and Remennikov, A.M., 2011, "Ultimate impact resistance and residual toughness of prestressed concrete railway sleepers." Australian Journal of Structural Engineering, 12(1): 87-97.
[9] Wakui, H. and Okuda, H., 1999. A study on limit-state design for prestressed concrete sleepers. *Concrete Library of JSCE*, **33**: 1-25.
[10] Esveld, C., 2001. *Modern Railway Track*, The Netherlands MRT Press.
[11] Remennikov, A.M. and Kaewunruen, S., 2015, "Determination of prestressing force in railway concrete sleepers using dynamic relaxation technique," ASCE Journal of Performance of Constructed Facilities, 29 (5), 04014134.
[12] Remennikov, A.M. and Kaewunruen, S., 2014, "Experimental load rating of aged railway concrete sleepers," Engineering Structures, 76(10): 147-162.
[13] Remennikov, A.M., Murray, M.H., and Kaewunruen, S., 2012, "Reliability based conversion of a structural design code for prestressed concrete sleepers," *Proc. of the Inst. of Mech. Engineers: Part F Journal of Rail and Rapid Transit*, 226(2): 155-173.
[14] Wang, N., 1996. Resistance of concrete railroad ties to impact loading, *PhD Thesis*, University of British Columbia, Canada.
[15] Leong, J., 2007, "Development of a limit state design methodology for railway track," Master of Engineering Thesis, Queensland University of Technology, QLD, Australia.
[16] Gustavson, R., 2002. Structural behaviour of concrete railway sleepers. *PhD Thesis*, Department of Structural Engineering, Chalmers University of Technology, Sweden.
[17] Kaewunruen, S. and Remennikov, A.M., 2011, "Experiments into impact behaviours of prestressed concrete sleepers in railway tracks," Engineering Failure Analysis, 18(8): 2305-2315.
[18] Kaewunruen, S. and Remennikov, A.M., 2009, "Impact capacity of railway concrete sleepers," Engineering Failure Analysis, 16(5): 1520-1532.
[19] Warner, R.F., Rangan, B.V., Hall, A.S., and Faulkes, K.A., 1998. *Concrete Structures*, Addison Wesley Longman, Melbourne, Australia.
[20] Kaewunruen, S. and Remennikov, A.M., 2013, On the residual energy toughness of prestressed concrete sleepers in railway track structures subjected to repeated impact loads. *Electronic Journal of Structural Engineering*, 13 (1), 41-61.
[21] Lake, M, Ferreira, L, Murray, M. (2002). 'Using simulation to evaluate rail sleeper replacement alternatives'. Transportation Research Record, Vol. 1785, p. 58-63.
[22] Kaewunruen, S., et al (2014), "Free vibrations of interspersed railway track systems in three-dimensional space," Acoustics Australia, 14(1): 20-26.
[23] Minoura, S., et al, Study on abrasion property of prestressed concrete sleeper and its influence on loading capacity, Proc. Japan Concr. Inst. (2015), 1345-1350 [In Japanese].
[24] Watanabe, T. et al, Wearing Characteristics of Aged PC Sleeper in the Operation Line National Convention on Civil Engineering, Japan(2015), V-527 [In Japanese].
[25] Railway Technical Research Institute, Design Standards for Railway Structures and Commentary (Concrete Structures), Maruzen Publishing, Japan (2013) [In Japanese].

International RILEM Conference on Materials, Systems and Structures in Civil Engineering
Conference segment on Service Life of Cement-Based Materials and Structures
22-24 August 2016, Technical University of Denmark, Lyngby, Denmark

NUMERICAL SIMULATION SINCE EARLY AGES OF THE RG8 BEAM TEST FROM CONCRACK BENCHMARK BY MEANS OF A 3D FIBRE FRAME MODEL

María D. Crespo [(1)], Denise Ferreira [(2)], Jesús M. Bairán [(3)], Antonio Marí [(3)]

(1) Department of Structures, School of Civil Engineering, Universidad Nacional de Rosario, Rosario, Argentina
(2) Institute of R&D in Structures and Construction - CONSTRUCT / LABEST, Department of Civil Engineering, Faculty of Engineering, University of Porto, Portugal.
(3) Department of Civil and Environmental Engineering, ETSECCPB, Universitat Politècnica de Catalunya, BarcelonaTECH, Barcelona, Spain

Abstract
This work presents the numerical analysis of the RG8 test performed by the French research program Concrack2 in 2011. It consisted in a large RC beam specimen loaded in bending after restrained shrinkage. The specimen is composed of a central thinner part and two massive heads linked by two cylindrical struts that restrained strains due to thermal effects and autogenous shrinkage occurring in the concrete central part. After 8 weeks, the beam was loaded near to its ultimate capacity. The numerical model is based on the 3D fibre beam approach, capable of reproducing the response since early ages. The cross-section is discretized into fibres to take into account the different maturity levels within the cross-section. The analysis is divided into three phases: i) the thermal analysis determines the development of temperatures due to cement hydration and heat transfer, solar radiation and night cooling effects, ii) nonlinear mechanical analysis for early ages including creep, autogenous shrinkage and ageing and iii) nonlinear mechanical analysis for loading phase includes the interaction of normal and shear forces. Performance is compared against experimentation and the development of early age stresses discussed.

1. Introduction

CEOS.fr carried out an experimental campaign for benchmark purposes in order to compare the accuracy of different approaches to describe cracking of RC structures [1, 2]. In [3], the results of the blind simulation of one of the experimental tests – the large RC beam specimen loaded in bending after free shrinkage (RL1 test) – performed with the fibre beam model and compared with other teams' predictions were published. This communication presents the simulation of the other beam test - the large RC beam specimen loaded in bending after restrained shrinkage (RG8 test). The approach used in the simulations is a fibre beam model

able to reproduce the strain and stress states of tridimensional reinforced and prestressed concrete frame structures since early ages.
The RG8 test is a massive structure composed of a central part, two massive heads and two cylindrical struts linked to the heads in order to restrain the deformations of the central part of the structure and consequently lead to cracking at early age (Figure 1) [1].
Early age stresses arise from the restraint to the volumetric changes (such as those produced by the temperature development and autogenous shrinkage) that develop from the hydration of cement. The restraint can be caused either by non-linear strain distributions, by internal (reinforcement) or external restraints. Such stresses depend on several factors, such as the development of the mechanical properties, creep, thermal deformations distribution in the cross section, development of autogenous shrinkage and level of restriction of these deformations.

Figure 1: RG8 test – large dimension beam with restrained shrinkage [1]

In the case of the RG8 beam, the strains that develop in the central part due to temperature variation and autogenous shrinkage are restrained by the heads and the struts. Accordingly, the restraint level depends not only on the stiffness of the struts, but also on the maturity of the concrete of the heads and temperature variations in the struts.
Cracking depends on the concrete strength which, due to sustained load, is lower than the strength measured in a concrete specimen with the same maturity. Moreover, cracking due to restrained imposed deformations leads to a diminishment of the normal forces [4].
In other words, determining the stress and strain states in the RG8 beam is not a simple task. This was evident in the results presented in the blind stage of the benchmark, in which the forces in the struts predicted by the different participating teams presented very high scatter and were far from the measured forces [5, 6].
Although the volumetric strains at early ages produce 3D effects, in case of beams and columns, the moisture and thermal flow in the longitudinal direction can be ignored without losing significant accuracy, except at the elements ends.
This work starts with an analysis of the influence of the different factors on the axial force in the struts. A comparative study is carried out to determine the influence of the strut temperature on the internal forces. Afterwards, the bending test is simulated and the numerical results are compared with the experimental data in terms of displacements.

2. Numerical model

2.1 General characteristics

The RG8 test is modelled by means of a staggered analysis divided into three phases: i) the thermal analysis that determines the development of temperatures at the cross sectional level, ii) the nonlinear mechanical analysis for early ages and iii) the nonlinear mechanical analysis for the loading phase.

The thermal analysis was performed with COMSOL multiphysics, taking into account solar radiation and night cooling effects, as described in [7].

The nonlinear mechanical analysis is performed by a 3D fibre beam model for time-dependent and phased analysis of concrete structures [3] (Figure 2).

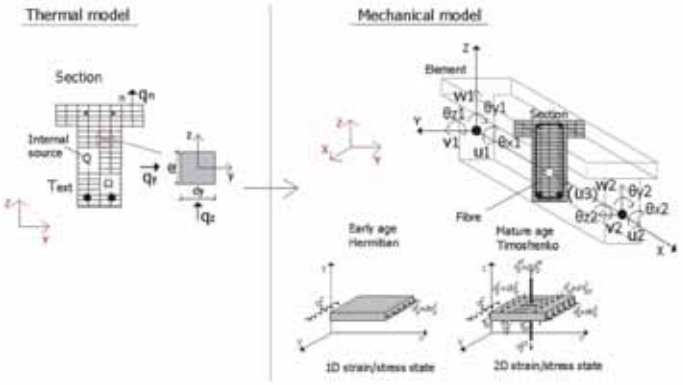

Figure 2: Fibre frame model a) early age model, b) 1D model with multiaxial force interaction

The strains at each instant are the sum of the mechanical and non-mechanical strains, such as creep, shrinkage, thermal strains and aging. The phased structural analysis consists of a time step-by-step procedure in which the time domain is divided into a discrete number of intervals and the increments of displacements and strains are successively added to those obtained in previous steps [8].

The cross section is discretized into concrete fibres and steel filaments. Each filament can have a different temperature, which permits considering different levels of maturity of concrete and studying the effects of arbitrary distributions of shrinkage and thermal deformations. The model considers perfect bond between concrete and steel.

The key aspects of the models are presented in the following sections; for more details see [9] for the early age model, [10] for the basis fiber beam model and [3] for the combination of the two models in a staggered analysis.

2.2 Early age mechanical model

The longitudinal geometry is discretized by linear Hermitian 13 degrees of freedom finite elements [11]. For each FE, the longitudinal reinforcement is parallel to the longitudinal axis.

Regarding their position in relation to the boundaries, the filaments achieve different temperatures during hydration and, consequently, different levels of maturity. The mechanical properties of concrete are not constant in the cross section due to the variation of the maturity

levels. This aspect is considered in the early age model, as it can be relevant for predicting cracking risk during the cement hydration process.
The mechanical characteristics of concrete are simulated through the concept of degree of hydration or maturity [12]. In this study, these are described as a function of the equivalent age. Details of the formulation and validation of the early age model can be found in [9].

2.3 Mature mechanical model

The fibre beam model [10] was used in the mechanical simulation of the loading test at mature age. The model is based on the Timoshenko beam theory with the cross section discretized into fibres of concrete and smeared stirrups and longitudinal steel filaments, as in the model for early age analysis. A sectional formulation accounts for nonlinear axial force-bending-shear interaction. Cracking of concrete is based on the smeared rotating crack approach.

3. Simulation of the Concrack2 RG8 test

3.1 Description of the experimental test

The experimental test under study here is the full scale beam subjected to restrained shrinkage (RG8 test) of ConCrack Benchmark [1, 2] (Figure 1). The central part is 5.9 m long, 0.50 m wide and 0.80 m high, longitudinal reinforcement of 2% and concrete cover equal to 50 mm. The two massive heads are 0.90 m long, 2.2 m wide and 0.90 m high. Two cylindrical struts with a diameter equal to 32.2 cm and thickness of 4 cm are anchored to concrete heads in both ends of the beam.
The beam was thermally insulated during the first 2 days after casting. Then, the insulation and the formwork were removed and the beam was kept at ambient conditions for 2 months. The heads were prestressed just before formwork removal. Subsequently, the beam was transferred to the testing bench and loaded until near bending capacity. Figure 3 shows a scheme of the RG8 beam on the testing bench. The two concentrated loads were applied in 16 loading steps of 50kN/jack (until a maximum of 800kN/jack). A pre-loading of 200 kN was applied and removed before the start of the test.
The beam was largely instrumented, both externally and internally with the following types of sensors: temperature; vibrating wire for deformations; displacement sensors for the loading phase; optical fibre sensors; electrical strain gauges placed on reinforcement bars. During the test, the observation of the development of cracks and forces was the prime focus.

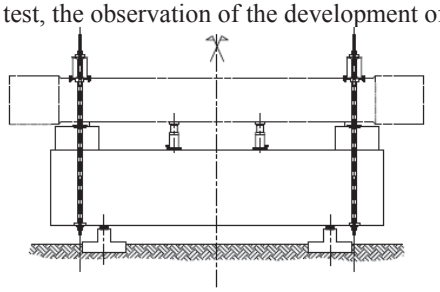

Figure 3: Loading scheme of the RG8 test [1]

3.2 Parameters of the model for early age analysis

The thermal characterization of concrete was done with the data provided by the benchmark: mix proportion, chemical composition of the cement, volumetric mass, ambient temperatures and the temperatures development in an adiabatic test (which for operational reasons began three hours after the beam was cast). As the adiabatic test should start right after mixing of concrete (5-10 min) in order to capture the entire hydration temperature, the hydration degree was modelled according to Freiesleben-Hansen and Pedersen [13], with the parameters suggested by Schindler and Folliard [14] depending on the water/cement ratio (w/c), cement fineness (specific surface area) and cement chemical composition [3].

In the 2D model for early age thermal-analysis, the cross section was discretized into 640 elements, 20 equal length divisions in the horizontal direction and 32 equal length divisions in the vertical direction. Time domain was discretized into 15 minutes steps.

The development of the mechanical properties was adjusted with the models of the Norwegian University of Science and Technology (NTNU) [15].

As the experimental information available about creep was limited to one loading age (2 days) the *Linear Logarithmic Creep Model* was used considering the parameters proposed by Larson and Jonasson [16, 17] for a concrete with a similar modulus of elasticity. For more details about the creep models used, see [3]. Due to the lack of experimental tests for the characterization of the instantaneous mechanical behaviour of concrete, a linear constitutive equation for concrete with effective tensile strength equal to 90% of the tensile strength was considered. This hypothesis may have a relevant effect in the stress state predicted for early ages [18].

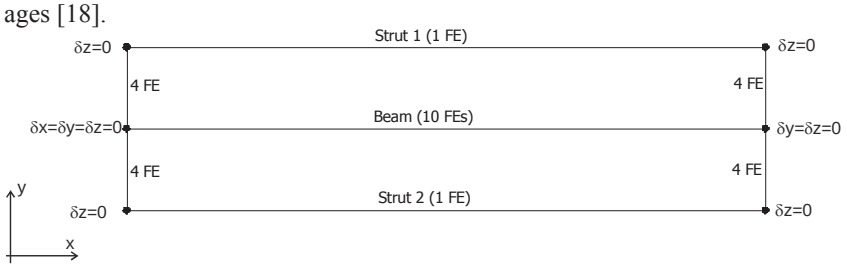

Figure 4: FE model for early age analysis

The model for the mechanical analysis is presented in Figure 4: the beam was divided into 10 elements of different lengths, the mesh of the cross section being the same as in the thermal analysis. The heads were modelled with eight elements and the struts with one element.

The input solicitations in the model were the temperatures generated by the heat of hydration and atmospheric environment and the degree of hydration in each filament. No friction was considered between the formwork and the beam. The heads were considered to have the same maturity as the central part of the cross section at each instant of time.

3.3 Parameters of the model for loading test at mature age

The longitudinal mesh is represented in Figure 5 consisting of 35 finite elements and the cross section discretization equal to the one used in early age thermo-mechanical analysis.

Pertaining to the boundary conditions, the elastic supports represent the stiffness of the Macalloy bars that tie the beam to the bending bench (k=503077 kN/m) and there is a

horizontal displacement restriction at the middle node. In the nonlinear analysis, the applied loads consisted on the dead weight (considering the effect of the end concrete heads as concentrated: P_1=42,5 kN and M_1=19,26 kN.m) and two nodal loads representing each line of jacks applied in 16 loading steps of 50 kN (total of 1600 kN). The material parameters considered in the model are listed in Table 1.
The strain-stress state of concrete and steel generated by the cement hydration phenomena and shrinkage determined in the early age analysis were inputted as initial state of the materials in the second stage of the simulation.

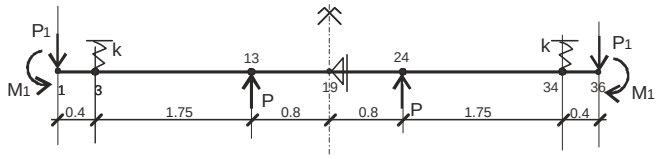

Figure 5: FE model for the loading test at mature stage

Table 1: Parameters of the mechanical model for the loading test

Property	Parameter	Value	Unit
Compression strength of concrete	f_c	63.7	MPa
Tensile strength of concrete	f_{ct}	4.65	MPa
Modulus of elasticity of concrete	E_c	40.2	GPa
Tension stiffening	K_c	0.5	-
	C	0.002	-
Yield strength of steel	f_y	500	MPa
Ultimate strength of steel	f_u	550	MPa
Modulus of elasticity of steel	E_s	200	GPa

4. Results and discussion

4.1 Early age

Figure 6 compares temperatures measured and numerically obtained at three points in the central section by the thermal analysis performed [7] where a very good agreement was achieved. In the upper point U - localized 11.5 cm below the top of the beam - the effect of solar radiation is noticed. The difference between maximum numerical and experimental temperatures can be due to some problems of insulation (no continuity in polystyrene) that were observed during the setting up, as reported by the authors of the tests [19].

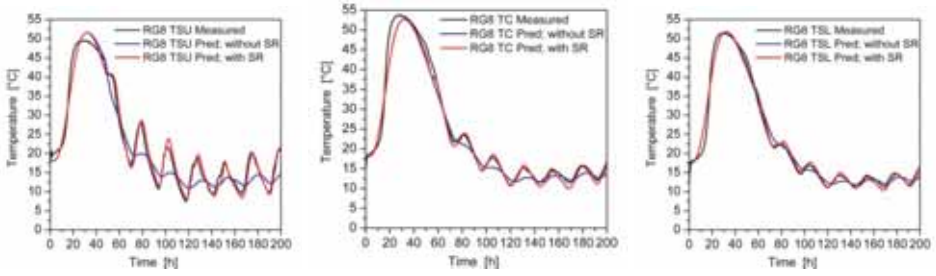

Figure 6: Temperature vs. time since casting at point SU, C and SL

No data was available related to strut isolation in order to perform a complete 3D thermal analysis needed to compute the temperatures in the struts with high accuracy. Hence, a parametric study was performed considering different temperatures for the struts (Figure 7): 18 ºC, ambient temperature and temperature measured in one cross section of the struts.

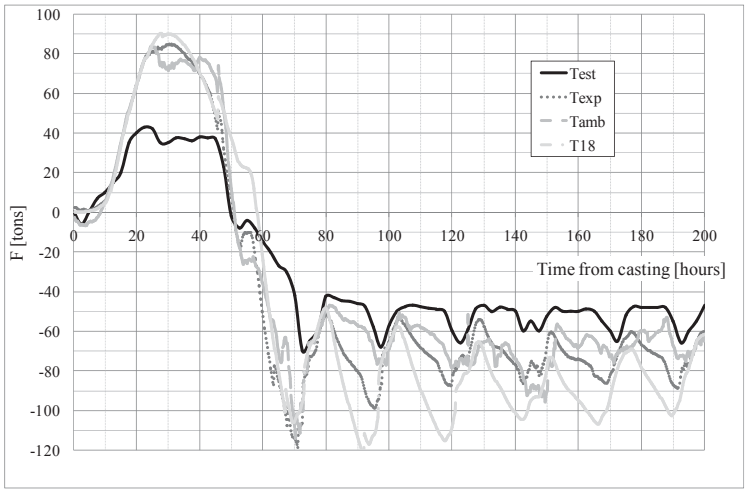

Figure 7: Influence of struts temperature on the development of strut forces

In the three cases, during the first hours, the forces in the struts are higher than those measured [6, 19]. For temperatures of 18 ºC and equal to the one measured in a section, the development of forces in the strut does not show the plateau that is experimentally observed. For temperatures in the struts equal to ambient temperature, the kinetics of struts forces between 20 and 50 hours is similar to the development of experimental temperatures.
It can also be observed that the maximum compression in the struts, which corresponds to tension in the beam, is higher than the maximum compression measured. This can be due to the effect of the sustained load, resulting into effective strength lower than the instantaneous strength.
Pertaining to the tension forces, the organizers of the benchmark pointed out the following [19]: "Experimentally a provisional stabilization was noted at 20 tons (per strut). This could be partially explained by an insufficient prestressing of the anchoring of struts as the system for anchoring the struts in the concrete heads was designed for compressive stress (when concrete is cooling). In this period, the concrete was dilating, which induces tensile stress in the struts. If the anchoring was insufficient, a sliding could be observed which would induce a plateau on the evolution of the force developed in the strut". In the authors' opinion, this difference in the kinetics may be also due to the effect of temperature in the struts.
Figure 8 shows the development of the stress profile in the uncracked sections produced by internal and external restraint for different time steps, considering an effective strength of 90% of the tensile strength. During the heating phase, the profiles are characterized by compressive stresses in the whole section.
In the cooling phase, the development of the modulus of elasticity causes a reversal of the

sign of the stresses. At 48 hours the formwork and isolation are removed, producing an abrupt decrease in temperature on the upper fibres and on both sides, which lead to further tensile forces in these parts.
The daily variations in temperature produce a change in the stress profile that approximately repeats every 24 hours. When outer temperatures increase, the outside tends to compress and the inside tends to tense more.

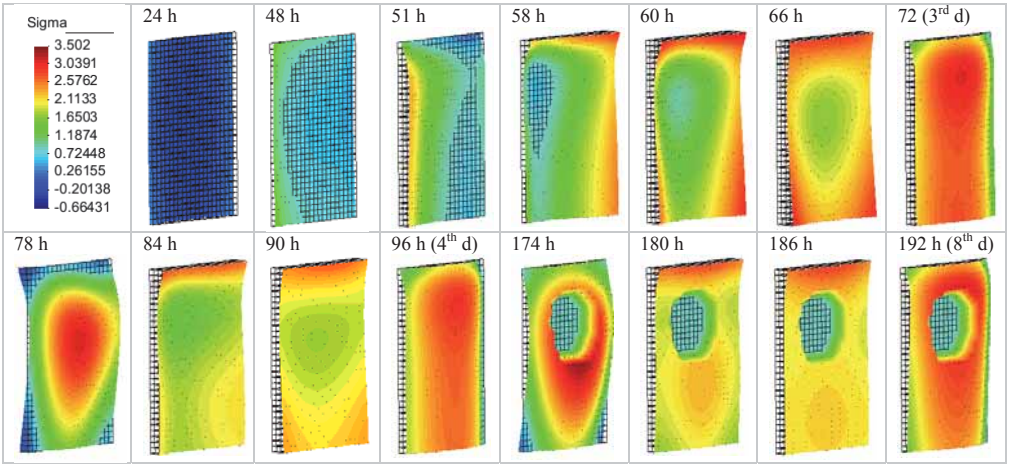

Figure 8: Development of the profile stresses in uncracked section

Maximum stresses appear at different locations and instants – at 51 hours on the left border (west side) and at 58 hours on the right border of the beam (east side). At 60 hours the highest stresses appear in the top and lateral fibres. Around 66 hours the stress profile is rather constant and around 72 hours the highest stresses appear in the inner part of the cross section.
In the following days, the stress flow has a similar variation to the fourth day: at first the corners and the top border of the cross section start to compress (maximum values appear at 78 hours). Between 84 and 90 hours the top area presents the highest tensile stresses. At 96 hours the stress profile is similar to the one corresponding to 72 hours. At 98 hours cracking appears in the centre of the cross section.
The experimental observations show that at early age 3 cracks appeared in the central part and the beam did not reach a stabilized cracking stage. The numerical model predicts cracking in 8 cross sections.

4.2 Loading test

Regarding the loading analysis, the experimental and computed displacements in one point are compared in Figure 9. It can be observed that numerical results present a good fitting with experimental results, with differences in the maximum displacements of approximately 14%.
In order to quantify the influence of the early age effects on the behaviour of the beam when loaded, a similar analysis was performed without considering the offset of early age strains. Early age stresses influence the reduction of stiffness due to cracking, which is relevant in the overall response under loading. The maximum displacement computed by the analysis since

early ages is approximately 8% greater than the one without considering early age effects.

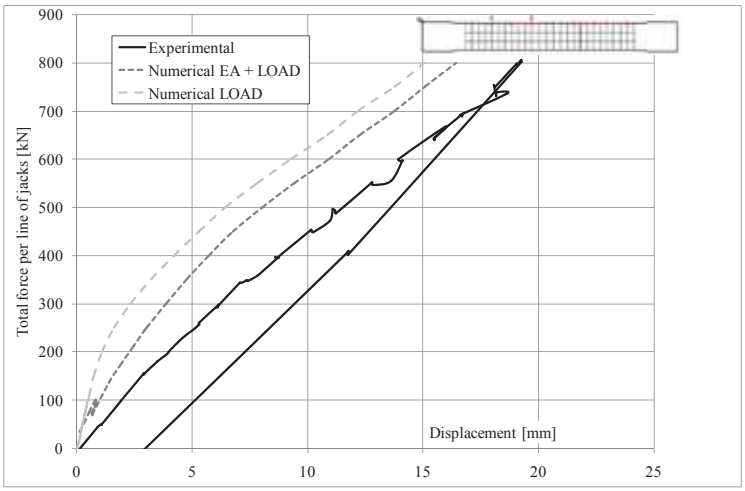

Figure 9**:** Comparison between numerical and experimental displacements at point 6

5. Conclusions

- During the first hours, the forces in the struts are greatly dependent on their temperature.
- When considering the temperature in the struts equal to the one measured in one of its cross sections, the computed tensile stresses are higher than the experimental results and do not present the plateau observed in the test.
- Maximum tensile stresses in the beam (corresponding to maximum compression stresses in the struts) depend on the concrete effective strength considered; a good agreement is achieved when it is considered as 90% of the instantaneous value.
- The results computed in the early age phase are dependent on the size of the mesh.
- The displacements obtained in the simulation of the load test are lower than the experimental ones (approximately 14%).
- Early age effects affect the response of the beam under load; maximum displacements increase around 8% when the early age effects are considered.

Acknowledgements

This work has been developed under the framework of the Research Project 'BIA2012-36848', funded by the Spanish Ministry of Economy and Competitiveness (MINECO) and co-funded by the European Regional Development Funds (ERDF).

Funding provided by the Portuguese Foundation for Science and Technology (FCT) to the second author through the Postdoctoral fellowship SFRH/BPD/102373/2014 (co-funded by the Portuguese Ministry of Education and Science and the European Social Fund (ESF)) is gratefully acknowledged.

References

[1] CEOS.fr., French national research project. Behaviour and assessment of special construction works concerning cracking and shrinkage; 2008. <http://www.ceosfr.org>
[2] CEOS.fr., Concrack 2: 2nd Workshop on Control of cracking in RC structures. Restitution of the International Benchmark ConCrack (2011) http://www.concrack.org/
[3] Ferreira D., et al., Thermo-mechanical simulation of the Concrack Benchmark RL1 test with a filament beam model, Eng Struct 73 (2014), 143-159
[4] Ghali A. and Favre R., Concrete Structures: Stresses and deformations, 2nd edition, E & FN Spon (1994)
[5] International Benchmark CONCRACK, Synthesis of the results, 2nd Workshop on Control of cracking in R.C. structures *ConCrack 2 June 20-22 (2011), Paris – France*
[6] Torrenti J-M et al, Experiments for crack control of concrete at early age, RILEM-JCI International Workshop on Crack Control of Mass Concrete and Related Issues concerning Early-Age of Concrete Structures, Paris (2012), 3-10
[7] Gastón A., Abalone R. and Crespo M. D., Estudio del comportamiento térmico a edades tempranas en vigas grandes dimensiones, Mecánica Computacional 31 (2012), 1997-2011
[8] Ferreira D., Bairán J., Marí A., Influence of time-dependent restrained strains in the shear response of RC frames, Mater Struct (2016), under revision
[9] Crespo M. D., Behaviour of reinforced concrete at early ages. Structural effects of the restrained imposed strains (in Spanish), PhD thesis, Univ. Politèc. de Catalunya, (2011)
[10] Ferreira D., Bairán J., Marí A. and Faria R., Nonlinear analysis of RC beams using a hybrid shear-flexural fibre beam model, Eng Computations 31(7) (2014), 1444-1483
[11] Marí A., Numerical simulation of the segmental construction of three dimensional concrete frames, Eng Struct 22 (2000), 585-596
[12] De Schutter G., Applicability of degree of hydration concept and maturity method for thermo-visco-elastic behaviour of early age concrete, Cement Concrete Comp 26 (5) (2004), 437-443
[13] Freiesleben-Hansen P. and Pedersen E.J., Curing of concrete structures. Draft DEB – Guide to durable concrete structures, Appendix 1 (1985)
[14] Schindler A. K. and Folliard K. J., Heat of hydration models of cementitious materials, ACI Mater J 102 (2005), 24–33
[15] Kanstad T., Hammer T. A. and Bjontegaard O., Mechanical properties of young concrete. Part II: Determination of model parameters and test program proposals, Mater Struct 36(4) (2003), 226-230
[16] Larson M. and Jonasson J.-E., Linear logarithmic model for concrete creep: I. Formulation and evaluation, J Adv Concr Technol 1(2) (2003), 172-187
[17] Larson M. and Jonasson J.-E., Linear logarithmic model for concrete creep: II. Prediction formulas for description of creep behaviour, J Adv Concr Technol 1(2) (2003), 188-200
[18] Rostásy F. S. and Kraub M., Effects of stress-strain relationship and relaxation on restraint, stress and crack formation in young concrete members, Control of Cracking in Early Age Concrete, Proceedings International Workshop on Control of Cracking in Early Age Concrete, Sendai, Japan (2002) 305-316
[19] Buffo-Lacarrière L., Sellier A. and Kolani B., Application of thermo-hydrochemo-mechanical model for early age behaviour of concrete to experimental massive reinforced structures with strain–restraining system, Eur J Environ Civ Eng 18:7 (2014), 814-827, doi: 10.1080/19648189.2014.896754

International RILEM Conference on Materials, Systems and Structures in Civil Engineering
Conference segment on Service Life of Cement-Based Materials and Structures
22-24 August 2016, Technical University of Denmark, Lyngby, Denmark

PREDICTING CHLORIDE INDUCED DEPASSIVIATION AND MINIMUM CONCRETE COVER WITH DIFFERENT BINDERS

Ingemar Löfgren [1 & 2], Tang Luping [1], Oskar Esping [2] & Anders Lindvall [2]

(1) Chalmers University of Technology, Gothenburg, Sweden
(2) Tomas Concrete Group, Gothenburg, Sweden

Abstract
Corrosion of steel reinforcement represents the major cause affecting durability of reinforced concrete structures in road and marine environments. To assure durability, standards attempt to provide specifications for long-term performance by simple deemed-to-satisfy rules for approximate environmental classification. This paper presents results from a study of modelling of chloride ingress in concrete with fly ash and ground granulated blast-furnace slag. Chloride threshold values for corrosion initiation are discussed. A physical model, ClinConc, was employed to calculate the chloride ingress profiles after exposure under marine (submerged) and road environments for 100 years. The model was validated using field data after exposure in the Swedish seawater for about 20 years. The results show that the addition of mineral additions in general increases the resistance of concrete to chloride ingress and allows smaller concrete cover thicknesses. However, one critical parameter is the chloride threshold value. In consideration of both the chloride resistance and the alkalinity, which influence the critical chloride threshold value, the concrete with mineral additions still reveals sufficient margin to allow a significantly lower chloride threshold for initiation of corrosion of reinforcement steel in concrete.

1. Introduction

Chloride induced reinforcement corrosion is still a big durability problem of reinforced concrete structures such as bridges and tunnels in road infrastructures. At the present, the specification of durability is mainly based on the establishment of various constraints to the mixture proportions of the concrete, such as cement type and water/binder (w/b) ratio, together with requirements on the cover thickness as function of the severity of the exposure. This approach does not consider the actual performance of concrete materials with different types of cement and mineral additions added to the cement or directly to the concrete. With the help of more sophisticated durability models safer structures can be designed with expected service life and reduced consumption of materials. This paper intends to evaluate the service life of reinforced concrete with binders blended with fly ash (FA) and ground

granulated blast furnace slag (GGBS) regarding chloride-induced corrosion of reinforcement steel, based on the current knowledge and models, see [1]. Moreover, the aim is to provide recommendations with respect to requirements on minimum concrete cover for different concrete compositions, with main focus on bridges and tunnels with a service life of 100 years.

2. Experiments

For the experiments, three different Portland cements (CEM I), one Portland-fly ash cement (CEM II/A-V), one Portland-slag cement (CEM II/B), one blast furnace cement (CEM III/A), two different GGBS, and one type of FA were used in the study, see Table 1 for properties. For the concrete mixes granite type of aggregates were used (maximum aggregate size 16 mm) and for all the mixes the air content was 5 to 6% by volume. For the mixes with mineral additions an efficiency factor (*k*-value) of 1.0 was used, i.e. comparison is made at equal *w*/*b* ratios.

Table 1: Materials.

ID	**Type**	**Density**	**Blaine**	**CaO**	**SiO_2**	**Al_2O_3**	**Fe_2O_3**	**Na_2O_{eqv}**
	Acc. to EN 197-1	kg/m^3	m^2/kg	M.-%	M.-%	M.-%	M.-%	M.-%
C1	CEM I 42,5 N SR3 MH/LA	3 200	330	64	22	3.7	4.5	0.51
C2	CEM I 42,5 N SR3 MH/LA	3 160	330	64	22	3.3	4.6	0.45
C3	CEM I 52,5 N	3 140	420	63	19	4.3	3.1	0.90
C4	CEM III/A 42,5 N/NA	3 000	450	52	28	8.9	1.2	0.70
C5	CEM II/A-V 42,5 N MH/LA	3 040	370					0.85
C6	CEM II/B-S 52,5 N	3 060	460	56	25	6.3	2.1	0.80
S1	GGBS	2 900	420	40	35	12		1.20
S2	GGBS	2 920	500	31	34	13		0.90
FA	Fly ash	2 100						2.40

C4: Contains about 49% GGBS.
C5: Is a FA cement with app. 14% FA and with the clinker of C1.
C6. Contains about 33% GGBS.
FA: The FA had a fineness of 16% (<45 μm) and a loss on ignition of 2%.

The compressive cube strength and the chloride migration coefficient was measured for all mixes. The chloride migration coefficient was determined according to NT BUILD 492 [2]. The compressive strength (water cured cubes) and chloride migration coefficient at 28, 56 and 180 days are presented in Table 3. As can be seen there are variations in the performance of the different materials with respect to the chloride migration coefficient, e.g. difference between GGBS S1 and S2, is probably due to their different fineness and/or chemical composition.

Table 3: Compressive strength (cube) and chloride migration coefficient of concrete.

Binder & *w/b*	**amount**	**Comp. strength [MPa]**			**Chloride mig. [$\cdot 10^{-12}$ m^2/s]**		
(See table 1)	[kg/m^3]	28 days	56 days	180 days	28 days	56 days	180 days
C1 0.45	400	45.2	52.2	58.2	17.6	14.5	13.9
C2 0.45	400	46.9	53.7	59.2	20.0	14.9	14.6
C3 0.45	400	42.8	48.6	50.1	10.9	9.0	8.6
C2+20%S1 0.45	400	45.6	54.1	63.5	11.4	8.7	6.1
C2+30%S1 0.45	400	39.4	48.8	56.0	11.5	7.2	4.3
C2+40%S1 0.45	400	37.5	49.1	59.9	15.2	6.5	2.9
C2+60%S1 0.45	400	37.0	48.3	66.6	8.9	4.7	2.5
C1+20%S1 0.45	400	45.5	52.7	58.4	9.4	6.4	4.7
C1+40%S1 0.45	400	36.8	46.3	55.5	7.6	4.1	3.8
C6 0.45	400	47.0	52.4	59.4	8.6	6.2	5.8
C4 0.45	400	50.4	57.8	66.4	5.0	3.3	2.3
C2+20%S2 0.45	400	48.6	57.8	63.2	12.0	8.5	5.6
C2 40%S2 0.45	400	38.7	49.1	57.9	11.1	6.1	3.6
C5 0.45	400	45.8	50.2	63.2	15.5	11.5	4.8
C1+20%FA 0.44	419	38.8	46.7	-	22.8	14.0	6.2 [1)]
C5 0.40	425	50.7	54.8	64.6	12.5	8.6	4.0
C1+20%FA 0.40	438	45.8	53.7	-	16.9	8.9	3.0 [1)]
C1+25%FA 0.39	465	49.1	58.4	-	16.4	9.3	3.6 [1)]
C2 0.40	425	50.5	57.4	61.5	19.0	14.9	13.1
C2+20%S1 0.40	245	50.0	57.0	66.8	12.9	7.8	5.7
C2+30%S1 0.40	425	48.4	56.8	68.7	10.4	5.5	4.5
C2+40%S1 0.40	425	45.6	57.0	72.6	9.3	5.3	3.5
C4 0.40	425	54.7	61.0	68.3	4.7	3.5	2.9
C6 0.40	425	59.2	61.7	68.6	6.3	4.5	4.4

[1)] Estimated from the data measured at 28 and 56 days using exponent time-dependent relationship.

3. Corrosion initiation

3.1 Chloride ingress modelling

Based on recent validation results from concrete specimens after over 20 years' exposure in the Träslövsläge harbour [3] and 10 years field exposure in road environment [4] in Sweden,

the ClinConc model [5] revealed the best agreement with the field data. Therefore, this model was used for modelling of chloride ingress in this study. The ClinConc model consists of two main procedures, see [5]: 1) Simulation of free chloride penetration through the pore solution in concrete using a genuine flux equation based on the principle of Fick's law with the free chloride concentration as the driving potential, and 2) Calculation of the distribution of the total chloride content in concrete using the mass balance equation combined with non-linear chloride binding. The ClinConc model uses free chloride as the driving force and takes non-linear chloride binding into account, thus describing chloride transport in concrete in a more scientific way than the empirical or semi-empiric models. The free chloride concentration in the concrete at depth, x, is determined using the following equation:

$$\frac{c-c_i}{c_s-c_i}=1-\mathrm{erf}\left(\frac{x}{2\sqrt{\frac{\xi_D D_{6m}}{1-n}\cdot\left(\frac{t_{6m}}{t}\right)^n\cdot\left[\left(1+\frac{t_{ex}}{t}\right)^{1-n}-\left(\frac{t_{ex}}{t}\right)^{1-n}\right]\cdot t}}\right) \quad (1)$$

where: c, c_s and c_i = the concentration of free chlorides in the pore solution at depth x, at the surface of the concrete and initially in the concrete, respectively; D_{6m} = the diffusion coefficient measured by the RCM test, e.g. NT BUILD 492 [1], at the age of t_{6m}; ξ_D is the factor bridging the laboratory measured D_{6m} to the initial apparent diffusion coefficient for the actual exposure environment; n is the age factor accounting for the diffusivity decrease with age; t_{ex} is the age of concrete at the start of exposure and t is the duration of the exposure.

Different from the empirical models, the factors ξ_D and n in the ClinConc can be calculated based on the physical properties of concrete including cement hydration, hydroxide content, water accessible porosity, time-dependent chloride binding, and the environmental parameters such as chloride concentration and temperature. The detailed descriptions of the factors ξ_D and n are given in [6].

The total chloride content is basically the sum of the bound chloride, c_b, and free chloride, c, expressed as (as mass % of binder):

$$C=\frac{\varepsilon\cdot(c_b+c)}{B_c}\times 100 \quad (2)$$

where: ε is the water accessible porosity at the age after the exposure; B_c is the cementitious binder content, in kg/m^3 concrete; and c_b, is the bound chlorides expressed in the same unit as free chloride.

In the modelling of the marine environment a chloride ionic concentration of 14 g/l and an annual mean water temperature of +11°C was used. For the road environment a chloride ionic concentration of 1.5 g/l and an annual mean air temperature of +10 °C were applied. For the initial chloride content 0.1% of binder was assumed, even though the actual values in the tested mixes were lower. Examples of calculated chloride profiles for marine environment (submerged, XS2) are shown in Figure 1. The chloride profiles for all mixes are not shown as there were minor differences for some of the mixes, e.g. with the different slags. Moreover,

for the mixes with GGBS the difference in chloride ingress between *w*/*b* 0.45 and 0.40 were in many cases very small because their chloride migration coefficient were similar.

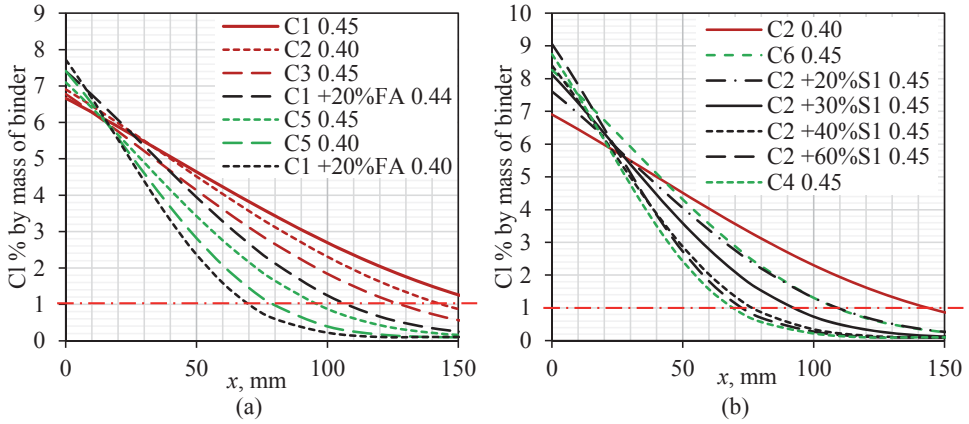

Figure 1: Comparison of calculated chloride profiles for marine environment (submerged, XS2) after 100 years exposure. (a) For CEM I and mixes with FA and (b) for some of the mixes with GGBS or GGBS cements.

3.2 Chloride-induced corrosion and minimum concrete cover

It is generally accepted that the active corrosion (depassivation) occurs when the chloride concentration reach a certain critical level, referred as the chloride threshold value C_{cr} [7] [8]. The chloride threshold value depends on many parameters. Comprehensive literature reviews on the subject [8] [9] show large scatter in the reported chloride threshold values with one order of magnitude, from 0.1% up to around 2% by mass of binder. One of the decisive factors is the pH value of the pore solution which is dependent on the type of binder [7] [8], because the passive film is formed and maintained under the alkali condition or the concentration of hydroxide ions. For reinforcement steel embedded in concrete additional factors such as moisture content, temperature, oxygen availability, defects on the concrete-steel interface are also important. Usually C_{cr} is expressed as the total or acid soluble chloride. In this case, the chloride binding capacity of cementitious hydrates has to be taken into account.

It is conventionally believed that the mineral addition in concrete results in lower chloride threshold value because of the pozzolanic reactions which consume $Ca(OH)_2$ from the cement hydration, resulting in a lower pH value in the pore solution [10]. This is still questionable, because the initial pH (13-14) of the pore solution is mainly attributed to the alkaline oxides K_2O and Na_2O, as expressed by equivalent $[Na_2O]_{eqv}$ in the binder whilst the long-term pH is dependent on the existence of portlandite in the hardened cement paste. It has been reported that for GGBS contents of $\leq 40\%$ the concentration of alkali in the pore solution is within the range of pure CEM I but high amounts (>75%) can have a strong influence on the alkalinity [11]. However, it has also been reported [12] [13] that even at a GGBS content >75% there is still portlandite remaining in 20 year old samples. At about 50% GGBS more than 9% portlandite by mass of binder remained after hydration for 3 and 20 years, see [13] [14] [15].

The same has been reported for concrete with FA [149 [15]; when FA <30% there is still portlandite remained. It is known that calcium leaching is a process much slower than chloride ingress. If there is no carbonation, very little amount of portlandite can keep the pH value of solution about 12.5 due to its low solubility (0.023 mol/l).

On the other hand, the higher chloride binding capacity, lower diffusivity and finer pore structure of concrete with mineral addition positively contribute to the resistance of concrete against corrosion initiation, as indicated in a study of reinforced concrete specimens after over 20 years' exposure in the Träslövsläge harbour [3]. According to [3], the estimated chloride threshold value from the field exposure is about 1% by mass of binder for most types of concrete with Portland cement and silica fume whilst the concretes with FA and GGBS did not show a corrosion tendency at a chloride content even higher than 1% by mass of binder. Therefore, the conventional opinion of low C_{cr} for the concrete with mineral additions due to its lower alkalinity is questionable, because on one side there is no sufficient evidence of a significant lower pH value in the pore solution and on the other hand the improved microstructures in such types of concrete may prevail the weakness of low alkalinity, if it is.

Assuming a service life of t_L = 100 years, the minimum cover thickness x_c can be estimated from the following equation in the ClinConc model, if the free chloride threshold value c_{cr} is given:

$$x_c = 2\sqrt{\frac{\xi_D D_{6m}}{1-n}\cdot\left(\frac{t_{6m}}{t_L}\right)^n\cdot\left[\left(1+\frac{t_{ex}}{t_L}\right)^{1-n}-\left(\frac{t_{ex}}{t_L}\right)^{1-n}\right]\cdot t_L}\cdot \mathrm{erf}^{-1}\left(1-\frac{c_{cr}-c_i}{c_s-c_i}\right) \quad (3)$$

In this study for estimation of the minimum cover thickness the value of 1% total chloride by mass of binder was used as criteria for concrete exposed under the marine environment and 0.4% total chloride by mass of binder for concrete exposed under the road environment due to the high availability of oxygen and possible carbonation. The corresponding free chloride threshold value c_{cr} used in equation (3) can be inversely obtained from equation (2).

The calculated minimum concrete cover required under the marine environment and for the road environment is presented in Figure 2. As can be seen, in the marine environment the minimum concrete cover predicted is 70 mm for C4 (CEM III/A) and those mixes with 60% GGBS. With lower GGBS content the required cover increase and becomes about 80 mm with 40%, 90 mm with 30% and 100 to 110 mm with 20%. For the mixes containing FA (with 15 to 20%), 100 to 110 mm is required at *w*/*b* 0.45 and 70 to 80 mm at *w*/*b* 0.40. The largest concrete cover is required for the sulfate resistant Portland cement (C1 and C2), with 160 mm at *w*/*c* 0.45 and 140 mm at *w*/*c* 0.40. In comparison, the ordinary Portland cement requires 130 mm at *w*/*c* 0.45. For the road environment the concrete mixes with GGBS or FA require 35 to 50 mm cover at *w*/*b* 0.45 and 35 to 45 mm at *w*/*b* 0.40. In comparison, the ordinary Portland cement requires 65 mm at *w*/*c* 0.45 and the sulfate resistant Portland cement a cover of 70 mm at *w*/*c* 0.40. In general, the required covers in the marine environment are much higher than the recommended values in EN 1992-1-1 [16] but are in line with the recommended value of 100 mm by the Norwegian road authorities [17].

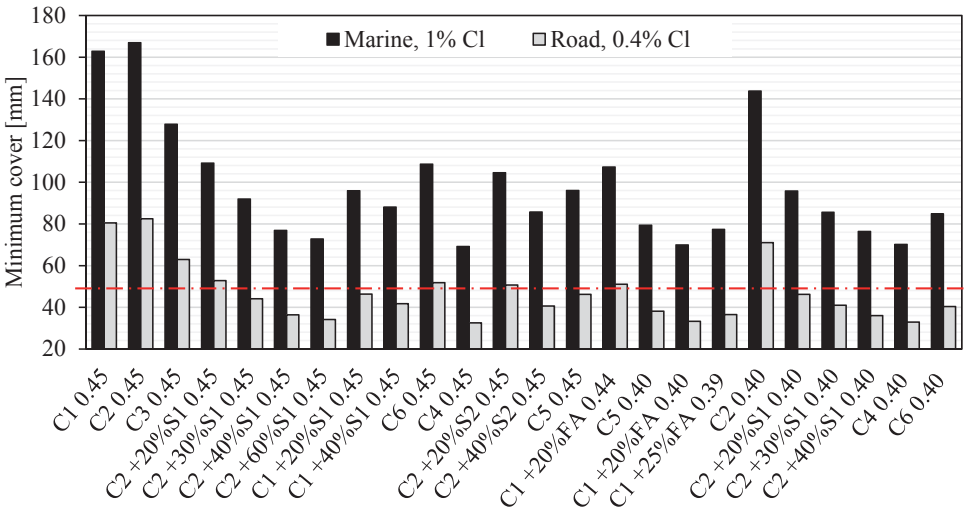

Figure 2: Calculated minimum concrete cover for marine (XS2) and road environment (XD3) for a service life of 100 years.

3.3 Allowable low limit of chloride threshold

So far it is still lack of actual chloride threshold value for concrete, especially for those with mineral additions, due to the absence of standard test method for the threshold value. Under the assumption of the same service life and cover thickness as concrete based on the mixes with C1 and C2 (sulfate resistant Portland cement), a chloride content at the cover depth in concrete with mineral additions can be calculated with the help of the ClinConc model. Thanks to the higher resistance of concrete with mineral additions to chloride ingress, this calculated chloride content will be lower than the chloride threshold for the reference concrete (with C1 or C2) and can thus be considered as a theoretical allowable low limit of chloride threshold for concrete with mineral additions. In this study, a cover thickness of 100 and 70 mm, and a chloride threshold value of 1% and 0.4% by mass of binder were assumed for the marine and road environment respectively. The results are illustrated in Figure 3. From Figure 3, it can be seen that under the marine and road environment, the theoretical low limit of threshold for all the other types of concrete with mineral additions is considerably lower than the reference threshold for concrete with C1 and C2 (sulfate resistant Portland cement). For the marine submerged condition the chloride threshold value could be allowed to be as low as 0.1% to 0.2%, 10 to 20% of that of a sulfate resistant Portland cement. This means that concrete with mineral additions, due to the improved resistance to chloride ingress, are expected to have more than sufficient margin to protect reinforcement steel from corrosion.

4. Discussion

The results from the above modelling together with the limited field data after exposure in the Träslövsläge harbour for 20 years have given a certain evidence showing the positive contribution of mineral addition to the resistance of concrete to chloride ingress. For the addition of GGBS up to 60% in this study (75% for the field exposure), the chloride

resistance increases with the addition level. Similarly, fly ash at an addition of 15 to 25 % increased the chloride resistance significantly. With respect to chloride threshold values, the field data from Träslövsläge harbour seem to indicate that 1% can be used for mixes with Portland cement as well as for mixes with GGBS or moderate amount of fly ash. In the literature mineral additions, such as fly ash and slag, have been reported to give rise both higher and lower threshold values [8]. But it has also established that the most influencing parameters are the steel-concrete interface (e.g. presence of defects) and the steel potential [8] which makes results from literature difficult to interpret.

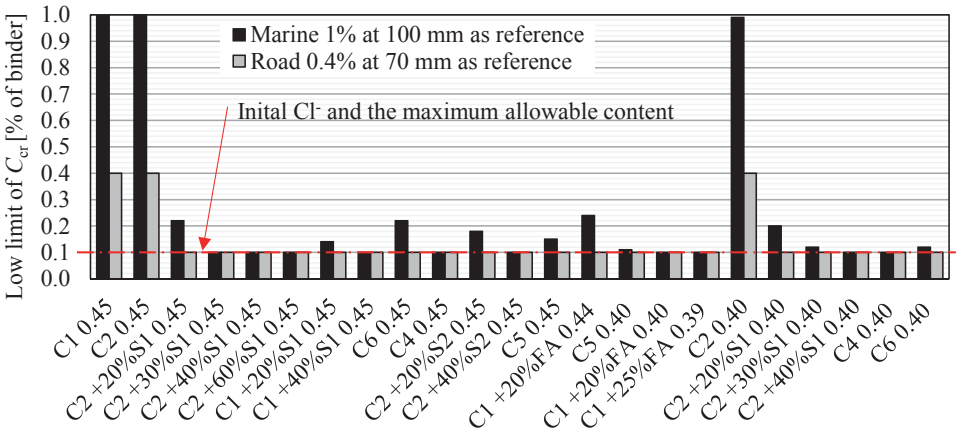

Figure 3: Allowable low limit of the chloride threshold value for the same concrete cover and service life compared with the concretes with cement C1 & C2 (CEM I 42.5N SR3 MH/LA).

Given the uncertainty regarding the chloride threshold value a possible low limit of chloride threshold was determined. The result from this back-calculation show that by reducing the chloride migration coefficient to one third compared to a mix with CEM I (sufate resistant) the low limit threshold can be as low as 0.1 to 0.2 % of binder if 1.0% is assumed for CEM I in submerged marine environment. In consideration of both chloride resistance and alkalinity, the concrete with mineral additions (at moderate amounts) still reveals sufficient margin to allow a significantly lower chloride threshold for initiation of corrosion of reinforcement steel in concrete. Most reported chloride threshold values for concrete with slag or fly ash [8] [9] do not indicate such low threshold values at moderate amount of mineral additions (up to 25% fly ash and 50% GGBS). The reduction in threshold value, for the cases where this has been found, reported is generally not more than 50% [18]. Hence, the improved resistance to chloride ingress, where moderate amount of mineral addition can reduce the chloride migration to one third compared to a CEM I, overcomes the potential negative effect on the chloride threshold value.

With the help of models, like ClinConc, rapid chloride test methods such as NT BUILD 492 [2] can be used for specification and verification by a performance based approach. As can be seen in Figure 2 there is a big variation in required concrete covers. With a prescriptive approach such variations are difficult to handle. Moreover, there is also variation in the

performance of the different materials with respect to the chloride migration coefficient which also cannot be considered with a prescriptive approach. This variation can, however, be considered with the performance based approach although it still requires a reliable test method to quantify chloride threshold values. Moreover, for large concrete covers the effects of more stable internal climate and less oxygen availability may have positive impact on the chloride threshold values and corrosion rate which needs to be considered.

5. Conclusions

The ClinConc model was used to model chloride ingress in concrete with Portland cement and with various mineral additions with the measured chloride migration coefficient as the key input parameter. Some limited field data measured from concrete exposed in the Träslövsläge harbour for about 20 years [3] and 10 years exposure in a road environment [4] were used for validation of the modelled results. From both the literature review and the experimental and modelling results [1] it can be concluded that, for the mineral additions:

- The chloride resistance of concrete increases with mineral addition. For GGBS, the higher the addition level (up to 60% GGBS in this study), the better the resistance is, whilst for FA, the addition level in the range of 13% and 25% reveals similar resistance.
- The alkalinity of concrete with GGBS may not necessarily be low because both the alkaline components in GGBS and the reduced porosity contribute to a high concentration of hydroxide ions in the pore solution. It is only at high addition levels that this might be a concern.
- The alkalinity of concrete with FA is proportionally reduced with the addition of FA, but the reduction is limited if the addition of FA is not more than 25%.
- In consideration of both chloride resistance and potential effect of alkalinity on the chloride threshold value, the concrete with mineral additions have significantly better resistance to chloride ingress which outperforms any negative effect on the chloride threshold value.

Values of minimum cover specified in current standards need to be revised by consideration of the type of binder used. From the ClinConc model and the concrete mixes tested, some suggested values are given in Figure 2. To assure the designed service life, the resistance of concrete to chloride ingress should be tested using e.g. the rapid chloride migration test or similar standardized tests and a performance based approach should be used to determine required concrete covers.

Finally, it can be point out that the overall effect of mineral additions in concrete is significant in terms of resistance to chloride ingress with a marginal influence on the chloride threshold value. Therefore, the use of mineral additions in concrete should have a clear, great advantage from viewpoint of sustainability in terms of technical performance, cost-effectiveness and ecological benefit.

Acknowledgment

This project has been financially supported by the Swedish Transport Administration.

References

[1] Tang L. and Löfgren I., Evaluation of Durability of Concrete with Mineral Additions with regard to Chloride- Induced Corrosion. Report No. 2016-4, Dep. of Civil and Env. Eng., Div. of Building Technology, Chalmers University of Technology, Gothenburg, 2016.
[2] NT BUILD 492 – Concrete, Mortar and Cement Based Repair Materials: Chloride Migration Coefficient from Non-steady State Migration Experiments, NORDTEST, Espoo, Finland, 1999.
[3] Boubitsas D., Tang L. and Utgenannt P., Chloride Ingress in Concrete Exposed to Marine Environment - Field data up to 20 years' exposure. CBI Report to SBUF Project 12684, Swedish Cement and Concrete Research Institute, Stockholm, Sweden, 2012.
[4] Tang L. and Lindvall A. Validation of models for prediction of chloride ingress in concrete exposed in de-icing salt road environment, International Journal of Structural Engineering, 4(1/2) (2013) 86-99.
[5] Tang L., Engineering expression of the ClinConc model for prediction of free and total chloride ingress in submerged marine concrete. Cem. & Conc. Research, 38, 1092-1097.
[6] Tang L., Service-life prediction based on the rapid migration test and the ClinConc model, in: Performance Based Evaluation and Indicators for Concrete Durability, RILEM PRO 047, 157-164, 2006.
[7] Bertolini L., Elsener B., Pedeferri P. and Polder R., Corrosion of steel in Concrete – Prevention, Diagnosis, Repair, Wiley-VCH, Weinheim, 2004.
[8] Angst U., Elsener B., Larsen C.K. and Vennesland, Ø., Critical chloride content in reinforced concrete – A review, Cement and Concrete Research, 39, 1122-1138, 2009.
[9] Alonso M.C. and Sanchez M., Analysis of the variability of chloride threshold values in the literature, Materials and Corrosion. 60, 631-637, 2009.
[10] Tuutti K., Corrosion of steel in concrete. CBI Report 4:82, Swedish Cement and Concrete Research Institute, Stockholm, 1982.
[11] Vollpracht A., Lothenbach B., Snellings R. and Haufe J., The pore solution of blended cements: a review. Materials and Structures, published online 15 October 2015.
[12] Gruyaert E., Effect of blast-furnace slag as cement replacement on hydration, microstructure, strength and durability of concrete, PhD thesis, Magnel Lab. for Concrete Research, Ghent University, Belgium, 2011.
[13] Taylor, R., Richardson, I.G., Brydson, R.M.D., Composition and microstructure of 20-year-old ordinary Portland cement-ground granulated blast-furnace slag blends containing 0 to 100% slag. Cement and Concrete Research, 40, 971-983, 2010.
[14] Luke, K., and Lachowski, E., Internal Composition of 20-Year-Old Fly Ash and Slag-Blended Ordinary Portland Cement Pastes. J. of American Cer. Soc., 91(12) 4084–4090.
[15] Taylor, H.F.W., Cement Chemistry. Academic press LTD, London, 1997.
[16] EN 1992-1-1:2004, Eurocode 2: Design of concrete structures - Part 1-1: General rules and rules for buildings, CEN.
[17] Statens Vegvesen, Bridge Projecting Handbook N400 (in Norwegian). Norwegian National Road Administration, ISBN: 978-82-7207-680-0, Oslo, 2015.
[18] Ann K.Y. & Song H.-W., Chloride threshold level for corrosion of steel in concrete, Corrosion Science, Vol. 49, Issue 11, Nov. 2007, pp. 4113-4133.

International RILEM Conference on Materials, Systems and Structures in Civil Engineering
Conference segment on Service Life of Cement-Based Materials and Structures
22-24 August 2016, Technical University of Denmark, Lyngby, Denmark

COUPLING LIMIT STATES OF CORROSION INITIATION AND CORROSION INDUCED CRACK OPENING – SENSITIVITY ANALYSIS OF MODEL PARAMETERS

Miguel Ferreira [(1)], Edgar Bohner [(1)], Olli Saarela [(1)]

(1) VTT Technical Research Centre of Finland Ltd., Espoo, Finland

Abstract
A normal approach to the Service Life Design of reinforced concrete will typically consider the limit state of corrosion initiation as the defining durability limit state. Rarely are other limit state considered such as corrosion propagation or corrosion induced cracking and spalling due to the greater uncertainties in the models that describe the deterioration mechanisms. Most models capture the process of the initial phase of degradation. These models disregard the actual damage, i.e. the corrosion of the reinforcing steel. As a result, the Service Life Design established to date only considers the end of the initiation phase of the degradation process, or, in other words, the onset of damage (time of depassivation or onset of corrosion) as a critical limit state. Corrosion and its consequences are not considered, which may lead to a substantially shorter estimated service life of the structures. Comprehensive investigations were recently undertaken on the depassivation of steel reinforcement and on crack formation in concrete which have resulted in an analytical prediction model for corrosion-induced cracking occurring in the surface zones of structural components. This paper presents a sensitivity study of the main model parameters for the corrosion induced cracking when coupled to the chloride induced corrosion initiation model.

1. Introduction

Reinforced concrete structures are subject to constant deterioration limiting their service life. The service life prediction of deteriorating structures is affected by the uncertainties associated with material properties, mechanical and environmental loads, and damage occurrence and propagation models [1]. Therefore, estimation of service life requires probabilistic models and methods to account for the uncertainties that govern the deterioration processes.

The service life design (SLD) of reinforced concrete structures requires material models

capable of reliably describing both mechanisms of damage and the general progression of damage over time. However, most models that are currently being used only capture the process of carbonation and chloride penetration into the uncracked concrete that is at the initial phase of degradation. Typically, these models disregard the actual damage, i.e. the corrosion of the reinforcing steel. As a result, the SLD established to date only considers the end of the initiation phase of the degradation process, i.e. the onset of damage (time of depassivation or onset of corrosion) as a critical limit state (LS). The corrosion of the reinforcement and its consequences, i.e. the crack formation and spalling of concrete, are not considered, which may lead to a substantially shorter estimated service life of the structures.

There are two distinct phases in the corrosion induced deterioration process of concrete. The first phase (initiation) is defined as the time necessary for chloride ions to reach a critical concentration at the depth of the reinforcement to cause its depassivation. Typically diffusion controls the process. This instant is defined as corrosion initiation. The second phase (propagation) is defined as the period of time that follows the initiation of corrosion. It can be separated in different deterioration phases, of which the first is cracking of concrete cover. Typically corrosion rate controls the process at the outset. After the appearance of the first crack, the continuous volume expansion due to rust formation as a consequence of the proceeding corrosion leads to crack propagation resulting in the spalling of the concrete cover.

In practice, it has been observed that time dependent reliability models do not consider the causational relationship between serviceability LS, dealing with each LS independently. As an example, corrosion initiation and propagation are usually dealt with independently, ignoring the dependency between them [2]. Commonly the propagation phase is ignored, i.e. considered to be on the safe side (conservative approach). This might stem from the lack of models, and confidence in models for this phase. As a consequence, design decisions based upon independent time-dependent reliability models will not produce optimal/realistic outcomes.

Comprehensive investigations were recently undertaken on the depassivation of steel reinforcement and on crack formation in concrete which have resulted in an analytical model for corrosion induced cracking occurring in the surface zones of structural components [3,4].

An attempt to bridge this gap is made with a basic methodology for the probabilistic determination of service life, combining both corrosion initiation and propagation phase models. The approach takes into account the time dependency of the individual phenomena, and the relationship between both phases.

The quantitative prediction of the time to cracking is needed in the development of a holistic deterioration model for the prediction of service life. A probabilistic methodology has been presented based on theoretical physical models for corrosion initiation and time from corrosion initiation to cracking of the concrete cover (time-to-cracking), and the causational relationship between them, i.e. time-to-cracking depends on the time to corrosion initiation [5,6]. Based on the methodology, it is demonstrated how the models influence the estimated time to corrosion induced cracking considering both deterioration mechanisms involved. This

approach helps to improve the prediction of durability for new or to define optimal repair strategies for existing concrete structures. The time from corrosion initiation to cracking of the concrete cover is a critical period for modelling the time to repair, rehabilitate, and replace reinforced concrete structures.

This paper presents a sensitivity study of selected model parameters for the corrosion induced cracking when coupled to the chloride induced corrosion initiation model (variations of the geometrical model parameters concrete cover depth and rebar diameter were not studied in this paper). By combining the limit states, the outcome of the SLD calculation is the probability of time to corrosion induced cracking, at any time starting after construction.

2. Reliability Analysis

2.1 Coupling of two limit states

In general, engineering design consists of proportioning the elements of a reinforced concrete structure so that it satisfies various criteria of performance, safety, serviceability, including durability under various loadings. A reliability analysis can be used to calculate the probability of reaching each LS at any time instant during the reinforced concrete structure's service life. The objective of durability design is to keep the probability of failure throughout the planned service life below a certain requirement that depends on the consequences of failure. The LS define the conditions beyond which a specified requirement for a structure (or component) is no longer met for a certain degree of reliability [7]. Limit states are represented by LS equations, generally of the form $g(x, t) < 0$, where x denotes depth from surface and t time. A LS violation (or failure) occurs when an undesirable condition for the structure is reached. The probability of occurrence of a LS violation is a numerical measure of the chances of its occurrence, based on long term observations or subjective estimates.

A reliability analysis can be performed by numerical integration, Monte Carlo simulation, or using approximate methods such as First Order and Second Order Reliability Methods (FORM/SORM). The reliability analysis in this study was performed using Monte Carlo simulation. Even for the computing of small probabilities, the development of variance reduction techniques such as importance sampling, and the evolution of computing power has reduced dramatically this once very time consuming process. The theoretical description of this method is given in many references [8-10]. The numerical integration was not preferred in this case because of the large dimensionality and the complexity of this problem.

A methodology presented in [5,6] describes the development of reliability-based approaches for the durability design and service life prediction of reinforced concrete structures that combines the probabilistic determination of two LS (corrosion initiation and corrosion induced cracking) in a single analysis.

By combining initiation with propagation until cracking, the combined service life covers the period from $t = 0$ until the time for the first crack with a width of a minimum of 0.05 mm to appear on the surface of the concrete, thus removing the need for one of the LS.
Assuming that corrosion is initiated at some time τ, for cracking to take place at time t the

corrosion process has to have duration of t-τ. Consequently, the combined probability distribution of the time of cracking is

$$f_{i,p}(t) = \int_{-\infty}^{\infty} f_p(t-\tau \mid T_i = \tau)\, f_i(\tau)\, d\tau \tag{1}$$

where $f_{i,p}$ = probability of failure; $f_p(t)$ = probability distribution function of the propagation model; and $f_i(t)$ = probability distribution function of the initiation model.

The start of corrosion propagation process depends on the corrosion initiation process; however the mechanisms that describe each of these processes are independent of each other. Therefore the modelling and computation of this distribution can be simplified by replacing the conditional probability density function with corresponding marginal probability distribution:

$$f_{i,p}(t) \approx \int_{-\infty}^{\infty} f_p(t-\tau)\, f_i(\tau)\, d\tau \tag{2}$$

The initiation model assumes chloride ingress starts at the time of construction ($t = 0$), and that the corrosion process starts when chloride has reached a critical threshold value at the depth of the reinforcement. Consequently,

$$f_p(t) = f_i(t) = 0 \quad \forall \; t < 0 \tag{3}$$

allowing the integration interval to be shortened. For $t \geq 0$

$$f_{i,p}(t) \approx \int_{0}^{t} f_p(t-\tau)\, f_i(\tau)\, d\tau \tag{4}$$

A consequence of this approach is that there is no need to define a LS requirement for corrosion initiation. By combining the two LS, only one LS requirement is necessary for the outcome of the coupled calculation. Furthermore, the uncertainties related to both processes, as modelled in the probability distribution functions, are properly considered.

2.2 Deterioration models

A reliability analysis begins with the formulation of a LS function, which represents the performance of a structure or an element, in terms of a number of basic random variables. The model parameters are characterised by probability density functions. Even the uncertainties associated with the model and the tests used should typically be considered. It is not the intention in this study to discuss the validity of the models in question. However, to study the effect of model coupling, it is an expected assumption that the models for corrosion initiation and propagation are sufficiently validated in order to provide realistic and representative results. Conformity is checked by verifying that the specified reliability is unsurpassed in the verification of the LS function over the service life of the structure. The LS function for time to corrosion initiation is defined by:

$$g_i(x,t) > 0 \Leftrightarrow C_{crit} - C(x,t) > 0 \tag{11}$$

where $g_i\ (x,t)$ = LS function for corrosion initiation; C_{crit} = critical chloride content leading to depassivation [%/weight of cement]; and $C(x,t)$ = chloride concentration at depth x and time t [%/weight of cement]; and described below.

The LS function for time to corrosion induced concrete cracking is given by:

$$g_p(x,t) > 0 \Leftrightarrow \Delta r_{crack}(t) - \Delta r_{corr}(t_{corr}) > 0 \tag{12}$$

where $g_p\ (x,t)$ = LS function for corrosion induced concrete cracking; Δr_{corr} = increase of rebar radius due to corrosion [mm]; Δr_{crack} = critical increase of rebar radius due to corrosion at time of cracking [mm]; t_{corr} = time of corrosion [years]; and described below.

The designers must define the criteria for which the LS are evaluated. There is still considerable debate as to what are the appropriate values for durability related LS [11,12]. With regards to reinforcement corrosion, this is in part due to the difficulty in practice to define a precise instant when corrosion actually starts, among other aspects. Values based on experience or set by conventions are required. In this study, a probability of LS failure of 10 % has been used based on values presented in literature and design guides [12]. It is not the focus of the study to determine the effect of the choice of LS criteria on the service life calculation, despite it being apparent that this would influence the outcome.

2.3 Models for time to corrosion initiation and time to first corrosion cracking

The corrosion initiation used in this study is based on the fib Model Code 2010 [13] approach, and considers the classical solution of Fick's second law with semi-infinite boundary and constant surface concentration. This model includes a time varying apparent diffusion coefficient and considers the time of initial exposure to chlorides [14].

The model used to describe the time from corrosion initiation to first corrosion induced cracking of the concrete cover is based on research work about the influence of concrete porosity on the corrosion morphology and the mechanical behaviour of the concrete cover affected by the corrosion process. Experimental and numerical investigations allowed for the detailed analysis of the stresses, strains and the crack formation within the concrete cover. An analytical prediction model for concrete cover cracking was derived and enables the damage prediction of the time dependent process under conditions of practical relevance [3,4].

3. Sensitivity analysis of model parameters

To study the coupling of LS, and understand the effect of model parameter changes on the outcome (SL calculation), a hypothetical semi-infinite reinforced concrete wall located in a tidal/splash zone is considered. This scenario enables the use of a 1-D analysis and diffusion being the main form of chloride transport in the concrete. Service life calculations have been performed considering a concrete made with CEM III/A 42.5 R and with w/b ratio 0.55.

For all model parameters, distribution type and values used are presented in Table 1. Service life calculations are performed for a 50 year period. It is considered that after 10 years, the effect of concrete ageing is no longer felt. For the corrosion propagation model, two distinct corrosion rates, which describe the rate of dissolution of steel, were chosen to simulate a "fast" (3.0 μA/cm2) and a "slow" corrosion process (0.3 μA/cm2). Corrosion rate can be defined as well as the reduction of the reinforcement cross section over time. It is defined by a lognormal distribution (CoV = 0.3) with an average value for rebar radius reduction of 0.0035 mm/year and 0.035 mm/year for "slow" and "fast" corrosion, respectively.

The influence of corrosion initiation model parameters is well known [15], therefore the focus of this study is on corrosion propagation model parameters on the effect of LS coupling.

Table 1. Parameter distributions/values for the time to corrosion initiation model, for the time from corrosion initiation to concrete cracking model, and variations for the sensitivity analysis.

Initiation parameters			Corrosion parameters			
Param.	Units	Dist./Values	Param.	Units	Dist./Values	Variation
C_{crit}	%/wt.c	LN[0.65, 0.13]	λ	–	C[2.1]	C[2.9] C[4.0]
C_0	%/wt.c	N[0.10, 0.005]	p	–	N[0.17, 0.017]	N[0.14, 0.014] N[0.2, 0.02]
C_S	%/wt.c	LN[2.00, 0.60]	dtz	mm	LN[0.17, 0.051]	N[0.12, 0.036] N[0.22, 0.066]
c	mm	LN[55.0, 6.25]	ds	mm	C[16.0]	–
$D_{RCM,0}$	$10^{-12}\cdot m^2/s$	LN[5.0, 1.25]	c	mm	LN[55.0, 6.25]	–
k_t	–	C[1.0]	f_{ct}	MPa	N[3.1, 0.31]	N[2.0, 0.02] N[4.0, 0.04]
b_e	K	N[4800, 700]	E_c	MPa	N[29300, 2000]	N[25000, 2000] N[35000, 2000]
T_{ref}	°C	C[20.0]	ν	–	C[0.20]	–
T_{real}	°C	C[18.3, 1.55]	k_{nonlin}	–	C[2.3]	–
n	–	B[0.45, 0.027, 0, 1]	k_{local}	–	C[0.70]	–
t_0	years	C[0.0767]	k_μ	–	C[1.0]	–
Δc	mm	N[3.87, 0.71]	D	–	C[0.0]	–
t_e	days	C[0]	φ	–	C[0.70]	–
t_n	years	C[10]	ρ	–	C[0.80]	–

Distribution types: LN – lognormal; N –Normal; B – Beta; C – Constant

where, for the corrosion initiation model: C_{crit} = critical chloride concentration in the concrete [%/weight of cement]; C_0 = initial chloride concentration in the concrete [%/weight of cement]; C_S = surface chloride concentration [%/weight of cement]; c = concrete cover depth [mm]; Δc = convection zone of concrete cover [mm]; $D_{RCM,0}$ = apparent diffusion coefficient

[m^2/s]; n = ageing factor of diffusion coefficient [-]; t_0 = reference time [years]; t = life time [years]; T_{real} = temperature of the water/air in contact with concrete [K]; T_{ref} = reference temperature [K]; b_e = Arrhenius slope [-]; k_t = transfer parameter [-]; t_e = time of exposure to chlorides [days]; t_n = period of concrete ageing [years]. For the corrosion crack model: λ = volume ratio [-]; p = porosity of the transition zone accessible for corrosion products [-], valid $0 \leq p < 1$; dtz = thickness of the transition zone accessible for corrosion products [mm]; ds = rebar diameter [mm]; c = concrete cover [mm]; f_{ct} = tensile strength of concrete [MPa]; $E_{c,eff,D}$ = effective modulus of elasticity of concrete [MPa]; ν = Poisson's ratio of concrete [-]; k_{nonlin} = factor for consideration of plasticity and cracking of concrete [-]; k_{local} = factor for consideration of a localisation of corrosion (pitting corrosion) [-]; k_μ = factor for consideration of percentage of reinforcement [-]; D = coefficient for consideration of a pre-existing crack in concrete cover [-]; φ = creep coefficient of concrete [-]; ρ = relaxation coefficient of concrete [-].

The parameters varied in the sensitivity analysis have been combined as a result of their affinity (correlation). Therefore, the parameters linked to the porosity of the concrete p and dtz have been varied simultaneously, as well as the parameters representing the mechanical properties of concrete $f_{ct}(t)$ and E_C When presenting the results, the index L indicates the use of the lower values, and the index H indicates the use of the higher values. The value λ, which is calculated as the ratio between the volume of the corrosion product or rust (iron oxide or hydroxide) and that of elemental iron, can only vary according to the molar volumes of the chemical compounds, and is usually larger than 2.1 [16] dependent on the availability of oxygen, the presence of chlorides and the level of pH in the concrete pore solution.

3.1 Simulation results and discussion

The service life calculations for both individual and coupled LS models were performed with a direct Monte Carlo simulation based on 5000 determinations for each time step (Δt = 0.1 year). The probability density function in Eq. 4 was computed with trapezoidal numerical quadrature, as described by [17]. The results are presented in Figs. 1a – 4a for "slow" corrosion, and Figs. 1b – 4b for "fast" corrosion. The horizontal axes indicate service life in years for initiation and coupled LS (the solid curves) and the time from initiation to crack appearance, i.e. propagation (the dashed curves). Table 2 shows the results for the calculated service life durations and their respective variations as a function of the models and the varying parameters.

The service life obtained by combining the two individual service life calculations depends on both the quality of concrete and the corrosion rate. However, the quality of concrete, mostly determining the time to corrosion initiation, dominates as it is the precursor for the corrosion propagation phase. Assuming a 10% probability requirement for the LS failure for corrosion initiation, it is expected that the probability requirement for the LS failure for corrosion propagation should be lower since the consequences are more severe, and already damage inducing.

The combination of both LS should naturally be judged by the requirement for the second LS since it is the phenomenon being observed, i.e. first cracking. However, for simplicity, it is assumed for both individual LS and coupled LS, an identical value of 10 % is used.

The service life obtained for the initiation model, irrespective of the reference case (slow/fast corrosion), is 21.4 years. This means that, based on the model used and the parameters chosen, it took 21.4 years for the probability, that the chloride content at the depth of the reinforcement was greater than the critical chloride content, to exceed 10 %. The service lives obtained for the propagation models were 14.1 years for slow corrosion and 1.4 years for fast corrosion, respectively, from the time of initiation. This means that, based on the model used and the parameters chosen, it took 14.1 (or 1.4 for fast corrosion) years for the probability, that a crack with a width of 0.05 mm had appeared on the concrete surface due to

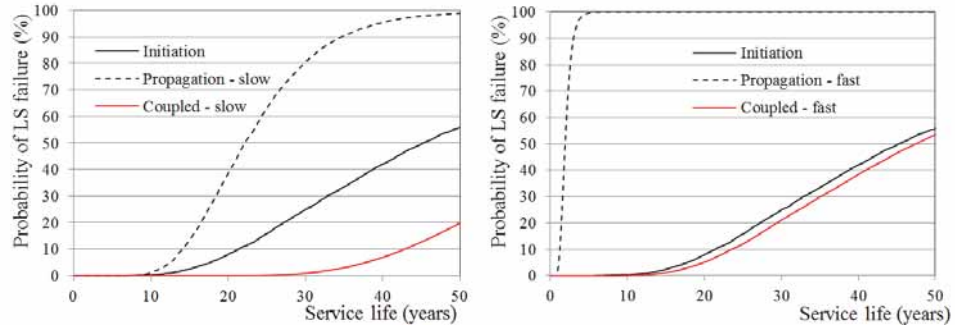

(a) (b)

Figure 1. Reference service life calculations for initiation, propagation and coupled LS, for slow corrosion (a) and fast corrosion (b).

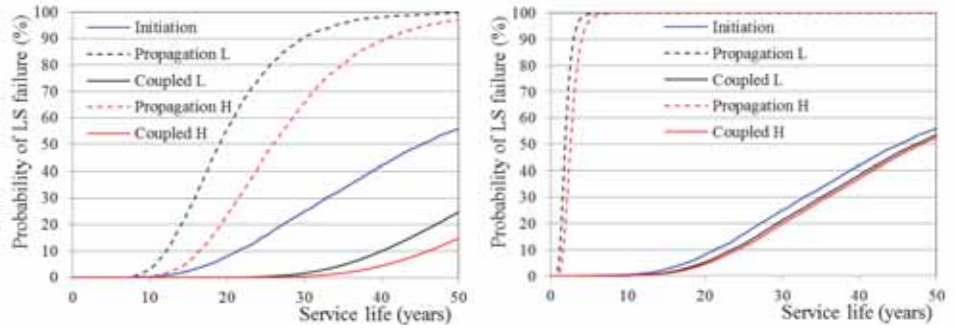

(a) (b)

Figure 2. Service life calculations varying *p* and *dtz* for initiation, propagation and coupled LS, for slow corrosion (a) and fast corrosion (b).

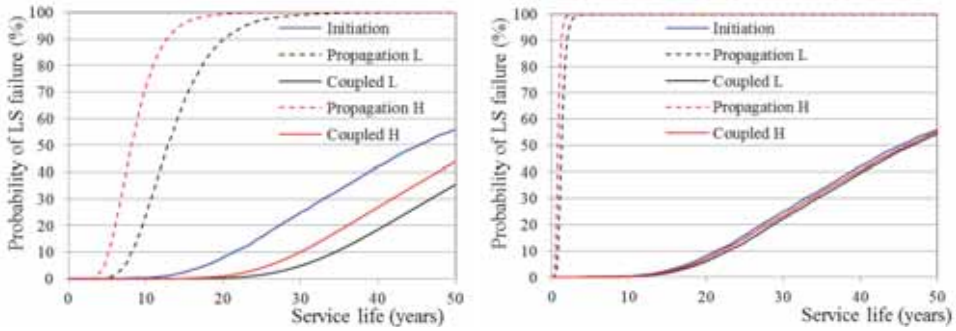

(a) (b)

Figure 3. Service life calculations varying λ for initiation, propagation and coupled LS, for slow corrosion (a) and fast corrosion (b).

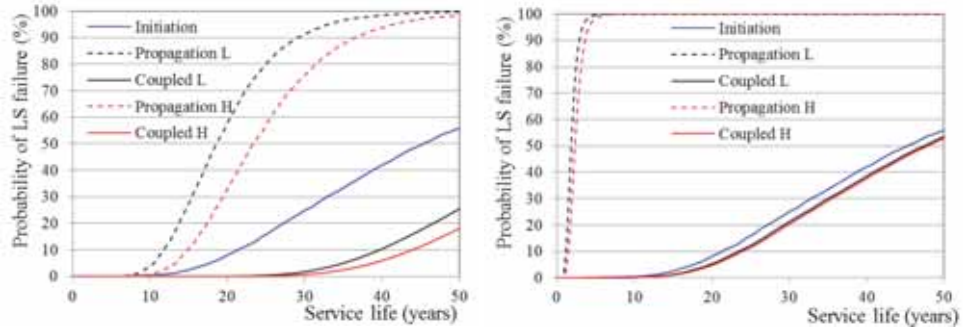

(a) (b)

Figure 4. Service life calculations varying f_{ct} and E_c for initiation, propagation and coupled LS, for slow corrosion (a) and fast corrosion (b).

reinforcement corrosion, to exceed 10 %. This effect of corrosion rate is clearly seen in Figs. 1a and 1b, where for the slow corrosion the coupled service life is extended by more than 20 years when compared to the initiation SL. In the case of fast corrosion, the increase in service life is less than 3 years. This result shows how the rate of corrosion is a crucial parameter to consider when determining the service life of a reinforced concrete structure. In situations where fast corrosion can be expected (poor concrete quality and/or aggressive environment), the propagation model does not extend the initiation phase model service life significantly. However, when slower corrosion rates are expected, this can impact positively the service life calculation by extending significantly the initiation phase model service life. In Table 2, the exact values for each service life calculation are presented. In Table 2, the reference calculation (Ref.) shows the service life obtained for the initial parameters considered. The remaining calculation present the resulting service life if a change in one or a pair of parameters is undertaken. The index L and H refer to weather the parameter has been increased (H) or decreased (L). The variation is determined in relation to the reference calculation.

When the corrosion rate is high (fast corrosion), the influence key propagation model parameters have on both the propagation model LS outcome and the coupled LS outcome is small. The maximum variation of the propagation model service life as a result of parameter changes is between 0.5 years and 1.65 years (reference = 1.4 years). The impact on the coupled service life calculation is also only marginal. The maximum variation of the coupled model service life as a result of parameter changes is between 22.0 years and 24.3 years (reference = 23.8 years). This shows that, when corrosion rate is high (fast corrosion) the influence key propagation model parameters can have on the overall service life calculation is less significant.

When the corrosion rate is low (slow corrosion), the influence key initiation model parameters have on both the propagation model LS outcome and the coupled LS outcome can be large. The maximum variation of the propagation model service life as a result of parameter changes is between 5.2 years and 16.4 years (reference = 14.1 years). While the direct effect of a change in concrete quality on the propagation phase duration is seemingly small, the impact on the coupled service life calculation is larger. As a consequence, the maximum variation of the coupled model service life as a result of parameter changes is 30 years to 46.1 years (reference = 42.9 years). This shows that, while an improvement of service life due to a better concrete quality is less noticeable, a decrease in service life can be significant, especially for the parameter λ, which depends on the presence of specific corrosion products as a consequence of the availability of oxygen among others.

Table 2. Service life durations and respective variations as a function of the models and the varying parameters.

Models	Ref.	p_L/dtz_L	p_H/dtz_H	λ_L	λ_H	f_{ctL}/E_{CL}	f_{ctH}/E_{CH}
Initiation (y)				21.4			
Propagation slow (y)	14.1	12.1	16.4	8.2	5.2	11.7	14.9
ΔSL_{PROP} (%)	–	-14.2	16.3	-41.8	-63.1	-17.0	0.0
Propagation fast (y)	1.4	1.1	1.65	0.8	0.5	1.2	1.5
ΔSL_{PROP} (%)	–	-21.4	17.9	-42.9	-64.3	-14.3	7.1
Coupled slow (y)	42.9	40.1	46.1	34.5	30	39.7	43.9
ΔSL_{COUP} (%)	–	–6.5	7.5	–19.6	–30.1	–7.5	2.3
ΔSL_{INI} (y)	21.5	18.7	24.7	13.1	8.6	18.3	22.5
ΔSL_{INI} (%)	100.5	87.4	115.4	61.2	40.2	85.5	105.1
Coupled fast (y)	23.8	23.5	24.3	22.85	22.0	23.5	24.0
ΔSL_{COUP} (%)	–	–1.3	2.1	–4.0	–7.6	–1.3	0.8
ΔSL_{INI} (y)	2.4	2.1	2.9	1.45	0.6	2.1	2.6
ΔSL_{INI} (%)	11.2	9.8	13.6	6.8	2.8	9.8	12.1

These results show that, when coupling corrosion initiation and corrosion propagation, the corrosion rate has a significant influence in the extension of the SL. Cairns & Law [18] suggest that the LS for propagation could be identical to that of the initiation because the

appearance of the first crack does not affect the mechanical performance of the reinforced concrete structures. In this case, a combination of LS would always result in an extension of the service life of the reinforced concrete structures.

With regards to the criteria chosen for the LS, while assumed constant in this analysis, it must be mentioned that there is currently not enough background information to understand the consequences of certain values, and while many values are being put forward based on those used in structural design, they do not necessarily represent adequately the complexity of the deterioration mechanism and the economic consequences of LS failure. The choice of LS requirement is still relatively subjective.

4. Conclusions

This paper presents a sensitivity analysis of a probabilistic design procedure which combines the calculation of two independent LS for concrete deterioration: chloride induced corrosion initiation and corrosion induced cover cracking of concrete. By combining these two limit states, the outcome of the service life calculation is the probability of time to corrosion induced cracking, at any time starting after construction. The design procedure is exemplified for a concrete with CEM III, and for two corrosion rates ("slow" and "fast").

Simulation results show that the corrosion rate is a major factor to consider when determining the service life of a reinforced concrete structure. In situations where fast corrosion can be expected, either due to poor concrete quality and/or an aggressive environment, the propagation model, when coupled to the initiation model, does not extend the service life calculation significantly (< 3 years for the cases studied). However, when slower corrosion rates are expected, this can impact positively the service life calculation by extending significantly the initiation phase model service life (up to almost 25 years for the given example).

Studying the effect other propagation model parameters (here: influence of porosity and mechanical properties of concrete cover) have on the service life calculation outcome, it was noticed that their impact depends on whether the corrosion rate was low or high. For high corrosion rates, other model parameters had little effect. For low corrosion rates, they could still influence significantly the outcome of the service life calculation. The effect of changing geometrical parameters, as e.g. concrete cover depth and rebar diameter, were not subject of this study.

This research has shown the benefit of using a coupled limit state analysis until the time to first corrosion induced crack to appear. The coupled limit state is of interest especially to the owners of reinforced concrete structures. Joint consideration of corrosion initiation and propagation describes the damaging mechanism more realistically and facilitates an extension of the service life of the structures. More accurate assessment of the performance capacity of the reinforced concrete structures allows better optimised resource management.

References

[1] Kim, S., Frangopol, D.M., Soliman, M. 2013. Generalized Probabilistic Framework for Optimum Inspection and Maintenance Planning. J. Struct. Eng. 139. pp. 435-447
[2] fib Bulletin 34. 2006. Model Code for Service Life Design. International Federation for Structural Concrete, 206 p.
[3] Bohner, E. 2013. Rissbildung in Beton infolge Bewehrungskorrosion. Doctoral Dissertation, Karlsruhe Institute of Technology (KIT) (*Translated title: Concrete cracking due to reinforcement corrosion*).
[4] Bohner, E., Müller, H. S.: Analytical model for predicting time to concrete cover cracking due to corrosion of reinforcement. In: Proceedings of the XXII Nordic Concrete Research Symposia (NCR 2014), August 13-15, 2014, Reykjavik, Iceland, Nordic Concrete Federation (ed.), Norsk Betonforening, Oslo, 2014, S. 421-424
[5] Ferreira, M., Bohner, E., Saarela, O., Modelling the time to concrete cover cracking due to reinforcement corrosion. SMIRT 23 Manchester, 10-14 August 2015 Div.I-221.
[6] Bohner, E., Ferreira, M., Saarela, O., Modelling the service life of concrete until cover cracking due to reinforcement corrosion. ICCRRR 2015. Leipzig 8-9 October 2015. pp.203-211.
[7] ISO/FDIS 16204:2012 Durability – Service life design of concrete structures. ISO. 40 p.
[8] Thoft-Christensen P, Baker M.J. 1982. Structural reliability theory and its applications. Springer Verlag: Berlin.
[9] Rubinstein, R.Y. 1981. Simulation and monte carlo method. John Wiley & Sons, New York.
[10] CSEP. 1995. Introduction to Monte Carlo methods. Computational Sci. Projects, ORNL
[11] Gulikers, J. 2006. Critical issues in the interpretation of results of probabilistic service life calculations. In International RILEM Workshop on Integral Service Life Modelling of Concrete Structures. University of Minho, Guimarães, Portugal, ISBN 972-99179-2-2. pp. 195-204
[12] Ferreira, R.M., Gulikers, J. 2008. Critical considerations on the assessment of the durability (serviceability) limit state of reinforced concrete structures. Pro.11th DBMC, Istanbul, 11-14 May. pp. 1425-1432
[13] fib Model Code for Concrete Structures 2010. International Federation for Structural Concrete, Lausanne. 2013, 436p.
[14] Ferreira, R.M., Implications on RC structures performance of model parameters sensitivity: Effect of chlorides. J. Civil Engn. & Management. 16(4). 2010. 561-566.
[15] Ferreira, R.M., Sensitivity analysis of model parameters for corrosion initiation and implications on design. Proc. of Int. RILEM Wksp. on Integral Service Life Modelling of Concrete Structures. Guimarães. 5-6.11.2007. 205-214.
[16] Weizhong, G., Raupach, M., Wei-Lang, J.: Korrosionsprodukte und deren Volumenfaktor bei der Korrosion von Stahl in Beton. In: Beton- und Stahlbeton 105 (2010), No. 9, pp. 572-578 (*Translated title: Corrosion products and their volume ratio at corrosion of steel in concrete*).
[17] Stoer, J., Bulirsch, R. 1980. Introduction to numerical analysis. Springer Verlag: Berlin.
[18] Cairns, J., Law, D. 2003. Prediction of the ultimate limit state of degradation of concrete structures. ILCDES 2003: Integrated Lifetime Engineering of Buildings and Civil Infrastructures, Rotterdam. 6 p.

International RILEM Conference on Materials, Systems and Structures in Civil Engineering
Conference segment on Service Life of Cement-Based Materials and Structures
22-24 August 2016, Technical University of Denmark, Lyngby, Denmark

BIO-BASED PH-RESPONSIVE SUPERABSORBENT POLYMERS FOR SELF-HEALING CRACKS IN CONCRETE

Arn Mignon [1,2], Dries Devisscher [2], Jolien Vermeulen[1], Peter Dubruel [2], Sandra Van Vlierberghe[2], Nele De Belie[1]

(1) Magnel Laboratory for Concrete Research, Ghent University, Belgium
(2) Polymer Chemistry and Biomaterials Group, Ghent University, Belgium

Abstract
Cracks endanger the durability of concrete. Introducing a superabsorbent polymer (SAP) during concrete mixing can create a self-sealing and -healing construction. SAPs are able to take up aqueous solutions up to several hundred times their own weight. Bio-based SAPs starting from polysaccharides have gained increasing interest in recent years due to their biocompatibility, non-toxicity and low price. The use of pH-responsive SAPs can also be extremely useful as they should only swell more upon crack formation and less during mixing of the SAPs in the concrete. The present work describes the development and the characterization of SAPs based on methacrylated polysaccharides (alginate and chitosan) combined with pH-responsive monomers dimethylaminoethyl methacrylate (DMAEMA) and dimethylaminopropyl methacrylamide (DMAPMA). The materials exhibited a high moisture uptake capacity up to 120% of their original weight with a negligible hysteresis. The pH-responsive swelling behavior was studied in aqueous and cement filtrate solutions with a varying pH. Chitosan combined with DMAEMA or DMAPMA showed the targeted pH-responsive swelling. Chitosan combined with DMAPMA also showed a limited compression strength reduction and a promising self-sealing and -healing behavior and could thus be considered as a very interesting future solution to seal and heal cracks in concrete.

1. Introduction

Concrete is nowadays still the most important building material, mostly due to its ease of use, good mechanical and durability properties and especially due to its relatively low cost compared to other construction materials. Annually, over 10 billion tons are produced [1]. However, it has a low tensile strength. Therefore, concrete is nearly always reinforced with steel bars. This low tensile strength can lead to crack formation, which is one of the most destructive problems in concrete applications as these cracks can endanger the durability of concrete. This can lead to corrosion of the reinforcement, since a pathway for harmful

particles dissolved in fluids and gases is generated [2]. Repairing of cracks often is performed with external techniques such as manual repair with epoxy [3], polyurethane [4], etc. The maintenance and repair with external techniques is often expensive, time-consuming and visually unattractive. These costs can even exceed half of the annual construction budget [5]. Therefore, efforts have been made by researchers to develop concrete that automatically seals and heals any cracks that may form. Standard concrete already possesses the ability to heal small cracks by deposition of calcium carbonate in a process called autogenous healing [6, 7]. Addition of superabsorbent polymers (SAPs) is a possibility to simulate the self-healing of concrete. SAPs are cross-linked polymer networks which can swell up to several hundred times their own weight in aqueous solutions. Previous work has already been performed in our research group regarding synthetic SAPs based on acrylic acid and acrylamide for self-sealing and -healing applications in concrete [8, 9]. These materials were already quite interesting for the intended application. However, they showed a severe effect on the strength upon incorporation. When these SAPs were mixed in mortar, they take up some of the added water which can subsequently be released inside the mortar during the hardening process. This leads to a higher degree of hydration and a more gradual drying, increasing the strength of the concrete and reducing the chance of cracks to manifest. However, as the SAP releases its water, it shrinks and leaves behind pores in the matrix which negatively influence the compressive strength. Which effect contributes the most depends on the water/cement ratio [10, 11]. For self-healing applications, high SAP amounts are required (up to 1% relative to cement mass). Therefore, the macropore formation becomes more critical especially when high amounts of additional water are used to compensate for the loss in workability. To minimize this effect, pH-responsive basic monomers were used here to control the swelling in such a way that the formed SAPs will almost not swell at a high pH (the pH of fresh mortar is 12.5-13), but when a crack occurs and water enters, they will swell more and do their job. In other previous work from the author, alginate biopolymers have been indicated as a high-potential and low-cost polymer for sustainable concrete repair [12]. Natural polysaccharides have the advantage of being renewable, environment-friendly and have a low cost. The current work will therefore report on the development, characterization and investigation of the self-healing potential of SAPs based on methacrylated polysaccharides combined with basic monomers.

2. Materials and methods

2.1 Materials

Sodium alginate and chitosan (used polysaccharides), methacrylic anhydride (MAAH, used for modification of the polysaccharide), sodium hydroxide (NaOH, used for creating aqueous solutions with varying pH-values), hydrochloric acid (HCl, used for creating aqueous solutions with varying pH-values), acetic acid (used to dissolve chitosan), dimethylaminoethyl methacrylate (DMAEMA, used monomer), dimethylaminopropyl methacrylamide (DMAPMA, used monomer) and ammonium persulfate (APS, used initiator for polymerization) were purchased from Sigma-Aldrich.

N,N-tetramethylethylenediamine (TEMED, used as activator for the polymerization) was obtained from Acros Organics.

2.2. Methacrylation and cross-linking of the polysaccharides

The reaction conditions are outlined in Table 1. The polysaccharide solution was prepared by stirring overnight. Subsequently, the MAAH was added dropwise. The reaction was left to proceed for the designated time, after which a dialysis was performed for 72 hours whilst changing the dialysis water twice per day. The resulting solution of methacrylated polysaccharide (AlgMOD or ChiMOD) was frozen and the water removed via lyophilization using a Christ freeze-dryer alpha 2-4-LSC at -85 °C and 0.37 mbar.

Table 1: Methacrylation reaction conditions.

Polysaccharide	Solvent	Polymer concentration [w%]	MAAH added[eq]	pH	Temperature	Stirring time
Alginate	Milli Q	2.00	2.00	8	r.t.	24 h
Chitosan	2 v% AcOH	1.50	0.80	5	r.t.	3 h

The cross-linking reaction of the methacrylated polysaccharides with either DMAEMA or DMAPMA took place by preparing a certain amount of modified polysaccharide, monomer and TEMED in a solvent (all amounts and solution types are specified in Table 2). The mixture was placed under nitrogen atmosphere by flushing the system after which the temperature was raised if needed. Subsequently APS was added to initiate the reaction. After 24 hours, the SAP was submersed in an excess of demineralized water for 24 hours to remove unreacted products after which it was frozen and dried by lyophilization. Finally the resulting material was grinded into a powder with an A11 basic Analytical Mill.

Table 2: DMAEMA/DMAPMA cross-linking reaction conditions.

Poly-saccharide	Solvent	Temperature [°C]	Polysaccharide concentration [w%]	Monomer conc. [w%]	TEMED conc. [v%]	APS conc. [w%]
AlgMOD	Milli Q	45	2	14	0.48	0.32
ChiMOD	6 v% AcOH	r.t.	2	14	0.96	0.64

2.3. Characterization of the synthesized SAPs

Gel fraction quantification

The gel fraction was determined by weighing a dried sample of the hydrogel directly after the cross-linking reaction before and after washing for 24 hours.

Moisture uptake measurements using dynamic vapor sorption (DVS)

Moisture uptake at 0, 30, 60, 90 and 95% RH was determined with a Cahn microbalance. Each subsequent step was initiated when a change in sample mass lower than 0.002 mg/min

was observed. The cycle continued with a desorption phase where the same sequence of RH levels was used but in reverse order.

Determination of the swelling capacity
0.2 g SAP (m_{SAP}) was added to 100 ml swelling medium (m_0) (i.e. demineralized water or cement slurry filtrate) and the pH was adjusted with NaOH or HCl if necessary. After 3 hours of incubation, the liquid was brought over a filter to remove the swollen hydrogel. The filtrate (m_f) was weighed and the swelling capacity in g absorbed water per g SAP was calculated using Equation 1:

$$S = (m_0 - m_f)/m_{SAP} \quad (1)$$

Cement slurry filtrate was prepared by stirring ordinary Portland cement in demineralized water for three hours. The suspension was subsequently filtered to remove solid cement particles. The resulting liquid is cement slurry filtrate with a pH of approximately 12.6.

2.4. Influence of SAP incorporation on mortar strength
A standard mortar mixer was used to prepare mortar samples according to the EN 196-1 standard by mixing 450 g (22 w%) ordinary Portland cement (CEM I 52.5 N; 510 kg/m^3) with 225 g (11 w%) water and 1350 g (67 w%) silica sand 0/2 (1530 kg/m^3). On top of these amounts, 2.25 or 4.50 g SAP (ChiMOD DMAPMA) for 0.5 and 1 w% respectively and additional water to account for the water uptake of the hydrogel (based on the water uptake in cement filtrate) were added. After a curing period of 28 days, the mortar samples were tested for their flexural and compressive strength by means of a three-point-bending test followed by a compression test on the resulting halves (complying to the EN 196-1 standard) using the Walter + Bai DB 250/15 machine.

2.5. Self-healing efficiency
The composition of the mixtures used for measuring the self-healing efficiency can be found in Table 3. First, the cement (CEM I 52.5N), fly ash (Class F) and SAPs (except for the reference mixture) were equally distributed with a mortar mixer. Then, water and superplasticizer were added and mixed for 30s at 140 rotations per minute (rpm). The fine silica sand (M34, Sibelco) was added during the next 30s at 140 rpm. To ensure a homogenous dispersion of all components, the speed was increased for the following 30s to 285 rpm. The edges of the bowl were then scraped during 30s and the mixture was resting for a period of 60s. Subsequently, at a speed of 140 rpm, synthetic PVA microfibers (RECS 15x8, Kuraray) were slowly added during 30s. The final step was mixing for 60s at 285 rpm. Molds (160 x 40 x 10 mm³ samples) were filled with the mixture. The samples were demolded after 48h and were stored at a relative humidity of 95 ± 5% and a temperature of 20 ± 2°C until the age of 28 days. Series used within this study consisted of a minimum of 3 samples with 2 v% of PVA microfibers to induce multiple cracking.

Cracks were created in the specimens by a four-point bending test at the age of 28 days. A servo hydraulic testing system (Walter+Bai DB 250/15) ensured a displacement-controlled test (0.0015 mm/s to imitate a quasi-static load). The lower span was 140 mm and the upper loading span was 40 mm. The strain at the bottom side of the specimen was limited to 1%,

theoretically calculated from the curvature and the vertical displacement during loading. This strain is lower than the maximum possible strain upon failure of such a strain-hardening specimen, so the service cracks could be studied before opening due to pullout of the fibers. After cracking, the samples were stored in a room at 20 ± 2°C by applying wet-dry cycles (alternatingly stored in water for 12h and at a relative humidity of 60% for 12h).

After a period of 28 days of healing, the specimens were reloaded in four-point bending until failure and the regain in first-cracking strength, obtained during the first and second loading cycle, was compared [13].

Table 3: Mortar composition of the studied mixtures.

Sample Code	m% SAP	Cement [kg/m³]	Fly ash [kg/m³]	Sand [kg/m³]	Water [kg/m³]	Additional water [kg/m³]	Super-plast [kg/m³]	Fibers [kg/m³]
Reference	0	608	608	426	365		12	26
ChiMOD DMAPMA	0.5	584	584	409	350	39	12	26
	1	577	577	404	346	51	12	26

3. Results and discussion

3.1 Characterization performed on SAP

Gel fraction quantification

Gel fraction of a SAP is the percentage of dry weight that is incorporated in the polymer network. It is calculated by weighing the dried material before and after purification, where the unreacted agents and non-covalently linked oligomers are removed. It gives an indication on the efficiency of the cross-linking reaction. All measurements were performed in triplicate and the results are shown in Table 4. It could be seen that the polymers with DMAEMA showed a higher gel fraction compared to their DMAPMA counterpart. This could be explained partly because the structure of the SAPs containing DMAPMA is more brittle and as such more prone to becoming damaged during purification.

Table 4: Gel fraction results.

Material	Gel fraction	Standard deviation
AlgMOD DMAEMA (high DS)	80.1	0.35
AlgMOD DMAPMA (high DS)	64.7	1.39
ChiMOD DMAEMA	64.7	5.01
ChiMOD DMAPMA	49.0	10.67

Moisture uptake capacity of the SAPs using DVS

To identify the behavior of the hydrogels in mortar or concrete in conditions where no direct contact with water is possible, moisture uptake capacity measurements were performed. In some applications, water cannot infiltrate into the formed cracks and only humidity from the

air can be absorbed. If this uptake capacity is high enough, these cracks could be partially sealed already.

The results are shown in Figure 1. It could be observed that the hydrogels, especially the ones containing DMAPMA have a high moisture uptake capacity (even up to 120% its own weight for ChiMOD DMAPMA). All materials showed a negligible hysteresis, which implies that all moisture initially absorbed will again desorb at equal relative humidity (RH) levels. This is advantageous as a slow desorption of this water during the curing of mortar leads to a gradual drying. This also lowers the probability of cracks to manifest during curing. In addition, this released water can lead to the deposition of $CaCO_3$ from dissolved $Ca(OH)_2$ and CO_2, which increases the self-healing of mortar.

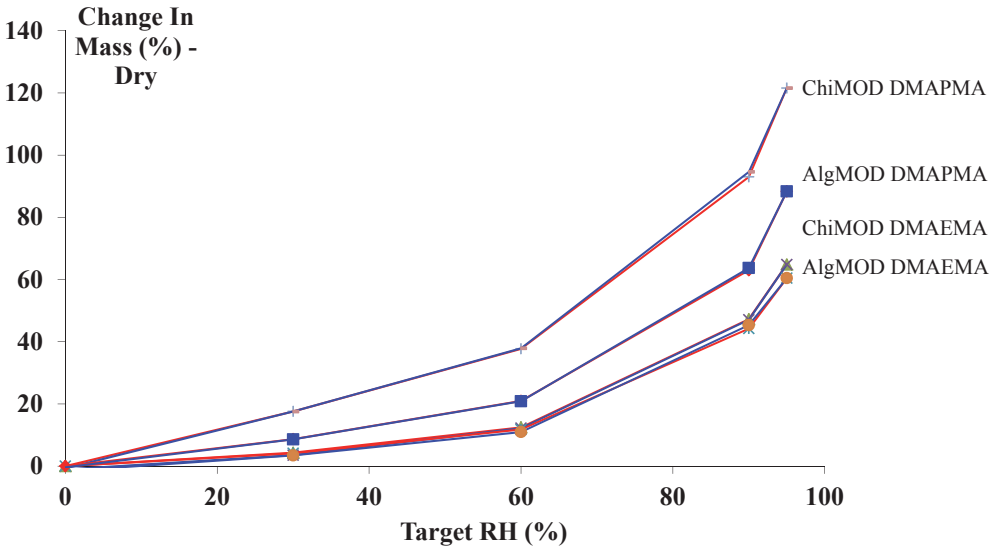

Figure 1: Sorption and desorption isotherms of the SAPs measured by DVS.

Swelling capacity as a function of the composition of SAP

The results of the swelling capacity are shown in Figure 2 (a,b). To understand these results, a first explanation needs to be given on the pH-responsiveness of these polymers.

Alginate contains carboxylic acid groups which will become negatively charged at pH higher than its pKa (~3.5). The amine group in the basic monomers becomes positively charged at pH values lower than the pKa values (8.4 for DMAEMA and 8.9 for DMAPMA). Chitosan also contains amine groups and has a pKa ~6.5. Similar charges will repel each other and create more possibility for swelling. The swelling tests have been performed in aqueous solutions with a varying pH (pH 3, 8 and 12) to indicate the pH-responsiveness of the SAPs.
Due to the combination of the carboxylic acids from alginate and the amine groups of the monomers, the SAPs (AlgMOD DMAEMA and AlgMOD DMAPMA) did swell at pH 3 (only positively charged amine groups) and at pH 12 (only negatively charged carboxylic acid

groups) as seen in Figure 2b. However, an association of the positive and negative charges at pH 8 leads to a denser physically cross-linked network, with less free volume for the absorption of water. This is the opposite trend as anticipated. For that reason these SAPs will be less useful in the intended application.

Chitosan in combination with the monomers is much more promising. In this case, at a pH of 12, no amines are positively charged and a low swelling is measured. However at a pH of 8, the amines of DMAEMA or DMAPMA start to become positively charged, leading to an increased swelling. At pH 3, both the amines of the monomers and of chitosan become positively charged and lead to an even further increase of the swelling. It is evident that these are better materials to incorporate in mortar. As the swelling is similar for both materials, but the moisture uptake capacity of ChiMOD DMAPMA is much higher than ChiMOD DMAEMA, the first one will be further tested on its effect on the strength and self-sealing and -healing efficiency.

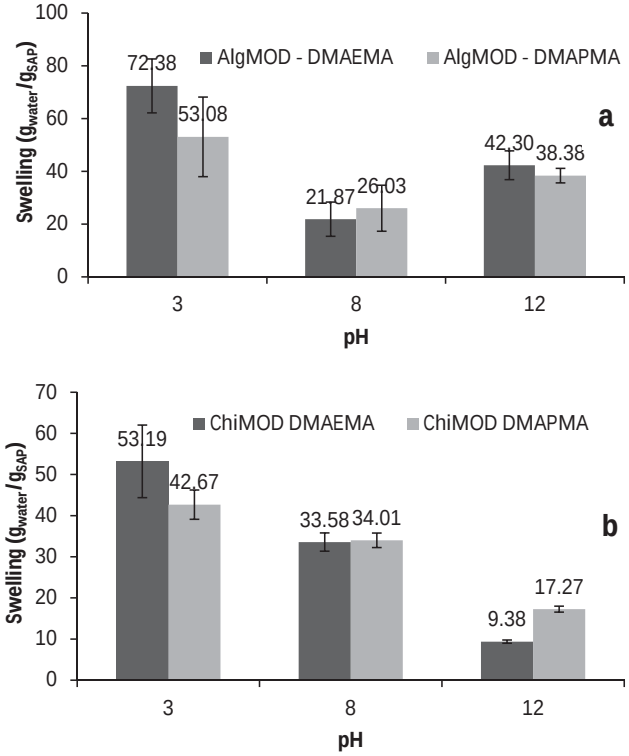

Figure 2: Swelling capacity of the SAPs. AlgMOD DMAEMA & AlgMOD DMAPMA (a), and ChiMOD DMAEMA & ChiMOD DMAPMA (b).

3.2. Influence of mortar strength upon SAP incorporation

Chosen as the best material of the above-mentioned series, ChiMOD DMAPMA has been incorporated in mortar in 2 different amounts (0.5 m% and 1 m% in function of the amount of cement) to indicate the effect on the strength. After a curing period of 28 days, the samples were tested by means of three point bending and compression strength tests (Table 5).

Table 5: Influence of SAP incorporation on mortar strength

	Bending strength			**Compression strength**		
Material	Mean	Stdev	% Loss	Mean	Stdev	% Loss
Reference	8.6	0.2		68.4	1.1	
ChiMOD DMAPMA 0.5 m%	8.1	0.14	5.8	58.1	1.4	15.1
ChiMOD DMAPMA 1.0 m%	7.3	0.4	15.1	51.8	1.3	24.3

Additional water was added to compensate for the absorption of mixing water by the polymers and to create mixtures showing a similar workability as the reference material with a water-to-cement ratio of 0.50 [8]. Samples containing SAPs have an effect on the strength, however this is very limited compared to addition of specific synthetic SAPs [8]. The higher the addition of SAP, the more pronounced the effect is on the strength, when using a high water-to-cement ratio [10]. Upon addition of ChiMOD DMAPMA, the bending strength decrease remains below 15% and for the compression strength below 24% (addition up to 1 m% SAP in function of the added amount of cement).

3.3. Self-healing efficiency of mortar samples by incorporation of SAPs

A different mixture was used for the self-healing efficiency as microfibers were needed to create several small cracks instead of 1 large crack. If fibers were added to the original mixture, the slump flow would not be as anticipated. Therefore this mixture was adjusted to the one as described in [13]. Due to the use of microfibers, multiple cracking was obtained. Multiple smaller cracks will make sure that enough SAPs are available for self-healing and will lead to a better autogenous healing as smaller crack widths show better healing compared to larger crack widths. In the samples with an addition of SAPs, macropores were formed during the mixing and hardening of the mortar, which could act as crack initiators [13]. This will increase the ductile behavior of the mortars. To study the self-healing capacity of the mortars with or without SAPs, the samples were cracked up to 1% strain. This was done to study the crack widths occurring during the lifetime of a structure, but not to complete failure. As the samples were stored in wet-dry cycles, a large amount of water was available for autogenous healing. To give an indication on the self-healing efficiency of the mortars, the strength regain after 28 days of self-healing was compared between the samples with and without SAP addition. However, a few things should be taken into account when comparing these results.

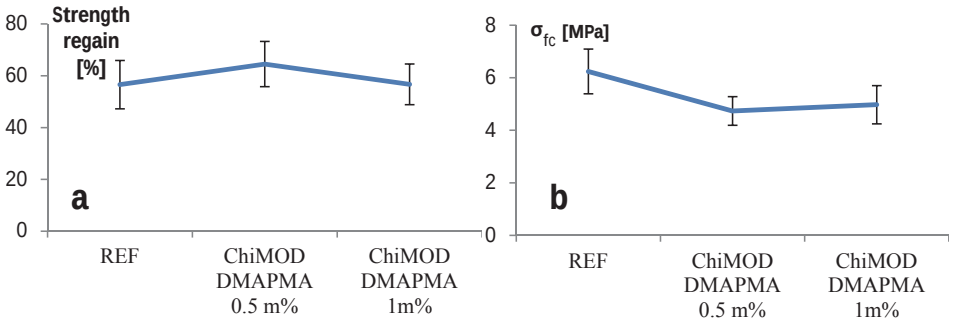

Figure 3: (a) strength regain values of the mortar samples and (b) first cracking strength.

As can be seen in Figure 3a, there is no significant difference ($p < 0.05$) between the reference and mortar with ChiMOD DMAPMA (1 m% addition). When comparing the first cracking strength ($\sigma_{fc,}$ Figure 3b), there is also no significant difference. However, there is a difference in the crack size distribution. Microscopy has shown that 90% of the cracks were between 1 and 47 µm for the reference and between 2 and 63 µm for ChiMOD DMAPMA 1 m%, meaning the latter would need an improved self-healing efficiency, to obtain a similar strength regain as the reference. This means that addition of 1 m% would lead to a reduced autogenous healing compared to the reference material. On the other hand, the water available in the SAPs should be used for improved autogenous healing. In literature, cracks up to 130 µm are able to close when using commercial SAPs. Here, partial recovery can be seen.

When now comparing the reference with ChiMOD DMAPMA 0.5 m%, a small increase in the strength regain was observed (however not a significant difference). σ_{fc} was actually significantly lower than the reference material and when investigating the crack size distribution, 90% of the cracks were situated between 1 and 33 µm. The combination of smaller cracks and lower σ_{fc}, could explain the small increase (again, not significant) in the strength regain.

It could be concluded that especially an addition of 1 m% SAP induced the strongest self-healing as larger cracks needed to be sealed and in addition a similar strength regain was obtained compared to the reference mortar. However, the improvement was more limited than envisaged, mainly due to the high self-healing capacity of the reference mortar, which was a fiber reinforced cementitious composite.

Further research will focus on the functionalization of these new types of SAPs, to further improve self-healing properties without reducing the strength.

4. Conclusion

It can be concluded that bio-based pH-responsive superabsorbent polymers could be very promising for self-healing of cracks in mortar and concrete. These SAPs showed a strong moisture uptake capacity up to 120% of the original weight and a swelling capacity up to 50-

70 times their weight, especially at a lower pH. The polymers will thus not swell during the mixing process (alkaline condition), but will swell when cracking occurs and water enters the crack (neutral to acidic condition). Therefore, upon incorporation of ChiMOD DMAPMA in mortar, the samples showed only a limited strength reduction (< 24% when adding 1 m% SAP, in function of the added amount of cement). An addition of 1m% also lead to a stronger self-healing capacity compared to reference samples, although the difference was limited due to the high self-healing capacity of the reference. These results can conclude that ChiMOD DMAPMA could be a promising polymer for self-healing of cracks. Further research could be performed to further optimize these materials for an even stronger self-healing.

References

[1] Meyer, C., The greening of the concrete industry, Cement and Concrete Composites, 31 (2009) 601-605.
[2] Wang, K., et al., Permeability study of cracked concrete, Cement and Concrete Research, 27 (1997) 381-393.
[3] Sanjay, P., et al., Feasibility of externally activated self-repairing concrete with epoxy injection network and Cu-Al-Mn superelastic alloy reinforcing bars, Smart Materials and Structures, 23 (2014) 105027.
[4] Bang, S.S., et al., Calcite precipitation induced by polyurethane-immobilized Bacillus pasteurii, Enzyme and Microbial Technology, 28 (2001) 404-409.
[5] Joseph, C., et al., Issues relating to the autonomic healing of cementitious materials, in: Proceedings of the 1st International Conference on Self-Healing Materials, Noordwijk, the Netherlands Springer, 2007.
[6] Edvardsen, C., Water Permeability and Autogenous Healing of Cracks in Concrete, Materials Journal, 96 (1999) 448-454.
[7] Wu, M., et al., A review: Self-healing in cementitious materials and engineered cementitious composite as a self-healing material, Construction and Building Materials, 28 (2012) 571-583.
[8] Mignon, A., et al., pH-responsive superabsorbent polymers: A pathway to self-healing of mortar, Reactive and Functional Polymers, 93 (2015) 68-76.
[9] Mignon, A., et al., pH-sensitive superabsorbent polymers: a potential candidate material for self-healing concrete, J Mater Sci, 50 (2014) 970-979.
[10] Snoeck, D., et al., Effect of high amounts of superabsorbent polymers and additional water on the workability, microstructure and strength of mortars with a water-to-cement ratio of 0.50, Construction and Building Materials, 72 (2014) 148-157.
[11] Jensen, O.M., Hansen, P.F., Water-entrained cement-based materials: II. Experimental observations, Cement and Concrete Research, 32 (2002) 973-978.
[12] Mignon, A., et al., Alginate biopolymers: Counteracting the impact of superabsorbent polymers on mortar strength, Construction and Building Materials, 110 (2016) 169-174.
[13] Snoeck, D., De Belie, N., Repeated autogenous healing in strain-hardening cementitious composites by using superabsorbent polymers, Journal of Materials in Civil Engineering, 28 (2015) 04015086.

International RILEM Conference on Materials, Systems and Structures in Civil Engineering
Conference segment on Service Life of Cement-Based Materials and Structures
22-24 August 2016, Technical University of Denmark, Lyngby, Denmark

COMPARISON OF MEASURED AND PRESCRIBED K-VALUES FOR THE EQUIVALENT PERFORMANCE OF FLY ASH CONCRETE

T. Altuğ Söylev [(1)]

(1) Gebze Technical University, Kocaeli, Turkey

Abstract
In the present study cement efficiency factor (k-value) for a Class F fly ash was determined in control and fly ash concretes with three different water/binder ratios (w/c = 0.40, 0.50 and 0.60). Fly ash replacement ratio was kept at 20% by mass of cement. The determination of k-value was based on compressive strength at 28 days age. The obtained k-values were compared to the prescribed k-value (k = 0.4) of EN 206 Standard with the compressive strength test (EN 12390-3). Water permeability specimens are still under testing. The results indicated that the prescribed k-value is unsafe for lower w/c ratios. Measured k-value can help to obtain safer values

1. Introduction

The use of mineral additions can provide many chemical and physical enhancements to the properties of concrete beside economical advantage and environmental impact. They are typically used in two ways: mixed with clinker during manufacture to obtain composite cements or directly added to concrete. Mineral additions (Type II in EN 206 Standard) have cementitious properties due to their oxide compositions. However, their cementitious capacity can be different than that of Portland cement. On the other hand, they are not cementitious in themselves but in the presence of $Ca(OH)_2$, they can hydrate. As a result of this, when they are used as a cement replacement material, their potential for hydration is limited to the amount of $Ca(OH)_2$ generated by the hydration of Portland cement.

EN 206 Concrete Standard allows the use of mineral additions as a cement replacement material. However their use is limited by the equivalent performance requirement. Cement replacement ratio should be selected properly to avoid an alteration from the strength and durability of concrete without addition.

For some mineral additions like fly ash, whose performance has been tested for years, the standard suggests a definite cement replacement ratio in order to secure the equivalent performance. Determination of the cement replacement is based on the cement efficiency factor (k-value) and the ratio of fly ash to cement.

However, the k-value prescribed in the standard is a general value. Cementing efficiency of mineral additions can significantly differ according to the type, source etc. Gruayert et al. tested much better performances for slag replacement (50, 70 and 85%) for chloride penetration. They determined k-values from the test results and compared them to the prescribed k-values in the standard (EN 206). Although, the better performance for chloride penetration, acid attack, alkali-silica reaction and sulfate attack, the performance of slag concrete was poor against carbonation [1]. Kaid et al. also found lower k-value than that of the control concrete for 20% natural pozzolan replacement, equivalent values for compressive strength, absorption and gas permeability. However, k-values against chloride attack and acid attack were more than 2 [2]. Similar result was found for carbonation resistance of 25% metakaolin replacement in concrete by San Nicolas et al. but better performance than the control concrete for gas permeability, chloride ion diffusion and long-term (one year) compressive strength [3]. However, according to study of Younsi et al., 50% fly ash replacement gives acceptable performance against carbonation attack [4]. Different tests, such as carbonation depth [5] and chloride diffusivity [5-6], were used to assess equivalent performance of concretes. Badogiannis determined the k-value for Greek kaolins by testing compressive strength at different ages and found three times higher value compared to the control concrete at 28 day [7].

In the present study, the cement efficiency of the fly ash used was measured in the laboratory. Measured and prescribed k-values was compared in terms of strength. The ratio of fly ash to cement is kept the same as the standard for all the fly ash concrete mixes (F/C = 0.33) for equivalent performance determination. Research significance of the study is based on testing the validity of the prescribed k-value for strength. Also, the advantage of using of the measured k-value will be assessed. The assessment of equivalent durability performance will be carried out by water permeability testing. Specimens for durability testing require further curing in order to eliminate the effect of hydration. Particularly for fly ash concrete can be significant. For this reason the results of water permeability are not ready and will be obtained soon.

2. Experimental Program

2.1 Materials

CEM I 42.5 R Portland cement and class f fly ash were used as binder. Two different sizes of crushed limestone aggregate were used and the maximum aggregate size was 20 mm. Two different sands were used: river sand and crushed sand. Superplasticizer was a melamine sulphonated based admixture

2.2 Concrete mixes

Three different effective water/cement ratios were used in this study: 0.40, 0.50 and 0.60 (C40, C50 and C60 respectively) for the control concrete (concrete without fly ash). For the determination of k-value, 20% fly ash replacement by mass of cement was used for mixes of 0.40, 0.50 and 0.60 water cement ratio (F40, F50 and F60 respectively).

For the equivalent testing of fly ash concretes, fly ash/cement ratio was taken as 1/3 for the prescribed mixes of 0.40, 0.50 and 0.60 water/cement ratios (Fp40, Fp50 and Fp60 respectively) and for the mixes with measured k-values (Fm40, Fm50 and Fm60). Equivalent performance was based on effective cement content by mass keeping the water content constant:

$$C = c + k \times f \quad (1)$$

C : mass of effective cement
c: mass of cement in fly ash concrete
f: mass of fly ash
k: cement efficiency factor

Concrete mixes for control and 20% fly ash replaced concretes are given in Table 1.

Table 1: Concrete mixes of control and 20% fly ash replaced concretes

kg/m^3 water/binder ratio	C60	C50	C40	F60	F50	F40
Cement	330	380	420	264	304	336
Fly Ash				66	76	84
Water	198	190	168	198	190	168
Aggregate, 20 mm	548	542	549	548	542	549
Aggregate, 10 mm	449	444	450	449	444	450
River sand	489	484	490	489	484	490
Crushed sand	327	323	327	327	323	327
Superplasticizer	1,5	3	9	1,5	3	9

2.3 Test specimens

Three cubes (150mm) for each concrete mix were tested for compressive strength testing (EN 12390-3) and the average value was used for the comparison of different mixes. Specimens were moist cured 28 days after casting.

2.4 Test procedure

First, the k-value which was determined for the fly ash used in this study. The determination of k-value is based on the Bolomey method, which is described in CEN TR 16639 (Figure 1). The relationship between strength and water/cement ratio was obtained for three different water/cement ratios (w/c = 0.40, 0.50 and 0.60). The same was obtained for fly ash concretes with 20% replacement by mass of cement. Extrapolation of the results gave two lines and equalizing line equations enabled to solve the k-value. The obtained k-values was compared with the prescribed k-value (k = 0.4) of EN 206 Standard within the equivalent concrete

performance concept. The equivalent performance was tested for the compressive strength (EN 12390-3). The determination of k-value is based 28 days testing values.

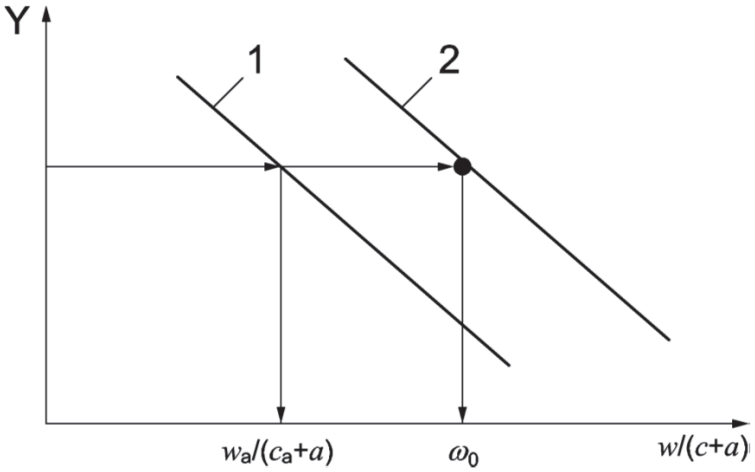

Figure 1: Determination of k-value by the use strength water/cement ratio relationship for concrete with and without fly ash

3. Results and Discussion

3.1 Determination of the k-value

The cement efficiency factor, k-value, was determined by testing compressive strength (f_c) of concretes at three different water/cement ratios (three different water/(cement+fly ash) ratios for fly ash concretes) after 28 days moist curing. The average of compressive strength results was shown in Fig. 2. The mix without fly ash (control) had higher f_c than that of the mix with 20% fly ash replacement at all w/b as expected. It is well known that the decrease in strength is due to the lower cement efficiency of fly ash compared to cement. However, the decrease in strength is not constant but it shows differences at different w/b ratios, which means that the cement efficiency factor (k) is a function of w/b ratio.

In order to quantify the variation of k-value as a function of w/b, linear approximation equations of f_c vs w/b ratio results for control and fly ash concretes were obtained (Figure 2.) and were set equal. Linear trendlines generally show good approximation. However the approximation fitted better to the results of fly ash concrete but it underestimates the results of control concrete at w/c = 0.50 and overestimates at other w/c ratios.

The equations for control and fly ash concretes are set equal:

$$-113.88x_1 + 111.93 = -107.88x_2 + 101.78 \quad (2)$$

where

x_1 : water/cement ratio of control concrete, w_o
x_2 : water/cement+fly ash) of fly ash concrete, w_f

The two unknowns can be reduced by setting the equality of $w_a = w_o$ (c + kf)

The solution of Eq. 2 gives the following solution for k-value:

$$k = - (0.47/w_o) + 1.278 \quad (3)$$

The following results were calculated from Eq. 2.

$k = 0.495$ ($w_o = 0.60$)
$k = 0.338$ ($w_o = 0.50$)
$k = 0.103$ ($w_o = 0.40$)

The results show that cement efficiency decreased as a function of w/c ratio.

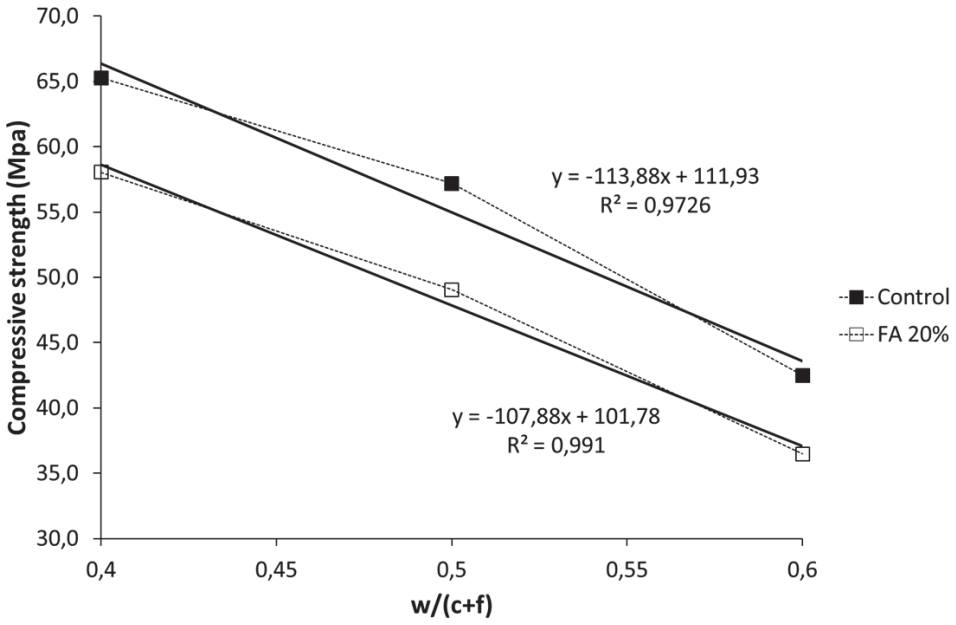

Figure 2: Compressive strength vs w/c (and c+f) with linear trendlines and their equations

Concrete mixes with prescribed and measured k-values are given in Table 2

Table 2: Concrete mixes with prescribed and measured k-values

kg/m^3 w/c (effective)	Fp60	Fp50	Fp40	Fm60	Fm50	Fm40
Cement	291	335	371	283	342	406
Fly Ash	97	112	124	94	76	135
Water	198	190	168	198	114	168
Aggregate, 20 mm	548	542	549	548	542	549
Aggregate, 10 mm	449	444	450	449	444	450
River sand	489	484	490	489	484	490
Crushed sand	327	323	327	327	323	327
Superplasticizer	1,5	3	9	1,5	3	9

3.2 Comparison of the prescribed and measured k-values

The results of compressive strength at 28 days moist curing were given in Figure 3.

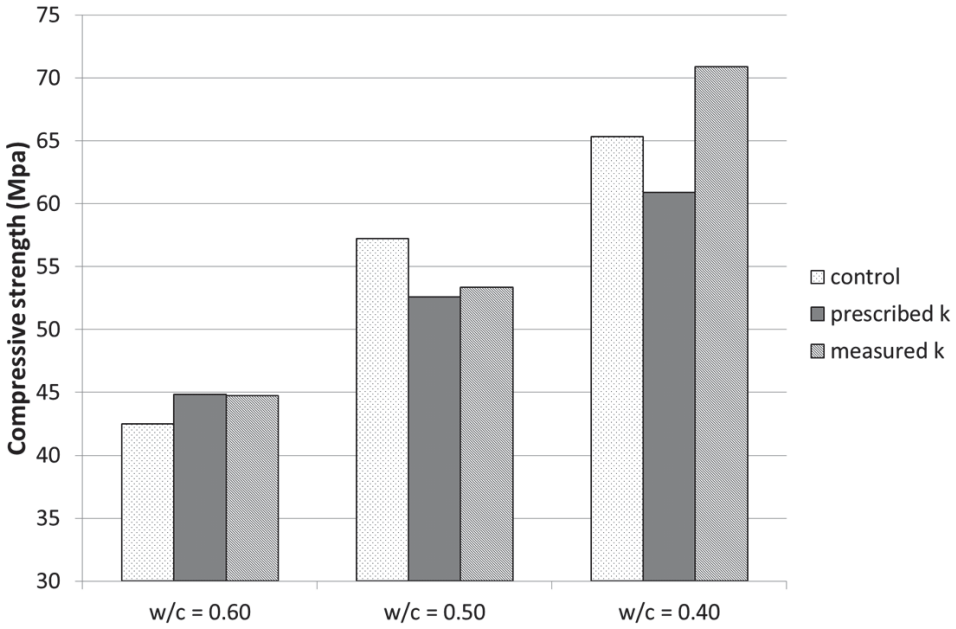

Figure 3: Compressive strength of control and fly ash concretes with prescribed and measured k

The results indicates the effect of higher cement efficiency of fly ash at w/c = 0.60. For prescribed and measured k, f_c is 5.5% and 4.9% higher compared to control concrete. Cement efficiency decreases with the decrease of effective water/cement ratio. At w/c = 0.50, there is a decrease of 8.1% and 7.4% for fly ash concretes with prescribed and measured k-values, respectively. The measured value was not able to compensate the decreasing cement efficiency at this w/c. At w/c = 0.40, the prescribed k-value is insufficient by 6.8% loss in f_c. The measured value showed its effectiveness by 9.2% increase in f_c compared to control concrete. These results show the better performance of measured k by 1.4% and 16.5% at 0.5 and 0.4 w/c ratios, respectively.

Compressive strength results can be reflected to the corresponding effective w/c by the use of the trendline equation: $f_c = -113{,}88w_o - 111{,}93$. Calculated w_o values are given in Table 3. These results indicate water/cement ratio for a given compressive strength.

Table 3: Water/cement ratio calculated from compressive strength

Original	Control	Prescribed k	Measured k
0.60	0.61	0.59	0.59
0.50	0.48	0.52	0.51
0.40	0.41	0.45	0.36

The first column in Table represents the calculated value by dividing mass of water to mass of cement. The second column gives the results obtained from the trendline equation. The difference between these values is due to linear approximation. However the differences are not so high but the comparison of k-value with control must be based on the second column as it gives the real value derived from f_c. The prescribed k-value led to a significant increase in effective w/c ratios (from 0.48 to 0.52 and from 0.41 to 0.45). Measured k was not able to correct the decrease at w/c = 0.50 but the improvement at w/c = 0.40 was very significant (from 0.41 to 0.36).

The results show that prescribed k-value can cause significant deviations from targeted water/cement ratio and strength. Use of measured k-values can give safer results for a given fly ash type.

4. Conclusion

Fly ash has been used as a cement replacement material for decades. Since its cement efficiency varies depending on the chemical and physical characteristics, EN 206 Standard requires the use of k-value, which can be assumed as safe for any fly ash type and concrete. However, as the results of this study emphasized, k-value is not a constant value but it changes as a function of w/c ratio. On the other hand, the prescribed k-value was shown to be significantly unsafe at lower water/cement ratios. The practical outcome of this finding is the insufficiency of the requirements for strength development and durability of fly ash concrete. A deviation of order 0.04 – 0.05 in w/c ratio corresponds to a degradation of concrete class. The degradation can be more severe depending on the characteristics of fly ash, which can lead to a serious miscalculation of the service life. Consequences on durability will be tested

with water permeability test soon as the continuation of the present study. Measured k-value helped to remain in safe side for compressive strength at high w/c ratio. However, linear approximation caused over- and under-estimations. This difficulty can be overcome by testing concretes at additional and closer w/c ratios, by using more specimens and by selecting different fly ash/cement ratios.

References

[1] Gruyaert E. et al., Performance of BFS concrete: k-Value concept versus equivalent performance concept, Constr Building Mater 47 (2013), 441–455
[2] Kaid N. et al., Durability of concrete containing a natural pozzolan as defined by a performance-based approach, Constr Build Mater 23 (2009), 3457–3467
[3] San Nicolas R. et al., Performance-based approach to durability of concrete containing flash-calcined metakaolin as cement replacement, Constr Buid Mater 55 (2014) 313-322
[4] Younsi A. et al., Performance-based design and carbonation of concrete with high fly ash content, Cem Concr Comp 33 (2011), 993–1000
[5] Badogiannis E. et al., Exploitation of poor Greek kaolins: Strengh development of metakaolin concrete and evaluation by means of *k*-value, Cem Concr Res 33 (2004), 1035–1041
[6] Rozière E. et al., A performance base approach for durability of concrete exposed to carbonation, Constr Build Mater 23 (2009), 190–199
[7] Hooton R.D. and Bickley J.A., Design for durability: The key to improving concrete sustainability, Constr Build Mater 67 (2014), 422–430

International RILEM Conference on Materials, Systems and Structures in Civil Engineering
Conference segment on Service Life of Cement-Based Materials and Structures
22-24 August 2016, Technical University of Denmark, Lyngby, Denmark

CARBON NANOPARTICLES CEMENT-BASED MATERIALS FOR SERVICE LIFE MONITORING

André O. Monteiro[(1,2)], Paulo B. Cachim[(1,2)], Pedro M. F. J. Costa[(3, 4)]

(1) Department of Civil Engineering, University of Aveiro, Portugal
(2) RISCO, University of Aveiro, Portugal
(3) Physical Sciences and Engineering Division, KAUST, Thuwal, Saudi Arabia
(4) Department of Materials and Ceramic Engineering, University of Aveiro, Portugal

Abstract
This paper investigates the sensing capacities of piezoresistive cement-based composites loaded with carbon black particles (CB), in order to develop embedded strain sensors for service life monitoring of civil engineering structures. Several cement-based composites, containing CB in concentrations up to 10% of binder mass (wt%), were mechanically characterized and tested under cyclic uniaxial loads, registering deformation vs electrical resistivity variations. Results showed reversible piezoresistive behaviour and quasi-linear relationships between the fractional change in resistivity (FCR) and the compressive strain, for compositions with higher amounts of CB. Gage factors (GF) of 28.09 and 24.42 were found for compositions containing 7 and 10 wt%. These findings suggest that the experimented material can become a promising alternative to monitor compressive strain along the service life of concrete structures and roadways.

1. Introduction

The monitoring of civil engineering infrastructures has been a growing preoccupation during the last decades, mainly related with health or stresses/deformations control in e.g. buildings, bridges and dams, or for roadways management and logistics, which led to the arising of a new technology known as Structural Health Monitoring (SHM). It aims to control continuously the structural behaviour of a structure and several service loads, and notify the engineers about important parameters such as corrosion rate, moisture, pH, stresses, strains or cracks. This continuous knowledge is an important key-point, providing safety enhancement, maintenance control, and management assistance for infrastructures, reducing costs and preventing eventual losses with appropriate interventions. Nevertheless, the high implementation cost of SHM sensing systems in large scale infrastructures has been a bottleneck for its widespread usage..

Besides the traditional sensors (potentiometers, optic fibre, strain gauges, etc.), a new technology has been developed during the last few years based on the piezoresistivity

principle. It proposes the use of a new family of cement-based conductive composites loaded with electrically conductive additions. These composites act as sensors due to their stimulus-dependent electrical properties (e.g. resistivity, the inverse parameter of the electrical conductivity) [1]. Piezoresistivity is the property that defines the dependence of the electrical resistivity of a certain material to its deformation. The resistivity depends on the spatial distribution of the conductive additive particles in the composite. In fact, the closer these are disposed, the easier the current can flow through the material. Therefore, the compression of a cement-based composite element can be associated with an electrical conductivity increase.

Cement-based composites can be used to replace other conventional building materials or to fabricate small sensors to be integrated in a infrastructure [2], being usually called as cement-based self-sensors (CBSS) or piezoresistive cement-based strain sensors (PCSS). Any change in a certain element, whether e.g. deformation, temperature or moisture, leads to a change in its electrical properties. This is the working principle of conventional sensors. The measurement of the variation of a certain property is done based on the variation of an easily measurable electrical parameter (e.g. voltage or current) and knowing the relationship between both. Thus, a concrete element can become a sensor of itself simply by including materials which make it partially conductive. This is an interesting monitoring alternative, with its main advantages being better mechanical properties, a high sensing ability, better compatibility with the infrastructure, reduced maintenance cost and a life span similar to the infrastructure itself.

The first proposition of intelligent concretes and piezoresistive cement-based materials dates back to 1993 with D. Chung [3], when carbon fibres (CF) were used to increase the conductivity of cement pastes. Electrical resistivity was found to be strain-dependent under compressive loading, besides identifying additional flexural and axial strength improvement, freeze-thaw durability and drying shrinkage reduction. Subsequent studies have been made using CF [4-11], carbon nanotubes (CNT) [4, 12-14], steel fibres (SF) [15-17] and carbon black [10, 18-22] for structural applications or roads monitoring [23]. CB particles demonstrated some advantages for SHM applications when compared with other conductive additions, emphasizing their lower cost. Notwithstanding, only few works have been found dealing with the addition of CB without the presence of any other conductive component. Thus, based on previous preliminary experiments [19], the purpose of this work is to further study the piezoresistive response of cement-based specimens, containing different amounts of CB when subjected to cyclic compressive loads and ultimately provide a practicable strain sensor material for long-term service monitoring.

2. Methods

2.1 PCSS Preparation

The materials used to build the PCSS were ordinary Portland cement 32.5N, carbon black type N330, polycarboxylate polymer-based superplasticizer (Sika AG), fine sand (<1mm) and copper plates which worked as electrodes.

Five different compositions were experimented, varying the amount of CB in function of the volume of aggregates (v.a.). Hence, the compositions studied were: without CB (CB0), with 1%v.a. (CB1), with 4%v.a. (CB4), with 7%v.a. (CB7) and with 10%v.a. (CB10). Such values

correspond to amounts of CB of 0, 1.03, 4.12, 7.20 and 10.29%, respectively, relatively to the binder mass. The water/cement relation was 0.5 in weight, for all the compositions and the cement/aggregate ratio was initially 1:3 in volume, for the reference composition CB0. The superplasticizer was used in amounts from 0% to 3% of mass of cement, thus compensating the lack of the necessary water for the correct cement hydration, caused by the CB particles and maintaining the workability level.

Carbon black is composed of small primary spheroidal particles, with the diameters of the N330 type being approximately 120nm. Their homogeneous dispersion in a mixture is a key point to reach an optimized tunnelling effect [18]. Several dispersion techniques were already studied and can be found in the literature [13, 14, 24-28]. Dispersion steps may, however, introduce foreign substances (e.g. surfactants) thereby altering the raw material. In this study, we aimed to study the integration of the CB in its as-received status so no steps were taken to disperse the particles.

Prismatic samples were casted (40x40x160mm) and cured for 28 days (Figure 1), at room temperature of 20 °C and >95% humidity. The resistivity measurements were based on the four electrodes method [9, 29]. The specimens were dried in oven at 60°C for 2 days before the experiments. This was to eliminate undesirable moisture on the electrical conduction of the PCSS and thereby simplify the interpretation of the present primary experiments. In fact, it is well known that moisture as a great influence in the electrical conduction composite materials. Studies showed that the polarization phenomenon [30] strengthens from certain values of moisture level, leading to inaccurate resistivity readings. Nonetheless, some experiments have been done in order to eliminate this effect, mainly based on epoxy-based resins coatings [15, 20].

Figure 1. Set of the 9 CB7 samples after casting.

2.2 Piezoresistivity Testing

The piezoresistivity of the CBSS was studied using cyclic loads, recording simultaneously the resistivity and the axial deformation. The resistivity $\rho(t)$ is calculated along the time

combining the 1st and 2nd Ohm laws, obtaining the equation 1.

$$\rho(t) = \frac{U(t)}{I(t)}\frac{A}{l} \quad (1)$$

where $U(t)$ is the potential difference across the inner electrodes, $I(t)$ is the current measured between the outer electrodes, A is the contact area between the electrodes and the material and l is the spacing between the inner electrodes. Figure 2 represents the resistivity measurement principle, the geometrical parameters and electrodes disposition.

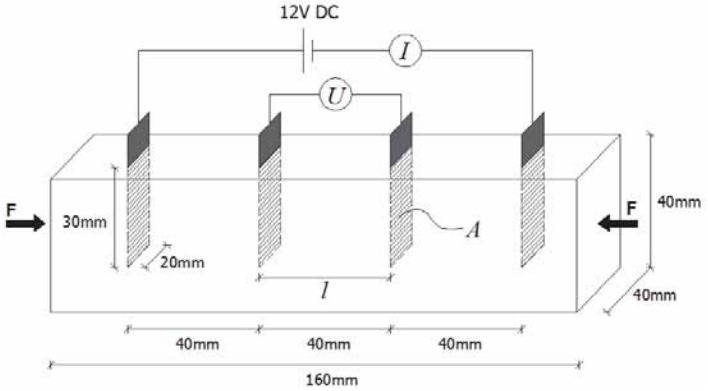

Figure 2. Representation of the resistivity measurement principle and the geometrical parameters of the PCSS.

First, a potential difference of 12V was applied through the outer electrodes using a DC power supply. The loading was then applied in two different steps. Initially, a 2kN load was maintained constant until reaching the stabilization of the resistivity. Then, a cyclic load was applied with amplitudes of 15kN, at a rate of 250N.s^{-1}. The resistivity variation was continuously monitored during the essay using a data acquisition device and the axial deformation measured with a 25mm 120Ω strain gauge. Figure 3a shows the implemented setup.

3. Results and Discussion

3.1 Mechanical Properties

Compressive and 3-point bending tests were carried out in order to characterize the various compositions in terms of strength. Figures 4a and 4b show the obtained compressive and tensile strengths after 14 and 28 days. Each point corresponds to the mean value of 3 essays.

As expected, the compressive and tensile strengths increase with the curing time (with an exception registered in the tensile strength of CB7). The maximum compressive strength was obtained for the composition CB4, which means that the addition of carbon black increases the compressive strength of the CBSS but only until 4 wt%. This effect was already reported in the literature [31] and it is associated with a first filling of some capillaries, leading to a higher strength. However, past this threshold, the mechanical benefits start to wane due to the

overload of CB particles and their adsorption on the surface of cement, affecting the hydration process and reducing the strength of the composite.

Figure 3. Experimental set-up used to perform the piezoresistive essays.

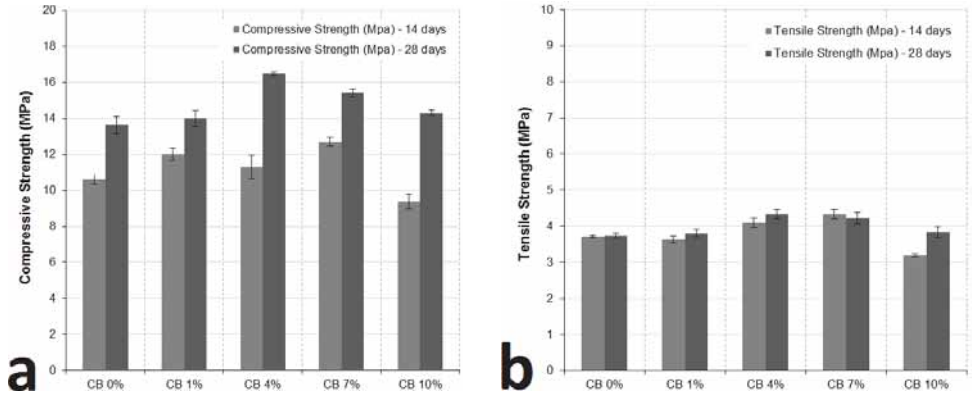

Figure 4. Results of the ultimate strength tests carried for: a) compression; b) tension.

3.2 Piezoresistive Properties

Piezoresistive essays were carried out for all the compositions. Notwithstanding, only the compositions CB7 and CB10 demonstrated piezoresistive behaviour and are thus analysed in the document. Figures 5 and 6 depict variations of the fractional change in resistivity (FCR, see equation 4) for the CB7 and CB10 PCSS, respectively, under cyclic compressive loading. Table 1 summarizes the results in terms of initial electrical resistance (R_i), initial resistivity (ρ_i) and piezoresistivity behaviour with maximum FCR, the gauge factor (GF) and sensitivity, which relates the variation of the FCR and the axial stress (as per equation 5).

$$FCR = \frac{\rho(t) - \rho_0}{\rho_0} \tag{4}$$

$$sensitivity_. = \frac{FCR}{\Delta\sigma} \tag{5}$$

Table 1. Some electrical and piezoresistive properties of the 5 compositions tested.

	R_i (Ω)	ρ_i (Ω.m)	max. FCR (%)	GF	Sensivity (%/MPa)
CB7	14294.94	214.42	2.68	28.09	0.286
CB10	302.54	4.54	1.61	24.42	0.172

The plots in figures 5a and 6a, show that the FCR decreases reversibly upon loading and increases reversibly upon unloading, almost linearly, allowing to establish easy relationships between deformation and resistivity. The repeatability of the piezoresistive behaviour can be evaluated in figures 5b and 6b which consist in a strain vs resistivity plot of all the loading cycles, with the superposition of the strain vs resistivity paths. Both showed a good repeatability and global linearity with satisfactory values of R^2. Notwithstanding, CB10 showed a better precision with a narrowest scatter distribution and a better linearity, despite of a lower gage factor and sensitivity value.

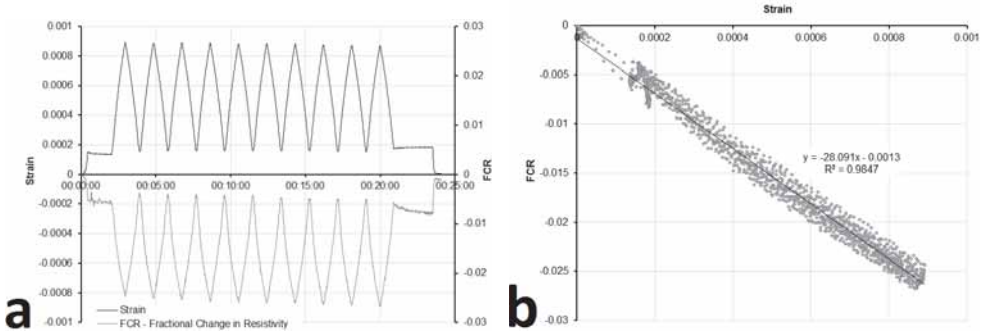

Figure 5. Results of the cyclic loading on CB7 samples. a) FCR and strain vs. time; b) FCR vs. strain for the 10 cycles.

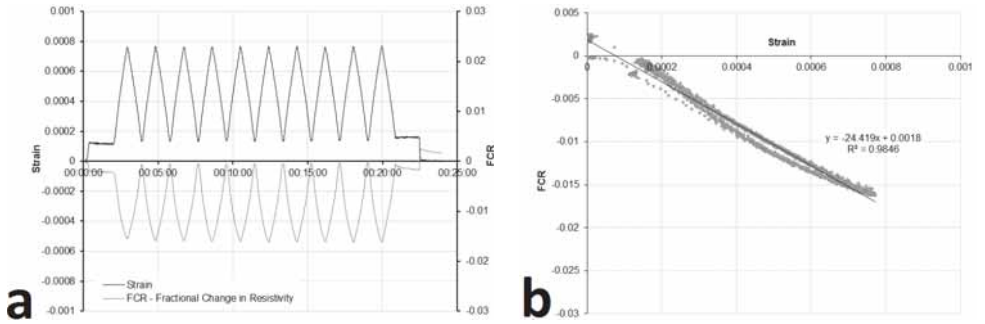

Figure 6. Results of the cyclic loading on CB10 samples. a) FCR and strain vs. time; b) FCR vs. strain for the 10 cycles.

Looking at both cyclic load results, the FCR value is not exactly returning to zero together with the deformation at the end of the cycles, once the sensors get unloaded, as expected. Such can be associated to insufficient time given for the electrical resistance stabilization before the next essay or to an electrodes contact resistance variation during the experiments.

4. Conclusions

This work investigated the addition of carbon black particles in cement-based materials with the purpose to develop a piezoresistive self-sensing material, to be embedded in civil engineering structures. The present experiments established piezoresistive compositions and allowed to understand how the carbon black inclusion influences the mechanical and electrical behaviour of a cement-based material. Carbon black was loaded in different amounts from 0 to 10 wt% and both mechanical and piezoresistive tests were carried out. It was verified that CB additions up to 4 wt% are favourable to enhance mechanical resistance, whilst amounts between 7 and 10 wt% provided better piezoresistive abilities. Quasi-linear relations were found between the axial deformation and the FCR. These findings suggest that the experimented materials can become promising alternatives for monitoring compressive strain in concrete structures and roadways.

References

[1] B. Han, X. Yu, and J. Ou, *Self-Sensing Concrete in Smart Struct.* 2014: Elsevier Science.
[2] B. Han, S. Ding, and X. Yu, *Intrinsic self-sensing concrete and structures: A review.* Measurement, 2015. **59**: p. 110-128.
[3] C. Pu-Woei and D.D.L. Chung, *Carbon fiber reinforced concrete for smart structures capable of non-destructive flaw detection.* Smart Materials and Struct., 1993. **2**(1): p. 22.
[4] F. Azhari and N. Banthia, *Cement-based sensors with carbon fibers and carbon nanotubes for piezoresistive sensing.* Cem. and Concr. Comp., 2012. **34**(7): p. 866-873.
[5] S. Wen and D.D.L. Chung, *Effects of Strain and Damage on Strain-Sensing Ability of Carbon Fiber Cement.* Journal of Materials in Civil Eng., 2006. **18**(3): p. 355-360.
[6] M. Chiarello and R. Zinno, *Electrical conductivity of self-monitoring CFRC.* Cement and Concrete Composites, 2005. **27**(4): p. 463-469.
[7] B.W. Ramme, J.J. Noegel, R.H. Setchell, and R.F. Bischke, *Electrically conductive concrete and controlled low strength mater. having carbon fibers*, 2010, Google Patents.
[8] S. Wen and D.D.L. Chung, *Electrical-resistance-based damage self-sensing in carbon fiber reinforced cement.* Carbon, 2007. **45**(4): p. 710-716.
[9] B. Han, X. Guan, and J. Ou, *Electrode design, measuring method and data acquisition system of carbon fiber cement paste piezoresistive sensors.* Sensors and Actuators A: Physical, 2007. **135**(2): p. 360-369.
[10] Y. Ding, Z. Chen, Z. Han, Y. Zhang, and F. Pacheco-Torgal, *Nano-carbon black and carbon fiber as conductive materials for the diagnosing of the damage of concrete beam.* Construction and Building Materials, 2013. **43**: p. 233-241.
[11] S. Wen and D.D.L. Chung, *Self-sensing of flexural damage and strain in carbon fiber reinf. cem. and effect of embedded steel reinf. bars.* Carbon, 2006. **44**(8): p. 1496-1502.
[12] G.Y. Li, P.M. Wang, and X. Zhao, *Pressure-sensitive properties and microstructure of carbon nanotube reinforced cement comp.* Cem. Concr. Comp., 2007. **29**(5): p. 377-382.
[13] X. Yu and E. Kwon, *A carbon nanotube/cement composite with piezoresistive properties.* Smart Materials and Structures, 2009. **18**(5): p. 055010.

[14] A. D'Alessandro, M. Rallini, F. Ubertini, A.L. Materazzi, and J.M. Kenny, *Investigations on scalable fabrication procedures for self-sensing carbon nanotube cement-matrix composites for SHM applications.* Cem. and Concrete Composites, 2016. **65**: p. 200-213.
[15] M.-q. Sun, R.J.Y. Liew, M.-H. Zhang, and W. Li, *Development of cement-based strain sensor for health monitoring of ultra high strength concrete.* Construction and Building Materials, 2014. **65**: p. 630-637.
[16] N. Banthia, S. Djeridane, and M. Pigeon, *Electrical resistivity of carbon and steel micro-fiber reinforced cements.* Cement and Concrete Research, 1992. **22**(5): p. 804-814.
[17] E. Teomete and O.I. Kocyigit, *Tensile strain sensitivity of steel fiber reinforced cement matrix composites tested by split tensile test.* Constr. Build. Mater., 2013. **47**: p. 962-968.
[18] H. Li, H.-g. Xiao, and J.-p. Ou, *Effect of compressive strain on electrical resist. of carbon black-filled cement-based composites.* Cem. Concr. Comp., 2006. **28**(9): p. 824-828.
[19] A.O. Monteiro, P.B. Cachim, and P.M.F.J. Costa, *Electrical Properties of Cement-based Composites Containing Carbon Black Particles.* Materials Today: Proceedings, 2015. **2**(1): p. 193-199.
[20] H. Li, H. Xiao, and J. Ou, *Electrical property of cement-based composites filled with carbon black under long-term wet and loading condition.* Composites Science and Technology, 2008. **68**(9): p. 2114-2119.
[21] V.W.J. Lin, M. Li, J.P. Lynch, and V.C. Li. *Mechanical and electrical characterization of self-sensing carbon black ECC*. 2011.
[22] S. Wen and D.D.L. Chung, *Partial replacement of carbon fiber by carbon black in multifunctional cement–matrix composites.* Carbon, 2007. **45**(3): p. 505-513.
[23] B. Han, et al., *Integration and road tests of a self-sensing CNT concrete pavement system for traffic detection.* Smart Materials and Structures, 2013. **22**(1): p. 015020.
[24] M.L. Miglietta, G. Rametta, and G. Di Francia, *Characterization of Carbon Based Nanoparticles Dispersion in Aqueous Solution Using Dynamic Light Scattering Technique.* Macromolecular Symposia, 2009. **286**(1): p. 95-100.
[25] S.M. Aldoshin, et al., *Study of the influence of single-wall carbon nanotube dispersion techniques upon the properties of epoxy resin-based nanocomposites.* Journal of Machinery Manufacture and Reliability, 2015. **44**(3): p. 271-275.
[26] Y. Liu, et al., *Dispersion and Modification of Carbon Nanotubes Using a Surface Gel–Sol Technique.* Chemistry Letters, 2006. **35**(11): p. 1258-1259.
[27] S. Parveen, et al., *Microstruct. and mechan. Prop. of carbon nanotube reinf. cementitious composites developed using a novel disp. techn.* Cem. Concr. Res., 2015. **73**: p. 215-227.
[28] X. Zeng, et al., *A new technique for dispersion of carbon nanotube in a metal melt.* Materials Science and Engineering: A, 2010. **527**(20): p. 5335-5340.
[29] C.-Y. Lee and S.-R. Wang, *Application of Four-electrode Method to Analysis Resistance Characteristics of Conductive Concrete.* World Academy of Science, Engineering and Technology, 2010. **4**: p. 77-80.
[30] F. Ubertini, S. Laflamme, and A. D'Alessandro, *Self-Sensing Concrete in Smart Structures*, in *Innovative Developments of Advanced Multifunctional Nanocomposites in Civil and Structural Engineering*, 2016, Woodhead Publishing: Cambridge. p. 97-120.
[31] B. Han, L. Zhang, S. Sun, X. Yu, X. Dong, T. Wu, et al., *Electrostatic self-assembled carbon nanotube/nano carbon black composite fillers reinforced cement-based materials with multifunctionality.* Composites Part A: Appl. Sci. and Manuf., 2015. **79**: p. 103-115.

International RILEM Conference on Materials, Systems and Structures in Civil Engineering
Conference segment on Service Life of Cement-Based Materials and Structures
22-24 August 2016, Technical University of Denmark, Lyngby, Denmark

CAN A RELIABLE PREDICTION OF CEMENT PASTE TRANSPORT PROPERTIES BE MADE USING MICROSTRUCTURE MODELS?

Ravi A. Patel[(1,2,*)], Janez Perko[(1)], Diederik Jacques[(1)], Geert De Schutter[(2)], Guang Ye[(2,3)], Klaas Van Breugel[(3)]

(1) Belgian Nuclear Research Centre (SCK•CEN), Belgium.
(2) Magnel lab of concrete research, Ghent University, Belgium.
(3) Microlab, Delft University of technology, Netherlands

Abstract
Physical and mechanical properties of cement-based materials are directly linked to their microstructure. In recent years, different microstructure modelling platforms have emerged (e.g., HMYOSTRUC, CEMHYD3D and μic) which simulate the evolution of the microstructure of cement paste during hydration. These microstructures can be utilized to obtain physical and mechanical properties. However, due to underlying assumptions in these models, morphologically different microstructures (different pore connectivity, pore size and percolation thresholds) are obtained from these platforms for the same water-cement ratio and cement composition. The question then arises whether the estimations of properties of cement paste using these microstructures is reliable or not. In this paper we discuss issues related to achieving reliable predictions of the transport properties using microstructures generated from these platforms.

1. Introduction

Since the early dawn of material science of cement-based materials, efforts have been laid to link the microstructure features to properties of cement paste [1]. Further, increasing understanding of the hydration process has laid to the development of different microstructure modelling platforms in last few decades [2]. These modelling platforms, provides a microstructure of a cement paste for a given degree or time of hydration using some basic input parameters. The initial purpose of these models was to obtain the evolution of the microstructure taking into account the reactions at the cement particle level as a starting point, and considering the effects of particle size distribution, chemical composition of cement paste, water-cement ratio (w/c) and curing on hydration. However, the output microstructures have other potential applications. For instance, these microstructures can serve as input to determine physical and mechanical properties of cement paste either analytically or by computational homogenization which involves solving of governing

physics equation through the microstructure. The advantage of such an approach is that, from a set of basic input parameters; one can predict the properties of cement paste at different stages of hydration. However, it should be noted that the properties of cement pastes obtained in this way is a "*by product*" of these hydration models. Hence series of question arises, such as: Are these microstructures representative for the actual cement paste morphology? Can reliable predictions of properties be achieved from these microstructures? And if so, what are further conceptual assumptions required to achieve these predictions? In this paper, discussion is put forward with regards to these questions for the prediction of transport properties from the microstructures generated using these platforms. Transport properties are of prime importance with regards to the durability and service life predictions of concrete structures. First a brief overview on microstructure modelling platforms and discussion on morphological differences in the microstructures generated using these platforms is presented. Thereafter, a discussion with regards to the prediction of transport properties from the generated microstructures is presented.

2. Microstructure modelling platforms for cement paste

Based on the conceptual assumption used for the representation of cement particles, the microstructure models can be classified as vector-based or lattice-based approaches [2]. In the vector-based approach, the cement particles are represented as spheres. The hydration products are assumed to grow concentrically around the cement particles. Dissolution of cement particles leads to decrease in the radii of cement particle and similarly precipitation of hydration products leads to increase in radii of hydration layers around the cement particle. Additional phases, such as portlandite, grow spherically from initially defined nuclei in such models. Well-known vector based microstructure models are HYMOSTRUC [3–5] and μic [6]. In the lattice-based approach, a 3D cement paste microstructure is digitized on a uniform cubic lattice and each volume element (voxel) is assigned a certain material (e.g., water-filled pores, clinker phase, etc). Two well-known lattice based models are CEMHYD3D [7] and HydratiCA [8]. In CEMHYD3D, changes to the microstructure are simulated through a set of rules which are used to mimic the dissolution of solids, diffusion of dissolved species according to a random walk algorithm, and nucleation and growth of hydration products such as portlandite and C-S-H gel. HydratiCA is a reactive transport model based on kinetic cellular automation and it directly simulates transport of ions, dissolution and growth of mineral phases, complexation reactions at surface and nucleation of new phases by considering chemical thermodynamics.

Due to the underlying differences in conceptualization, microstructures generated from these platforms can differ substantially in terms of pore connectivity even for the same fraction of capillary pores. Fig. 1 shows the fraction of connected pores for a given capillary porosity for microstructures generated using CEMHYD3D (a voxel based approach) and HYMOSTRUC (a vector based approach) for different w/c (cement composition as of Bejaoui et al. [9]). It should be noted that this computation of percolation thresholds has been carried out using the resolution of microstructure as 1 μm. In case of CEMHYD3D, capillary pores are depercolated at capillary porosities smaller than approximately 18%, whereas, for HYMOSTRUC, capillary pores remain connected even at very low capillary porosity. The reason for the high percolation threshold for the microstructures generated using

CEMHYD3D is the more dispersed pore space generated by CEMHYD3D compared to HYMOSTRUC (see Fig. 2). Thus in case of CEMHYD3D, at capillary porosity below 18% C-S-H would be the dominant pathway for transport, whereas, in case of HYMOSTRUC capillary pores are always the dominant pathway. A percolation threshold at a capillary porosity of about 18% is supported by experimental measurements of permeability by Powers [1] and electric conductivity measurements of frozen cement paste using impedance spectroscopy by Olson et al. [10]. For transport properties such as permeability, the capillary pore diameter can also play a significant role. Fig. 2 shows that for a similar pore fraction, pore space geometry varies extensively for microstructures generated using HYMOSTRUC and CEMHYD3D. As a result, pore throats and diameters also differ for both models. Ye [11] has found a good agreement for the pore size distribution between HYMOSTRUC generated microstructures and SEM images. Thus not all the morphological features are correctly represented in both the hydration model and accuracy of predictions of transport property from these microstructures depend on whether the morphological features governing a specific transport property are correctly represented or not.

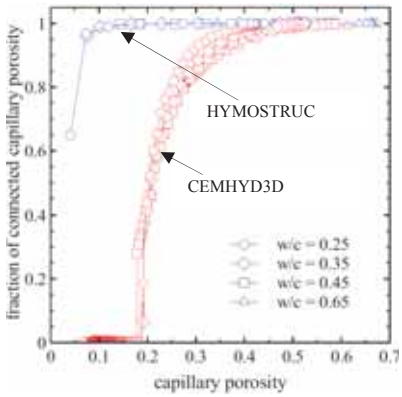

Fig. 1 Fraction of connected capillary pores as a function of capillary porosity for different w/c. Microstructure resolution is 1μm (CEM-I cement with composition of Bejaoui et al. [9]).

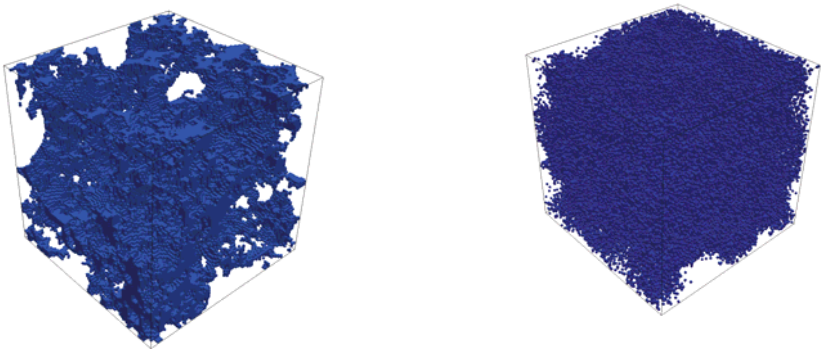

(a) (b)

Fig. 2 Pore space generated using (a) HYMOSTRUC and (b) CEMHYD3D for a capillary porosity of about 14% for a w/c =0.45 (CEM-I cement with composition of Bejaoui et al. [9]).

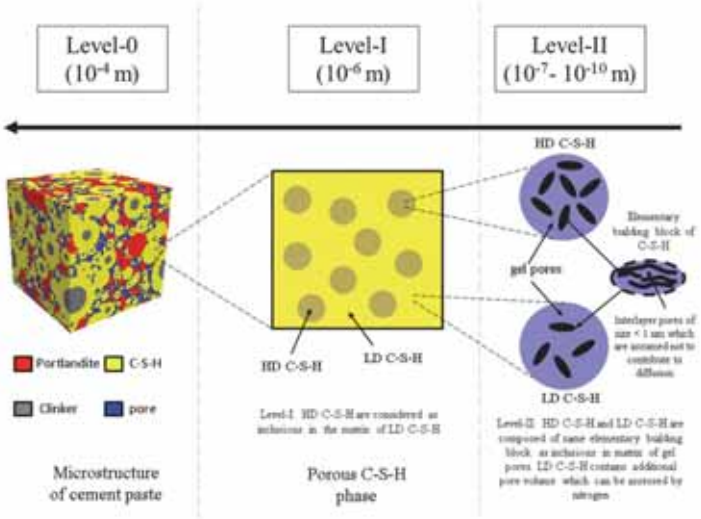

Fig. 3 Morphological representation of C-S-H phase considered for diffusivity model [12]

3. Obtaining transport properties from virtual cement paste microstructures

In order to obtain the transport properties using computational homogenization from virtual cement paste microstructures generated using these modelling platforms, one needs to solve the governing field equations on the microstructure of a representative size. For cement paste, microstructure of a cubic volume of 100 μm^3 is usually considered as representative [13,14]. The appropriate resolution of the virtual microstructures is a critical parameter as percolation threshold and capillary porosity depend on the resolution of the microstructure [15,16]. However, for this size of microstructure and considering computational constrains to obtain transport properties, simulations are usually carried out with resolution of microstructure as 1μm [12,17–21]. Only capillary pores are resolved at this resolution. Hence, an additional conceptualization is required to consider the transport through the gel pores which consists of considering cement paste as an multilevel porous system with (i) C-S-H represented as a continuum porous phase through which transport can occur, (ii) capillary pores with transport properties of pore fluid, and (iii) solid phases such as unhydrated cement particles, portlandite, etc., through which transport do not occur.

Recently, the authors have developed an approach to predict the diffusivity from virtual microstructures [12]. In this approach, the mass transport equation (Fick's law) is solved using a lattice Boltzmann method. Additionally, an analytical model based on continnum-micromechanics theory has been developed to obtain the diffusivity of the C-S-H phase. In this approach, at lowest level (Level II) two types of C-S-H phases are considered viz., high density C-S-H (HD C-S-H) and low density C-S-H (LD C-S-H). Both HD C-S-H and LD C-S-H are made of the same elementary solid phase but LD C-S-H has additional porosity which can be accessed by nitrogen during BET experiments. It has been considered in the

model that transport of ion and tracers only occurs through this nitrogen-accessible porosity. However, all C-S-H pores contribute to transport in case of electric resistivity. This results in a higher relative diffusivity measurements using electric resistivity techniques compared to other techniques [22]. At Level I, HD C-S-H are considered as spherical inclusions in a matrix of LD C-S-H as HD C-S-H is formed in a later stage during hydration. Diffusivity at each level is estimated using the differential effective media theory.

Fig. 4 (b) shows the results obtained using the developed approach for experimental data of Bejaoui et al. [9]. The diffusivity predicted by HYMOSTRUC is always higher compared to CEMHYD3D and differences are larger for porosity smaller than 25%. This is due to differences in the morphology of microstructures generated from these platforms. As discussed previously, capillary pores in the CEMHYD3D model are depercolated below 18% capillary porosity, which is consistent with experimental data. As a consequence, below 18% capillary porosity, C-S-H phase which has few order lower diffusivity as compared to capillary pores is as dominant diffusing phase. A detailed comparison with a wide range of experimental data has been previously carried out by the authors [12]. It was found that with the proposed approach around 48% and 80% of the predictions using CEMHYD3D generated microstructures for through-diffusion/electro-migration and electric resistivity data, respectively fall within factor 2-bounds. This is better compared to the existing analytical models. For discussion on performance of existing analytical models refer to [22].

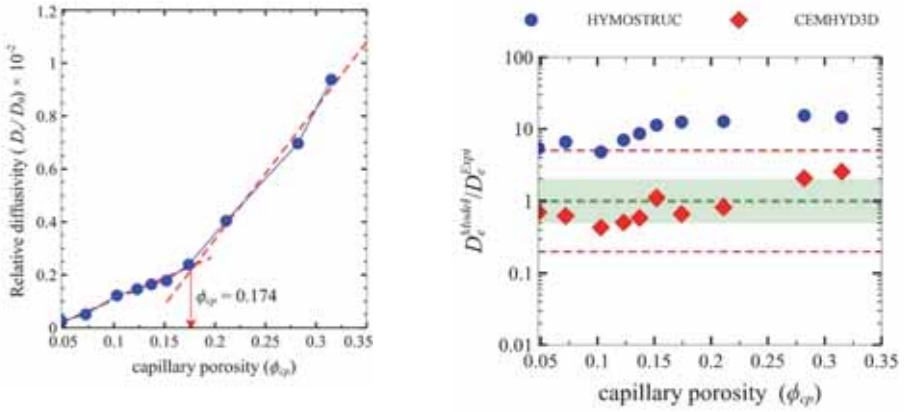

(a) (b)

Fig. 4 (a) Experimental data of Bejaoui et al. [9] (b) Ratio of estimated diffusivity using microstructures (D_e^{model}) to experimental diffusivity (D_e^{expt}) for experimental data of Bejaoui et al. [9]. In (b) Shaded region represents factor 2-bounds and the red dash lines represent factor 5-bounds.

For water permeability (referred here as permeability), C-S-H phase is usually considered as non-permeable due to its very low permeability [21,23,24]. Recently, Zalzale et al. [25] treated C-S-H as a permeable phase while computing permeability from microstructures generated using μic. They found that it is essential to consider C-S-H as a permeable phase in

case of very low porosities. Zhang et al. [21] tried to estimate permeability using HMYOSTRUC generated microstructures. They obtained good agreement for permeability for capillary porosity higher than 20%. However, at low porosity large deviations were observed between experiments and predictions. Zalzale et al. [23] compared the estimates of permeability obtained from microstructures generated using μic and CEMHYD3D. They observed that at high capillary porosity good agreement is observed between μic and CEMHYD3D generated microstructures. However, at low differences up to several orders of difference are observed between μic and CEMHYD3D generated microstructures with μic generated microstructures giving lower value closer to experiments compared to CEMHYD3D. The result of these analysis are quite surprising as at lower porosity one would expect that in case of CEMHYD3D generated microstructures capillary pores are depercolated, whereas, μic being vector based model capillary pores would still be percolated. As a consequence, CEMHYD3D generated microstructures should have lower permeability. It should be noted that their results are plagued with the diagonal leak error arising from lattice Boltzmann method which have a large influence at low porosity, giving higher permeability than actual at lower porosity. At present there are no comprehensive studies comparing permeability obtained from microstructures generated using different platforms and experiments. One of the issues is that there exist several orders of differences between permeability values from different experimental techniques. Zalzale et al. [25] suggested that a main issue in comparing results with different experimental techniques is a difference in saturation degree which result in large variation in magnitude of permeability measured by these techniques. Recently, Phung et al. [26] has developed a constant flow permeability setup for measuring water permeability of cement paste which can ensure that permeability is measured at complete saturation. This technique is a fast and more reliable method for measuring water permeability and can be used in future to carryout comparison with predictions from microstructures.

4. Conclusions

While the microstructure modelling platforms may provide accurate estimates of the evolution of hydration degree and microstructure phase fractions, the microstructures generated from them vary substantially. Not all features are correctly captured in any particular microstructure modelling platforms. The reliability of prediction of transport properties from microstructures generated using microstructure modelling platforms depends on whether a morphological feature governing a given transport process is correctly captured in the microstructure. For instance, in case of diffusivity, the capillary porosity at which depercolation occurs is important as below that point, the major transport pathway is through the C-S-H phase. This feature is correctly captured in microstructures generated using CEMHYD3D and therefore better predictions are achieved with CEMHYD3D generated microstructures compared to HYMOSTRUC. In case of permeability, other morphological features such as pore size distribution and surface area in addition to percolation threshold needs to be correctly represented. However, till date, a comprehensive study comparing the performance of different microstructure modelling platforms to predict permeability does not exist. An important issue is that the experimental value of permeability varies substantially from one experimental setup to another.

References

[1] T.C. Powers, Structure and Physical Properties of Hardened Portland Cement Paste, J. Am. Ceram. Soc. 41 (1958) 1–6.
[2] J. Thomas, J. Biernacki, J. Bullard, Modeling and simulation of cement hydration kinetics and microstructure development, Cem. Concr. Res. 41 (2011) 1257–1278.
[3] K. Van Breugel, Numerical simulation of hydration and microstructural development in hardening cement-based materials (I) theory, Cem. Concr. Res. 25 (1995) 319–331.
[4] K. Van Breugel, Numerical simulation of hydration and microstructural development in hardening cement-based materials:(II) applications, Cem. Concr. Res. 25 (1995) 522–530.
[5] G. Ye, K. Van Breugel, Three-dimensional microstructure simulation model of cement based materials, Heron. 48 (2003) 251–275.
[6] S. Bishnoi, K.L. Scrivener, Cement and Concrete Research μic : A new platform for modelling the hydration of cements, Cem. Concr. Res. 39 (2009) 266–274.
[7] D.P. Bentz, P.V. Coveney, E.J. Garboczi, M.F. Kleyn, P.E. Stutzman, Cellular automaton simulations of cement hydration and microstructure development, Model. Simul. Mater. Sci. Eng. 2 (1994) 783.
[8] J.W. Bullard, E. Enjolras, W.L. George, S.G. Satterfield, J.E. Terrill, A parallel reaction-transport model applied to cement hydration and microstructure development, Model. Simul. Mater. Sci. Eng. 18 (2010) 025007.
[9] S. Bejaoui, B. Bary, Modeling of the link between microstructure and effective diffusivity of cement pastes using a simplified composite model, Cem. Concr. Res. 37 (2007) 469–480.
[10] R.A. Olson, B.J. Christensen, R.T. Coverdale, S.J. Ford, G.M. Moss, H.M. Jennings, et al., Interpretation of the impedance spectroscopy of cement paste via computer modelling Part lll Microstructural analysis of frozen, J. Mater. Sci. 30 (1995) 5078–5086.
[11] G. Ye, Experimental Study and Numerical Simulation of the Development of the Microstructure and Permeability of Cementitious Materials, 2003.
[12] R.A. Patel, P. Janez, D. Jacques, G. De Schutter, G. Ye, K. van Breugel, Effective diffusivity of cement pastes from virtual microstructures: role of gel porosity and capillary percolation, (In Prep.).
[13] N. Ukrainczyk, E. a B. Koenders, Representative elementary volumes for 3D modeling of mass transport in cementitious materials, Model. Simul. Mater. Sci. Eng. 22 (2014) 035001.
[14] M.Z. Zhang, G. Ye, K. Van Breugel, A numerical-statistical approach to determining the representative element volume (REV) of cement paste for measuring diffusivity, Mater. Construcción. 60 (2010) 7–20.
[15] G. Ye, Percolation of capillary pores in hardening cement pastes, Cem. Concr. Res. 35 (2005) 167–176.
[16] E.J. Garboczi, D.P. Bentz, The effect of statistical fluctuation, finite size error, and digital resolution on the phase percolation and transport properties of the NIST cement hydration model, Cem. Concr. Res. 31 (2001) 1501–1514.

[17] M. Zhang, G. Ye, K. van Breugel, Multiscale lattice Boltzmann-finite element modelling of chloride diffusivity in cementitious materials. Part I: Algorithms and implementation, Mech. Res. Commun. 58 (2014) 53–63.
[18] M. Zhang, G. Ye, K. van Breugel, Microstructure-based modeling of water diffusivity in cement paste, Constr. Build. Mater. 25 (2011) 2046–2052.
[19] D.P. Bentz, O.M. Jensen, A.M. Coats, F.P. Glasser, Influence of silica fume on diffusivity in cement-based materials I. Experimental and computer modeling studies on cement pastes, Cem. Concr. Res. 30 (2000) 953–962.
[20] D.P. Bentz, E.J. Garboczi, Modelling the leaching of calcium hydroxide from cement paste : effects on pore space percolation and diffusivity, Mater. Struct. 25 (1992) 523–533.
[21] M. Zhang, G. Ye, K. Van Breugel, Microstructure-based modeling of permeability of cementitious materials using multiple-relaxation-time lattice Boltzmann method, Comput. Mater. Sci. 68 (2013) 142–151.
[22] R.A. Patel, Q.T. Phung, S.C. Seetharam, J. Perko, D. Jacques, G. De Schutter, et al., Diffusivity of saturated ordinary Portland cement-based materials: A critical review of experimental and analytical modelling approaches, Cem. Concr. Res. (under Rev. (2016).
[23] M. Zalzale, P.J. McDonald, Lattice Boltzmann simulations of the permeability and capillary adsorption of cement model microstructures, Cem. Concr. Res. 42 (2012) 1601–1610.
[24] E.J. Garboczi, D.P. Bentz, The effect of statistical fluctuation, finite size error, and digital resolution on the phase percolation and transport properties of the NIST cement hydration model, Cem. Concr. Res. 31 (2001).
[25] M. Zalzale, P.J. McDonald, K.L. Scrivener, A 3D lattice Boltzmann effective media study: understanding the role of C-S-H and water saturation on the permeability of cement paste, Model. Simul. Mater. Sci. Eng. 21 (2013) 085016.
[26] Q.T. Phung, N. Maes, G. De Schutter, D. Jacques, G. Ye, Determination of water permeability of cementitious materials using a controlled constant flow method, Constr. Build. Mater. 47 (2013) 1488–1496.

International RILEM Conference on Materials, Systems and Structures in Civil Engineering
Conference segment on Service Life of Cement-Based Materials and Structures
22-24 August 2016, Technical University of Denmark, Lyngby, Denmark

MEASURING THE INFLUENCE OF TEMPERATURE ON ELECTRICAL PROPERTIES OF CONCRETE

Alex Coyle [(1)], Robert Spragg [(1,2)], Armen Amirkhanian[(1)], Jason Weiss [(1)]

(1) Oregon State University, Corvallis, Oregon
(2) Purdue University, West Lafayette, Indiana

Abstract
Electrical measurements are becoming a popular method to examine transport properties of concrete due to their ability to be performed rapidly and their ease of use. Previous work has shown that specimen geometry, temperature, and storage conditions influence electrical readings. As such, caution must be taken when correlating such readings with transport properties. It is important to correct these factors so that measurements more accurately describe the material. The work presented in this paper looks specifically at the role temperature of the specimen play in resistivity measurements. This is done by cycling samples through a temperature range and developing corrections characterizing their behavior. A normalized formation factor is proposed to describe transport through the microstructure. This allows for the determination of a transport property that can be used for service life prediction. The work is currently being developed as a part of a nation-wide project aimed at investigating the possibility of moving towards performance based specifications.

1. Introduction

Measurement of the electrical properties of concrete is a practical, rapid, nondestructive method used to study transport properties in concrete. Prior research has shown that measurements of resistivity are affected by factors including pore solution [1]–[3], testing temperature [4]–[7], conditioning [3], [6], [8], and degree of saturation [9]–[12]. Resistivity measurements can be used to determine the formation factor, which is a numerical parameter that describes the volumes and connectivity of the pore network [13]–[16] and has been related to ionic transport properties [10], [11], [17].
In general, resistivity measurements of porous material can be described in Equation 1:

$$\rho = \rho_0 \cdot \frac{1}{\phi\beta} = \rho_o \cdot F \quad (1)$$

where ρ is the total bulk resistivity, ρ_0 is the resistivity of pore solution, ϕ is the fluid filled porosity, β is the connectivity of the pores, and F is the formation factor. The formation factor can be calculated by dividing the bulk resistivity by the resistivity of the pore solution [11].
The measured resistivity, discussed in the next section, is highly dependent on testing temperature, e.g. [4], [6], [18], [19]. This work will discuss an activation energy based correction for resistivity measurements, utilizing a tabletop temperature cycling system [18]. This is an improvement over previous methodologies, as it allows the operator to start and finish the test with the value needed for a correction [20]. This work is conducted as part of a multi-state study, and the data gathered here will be used to inform the development of a standard test method [21].

2. Background

Previous literature has shown that an activation energy based relationship can be developed to account for the influence of temperature on the measured resistivity, e.g. [4], [22], shown in Equation 2.

$$\frac{\rho_{T_{ref}}}{\rho} = \exp\left[\frac{-E_{a-cond}}{R}\left(\frac{1}{T} - \frac{1}{T_{ref}}\right)\right] \quad (2)$$

Where $\rho_{T_{ref}}$ is the resistivity at temperature T_{ref} , ρ is the measured resistivity at temperature T, $E_{a\text{-}cond}$ is the activation energy of conduction, R is the universal gas constant, T is the temperature of the measured sample in K, and T_{ref} is the reference temperature, typically 23 °C = 296 K. It should be noted that the activation energy of conduction represents only the influence of the temperature at the time of test and as such, it differs from the activation energy of hydration which describes the role of temperature on the hydration process [6].
Previous research evaluated the E_{a-cond} for a variety of different ages, and found that after approximately 7 days a sufficient extent of hydration has occurred and the value does not change appreciably [8]. This study will evaluate the specimens at an age of 180 days.

3. Testing Procedure

The specimens used in this study were standard 4” x 8” (~102 x 204 mm) concrete cylinders made from various pavement and bridge deck mixtures from across the United States. Mixtures in this study include various straight cement, binary, and ternary mixtures, and unless otherwise noted cementitious materials were each batched separately. The water-to-cementitious ratio (w/cm) and cementitious materials content are summarized in Table 1 and unless noted cement and supplementary materials were batched separately.

Table 1: Summary of the paste portion of the mixture designs, with Mixture ID noting the cement, fly ash, slag, and ternary mixtures.

Mixture ID	w/cm	Water (kg/m^3)	Cement (kg/m^3)	Fly Ash (kg/m^3)	Slag (kg/m^3)
C-1	0.42	141	335	-	-
C-2	0.41	185	390	-	-
FA-1	0.40	135	335*	-	-
FA-2	0.37	154	332	82	-
FA-3	0.42	144	273	68	-
FA-4	0.39	122	248	62	-
FA-5	0.45	143	279	43	-
S-1	0.43	141	247	-	82
Ter-1	0.40	125	262†	66	-

* denotes an ASTM C595 IP(25) cement [23]
† denotes an ASTM C595 IS(20) cement [23]

As part of the multi-laboratory study, the specimens were prepared at different laboratories and shipped to the testing lab at Oregon State University. Specimens were sealed and cured in a sealed condition by placing the concrete into double 6 mil (~0.15mm) thickness plastic bags until the beginning of the test. The testing for temperature correction discussed here was conducted at an age of 180 d.

The procedure described here continuously measures the resistivity of the sample while the temperature of specimen is varied from 5 °C to 30 °C. A diagram of the testing apparatus can be seen in Figure 1, which is a similar setup as that used by [18]. This setup has the ability to use a full standard concrete cylinder.

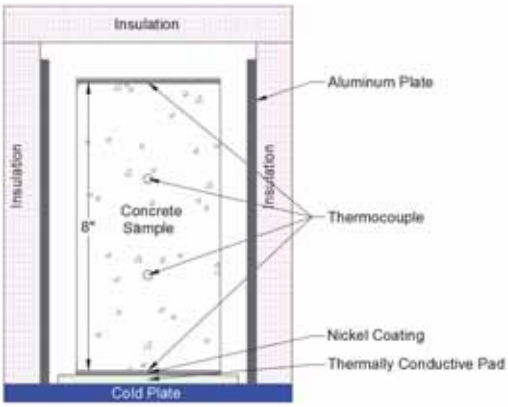

Figure 1: Diagram of Testing Apparatus, not shown is the 18 gauge wire used to connect the nickel coating electrode to the resistivity meter and the plastic wrap placed on the concrete cylinder to prevent excessive drying during the testing period.

A 4" x 8" (102 mm x 204 mm) sample was prepared by applying a conductive nickel coating at the top and bottom of the sample. Surfaces were scarified with a 20 grit concrete sanding block to ensure proper adhesion between the concrete surfaces and the coating. This nickel coating forms the electrodes as typically seen in uniaxial concrete measurements. The nickel coating electrodes are connected to the resistivity meter using 18 gauge copper wire. The top and bottom surfaces are then covered with aluminum tape to ensure sufficient contact with the wire and electrode as well as to prevent moisture loss from evaporation. Additionally, thin plastic is wrapped around the exposed sides to prevent moisture loss as the test is performed. Type T thermocouples with an accuracy of ±0.713 °C [24] were placed at the bottom, top and middle thirds of the sample to continuously monitor measurements of the temperature.
The temperature of the sample is controlled by a thermoelectric cold plate. A thermally conductive pad (ThermaCool TC3008™) is placed in-between the cold plate and the sample to ensure appropriate thermal connection between the plate and the sample as well as to protect the cold plate from abrasion. The sample is isolated from the exterior environment through the use of aluminum shrouding which is connected to the cold plate. The aluminum shrouding is surrounded by R-10 insulating foam board. This promotes unidirectional cooling and heating. A preliminary test was performed where a hole was drilled and a thermocouple was place inside. It showed that the temperature inside the sample and the temperature at the surface were nearly identical.
Two types of resistivity meters were used to track the resistivity of the specimen. The Giatec RCON2™ applies an AC current at a frequency of 1000 Hz and measures total impedance and phase angle. The Proceq Resipod Resistivity Meter, set in its uniaxial configuration, also applies an AC current but with a frequency of 40 Hz and measures total impedance. Once the testing apparatus is prepared, the data acquisition software measures resistance and temperature at a frequency of 0.1 Hz. Initially, the cold plate is set to allow the sample to equilibrate to 5°C. The sample temperature is then raised at a set rate of 0.6 °C / h.
The average specimen temperature was determined as the average of the top three thermocouples, as the temperature measured by the bottom thermocouple is more representative of the cold plate temperature. The heating rate was chosen to minimize thermal gradients in the specimen. It should be noted that during the test the testing device stays in a temperature controlled environment at 23°C.
Resistivity of the specimen is determined by using the real component of impedance, determined by multiplying the cosine of the phase angle and the measured total impedance, and then multiplied by the geometry factor. The geometry factor for the uniaxial test used in this study is simply the ratio of cross-sectional area to length. [6]

4. Results and Discussion

The activation energy of conduction, E_{a-cond}, is a single parameter that can be used in an exponential, Arrhenius-type correction for resistivity measurements. The E_{a-cond} can be calculated from the slope of the best fit line for a figure of the natural log of resistivity versus the inverse of the absolute temperature, as shown in Figure 2. The slope of the best fit line is then multiplied by the universal gas constant (R=8.314 J/ (K·mol)) to determine E_{a-cond}.

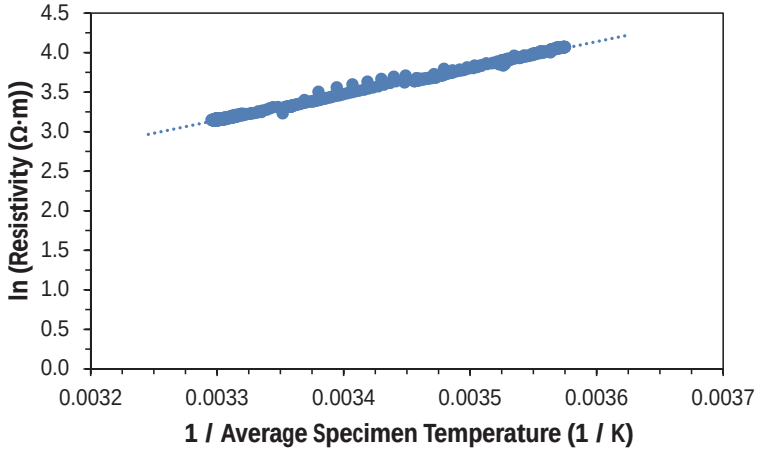

Figure 2: Arrhenius type plot of natural logarithm of resistivity vs. inverse of absolute temperature, the slope of the best fit line used to calculate the activation energy of conduction.

Using the measured resistivity at 23 °C and the E_{a-cond} determined as described above, the resistivity of the concrete sample at any temperature can be estimated. An example is shown in Figure 3 for mixture FA-5, with the other mixtures showing similar results. It can be observed that the correction of the temperature following the activation energy concept provides data that is similar to that which was experimentally measured.

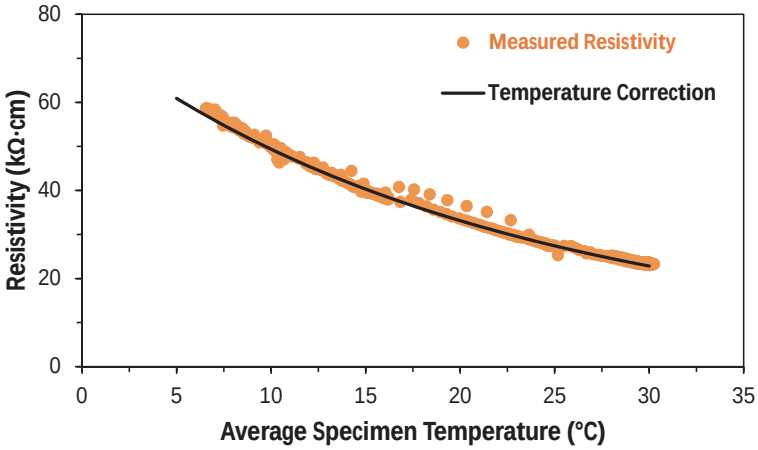

Figure 3: Typical experimental results showing resistivity and average specimen temperature, results for mixture FA-5.

Values for E_{a-cond} were determined for all of the mixtures in this study, and the results are shown in Table 2. Results indicate an average value of 27.4 kJ/mol.

Table 2: Activation energies of conduction for each of the mixtures in this study.

Mixture ID	E_{a-cond} (kJ/mol)
C-1	25.1
C-2	25.4
FA-1	32.2
FA-2	25.9
FA-3	31.4
FA-4	25.9
FA-5	27.5
S-1	28.8
Ter-1	24.8
AVG	27.4
SD	2.8

As most of the conduction occurs through the pore solution, a relationship was investigated between E_{a-cond} and the pore solution. The pore solution properties, specifically the ionic strength, was estimated based upon the mixture designs and alkali contents of the cementitious materials, using the pore solution calculator developed by NIST, available at http://concrete.nist.gov/poresolncalc.html [25]. Figure 4 shows that a higher pore solution ionic strength, which corresponds to a higher concentration pore solution or a lower pore solution resistivity, in general shows a lower activation energy. The relationship of higher ionic strength to lower activation energy of conduction has been reported previously for extracted pore solutions as well [26]. A linear fit is shown to help guide the eye, as well as symbols for the different types of mixtures. With a larger data set, this correlation could potentially help to estimate E_{a-cond} based upon the pore solution properties.

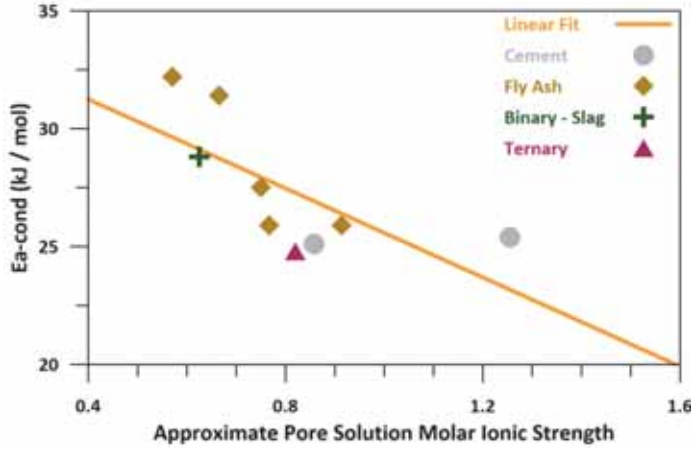

Figure 4: Activation energy of conduction versus pore solution molar strength shows the general trend that mixtures with high concentration pore solutions showed a lower temperature sensitvity, i.e. a lower E_{a-cond}.

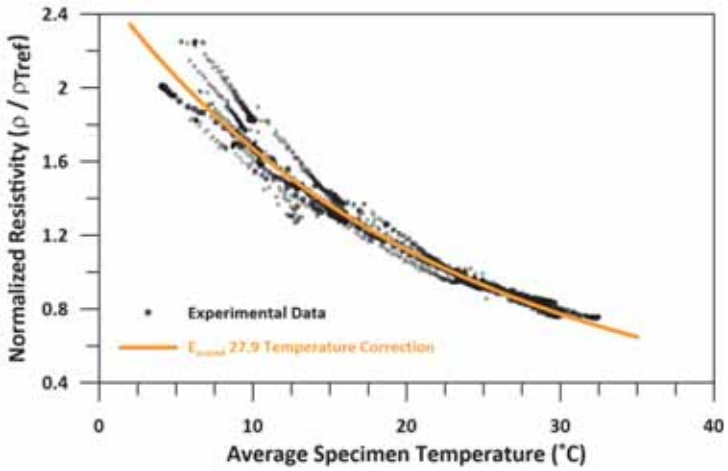

Figure 5: Experimental results showing resistivity versus average specimen temperature for the mixtures in this study, overlaid with the temperature correction fit based on the average activation energy of conduction.

One objective of this work is to evaluate the possibly of a single value of E_{a-cond} being used as a temperature correction for a wide range of mixture compositions. While that evaluation is still being conducted, Figure 5 shows data from each of the mixtures used in this study. It can be seen that when the normalized resistivity, $\rho/\rho_{T_{ref}}$, is plotted against temperature the Arrhenius function captures the general trend of the data. The data points are overlaid with a temperature correction based upon the average E_{a-cond} of 27.9. A reasonable agreement is noted, suggesting that a single value of E_{a-cond} could be used for sealed samples using the standard deviation noted in Table 2. Future work may however show estimating E_{a-cond} based on pore solution concentration to be more suitable.

5. Ongoing Work

Additional testing will be performed on these samples to determine the role that degree of saturation has in terms of activation energy. For this testing, specimens will be saturated using a 7 torr vacuum level [27], and the E_{a-cond} will be evaluated as the specimen loses moisture. Preliminary analysis of the C-1 samples shows that activation energy can change by approximately 20 % as the specimen moves from a sealed state to a saturated state. This is expected as although the pore solution may become more diluted, the effect of filling in the pores will increase the conductive volume and connectivity enough that resistivity measurements are less affected by temperature. This behavior has been noted by previous researchers [6], [28].

6. Conclusions

This paper presented a methodology to determine the activation energy of conduction, E_{a-cond}, based upon a continuously monitored electrical resistivity setup that incorporates a thermoelectric cold plate. This method demonstrates potential for use in determining a temperature correction for resistivity measurements. The method simply requires a standard test cylinder to be placed into the apparatus, and monitored with a resistivity meter and thermocouple.

The E_{a-cond} was calculated for a wide range of mixtures in their sealed state, and results indicate that an average value of 27.9 provides reasonable agreement with all of the mixtures in this study. These mixtures were made using a wide variety of constituent materials that ranged from w/cm = 0.37 to 0.45 with Type I OPC cements, to ternary blends including fly ash and slag cement. A correlation between E_{a-cond} and pore solution ionic strength was noticed with systems of a higher ionic strength, i.e. higher concentration, typically having lower values of E_{a-cond}. Furthermore, ongoing work with these samples demonstrates a value that can vary more than 20 % as the mixture goes from sealed to a saturated state.

7. Acknowledgements

This work was conducted through the National Concrete Consortium and the mixtures were produced by members of the Performance Engineered Mixtures (PEM) Champion States. Gratitude is extended for their effort as the data shown here would not have been possible without their assistance. The experiments were conducted at the Infrastructure Materials Research Laboratory at Oregon State University. The authors are grateful for contributions that have made the operation of the laboratory possible. The contents of this paper reflect the views of the authors, who are responsible for the facts and the accuracy of the data presented herein, and the contents do not constitute a standard, specification, or regulation.

References

[1] F. Rajabipour, G. Sant, and J. Weiss, “Development of Electrical Conductivity-Based Sensors for Health Monitoring of Concrete Materials Development of Electrical Conductivity-Based Sensors for Health Monitoring of Concrete Materials,” in *Proceedings of the Transportation Research Board*, 2007, pp. 1–16.

[2] Y. Bu, R. P. Spragg, C. Villani, and J. Weiss, “The influence of accelerated curing on the properties used in the prediction of chloride ingress in concrete using a Nernst-Planck approach,” *Constr. Build. Mater.*, vol. 66, pp. 752–759, 2014.

[3] R. P. Spragg, S. Z. Jones, Y. Bu, Y. Lu, D. P. Bentz, K. A. Snyder, and J. Weiss, “Alkali-Leaching in Cementitious Systems : Implications to Measurements of Electrical Resistivity,” Submitt. to *Model. Simul. Mater. Sci. Eng.*, 2016.

[4] G. Sant, F. Rajabipour, and W. J. Weiss, “The influence of temperature on electrical conductivity measurements and maturity predictions in cementitious materials during hydration,” *Indian Concr. J.*, vol. 82, pp. 7–16, 2008.

[5] T. M. Chrisp, G. Starrs, W. J. McCarter, E. Rouchotas, and J. Blewett, “Temperature-

conductivity relationships for concrete: An activation energy approach," *J. Mater. Sci. Lett.*, vol. 20, no. 12, pp. 1085–1087, 2001.

[6] R. Spragg, C. Villani, K. Snyder, D. P. Bentz, J. W. Bullard, and J. Weiss, "Factors That Influence Electrical Resistivity Measurements in Cementitious Systems," *Transp. Res. Rec. J. Transp. Res. Board*, vol. 2342, pp. 90–98, Dec. 2013.

[7] G. A. Julio-Betancourt and R. D. Hooton, "Study of the Joule effect on rapid chloride permeability values and evaluation of related electrical properties of concretes," *Cem. Concr. Res.*, vol. 34, no. 6, pp. 1007–1015, Jun. 2004.

[8] R. Spragg, Y. Bu, K. A. Snyder, D. P. Bentz, and J. Weiss, "Electrical Testing of Cement-Based Materials: Role of Testing Techniques, Sample Conditioning, and Accelerated Curing," Purdue University, West Lafayette, Indiana, FHWA/IN/JTRP-2013/28, Dec. 2013.

[9] J. Weiss, K. Snyder, J. Bullard, and D. P. Bentz, "Using a Saturation Function to Interpret the Electrical Properties of Partially Saturated Concrete," *J. Mater. Civ. Eng.*, vol. 25, no. 8, pp. 1097–1106, Aug. 2013.

[10] T. Barrett, "Improving Service Life of Concrete Structures Through the Use of Internal Curing: Impact on Practice," PhD, Purdue University, West Lafayette, Indiana, 2015.

[11] R. Spragg, C. Villani, and J. Weiss, "Electrical Properties of Cementitious Systems : Formation Factor Determination and the Influence of Conditioning Procedures," *Adv. Civ. Eng. Mater.*, vol. 5, no. 1, 2016.

[12] A. Schiessel, W. J. Weiss, J. D. Shane, N. S. Berke, T. O. Mason, and S. P. Shah, "Assessing the Moisture Profile of Drying Concrete using Impedance Spectroscopy," *Concr. Sci. Eng.*, vol. 2, no. 6, pp. 106–116, 2000.

[13] G. E. Archie, "The Electrical Resistivity Log as an Aid in Determining Some Reservoir Characteristics," *Pet. Technol.*, vol. 146, no. 1, pp. 54–62, 1942.

[14] F. A. L. Dullien, *Porous media: fluid transport and pore structure*, 2nd ed., vol. 1991. San Diego: Academic Press, 1991.

[15] F. Rajabipour and W. J. Weiss, "Parameters Affecting the Measurements of Embedded," in *Health Monitoring Systems & Sensors for Assessing Concrete*, 2008, vol. SP252–08, pp. 7–22.

[16] X. Feng, E. Garboczi, J. Bullard, D. P. Bentz, K. Snyder, P. Stutzman, and T. Mason, "Expanding a tool for predicting chloride diffusivity in concrete so it can be used by manufacturers to evaluate the durability of concrete made with blended cements. Part I: Characterizing blended cement materials.," Gaithersburg, MD, NISTIR 7135, 2004.

[17] C. Qiao, "Influence of Mineral Admixtures and Shrinkage Reducing Admixtures on Transport Properties of Concrete," Phd. Dissertation, University of Science and Technology Beijing, Beijing, 2016.

[18] Y. Farnam, H. Todak, R. Spragg, and J. Weiss, "Electrical response of mortar with different degrees of saturation and deicing salt solutions during freezing and thawing," *Cem. Concr. Compos.*, vol. 59, pp. 49–59, May 2015.

[19] M. Castellote, C. Andrade, and C. Alonso, "Temperature correction, from 3 to 25C of the electrical resistivity of mortars and concretes," *Ind. Ital. del Cem.*, vol. 71, pp. 916–923, 2001.

[20] R. P. Spragg, "The Rapid Assessment of Transport Properties of Cementitious Materials Using Electrical Methods," MSCE, Purdue University, West Lafayette, IN, 2013.

[21] R. P. Spragg, A. Coyle, T. Fu, and J. Weiss, "Formation Factor Round Robin : A Multi State Study," Report submitted to National Concrete Pavement Tech Center. Ames, IA, 2016.
[22] W. J. McCarter, G. Starrs, and T. M. Chrisp, "Electrical conductivity, diffusion, and permeability of Portland cement-based mortars," *Cem. Concr. Res.*, vol. 30, no. 9, pp. 1395–1400, 2000.
[23] ASTM C595, "Standard Specification for Blended Hydraulic Cements." ASTM International, West Conshohocken, PA, 2016.
[24] Measurement Computing, "USB-TEMP Multi-sensor Temperature Measurement User's Guide," no. Revision 13. Measurement Computing Corporation, Contoocook, NH, 2014.
[25] D. P. Bentz, "A virtual rapid chloride permeability test," *Cem. Concr. Compos.*, vol. 29, no. 10, pp. 723–731, 2007.
[26] J. Castro, R. Spragg, P. Kompare, and J. Weiss, "Portland Cement Concrete Pavement Permeability Performance," West Lafayette, Indiana, FHWA/IN/JTRP-2010/29, Nov. 2010.
[27] Y. Bu, R. Spragg, and J. Weiss, "Comparison of the Pore Volume in Concrete as Determined Using ASTM C642 and Vacuum Saturation," *Adv. Civ. Eng. Mater.*, vol. 3, no. 1, 2014.
[28] W. J. McCarter and S. Garvin, "Dependence of electrical impedance of cement-based materials on their moisture condition," *J. Phys. D. Appl. Phys.*, vol. 22, no. 11, pp. 1773–1776, 2000.

International RILEM Conference on Materials, Systems and Structures in Civil Engineering
Conference segment on Service Life of Cement-Based Materials and Structures
22-24 August 2016, Technical University of Denmark, Lyngby, Denmark

MODELLING OF CHLORIDE TRANSPORT IN UNSATURATED CONCRETE: STUDY OF ELECTROCAPILLARY EFFECT

Phu Tho Nguyen [(1)], Ouali Amiri [(1)]

(1) University of Nantes (IUT de Saint Nazaire), Saint Nazaire, France

Abstract
In this paper a multispecies transfer model is used to simulate the chloride profile in unsaturated concrete. Particularly, this model takes into account the electrical double layer (EDL) occurring at the interface between a pore wall and a pore solution. The obtained numerical simulations show that the chloride profile is mainly affected by the two main parameters of EDL i.e: the zeta potential and the pore diameter. The overlapping of EDL occurs when the pore diameter is smaller than 3nm and the zeta potential is around 30mV.
The simulations also show that the composition of concrete affects the evolution of the chloride profile. Among the tested concretes, the one containing slag shows an overlapping of EDL greater than ordinary Portland concrete or concrete made with fly ash. This result could be explained by the ferrous ions of slag which affect the ionic strength of the pore solution as well as by the finer pore size distribution of such materials.

1. Introduction

One of the most important causes of degradation of concrete structures is the corrosion of steel reinforcement which is due mainly either to chloride ingress in the sea side areas or to carbonation process. In the case of chloride ingress, when the chloride concentration reached the threshold value, the corrosion of steel began until the macroscopic degradation of the structure according to Tuutis's model [1]. Consequently, the service life of the structures is reduced.
To predict correctly the chloride ingress and hence the service life, it is important to take into account in the chloride transfer model, the main chemical and physical phenomena's occurring in cement based materials [2-6] such as the chloride chemical binding, the activity of pore solution, the electrostatic interaction between the ions contained in the pore solution and the electrical double layer (EDL) which is known under 'electrocapillary effect' [7]

To our knowledge, the studies dealing with the EDL effect on chloride transport from a quantitative point of view, mainly in unsaturated concrete, are few. So the aim of this research is to highlight the EDL effect in unsaturated concrete submitted to chloride ingress coupled to wetting-drying cycles. To reach this purpose, we should combine ions and humidity transports with the EDL effect at a macroscopic scale. Simulations of chlorides profiles in concretes containing fly ash and slag were carried out in order to show the effect of the sign of EDL and the drying-wetting cycles on chloride ingress.

2. Description Electrical double layer (EDL) phenomenon

In order to understand the EDL effect, we just give a brief description of this phenomenon. More details are given in [7-11].

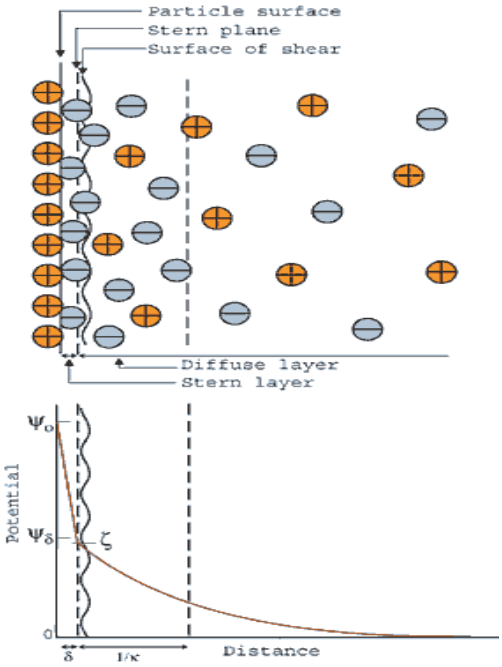

Figure 1: Schematic view of the EDL according to Stern Model

The Stern model (figure 1) [12] is generally adopted to describe EDL phenomenon. At the interface between the pore walls (cement matrix) and the pore solution, ions are physically adsorbed by Van der Waal's forces. An ionic imbalance is then established, but the bulk remains in equilibrium.
The interface is structured in two parts, a diffuse layer and a compact layer: the two parts form an electrical double layer. The compact layer is made of solvated ions, adsorbed at the surface. The potential in the EDL is due to the ionic imbalance following Poisson's equation.

At the compact layer, the potential is known as "the zeta potential" and can be measured by a zetameter. The extension of the potential occurs on a distance called "Debye length" which depends on the temperature, the ionic concentration of the bulk solution and its dielectric permittivity. In this paper, we consider a microstructure with a single pore which can be schematically represented by two parallel flat plates distant from d which is considered as the pore diameter. In this case, two diffuse layers are positioned face to face and overlap when the pore diameter is close to Debye length.

3. Physical modeling: coupled transfer ions and humidity

In this section, we summarize the physical modeling used in this study. This modelling combines ions and humidity transfer. First, for the ionic transfer the classical equation of Nernst-Planck extended to unsaturated transport is used:

$$\frac{\partial(\mathrm{WK_{\mp}C_i})}{\partial t} + (1-\epsilon)\frac{\partial C_{i,b}}{\partial C_i}\frac{\partial C_i}{\partial t} + \mathrm{div}\left(\underbrace{-D_i \mathrm{WK_{\mp}grad}(C_i)}_{\text{diffusion}} - \underbrace{\frac{D_i z_i F}{RT}\mathrm{WK_{\mp}C_i grad}\Psi}_{\text{migration}} + \underbrace{K_{\mp}C_i V_e}_{\text{convection}}\right) = 0 \quad (1)$$

Where K_+ and K_- are two coefficients which express the EDL effect on cation and anion fluxes, respectively.

ϵ is porosity of the material, W is water content. C_{ib} is the concentration of chemical specie contained in the pore solution. Ψ is the electrical potential in the pore solution. D_i is the diffusion coefficient of the specie i and Z_i is its valence. F is the Faraday's constant, R is the gas constant and T is the temperature.

In the pore solution, the ions interact with each other, producing an electrostatic potential Ψ which can be generated from the Eq.(1) in the case of a natural diffusion (current density equal to zero):

$$\nabla\psi = -\frac{\sum_{i=1}^{n} D_i K_{\mp} C_{ib} z_{ib} W \nabla C_{ib} - \sum_{i=1}^{n} z_i \mathrm{WK_{\mp}} C_{ib}}{\frac{F}{RT}\sum_{i=1}^{n} D_i K_{\mp} C_{ib} z_i^2 W \nabla C_{ib}} \quad (2)$$

$$K_+ = \frac{A(\kappa d)^2}{1 - AB\kappa d + A(\kappa d)^2} + \frac{1+Z}{2}\frac{2q}{FdC_{pc}} \quad (3)$$

$$K_- = K_+ - \frac{2q}{FdC_{pc}} \quad (4)$$

where A and B are the two parameters which depend on the zeta potential ζ and the pore diameter d, the concentration of the bulk C_{pc} and on the surface density charge q [7, 11].

We can note that EDL affects the transport through the coefficients K± which depend on both the pore structure (pore diameter d) and potential zeta (see Eq.3).
For the humidity transfer, the mains assumptions considered are:

- The liquid phase constituted by water. The gas phase make up of dry air and steam. The pressures in these two phases are respectively noted p_a and p_v.
- The gravity effect is negligible.

The balance equations for each phase both liquid (w), (water vapor) (v) and air (*a*) are:

$$\frac{\partial[\rho_w W]}{\partial t} = -\mathrm{div}(\rho_w v_w) - \dot{m} \tag{5}$$

$$\underbrace{\frac{\partial[\rho_v(\epsilon - W)]}{\partial t}} = -\mathrm{div}(D_{va}\mathrm{grad}(\rho_v)) + \dot{m} \tag{6}$$

$$\underbrace{\frac{\partial[\rho_a(\epsilon_0 - W)]}{\partial t}} = -\mathrm{div}(D_{va}\mathrm{grad}(\rho_a)) \tag{7}$$

Where ρ_w, ρ_v and ρ_a are respectively the densities of water, vapor and air. Equations (8) and (9) give respectively the velocity of liquid phase and the capillary pressure.

$$v_w = -\frac{K_l K_{rl}}{\mu_l}\mathrm{grad}(P_l) \tag{8}$$

$$P_c = P_g - P_l \tag{9}$$

For capillary pressure calculation, we consider the GAB model, modified by Bazant [13-14]:

$$P_c = -\frac{\rho_w RT}{M_v}\ln\left(\alpha_c + \frac{1}{2}\sqrt{\beta_c + \gamma_c\frac{\varepsilon}{W}}\right) \tag{10}$$

$\alpha_c, \beta_c, \gamma_c$ are the parameters which depend on the material properties [15].
K_l, K_{rl}, μ_l are respectively the intrinsic permeability, relative permeability and the density of water
D_{va} is the vapor diffusion coefficient in concrete and can be expressed by:

$$D_{va} = 2.17x10^{-5}\left(\frac{T}{T_{ref}}\right)^{1.88} * f_{res} \tag{11}$$

T, T_{ref} are respectively the temperature of the concrete and the reference one.
f_{ref} is the tortuosity factor which depends on the water content and porosity according to Milligton model [16].
The sum of equations (6) and (7) gives:

$$\frac{\partial W}{\partial t} - \mathrm{div}\left(D_w\mathrm{grad}(W)\right) = 0 \tag{12}$$

D_w is the water diffusion coefficient written as:

$$D_w = -\frac{K_l K_{rl}}{\mu_l}\frac{\partial P_c}{\partial x} + \frac{D_{va}}{\rho_w}\frac{\partial \rho_v}{\partial W} \quad (13)$$

4. Numerical simulations and discussion

The model of ionic and humidity transport is described by the partial differential Eq.1 and Eq.12. These equations are solved numerically in the one-dimensional case by using volume finite method with an explicit scheme. For the simulations, a cubic concrete sample with 5cm of thickness is considered. Only one side is exposed to a saline solution (500 mol/l), this concentration is chosen in order to simulate sea water.
The simulations of chloride profile were carried out in 4 types of concrete: the concrete reference (CR) manufactured with ordinary cement (CEM I), 3 others concrete where the ordinary cement is substituted by 30% (CS30) and 75% (CS75) of blast furnace slag and by 30% of fly ash (CA30). The main characteristics of these concretes are summarized in table 1 and full details are given in [14].

Table 1 : Characteristics of the used materials

Concrete	CR	CS30	CS75	CA30
Gravel 6/10 (kg/m^3)	1012.7	1077.4	1037.1	1048.2
Sand (0/4) (kg/m^3)	855	848.3	816.5	824.5
CEM I 52.5 (kg/m^3)	330	218.7	102.8	241.1
Slag (kg/m^3)	-	93.7	309.6	-
Fly ash (kg/m^3)	-	-	-	103.3
Water (kg/m^3)	198	181	170	182.1
W/C	0.6	0.63	0.44	0.57
Pore diameter *d*(nm)	95.6	21.1	3	120.7
Diffusion Coefficient x(10^{-12}) m^2/s	12.5	7.2	1.4	6.2
Water porosity (%)	15.9	17.5	14.3	16.5

Figures (2-5) show the chloride profile obtained for the four concretes. The simulations are performed for 1 year. We have to note that the EDL effect is greater in the case of saturated concrete comparatively to an unsaturated one. This is due to the continuity of the liquid phase in the first case (saturated concrete) and the EDL occurs only in the liquid phase.
Also, according to the table 1, the pore diameter of concrete containing slag (CS75) is 3nm, in such condition the overlapping of EDL is higher.

The simulations show also that the positive EDL affects the chloride profile more than the negative EDL. This result would be explained by the high ionic strength mainly for concrete containing 75% of slag which releases in the pore solution ferrous ions Fe^{++}.

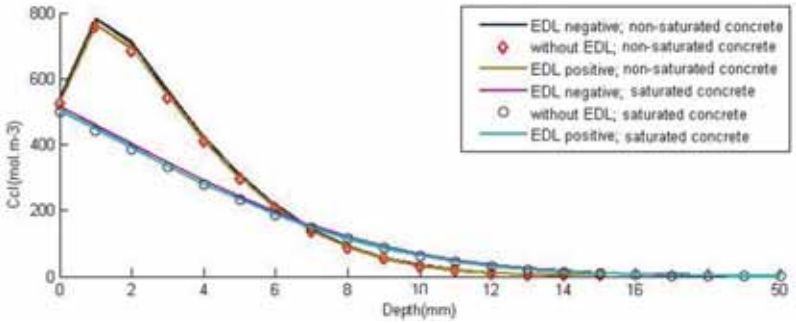

Figure 2: Chloride profile of concrete Ref

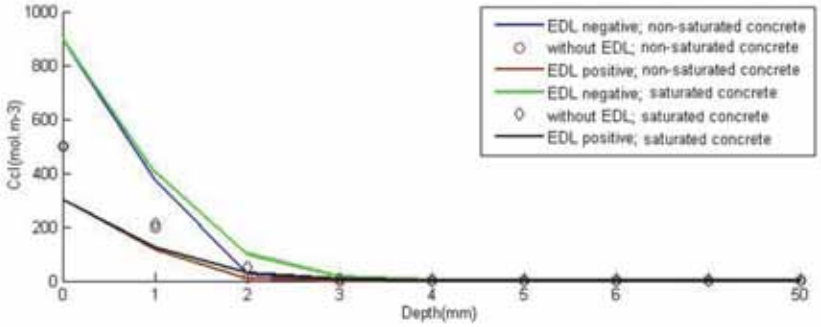

Figure 3: Chloride profile of concrete CS75

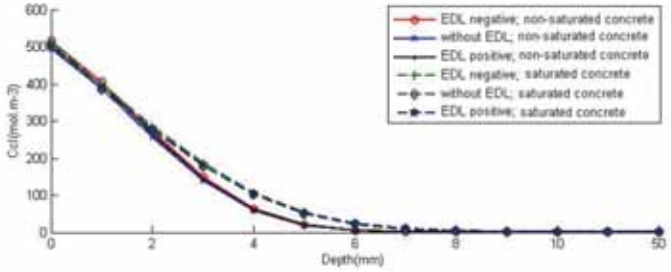

Figure 4: Chloride profile of concrete CA30

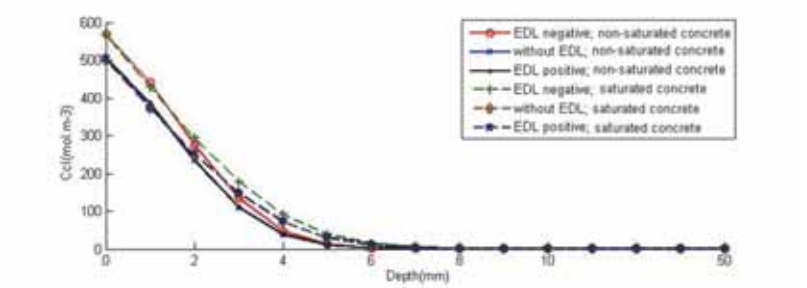

Figure 5: Chloride profile of concrete CS30

The two main parameters of EDL are the zeta potential and the pore size (pore diameter d). In order to show the sensitivity of the model according to a set of parameters, we simulated the profile of chloride ions for 3 values of zeta potential and pore diameters. Figure 6 shows that chloride concentration is inversely proportional to the pore diameter. The EDL effect is greater when the pore diameter is close to Debye length (3nm). Any variation of the pore size leads to a significant change of chloride concentration. This explains the weak effect of EDL for the concretes CR, CA30.
The simulations were carried out for a short-term (1 year). Therefore, the chloride ingress did not exceed 10mm. The ionic diffusion coefficients of the tested concretes are also weak (see the Table1). In such conditions, the chloride ingress is slow.

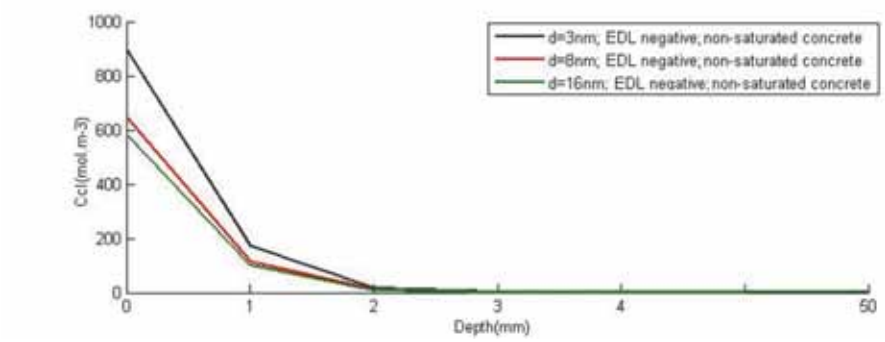

Figure 6: Influence of size pore on chloride profile in the concrete CS75

Concerning the zeta potential effect, figure 7 shows that the chloride profile increases with the zeta potential. This is due to the fact that the overlapping of EDL within a pore is related to the intensity of physical adsorption which is strongly linked to the zeta potential.

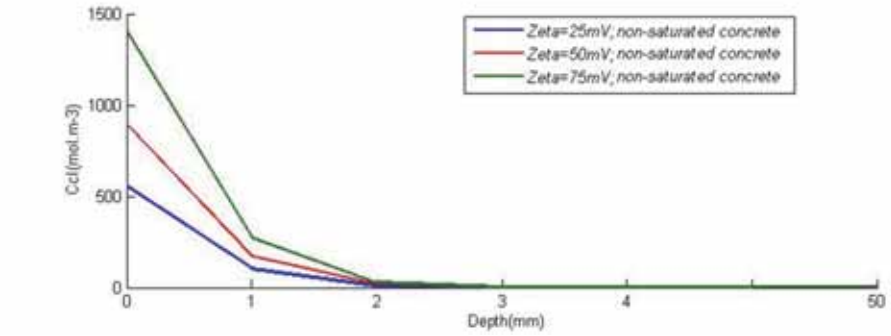

Figure 7: Influence of zeta potential on chloride profile in the concrete CS75

5. Conclusions

The effect of electrical double layer (EDL) on chloride transport in unsaturated concretes is studied in this paper. We can highlight the following results:

- The chloride concentration is linked to the two parameters of electrical double layer zeta potential and pore diameter. However when the pore diameter is greater than the Debye length, the EDL effect becomes insignificant.
- The EDL occurred mainly in the liquid phase, so its effect is higher in such condition (saturated material). The variation of chloride concentration depends also on saturation degree. Thus, if the drying is strong (high gas permeability), the chloride concentration increases in the pore solution.
- The EDL effect is stronger in the concrete containing slag than in those manufactured with fly ash. This is due to the ferrous ions of slag which increases the ionic strength of the pore solution.

References

[1] Tuuti K., Corrosion of Steel in Concrete, report of Swedish Cement and Concrete Research Institute, Stockholm, (1982).
[2] Fredrik P., Glasser *et al*. –Durability of concrete – Degradation phenomena involving detrimental chemical ractions- Cem Concr Res 38 (2008) 226-246.
[3] Samson E., J. Marchand J, Beaudoin, Modeling the influence of chemical reactions on the mechanisms of ionic transport in porous materials: An
[4] Samson E. Marchand J., Modeling chemical activity effects in strong ionic solutions computational materials science 15(1999)285-294.
[5] Samson E., Marchand J., Modeling the effect of temperature on ionic transport in cementitious materials, Cem Concr Res 37 (2007) 455-468.

[6] Amiri O., Aït-Mokhtar A., Dumargue P., Touchard G., Electrochemical modeling of chloride migration in cement based materials, Part I: Theoretical basis at microscopic scale, Electrochemical Acta 46 (2001) 1267-1275.
[7] Friedmann H., O.Amiri O., Aït-Mokhtar A., hysical modeling of the electrical double layer effects on multispecies ions transport in cement-based materials, Cem Concr Res 38 (2008) 1394-1400.
[8] Dubois M., Zemb T., Belloni L.,. Osmotic pressure and salt exclusion in electrostatically swollen lamellar phases. J.chem. Phys. 96(3), 1 February 1992.
[9] Nagele E., The zeta-potential of cement, Cem. Concr.Res. 15 (1985) 453-462.
[10] Viallis-Terrisse H., Nonat A., Petit J.C, Zeta-potential study of calcium silicates hydrates interacting with alkaline cation, J.Colloid Interface Sci.244(2011) 58-65.
[11] Dufêche J.F., Marry V., Bernard O., Turq P., Models for electrokinetic in montmorillonite, Colloids and Surfaces A, 195 (2001) 171-180
[12] Stem O. Z., *Electrochem.* 30**,** 508 (1924).
[13] Xi Y., Bazant Z.P, and Jennings H.M, Moisture Diffusion in Cementitious Materials Adsorption Isothermes, Advances Cement Based Materials 1 (1994) 248-257.
[14] Xi Y., Bazant Z.P, Molina L., Jennings H.M., Moisture Diffusion in Cementitious Materials-Moisture Capacity and Diffusivity, Advances Cement Based Materials, 1 (1994) 258-266.
[15] P.T. Ngyen "Étude multiphysique du transfert de chlorures dans les bétons insaturés : Prédiction de l'initiation de la corrosion des aciers" phD Thesis of La Rochelle University (France), 2014.
[16] Millington R., Shearer R.C., diffusion in aggregated porous media, soil science, 3 (1970), 372-378.

International RILEM Conference on Materials, Systems and Structures in Civil Engineering
Conference segment on Service Life of Cement-Based Materials and Structures
22-24 August 2016, Technical University of Denmark, Lyngby, Denmark

INFLUENCE OF FIBRE REINFORCEMENT ON THE INITIATION OF CORROSION-INDUCED CRACKS

Carlos G. Berrocal [(1)(2)], Ignasi Fernandez [(1)], Karin Lundgren [(1)], Ingemar Löfgren [(1)(2)]

(1) Chalmers University of Technology, Göteborg, Sweden
(2) Thomas Concrete Group AB, Göteborg, Sweden

Abstract
The initiation of corrosion-induced cracks, often running parallel to the reinforcement, becomes a turning point in the service life of a reinforced concrete (RC) structure as they promote increased corrosion rates, thus accelerating the degradation process of the structure. Compared to plain concrete, fibre reinforced concrete (FRC) provides additional confinement to the reinforcement, which has been reported to delay or even prevent the appearance of mechanically induced splitting cracks. In this study, an experimental programme has been carried out to investigate the influence of fibres on the onset of corrosion-induced splitting cracks. Cylindrical lollipop specimens with a centrally positioned Ø16 mm bar and varying cover depths from 40 to 64 mm were subjected to accelerated corrosion. A constant current of 100 $\mu A/cm^2$ was impressed through the specimens and the electrical resistance between each rebar and an external copper mesh acting as cathode was monitored. Crack initiation, determined from a drop in electrical resistance, and confirmed by visual inspection, revealed that fibre reinforcement may delay corrosion-induced cracks, an effect that was more noticeable for reduced *c/Ø ratios*, featuring up to 50% higher corrosion levels at crack initiation compared to plain concrete.

1. Introduction

Corrosion of reinforcement is one of the main causes leading to the premature deterioration of reinforced concrete (RC) structures with the consequent reduction of their service life. In advanced stages of the corrosion process, the accumulation of corrosion products at the steel-concrete interface induces splitting stresses at the concrete cover. If the corrosion does not cease, the stress level may eventually reach the tensile strength of the concrete and cracking of the cover will occur. Corrosion-induced cracks are typically longitudinal cracks running along the reinforcement. This type of cracks have been reported to accelerate the corrosion rate of reinforcement [1] and might result in spalling of the concrete cover. Thus, they are

especially harmful for the integrity of the structure and potentially dangerous as concrete pieces can fall off.

Similar to the mechanism of corrosion-induced cracking, the normal bond stresses arising when rebars are subjected to large slips may induce longitudinal cracks along the concrete cover, which are known to severely affect the bond of reinforcement due to the loss of confinement and are often called bond-splitting cracks. Several studies aimed at investigating the influence of fibres on bond of reinforcement in RC tie-elements, see e.g. [2], [3], reported an enhanced control of such splitting cracks when fibre reinforcement was incorporated.

Research focused on the effect of fibre reinforcement on corrosion-induced cracks is sparse. Hybrid fibre reinforced concrete (HyFRC), i.e. concrete incorporating a combination of fibres featuring different sizes and materials, proved to be effective in supressing crack formation in specimens subjected to accelerated corrosion with an impressed current of 1 mA/cm^2 for 48 h [4]. In that study, however, a relatively high fibre dosage (1.5% vol.) was needed to obtain a concrete exhibiting strain hardening. In another study [5], the role of fibres in controlling crack initiation and reducing bond degradation was experimentally investigated for synthetic fibres added at low dosages (0.15 to 0.30 % vol.). Results from that study showed a delay in crack initiation for increasing fibre dosage in terms of the number of exposure cycles needed to observe cracking. However, none of the aforementioned studies determined the actual steel loss needed to cause corrosion-induced cracking.

The present study aimed at understanding how the addition of steel fibre reinforcement at low dosages might influence the onset of splitting cracks induced by accumulation of corrosion products around an embedded rebar. In particular, the actual steel loss necessary to induce cracking was investigated as a function of the cover to bar diameter ratio. The results presented here are part of a larger experimental programme currently ongoing in which the effect of fibre reinforcement on the residual bond capacity of corroded bars will be investigated.

2. Experiments

For the assessment of crack initiation, experiments were conducted including a total of 30 specimens which can be divided into two groups: (i) specimens corroded until crack detection, here referred to as *low corrosion*, which are the main focus of this paper and (ii) specimens corroded beyond cracking, here referred to as *high corrosion*. The nomenclature of the specimens consists of three letters. The first letter indicates the type of concrete, either plain concrete (P) or fibre reinforced concrete (F). When referring to the concrete mixes alone, the abbreviations PC or FRC will be used, respectively, in the following. The remaining two letters indicate the relative size of the specimen, Small (S), Medium (M) or Large (L) and the corrosion level, either Low corrosion (L) or High corrosion (H). Tab. 1 summarizes the details of the experimental programme.

Table 1: Experimental programme. (Number of specimens in brackets)

	Estimated corrosion level and concrete type			
	Low corrosion - cracking		**High corrosion – (7.5%)***	
c/Ø ratio	**PC**	**FRC**	**PC**	**FRC**
2.5	PSL (3)	FSL (3)	PSH (3)	FSH (3)
3.25	PML (3)	FML (3)	-	-
4.0	PLL (3)	FLL (3)	PLH (3)	FLH (3)

*Estimated steel loss based on Faraday's Law

2.1 Specimen geometry and materials

The specimens designed for the present study were cylinders reinforced with a single ∅16 mm ribbed bar at the centre, which stuck out from one of the circular sides, also known as "lollipop" specimens. The cylindrical shape of the specimens and the position of the rebar in the centre were chosen to obtain uniformly distributed corrosion around the rebar and to prevent preferential cracking directions. The cylinders featured a total height of 100 mm while the rebar was partially encased into a PVC tube, thus providing an effective embedment length of 70 mm. Three different concrete cover to bar diameter ratios (*c/∅*) were investigated, namely 2.5, 3.25 and 4, corresponding to cover depths of 40, 52 and 64 mm, respectively. These cover depths comply with the specifications included in current design codes for reinforced concrete structures exposed to a variety of aggressive environments. Fig. 1 presents the specimens geometry.

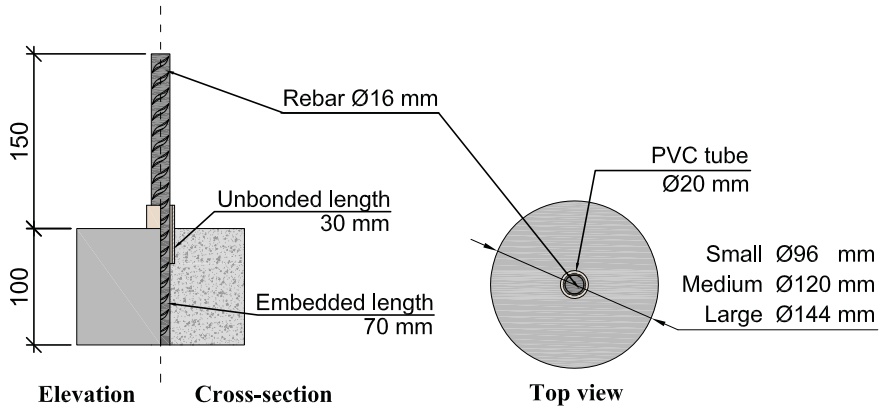

Figure 1: Specimen geometry.

A self-compacting concrete mix with a water to cement ratio (*w/c*) of 0.47 was prepared to cast all the specimens. The same mix composition was used to prepare both the plain and the steel fibre reinforced concrete, except for minor variations in the aggregate content to incorporate the fibres. To promote a fast corrosion initiation, 4% sodium chloride by weight of cement was incorporated into the mix. Tab. 2 shows the detailed concrete composition.

Table 2: Concrete mix proportions, kg/m^3

	Concrete mix designation	
Component	PC	FRC
Cement (CEM I 42.5N SR 3 MH/LA)	360	360
Limestone filler (Limus 40)	150	150
Fine aggregate (sand 0/4)	718	711
Coarse aggregate (crushed 5/16)	987	977
Effective water	169	169
Superplasticizer – Glenium 51/18	5.4	6.48
Air entrainer – MicroAir 105	0.36	0.36
Sodium Chloride (NaCl)	14.4	14.4
Steel – Dramix 65/35-BN	-	40

The compressive cube strength, f_{cm}, and the splitting tensile strength, f_{ctm}, were assessed for both mixes 28 days after casting through material tests. The former was tested on 100 mm cubes according to [6] while the latter was tested in accordance to [7] on 150 mm cubes. A summary of the material properties is presented in Tab. 3.

Table 3: Compressive and splitting tensile strength, in *MPa*

	f_{cm} (cube)		**f_{ctm}**	
	Avg.	**Std. Dev**	**Avg.**	**Std. Dev**
PC	56.0	1.3	4.2	0.2
FRC	52.5	0.3	4.6	0.2

All the specimens of the same concrete mix were cast in a single batch and were demoulded 24 h after casting. Subsequently, the reference specimens were cured in potable water whereas the remainder, the specimens designated to undergo accelerated corrosion, were cured in 3.5% NaCl solution, all of them at a constant temperature of 22 ºC.

2.2 Experimental setup

Accelerated corrosion tests were carried out in order to hasten the rate of steel dissolution, thus shortening the time necessary to observe corrosion-induced splitting cracks on the concrete cover, which otherwise could take place over a period of months or years. Since detecting the onset of splitting cracks was the main objective of these tests, a specific setup was conceived.

The specimens were introduced into plastic buckets with the reinforcement bar passing through a hole centrally bored at the bottom of the bucket. Silicone was applied at the cylinder surface in order to create a water-tight seal between the specimen and the bucket. A 1 mm thick copper wire mesh, spanning the entire height of the cylinders, was fastened around each specimen using rubber bands. After a 24 h period during which the silicone was left to harden, the buckets were filled with 3.5% NaCl solution, setting the water level about 2 cm below the top of the cylinders. In Fig. 2, the setup of the accelerated corrosion tests is illustrated.

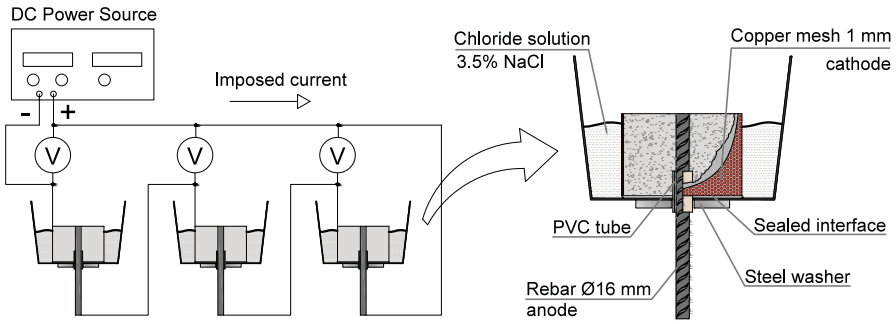

Figure 2: Experimental setup for accelerated corrosion tests

Leads were attached to the reinforcement bar, acting as the anode, and to the copper mesh, acting as the cathode, to connect them to the positive and negative terminals of a power source, respectively. It has been reported in the literature [8] that current densities above 350 $\mu A/cm^2$ may result in deviation of test conditions from a natural corrosion process. Therefore, a steady DC current equal to 3.52 mA was impressed through each specimen which, based on the exposed steel area of embedded rebar, was equivalent to a current density of 100 $\mu A/cm^2$. The electrical resistance of each specimen was monitored during the entire duration of the accelerated corrosion tests to determine the point in time when corrosion-induced cracking initiated. The potential between each cathode and the positive terminal of the power source was measured and recorded hourly using a data logger. The electrical resistance was calculated, according to Ohm's law, from each individual potential divided by the current intensity passing through the specimen.

In addition to electrical resistance measurements, visual confirmation of the first crack appearance was sought-after. Despite cracks were not easily detectable on the lateral sides of the cylinder due to the copper mesh, the configuration shown in Fig. 2 enabled easy access to the top surface of the specimens on which cracking was likely to be earliest detectable.

Once the accelerated corrosion procedure was completed, the reinforcement bars were extracted and cleaned for gravimetric steel loss measurements. Corrosion products were chemically removed according to ASTM recommendations [9] by repeated immersion of the bars in a solution of hydrochloric acid and urotropine. The corrosion level was calculated for each reinforcing bar assuming that the measured steel loss was concentrated on the 70 mm bar length embedded in the concrete, according to Eq. 1:

$$\nu = \frac{M_0 - M_f}{L_e \cdot A_s \cdot \rho} \cdot 100 \quad (1)$$

where υ is the corrosion level in %, L_e is the embedded length equal to 70 mm, A_s is the nominal cross-sectional area of the bar equal to 201 mm^2, ρ is the density of steel equal to 7.85 g/cm^3 and M_0 and M_f is the steel weight of the bar before and after the accelerated corrosion, respectively.

3. Results and discussion

Corrosion-induced cracks, which facilitate the transport of ions through concrete, usually result in a sudden drop of the concrete's electrical resistance. Ideally, such phenomenon could be used as a criterion to determine crack initiation. In practice, if cracks are below a certain threshold, the change in transport properties is very limited and the loss of electrical resistance might not be significant.

The electrical resistance of concrete is, furthermore, influenced by numerous factors, e.g. the temperature, the degree of saturation, the chemical composition of the pore solution, etc., while measurements may also be affected by small perturbations in the impressed current. The result is that the development of electrical resistance in time, when observed locally, may continuously fluctuate. Consequently, the specimens in the *low corrosion* series underwent accelerated corrosion until a crack was visually detected, meaning that the corrosion level assessed by gravimetric methods exceeded the actual corrosion level at crack initiation by a certain amount.

In order to determine the corrosion level at crack initiation, electrical resistance results are presented versus the corrosion level based on the steel loss measured at the end of the tests and assuming a linear dependence between time and mass loss. This assumption was based on Faraday's law, provided that a constant corrosion rate was enforced through the impressed current. Fig. 3 presents the variation of the electrical resistance monitored during the time period of the accelerated corrosion procedure for each specimen in the *low corrosion* series. For comparison purposes, in Fig. 4, the variation of the electrical resistance versus corrosion time is presented during the initial 40 days for specimens in the *high corrosion* series, which are still subjected to accelerated corrosion.

As observed, the electrical resistance generally followed a similar pattern in all cases: after an initial drop, it increased and remained rather stable, until it finally decreased again. Crack initiation was determined as the moment when electrical resistance started decreasing with no subsequent significant increase, which is indicated in Fig. 3 and Fig. 4 by arrows. The crack initiation results are summarized in Fig. 5, in which the effect of varying the *c/Ø* ratio and the effect of fibres can be interpreted.

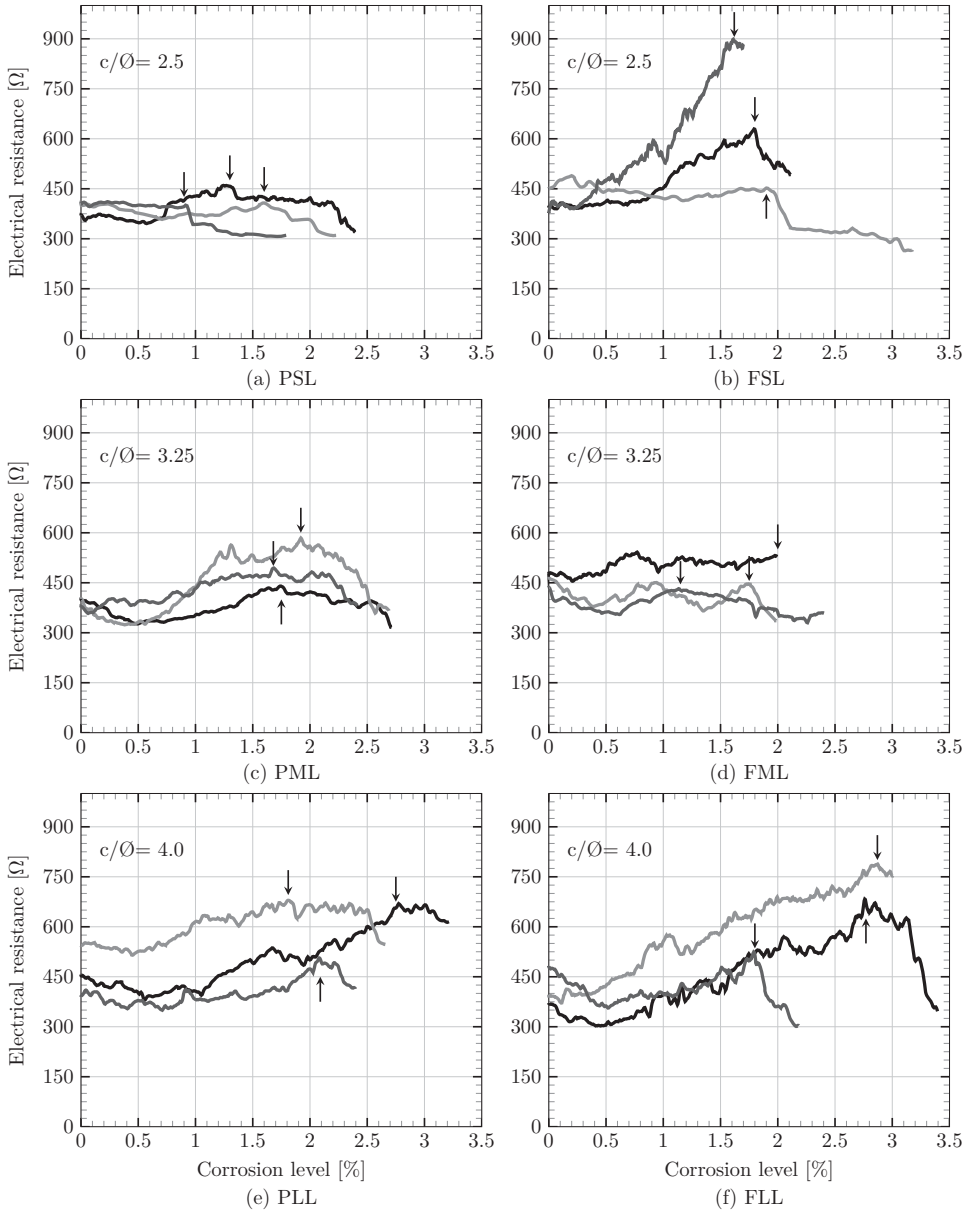

Figure 3: Electrical resistance measurements for *Low corrosion* specimens. Crack initiation is indicated by arrows.

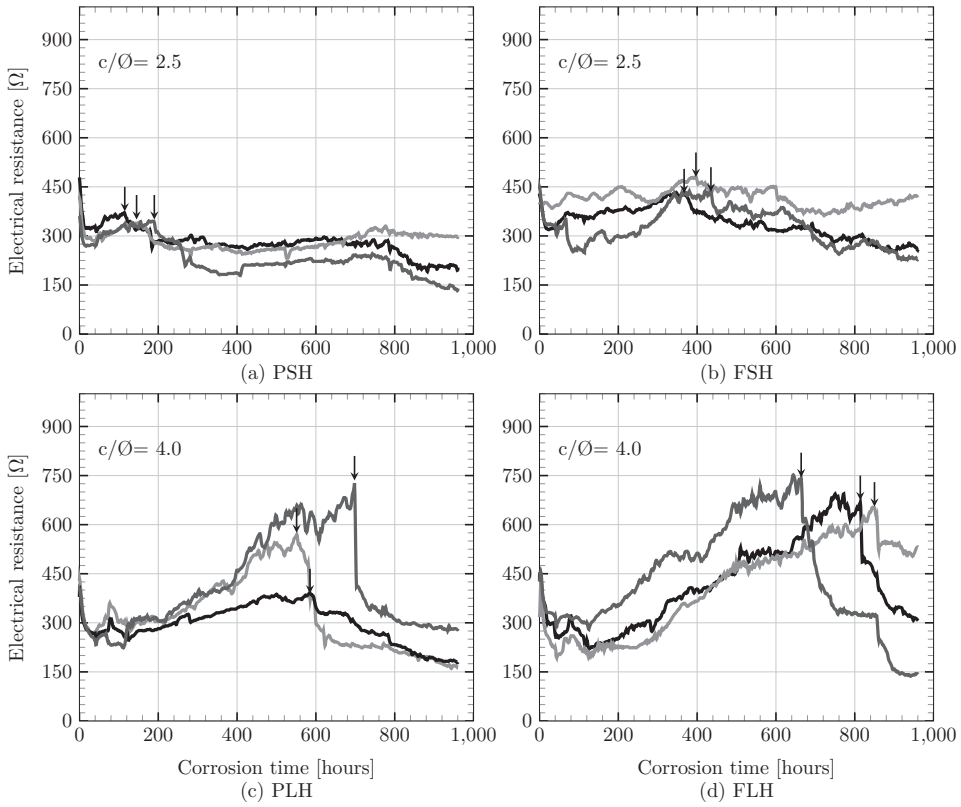

Figure 4: Electrical resistance measurements for *High corrosion* specimens. Crack initiation is indicated by arrows.

It is clear from Fig. 5 that the *c/Ø* ratio played an important role in delaying crack initiation, which based on Fig. 5(a) seemed to keep an almost linear relationship with the corrosion level required to induce cracking. Note that the specimens in the FML group exhibited an unexpectedly low corrosion level, even lower than that of the specimens with smaller dimensions. Consequently, they were considered as outliers but are included here for completeness. The addition of steel fibres at 0.5% vol. also showed a beneficial effect in terms of delayed corrosion-induced cracks although this effect seemed to be dependent on the *c/Ø* ratio. For the smallest specimen size, fibres had a significant impact, which decreased as the *c/Ø* ratio increased. This was likewise observed in Fig. 5(b) for the *high corrosion* series. This size dependent effect was attributed to differences in how cracks propagated in the various size specimens, more gradually in small specimens allowing a greater contribution of the fibres and more suddenly in large specimens due to higher built-up internal pressure. This finding is corroborated by the electrical resistance evolution curves, in Fig. 3 and particularly in Fig. 4, which show a larger sudden drop for large *c/Ø* ratios and a smoother transition for small *c/Ø* ratios.

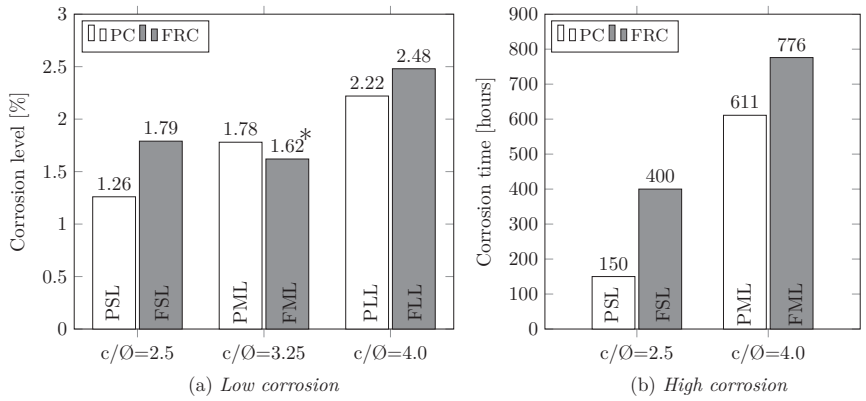

Figure 5: Crack initiation determined from corrosion level (a) and from corrosion time (b). *FML specimens yielded results in contradiction with the general trend shown by the remaining specimens.

It is also noteworthy that the initial range of electrical resistance in Fig. 3 and Fig. 4 showed no significant difference for plain and fibre reinforced concrete. This suggests that steel fibres were not conducting current under the applied DC field, hence the resistivity of FRC remained unchanged, a result that contradicts resistivity measurements carried out under AC [10].

A closer look to the embedded fibres, once the specimens had been split to extract the reinforcing bar, revealed that fibres were generally free of any signs of corrosion despite mixing 4% NaCl by weight of cement in the concrete and placing the specimens in 3.5% NaCl solution. This observation supports previous research indicating that steel fibres have higher resistance to chloride induced corrosion in concrete than steel reinforcement [11]. Nevertheless, some fibres located near the reinforcing bar presented evidences of light corrosion as shown in Fig. 6. Local defects, corrosion-induced cracks or a locally altered chloride-rich environment near the rebar promoted by ion migration under the applied DC field, might have been factors impairing the corrosion resistance of the observed corroded fibres.

Figure 6: Example of embedded fibres located near the rebar revealing light corrosion.

4. Conclusions

In this study experiments were carried out to determine the influence of adding 0.5% vol. steel fibres into concrete on initiation of corrosion-induced cracks in conventionally reinforced specimens. The results showed that fibres had a beneficial effect in terms of delayed crack initiation, which was more evident for small *c/Ø* ratios. This was attributed to a change in crack propagation from sudden for large cover, to gradual for small cover. Although fibres did not suppress cracking, it is argued that they would limit the crack width and prevent cover spalling at later stages. The experiments also revealed that steel fibres did not decrease the electrical resistivity of concrete based on the measured electrical resistance. The high corrosion resistance of steel fibres was confirmed by the lack of corrosion signs in the vast majority of embedded fibres.

References

[1] A. Poursaee and C. M. Hansson, "The influence of longitudinal cracks on the corrosion protection afforded reinforcing steel in high performance concrete," *Cem. Concr. Res.*, vol. 38, no. 8–9, pp. 1098–1105, Aug. 2008.

[2] H. Abrishami and D. Mitchell, "Influence of steel fibers on tension stiffening," *ACI Struct. J.*, vol. 94, pp. 769–776, 1997.

[3] F. Minelli, G. Tiberti, and G. A. Plizzari, "Durability and Crack control in FRC RC elements : an experimental study," in *International RILEM Conference on Advances in Construction Materials Through Science and Engineering*, 2011, pp. 435–443.

[4] G. Jen and C. P. Ostertag, "Resistance to Corrosion Induced Cracking in Self Consolidating Hybrid Fiber Reinforced Concrete," in *High Performance Fiber Reinforced Cement Composites 6*, vol. 2, 2012, pp. 163–170.

[5] R. H. Haddad and A. M. Ashteyate, "Role of synthetic fibers in delaying steel corrosion cracks and improving bond with concrete," *Can. J. Civ. Eng.*, vol. 28, no. 5, pp. 787–793, 2001.

[6] "EN 12390-3:2009 Testing hardened concrete. Part 3: Compressive strength of test specimens." 2009.

[7] "EN 12390-6:2001 Testing hardened concrete. Tensile splitting strength of test specimens." 2001.

[8] T. El Maaddawy and K. Soudki, "A model for prediction of time from corrosion initiation to corrosion cracking," *Cem. Concr. Compos.*, vol. 29, no. 3, pp. 168–175, 2007.

[9] ASTM G1, "Standard Practice for Preparing , Cleaning , and Evaluating Corrosion Test," 1999.

[10] C. G. Berrocal, K. Lundgren, and I. Löfgren, "Corrosion of steel bars embedded in fibre reinforced concrete under chloride attack: State of the art," *Cem. Concr. Res.*, vol. 80, pp. 69–85, Feb. 2016.

[11] P. S. Mangat and K. Gurusamy, "Corrosion Resistance of Steel Fibres in Concrete under Marine Exposure," *Cem. Concr. Res.*, vol. 18, pp. 44–54, 1988.

International RILEM Conference on Materials, Systems and Structures in Civil Engineering
Conference segment on Service Life of Cement-Based Materials and Structures
22-24 August 2016, Technical University of Denmark, Lyngby, Denmark

WATER RELEASE PROCESS OF SUPERABSORBENT POLYMERS IN CEMENT PASTE AT EARLY AGE

Yujiang Wang [(1)(2)], Ming Li [(2)], Qian Tian [(2)]

(1) School of Materials Science and Engineering, Southeast University, China
(2) State Key Laboratory of High Performance Civil Engineering Materials, Jiangsu sobute new materials CO., LTD, China

Abstract
Internal curing by means of superabsorbent polymers (SAPs) is an effectively method to decrease the self-desiccation of high performance concrete. This paper focus on the water release process of SAPs in cement pastes at early age, which is an important aspect to understand the effectiveness of internal curing. In this paper, cement pastes with SAP were broken, and the particle sizes of the SAP were observed, at certain time intervals, meanwhile, the water release process was analyzed, according to the variation of the particle size of the SAPs. The results show that the SAPs starts to release water before initial setting, and, there's no obviously interspace between the SAP and cement matrix before final setting. Furthermore, the diameter of the SAPs becomes to be smaller than that of the surrounding pore, about 1h after final setting.

1. Introduction

High performance concrete (HPC) with low water to cement ratio (w/c) has been widely used in the world. However, a related issue in HPC with a low w/c is that of self-desiccation [1], which results in a considerable autogenous shrinkage. Internal curing by means of superabsorbent polymers (SAPs) that firstly proposed by Jensen and Hansen [2, 3] has been proved to be effectively to mitigate the self-desiccation as well as autogenous shrinkage HPC [4].
In general, the mechanisms of SAPs are as follows: SAPs adsorb water during the mixing of concrete. Thereafter, with hydration of the cement, the SAPs progressively releases its adsorption water, which migrates to the surrounding matrix. The migrated water inhibits the self-desiccation and decrease the autogenous shrinkage of HPC. Therefore, the water release process of the SAPs is an important aspect to understand the effectiveness of internal curing. In practical, the adsorption capacity of the SAPs in the paste needs to be studied, in order to characterize this process. Some methods have been applied for the determination of

absorbency of SAPs in the liquid (e.g., [5-7]). However, there is still lack of relationship of adsorption capacity of the SAPs in the paste and in solution. Trtik et al [8] applied neutron tomography to characterize the water adsorption/release of the SAPs in a cement paste with a w/c of 0.25 during the first day of hydration. In his study, the SAP particles was about 2 mm in the swollen state, which was much larger than the dimensions of the SAP that commonly used for internal curing. Furthermore, image analysis of the cross-section was used to determine the adsorption capacity in hardened cementitious paste (e.g., [9]). This method can only be implemented when the paste has certain strength, and the particle size of the SAP at different time can be hardly obtained. Moreover, some new methods such as NMR and x-ray computed tomography are expensive and complicated.
In this paper, a simple method is applied for characterization of adsorption capacity of the SAPs in the cement paste at early age, furthermore, water release process of the SAPs and the sizes of the pore that formed by SAPs are discussed.

2. Materials and methods

2.1 Materials

Ordinary Portland cement with 52.5 grade was used, whose oxide compositions were listed in table 1. A commercial polycarboxylate-based superplasticizer with 40% solid content was used for all mixtures.

Table 1: Composition of Portland cement (wt%)

SiO_2	Al_2O_3	Fe_2O_3	CaO	MgO	SO_3	K_2O	Na_2O	TiO_2
20.17	4.39	2.84	63.05	1.60	3.77	0.65	0.17	0.29

Superabsorbent polymers (SAPs) is covalently cross-linked acrylamide/acrylic acid copolymers by means of inverse suspension polymerization. The SAPs was treated by sieves, and the SAP with particle size of 100 – 105 μm was chosen for this study (Fig.1). The density of the SAP was 1310 kg/m^3.

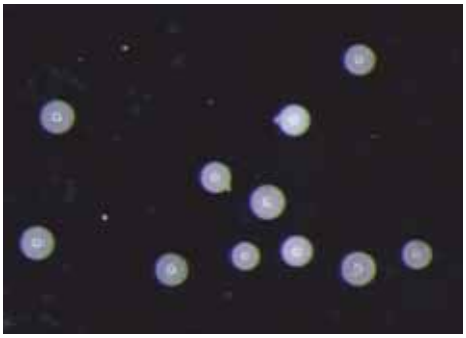

Fig.1 Image of SAPs sample at dry state

Water adsorption abilities of the SAP in distilled water and in synthesized pore solution were 72 g/g and 21g/g, respectively. The synthesized pore solution was composed of [Na^+] =400mmol/L, [K^+] =400mmol/L, [Ca^{2+}] =1 mmol/L, [SO_4^{2-}] =40 mmol/L, [OH^-] =722 mmol/L as shown in the reference [3]. The test procedures of water adsorption were as follows: certain amount of dried SAP samples were immersed into enough distilled water (or the synthetic pore solution) for 30 min. Then, the swollen hydrogel was filtered through a sieve with mesh sizes of 300 to remove the non-absorbed water. Finally, the water adsorption rate was calculated by the weight ratio of the SAP with and without adsorption water.

2.2 Pastes preparation

The cement pastes with w/c of 0.3 were prepared in the room with temperature of 20±2 ^oC, by mixing the solid powder with liquid for 2 min at low speed (140 ± 5 r/min) and a further 2 min at high speed (285 ± 10 r/min). The dosage of the SAPs and the superplasticizer were all 0.4%.

2.3 Absorption capacity of SAP in the pastes

The adsorption capacity of the SAP is determined by the volume increase between the vacuum dried state and the absorbing state. As shown in Fig.1, the shape of the SAP used in this paper is approximate to be spherical. Therefore, the volume of the SAPs with or without adsorption water is calculated from their average diameter. The SAPs particles in the cement paste are analyzed by a stereo optical microscope (NIKON SMZ 800), and the methods are as follows:

Before initial setting: in theoretical, the state of the SAP should be observed as soon as after mixing. However, in practical, it is difficult to do this for high workability of the cement paste and the effects of bleeding water between SAP particle and matrix. So, in this paper, the analysis is implemented 1h after mixing. At this time the workability of the paste can be ignored, and the results of isothermal calorimetry measurements indicated that the induction stage of the cement hydration was not over yet. In the test, the SAPs was carefully separated from the matrix under the stereo optical microscope, and the images of SAP were recorded. Furthermore, for a particular SAPs particle, the separating process is controlled in 30s, in order to decrease the effects of the environment on the adsorption capacity.

After initial setting: at this stage, the solid structure of the paste begins to form, and the strength of the pastes generate. In the test, the paste was bent to break off, and the SAPs particles on the fracture surface were observed. It should be noted that the measured diameter of the SAP particle may be smaller than its real value, because the SAP particle can be buried by the matrix. Therefore, during the measurements, the SAP particles that above the fracture surface were analyzed.

The adsorption capacity of the SAPs is calculated by equation (1).

$$S_{SAP} = (D_s^3 - D_0^3)\rho_w / (D_0^3 \rho_{SAP}) \quad (1)$$

Where D_s is the average diameters of the SAP particle in cement paste, D_0 is the average diameter of the SAPS particle at dry state, ρ_w and ρ_{SAP} are the density of water and SAPS, respectively.

In addition, a large number of repeat tests should be implemented, in order to obtain the ideal testing sample, although the above methods were relatively simple. Furthermore, the diameter of the SAP particle is measured by Image – Pro Plus.

3. Results and discussions

In this section, a part of images of the SAPs in cement paste at different time are presented.

3.1 images of the SAPs in the pastes

The separated SAPs particles are shown in Fig.1 at about 1h after mixing. In the figure, The SAPs particles can be observed clearly.

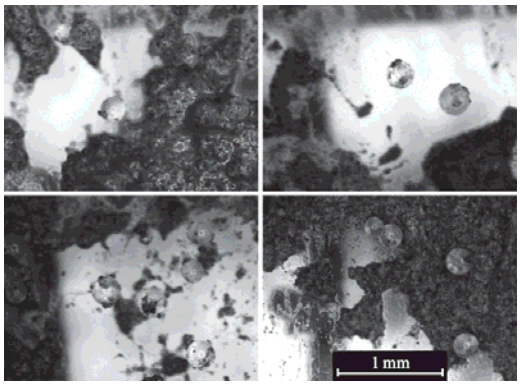

Fig.2 SAPs particles at about 1h after mixing

The SAPs particles on the fracture surface at the time of initial/final setting are shown in Fig.3, while the state of the SAPs particles that are partly buried by the matrix are shown in Fig.4.

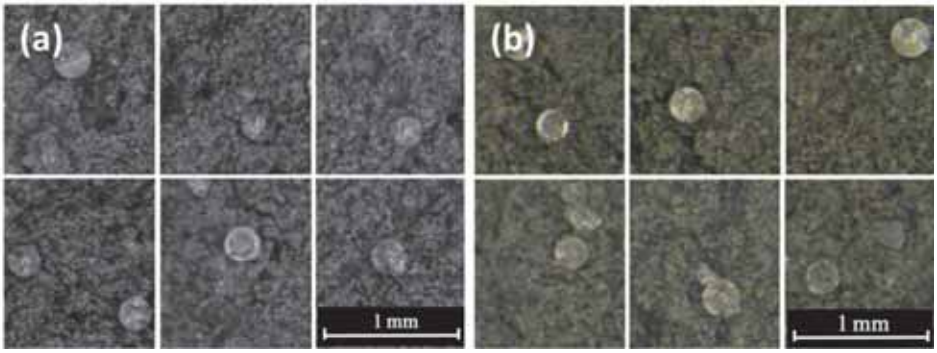

Fig.3 SAPs particles at initial and final setting: (a) initial setting (b)final setting

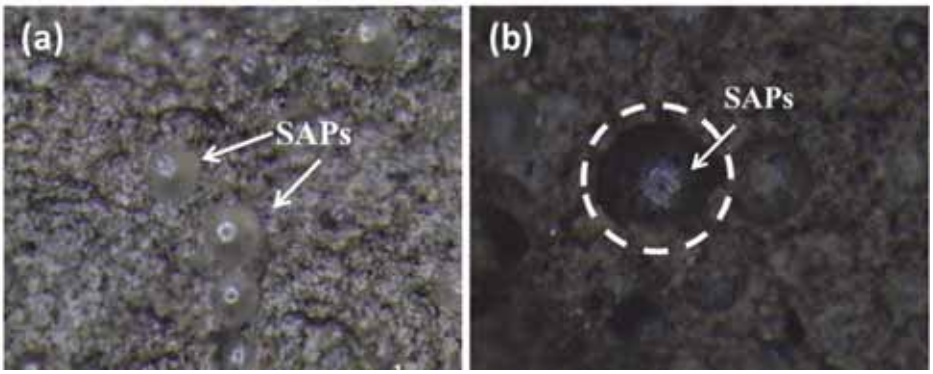

Fig.4 Combination of the SAPs with matrix at initial and final setting: (a) initial setting (b) final setting

The images of the SAPS in cement paste at approximately 1h after mixing are shown in Fig.5. The SAPs are visible as white, while the surrounding matrix appears gray, meanwhile, the obviously dark gray interspace between the SAPS particles and the matrix can be observed.

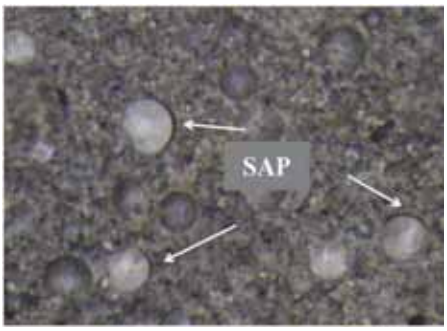

Fig.5 Combination of the SAPs with matrix at about 1h after final setting

3.2 Discussions

The diameter of the SAPS in cement paste is measured by Image – Pro Plus, and average diameter is also calculated. The results are shown in Fig.6.

From Fig.6, the adsorption capacity of SAPs in cement paste can be obtained:

(1) At about 1h after mixing, the average diameter of the SAPs increases about 2.63 times, which indicates that the adsorption capacity is about 13.10 g/g.

(2) The average diameters of the SAPs at initial and final setting increase about 2.37 and 2.33 times, respectively, and the corresponding adsorption capacity are 9.41 g/g and 8.94 g/g.

(3) At about 1h after final setting, the average diameters of the SAPS increases about 2.26 times, while the adsorption capacity is about 8.01 g/g.

The above results show that the SAPs starts to release water before initial setting. At initial setting, the capillary pressure of the paste is about 10 kPa [10], and the self- desiccation can be neglected. Before initial setting, water release of the SAPs can be attributed to the increase of the ion concentration of the pore solution with hydration of cement. After initial setting, the

effects of self- desiccation (decrease of relative humidity) begin to appear. And desorption of SAPs at different relative humidity has been studied by many researchers (e.g. [2]). Furthermore, Fig.6 shows an obvious increase of water release rate of the SAPs after final setting.

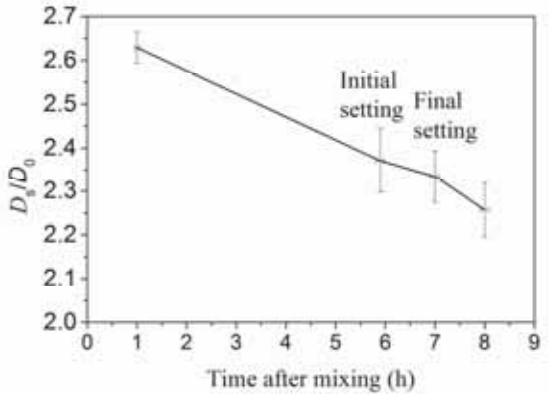

Fig.6 Average diameter of the SAPs particle

Meanwhile, during the process of water adsorption/release of the SAPs, the volume of the SAPs particle increases/decreases, and a pore that surrounding the SAPs particle forms. As shown in Fig.4, before final setting, there's no obvious interspace between the SAPs and matrix, which means that the diameter of the surrounding pores can be seen as same as that of the SAPS particle. The results also imply that the SAPs has less effect on the autogenous shrinkage of the pastes at this stage, due to there's no obvious unsaturated space forms. After final setting, as shown in Fig.5, the diameter of the surrounding pores is larger than that of the SAPs particle. Meanwhile, it can be deduced that the space between the SAPs and matrix is not partly saturated due to self-desiccation. In this case, autogenous shrinkage is inhibited by water migration from the SAPs to cement paste. As results, the diameter of the pore that surrounding the SAPs particle is not constant at early age.

4. Conclusions

In this paper, the state of SAPs (100-105μm in dry condition) in cement paste with w/c of 0.30 was observed by a stereo optical microscope, and the diameter of the SAPs particle was measured. Then, the adsoption capicity, water release process and the pores that formed by SAPs were studied. Main conclusions are as follows :

For the SAPS used in this paper, comparing to its dry state, the times of its diameter increases in cement paste at 1h after mixing, initial setting, final setting and 1h after final setting are 2.63, 2.37, 2.33, 2.26, respectively, while the corresponding adsorption capacity are 13.10 g/g , 9.41 g/g, 8.94 g/g and 8.01g/g, respectively. Results show that the SAPs release its adsorption water before initial setting, and release rate of adsorption water increase after final setting.

Before final setting, the particle combines closely with its surrounding matrix, which indicates that the diameter of the pores formed by the SAPs can be seen as same as that of the SAPs. After final setting, the diameter of the pores is larger than that of the SAPs particle. Results indicate the size of the pore that surrounding the SAPs particle is not constant.

Acknowledgements

This work is financially supported by National Basic Research Program of China (Grant No. 2015CB655105) and National Natural Science Foundation of China (Grant No. 51438003 and 51578268).

References

[1] Neville, A. M., Properties of Concrete, 4th Edition,Wiley (1996), 844
[2] Jensen, O. M. and Hansen, P. F., Water-entrained cement-based materials: I. Principles and theoretical background. Cem Concr Res, 31 (2001), 647-654
[3] Jensen, O. M. and Hansen, P. F., Water-entrained cement-based materials: II. Experimental observations. Cem Concr Res, 32 (2001), 973-978.
[4] Mechtcherine, V. and Reinhardt, H. W., Application of super absorbent polymers (SAP) in concrete construction, State-of-the-art Report Prepared by Technical Committee 225-SAP, Springer Science & Business Media (2012).
[5] Schröfl, C. et al, Relation between the molecular structure and the efficiency of superabsorbent polymers (SAP) as concrete admixture to mitigate autogenous shrinkage. Cem Concr Res, 42 (2012), 865-873.
[6] Jensen, O. M., Water absorption of superabsorbent polymers in a cementitious environment, RILEM proceedings pro 79 from the International RILEM Conference on Advances in Construction Materials Through Science and Engineering, Hong Kong (2011), 22-35
[7] Mechtcherine, V. et al, Effect of internal curing by using superabsorbent polymers (SAP) on autogenous shrinkage and other properties of a high-performance fine-grained concrete: results of a RILEM round-robin test. Mater Struct, 47 (2014), 541-562
[8] Trtik, P. et al, Neutron tomography measurements of water release from superabsorbent polymers in cement paste, RILEM proceedings pro 77 from the International RILEM conference on material science, Germany (2010), 6-10
[9] Justs, J. et al, Internal curing by superabsorbent polymers in ultra-high performance concrete. Cem Concr Res, 76 (2015), 82-90
[10] Tian, Q. et al, In-situ monitoring of setting of concrete based on pore water pressure measurement, Second international conference on microstructural-related durability of cementitious composites, The Netherlands (2012).

International RILEM Conference on Materials, Systems and Structures in Civil Engineering
Conference segment on Service Life of Cement-Based Materials and Structures
22-24 August 2016, Technical University of Denmark, Lyngby, Denmark

HARDENING INDUCED STRESSES IN VERY THICK CONCRETE MEMBERS – INSIGHTS FROM COMPREHENSIVE FE-STUDIES

Peter Joachim Heinrich [(1)], Dirk Schlicke [(1)]

(1) Graz University of Technology, Graz, Austria

Abstract
This contribution presents first results of comprehensive FE-studies on hardening-induced stress histories of very thick concrete members with compact dimensions. The motivation is to improve the understanding of their structural behaviour in order to provide an efficient but safe crack width control of such members. The strict application of current design rules would lead to very high reinforcement amounts, even though observations in practice indicate that serviceability can be ensured with much less reinforcement. Finally, the insights of these investigations will provide a basis on which efficient design rules can be developed for very thick concrete members. The FE-studies were conducted with a new constitutive law for hardening concrete whereby special regard was put on the influence of the member thickness, the ambient temperature as well as production conditions. In general, the results confirm the predominance of residual stresses or so called Eigenstresses in such structural elements, while restraint forces and restraint moments are of minor importance for usual subsoil conditions.

1. Introduction

Very thick concrete members experience remarkable temperature histories due to hardening since the majority of the heat, which is released during the exothermal cement hydration, is firstly stored in the interior of the member before it flows out very slow according to the limited thermal conductivity of the concrete. These temperature histories are characterized by transient temperature field changes consisting of uniformly (constant) in the cross section distributed parts, temperature gradients over the cross sections width and height as well as non-linear parts resulting from temperature differences between the interior and the surface regions of the member. The accompanying temperature deformations lead to thermal stresses according to the restraining situation. In general, very thick members usually have rather compact dimensions. Former investigations show that such members are predominantly stressed by the non-linear parts, which are almost completely restrained since the cross

section tends to remain plane. At the same time, real length changes due to constant parts and curvatures due to temperature gradients are hardly restrained. The main reason is the very high axial stiffness of the hardening member itself and the limited bending restraint of members with low length-to-height ratios.

Although the precise dimensions of hardening-induced residual stresses and their interaction with additional restraints due to seasonal temperature changes are needed for an efficient structural design of very thick and compact concrete members, this has not been investigated systematically yet. Neither national nor international design rules provide satisfying design rules of such special cases because they are rather based on empiricism than on mechanically consistent aspects, see [1]. Thus, the main aim of the presented studies is to develop a mechanically consistent design concept that takes geometric dimensions, boundary conditions and/or the material properties itself into account with special regard to the safety-concept of Eurocode 2 [2].

2. Calculation model

A reliable determination of the resulting stress distribution calls for a comprehensive time-step calculation model, which uses well-established material models as well as realistic boundary conditions. Here, a FE-based model is generated in the modular FE-framework SOFiSTiK. Its mesh is exemplified for the reference case of the study in Fig. 1. It can be seen that the mesh is refined in the surface regions because of the expected higher influence of the ambient temperature.

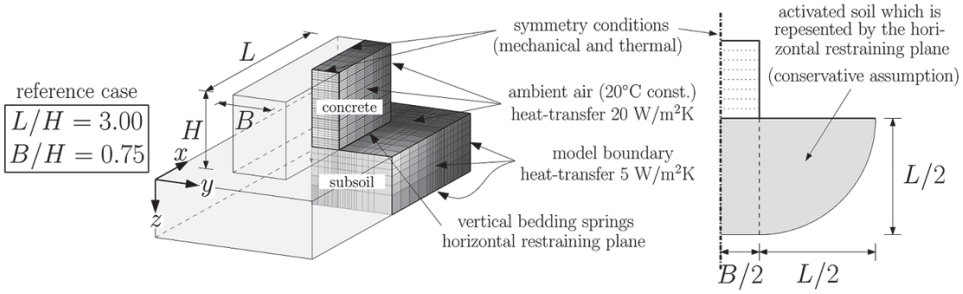

Figure 1: FE-Mesh

To generate a regular mesh, the included module SOFIMSHA uses given geometric node definitions. For each time-step, the module HYDRA determines the temperature-field in the structure. Later, the module ASE follows the procedure and calculates the resulting stresses, while it takes the temperature-field directly from HYDRA as thermal loading. The module SOFILOAD applies additional loads, e.g. further deformation impact from shrinking.
At this point, it should be mentioned that the calculation model was comprehensively verified by satisfying recalculations of in-situ monitorings of several mass concrete applications, e.g. a 4.0 m thick power plant slab or a 2.5 m thick chamber wall of a sluice. Further details are given in [3].

2.1 Structural idealization

The basic model consists of several 3D elements (8 nodes with linear shape functions) and it represents only a quarter of the whole structure. This reduces the complexity of the calculation and increases the speed of the whole simulation. Appropriate boundary conditions consider the symmetry as well as bedding and thermal conditions. During the temperature-field calculation, the modelled soil acts as heat storage. For the stress calculation, the soil body is replaced by a vertical bedding with non-linear compression-springs and horizontally arranged 2D elements (4 nodes with linear shape functions). The vertical bedding springs allow a realistic self-weight activation in cases of temperature gradients over the height as well as eccentric external restraint at the bottom of the member. This is of major importance in the considered cases with length-to-height ratios of three. The horizontal soil stiffness will be represented by the horizontally arranged 2D elements with regard to the activated soil below the member, as illustrated in Fig. 1.

The structures dimensions are fully variable in every direction; it is possible to control each surrounding condition and furthermore to investigate different types of construction-methods (e.g. fresh-in-fresh concrete placement in layers).

2.2 Simulated material behaviour and models used

The simulated material behaviour represents a typical mass concrete with a strength class of C35/45. All relevant properties of this concrete are extensively presented, cf. [3]. The hardening process of this concrete was simulated time-discretely with a thermo-mechanical coupling on basis of the so-called equivalent (effective) concrete age. The equivalent concrete age is a state variable that takes the maturity (influence of the real concrete temperature in the structure on the speed of hydration and hardening) into account. In the applied material model, this state variable controls the release of hydration heat by the JONASSON approach, the simultaneously developing strength properties of the hardening concrete by the WESCHE approach, the appearance of autogenous shrinkage as well as the viscoelastic behaviour according to the stress history by an approach proposed by SCHLICKE. In particular, the occurring viscoelastic strains of a time step were determined according to a time-discrete analysis of the EC2 creep curves and implemented independently for each element and direction in every time step. Further details are given in [3] and [4].

2.3. Analysis of the determined temperature and stress fields

The results of such an analysis are temperature and stress fields for each time step. On the one hand, it is important to know their absolute values in the material points (nodal results) to assess the risk of cracking. On the other hand, it is important to draw clear conclusions on the restraining situation as well as the type of cracking. Thus, it is important to analyse these fields with regard to uniformly (constant), gradual (linear) and non-linear distributed parts that can directly be related to stress resultants and residual stresses or so-called Eigenstresses. In general, it can be said that

- the *constant* temperature-part leads to an expansion or shortening of the member in the considered direction and this results in case of external restraint in a force or in case with eccentric restraining in a force and two bending moments (an inner moment according to the cross section compatibility and an outer moment according to self-weight activation)

- the *linear* temperature-part leads to a curvature of the cross section around the considered axis and this results in the case of restraint in another bending moment and
- the *non-linear* temperature-part is self-balanced within the cross section and has therefore no resultants. However, these deformations are usually almost fully restrained by the plane cross section, which leads to residual stresses, or so-called "Eigenstresses" which are also self-balanced within the cross section.

The following part gives a short summary of the separation of an arbitrary resulting temperature- or stress-field into the described parts. The procedure is in general the same for both of them. At this point it should be noted that the stress field changes are solely caused by the relative temperature field changes. For a comparison of both, the analysis of the temperature field changes has therefore to be done separately in each time step only for the change in this time step. The course of the specific part can then be drawn by summing up the single changes per time step. There exist a few ways to perform the temperature- or stress-field separation: [4] and [5] describe one simple and efficient way, if resulting temperature- or stress-fields are more or less "well" known in advance. If the resulting distributions are more "doubtful", it is better to use the way of a general (numerical) integration of the temperature- or stress-field over the whole cross-section. This is possible, if the temperature- or stress-field is known as a function $f(y, z)$. Here, a MATLAB-routine is used to determine these functions for each single time-step by the usage of a 2D-least-squares-fit for a fourth-order-polynomial in y and z. Fig. 2 illustrates the procedure of fitting, integration and separation respectively.

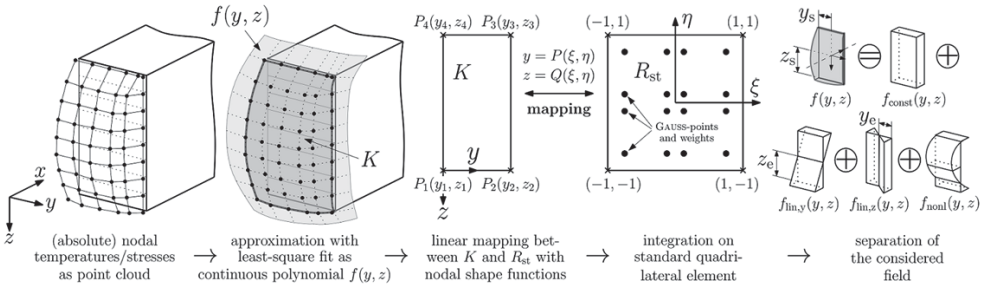

Figure 2: fitting, integration and separation of an arbitrary temperature- or stress-field

After the fitting, it is possible to integrate the received functions over the region K. A numerical well-established way is to use a 2D-GAUSSian quadrature formula of order N, given in (1). The mapping $x = P(\xi, \eta)$ and $y = Q(\xi, \eta)$ can be achieved conveniently by using nodal shape functions; $J(\xi, \eta)$ is the Jacobian of the transformation, and w_i, w_j are the weights, see [6].

$$\int \int_K f(y,z)\,\mathrm{d}y\mathrm{d}z \approx \sum_{i=1}^{N}\sum_{j=1}^{N} w_i \cdot w_j \cdot f\left(P(\xi_i,\xi_j), Q(\xi_i,\xi_j)\right) \cdot \left|J(\xi_i,\xi_j)\right| \tag{1}$$

Dividing (1) by the area of the considered cross-section leads to the resulting constant part, (2). Multiplying each point of (1) by its moment arm in z-direction and dividing it finally by the corresponding moment of inertia around the y-axis multiplied by the distance z_e from the

centre of gravity, leads to the corresponding linear part around y. The linear part around z could be gained analogous (3).

$$f_{\text{const}} = \frac{1}{A_{\text{c}}} \cdot \left(\sum_{i=1}^{N} \sum_{j=1}^{N} w_i \cdot w_j \cdot f\left(P(\xi_i, \xi_j), Q(\xi_i, \xi_j)\right) \cdot \left|J(\xi_i, \xi_j)\right| \right) \tag{2}$$

$$f_{\text{lin,y,e}} = \frac{1}{I_{\text{y}} \cdot z_{\text{e}}} \left(\sum_{i=1}^{N} \sum_{j=1}^{N} w_i \cdot w_j \cdot f\left(P(\xi_i, \xi_j), Q(\xi_i, \xi_j)\right) \cdot \left|J(\xi_i, \xi_j)\right| \cdot (z_{i,j} - z_{\text{s}}) \right) \tag{3}$$

Subtracting $f_{\text{const.}}(y, z)$, $f_{\text{lin.,y}}(y, z)$ and $f_{\text{lin.,z}}(y, z)$ from the original distribution $f(y, z)$ finally leads to the residual part $f_{\text{nonl.}}(y, z)$. Note that if the geometry and the boundary as well as the loading conditions are symmetric to one axis, the corresponding linear part is zero. For the present case, this is the case for the zx-plane so that $f_{\text{lin,z}}(y,z)$ is not pursued any further.

3. Case Study

3.1 Set up and investigated parameters

From a geometric point of view all considered cases represent a kind of "bloc", neither a slab (because $B \sim H$) nor a wall (because $H / B << 4$). Besides, all cases have an L / H-ratio of 3 which is the lower boundary to be considered as a wall – even if this is a common ratio to define the length of a construction stage respectively the distance between expansion joints of walls. The case study investigates the variation of several factors that are known to influence the temperature- and stress-field in ground slabs as well as in walls on foundations significantly. The variation of these factors varies within the range of typical conditions of practical cases. It is possible to summarize these conditions in three groups, which are geometry, initial and ambient temperatures and material/construction. Here, the presented results solely display the reference concrete C35/45. Fig. 3 shows the set up of the study and the different cases that have been simulated.

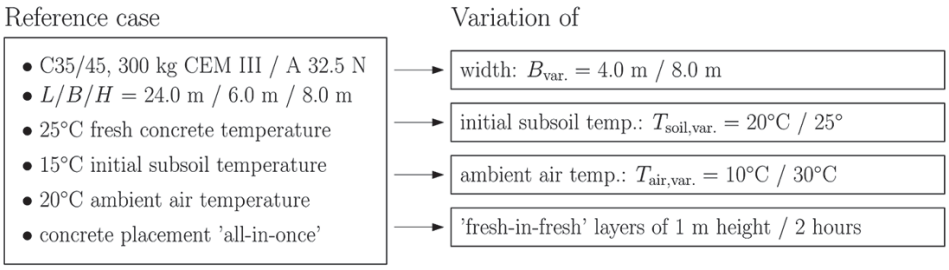

Figure 3: parameter variation of the case study

Any other boundary condition is similar in all cases. This refers mainly to the heat exchange over the free surfaces which is set with 20 W/m²K without any further consideration of formwork and its removal. The heat exchange at the bottom depends on the thermal properties

of the soil, whereby a conductivity of 1.6 W/Km and a thermal capacity of 1900 kJ/Km³ has been considered. The support in the bedding area was estimated according to the stiffness of common subsoil. In vertical direction, a stiffness of 10000 kN/m³ was considered in case of compression whereas the transfer of vertical tensile forces in the bedding was totally excluded with the non-linear bedding springs. In contrast to this very realistic assumption in vertical direction, the horizontal restraint in the bedding area was set up to a value, up to where macrocracking cannot be excluded for the reference case, as explained in section 3.2.

3.2 Results of the reference case

Fig. 4 gives the course of absolute results in selected nodes in the symmetry in length direction. It can be seen that the structure reaches its absolute temperature maximum at t = 160 h (~60°C), while temperature equalization occurs after about 5 months. As expected, there are huge temperature differences within the cross section with almost adiabatic conditions in the interior, whereas the temperatures on the free surfaces are very close to the ambient air temperature and do not pass 30°C. The temperatures at the bottom increase delayed but are still remarkable. The accompanying stresses reflect this temperature impacts only partly: on the one hand, the resulting stresses of a given temperature change in a time step increase during the hardening according to the stiffness evolution; on the other hand, viscoelastic effects distort the course considerably. But what one can see already is the predominance of Eigenstresses since almost all absolute stresses of the surface have an opposite sign as the interior stresses. Besides, the comparison of absolute stresses in Fig. 4 with the mean value of the lower limit of the tensile strength ($f_{ctk;0.05}$) indicates that cracking cannot be excluded in general.

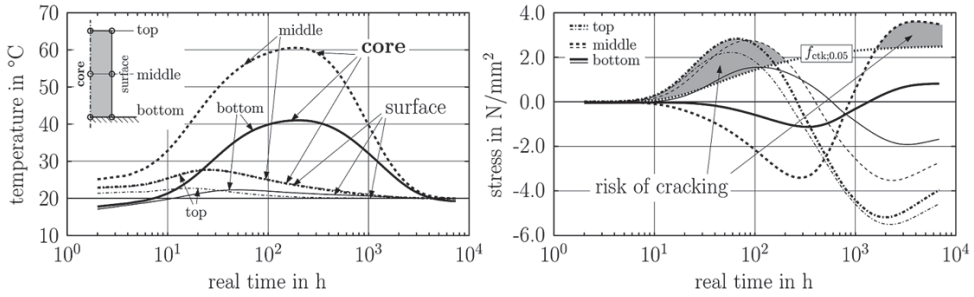

Figure 4: nodal results (temperature and stress) of the reference case

To clarify the type of cracking to be expected, Fig. 5 gives the course of constant and linear parts in the temperature and stress field history. Linear parts around the *z*-axis were not pursued since they are zero in the considered case due to symmetrical conditions over the width as remarked in section 2.3. As mentioned before, the horizontal restraining condition in the bedding area was iteratively increased up to where macrocracking would occur in the reference case. Hereby, the risk of macrocracking is assessed by the comparison between maximum stresses due to restraint force and restraint moments ($\sigma_{const.+lin.,y,bottom}$) with the mean value of the tensile strength (f_{ctm}). Eigenstresses, however, are neglected since they are self-balanced in the cross section and have therefore no significant influence on macrocracking. Further details on this assumption are given in [7] and [8].

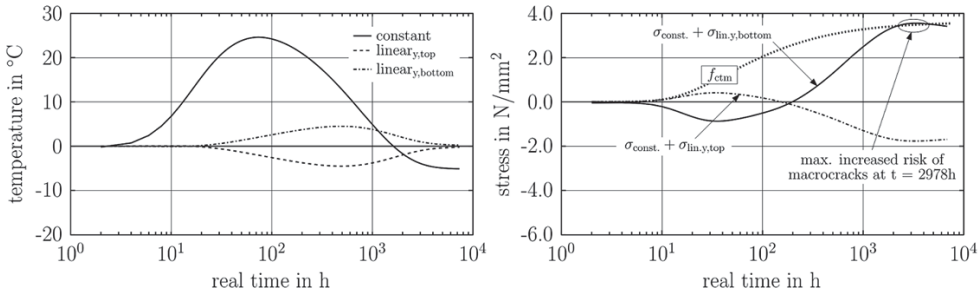

Figure 5: analysis of temperature and stress field changes of the reference case

As expected, macrocracking would predominantly result from the constant temperature changes, which are huge in these thick members. However, the eccentric restraining of these parts at the member bottom in combination with a limited *L* / *H*-ratio causes always a distinct linearity in the stress distribution over the height. Altogether, the risk of macrocracks is the highest at temperature equalization where restraint force and restraint moment superimpose both in tension at the bottom. The indicated risk of macrocracks is very low in this example since the required horizontal subsoil stiffness exceeds conventional conditions by several orders of magnitude (over 10 000 times higher in this case). Of course, this factor would vary since subsoil activation depends predominantly on the member length, however, increasing *L* / *H* would also reduce critical linearity in the stress distribution over the height and thus require higher horizontal stiffness.
In case of a realistic consideration of horizontal subsoil stiffness, restraint force and restraint moments are much smaller, whereas Eigenstresses would remain in the above shown size. Thus, the risk of macrocracks is usually very small, whereas the risk of microcracks as well as locally restricted cracks is still very high at early ages in the surface region. At temperature equalization, the risk of microcracks is also indicated in the interior, but this is overestimated since all calculations assume a fully linear-elastic cross section which is not the case for the surface region after early cracking.

3.3 Parameter variation

Fig. 6 and Fig. 7 show the determined courses of temperatures and stresses in the specific points at the surface and in the interior for all considered cases.

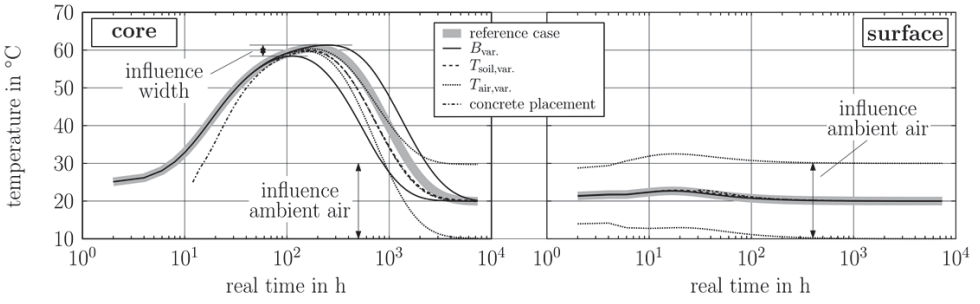

Figure 6: absolute temperatures in specific core- and surface-points

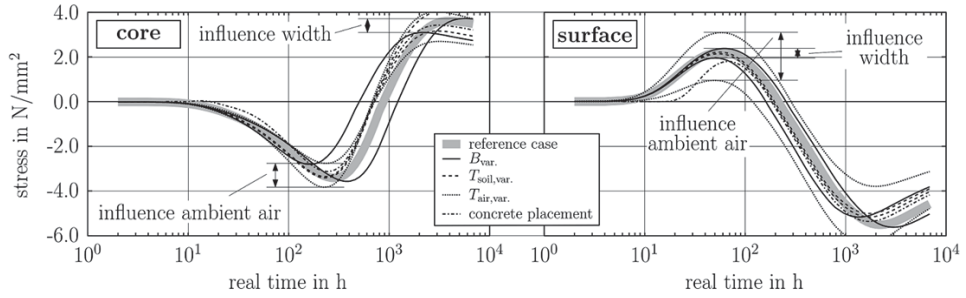

Figure 7: total stress in specific core-and surface-points

Fig. 8 and Fig. 9 show the course of the constant and linear temperature parts around the *y*-axis, whereby the stress resultants are illustrated in form of a superposition at the members bottom to see the most critical value in tension.

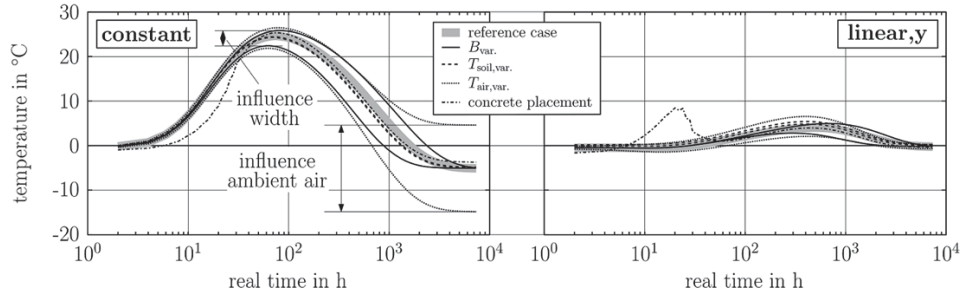

Figure 8: constant and linear (bottom) temperature part

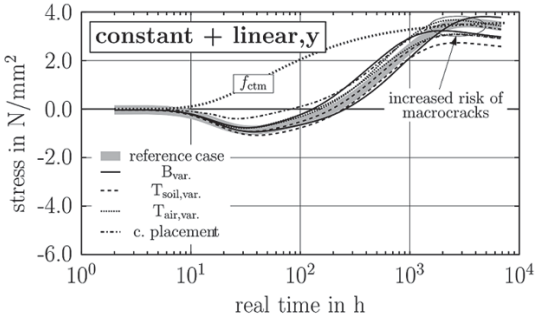

Figure 9: superposition of constant and linear (bottom) stress part

4. Discussion

4.1 General findings

As expected, very thick concrete members show a significant hardening-induced temperature history consisting of huge constant temperature changes as well as significant temperature

differences within the cross section. The accompanying stress field consists predominantly of Eigenstresses whereas the build up of critical restraint forces and restraint moments would require very high external restraint which is in the present case around 10 000 times higher than the horizontal stiffness of conventional soil.

4.2 Influence of member width

Although the member width has a clear influence on the duration of the whole process, the effect on absolute resulting stresses is small. The main reason is that there are almost adiabatic conditions in each member anyway so that the differences in the deformation impacts are insignificant.

4.3 Influence of subsoil temperature

The subsoil temperature has a significant influence on the temperature history at the bottom of the thick member. This affects the temperature gradients. Depending on the bending restraint this could increase the risk of bending cracks at temperature equalization in case of much stiffer subsoil. In the considered conditions this is of minor importance. Here, solely the effect on the absolute maximum temperature in the interior matters in terms of intensification of surface cracking.

4.4 Influence of ambient air temperature

Of course, the ambient air temperature has a significant influence on the temperature field. But as in the previous cases, the effect on the risk of macrocracking is rather small due to the limited external restraint. What can be said is that a delayed decrease of ambient air temperature after casting will have a negative effect on the intensity of surface cracking.

4.5 Influence of construction method

If the process of concrete placement is taken into account, the temperature and stress field are significantly influenced in the beginning. However, decisive stresses are comparable with the results without consideration of the process of concrete placement. Of course, this statement is only valid for temperature induced stresses. In reality, the construction process introduces high tensile stresses at the bottom due to the higher stiffness in the bottom layer when the new layer will be placed. However, the latter affects also the viscoelastic behaviour which depends on the absolute stresses.

5. Conclusion and Outlook

Considering the resulting temperature-parts, only the variation of width as well as the variation of the ambient temperature have a significant influence on the constant part. Linear parts were not influenced significantly in any case. Finally, it has to be outlined that none of the parameters has a high influence neither on the restraint force nor on the restraint moments. This leads to the conclusion that typical compact mass concrete members are predominantly stressed by Eigenstresses. The expected crack pattern of such members will be characterized by surface cracking, whereby these cracks may reach a depth up to 1.0 m.

It should be noted that all cases show huge constant temperature changes. A critical restraining of these deformations is very unlikely since it requires very high external restraint which is in the present case around 10 000 times higher than the horizontal stiffness of conventional soil. Of course, this factor would vary since subsoil activation depends

predominantly on the member length, however, the factor would also not decrease significantly for longer members since its size depends on the linearity in the stress distribution according to L / H as well. And even if a macrocrack could be triggered at the bottom, separating cracks over the whole member height can still be excluded for L / H ratios smaller or equal to three. The reason is that the stress distribution without Eigenstresses has in such cases still a distinct linearity due to the eccentric localization of the restraining condition at the bottom. Hereby, the top of the member is always significantly compressed when the tensile strength may be reached at the bottom, which gives cracks stopping by itself in the lower part of the member.

There have to be done further investigations, concerning the continuance of the present parametric study which should be expanded on more influence factors. Such factors are the investigation of various thermal boundary conditions (like retaining walls, or underwater structures), various geometrical conditions (mainly increasing L / H) or various bedding conditions.

Another essential step will be the superposition with further deformation impacts due to seasonal changes of ambient temperature.

Acknowledgement

This research project is funded by Austrian Research Promotion Agency (FFG), pr.-nr. 843489.

References

[1] Heinrich, J. P. and Schlicke, D.: Normative Regelungen zur unbewehrten Ausführung von massigen Betonbauteilen, In: Proceedings of 2. Grazer Betonkolloquium, Graz, (2014)

[2] EN 1992-1-1:2004 + AC:2008: Eurocode 2: Design of concrete structures - Part 1-1: General rules and rules for buildings

[3] Schlicke, D.: Mindestbewehrung für zwangbeanspruchten Beton, PhD thesis, Graz University of Technology (2014) http://lamp.tugraz.at/~karl/verlagspdf/buch_schlicke_25052016.pdf

[4] Schlicke, D.: Consideration of Viscoelasticity in Time Step FEM-Based Restraint Analyses of Hardening Concrete, Journal of Modern Physics 4 (2013), SCIRP, 9-14

[5] Eierle, B. and Schikora, K.: Zwang und Rissbildung infolge Hydrataionswärme – Grundlagen, Berechnungsmodelle und Tragverhalten, DAfStb Heft 512, Berlin (2000)

[6] Shaozhong, D.: Quadrature Formulas in Two Dimensions, online Lecture notes http://math2.uncc.edu/~shaodeng/TEACHING/math5172/Lectures/Lect_15.PDF (date of access: 11.04.2016), University of North Carolina at Charlotte (2010)

[7] Schlicke, D. and Tue, N. V.: Crack width control – verification of the deformation compatibility vs. covering the cracking force, Proceedings of MSSCE2016/Service Life Segment, Lyngby, Denmark (2016)

[8] Knoppik-Wróbel, A. and Schlicke, D.: Computational prediction of restraint-induced crack patterns in reinforced concrete walls. In: Proceedings of MSSCE2016 / Service Life Segment, Lyngby, Denmark (2016)

International RILEM Conference on Materials, Systems and Structures in Civil Engineering
Conference segment on Service Life of Cement-Based Materials and Structures
22-24 August 2016, Technical University of Denmark, Lyngby, Denmark

BENCHMARKING OF COMPLEX SYSTEMS: APPLICATION TO CEMENT BASED MATERIALS

Janez Perko [(1)], Diederik Jacques [(1)], Ravi A. Patel [(1)], Joan Govaerts [(1)]

(1) Belgian Nuclear Research Centre SCK•CEN, Mol, Belgium

Abstract
In modern science and engineering, computer modelling forms an inevitable part in the assessments of risk or engineering performance. With the increasing amount of experimental data and process knowledge also the complexity of underlying models increases. However, the increasing model complexity involves certain consequences. Firstly, increasing model complexity is prone to errors during numerical implementation. Secondly, each model definition requires a certain level of abstractions and conceptualizations of processes, parameters, boundary and/or initial conditions. Finally, the numerical simulations can induce non-physical behaviour when several processes are coupled together. Several approaches are possible to assure the quality of the numerical results and built confidence. For simple models analytical or closed-form solutions can be used for model verification. However, this situation is rarely true with complex systems. Alternative is to perform benchmarks with different numerical codes and different authors under the assumptions which allow for an adequate comparison. This paper summarizes some important elements of benchmarking which are underpinned by practical examples.

1. Introduction

Increasing computational power of computers, experimental data and process understanding open the route for increasing aspirations towards complex conceptual and numerical models. Although numerical modelling will lead to throughout process understanding, increasing model complexity carries certain threats such as higher probability for almost undetectable implementation errors. Further, numerical simulations can become unstable or induce non-physical behaviour when several processes are coupled together. This is typically the case when the coupled physical processes manifest themselves at different time scales, for example reactive transport with very different reaction rates, two-phase flow and similar. In order to assure the quality of numerical results, several approaches are possible. For geometrically

simple models with a limited number of processes and simple boundary conditions, analytical or closed-form solutions can be used for benchmarking. However, analytical solutions are rarely available for complex systems. An alternative approach is to numerically verify different codes by defining a well-defined benchmark. In modern terms, benchmarking represents an essential element for confidence building from the point of view of computational performance, verification and validation, uncertainty qualification and simulation process and data management.

The need for benchmarking of numerical codes exists from the early beginning of computer modelling. One of the first systematic benchmarking platforms, still active at present is the NAFEMS platform [1]. The focus of this platform is on the Finite Element Method (FEM) and the principal aims are to establish best practice in engineering simulation, to act as an advocate for the deployment of simulation and to improve the education and training in the use of simulation techniques. NAFEMS includes several technical modelling areas which encompass single physics benchmark, high performance computing and multiphysics problems. In the field of cement based materials, NAFEMS benchmarks mostly involve structural mechanics models. In a recent benchmarking initiative for subsurface environmental modelling [2] with focus a reactive transport also some examples related to cement based materials were proposed – decalcification of cracked cement [3] and interactions between cement and clay [4].

In this paper we discuss some pertinent lessons learned and challenges when defining and coordinating a benchmark problem of a complex system. First we discuss different types of benchmarking with their particular properties; next the attention is laid on defining indicators on the basis of which the results from benchmarking exercise can be compared. Another focus point of the discussion is on the level of complexity of the benchmark and the approach to alleviate too stringent conditions which would be difficult to follow by benchmark participants. By complexity we refer to properties related to geometry, processes, constitutive relationships or couplings. Some examples are given regarding the description of the benchmarking case. The paper concludes with practical organisational issues which need to be thought of when defining the benchmark. The cases presented in this paper are situated within the field of (reactive) transport problems. However, the conclusions and lessons learned can be easily applied to other physical domains.

2. Scope of benchmarking

As benchmarks can serve different purposes, their scope also varies. Benchmarks with simple geometry, single physics and no couplings can be used for the purpose of training. With a predefined set of simple tasks, the new user can get acquainted with the code. This type of benchmarks can also be used for verification of the correctness of newly developed code. However, this paper focusses to more complex problems involving coupling of different physics, spatial and temporal scales, reactions or constitutive models for which experimental validation is not straightforward or even almost impossible (e.g. large spatial and/or temporal scales, heterogeneity, amongst others). In this section we divide benchmarking exercise into three types which are specific in terms of problem description, indicators and approach.

2.1 Types of benchmarking

Benchmarking can be applied to different levels, depending on the indicators that needs to be tested. Hence, we here define three types of benchmarking; benchmarking of the numerical, the mathematical or the conceptual model. A benchmark can comprise one, two or all three benchmarking types. One has to bear in mind that the difference between models are more difficult to pinpoint when the benchmarking is on the conceptual level than when it is on the numerical level. The distinction between different types is not always clear because the choice of mathematical or constitutive model can also be seen as the conceptual choice. However, in this paper we consider the benchmarking as "conceptual" when different conceptual approach is used and not only different mathematical description.

Numerical benchmarking aims to test whether the mathematical model is correctly solved. Typically, this encompasses temporal or spatial discretization, integration scheme, numerical solution schemes or coupling procedures, either the coupling of different physics or the coupling of forcing terms (e.g. volumetric sources). This kind of benchmarking is often used for code development and for testing newly written numerical codes or new numerical methods to solve the governing partial differential equations (PDE). Boundary conditions, initial conditions, material properties, geometry and underlying physics with respective constitutive laws or reactive network are precisely defined. In principle the differences between different models should be small. The differences in results may arise due to wrong implementation, instabilities or discretization errors. However, these differences are relatively easy to analyse and amend.

Benchmarking of mathematical models focuses on the question “is the mathematical description of the physical reality adequate”. Here the exact PDE, couplings, constitutive laws are not necessarily given in the benchmarking description. For example, fluid flow in porous media at the continuum scale is usually defined by Darcy’s equation (1) which in isotropic porous media and under steady-state conditions is given as:

$$\nabla p = -{}^{\mu}/_{\kappa}\, \boldsymbol{q} + \boldsymbol{F} \tag{1}$$

where $\boldsymbol{q}$ is Darcy’s flux [m/s], p is pressure [Pa], $\boldsymbol{F}$ is forcing term [Pa/m], κ is permeability of a porous medium [m^2] and μ is viscosity [Pa·s]. The Darcy’s equation describes water flow in porous media as long as the flow is sufficiently slow. For porous media with high porosities and for larger pressure gradients [5] other formulations can be used, such as the Darcy-Brinkman with an additional effective viscosity μ_{eff} as:

$$\nabla p = -{}^{\mu}/_{\kappa}\, \boldsymbol{q} + \nabla \cdot (\mu_{eff} \nabla \boldsymbol{q}) + \boldsymbol{F} \tag{2}$$

or Darcy-Forscheimmer [6] formulations which include viscous dissipation or even complete Navier-Stokes equation where the porous structure is explicitly represented. The influence and sensitivity of assumptions involved in different mathematical models can be evaluated. Another example is the tortuosity factor to describe diffusion in cement-based materials. Instead of invoking a simple Archie’s relationship (see equation (5) further), alternative formulations, alternative models accounting for a percolation threshold of the cement matrix can be used.

Usually models with low "intensity" (e.g. low Reynolds number, low Peclet number) tend to be insensitive to the choice of the mathematical model. However, when processes become more intensive, the solution can progressively diverge between the models. This is nicely demonstrated by a numerical exercise performed for the problem of melting from an isothermal vertical wall [7]. While the results between 13 models clearly overlapped for low Pr and Ra numbers, the patterns became completely different for different models with higher Ra number. Differences further increased with increase in Pr number.

Finally, benchmarking of the conceptual model is foreseen to answer whether the governing processes are adequately captured, for example in terms of how the heterogeneities are represented in the model. The only defined information is limited to boundary and initial conditions. Depending on the type of problem, also material properties are given, but they can be the part of the conceptual benchmark itself. For example, when benchmark includes the comparison between an explicit microstructural model and a continuum model, material properties are not included in the benchmark definition. In the continuum model the material properties are averaged, while in the microstructural model each phase can have a different property. Benchmarking of different microstructural models (so called integrated kinetic models) used for cement paste [8] also belong to this conceptual model benchmarking type. Namely the microstructure, although based on the same initial clinker properties and water-to-cement ratio can give different mineral distribution and different percolation threshold when based on vector or voxel hydration model [9]. Another aspect of benchmarking of the conceptual model is related to model abstraction in terms of complexity of processes. For example, the use of a geochemical solver in reactive transport modelling often takes more computational resources than the transport modelling part especially when the reaction network is complex. One way to alleviate this computational effort is to make an abstraction of the reaction network in a way that speciation depends on few independent variables. In case of cement, the pore water Ca concentration can be determined on the basis of solid Ca or alternatively by Si/Ca ratio in solid [10]. Another possible conceptualization relates to the decrease of dimensionality, e.g. modelling in 2D or 1D spatial dimensions. Table 1 gives an overview of the defined parameters in order to perform different types of benchmarking.

Table 1: Overview of required information for different benchmark types. Brackets are optional.

Type benchmarking	Numerical	Mathematical	Conceptual
Geometry	✓	✓	(✓)
Discretisation		(✓)	
Boundary conditions	✓	✓	✓
Initial conditions	✓	✓	✓
Material properties	✓	✓	(✓)
PDE	✓		
Coupling			
Constitutive laws	✓		

Let us demonstrate these definitions on an example of simulation of carbonation front in concrete. In the first instance we can benchmark the numerical model. This is preferred because the problem of carbonation is quite complex [11]. In this case we would choose for continuum model where we specify which PDEs need to be solved (e.g. advection-dispersion equation, Richards equation for water transport). Further we would define a geochemical model and reaction network (species, thermodynamic constants, activity correction model) and constitutive relations (e.g. tortuosity, porosity). In the next step the problem could be solved by different approaches to determine water retention characteristics or alternative constitutive relations. In the last step, benchmarking of the conceptual model, the only defined properties would be boundary conditions (RH in atmosphere, CO2 concentration), concrete/cement (w/c, aggregate volume, amount of cement, cement composition (clinker composition)). However, the problem could be solved in different ways, such as pore-scale model, continuum model…
Often, especially when dealing with complex problems, all three types are represented in the same benchmarking exercise because of different capabilities, options and available specific processes or constitutive laws of the numerical codes involved. For example, in a benchmarking exercise which dealt with the decalcification of cracked cement structures [3] material properties, boundary conditions, initial conditions, reaction network, geometry, PDE and constitutive relations were given. This set of given data is sufficient to perform a benchmarking of a numerical model since PDE solvers were different. The second type of benchmarking was introduced through the representation of C-S-H phases. While some codes used several pure phases to represent the decrease of Ca/Si ratio during Ca leaching, other codes used solid-solutions. Some codes involved also differed in the way they solve the geochemical system such as solving a system of mass action laws (PHREEQC [12], ORCHESTRA [13]), or with a Gibbs free energy minimization approach (GEM selector [14]), or utilizing different coupling approaches between geochemistry and transport such as an sequential non-iterative operator-splitting approach (SC3K (iPhreeqc-COMSOL) or OGS-GEM) or global-implicit (MIN3P [15]). The conceptual part of benchmarking was represented through the crack in the domain which has been conceptualized differently within different models. The reason was that a crack is typically a geometrically small feature which required finer discretization that not all codes could effectively solve. In some cases, the crack was approximated by a larger opening with the properties of the defined crack, in some cases was modelled as an implicit boundary type feature and in other cases a very fine discretization was used. As a result of the problem complexity it was not always possible to univocally identify the reason for a differences between involved codes.

2.2 Indicators

In any benchmarking it is very important to define the indicators on which the comparison is based. Although this seems to be an easy and straightforward task, it plays a crucial role in the quality of benchmarking. Again, the choice of indicators depends on the type of benchmarking, complexity of the problem including its dimensionality. The main indicator of benchmarking a numerical model is usually the primary variable at a defined location (and time when the model is transient). For example, the NAFEMS benchmark for a 2D heat conduction problem [16] (Figure 1) specifies beside the exact boundary and initial conditions, also the point where the primary variable (temperature in this case) is recorded. Also, the formula to calculate the accuracy and model performance are typically defined.

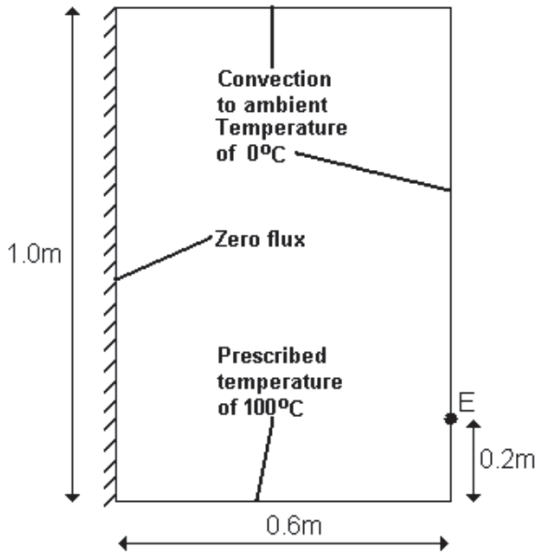

Figure 1. Benchmark indicators for steady-state numerical model benchmark.

In the case of a transient model, a time series at a certain point can be given as an indicator or alternatively, the field solution at a specified time either for the dimensionality of the benchmark (although more difficult in 3D and is usually not used) or a reduced dimensionality such as a 2D slice for a 3D problem or a 1D for a 2D or 3D problem. The choice of the location a profile is not trivial because the "most sensitive" location changes with time. Typically, it should be in the most sensitive region which needs to be tested in advance (for example with different discretization). In dynamic systems, a good practice is to choose the profile such that it covers the largest gradients of a primary variable.
On the other hand, when the conceptual model is compared, not all primary variables can always be compared. Consider two microstructural integrated kinetic models which calculate the hardened cement paste from the same clinker properties (fineness, composition) and water-to-cement ratio but with a different conceptual model of hydration. At the same degree of hydration, they give the same capillary porosity and volume of hydration products. Hence comparing the “primary” variables porosity would give a very good correspondence. If a concentration gradient of non-sorbing species is applied, the diffusion properties of the material can be obtained. However, it is not useful to compare solute concentration at the same point in space because that specific point could be occupied by liquid or solid in different models. Therefore, we have to use averaged properties over a predefined surface or within a predefined volume. Figure 2 gives an example of the percolation threshold differences for two models with the same boundary conditions. The figure also demonstrates that the correspondence of a primary (porosity) or a derived variable (here the percolation threshold which affects diffusivity and permeability) between two conceptual model can differ.

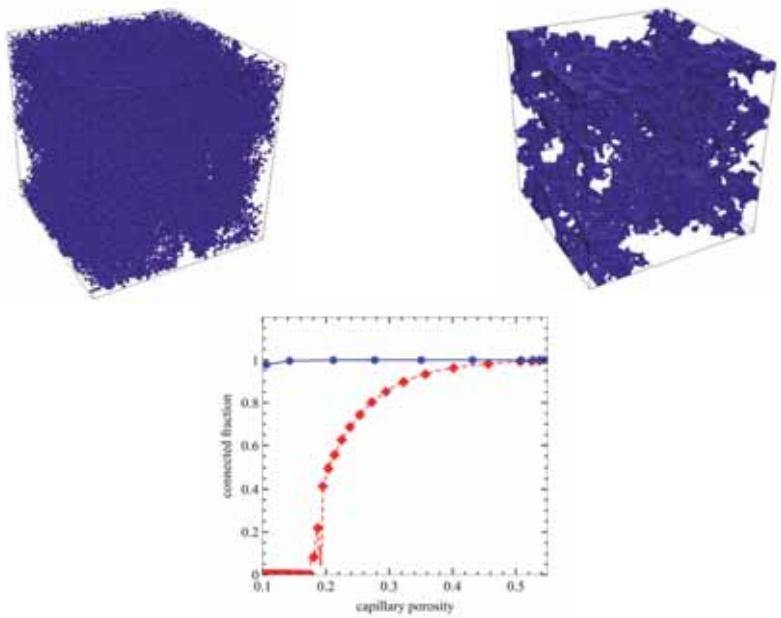

Figure 2. Benchmarking of two microstructural models. Capillary structure (top), percolation threshold (bottom)

For mixed benchmarking problems (numerical, mathematical, conceptual) it is advisable to define several indicators, some of which are related to the primary variable and others to a derived values. For example, in cement systems pH is buffered by soluble phases such as portlandite and simulated pH profiles will be similar between the different models (see for example [3]). On the other hand, the dissolved calcium profiles and porosity profiles may differ considerably due to the sensitivity of parameters in liquid regions close to solids. Hence, in this case it is useful to use the most sensitive indicator (e.g. porosity) for the comparison.
Comparison can be made qualitatively, for example with comparing different profiles, or – preferably – by numerical values indicating the maximum, averaged indicator variable value or indicator variable at a defined time(s). However the exact way of comparison has to be defined by the benchmark leader as the spectra of benchmarking problems can be large.

3. Tips and tricks

In this section we list some salient experiences from benchmark exercises in order to provide the reader with points of attention when designing a benchmark.

3.1 Difficulty

The complexity of benchmarks increases owing to the amount of experimental data, the level of process knowledge and the maturity of numerous numerical methods. Nowadays, the focus

is laid on the coupled multiphysics problems. However, most of the codes are specialised towards a given process or sub-set of processes and may not be capable of solving many complex couplings. Moreover, complex models require more time to implement. On the other hand, benchmark author(s) in most cases do not know who will participate in a benchmark and what are the capabilities of the participants/codes. Absolute compliance with lowest common denominator usually leads to over-simplification and in most cases the point of benchmarking is not met.
To alleviate the above-mentioned difficulties, it is advised to define benchmark in consecutive steps using a **graded difficulty approach.** The first step might begin with numerical benchmarking with low intensity processes, continuing by more difficult physical conditions (i.e. more intense processes), additional constitutive relations or coupling with additional physics to continue with the mathematical and/or conceptual benchmarking. Indicators could be defined differently for each steps. In this way more authors can participate because they can define the ability and time devoted to a benchmark.

3.2 Description

All elements need to be explicitly defined by equation and not by reference. Poorly defined problem may lead to wrong interpretations. This is especially true with more complex problems because same conclusions can be a consequence of different processes or parameters.
For demonstration purpose, consider the diffusion equation (3)

$$\theta \frac{\partial C}{\partial t} = -\nabla \cdot \left(-\theta D_p \nabla C\right) + S \tag{3}$$

where θ is porosity [-], D_p is the pore water diffusion coefficient [m²/s] and S is a volumetric source [mass/s].

Some models use the formulation with effective diffusivity D_e which is defined as $D_e = \theta D_p$

$$\theta \frac{\partial C}{\partial t} = -\nabla \cdot (-D_e \nabla C) + S \tag{4}$$

Now consider that porosity changes and the tortuosity also changes with porosity. Change in pore diffusion as a function of porosity is often described by Archie's relation that can be introduced in Eq. (3) as variable pore diffusion$D_p(\theta)$ defined as

$$D_p(\theta) = D_p(\theta_0)\left(\frac{\theta}{\theta_0}\right)^a \tag{5}$$

where θ_0 is initial porosity [-] and a is the cementation factor. On the other hand, the formulation in Eq. (4) gives the following variable effective diffusion $D_e(\theta)$ relation $D_e(\theta) = D_e(\theta_0)\left(\frac{\theta}{\theta_0}\right)^m$. We use here exponent m to denote a different value as a. Knowing the definition of effective diffusivity $D_e(\theta) = \theta D_p(\theta)$ we can write
$\theta D_p(\theta) = \theta_0 D_p(\theta_0)\left(\frac{\theta}{\theta_0}\right)^m$ and after rearranging

$$D_p(\theta) = D_p(\theta_0)\left(\frac{\theta}{\theta_0}\right)^{m-1} \tag{6}$$

or comparing equations (5) and (6) this gives the relation $a = m - 1$. In other words, the cementation factor given for equation (3) should be adapted if the code uses formulation (4).

Keep in mind, that especially definitions related to material properties can have progressively large impact on the numerical solution with time. The reason for this is that the solution has a positive response to material properties changes. For example higher diffusion coefficient of chemically leached concrete results in faster dissolution which, in turn, increases diffusion coefficient. Consequently the differences increase cumulatively with time.

3.3 Rules of the game

Benchmarking is a living-interacting process which includes more than one participant. It is difficult to estimate what the available time and capabilities of participants and numerical codes are. It is likely that the benchmark participants further shape the initial proposal with their own suggestions mostly closely related to their numerical code. This usually improves the quality, but the time when the problem definition is "cemented" should be clearly communicated. It is the leader who decides which changes will be implemented. Participants who already performed calculations are reluctant to repeat the same calculations when the problem definition changes!

Another difficulty is to define the number of iterations and interactions between participants. There is a possibility to demand a blind benchmark where participants do not know the results of other participants. In practice this is difficult to manage because commonly a sharepoint is used to collect data. Viewing the results, the participants might reconsider some modelling choices (nobody wants to have the “worse” code) to be more in-line with the majority of participants. This, however, may lead to loss of important information on why the differences initially occurred. Hence, be sure to record all improvements during the benchmarking process as this might be valuable information on the preferred approach used.

4. Conclusions

In this paper we tried to share some experiences from different benchmarking activities. The examples in this paper are limited in terms of physics involved but the principles are similar when dealing with other physical systems (e.g. structural mechanics). A benchmarking exercise begins with the question what do we want to benchmark? As discussed here, there is a big difference in problem definition as well as the indicators used whether the aim of benchmark is to test the ability of a code to solve complex coupled problem or to test which approach better describes experimental evidences. Preferably, each benchmark exercise should include a graded approach where different benchmark types or complexities are added step-by-step. In this way also the differences are easier to interpret. Moreover, participants can choose into which levels of benchmark they want or are able to participate. Secondly, we discussed the need for a good problem description with some practical examples. This includes a clear definition of all parameters and their meaning to avoid different interpretations and indicators we want to test or compare. This is complemented by some practical guidelines and lessons learned during the past benchmark exercises.

References

[1] NAFEMS, The International Association for the Engineering Modelling, http://www.nafems.org/
[2] Steefel, C.I., Appelo, C.A.J., Arora, B., Jacques, D., Kalbacher, T., Kolditz, O., Lagneau, V., Lichtner, P.C., Mayer, K.U., Meeussen, J.C.L., Molins, S., Moulton, D., Shao, H., Šimůnek, J., Spycher, N., Yabusaki, S.B., Yeh, G.T. (2014) Reactive transport codes for subsurface environmental simulation, Computational Geosciences, DOI: 10.1007/s10596-014-9443-x
[3] Perko, J., Mayer, K. U., Kosakowski, G., De Windt, L., Govaerts, J., Jacques, D., Su, D., Meeussen, J.C.L., Decalcification of cracked cement structures, Computational Geosciences, 19 (2015), pp 673-693.
[4] Marty, N. C. M., O. Bildstein, P. Blanc, F. Claret, B. Cochepin, E. C. Gaucher, D. Jacques, J.-E. Lartigue, S. Liu, K. U. Mayer, J. C. L. Meeussen, I. Munier, I. Pointeau, D. Su and C. Steefel, Benchmarks for multicomponent reactive transport across a cement/clay interface. Computational Geosciences 19 (3), 635-653 (2015).
[5] Bear, J., Bachmat, Y., Introduction to Modeling of Transport Phenomena in Porous Media, Springer, New York, (1990).
[6] Nield, D.A., Bejan, A., Convection in porous media, Springer, New York, (1998).
[7] Gobin, D, Le Quéré, P, Melting from an isothermal vertical wall. Synthesis of a numerical comparison exercise, Computer Assisted Mechanics and Eng Sciences 7 (2000), 289-306.
[8] Patel, R.A., Effective diffusivity of cement pastes from virtual microstructures: role of gel porosity and capillary pore percolation (submitted)
[9] Ye, G., Percolation of capillary pores in hardening cement pastes, Cement and Concrete Research, 35(1), 167-176 (2005)
[10] Perko, J., Seetharam, S.C., Jacques, D., Mallants D., Modelling Long-term Chemical Degradation of a Concrete Container under Near Surface Disposal Conditions, In proceeding of the 1st International Symposium on Cement-Based Materials for Nuclear Wastes, 2011, Avignon, France (2011).
[11] Phung, Q. T., Maes, N., Jacques, D., De Schutter, G., Ye, G., Perko, J., Modelling the carbonation of cement pastes under a CO2 pressure gradient considering both diffusive and convective transport, Construction and Building Materials 114, 333-351 (2016).
[12] Parkhurst, D.L., Appelo, C.A.J.: User's guide to PHREEQC (version 2) - a computer program for speciation, reaction-path, 1D-transport, and inverse geochemical calculations. US Geol. Surv. Water Resour. Inv. Rep. 99-4259, 312 (1999)
[13] Meeussen, J.C.L., ORCHESTRA: An object-oriented framework for implementing chemical equilibrium models. Environ Sci. Technol. 37, 1175–1182 (2003)
[14] Kulik D.A., Wagner T., Dmytrieva S.V., Kosakowski G., Hingerl F.F., Chudnenko K.V., Berner U.: GEM-Selektor geochemical modeling package: Numerical kernel GEMS3K for coupled simulation codes. Computational Geosciences. 17, 1-24 (2013).
[15] Mayer, K.U., Frind, E.O., Blowes, D.W.: Multicomponent reactive transport modeling in variably saturated porous media using a generalized formulation for kinetically controlled reactions. Water Resour Res. 38, (2002)
[16] Barlow, J. and Davies, G.A.O., Selected FE Benchmarks in Structural and Thermal Analysis, NAFEMS (National Agency for Finite Element Methods & Standards), National Engineering Laboratory, Glasgow, U. K.(1987)

International RILEM Conference on Materials, Systems and Structures in Civil Engineering
Conference segment on Service Life of Cement-Based Materials and Structures
22-24 August 2016, Technical University of Denmark, Lyngby, Denmark

A NEW ANALYTICAL APPROACH IN MODELLING OF CRACKING OF RC MEMBERS

Gintaris Kaklauskas [(1)], Regimantas Ramanauskas [(1)]

(1) Vilnius Gediminas Technical University, Vilnius, Lithuania

Abstract
Cracking is one of the most complicated phenomena of concrete structures. Multiple theoretical models have been proposed to predict cracking characteristics, but most rely on empiricism. The present paper proposes a simple, mechanically sound and transparent analytical approach for crack distance analysis of RC ties. The philosophy behind the proposed methodology is to establish the mean crack spacing through the compatibility of the discrete cracking and smeared cracking approaches. The mean crack spacing is obtained by equating the mean strains of both approaches. The bond stress-transfer approach governs the strain distribution of the reinforcement between the consecutive cracks, whereas the smeared approach provides the estimated mean strain of the element. The mean crack spacing can be determined for any bar diameter and reinforcement ratio combination in relation to a single mean crack distance established experimentally for the reference RC member. To ensure compatibility between the bond stresses and the applied load, the concept of damage zones is introduced: bond in the area adjacent to the cracks is considered to be fully damaged. A mean crack spacing model derived using the load-strain analysis method of the Eurocode 2 was shown to be in good agreement with experimental data of RC ties.

1. Introduction

Predicting cracking behaviour of reinforced concrete elements has always been a very difficult and highly inaccurate process. Numerous aspects influence this behaviour, with some key ones such as the interaction between reinforcement and surrounding concrete, spatial distribution of aggregates within the RC prism, redistribution of stresses within the element after every newly appeared crack. In general, the highly non-linear nature is the predominant reason why current cracking investigation methods rely on high degrees of empiricism. While many approaches exist, most can be grouped into two distinct categories, where the first is

directly related to the reinforcement cover height and uses the following generalized expression for crack width [1]:

$$w = k_2 \cdot c \tag{1}$$

where k_2 is again an empirical coefficient and c is the reinforcement concrete cover

The other group is based on concrete and reinforcement bond, often used in design codes and considered a classical approach [2]. The generalized form of this group is:

$$w = k_1 \cdot \frac{\emptyset_s}{\rho} \cdot \varepsilon \tag{2}$$

where k_1 is an empirical coefficient, $\emptyset_s$ is the diameter of reinforcement, ρ is the reinforcement ratio and ε is the average reinforcement strain value.

Variations of these groups mostly alter the empirical coefficients or sometimes introduce additional parameters such as reinforcement spacing within the RC element [3], but ultimately fail to provide consistent crack spacing results.

A new approach is presented by the authors for predicting crack spacing of RC ties that circumvents the reliance on empirical constants. The method is intended for the stabilized cracking stage. Exploring crack spacing through combination of two distinct approaches, the smeared crack and the stress-transfer approach enables to take full advantage of the benefits of both of these methods, as the former provides knowledge of the mean strains and the latter – strain distribution between adjacent cracks. In order to ensure compatibility of these distinct methods mean strains of both said methods must be equal. Additionally, concepts of damage and effective zones are introduced, that exhibit different strain distribution behaviour, due to the assumption of fully damaged bond in the damage zones. The aim of this paper is to provide a new methodology for the evaluation of the cracking behaviour of concrete elements and to encourage scientific discussion of this topic to ensure future development of the ideas presented herein, as these ideas are quite new and are in need of a solid foundation.

2. Basic principles and assumptions of the modelling approach

2.1 Compatibility of the discrete and the smeared crack approaches.

The key principle behind the approach is to combine the discrete and smeared crack approaches through the equality of the mean strains. By ensuring that the mean strains obtained by these methods are identical, full advantage of both approaches is exploited, thereby the mean crack spacing $l_{cr,m}$ can be obtained from the strain distribution obtain from the stress-transfer approach.

2.2 Introduction of the effective and the damage zones.

The distance between two consecutive cracks is divided into two separate regions defined by different strain behaviours. The regions next to the cracks are called the *damage zones*. The bond between the concrete and reinforcement bar is damaged due to local damage effects in

the concrete surrounding the reinforcement bar, thus the strains cannot be defined by the same shape function as for the undamaged parts (Fig. 1). The length of these *damage zones* is further denoted by l_d. The remaining part with undamaged bond is called the *effective zone* l_{eff}. Reinforcement strains within this region are defined by a known shape function:

$$\varepsilon_s(x) = \varepsilon_0 + a_1 x \tag{3}$$

where $\varepsilon_s(x)$ is the reinforcement strains at distance x from the centre of the segment between cracks, ε_0 is strain value at the said centre and a_1 is the slope of the strain curve.

For simplification, the bond in the damage zones is assumed to be fully damaged, i.e. not able to transfer any stresses between reinforcement and the surrounding concrete, therefore reinforcement strains would remain constant and equal to strains within the crack. The distance between cracks l_{cr} can further be expressed through these damage zones and the effective zone as:

$$l_{cr} = l_{eff} + 2l_d \tag{4}$$

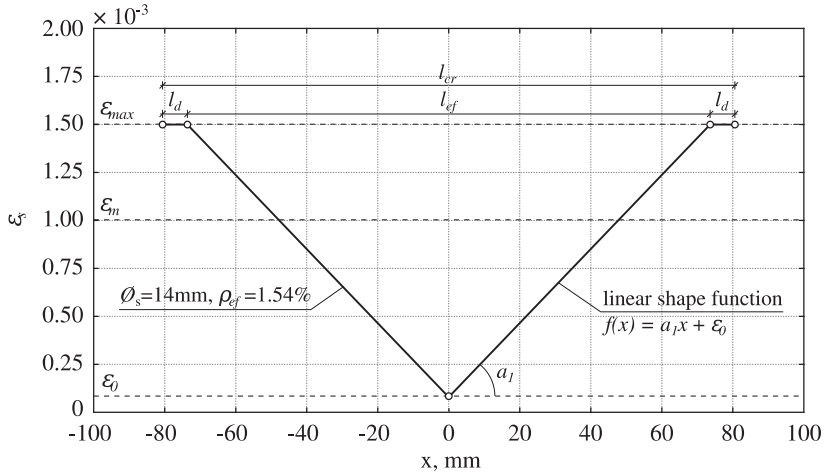

Figure 1. Strain profiles composed of the effective and damage zones

The length of the damage zone needs to be known in order to take full benefit of the approach suggested in this paper. In order to obtain a quantitative expression for the damage zone length, a first order polynomial as given in Eq. (3) and similarly proposed by Marti et al. [4] is used for approximating the effective zone. The reinforcement bar experimental strain profile data of a 400mm length RC prism published by Houde [5] is further used as the basis for the explanation of the procedure. Since the strain data is unsymmetrical, as can be easily seen in Fig. 2a, both sides of the strain profile were averaged out to obtain a single smoothed out curve (Fig. 2b) for every available load level. A linear fitting procedure was carried out for the middle part of the averaged strain profile for every load level. The point at which the

approximated line intersects the maximum strain for the appropriate load level is considered the end of the damage zone, therefore the length is the distance from the edge of the RC element to this point. For a visual comparison the fitted lines are plotted over the original strain profiles in Fig. 2c.

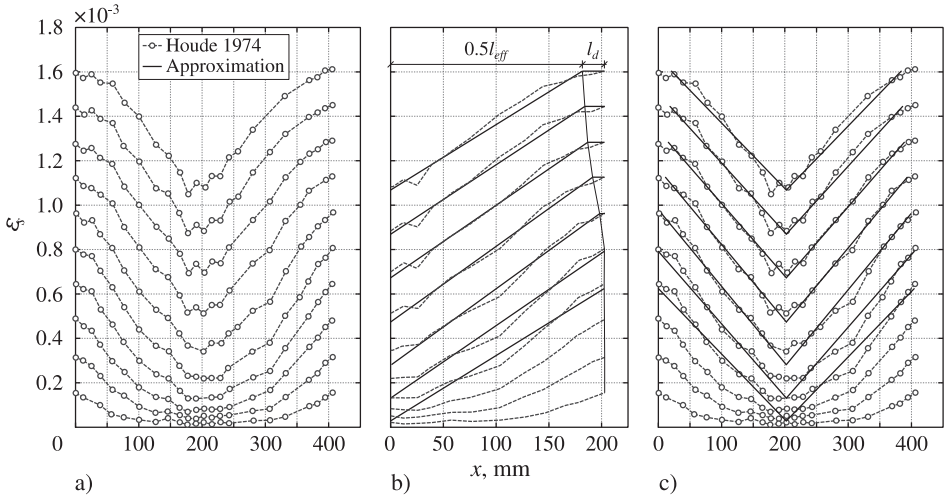

Figure 2. a) Experimental reinforcement strain distributions, b) linear approximations at different load levels on the experimental strain profiles with both sides averaged out and c) the linear approximations superimposed on the full strain profiles load levels

Following the same approach, the damage zone length was established for other tensile specimens presented by Houde [5] and Kankam [6]. The obtained lengths were then normalized by the bar diameter and plotted against the stress level instead of reinforcement strains. This way, the further regressed damage zone model is more universal, i.e. can be easily applied to other reinforcement types, such as glass or carbon fibre reinforced plastic bars (GFRP, CFRP and etc.). Linear regression is applied to the data points and the achieved fit is shown in Fig. 3 by the solid line, for simplicity another regression model with an intercept at zero point is developed.

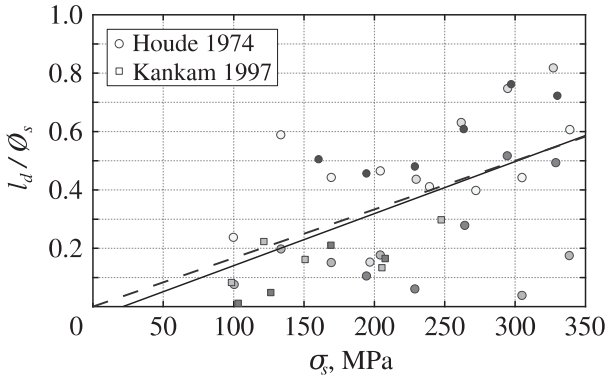

Figure 3. The regressed (solid line) and simplified (dashed line) damage zone models normalized by reinforcement bar diameter

Since the original data is of strain profiles, both simplified damage zone models are shown in Eq. (5), related to strains and stresses, obtained by multiplying the strain values with the appropriate elasticity modulus.

$$l_d = \frac{1}{3}\varepsilon_s \emptyset_s \approx 0.00167 \sigma_s \emptyset_s \tag{5}$$

2.3 Relating mean crack spacing to a reference $l_{cr,ref}$ value

The suggested technique enables the estimation of mean crack spacing for a variety of combinations of bar diameter and reinforcement ratio values. This is achieved by relating them to a known l_{cr} value of a reference RC element. The crack spacing value can be found by either numerical means or experimentally. As the proposed method depends on just a single reference RC prism with a reference bar diameter $\emptyset_{ref}$ and reference reinforcement ratio ρ_{ref} for which the reference mean crack spacing $l_{cr,ref}$ is known, it is best to use the bar diameter for which a significant number of specimens exists. A 14mm steel reinforcement bar is chosen as the reference, based on experimental data [7]-[13]. The mean crack spacing value l_{cr} = 162mm was established from 45 specimens, all with 100x100mm concrete cross-section (represents a reinforcement ratio of 1.54% for the 14mm bar) but variable concrete strengths. The mean crack spacing has been shown previously [10] to be independent from concrete strength. The spacing values are slightly scattered but visibly unaffected by concrete class, as shown in Fig. 4. The chosen concrete section dimensions are fixed in this investigated in order to further isolate one key variable, the reinforcement bar diameter and the connected reinforcement ratio.

While in this paper further explanations are based on this reference data, any other combination can be taken as the reference starting point, as long as the crack spacing value for that combination is known with enough certainty.

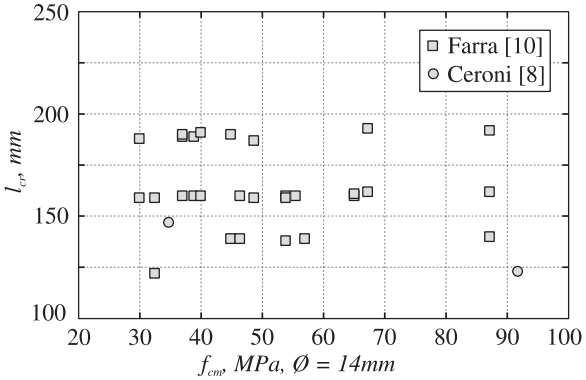

Figure 4. Crack spacing against concrete mean compressive strength for elements with 100x100mm section reinforced with a 14 mm steel bar

2.4 Assumptions of the model

With respect to the main principles presented above, the following assumptions can be deducted:

- The approach considers the stabilized cracking stage, thus the distance between cracks will not change as no new cracks will appear.
- Reinforcement strains within the effective zone are defined by a linear shape function.
- The bond-slip model for the effective zone is identical for all RC elements under investigation, regardless of reinforcement ratio or bar diameter.
- Tension softening stresses in the cracked sections are neglected.

3. Derivation of the Crack Spacing Model

1) Initially, the reference mean crack spacing value $l_{cr,ref}$ is established numerically or experimentally for a reference tension RC element with a reference steel bar diameter $Ø_{ref}$ and reference reinforcement ratio ρ_{ref}.

2) For the selected reference element, the mean strain value ε_m is calculated for a given axial load P_i using the method given by Eurocode 2 [14] (any method based on the smeared crack approach can be used).

3) Since the initial load level is given, the reinforcement strains ε_{smax} at the location of the crack are known and the damage zone length l_d can be established.

4) Due to the assumption of fully damaged bond in the damage zones, the reinforcement strains at the end of the effective zone are the same as at the location of the crack, hence the general reinforcement strain shape function (Eq. 3) can be further adapted for half of the effective zone to reflect this:

$$\varepsilon_{smax} = \varepsilon_0 + a_1\left(0.5 l_{eff}\right) \tag{6}$$

5) Following the key principle of this approach, the mean strains calculated by the smeared crack approach (Eurocode 2) are equated to the mean strains obtained by the stress-transfer approach. Given the damage zone with constant strains and effective zone described by a linear shape function, this equality can be expressed as:

$$\varepsilon_{smax} \cdot l_d + \varepsilon_0\left(0.5 l_{eff}\right) + 0.5 \cdot a_1\left(0.5 l_{eff}\right)^2 = \varepsilon_m \cdot \left(0.5 l_{cr,ref}\right) \tag{7}$$

6) The reinforcement minimum strains ε_0 and slope a_1 are then found for the reference element by solving the system of equations comprised of Eq. 6 and Eq. 7.

7) Bond stresses can then be found by differentiating the reinforcement strain shape function. For simplicity, concrete strains are neglected. The final differentiated expression reveals constant bond stresses:

$$\tau(x) = \frac{E_s \emptyset_s}{4} \frac{d\varepsilon_s(x)}{dx} = \frac{E_s \emptyset_s}{4} \cdot a_1 \tag{8}$$

8) Having established the bond stress for the reference RC prism, average distances between cracks can be estimated for any combination of bar diameter and reinforcement ratio. The assumption that bond-slip relationship is the same for other RC ties, regardless of bar diameter or reinforcement ratio ensures that the minimum strain ε_0 is fixed for all investigated cases and that the slope a_1 for any other bar size can be easily found by rearranging Eq. 8:

$$a_1 = \frac{4\tau}{E_s \emptyset_s} \tag{9}$$

9) With the shape function coefficients easily obtainable for other RC elements, the principle of compatibility of mean strains of the smeared and stress-transfer approaches must be ensured in order to obtain the appropriate mean crack spacing value. This can be easily solved numerically, by altering the required loading level, expressed as reinforcement strains ε_{smax}, or the effective zone length l_{eff} until the mean strain equality condition is met. The distance between cracks l_{cr} is then found from Eq. 4 for the element under investigation.

4. Crack spacing analysis

The newly proposed approach is applied for investigating crack spacing of a variety of bar diameters and reinforcement ratios, including the experimentally gathered data. In order to obtain results with greater validity, experimentally obtained mean crack spacing values were collected from different experimental programs of 100x100mm RC ties with bar diameters ranging from 10 to 20mm [7]-[13]. In total 173 different specimen crack spacing values are gathered, of which 49, 11, 45, 20 and 48 specimens were of RC prisms reinforced with 10, 12, 14, 16 and 20mm bars respectively. Average crack spacing values were further calculated and

found to be 216mm, 183mm, 161mm, 150mm and 138mm respectively for the 10, 12, 14, 16 and 20mm diameter bars. As previously discussed, the selected reference reinforcement ratio and reference bar diameter are based on this experimental data and taken as ρ_{ref} = 1.54% and $Ø_{ref}$ = 14mm, respectively. Accordingly, $l_{cr,ref}$ is taken as the mean value from 45 specimens as 162mm. The loading level for the reference member was taken as a service load inducing 300MPa stresses in the reinforcement. An example of the strain profiles obtained for 10, 14 and 20mm bars by this approach is shown in Fig. 5 for f_{cm} = 30MPa and f_{ct} = 2.9MPa. Varying reinforcement ratios of 1.54%, 2% and 3% are shown as well. Several important aspects are clearly illustrated such as the constant strains representing the damage zone, the fixed minimum strain ε_0 for all cases and varying slope a_1, depending on the reinforcement bar size.

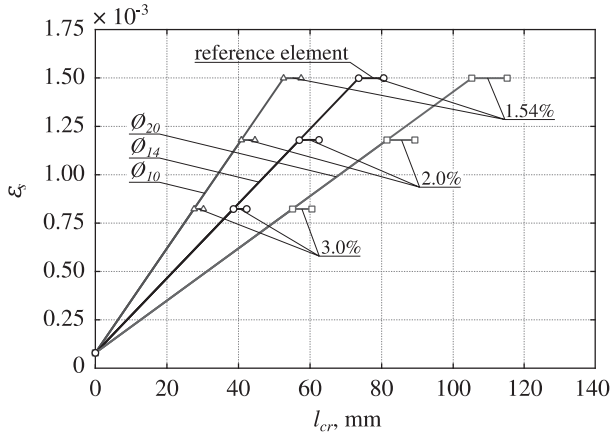

Figure 5. Strain profiles of 10, 14 and 20mm diameter bars for 1.54, 2 and 3% reinforcement ratios

For comparison with the experimental data, analyses were carried out for three mean concrete compressive strength values of 30, 40 and 50MPa, respectively the tensile strength was estimated from Eurocode 2 for the given concrete strengths. The averaged results are presented in Fig. 6 together with the experimental average crack spacing values and values obtained by Model Code 2010 [15] for comparison. The data obtained by the suggested approach is of excellent agreement with the experimental results and of greater accuracy than values estimated by the Model Code 2010. While comparisons were made to the code predictions, the authors would like to emphasise the early development stage of these ideas. The methodology should be used at the conceptual level, to further research the underlying ideas. The proposed approach relies on two limited deformation parameters, the reinforcement strain value at the middle of the investigated concrete block ε_0 and the reinforcement strain value at the location of the crack ε_{smax}. This is due to the assumption of the linear deformation profile, obtained from relatively limited experimental data. As the proposed approach equates the mean strains of the strains obtained from the code to the mean strains determined by the strain profile, either of the two strain parameters ε_0 or ε_{smax} are the key parameter that can be modified to ensure this strain compliance condition. The authors chose the minimum strain in this paper but would like to point out the benefit of relying on the fixed strain at the crack: the

iterative procedure could be removed altogether, as there would be no need to recalculate the mean strains predicted by the chosen method.

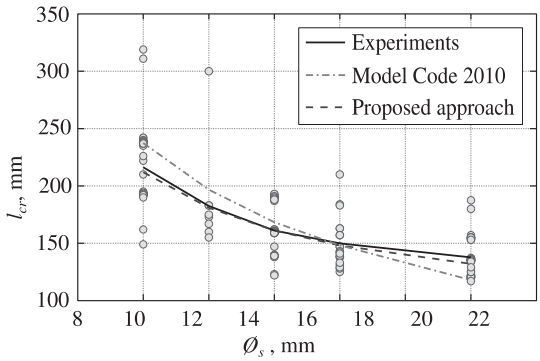

Figure 6. Crack spacing comparison between the proposed approach, Model Code 2010 and experimental data and their average values

5. Conclusions

An innovative new approach for modelling crack spacing of RC tension elements is presented in this study. The suggested method relies on several key principles, such as dividing the distance between cracks into separate regions identified as the effective and damage zones for which strains are described by different behaviours. The most significant aspect is the compatibility of two different approaches, the smeared crack and the stress-transfer approaches, which is ensured by the equality of mean strains estimated by said approaches. Keeping bond-slip relationship identical for every investigated element allows the mean crack spacing value to be determined. The key benefits of the suggested method are that it is a simple, mechanically sound and transparent approach, which does not rely on empirically obtained relations or constants. These attributes make it a very attractive option for investigating cracking behaviour, particularly crack spacing, instead of relying on semi-empirical approaches, commonly found in design codes. The only requirement by the approach is to have a single validated data point for a chosen reference tension RC element and any other configuration of reinforcement ratio and bar size can be investigated. A crack spacing analysis was carried out for the experimental data and the findings revealed that the proposed approach produces very accurate results when compared to experimental data. Finally, the authors want to encourage future discussion and research into this proposed methodology for investigating the cracking behaviour of concrete elements, as the ideas are quite new and are in the early stages of development, still in need of solid ground to build from.

Acknowledgements

The authors gratefully acknowledge the financial support provided by the Research Council of Lithuania (Research project No. MIP-093/2015).

References

[1] Broms, B.B., Crack width and crack spacing in reinforced concrete members, Journal of the American Concrete Institute, 62(10) (1965), 1237-56.
[2] Beeby, A.W., The influence of the parameter ϕ/ρ eff on crack widths, Structural Concrete 5(2) (2004), 71-83.
[3] Borosnyói, A. and Balázs, G.L., Models for flexural cracking in concrete: the state of the art, Structural Concrete 6(2) (2005), 53-62.
[4] Marti, P. et al, Tension chord model for structural concrete, Structural Engineering International 8(4) (1998), 287-98.
[5] Houde, J., Study of Force-Displacement Relationships for the Finite-Element Analysis of Reinforced Concrete, PhD thesis, McGill University, Montreal, Quebec, Canada (1974).
[6] Kankam, C.K., Relationship of bond stress, steel stress, and slip in reinforced concrete, Journal of Structural Engineering 123(1) (1997), 79-85.
[7] Bischoff, P.H. and MacLaggan, D.A., Bond and tension stiffening in concrete tension members with plain reinforcement, Proceedings of the First International Structural Specialty Conference, Canada (2006)
[8] Ceroni, F. et al, Tension stiffening of reinforced concrete ties strengthened with externally bonded fiber-reinforced polymer sheets, Journal of Composites for Construction 8(1) (2004), 22-32.
[9] Choi, K.Y. and Maekawa, K., Bond behaviour in RC tension members based on the change of concrete fracture characteristics with temperature, Proceedings of the Japan Concrete Institute, Japan (2003), 991-996.
[10] Farra, B. and Jaccoud, J.P., Bond behaviour, tension stiffening and crack prediction of high strength concrete, Proceedings of International Symposium 'Bond in Concrete', Latvia (1992).
[11] Lorrain, M. et al, Cracking behavior of reinforced high-strength concrete tension ties, Structural Journal 95(5) (1998), 626-35.
[12] Scott, R.H. and Gill, P.A., Short-term distributions of strain and bond stress along tension reinforcement, The Structural Engineer 65(2) (1987), 39-43.
[13] Wu, H.Q and Gilbert R.I., An experimental study of tension stiffening in reinforced concrete members under short-term and long-term loads, UNICIV Report no. R-449, The University of New South Wales, Sydney, Australia (2008).
[14] Eurocode 2: Design of Concrete Structures: Part 1-1: General Rules and Rules for Buildings, EN 1992-1-1, Comité Européen de Normalisation (CEN), (2004).
[15] Model Code 2010. Fédération Internationale du Béton fib/International Federation for Structural Concrete, (2010).

International RILEM Conference on Materials, Systems and Structures in Civil Engineering
Conference segment on Service Life of Cement-Based Materials and Structures
22-24 August 2016, Technical University of Denmark, Lyngby, Denmark

EXPERIMENTAL INVESTIGATION ON STRAIN DISTRIBUTION IN REINFORCEMENT OF RC SPECIMENS UNDER TENSION LOADING

Gintaris Kaklauskas [(1)], Mantas Juknys[(1)], Ronaldas Jakubovskis[(1,2)], Eugenijus Gudonis[(1)], Regimantas Ramanauskas [(1)], Viktor Gribniak [(1, 2)], Aleksandr Sokolov [(2)]

(1) Vilnius Gediminas Technical University, Vilnius, Lithuania
(2) Research laboratory of Innovative Building Structures, Vilnius, Lithuania

Abstract
The interaction of reinforcement and the surrounding concrete is fundamental to the understanding of the behaviour of reinforced concrete. There are a number of aspects to this problem which include an understanding of bond behaviour, cracking behaviour and the related problem of tension stiffening. The phenomenon of cracking and the structural behaviour of cracked reinforced concrete are topics of current investigation. This paper presents the use of a Fibre Bragg Grating optical system for measuring steel strains, bond stress and slip of a reinforcing bar relative to its surrounding concrete, between cracks. Tests were performed on concrete prisms of 260 mm length. Specimens were reinforced with 10 and 20 mm diameter ribbed bars. The bars had been instrumented along the edge to accommodate a longitudinal narrow groove in which two arrays of FBG sensors were installed. The obtained strain profiles of the specimens for various loading levels are presented. A brief description is given a newly proposed method to determine the mean crack spacing of RC ties. The experiments serve in part as a way to validate key assumptions of the proposed approach and in part as a way to test the Fibre Brag Grating optical sensing system for strain measurement.

1. Introduction

Recently the authors proposed a simple, mechanically sound and transparent analytical approach for crack distance analysis of RC ties [1]. The philosophy behind the proposed methodology is to establish the mean crack spacing through the compatibility of the discrete cracking and smeared cracking approaches. The mean crack spacing is obtained by equating the mean strains of both approaches. The bond stress-transfer approach governs the strain distribution of the reinforcement between the consecutive cracks, whereas the smeared approach provides the estimated mean strain of the element. The strain distributions of reinforcement are investigated in this paper experimentally for short RC prisms as the average

deformation behaviour of a cracked concrete element can be reasonably represented by a reinforced concrete block of the same length as the mean crack spacing value $l_{cr,m}$, furthermore, bond stress can be estimated from the strain distributions as given in Eq. (1).:

$$\tau(x) = \frac{E_s \emptyset_s}{4} \frac{d\varepsilon_s}{dx} \tag{1}$$

where E_s is the Young's modulus of reinforcement, $\emptyset_s$ is the diameter of the bar, ε_s is the strain.

Reinforced concrete as a structural material is defined by very intricate characteristics that are highly nonlinear in nature that are essential to better understanding of the physical behaviour of this composite material. One of the more complex of these aspects is the bond behaviour between concrete and reinforcement bars. This interaction is often assumed to be perfect in classical modelling approaches for simplicity but actually highly complicated local phenomena occur at this interaction zone that causes effects, such as slippage, when the longitudinal displacements of the surrounding concrete and reinforcement at any section are different. This bond-slip behaviour affects the distribution of strains within the reinforcement bars and concrete. While it is possible to investigate the bond directly, as done by Lahnert et al [2] using a magnetic approach, other simpler indirect experimental methods are often employed. The most commonly used ones focus on measuring the strain distribution within the reinforcement bars. One way to accomplish this is to glue the strain gauges on the surface. The other common way is to install the strain gauges inside the reinforcement bar. Mains et al [3] was one of the first to apply this method by cutting the bars in half, and setting up the strain gauges inside a longitudinal groove along the centre of the bar then welding the two sides back together. This approach is commonly used by researchers [4]-[6]. Recently, more sophisticated solutions have been introduced [7]-[8] for measuring the strains within the bars, like Fibre-optical sensing using a Bragg Grating system. While a Fibre Bragg Grating system allows to measure strains at specific locations spaced at certain distances, another advanced method involving optical frequency domain reflectometry that allows to obtain more truly distributed strain measurements along the entire length of the fibre [9]-[10].

FBG based optical sensors are employed in this work for measuring reinforcement strains of RC prisms, reinforced with 10 and 20mm diameter bars. A longitudinal groove is milled in the bars in which fibre optic arrays with FBG sensors are installed. Strains are measured up to 500MPa of induced stresses in the 10mm bar and 300MPa induced stresses in the 20mm bar specimen. Along with the experimental results, a brief introduction to an innovative crack spacing modelling approach is presented in this paper as well as a flowchart of the algorithm. Reinforcement strain profiles are necessary to validate the proposed crack spacing modelling technique, which relies on several key assumptions, such as the introduction of the effective and damage zone concepts. A linear shape function is assumed for the strain distribution within the effective zone. The obtained strain distributions are used to provide insight on this approach and the underlying assumptions, as well as to advance the theoretical research.

2. Crack spacing estimation using an innovative approach

A new approach is proposed for predicting mean distance between cracks of RC elements undergoing tension [1]. The main concepts involved in this method are the compatibility of the discrete (stress-transfer) and smeared crack approaches, introduction of the effective and damage zones. Reinforcement strain distribution is considered to follow two separate laws in these zones, strains are constant in the damage zone near the cracks, due to the assumption of fully damaged bond, whereas strains in the effective zone are governed by a known shape function, assumed to be a linear function with a_1 and ε_0 describing the slow and constant of the equation, respectively. The expression for the shape function is given in Eq. (2). The shape function is assumed for half of the strain distribution, starting from the middle and moving towards the crack. Applying the shape function to only half of the effective zone further simplifies the relationship and has the added benefit of defining the shape function constant as a physical parameter, the minimum strains at the centre of the block between cracks.

$$\varepsilon_s(x) = \varepsilon_0 + a_1 x \tag{2}$$

where ε_0 is the constant term of the shape function, representing the minimum strains, a_1 is the slope.

The damage zone was found to be dependent on the loading level [1] and was expressed in relation to the reinforcement bar strains at the location of the crack and the diameter of the bar. This relationship was further modified and the equation given in Eq. (3) was obtained. This equation was further related to the stresses in the reinforcement, as this enables the damage zone model to be applied for other types of reinforcement, such as GFRP, AFRP or CFRP bars.

$$l_d = \frac{1}{3}\varepsilon_s \emptyset_s \approx 0.00167 \sigma_s \emptyset_s \tag{3}$$

Where ε_s is the strains of the reinforcement at the location of the crack, σ_s is the stress in the reinforcement.

The mean reinforcement strains obtained by the smeared crack and discrete crack approaches are equated in order to guarantee compatibility. Another significant aspect is relating the crack spacing of elements to a specific reference RC element, with a reference bar diameter, reinforcement ratio and a well mean established mean crack spacing value. A simplified flowchart of the suggested approach is given in Fig. 1. As this method relies on several assumptions related to the distribution of strains within the reinforcement bar, additional experimental data is necessary to further increase the validity of this method. This is achieved by measuring the experimental strains in RC ties of a certain length, representing the distance between cracks, of specimens with different bar diameters. Details of the carried out experiments are presented further in this work.

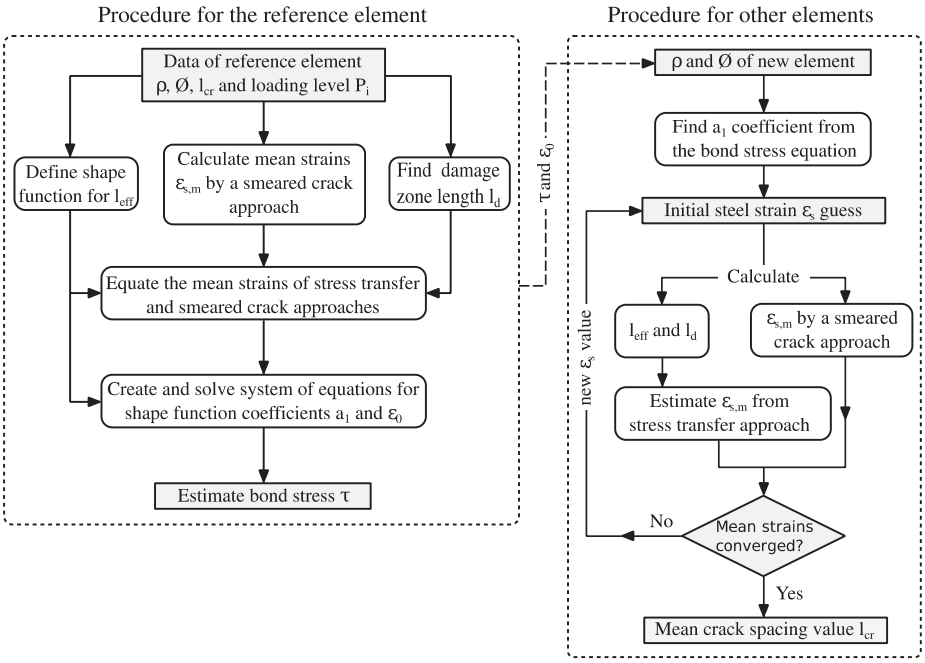

Figure 1. Flowchart of the proposed approach

3. Experimental setup

3.1 Specimens

Double pull-out experiments were carried out on 150x150mm and 100x100mm section reinforced concrete prisms reinforced with 20 and 10mm diameter steel bars, respectively. Both prisms were of 260mm length. The length of the prism was estimated to represent a crack spacing long enough to accommodate the full stress transfer distance but short enough for transverse cracks to appear.

3.2 Material properties

The concrete was made with ordinary Portland cement, natural pit sand (4mm maximum grain size) and graded gravel of 10mm maximum size. The exact proportion by weight is 1:2.5:3, the water to cement (w/c) ratio is 0.5. Tests of standard concrete cube samples revealed the cubic strength to be 54.34MPa after 28 days and the cylindrical strength to be 45.45MPa. The elasticity modulus of the steel bars were found to be 202.5GPa and 204.4GPa for the 10 and 20mm diameter bars, respectively.

3.3 Fibre Bragg Grating system

A Fibre Bragg Grating sensor based system was adopted for the experimental tests. These sensors are relatively small in size and many can be fitted in series on a fibre, therefore they

are well suited for the intended reinforcement bar sizes, specifically the 10mm bar. Since the system incorporates less cables, uses less space for the sensors, the 10mm bar will retain more cross-sectional area after bar preparation than the alternative strain measurement method of milling the bars and installing strain gauges in a cut out longitudinal groove along the centre of the bar (Fig. 2). The steel bars were prepared in advance and fitted with Fibre Bragg Grating (FBG) sensors for strain measurement at specific distance from each other.

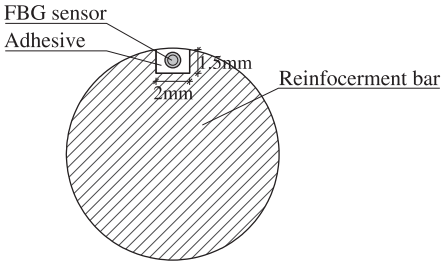

Figure 2. Reinforcement bar section with installed FBG sensors along a longitudinal groove

Two separate arrays were installed with 6 FBG sensors each (Fig. 3), with 1 FBG sensor on one array reserved for measuring thermal data instead of strains. This sensor is required for compensating the thermal effects on FBG sensors. The temperature sensor is placed approximately at the centre of the specimen.

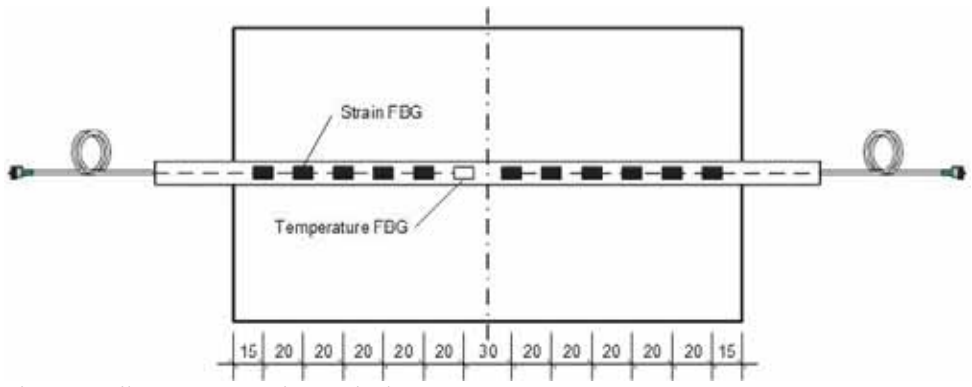

Figure 3. Fibre Bragg Grating optical sensor arrays

Tests were carried out with displacement controlled loading, but the equipment used allowed to record the appropriate load as well, that was used to estimate the stress level in the bars. Experiments were performed in a controlled environment, where the temperature was set at 20ºC and relative humidity was of 65%. The specimens were tested up to different loading levels, as the testing machine was limiting the achievable deformations for the bars. The results is that the 10mm reinforcement bar was tested up to an equivalent of 500MPa stresses induced in the steel bar and the 20mm diameter bar specimen was tested up to 300MPa

equivalent stress in the bar at the edge of the RC prism. Data from the FBG sensors was recorded after every displacement increment.

4. Experimental results

The data collected by the FBG sensors was processed to obtain the experimental strain distribution within the reinforcement bars. The strain profiles for the 10 and 20mm bars are presented at different loading levels in Fig. 4. As mentioned above, one sensor was used for monitoring temperatures required for calibration of the system, therefore no strain data is recorded for that segment. The grey dotted line in the figure represents this gap, as the thermal sensor was omitted.

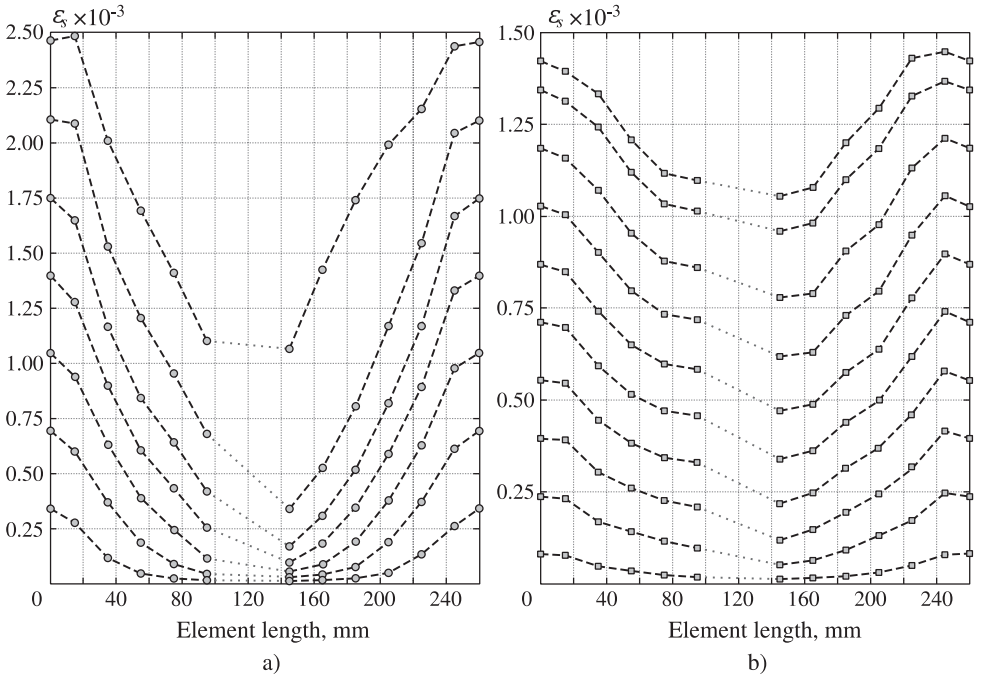

Figure 4. a) Reinforcement strain profiles of a RC prism reinforced with 10mm bar and b) 20mm bar.

Based on the deformations presented in Fig. 5, the following findings can be mentioned:

1. Reinforcement strains of 10 and 20mm diameter bars are visibly different. The assumption of a linear strain shape function in the proposed theoretical approach seems to be valid for the 10mm bar, whereas the strain distribution of the 20mm bar exhibits a different character with a clearly expressed horizontal part in the centre of the prism. Omitting this flat segment, the strains are visibly closer to the ones of the 10mm bar.

2. The growth of reinforcement strains in the zones close to the cracks significantly decreases for both specimens. The bond stress equation given in Eq.1, implies that bond in the vicinity of the cracks is damaged. Current tests support the previously reported results that relate the length of the damage zone with the diameter of reinforcement bar [1].

6. Conclusions

Experimental strain profiles of two RC prism specimens reinforced with 10 and 20mm diameter bars undergoing tension are obtained for various loading levels using a Fibre Bragg Grating optical sensing system. The strain distributions revealed the presence of damage zones in the areas next to the cracks and different behaviour between strains of 10 and 20mm diameter bars. The middle section of the 20mm bar strain profiles is visibly more horizontal, therefore a change in bond behaviour can be deducted. The 10mm bar strain distributions can be approximated using a linear strain shape function that validates the assumption of the theoretical model. The strains of the 20mm bar are visibly not linear but neglecting the horizontal segments gives similar strain profiles as for the 10mm bar, that clearly displays more linear behaviour. The FBG system yielded precise and reliable strain measurements of reinforcement up to high loading levels, representing the yielding of reinforcement without the fibres getting damaged due to excessive deformations.

Acknowledgements

The authors gratefully acknowledge the financial support provided by the Research Council of Lithuania (Research project No. MIP-093/2015).

References

[1] Kaklauskas, G. et al, A new method for formulating crack spacing models of RC ties, Proceedings of the second international conference on performance-based and life-cycle structural engineering (PLSE 2015), Australia (2015), 582-590.
[2] Lahnert, B.J. et al, Measurement of slip between steel and concrete core, In Journal Proceedings, ACI J 83(6) (1986), 974-982.
[3] Mains, R. M., Measurement of the distribution of tensile and bond stresses along reinforcing bars, In Journal Proceedings, ACI J 48(11) (1951), 225-252.
[4] Houde, J., Study of Force-Displacement Relationships for the Finite-Element Analysis of Reinforced Concrete, PhD thesis, McGill University, Montreal, Quebec, Canada (1974).
[5] Scott, R.H. and Gill, P.A., Short-term distributions of strain and bond stress along tension reinforcement, The Structural Engineer 65(2) (1987), 39-43.
[6] Kankam, C.K., Relationship of bond stress, steel stress, and slip in reinforced concrete, Journal of Structural Engineering 123(1) (1997), 79-85.
[7] Kenel, A. et al, Reinforcing steel strains measured by Bragg grating sensors, Journal of materials in civil engineering 17(4) (2005), 423-31.

[8] Kenel, A. and Marti, P., Faseroptische Dehnungsmessungen an einbetonierten Bewehrungsstäben [Fiber-optic steel strain measurements on embedded reinforcing bars], IBK Rep. No. 271, Institute of Structural Engineering, ETH, Zurich (2002).
[9] Michou, A. et al, Reinforcement–concrete bond behavior: Experimentation in drying conditions and meso-scale modelling, Engineering Structures 101 (2015), 570-82.
[10] Henault, J.M. et al, Quantitative strain measurement and crack detection in RC structures using a truly distributed fiber optic sensing system, Construction and Building Materials 37 (2012), 916-23.

International RILEM Conference on Materials, Systems and Structures in Civil Engineering
Conference segment on Service Life of Cement-Based Materials and Structures
22-24 August 2016, Technical University of Denmark, Lyngby, Denmark

NUMERICAL MODELLING OF FRACTURE OF MACRO-POLYMER FIBER REINFORCED CONCRETE

Marcos G. Alberti [(1)], Alejandro Enfedaque [(1)] Jaime C. Gálvez [(1)] and Encarnación Reyes [(1)]

(1) Departamento de Ingeniería Civil: Construcción, E.T.S de Ingenieros de Caminos, Canales y Puertos, Universidad Politécnica de Madrid.

Abstract
Research has shown that polyolefin fibres can meet the requirements of the standards that consider post-cracking effectiveness of fibres when it comes to the design of structures made of fibre reinforced concrete (FRC). Experimentally observed fracture behaviour has shown a remarkably reliable performance of polyolefin FRC, even when modifying the concrete type, the pouring and compaction procedures as well as mould sizes. A numerical model, based on the cohesive fracture approach, is proposed for modelling the fracture processes of macro-polymer fibre reinforced concrete (PFRC). Such a model has been successfully applied by the authors to plain concrete and even non-isotropic cohesive materials. In this work, it is extended to PFRC by means of an adapted tri-linear softening law. The model is implemented in a finite element programme by means of an embedded crack. The main advantage in comparison with other approaches is that it does not require re-meshing during crack growth. Numerical simulations of experiments carried out by the authors, show how the proposed model may simulate fracturing of PFRC. The conclusions of this study provide a better understanding mode I fracturing and could enhance future modelling and structural design of PFRC.

1. Motivation

Concrete brittleness has been conventionally reinforced with continuous steel-bar reinforcing placed in the tensile zone of structural members such as beams, slabs and columns. The combination of steel corrugated bars and concrete has been the most common composite material in construction [1]. The section forces can be balanced in structural members by taking advantage of the best performance of each material: compression stresses by concrete and tensile stresses by steel. Nonetheless, the developing of micro-cracks and macro-cracks by the sole use of continuous reinforcing still cannot be even slowed [2]. Having steel-bar reinforced concrete (RC) has become the par-excellence solution for structures over the last

100 years. In such a sense, the possibility of partial or even total substitution of steel-bars by steel fibres not only allows a reduction of the cost of the structure but also provides other improved properties, mainly due to the increase in ductility. Once accepted as being viable, such substitution boost industrial developments and research into fibres and leads to production of new types of fibres with varied shapes and possibilities.

While the good performance of steel combined with concrete is widely reported, it does also have certain drawbacks. For example, steel is potentially corrodible in nature and, in addition, is expensive to purchase, store and handle. Durability issues about steel fibre reinforced concrete (SFRC) continue to concern engineers and industry and the development of plastic industry allowed the production of chemically stable fibres [3]. The efforts of plastic industry have recently sought a new generation of polyolefin-based fibres inert in an alkaline environment and with structural benefits [4]. While polyolefin fibre reinforced concrete (PFRC) has considerable residual tensile strengths, additional research is required for better comprehension of this composite material.

The contribution of polyolefin fibres in the residual stages of PFRC has been the topic of previous research work, mainly focused on flexural tensile strength [5, 6]. These polyolefin fibres appeared as an alternative to steel fibres which a contribution to the structural design that was provided by using residual flexural strengths obtained in standard bending tests on notched beams [7]. Such strengths were considered in some concrete design standards [8, 9, 10] in design for the service life and ultimate state of the structure. In order to do so, constitutive relations could be built by using the procedure based on steel-fibre reinforcement [11]. However, the assessment of the fracture properties of PFRC has shown various significant differences from that of SFRC, especially for larger deformations than those typically considered [12, 13]. Considering the constitutive relations of SFRC in the codes for PFRC, there is an absence of extensive studies, with some authors even concluding that it overestimates use of polyolefin fibres [14]. As analysis is still needed, building a constitutive relation suitable for the structural design of PFRC is a topic of this study.

When providing constitutive relations of PFRC in associating the stress with the deformations, the use of inverse analysis approaches has reproduced the behaviour under flexion of SFRC [15]. There is a lack of published research on polyolefin macro-fibre reinforcement of concrete. Based on the post-cracking response of the experimental campaign of PFRC, it is possible to perform a numerical inverse analysis and hence obtain the parameters that define the material behaviour. That is to say, it is possible to fit experimental data with an iterative method and numerical simulations by using, in this study, a cohesive crack approach. Such a procedure was followed with the aim of fitting the constitutive relations from the experimental tests performed in PFRC fracture tests.

The significance of this research lies in the reproduction of the fracture behaviour of PFRC of previous experimental campaigns [16, 17] by means of cohesive fracture models and the finite element method (FEM). It is worth emphasising that the fracture results used for the inverse analysis were obtained with a dosage of 6kg/m³ of 60mm-long polyolefin fibres with several modifications in the concrete properties, pouring methods and specimen sizes. Therefore the constitutive models supplied by this study encompass a wide range of possibilities in the use of PFRC.

2. Experimental curves

The shapes of the fracture curves of PFRC are remarkably different from those of SFRC, as well as the fracture behaviour decribed in previous research [16] . The typical curves showed three remarkable turning points, as first examined in reference [13]. As can be seen in Figure 1, the first turning point took place when the loading-process reached the maximum value and only a few inelastic processes were apparent (the behaviour of concrete is mostly linear if compared with subsequent stages). The turning point where the load reaches the maximum is commonly known for all types of FRC as load at the limit of proportionality (L_{LOP}), with it being the overall maximum load also in the case of plain concrete. A softening behaviour may also be identified for PFRC after L_{LOP}. The softening behaviour is a distinctive characteristic in plain concrete fracture leading to the specimen failure and collapse. Yet the polyolefin fibres can absorb the energy released by the concrete in the fracture processes by so-called fibre bridging and change the loading tendency. At such a point, the curve reaches the minimum post-cracking load (L_{MIN}), while another uploading process starts again. The end of the load-increasing-ramp is the third remarkable point of the curve (the maximum post-cracking remaining load (L_{REM}) is shown in Figure 1). The descending slope drawn after L_{REM} continues until the end of the test. It should be noted that all the PFRC specimens had this behaviour and none failed or collapsed, showing improvements in ductility and toughness with respect to plain concrete. This description of the fracture curves was found in previous literature [10, 16 and 28] and compared with SFRC. The references established that beyond the strength values of the regulations, the behaviour of PFRC was defined by the definition of three such turning points (L_{LOP}, L_{MIN} and L_{REM}) in contrast with the use of SFRC.

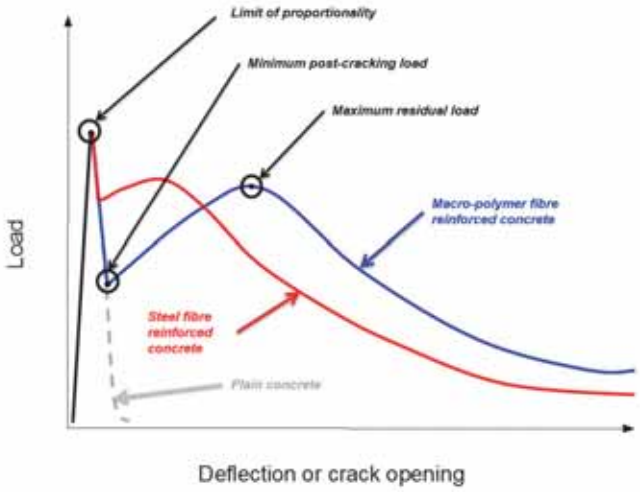

Figure 1: Schematic shape of the typical load-deflection curve obtained in a fracture test of polyolefin fibre reinforced concrete with its singular three turning points as described in references [10, 16, 28]

The comparison with steel fibres and even the combination of steel and polyolefin fibres has also been assessed in previous studies [18]. However, not only the fibre characteristics and dosages but also the placing conditions and formwork geometry influence the final behaviour of the material [19, 20]. In order to assess such variations, specimens manufactured with two types of concrete, several sizes and pouring methods were tested with the aim of analysing the fracture behaviour in previous references [16, 17]. All had an influential factor compared with the reference standardised self-compacting concrete (SCC) and vibrated conventional concrete (VCC). This can be better understood by seing Figure 2. It should be noted that the only common feature is that all had the same fibre dosage.

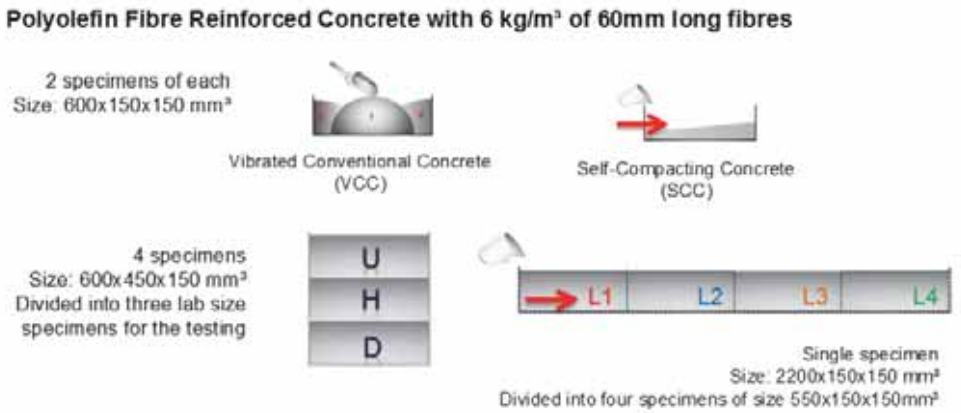

Figure 2: Specimens and structural elements manufactured with concrete reinforced with 6 kg/m³ of 60 mm-long polyolefin fibres in the reference [16]

Additional information about the experimental campagin can be found in reference [16]. It is worth noting that several material parameters are needed in order to simulate the behaviour. In the study, fracture energy as a function of several deformations, compressive strength, elasticity modulus and indirect tensile strength was asssesed. Therefore, the starting point of these numerical calculations was based on the results of a wide experimental campaign. Regarding the mechanical properties, the overall results of compressive strength, indirect tensile strength and elasticity modulus were in line with those of reported in the literature [12, 13]. There was no decreasing of the main mechanical properties in the hardened state. As regards the two types concrete, SCC and VCC, it should be highlighted that mix proportionings were designed in order to provide similar fracture energy in the formulations of plain concrete. In such a way, the differences found in the fracture results could be analysed in terms of the variations produced in the fibre positioning.
With the aim of obtaining an overall view of the behaviour of PFRC with 6 kg/m³ (PFRC6), the results under flexural tensile tests of all the concrete types are shown in Figure 3. The fracture energy obtained was similar for all the deformations and the coefficient of variation remarkably limited. This means that PFRC6 behaved in a significantly similar manner even with the large variety of affecting factors. This is shown in the fracture curves obtained which did not show significant differences either in shapes or in residual loads. The figure shows the confidence interval that would be obtained by keeping the fibre dosage and length steady. The

works performed in this study were focussed on achieving the constitutive models capable to reproduce such a confidence interval and the mean curve with deformations up to 6mm and with this dosage of 6 kg/m³.

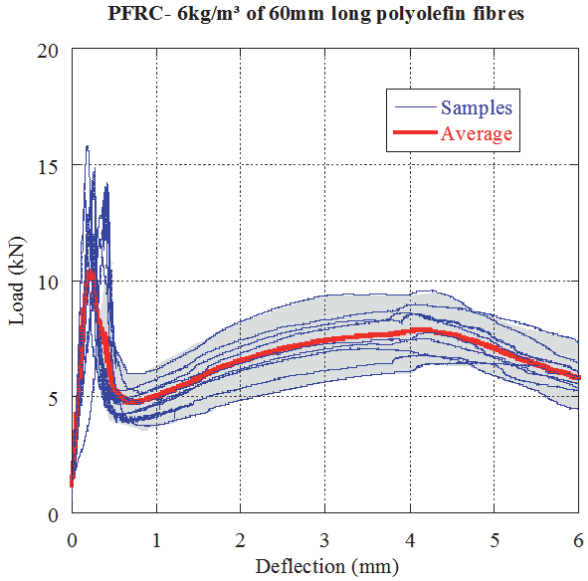

Figure 3: Load – deflection curves of the PFRC6 with 60 mm-long fibres [16].

3 Numerical calculations

The use of the cohesive crack model proposed by Hillerborg [21] to approach the fracture behaviour of quasi-brittle materials has obtained successful results for concrete-like materials, as shown in [22]. It requires the definition of a softening function as a material property that relates the stress across the crack σ with the crack opening w. Hillerborg later extended the proposal to fibre reinforced concrete [23]. It was also shown as a suitable model in assessing the fracture behaviour of anisotropic materials such as brickwork masonry or functionally graded FRC [24, 25, 26]. In such a sense, the use of embedded crack models has allowed analysis to be performed in which the need of a tracking algorithm is avoided. This permits the finite element to adapt itself in the stress field as long as the crack opening remains under a low threshold [27]. These elements have the crack embedded on them. The main assumptions and the mathematical description of the model are described in detail in such published research.

In the case of the present study, the model previously described has been implemented in ABAQUS by using the subroutine UMAT and an auxiliary external file with the coordinates of the nodes and elements. When the crack remains at null, w=0, the element behaves elastically. Once the tensile strength is exceeded, the crack is introduced perpendicularly to the direction of the maximum principal stress. In such a situation, the computational procedure avoids the formation of quasi-orthogonal cracks and the crack adaptation at the

element level fixes a crack direction with no further adaptation. Previous works have shown that these procedures bear resemblance to other work in avoiding crack locking [24].

3.1 Material behaviour and softening curves

The cohesive models have shown themselves to be apposite in order to reproduce the post-cracking behaviour of FRC. The model implemented behaves elastically until the tensile strength of the material is reached. Up to this limit the crack opening remains null. Once the tensile strength is exceeded, the material behaves according to the proposed softening function. At the time of writing, the constitutive relations proposed by recommendations [8, 9, 10] were bilinear or tri-linear softening functions that could not represent the reloading branch of PFRC in fracture. Research has shown that after the first unloading process [26] there is a branch that represents the fibre bridging. Such an intermediate stage is dependent on the type of fibres used and continues up to deformations in which the fibres fail or slip. Nonetheless, it is worth noting that these types of tri-linear curves have been successfully used for the cases of intermediate branches with soft-unloading or even flat stages. Figure 4(a) and Figure 4(b) show tri-linear constitutive relations used for SFRC which may be studied in more detail in references [28, 29]. The need of a branch with recharging strength, such as that presented in this paper, can be considered as a significant advance for the simulation of PFRC and other materials with this residual behaviour. The shape chosen for the numerical simulations presented may be seen in Figure 5.

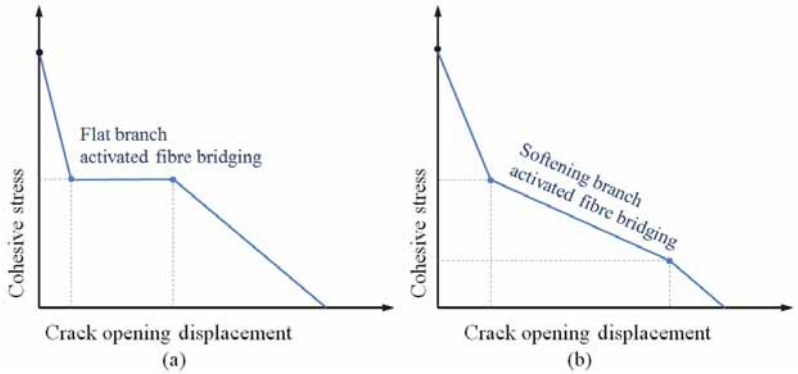

Figure 4: (a) tri-linear softening curve including an initial softening branch [28]; (b) tri-linear softening curve including a kink point [29].

The position of each of the turning points defines the subsequent stretch of the constitutive relation. Since the initial slope after L_{LOP} (see Figure 5) was similar to the well known one found in plain concrete, the first branch was defined by following the exponential function widely accepted for such a type of concrete. That is to say, the softening curve initially followed this exponential shape up to a value of cohesive stress and crack opening denominated C_{min} in which the cohesive stress started to reload. This strength recuperation was defined with a straight step that ended when the turning point named C_{REM} was reached. After C_{REM}, the final failure was simulated with another straight branch that finished at the point called C_F with null cohesive stress. The bounds of the performance of PFRC with a dosage of 6 kg/m³ were considered to be those shown in Figure 3. The use of the data

obtained in this paper is noteworthy and can represent all the changes in rheology and formworks typical in real construction tasks. Therefore, if the model represents these changes, the finding would be of significance for any future structural design. In order to do so, the values of C_{min} and C_{REM} were moved up and down with the experimental scatter in order to capture the confidence interval of the experimental testing by means of the numerical simulations. It is also worth noting that the first point of the constitutive relation, f_t, was considered with a stress value of 3.5 MPa.

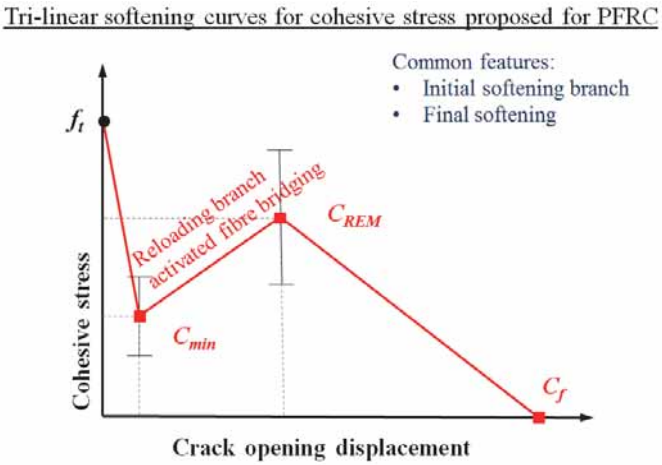

Figure 5: Tri-linear softening curve proposed for PFRC in this paper.

3.2 Results of the numerical simulations

As can be seen in Figure 6, the results of the numerical calculations were remarkably close to those of the experimental campaign. Table 1 supplies the values of the key point in the previously mentioned constitutive relations. The significance of these results is shown in the better understanding of the material behaviour subjected to Mode I of fracture. That is to say, future modelling and design procedures and codes could be significantly enhanced by considering the results of this study.

Table 1: Position of the turning points for the numerical simulation of PFRC with 6 kg/m³ of polyolefin fibres

	C_{min}		C_{REM}		C_F	
	w(mm)	σ(MPa)	w(mm)	σ(MPa)	w(mm)	σ(MPa)
Upper performance	0.072	0.503	2.250	0.784	7.500	0.000
Mean performance	0.082	0.389	2.250	0.900	7.500	0.000
Lower performance	0.090	0.311	2.250	1.200	7.500	0.000

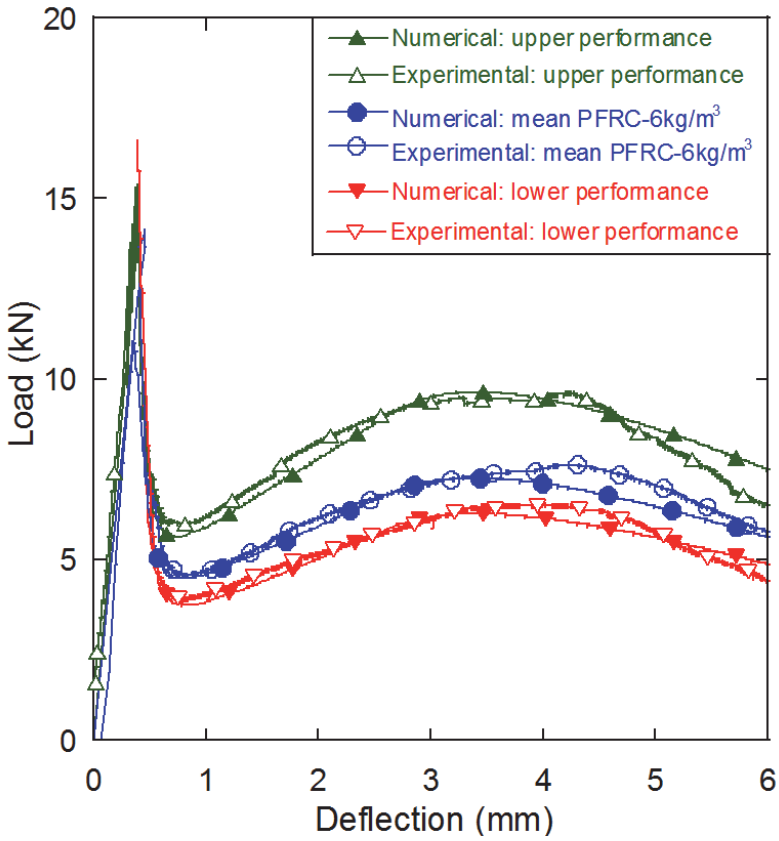

Figure 6: Numerical calculations and mean experimental results for the upper, mean and lower performance of PFRC.

4. Concluding note

A cohesive fracture approach was proposed for numerical modelling the fracture behaviour of PFRC. The model has been implemented successfully and can be used for a class of materials ranging from plain concrete to non-isotropic cohesive materials. In the present contribution, it has been extended to PFRC by means of adapting a tri-linear softening law. Numerical simulations of experiments underline that the proposed model may simulate fracturing of PFRC. Experimentally observations scatter intervals could be accurately reproduced by modifying the parameters of the softening function.

Acknowledgements

The authors gratefully acknowledge the financial support provided by Ministry of Economy and Competitiveness of Spain by means of the Research Fund Project DPI 2011-24876. They also offer their gratitude to Sika SAU for supplying the polyolefin fibres.

References

[1] A. M. Neville, Properties of concrete, Third Edition, London: Pitman, pp. 549-551, 1981.

[2] E. Nawy, Construction Engineering Handbook. 2ed. FL, USA: Taylor & Francis group, 2008.

[3] V. Ramakrinshnan, "Structural Application of Polyolefin Fiber Reinforced Concrete," ACI Special Publication 183(13), pp. 235-253, 1999.

[4] S. C. Ugbolue, Polyolefin fibres: industrial and medical applications, CRC Press, 2009.

[5] M. G. Alberti, "Polyolefin fibre-reinforced concrete: from material behaviour to numerical and design considerations," Doctoral dissertation, Universidad Politécnica de Madrid, E.T.S.I. Caminos, Canales y Puertos, 2015.

[6] M. G. Alberti, A. Enfedaque and J.C. Gálvez, "Improving the Reinforcement of Polyolefin Fiber Reinforced Concrete for Infrastructure Applications," *Fibers,* 3(4), pp. 504-522, 2015.

[7] RILEM TC-162-TDF, "Bending test: Final recommendations," 2002.

[8] CNR-DT 204, "Guide for the design and construction of fiber-reinforced concrete structures," Consiglio Nazionale delle Riserche, Roma, 2006.

[9] EHE-08, Spanish Structural Concrete Code, Spanish Minister of Public Works, 2008.

[10] fib Model Code, Model Code, Paris: Fédération Internationale du Béton fib/International Federation for Structural Concrete, 2010.

[11] A. Blanco, P. Pujadas, A. de la Fuente, S. Cavalaro and A. Aguado, "Application of constitutive models in European codes to RC–FRC," *Construction and Building Materials*, 40, pp. 246-259, 2013.

[12] M. G. Alberti, A. Enfedaque and J. C. Gálvez, "Comparison between polyolefin fibre reinforced vibrated conventional concrete and self-compacting concrete," *Construction & Building Materials*, 85(15), pp. 182-194, 2015.

[13] M. G. Alberti, A. Enfedaque and J. C. Gálvez, "On the mechanical properties and fracture behavior of polyolefin fiber-reinforced self-compacting concrete," *Construction and Building Materials*, 55, pp. 274-288, 2014.

[14] P. Pujadas, A. Blanco, S. Cavalaro and A. Aguado, "Plastic fibres as the only reinforcement for flat suspended slabs: Experimental investigation and numerical simulation," *Construction and Building Materials*, 57, pp. 92-104, 2014.

[15] A. G. Kooiman, C. Van Der Veen and J. C. Walraven, "Modelling the post-cracking behaviour of steel fibre reinforced concrete for structural design purposes," Heron, 45(4), pp. 275-308, 2000.

[16] M. G. Alberti, A. Enfedaque, J. C. Gálvez and V. Agrawal, "Reliability of polyolefin fibre reinforced concrete beyond laboratory sizes and construction procedures," *Composite Structures*, 140(15), pp. 506-524, 2016.

[17] M. G. Alberti, A. Enfedaque and J. C. Gálvez, "Fracture mechanics of polyolefin fibre reinforced concrete: Study of the influence of the concrete properties, casting procedures, the fibre length and specimen size," *Engineering Fracture Mechanics*, 154, pp. 225-244, 2016.

[18] M. G. Alberti, A. Enfedaque, J. C. Gálvez, M. F. Cánovas and I. R. Osorio, "Polyolefin fiber-reinforced concrete enhanced with steel-hooked fibers in low proportions," *Materials and Design*, 60, pp. 57-65, 2014.

[19] M. C. Torrijos, B. E. Barragán and R. L. Zerbino, "Placing conditions, mesostructural characteristics and post-cracking response of fibre reinforced self-compacting concretes.," *Construction and Building Materials*, 24(6), pp. 1078–1085, 2010.

[20] F. Laranjeira, A. Aguado, C. Molins, S. Grünewald, J. Walraven and S. Cavalaro, "Framework to predict the orientation of fibers in FRC: a novel philosophy," *Cement and Concrete Research*, 42(6), pp. 752-768, 2012.

[21] A. Hillerborg, M. Modéer and P. E. Petersson, "Analysis of crack formation and crack growth in concrete by means of fracture mechanics and finite elements," *Cement and concrete research*, 6(6), pp. 773-78, 1976.

[22] D. A. Cendón, J. C. Gálvez, M. Elices and J. Planas, "Modelling the fracture of concrete under mixed loading," *International Journal of Fracture*, pp. 293–310, 2000.

[23] A. Hillerborg, "Analysis of fracture by means of the fictitious crack model, particularly for fibre reinforced concrete," *The International Journal of Cement Composites*, 1980.

[24] E. Reyes, J. C. Gálvez, M. J. Casati, D. A. Cendón, J. M. Sancho and J. Planas, "An embedded cohesive crack model for finite element analysis of brickwork masonry fracture," *Engineering Fracture Mechanics*, 76(12), pp. 1930-1944, 2009.

[25] J. C. Gálvez, J. Planas, J. M. Sancho, E. Reyes, D. A. Cendón and M. J. Casati, "An embedded cohesive crack model for finite element analysis of quasi-brittle materials," *Engineering Fracture Mechanics*, 109, pp. 369-386, 2013.

[26] K. Park, G. H. Paulino and J. Roesler, "Cohesive fracture model for functionally graded fiber reinforced concrete," *Cement and Concrete Research*, 40(6), p. 956–965, 2010.

[27] J. M. Sancho, J. Planas, D. A. Cendón, E. Reyes and J. C. Gálvez, "An embedded crack model for finite element analysis of concrete fracture," *Engineering Fracture Mechanics*, 74(1), pp. 75-86, 2007.

[28] J. A. Barros, V. M. Cunha, A. F. Ribeiro and J. A. B. Antunes, "Post-cracking behaviour of steel fibre reinforced concrete," *Materials and Structures*, 38(1), pp. 47-56, 2005.

[29] D. Y. Yoo, S. T. Kang and Y. S. Yoon, "Effect of fiber length and placement method on flexural behavior, tension-softening curve, and fiber distribution characteristics of UHPFRC," *Construction and Building Materials*, 64, pp. 67-81, 2014.

International RILEM Conference on Materials, Systems and Structures in Civil Engineering
Conference segment on Service Life of Cement-Based Materials and Structures
22-24 August 2016, Technical University of Denmark, Lyngby, Denmark

BENDER-EXTENDER ELEMENTS FOR CHARACTERIZATION OF CEMENT PASTE AT EARLY AGES

José Granja [(1)], Miguel Azenha [(1)]

(1) University of Minho, Guimarães, Portugal

Abstract
The embedment of bender-extender elements in cement-based materials for assessment of the early development of mechanical properties is a relatively unexplored field. This technique provides the opportunity of embedding piezoelectric elements (emitter and receiver) into the tested material at the fresh state, generate waves and assess the velocity of propagation. It has the interesting feature of allowing distinct frequencies of wave to be explored at the several stages of stiffening of the testing material, thus maximising signal intensity and facilitating the identification of velocities. This paper presents an exploratory application of bender-extender elements to cement paste specimens, in parallel with other established experimental techniques, such as the Vicat needle, ultrasound pulse velocity measurements (with external probes), measurement of E-modulus through cyclic compressive testing and continuous assessment of the E-modulus of the cement paste through EMM-ARM. The results are evaluated and discussed in an integrated manner and conclusions are drawn in regard to the potential of using bender-extender elements in cement-based materials.

1 Introduction

The experimental characterisation of the behaviour of cement-based materials since early ages has been tackled by many researchers through a wide range of techniques. The use of non-destructive techniques based on wave propagation has been subject of wide discussion and developments, both in view of the type of propagated waves (e.g. P or S wave) [1], but also on the methods to identify the velocity of the waves (e.g. time or frequency domain methods) [2]. A relatively recent contribution by Zhu J., et al. [3] has shown the feasibility of adopting bender extender elements for wave propagation assessment in cement based materials. Bender extender elements are composed of piezoelectric plates that are normally coated by an epoxy resin, which are able to generate and measure waves in the tested material. Even though this technique has been widely applied in the study of cohesive soils, the application to cement-

based materials is still at its infancy. The present work aimed to contribute in such field of research, particularly by implementing and testing the application of bender-extender elements in the evaluation of hardening cement pastes since very early ages.
This paper reports a proposed test setup and its pilot experiment applied for two distinct cement pastes. In parallel to this, complementary experimental techniques have been used for comparative purposes: (i) EMM-ARM, (ii) cyclic compression tests for E-modulus assessment, (iii) ultrasound pulse velocity measurement, and (iv) Vicat needle testing. The discussion of obtained results allows obtaining insights about the possibilities and challenges brought about by applying bender-extender elements to the characterisation of cement-based materials.

2 Experimental Program

2.1 Materials

The experiments were conducted on two cement pastes containing Type I and II Portland cement, respectively, while having the same water-to-cement ratio. The mixture proportions of the cement pastes as well as the corresponding nomenclatures are presented in Table 1.

Table 1: Cement pastes adopted in this research work.

Reference	*Cement type*	*w/c ratio*	*Density (kg/m^3)*
c32.5	CEM II/B-L 32.5 N	0.50	1787.4±4.0
c42.5	CEM I 45.5 R	0.50	1840.3±4.1

2.2 Experimental program and procedures

The experimental program involved the assessment of the E-modulus of both cement pastes through 4 distinct methods: bender-extender elements (BE), ultrasonic pulse velocity (UPV), EMM-ARM, and classic cyclic compression (CC). Penetration resistance was also measured through Vicat needle testing, according to EN 196-3:2005. The details about the procedures used in each method are presented in the next section. The list of all the specimens used during this experimental program, comprising the two cement pastes under study is shown in Table 2. BE, UPV and EMM-ARM tests were performed continuously since casting, whereas the cyclic compression tests were conducted at the ages of 2, 3, 7, 14 and 28 days.

Table 2: Specimens used in the study.

Specimen	*Cement paste*	*Monitoring method*
32.5-Vic	c32.5	Vicat
32.5-CC	c32.5	CC
32.5-BE	c32.5	BE
32.5-UPV	c32.5	UPV
32.5-EMM	c32.5	EMM-ARM
42.5-Vic	c42.5	Vicat
42.5-CC	c42.5	CC
42.5-BE	c42.5	BE
42.5-UPV	c42.5	UPV
42.5-EMM	c42.5	EMM-ARM

In specific regard to the preparation of the cement pastes, the mixing operations were performed in an automatic mixer, according to the following procedure that conforms the recommendations of EN 196-1:2005: (i) introduce the cement in the mixer and immediately after add water (instant defined as "t=0"); (ii) start mixing at 500 rpm for 90 seconds; (iii) stop mixing during the following 90 seconds; (iv) resume mixing operation at 500 rpm for another 30 seconds. After the mixing process, the resulting cement pastes were poured into the moulds, which were simultaneously slightly vibrated for removal of air bubbles during the casting process. The time elapsed between mixing and the beginning of monitoring did not exceed 20 minutes for any of the continuous methods (BE, UPV and EMM-ARM). All these tests on c32.5 and c42.5 were performed under moist sealed conditions at 20°C and carried out for at least 7 days. The only exception to the mentioned situation corresponded to the CC specimens that were demoulded right before the first test (t = 2days) and were placed, unsealed, in a controlled environment with T = 20ºC and RH = 60%.

3 Experimental techniques and protocols

3.1 Bender-extender elements (BE)

In the present work, the evolution of the velocity of ultrasonic waves was measured along hydration through bender-extender elements (BE), according to the test configuration shown in Figure 1a. In this study, T-shaped bender-extender elements made in the University of Western Australia were used, and they are schematically depicted in Figure 1b. These BE enable the measurement of P and S waves and operate in a wide frequency range, common for this type of probes. The setup consists of two BE probes, one transmitter placed on one side of the sample, as depicted in Figure 1b, and a receiver positioned on the opposite side. A single period wave, defined in a function generator (model TTI - TG1010A) with 0.1 mHz resolution, an accuracy of <10 ppm and a range of 0.1 mHz to 10 MHz, is transmitted to the sample and received in the opposite side of the sample by another BE probe. An oscilloscope with 16-bit resolution and a sensitivity of 10 mV/div to 20 V/div (PicoScope 4424) performs the analog-to-digital conversion of both emitted and received waves and transmits the digitised waves to the computer for signal processing.

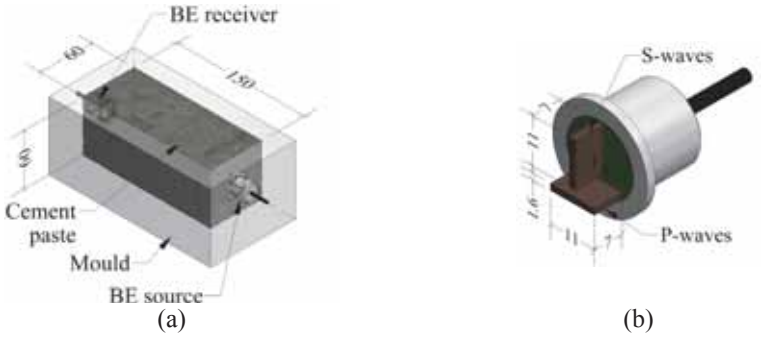

(a) (b)

Figure 1: BE method (a) experimental set-up; (b) BE probe [units: mm].

In order to avoid errors in the identification of the wave propagation time, special attention had to be given to the mould used for the BE methodology, due to the possible existence of

"cross talk" parasite waves [4]. However, as the usual operation of BE elements involves a wide frequency range that can start as low as 1 kHz, the distance between the probes must hence be higher, in comparison with the distance adopted for the UPV method. Preliminary tests in the scope of this research work have shown that a specimen sized 60×60×150 mm^3, moulded inside extruded polystyrene walls is suitable for BE experiments on cement pastes. The probes were placed in the opposite faces of the mould that are separated by 150 mm, as shown in Figure 1a. In order to have a good coupling between the BE probes and the material they were fixed to the mould prior to casting and to allow measurements immediately after mixing. The choice of the best frequency for wave velocity assessment at each instant of testing was made by manually sweeping several frequencies in the range 1 to 50 kHz to obtain the highest output signal amplitude. At such frequency, the identification of the wave arrival time is facilitated, since the noise-to-signal ratio is at its lowest. It is considered reasonable to assume that within the range of frequencies used in this method, the travel time is independent of frequency, that is, the travel time remains the same regardless of the applied input frequency [5].

3.2 Ultrasound Pulse Velocity (UPV)

The test configuration adopted for this methodology is quite similar to the one described in the previous section for BE, except for the use of ultrassonic contact probes instead of BE probes. The contact probes were P-wave probes with operating frequency of 150 kHz and diameter of 25 mm. The size of the probes is considered to be adequate for application to cement pastes since its diameter is greater than the largest expected heterogeneity. The same prismatic mould mentioned for BE testing was used: 60×60×150 mm3. To allow measurements immediately after mixing, the UPV probes were positioned in advance in the opposite faces of the cross-section of the mould, at a distance of 60mm, as shown in Figure 1a.

3.3 EMM-ARM

The cement pastes were tested with the corresponding version of EMM-ARM, as suggested by Granja J. [6]., with the test apparatus shown in Figure 2. The accelerations at the free end of the composite beam were measured with an accelerometer 352C04 (sensitivity: 1 V/g; range: ±5 g) connected to a dynamic acquisition system NI 9234 with 24-bit resolution. The accelerations were recorded at an acquisition frequency of 200 Hz in packages of 120 seconds each 10 minutes.

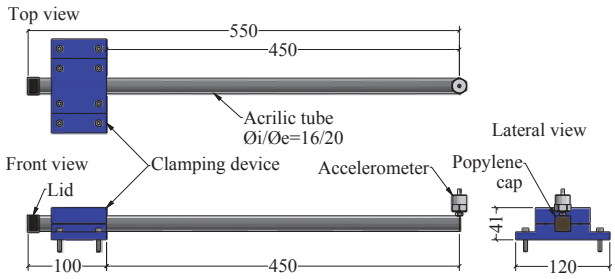

Figure 2: Experimental setup for EMM-ARM testing [units: mm].

3.4 Classical cyclic compression tests (CC)

Classical cyclic compression tests (CC) with on-sample strain measurements were performed to quantify the E-modulus of cylindrical specimens. The cement paste cylindrical specimens utilised in this study had a diameter/height of 50/100 mm. The testing apparatus includes a hydraulic actuator with 50 kN capacity and 3 displacement transducers (LVDTs), supported by 2 aluminium rings attached to the specimens (spaced 40 mm). The test protocol adopted in this work was based on the experiments reported by Maia L., et al. [7]. Each test involved 3 loading/unloading cycles, with a loading rate of 200 kPa/s, and the E-modulus was computed in the loading branch of the last load/unload cycle. The maximum cyclic load reached 33% of the compressive strength of the cement paste at the age of testing, obtained through destructive compressive tests in 50×50×50 mm^3 cubes.

4 Results and discussion

4.1 Bender-extender elements (BE)

As opposed to the UPV method, the use of BE easily allows to perform high quality measurements immediately after casting. This is mainly due to the high efficiency over a wide frequency range that the BE probes possess, which enables an adjustment of the input frequency to provide better results at each instant of measurement. However, despite this benefit, the use of BE is often accompanied by difficulties associated with a high sensitivity to external disturbances (such as the existence of electrical noise in the testing room), that poses relevant hurdles for the interpretation of test results. This high sensitivity can be partly explained by the relatively low power of the signal generator adopted in this research that solely allowed a maximum excitation amplitude of 20 V. On the other hand, the use of power amplifiers (to boost the input signal) is limited by the transducer itself, which depolarises approximately above 60 V. Figure 3 shows four S-wave signal readings performed for the paste c42.5 at ages of 2.9, 9.0, 26 and 172 hours. These readings were conducted at optimum increasing frequencies between 1 kHz at 2.9 hours and 50 kHz at 172 hours (see Figure 3a). In the four measurements presented in Figure 3b, one can clearly observe the difficulty the identification of the first arrival of the wave. This problem was already mentioned in the works of Ferreira C. M. [8] and Viana da Fonseca A., et al. [5] regarding the performance of BE in stiff materials.

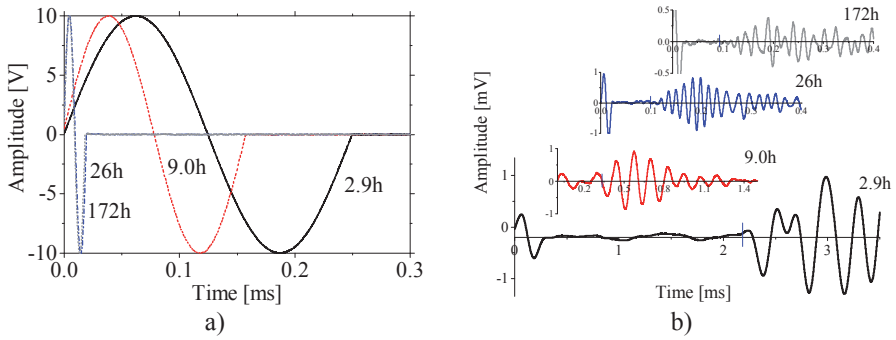

Figure 3: BE Signal readings during tests of c42.5: a) Input; b) Output.

The BE used in these tests have the capability of measuring compressional (P) and shear (S) waves, hence initially all tests included the recording of both wave types. However, after some measurements, it was found that both sensors measured exactly the same type of wave: S-waves (noted by the same wave shape and the order of magnitude of the recorded velocities). The justification for this phenomenon is likely to rely on the characteristics of the BE probes, as mentioned by Lee J.-S. and Santamarina, J. C. [9], and schematically shown in Figure 4a: the probe generates two P-wave side lobes normal to their plane and a S-wave frontal lobe. Therefore, since the generation of response signal in the receiver demands that the sensor itself bends, when the BE transmitter and BE receiver are perfectly aligned (which is the case in our work), the P-waves are parallel to the longitudinal axis of the receiving transducer, thus being unable to flex it. On the other hand, the S waves disturb the transducer in the direction perpendicular to its longitudinal axis, thus causing a larger bending motion and as a result a larger signal output. This feature causes them to lose the ability to adequately receive P-waves, while having a significant resolution in the measurement of S-waves. Additionally, at very early ages, i.e. in fresh pastes, the propagation of P-waves is difficult, due to the presence of entrapped air and to the high stiffness impedance between the transducer and the material. As the paste hardens, the compressional wave velocity increases rapidly and the frequency required to measure such high velocity causes the BE to vibrate in complex mode shapes, which in turn strongly reduces the amplitude of the effectively propagated wave and makes it difficult to detect the P-wave in the received signal.

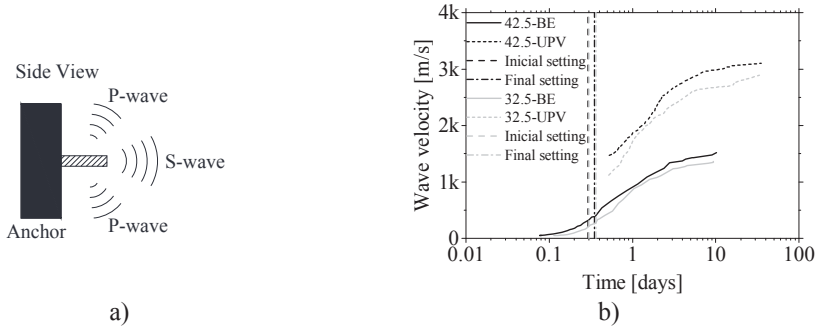

Figure 4: a) Waves in a BE probe. Adapted from [9]; b) Results for c32.5 and c42.5 (waves).

Consequently, the attempt to measure P-waves with BE in the scope of this research work was abandoned. Moreover, these results demonstrate that the use of S-waves is more suited to monitor these complex evolving processes than P-waves, since shear waves only propagate through the solid skeleton of the specimens, providing a higher sensitivity towards the structural changes that occur during setting. After obtaining the propagation time of the S-waves, the evolution of the wave velocity was computed, as shown in Figure 4b. It can be observed that there are no significant differences in the recorded wave velocities for the two types of pastes. However, the S-wave velocity is higher in the c42.5 paste throughout the entire curing period. It should also be noted that the difference in the wave velocity increases along the curing process. Therefore, the application feasibility of this methodology to cement

pastes was confirmed in coherence with the conclusions of the research work conducted by Zhu J., Tsai, Y.-T. and Kee, S.-H. [3].

4.2 Ultrasonic Pulse Velocity (UPV) and Vicat

The evolution of the P-wave velocity for c42.5 and c32.5 is shown in Figure 4b, together with information collected by Vicat testing. Firstly, it should be noted that UPV was unable to provide measurements of P-wave velocity in the cement pastes at very early ages, including the setting period. The earliest measurement was only possible at t = 12.4 hours for both pastes (see Figure 5). The reason for this problem can be attributed to the presence of air bubbles in the samples, which have been reported to attenuate and delay the wave propagation, the low power used to excite the transducer (10Vpp as opposite to >100Vpp used by other authors), as well as due to the high impedance mismatch between the transducers and the fresh cement paste [3]. In fact, in order to monitor the evolution of the P-wave velocity in cement pastes, some authors [10] used de-aired samples (previously placed in vacuum) with successful results. However, since the 'real' cement pastes always contain some air bubbles the de-airing of the samples may end up producing unrealistic results. In order to avoid this drawback in UPV, some authors [2, 3] successfully performed measurements during the setting by using smaller distances between the probes and more energetic excitation signals (with higher voltage) even with the wave attenuation. Such alternative was not available in this research work. However, despite the absence of UPV measurements in this initial period (~12 hours), the wave velocity measurements of Figure 4b exhibit an evolution which can be considered plausible. In fact, the various stages usually observed in the cement hydration kinetics after the dormant period can be identified: (i) an initial stage where a substantial increase in wave velocity occurs; (ii) a subsequent stage in which the velocity evolution becomes less significant. Lastly, it can be noted that the c42.5 paste shows a greater increase in wave velocity, which is consistent with the results of the EMM-ARM that were already reported.

4.3 EMM-ARM and CC

The E-modulus evolution identified by the EMM-ARM method for two cement paste mixtures under study are shown in Figure 5. When comparing the results obtained with the two pastes containing the same w/c ratio (c42.5 and c32.5), it can be seen that the cement paste containing the CEM I 42.5R cement has a higher stiffness, with a difference of ~2 GPa at the age of 7 days (168 hours) - see Figure 5. However, even though the cement paste c42.5 has reached a higher stiffness after the first day of curing, the E-modulus evolution at very early ages is fairly similar to that of paste c32.5. In fact, this would not be expected by strictly considering the chemical composition of the utilized cements, namely due to the higher C3S content of cement CEM I 42.5R. Nonetheless, another important characteristic might justify this behaviour at very early ages: the specific surface or Blaine index. In fact, the Blaine index of CEM I 42.5 R is lower than that of CEM II/B-L 32.5N (3891 against 4899 cm^2/g). The similarity of the E-modulus evolution at very early ages between the two pastes can thus be considered reasonable, taking into account these two aspects that justify the apparent inverse trends: clinker composition and specific surface.

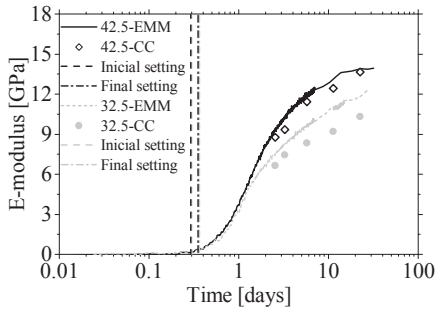

Figure 5: Comparison of the results of EMM-ARM, Vicat, and cyclic compression for cement pastes c32.5 and c42.5.

The comparison between the elastic modulus results obtained by EMM-ARM and by classic methods (CC and Vicat) for the cement pastes c32.5 and c42.5 is shown in Figure 5. It can be seen that the values obtained through the EMM-ARM are similar to those collected in CC tests in terms of magnitude and evolution kinetics. However, the results for c32.5 (Figure 5) show a non-negligible difference of 1.4 GPa at t = 22.4 days (538 hours). This deviation may possibly be explained by differences in the curing conditions of the samples. In fact, the EMM-ARM samples remained in perfectly sealed conditions during the whole test, while the samples used for the CC tests were exposed to drying during the testing period. This small variation in the curing conditions may have influenced the hydration process at the surface of the CC specimens [11], which may have significant effects in view of the small size of the specimen, thus resulting in lower stiffness. As the porosity of c32.5 is higher than that of c42.5, it is plausible that this deficient curing of CC specimens may have affected c32.5 more significantly, as opposed to c42.5. The results presented in Figure 5 also show good agreement between EMM-ARM and the data collected by the Vicat needle, in the sense that the end of setting determined by Vicat testing coincides with the end of the dormant period observed in EMM-ARM, followed by a strong acceleration of the hydration kinetics.

4.4 Overall comparison

Taking into account that the methodologies based on wave propagation measure dynamic parameters, for the purpose of comparison of all methodologies under study, the results were normalized ('Norm' in Figure 6) by dividing all results of each specimen/methodology by their corresponding values at t = 7 days. Moreover, in order to simplify the analysis and to compare both methods based on wave propagation (BE and UPV) with the results of quasi-static methods, the velocity values were squared (V^2) prior to normalization, as V^2 is proportional to the elasticity modulus [2].

The results of all experimental methods involved in this comparison is given in Figure 6, which demonstrates a quite reasonable reciprocal agreement, thus mutually validating the studied methodologies. The good performance of EMM-ARM in the scope of this comparative study, together with its ability to provide precise, continuous and quantitative estimates of E-modulus confirms the versatility and applicability of this methodology.

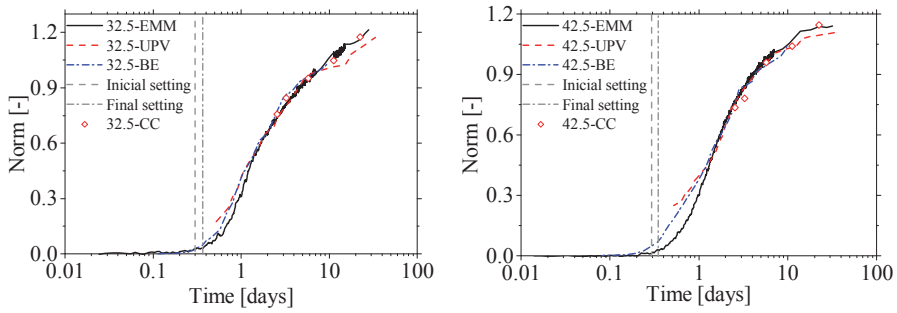

Figure 6: Comparison of the results of all methodologies used in this study for cement pastes a) c32.5 and b) c42.5.

In regard to setting times, there is also a good coherence between Vicat, EMM-ARM and BE, as observable in Figure 6. Thus, these results have confirmed the applicability of the wave propagation methods to monitor the stiffness of cement pastes since the fresh state and throughout the entire hardening process, as already mentioned by other authors [2, 10]. Despite this fact, the results obtained by these wave-propagation based methods should be regarded qualitatively, since these refer to dynamic properties, whose conversion to static properties is often arguable, particularly at very early ages, due to the evolution of Poisson's ratio during curing [12]. However, it should be noted that these wave velocity methods (BE and UPV) seem to exhibit a slightly more accelerated evolution kinetics than EMM-ARM, which is more evident for the c42.5 paste, as shown in Figure 6b. This fact may be related to the early evolution of Poisson's ratio. Similar findings have been reported in other research works, where the consideration of constant Poisson's ratios led to apparent earlier acceleration of stiffness when estimated through pulse velocity methods.

5 Conclusions

This paper has presented an experimental work devoted to a pilot experiment for application of Bender Extender elements for monitoring early age stiffness of cement pastes. This study involved two cement paste mixtures, which were tested through several techniques for benchmarking purposes: bender extender elements, EMM-ARM, compressive cyclic testing, ultra-sound pulse velocity and Vicat needle testing.

It was found that the application of bender-extender elements to cement paste is viable and provides relevant data at early ages, which relates well to the properties assessed through the other competing experimental techniques used in this work. Indeed, the bender extender elements were found to have special aptitude to assess the behaviour at very early ages through S-waves, with capacity to capture evolution of stiffness even before the setting period, with the best resolution among the techniques used in this research work. In spite of the capacity of bender-extender elements to be excited at variable frequencies, which offers better opportunities of increasing the amplitude of signals at all ages of testing, significant

hurdles were identified in the assessment of wave velocity in view of the high noise-to-signal ratio.
The advantages and pitfalls observed for bender extender elements lead the authors to consider that this is a technique that is worth of further research.

Acknowledgments

This work was partly financed by FEDER funds through the Competitivity Factors Operational Programme - COMPETE and by national funds through FCT – Foundation for Science and Technology within the scope of the projects POCI-01-0145-FEDER-007633 and POCI-01-0145-FEDER-016841.

References

[1] Voigt, T., et al., Comparison of ultrasonic wave transmission and reflection measurements with P- and S-waves on early age mortar and concrete, Materials and Structures 8 (2005), 729-738.
[2] Reinhardt, H. W. and Grosse, C. U., Continuous monitoring of setting and hardening of mortar and concrete, Construction and Building Materials 3 (2004), 145-154.
[3] Zhu, J., et al., Monitoring early age property of cement and concrete using piezoceramic bender elements, Smart Materials and Structures 11 (2011), 115014.
[4] Santamarina, J., et al., Soils and waves:Particulate materials behavior, characterization and process monitoring, Journal of Soils and Sediments 2 (2001), 130.
[5] Viana da Fonseca, A., et al., A Framework Interpreting Bender Element Tests, Combining Time-Domain and Frequency-Domain Methods, Geotechnical Testing Journal 2 (2009), 1-17.
[6] Granja, J., Continuous characterization of stiffness of cement-based materials: experimental analysis and micro-mechanics modeling, PhD Thesis, University of Minho (2016).
[7] Maia, L., et al., E-modulus evolution and its relation to solids formation of pastes from commercial cements, Cement and Concrete Research 7 (2012), 928-936.
[8] Ferreira, C. M., The Use of Seismic Wave Velocities in the Measurement of Stiffness of a Residual Soil, PhD Thesis, Faculty of Engineering of the University of Porto (2009).
[9] Lee, J.-S. and Santamarina, J. C., Bender Elements: Performance and Signal Interpretation, Journal of Geotechnical and Geoenvironmental Engineering 9 (2005), 1063-1070.
[10] Boumiz, A., et al., Mechanical properties of cement pastes and mortars at early ages : Evolution with time and degree of hydration, Advanced Cement Based Materials 3-4 (1996), 94-106.
[11] Parrott, L. J., A review os methods to determine the moisture conditions in concrete, (1990), 28
[12] Popovics, J. S., et al., ACI-CRC final report – a study of static and dynamic modulus of elasticity of concrete, (2008),

International RILEM Conference on Materials, Systems and Structures in Civil Engineering
Conference segment on Service Life of Cement-Based Materials and Structures
22-24 August 2016, Technical University of Denmark, Lyngby, Denmark

DEVELOPING AN ENGINEERING APPROACH FOR MIGRATING FROM PRESCRIPTIVE TO PERFORMANCE-BASED SPECIFICATION FOR CONCRETE

Sreejith Nanukuttan [(1)], P. A. Muhammed Basheer [(2)], W. John McCarter [(3)] and Tang Luping [(4)]

(1) Civil Engineering, Queen's University, Belfast, Northern Ireland, UK.
(2) School of Civil Engineering, University of Leeds, England, LS2 9JT, UK
(3) School of Energy, Geosci., Infrastruct. and Env., Heriot Watt Univ., Edinburgh, UK
(4) Chalmers University of Technology, Gothenburg, Sweden

Abstract
The integral variability of raw materials, lack of awareness and appreciation of the technologies for achieving quality control and lack of appreciation of the micro and macro environmental conditions that the structures will be subjected, makes modern day concreting a challenge. This also makes Designers and Engineers adhere more closely to prescriptive standards developed for relatively less aggressive environments. The data from exposure sites and real structures prove, categorically, that the prescriptive specifications are inadequate for chloride environments. In light of this shortcoming, a more pragmatic approach would be to adopt performance-based specifications which are familiar to industry in the form of specification for mechanical strength. A recently completed RILEM technical committee made significant advances in making such an approach feasible. Furthering a performance-based specification requires establishment of reliable laboratory and on-site test methods, as well as easy to perform service-life models. This article highlights both laboratory and on-site test methods for chloride diffusivity/electrical resistivity and the relationship between these tests for a range of concretes. Further, a performance-based approach using an on-site diffusivity test is outlined that can provide an easier to apply/adopt practice for Engineers and asset managers for specifying/testing concrete structures.

1. Why there is a need to change the current practice and specification?

Chloride transport into concrete is controlled primarily by the availability of chloride ions on the surface and properties of cover concrete such as diffusivity, porosity and ionic concentration of pore fluid. There are several other factors that also contribute to the transport and subsequent corrosion of reinforcement including temperature, moisture gradient, chloride binding, pore refinement and critical chloride threshold.
In order to specify a concrete that will last the design life of, say, 120 years, it is necessary to understand the contributing factors and their interconnectivity. It is also known that effects

such as shrinkage, structural loading and other deterioration mechanisms can increase the rate of chloride transport which may not be obvious from controlled laboratory testing on unloaded, small concrete specimens. Fig. 1 shows the chloride ingress data from two concrete structures exposed to marine environment. The mix design shows that both concretes conform to BS 8500 design requirements [1]. However, as the 7 year and 18 year data show, chlorides have reached the rebar location in sufficient quantity to initiate corrosion. It is interesting to note that Fig.1b refers to a concrete designed to a higher specification, with 460 kg/m^3 of CEM I, 0.4 water/binder (w/b) ratio, and a 28-day strength of 66 MPa. These are not isolated structures with high chloride ingress, but it is well known that the majority of the structures in XD and XS environments will not reach the 120 year design life without several significant interventions during their lifespan. In this context, one of the options for asset owners is to test concrete to determine its initial performance or invoke the option of Designed or Proprietary concretes outlined in BS 8500 [2]. For chloride ingress, there are several factors that control or govern performance, but as an interim method, determining/specifying diffusivity as well as capturing the mix details in sufficient depth for further analysis is a step in the right direction. In the next section, test methods commonly used in Europe to determine diffusivity are reviewed and the relationship between the methods is studied with a view to identify suitable methods for site and laboratory application.

2. Laboratory and onsite test methods for assessing chloride ingress

Chloride transport through a small section of concrete can be classified into three phases, non-steady (when the inward flow is not equal to outward flow – binding is effective), steady state (when inward and outward flow is equal) and attenuation state (when other ions take priority over chloride ions). Test methods mimic these phases in a small specimen and with an appropriate mathematical expression, it is possible to determine a diffusion coefficient when the test is concentration driven. Non-steady tests are more rapid and can replicate flow similar to the real structure, but decoupling the effect of binding is difficult, unless binding capacity is determined separately. Steady-state tests take longer to establish but it is perceived that they replicate the flow of free chloride ions and therefore can better assess the risk of reinforcement corrosion. An electrical field can be applied to accelerate the flow of chlorides in a test and therefore complete the test in short duration. These are classified as migration tests, and the resulting coefficient is either steady or non-steady state migration coefficient, similar to the phases in a diffusion test.
Results from different methods are presented below and the discussions will focus on the sensitivity of the coefficient to mix properties such as w/b ratio and type of binder and also on the standard error between the three replicate tests.

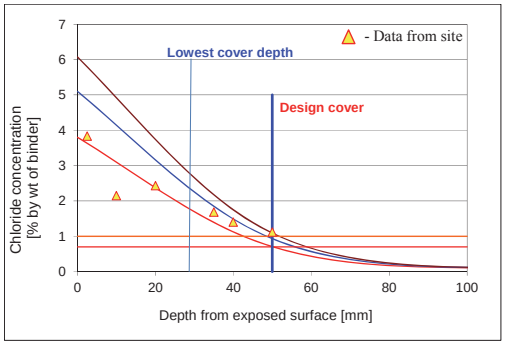

Fig. 1a, chloride profile from a concrete pier situated off the Atlantic coast (Cl^- concentration 15,700 ppm) after 7 years of exposure. Concrete mix information available are 0.46 w/b, 400 kg CEM I, C40/50 with a design cover of 50 mm and minimum cover on site of 27 mm.

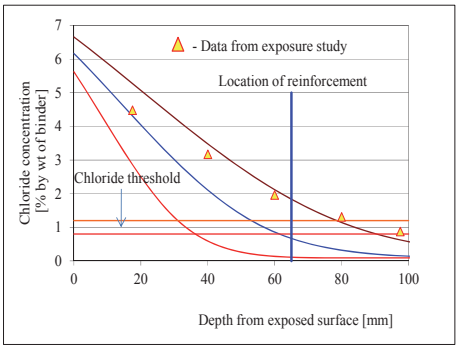

Fig. 1b, chloride profile from a concrete pier off North sea (Cl^- concentration 8,800 ppm) after 18 years of exposure. Concrete mix information available are 0.40 w/b, 460 kg CEM I, sample taken from XS2, compressive strength f_{28} = 66 MPa, design and actual cover is 65 mm.

Non-steady state measurement

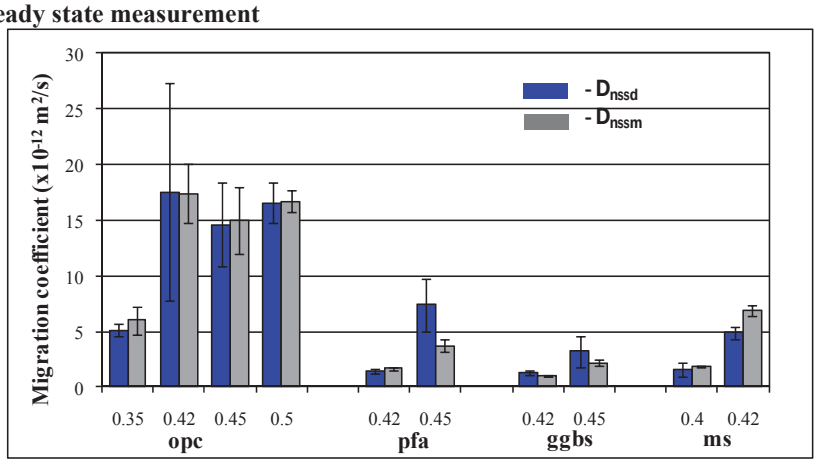

Fig. 2 Effect of mix properties on the non-steady state coefficient. D_{nssd} – Represent non-steady state diffusion coefficient as per NT Build 443, and D_{nssm} – represents non-steady state migration coefficient as per NT Build 492. Mix design and test details are given elsewhere [3].

Fig. 2 shows that both coefficients are sensitive to mix variables such as w/b and type of binder. For the exception of 0.42 w/b opc, which was found to have large cavities, all the other results are in line with previous published literature. In order to evaluate the effectiveness of other methods, the D_{nssd} was considered as reference value. This is mainly due to the fact that this test replicates the real-life scenario in which chloride ions move

through concrete under a concentration gradient. However, this highlights the challenge in conducting the non-steady state test as it is lengthy and requires considerable effort/man power including chemical analysis. The advantage of the migration-based test over diffusion test is that it is more rapid (1-4days), chemical analysis is not required, utilizes considerably less man power, but requires chemicals and a dedicated test set-up as described in NT Build 492. The relationship between the two coefficients is known to be linear with a high coefficient of regression [4, 5]. In addition, a lower standard error for D_{nssm} as compared to D_{nssd} would provide more confidence in the migration test method. Since the completion of the study, this test was successfully utilized as a quality control test for a major construction work in Ireland. One of the major advantages is that both D_{nssd} and D_{nssm} are commonly used for service-life prediction with the help of Fick's law based models.

Bulk electrical resistivity

Bulk resistivity was measured on concrete specimens prepared for non-steady state migration test: 50 mm thick and 100 mm diameter concrete cylinders were vacuum saturated in $Ca(OH)_2$ solution.

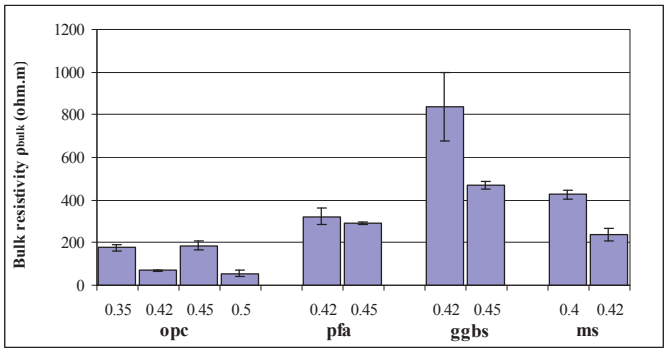

Fig. 3 Effect of mix properties on the bulk resistivity, ρ_{bulk}

Resistivity is a very rapid (5 mins) test and the results presented in Fig. 3 show a very high repeatability. Use of ionic saturated test specimens, lack of polarization due the use of AC voltage source, instantaneous measurement as compared to tests that run over days, all must have contributed to improving the repeatability. Moreover, published literature suggests that bulk resistivity of either water saturated or ionic saturated concrete specimens can be used to predict the steady or non-steady state migration coefficients [6-7]. This relationship is further explored by researchers for predicting the chloride transport as well as the onset and the propagation of reinforcement corrosion [8-9].

Steady state measurement

Similar to the coefficients discussed previously, steady-state migration coefficient, D_{ssm} in Fig. 4 shows that it is sensitive to mix variables and, generally, decreased with a decrease in w/b. The coefficients were significantly lower for concretes containing supplementary cementitious materials, with the exception of pfa concretes. The beneficial effect is more evident for concrete with higher w/b. A higher value for D_{ssm} for pfa concretes could be attributed to the low reactivity of the pfa blend used in this experimental programme. Tests

undertaken after two years on samples matured in an ideal laboratory condition showed a substantial reduction in the coefficients. It is expected that for all concrete mixes, hydration process continues beyond 28 days and further hydration products that are formed within the available space including pore walls. This will refine the pore structure and make the concrete less permeable.

The steady-state migration test can be considered as more rapid than the non-steady state diffusion test, but it requires 3-7days to complete which makes it less rapid than non-steady state migration test and bulk electrical resistivity test. Test requires a dedicated experimental set-up and set of skills for determining the coefficients.

$D_{in\ situ}$ refers to in situ migration coefficient determined using a surface based chloride migration test (Permit Ion Migration Test) and the figure 4 clearly shows that $D_{in\ situ}$ is sensitive to both w/b and type of binder. This figure also shows that the error associated with $D_{in\ situ}$ is low (similar to D_{ssm}). The data obtained from test carried out after 2 years reveal that the coefficient has halved in most cases. This confirms that the test is also sensitive to the maturity of the concrete. The advantage of the Permit is that as it is a surface-based test, it requires no coring and therefore no physical damage to concrete structure, it can test concrete in-situ. The coefficient will reflect, therefore, the interaction of structural loading, shrinkage, thermal strains, damage/pore blocking due to carbonation or damage due to other durability mechanisms, leaching, etc.

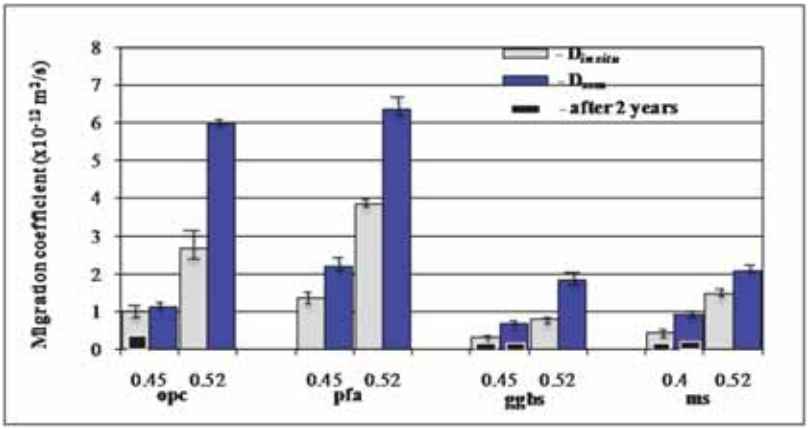

Fig. 4 The effect of mix properties on the steady state migration coefficient, D_{ssm}
Note: test voltage 12-60 v, 0.55 M NaCl solution, for further details refer to [3]

Relationship between the coefficients

The relationship between the various test results are discussed in the following section with a focus on the relationships between the coefficients and existing service life prediction models and also to identify further details regarding chloride ingress into concrete viz. chloride binding, volumetric porosity, etc.

It is worth noting that the discussion is limited to the concrete studied, mainly, 0.45-0.52 w/b, a higher w/b may warrant a higher slope ≥ 0.3, as reported elsewhere [7].

Nilsson et al (1996) suggested a relationship between steady and non-steady coefficient, and the mathematical expression is given in Eq. 1

$$D_{nssd} = \frac{D_{ssd}}{\varepsilon\left(1+\frac{\partial C_b}{\partial C_f}\right)} \quad \text{Eq. 1}$$

ε - porosity, and $\frac{\partial C_b}{\partial C_f}$ – represents binding capacity

The data presented in Fig. 5 show that this relationship can be proven experimentally. Therefore, the slope of the line, 4.42, represents the combined effect of binding and porosity on chloride transport. Therefore, in modelling the chloride transport, knowledge of three of these parameters will be invaluable. Porosity and diffusivity can be determined relatively easily, binding capacity may be estimated from the literature for the binder type and quantity, and this will make service life modelling easier to perform. Note that the slope of the line may change due to the experimental set-up; for Example, if 1.0 M NaCl solution is used instead of 0.55 M used in this study, then the slope decreases.

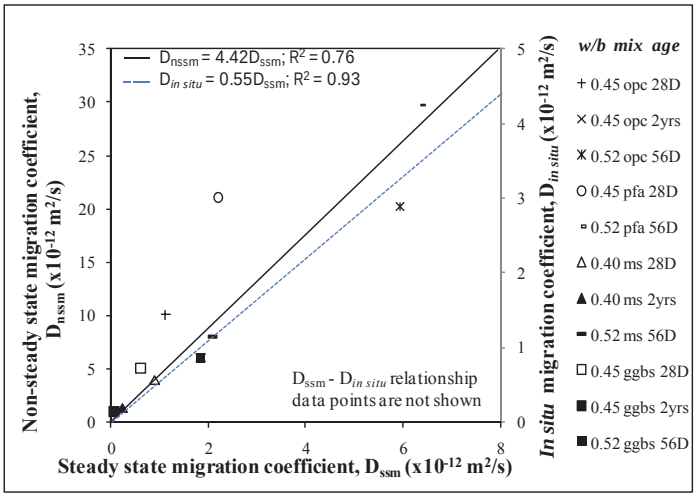

Fig. 5 Relationship between different migration coefficients [3].

Also presented in Fig. 5 is the relationship between coefficients evaluated from Permit and a conventional steady-state migration test (D_{ssm}). If both tests use the same principle, the coefficients should be linearly related and equal in magnitude; however, the slope is 0.55 and not unity. This is attributed to the difference in test set-up. The conventional steady state test uses 1.2 L of 0.55 M NaCl solution whereas PERMIT uses 0.45 L of 0.55 M NaCl. The Permit will electrically charge a region for accelerating the chloride flow. As the effective zone of influence of the electrical filed depends on the quality of concrete, cracking and contamination, this cannot be equated directly to a laboratory based test set-up which assumes a linear voltage drop per meter of specimen. These differences could influence the relationship and can be considered the reason as to why $D_{in\ situ}$ is lower than D_{ssm}.

Nevertheless, the coefficients are linearly related and therefore one can represent the other within the range of concrete studied.
Electrical resistivity, whether bulk or surface based, can be related to diffusion/migration coefficient and is reasonably well established [3-9]. The mathematical expression between surface resistivity, determined using the Wenner four probe technique, and $D_{in\ situ}$ is [3]:

$$D_{in\,situ}\,(x10^{-12}) = \frac{140}{\rho_{Wenner}} \qquad \text{Eq. 2}$$

Where, ρ_{Wenner} represents the surface resistivity in Ω-m. The coefficient of regression for the relationship is 0.72.
The benefit of using a relationship such as Eq. 2, is that assessing a large structure becomes easier. Resistivity measurements and mapping can be easily performed. This allows identification of areas of relative weakness/strength for further analysis. Once such a mapping has been produced, Engineers can decide to further investigate weak areas by gathering concrete dust-drillings for chloride analysis and Permit testing. Diffusivity from Permit or similar test can be used for chloride modelling and relationships, as in Eq. 2 will allow extension in prediction to all areas of the structure. Further, by superimposing the above information on cover meter data will assist engineers in the decision regarding the remaining life of a structure across the various locations. It is important to note that resistivity data will be influenced by moisture distribution, presence of chloride ions or carbonation and surface emanating cracks. Therefore the resistivity mapping alone should not be used in decision making, but further analysis as suggested before should be performed. The mapping, however, can be used as a progressive asset management tool for critical structures (or sections), where regular monitoring is a necessity.

3. Developing an approach for performance testing and modelling – Venlo RRT programme

The recently completed RILEM PSC technical committee held a round-robin test program (RRT) to establish the validity of site-based methods and the performance-based approach they can offer for testing/specification. Eight concrete mixes were considered, and the mix details are shown below in Fig. 6. Further details are available in the state-of-the-art report [11].
The Permit test was performed to determine $D_{in\ situ}$ for all the eight mixes. The concrete samples were just over two weeks old at the time of testing, so concrete maturity was determined using resistivity data, so that $D_{in\ situ}$ at 180 days could be determined. This approach was validated by repeating the test at a later age (refer to [11]). Using $D_{in\ situ}$ at 180 days, chloride transport modelling was performed using ClinConc [12]. The time for the chloride concentration to reach an assumed chloride threshold of 0.1% by mass of concrete was considered as the end of service life (time for corrosion initiation). Although such an approach ignores the corrosion propagation time, it should be considered as a conservative and safe option for designing concrete structures. Safety refers to the reliability/repeatability of the testing and prediction methods for quantifying chloride transport. Users can add the propagation time, if available for their structures to get a more realistic service life.

Sample	w/b	CEM	Date	Age at testing (days)	Measured $D_{in\ situ}$ (10^{-12} m²/s)
1	0.44	I	15-Apr-12	18	0.62
2	0.44	I		18	0.14
3	0.54	I		17	0.85
4	0.54	I		17	1.85
5	0.40	II B/V		16	0.95
6	0.40	II B/V		16	1.05
7	0.59	II B/V		14	2.64
8	0.59	II B/V		14	1.89

Fig. 6 Concrete panels used in Venlo RRT programme and the mix design and test details.

Table 1 Summary of the predicted performance of Samples 1-8 in XS3 exposure environment for C_s = 14 g/L

Sample	Predicted D value at 180 days ($D_{in\ situ}$ x 10^{-12}m²/s)	Actual Cover (mm)	Predicted Corrosion Initiation Time	Acceptable for XS3 exposure for 100 years of service Life	Suggested Improvement for 100 year Service Life
1	0.44	30	<10 years	No	Proper curing, increase binder content and cover ≥ 80mm
2	0.10	30	~ 50 years	No	Increase cover to 40mm
3	0.34	30	~ 10 years	No	Increase cover to 80mm
4	0.75	30	<10 years	No	Not suitable
5	0.25	30	~ 20 years	No	Increase cover to 70mm
6	0.27	30	~ 15 years	No	Proper curing, increase binder content and cover ≥ 70mm
7	0.51	30	≤ 10 years	No	Not suitable >> 80mm cover
8	0.37	30	~ 10 years	No	Increase cover to 80mm

Note: Covers higher than 70mm, are not viable for structural concretes due to lack of shrinkage control, so alternative mix design or surface treatment/cladding should be sought in such cases.

For the purpose of RRT, it was assumed that specimens are exposed to XS3 environments (i.e., salt concentration of 14 g/L) and for a cover of 30 mm, the time for initiation of corrosion (service life) was determined, refer to Table 1. The table also provides suggestions for improving the service life either by increasing the cover or by better curing the specimens. The procedure outlined in Fig. 7 shows how a performance-based specification can be developed using $D_{in\ situ}$ for a range of concrete specimens. As $D_{in\ situ}$ is a steady state coefficient, the critical value of 0.35x 10^{-12} m²/s can be adopted irrespective of the binder type (binding capacity). Binding capacity can be considered at the modelling stage and as shown

before this can be either estimated from the binder type/quantity or experimentally determined. This makes testing much easier and less complicated for industrial adaptation.

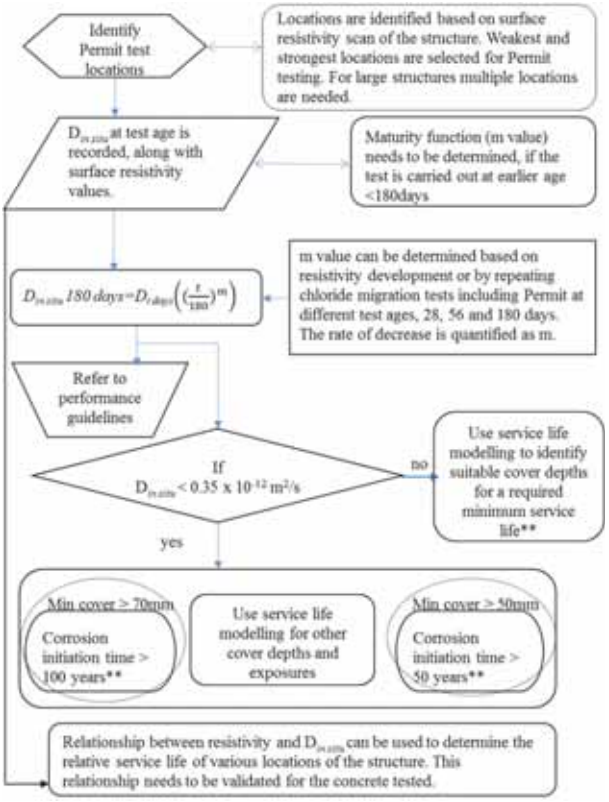

Moreover test can be repeated as and when required to confirm the quality (or quantify deterioration), estimate the remaining service life and decide on early remedial actions if necessary. Relationships presented in section 2 can be utilized as discussed before for estimating the remaining service life using a combination of surface resistivity and $D_{in\ situ}$. Such an approach is ideal for asset management where regular detailed inspection is a necessity.

4. Concluding remarks

This article reviewed the performance of two concrete structures in marine environments and shows the need for a performance-based approach for concrete specification. A review of the different test methods that can be successfully employed as quality control measures was carried out and the interrelationship between these tests also provided. The discussions in this paper gave emphasis to site based tests. Further, a methodology for developing performance-

based specification was outlined using Permit (a site based chloride diffusivity test) and chloride ingress modelling. The advantages of this approach include, and are not limited to, (1) determination of diffusivity in a larger undisturbed specimen, on site, with all the stresses / stain of a real structure and (2) providing a means to benchmark the performance measure at an early age, so that any further deterioration can be quantified easily and timely interventions carried out.

References

[1] British Standard 8500-1:2012, Complementary British Standard to BS EN 206-1, Part 1 Method of specifying and guidance for the specifier, (2012).
[2] Specifying Sustainable Concrete - Understanding the role of constituent materials, Concrete Centre, www.concretecentre.com/, Publications, (2011), revised in 2015.
[3] Nanukuttan, SV, et. al., 2015, 'The performance of concrete exposed to marine environments: predictive modelling and use of laboratory/on site test methods' CBM, vol 93, (2015) pp. 831-840.
[4] Chlortest- Resistance of concrete to chloride ingress-from laboratory test to in-field performance, CHLORTEST, Final Technical Report EU FP5 Growth Initiative (GRD1-2002-71808), (2006).
[5] Baroghel-Bouny, V., et al., Which toolkit for Durability Evaluation as regards Chloride ingress into concrete?, Part I: Comparison between various methods for assessing the chloride diffusion coefficient of concrete in saturated conditions, Proc 38, (2002).
[6] Andrade, C., et al, Methodology based on the electrical resistivity for the calculation of reinforcement service life, Fifth CANMET/ACI International Conference on Durability of Concrete, (2000), pp. 899-915.
[7] Baroghel-Bouny, V., et. al., (2010), Easy assessment of durability indicators for concretes with high volume of SCMs, 2nd International Conference on Sustainable Construction Materials and Technologies, June 28-30, (2010).
[8] Andrade, C and d'Andrea, R., , 'Electrical resistivity as microstructural parameter for modelling of service life of reinforced concrete structures", 2nd International symposium on Service Life Design for Infrastructure, 4-6 October 2010, Delft, The Netherlands, Volume 1, (2010), pp. 379-388
[9] Otieno, M., Beushausen. H. and Alexander, M., Resistivity-based chloride-induced corrosion rate prediction models and hypothetical framework for interpretation of resistivity measurements in cracked RC structures, Materials and Structures, June (2015), DOI 10.1617/s11527-015-0653-z.
[10] Nilsson, L., et. al., HETEK, Chloride penetration into concrete, State-of-the-art-report, Report No. 53, (1996), pages. 151.
[11] Beushausen, H, et. al, 'Application examples of performance-based specification and quality control'. in H Beushausen & L Fernandez Luco (eds), Performance-based specification and control of concrete durability: RILEM State-of-the-Art Reports, vol. 18, (2016) Springer, pp. 197-266., 10.1007/978-94-017-7309-6_8
[12] Tang, L. 'Service-life prediction based on the rapid migration test and the ClinConc model', Proc of Int RILEM workshop on Performance Based Evaluation and Indicators for Concrete Durability, 19-21 March (2006), Madrid, RILEM PRO 47, pp. 157-164.

International RILEM Conference on Materials, Systems and Structures in Civil Engineering
Conference segment on Service Life of Cement-Based Materials and Structures
22-24 August 2016, Technical University of Denmark, Lyngby, Denmark

PROPERTIES OF CONCRETE RECYCLING CLAY-RICH DREDGING SEDIMENTS AS A NOVEL SUPPLEMENTARY CEMENTITIOUS MATERIAL

Céline Van Bunderen [(1)], Ruben Snellings [(2)], Liesbeth Horckmans [(2)], Joris Dockx [(3)], Jos Vandekeybus [(4)], Koenraad Van Balen [(1)], Lucie Vandewalle [(1)], Özlem Cizer [(1)]

(1) Department of Civil Engineering, KU Leuven, Leuven, Belgium
(2) VITO (Flemish Institution for Technological Research), Mol, Belgium
(3) Department for Mobility and Public works, Flemish Government, Antwerp, Belgium
(4) Seneka, Kalmthout, Belgium

Abstract
Treated dredging sediments of the port of Antwerp are rich in clays (2:1 clays and kaolinite) and contain relatively low contents of sulfur and chloride. When flash calcination is applied to activate the clay minerals and to reduce the total organic content, the sediments show pozzolanic properties superior to siliceous fly ash. This paper investigates the applicability of the calcined dredging sediments as a supplementary cementitious material replacing Portland cement in concrete, and evaluates the basic properties of fresh and hardened concrete in comparison with two reference concrete mixes composed of Portland cement and Portland fly ash cement. When cement is replaced at 20, 30 and 40 wt.% ratios by dredging sediments, compressive and flexural strength values of concrete at 7 days decrease respectively. Low early strength is, on the other hand, compensated by the pozzolanic reactions taking place up to 28 days when the strength of blended concrete compositions reaches that of the reference Portland cement concrete. The initial results clearly indicate that flash-calcined clay-rich dredging sediments can potentially be used as a new pozzolanic supplementary cementitious material in concrete.

1. Introduction

Supplementary cementitious materials (SCMs) are commonly and increasingly used as a partial cement replacement or as mineral addition in concrete nowadays. [1,2] The rising demand for cement and concrete, increasing environmental concerns about cement manufacturing, and supply-and-demand concerns due to the limited (or even decreasing) amounts of high-quality SCMs prove the need for new alternative SCMs. Furthermore, environmental challenges related to the production and disposal of wastes and industrial by-products allow us to research the possibilities for their valorisation as SCM in sustainable cement and concrete. [1,3,4] In this respect utilisation of calcined clays as a pozzolanic material for concrete has received considerable interest in recent years. [4,5]

An alternative SCM presented in this paper originates from the dredging sediments of the port of Antwerp. Each year, about 450.000 tonnes (dry matter base) of sediments are dredged and treated by mechanical dewatering with membrane filter presses, resulting in a continuous supply of homogeneous filter cakes. These treated dredging sediments are rich in clays (2:1 clays and kaolinite) and contain relatively low contents of sulfur and chloride. [6] When flash calcination is applied to activate the clay minerals and to reduce the total organic content, the sediments show pozzolanic properties superior to siliceous fly ash. This paper investigates the applicability of the calcined dredging sediments as a novel and alternative SCM replacing Portland cement in concrete, and evaluates the basic properties of fresh and hardened concrete in comparison with two reference concrete mixes composed of Portland cement and Portland fly ash cement.

2. Experimental program

2.1 Materials

The materials used in this investigation are ordinary Portland cement (OPC, CEM I 52.5 N), Portland cement containing 21-35% siliceous fly ash (CEM II/B-V 42.5 N), calcined dredged sediments from the port of Antwerp (FC: filter cakes), natural river sand 0/4 and river gravel 4/14 (fully dry aggregates). The chemical compositions of the OPC, CEM II and FC are given in Table 1. FC is mainly composed of SiO_2 beside the other major components of CaO, Al_2O_3 and Fe_2O_3 [6]. Sulfur and chloride contents are 1.1 and 0.1 wt.% respectively, which is relatively low and complies with the regulations for non-reinforced and normal reinforced concrete according to EN 206 [7]. The total concentrations of heavy metal contaminants are below the target values set by the Flemish (Belgium) authorities for reuse as a construction material. As a PCE superplasticizer, Tixo® from Sika was added to the different concrete mixtures (dry matter content: 25.0% and density: 1.090 kg/l).

Table 1: Chemical composition of the cement and FC (wt.%)

	CaO	**SiO_2**	**Al_2O_3**	**Fe_2O_3**	**SO_3**
CEM I 52.5 N	63.9	20.0	5.1	3.4	3.1
CEM II/B-V 42.5 N	47.0	28.0	10.0	4.3	3.0
FC	15.9	54.3	14.6	12.0	3.2

2.2 Mix proportions

In the experimental part of the research, 5 different concrete compositions, including 2 reference mixes and 3 concrete mixes containing the dredging sediments, were tested. An overview of the compositions of the concrete mixes is given in Table 2. The two reference mixes were respectively made from OPC (CEM I) and Portland fly ash cement (CEM II), while the other mixes were prepared by replacing OPC at 20, 30 and 40 wt.% FC. The water/binder ratio was kept constant in all mixes as 0.5. It was found that the replacement of cement with FC increases the water demand and thereby reduces the workability of the fresh concrete, so that the use of a superplasticizer was necessary to achieve a good workability.

The reduced workability is due to the higher BET surface area of FC (4.94 m^2/g) than cement (0.93 m^2/g). The amount of superplasticizer was determined experimentally with the aim to obtain the same workability for all compositions (slump class S2 and flow class F2). As can be seen in Table 2, no superplasticizer was needed for the CEM II mixture since the spherical shape and glassy surface of the fly ash particles permit greater workability for equal water/cement ratios. [8,9] On the other hand, the amount of superplasticizer had to be increased for increasing amount of FC.

Table 2: Mix proportions of the concrete mixtures

	CEM I (kg/m^3)	**CEM II (kg/m^3)**	**FC (kg/m^3)**	**Sand (kg/m^3)**	**Gravel (kg/m^3)**	**Water (kg/m^3)**	**SP (kg/m^3)**
RC-I	360	-	-	640	1225	180	0.36
RC-II	-	360	-	640	1225	180	0.00
FCC-20	288	-	72	640	1225	180	1.08
FCC-30	252	-	108	640	1225	180	2.16
FCC-40	216	-	144	640	1225	180	3.24

2.3 Testing of concrete

Both fresh and hardened concrete parameters were investigated according to the European standards. The fresh concrete parameters (workability, air content and bulk density) were measured on the concrete immediately after mixing. To evaluate the workability of the fresh concrete, both slump and flow tests were carried out on each mix, respectively according to EN 12350-2 and EN 12350-5. Air content and bulk density were determined respectively according to EN 12350-7 and EN 12350-6. To evaluate the strength characteristics of the reference and blended cement concretes, compression tests were carried out on cube specimens (150x150x150 mm) according to EN 12390-3, by means of a 5000 kN capacity testing machine. Flexural strength and tensile splitting strength tests were conducted on prismatic test specimens (respectively of dimensions 150x150x600 mm and 150x150x300 mm) according to EN 12390-5 (three-point bending test) and EN 12390-6. The strength measurements were performed at ages of 7, 28 and 90 days and the specimens were cured at 20 ± 2 °C and ≥ 90 % relative humidity during hardening. Six specimens were used for each testing age; except for the flexural strength measurements, which were carried out on 3 test specimens. For each concrete composition, two batches of concrete were made. One batch of 90 liters for preparation of the cube specimens and one batch of 150 liters for preparation of the prisms.

3. Results and discussion

3.1 Fresh concrete parameters

Table 3 shows the results of the fresh concrete parameters, both for mixes of 90 liters and 150 liters of concrete. The RC-II composition was only made for mixtures of 150 liters. For the 90 liters mixtures, slump class S2 and flow class F2 were reached mostly, while this was not the

case for the concrete mixtures with a volume of 150 liters. It can be seen that the workability of the FCC mixes (especially the slump value) decreases for larger volumes of concrete. The amount of superplasticizer was experimentally determined on concrete mixes of 90 liter volumes. However, when larger volumes of concrete at 150 liter were made, the workability changes significantly, resulting in a decreasing workability for increasing replacement levels of OPC. The difference is less visible for the flow values. In order to find an explanation for the observed behaviour, further workability tests need to be carried out. The values of the air content were approximately constant for all mixes, except for the RC-II composition with Portland fly ash cement, which shows a significantly lower air content. This is due to the greater surface area of fly ash in concrete, since fly ash is generally finer than ordinary Portland cement. [8]

Table 3: Fresh concrete properties (90 liter | 150 liter concrete mixtures)

	Slump (mm)	**Flow (mm)**	**Air content (%)**	**Density (kg/m³)**
RC-I	50 | 50	380 | 380	2.8 | 2.5	2330 | 2320
RC-II	- | 50	- | 390	- | 1.5	- | 2360
FCC-20	50 | 30	380 | 370	2.1 | 2.7	2330 | 2310
FCC-30	80 | 10	370 | 320	2.4 | 2.0	2310 | 2330
FCC-40	80 | 10	- | 320	2.3 | 2.4	2340 | 2300

3.2 Compressive strength

The compressive strength results of the reference mixes and blended concrete compositions, measured on cubes at 7, 28 and 90 days, are shown in Figure 1. The mean and standard deviation for six specimens per mix are also given. At 7 days, a lower compressive strength for the concrete compositions blended with FC (FCC) is observed in comparison with the reference Portland cement concrete (RC-I), with a decreasing strength for increasing amount of FC. However, comparison with the Portland fly ash cement concrete (RC-II) shows slightly higher compressive strengths for the FCC-20 and FCC-30 mixtures. Therefore, compared to fly ash, higher early-age compressive strengths are reached for the FCC compositions at 7 days. At 28 days, the low early-age strength for the RC-II and FCC mixtures is compensated by the pozzolanic reactions taking place. The compressive strengths of both the RC-II as the FCC concrete mixtures (approximately) reach that of RC-I. An important factor to keep in mind here is the lower air content of the Portland fly ash cement concrete compared to the other compositions, which results in a higher compressive strength. This will be further validated by porosity measurements. Up to 90 days, compressive strength values further increase, except for the FCC-30 mixture. Although the compressive strength values of all three FCC are slightly lower than the traditional OPC concrete, the FCC mixes are still suitable for a range of applications and reach a strength class of C35/45.

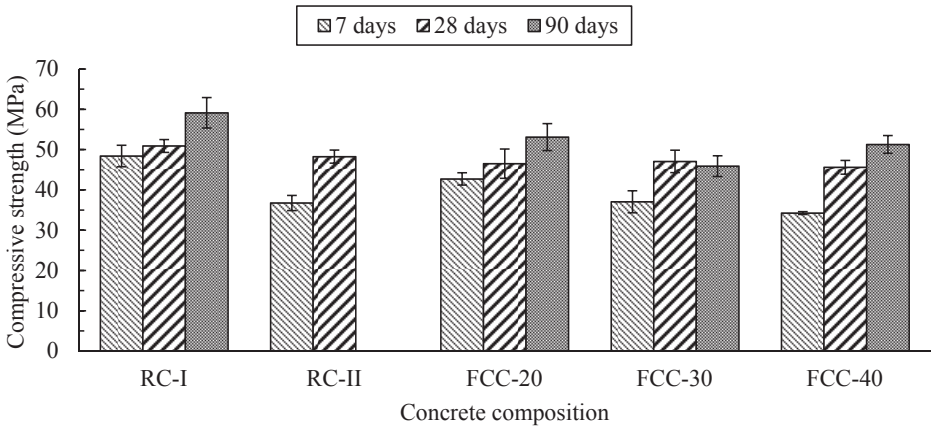

Figure 1: Compressive strength of the different concrete mixtures

3.3 Flexural strength

Figure 2 presents flexural strength of the concrete compositions. It can observed that at 7 days the flexural strength of the FCC compositions is lower than the flexural strength of the reference Portland cement concrete (RC-I). Up to 28 and 90 days, on the other hand, the flexural strength of the FCC-30 and FCC-40 compositions exceeds that of the RC-I mixture due to the pozzolanic reactions taking place. Comparison with the Portland fly ash cement concrete (RC-II) shows higher strength values at 7 and 28 days. Two abnormalities can be observed (RC-I at 28 days and FCC-20 at 90 days), which need to be further investigated for clarification.

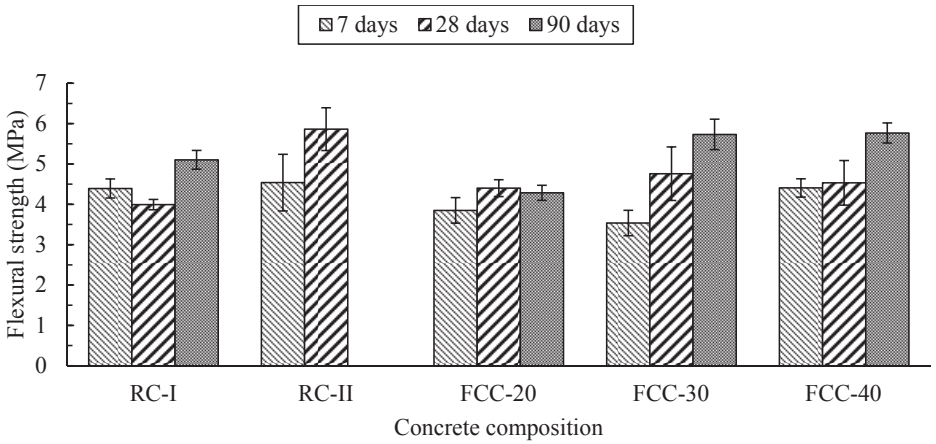

Figure 2: Flexural strength of the different concrete mixtures

3.3 Tensile splitting strength

The results of the tensile splitting strength testing of the concrete compositions are compared in Figure 3. With the exception of three inexplicable abnormalities (RC-I at 7 days and FCC-30 and FCC-40 at 90 days), similar values have been achieved for tensile splitting strengths of the FCC mixtures as for RC-I. When looking at the tensile splitting strength of RC-II, both for 7 and 28 days, much lower values are observed, compared to the RC-I and FCC compositions. Furthermore, large standard deviations can be observed in the results.

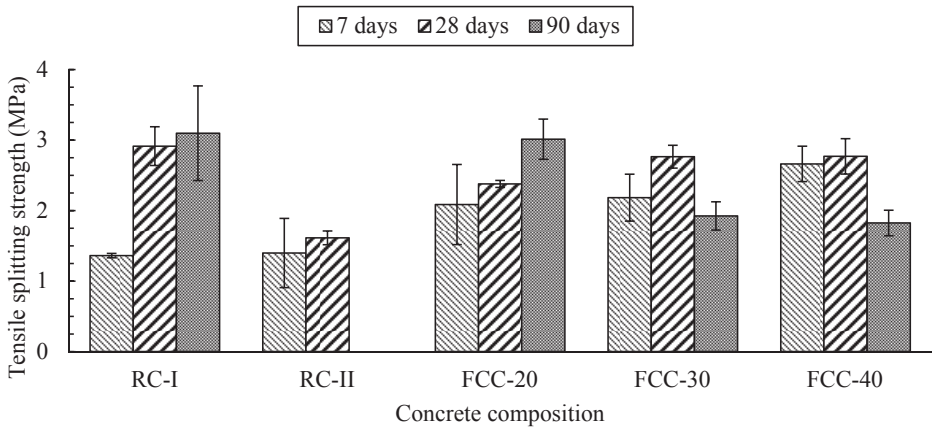

Figure 3: Tensile splitting strength of the different concrete mixtures

3.4 Relation between compressive and tensile strength

According to Neville [10], the compressive strength (f_{ck}) and tensile strength (f_{ctm}) of concrete are closely related. As the compressive strength increases, the tensile strength also increases, but at a decreasing rate. Several empirical formulas connecting the compressive and tensile strength have been suggested by many researchers. Probably the best fit overall, also mentioned by the *fib* Model code [11] and Eurocode 2 [12], is given by the following expression [10]:

$$f_{ctm} = 0.3 \cdot f_{ck}^{2/3} \tag{1}$$

Where f_{ctm} is the average tensile strength and f_{ck} the characteristic compressive strength measured on cylinders. Figure 4 shows the relation between the tensile strength calculated from the compressive strength (equation (1)) and the tensile strength calculated from flexural (black) or splitting (grey) strength, according to equations (2) and (3).

$$f_{ctm} = 0.6 \cdot f_{ctm,fl} \tag{2}$$

$$f_{ctm} = 0.9 \cdot f_{ctm,sp} \tag{3}$$

It can be seen from Figure 4 that the values for the tensile strength calculated from the compressive strength are in almost all cases higher than the one calculated from the flexural and splitting tensile strength. This shows that the values of the flexural and tensile splitting strength are on the low side and confirms the large standard deviations for the tensile strengths.

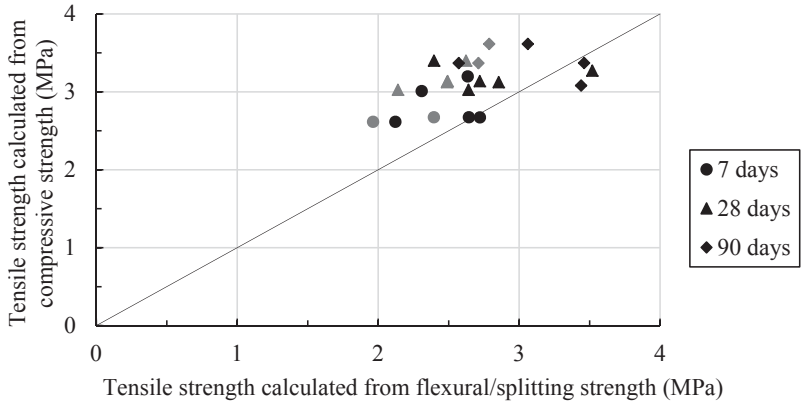

Figure 4: Relation between the tensile strength calculated from the compressive strength and calculated from the flexural (black) / splitting (grey) strength

4. Conclusions

Compressive, flexural and tensile strength results demonstrate the potential of the calcined clay-rich dredged sediments of the Port of Antwerp as a novel SCM in sustainable concrete production. Although the blended cement concretes develop low compressive strength at early-ages, the strength values catch up with that of the reference mix with ordinary Portland cement up to 28 and 90 days as a result of pozzolanic reactions induced by the calcined dredging sediments. The addition of superplasticizer is necessary to achieve a good workability in the blended concrete mixes. These results are promising to further investigate the other properties of FCC such as shrinkage, creep, microstructure and durability.

References

[1] Juenger, M. C.G. and Siddique, R., Recent advantages in understanding the role of supplementary cementitious materials in concrete, Cement and Concrete Research 78 (2015), 71-80
[2] Lothenbach, B. et al, Supplementary cementitious materials, Cement and Concrete Research 41.12 (2011), 1244-1256
[3] Flatt, R.J. et al, Concrete: An eco material that needs to be improved, Journal of the European Ceramic Society 32.11 (2012), 2787-2798

[4] Sabir, B.B. et al, Metakaolin and calcined clays as pozzolans for concrete: a review, Cement & Concrete Composites 23.6 (2011), 441-454
[5] Scrivener, K., and Favier, A., Proceedings of the 1st International Conference on Calcined Clays for Sustainable Concrete, Lausanne (2015)
[6] Horckmans, L., et al, BIND-AMOR: Reuse of dredged sediments as supplementary cementitious materials, 1st International Conference on Calcined Clays for Sustainable Concrete, Lausanne (2015), 571-572
[7] EN 206, Concrete: Specification, performance, production and conformity, European Standardization Committee (2013)
[8] Siddique, R. and Khan, M.I, Supplementary Cementing Materials, Springer (2011)
[9] Snellings, R., Mertens, G., and Elsen, J., Supplementary cementitious materials, Reviews in Mineralogy and Geochemistry, 74.1 (2012), 211-278.
[10] Neville, A.M., Properties of concrete, Pearson Education, Essex (2012)
[11] fib Model Code for Concrete Structures, Internatial Federation for Structural Concrete, Lausanne (2010)
[12] NBN EN 1992-1-1, Ontwerp en berekening van betonconstructies – Algemene regels en regels voor gebouwen, Bureau voor Normalisatie, Brussel (2005)

International RILEM Conference on Materials, Systems and Structures in Civil Engineering
Conference segment on Service Life of Cement-Based Materials and Structures
22-24 August 2016, Technical University of Denmark, Lyngby, Denmark

EXPERIMENTAL AND NUMERICAL ANALYSIS OF DRYING SHRINKAGE ON CEMENT-BASED MATERIALS

Marie Malbois [(1)], Adrien Socie [(1),(2)], Aveline Darquennes [(1)], Caroline De Sa [(1)], Farid Benboudjema [(1)]

(1) LMT, ENS Cachan, CNRS, Université Paris Saclay, France
(2) EPF – Ecole d'ingénieurs, Sceaux, France

Abstract
The drying of concrete induces surface microcracking due to hydric gradients, and internal microcracking due to drying shrinkage incompatibilities between cement paste and aggregates. The difficulty of separating each phenomena on concrete cracking makes it hard to quantify aggregates effects with classical experiments. An ongoing parametrical experimental study aims at quantifying the impact of drying and of inclusions by using morphologically controlled materials. In these materials, the aggregates size and volume fraction is controlled. The samples are then submitted to drying and their mechanical and transport properties are regularly characterized. The first results indicate noticeable impacts of both parameters. The study is to be enhanced of several results: different formulations and tests to assess the evolution of mechanical and transport properties at several ages are currently undertaken, and comparisons are made with results from numerical modelling.

1. Introduction

ANR MOSAIC. The French project ANR MOSAIC (MesoscOpic Scale durAbility Investigations for Concrete) is a collaboration between four French laboratories all recognized for their expertise within the field of cement-based materials durability: LML (Lille, France), LMT Cachan (Cachan, France), LMDC (Toulouse, France) and IFSTTAR (Champs-sur-Marne, France).
This project investigates, experimentally and numerically, the effect of drying and delayed ettringite formation on the mechanical and transport properties at a mesoscopic scale.
First, this project plans to set up an experimental methodology based on studying the two types of pathologies on two classes of materials:

- Materials where the mesoscale morphology is completely controlled : "morphologically controlled" materials
- Materials where the mesoscale morphology is uncertain : "real" materials

The study of the morphologically controlled materials aims at easily uncoupling the influent parameters (as aggregates size or aggregates distribution) on the global concrete behavior.

In order to assess the role of the morphology within the pathologies development, but also to allow the gathering of results of all the members of the project, these materials must be built from the same components: cement, aggregates, water to cement ratio.
In a second time, the MOSAIC project aims at developing a predictive way of modeling the consequences of the two phenomena at a mesoscopic scale.

Drying. The drying phenomenon is inherent to the life of concrete structures. It is triggered by the hydric imbalance of the structure with its environment and consists in water departure from the structure. The water loss leads to internal strains and stresses gradients that may lead to superficial microcracking, perpendicular to the surface of the structure. Besides under drying, the cement paste tends to contract while the aggregates are generally inert. Therefore, a restraint of the cement paste shrinkage by the aggregates can appear, leading to strains and stresses gradients between cement paste and aggregates. This last phenomenon induces the debonding at the cement paste - aggregates interfaces (circumferential cracks) and the development of inter-granular cracks (radial cracks) as displayed Figure 1 ([1], [9], [11], [15]). This cracking may impact significantly mass transfer properties, which are of major importance for civil engineering structures durability.

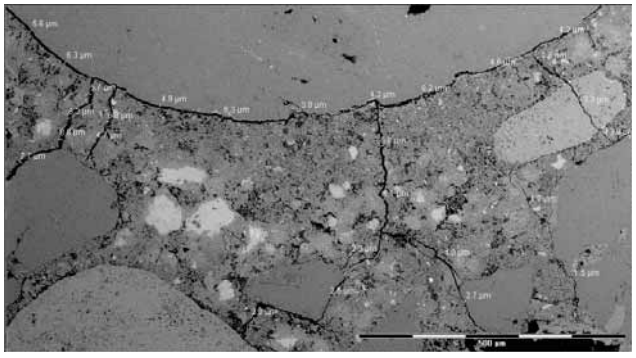

Figure 1 - Low magnification image of a sample after drying at 105°C, displaying cracking induced by aggregates restraint. Microcracks widths: 0.5-10 µm. (1182 x 655 µm). [15]

Many papers deal with the structural effects of drying, reporting qualitative and quantitative experimental ([4], [5], [14]) and numerical studies ([5] [7]). Few works have been devoted to cement paste and aggregates strain incompatibilities ([1][2][13]). The difficulty of studying this hererogeneity effect lies in, on one hand, the problem of separating each size effect on concrete cracking, and on the other hand, in assessing the effects of the numerous parameters linked to aggregates (e.g. shapes, size distribution, aggregates type, surface rugosity and interfacial transition zone).
Some recent works have investigated the experimental decoupling of macroscopic and mesoscopic effects, studying more particularly the influence of concrete heterogeneity on cracking due to drying ([11] [15]). The preliminary work of Lagier et al. [11], based on 2D digital image correlation experiments on morphologically controlled materials, has shown the ability of quantifying cracking due to drying and the impact of the heterogeneities (Figure 2). Numerically, several strategies can be considered to study drying effects. The literature

([6][8] [11]) has already underlined the interest of working at mesoscopic scale to describe the effects of heterogeneity. Yet, those works have not demonstrated the entire predictive feature of mesoscopic models.

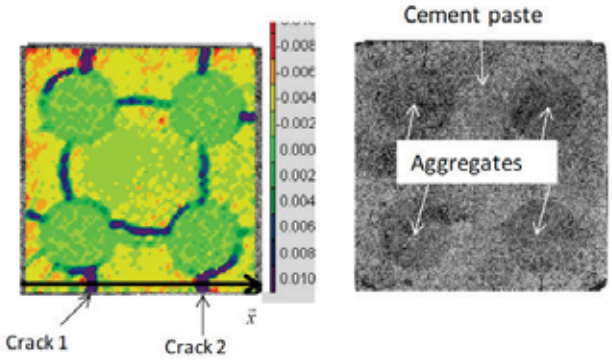

Figure 2 - 2D digital image correlation study on morphologically controlled materials investigating cracking due to drying incompatibilities between cement paste and aggregates. [11]. Trace of the strain tensor.

In this paper we will focus on the ongoing experimental study led in the LMT Cachan dealing with the drying phenomenon and its impact on morphologically controlled materials. First, we will present the different materials studied. Next we will take interest in the different technics to assess the macroscopic effects of drying and the morphology impact. Then we will present the first investigations of multi-scale modelling. We will finally present and discuss the results.

2. Experimental approach

2.1 Materials

The main objective of this study is to perform a parametric study on drying of cementitious morphologically controlled materials. In order to stay representative of the interactions between aggregates and cement paste, the inclusions are real calcerous aggregates (Boulonnais aggregates). Calcia cement CEM II (42.5 MPa) is used in Water-Cement Ratio of 0.57.

The two parameters selected for this parametric study are :

- Inclusions sizes: aggregates diameter between 6.3 and 8mm and between 10 and 12.5mm.
- Inclusions volume fractions: 30% and 50% of the total volume.

As these morphologically controlled materials lack most of the granular skeleton that would have insured a homogeneous distribution of the aggregates in the sample, the risks of segregation are significant. Thus an optimization of the composition was performed by the use of a viscosity modifying admixture. Then, the first three compositions that will allow us to assess the impacts of the two selected parameters were made:

- Cement paste with 6-8 mm inclusions in a 50% volume fraction
- Cement paste with 10-12.5 mm inclusions in a 50% volume fraction
- Cement paste with 10-12.5 mm inclusions in a 30% volume fraction

We will now see by which means we will assess the different effects of drying and of aggregates.

2.2 Procedure

Drying. Drying is studied on 70*70*280 mm prismatic specimens. For each formulation, 3 samples are made. They are removed of their mold after 24h and immediately protected against drying with two layers of aluminum foil. They are kept during 28 days under sealed conditions. Then, they are unwrapped to begin a drying phase, in a room controlled in temperature, 25 ± 1°C, and relative humidity, 35± 5%HR, until 200 days. To guarantee a unilateral drying, layers of aluminum foil are applied on the superior and inferior square faces of the prisms. The samples are regularly controlled for mass loss and shrinkage via an embedded apparatus made of brass, allowing the positioning of sample between a fixed support and a comparator. 3 prisms of each composition are also studied under sealed conditions.

Mechanical tests. 3 points flexural test. 3 points flexural tests are performed at 200 days, on 70*70*280 mm prims which have followed the same preservation conditions than detailled before. For each composition and for each conservation condition, 3 samples are charge operated at a 0,5mm/s speed.

3. Multi-scale modelling

Different modelling strategies have been investigated to improve their ability to reproduce the effects of aggregates during drying: analytical homogenisation technics and finite element calculations.

3.1 Homogenisation

The homogenisation model chosen for this study was developed by Le Roy [12] as it takes into account the effects of inclusions compactness. Only mechanical effects of the inclusions are considered, meaning that the gradient effects are neglected and a homogenous drying deformation is imposed in the cement paste.

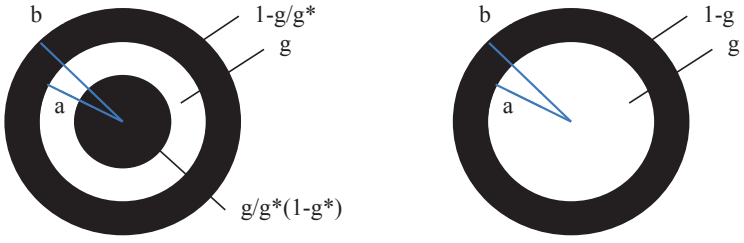

Cell 1 :
Random concentration

Cell 2 :
Inclusion in cement matrix

Figure 3 - Elementary cell of Le Roy's model [12]

For this study, the model of the cell with a random concentration is chosen (Figure 3, cell 1). The equation giving access to the shrinkage, with the hypothesis that $g^* = 1$ (case we considered, (Figure 3, cell 2)), is:

$$\frac{\varepsilon}{\varepsilon_p^r} = \frac{\left(1 - \frac{1-f_p}{g^*}\right) \times \left(1 + \nu_p + 2\left(1 - 2\nu_g\right)\frac{E_p}{E_g}\right)}{1 + \nu_p + 2\left(1 - 2\nu_g\right)\frac{E_p}{E_g} \times f_p + 2\left(1 - f_p\right)\left(1 - 2\nu_p\right)} \quad (1)$$

Where ε is the total deformation, ε_p^r is the cement paste deformation, ν_i is the Poisson coefficient, E_i is the Young Modulus and f_i is the volume fraction. The subscripts "p" stands for cement paste and "g" for aggregate.
We can now assess the effect volume fraction of aggregate $(1 - f_p)$ on deformation.
The other parameters are the characteristics of the materials used in the experimental campaign.
The results are compared to the limits of Hill [10], consisting in the serial and parallel models which are respectively, in the case of shrinkage, the superior and inferior limits.

3.2 Finite elements calculations

The analytic model used doesn't take into account the aggregate shape. Therefore numerical simulations were also tested, using CAST3M software [16]. Figure 4 displays the chosen geometries: a) spherical aggregate in cement paste, with an axisymmetric model, b) cubical aggregate in cement paste, with a 3D model.

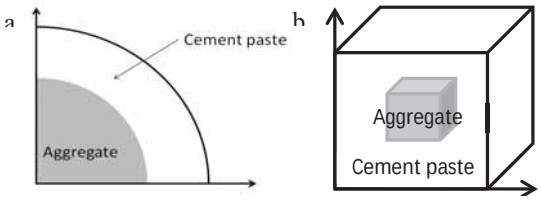

Figure 4 - a) spherical aggregate in cement paste, with an axisymmetric model, b) cubical aggregate in cement paste, with a 3D model

The same hypothesis than for the homogenisation are applied for the simulations: gradient effects are neglected and a homogenous drying deformation in the cement paste. The results of these simulations are compared to the ones of the analytic modelling(see part4.2, Figure 8)Figure 1.

4. Results and discussion

4.1 Experimental results

Morphology effects: impact of size and volume fraction of aggregates.

Figure 5 displays the mass loss of the different formulations express in function of the root of time on the average radius (Rm) of the samples followed, in order to be exonerated from samples size effects.

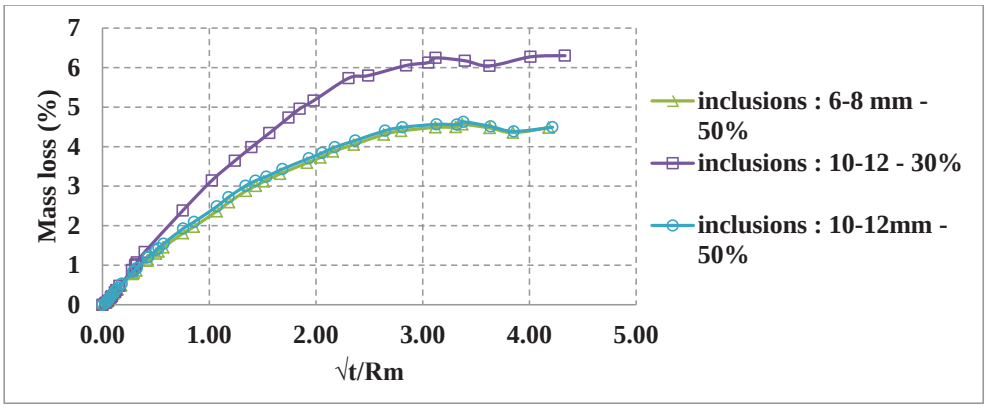

Figure 5 - Mass loss evolution of different compositions with time under drying conditions

First these curves reveal that the drying phenomenon seems stabilized after 200 days. In order to more clearly observe the effect of the aggregates on the diffusion phenomenon, Figure 6 shows the mass loss of the samples, normed by the volume fraction of cement paste. The curves are surimposed on each other, which can raise the question of the role of the interfacial transition zone and of cracking on mass transport.

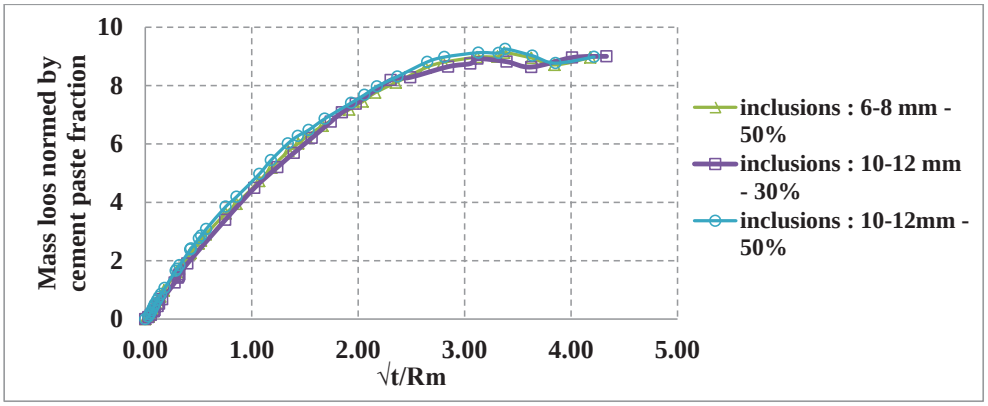

Figure 6 - Evolution of mass loss normed by cement paste volume fraction with time under drying conditions

Total shrinkage of the different compositions is displayed on Figure 7. As expected under drying conditions, a decrease of apparent shrinkage with the increase of the volume fraction of aggregates can be observed. Besides it can also be noticed that, at the same volume fraction, the formulations with smaller inclusions have an apparent shrinkage more important than the ones with bigger inclusions, meaning that the size of inclusions has an influence.

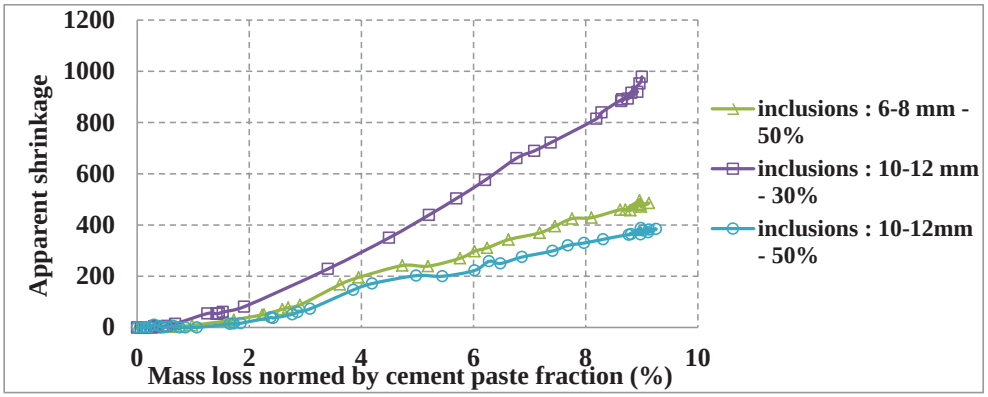

Figure 7 - Total shrinkage of different mesostructures versus relative mass loss percentage under drying conditions

Drying effects on mechanical properties.

On this day, only two compositions were tested. Flexural resistance results are gathered in Table 1. Comparing the behavior in autogenous conditions, the inclusions size does not seem to have any impact. Comparing the behavior between drying and autogenous conditions, drying causes a sizable decrease for both compositions, but not in the same measure :

- A 35% decrease for samples with 6-8 mm inclusions
- A 55% decrease for samples with 10-12 mm inclusions

These results reveal the impact of aggregates size on the damaging of samples.

More tests are currently performed to confirm this observation and to assess the impact of volume fraction of inclusions.

Table 1- Flexural resistances

Composition ***Inclusions***	**Drying conditions**	**Standard deviation**	**Autogenous conditions**	**Standard deviation**
6-8mm – 50 %	3,33 MPa	0,219	5,08 MPa	0,310
10–12 mm – 50%	2,30 MPa	0,212	5,10 MPa	0,586

Comparing the failure characteristics, different observations could be made between samples in drying conditions and the ones in autogenous conditions.

- In autogenous conditions: most of the aggregates are ruptured and some are ripped off.
- In drying conditions: most of the aggregates are ripped off and few are ruptured.

The difference could reveal a debonding phenomenon at the aggregate – cement paste interface.

4.2 Comparison with analytical and simulation results

Results of the homogenisation and simulation analysis are displayed on Figure 8. Relevant experimental results were added in comparison: Lagier et al. [11] followed the shrinkage of the cement paste used in the experimental campaign of this study and Bissonette et al. [3] and Pickett [13] also studied drying shrinkage with aggregates content. The results of the experimental campaign will later be compared also to these different modelling strategies results, once cement paste shrinkage will also be obtained.

First, we can confirm that the results of Le Roy's model are contained in-between Hill's limits. Then, spherical simulations are an exact match to the homogenisation simulation as expected, whereas the cubic simulation is not, but is close. Aggregate shape seems to have a small influence on shrinkage deformation. Homogenisation results then tend to show the analytical homogenisation seems to be sufficient to represent aggregates effects on deformation of concrete. Nevertheless, this kind of modelling cannot represent cracking due to incompatibilities between cement paste and aggregates which will have an effect on the mechanical properties of concrete (e.g. see Table 1). So new investigations on numerical modelling are undertaken to improve this second type of modelling.

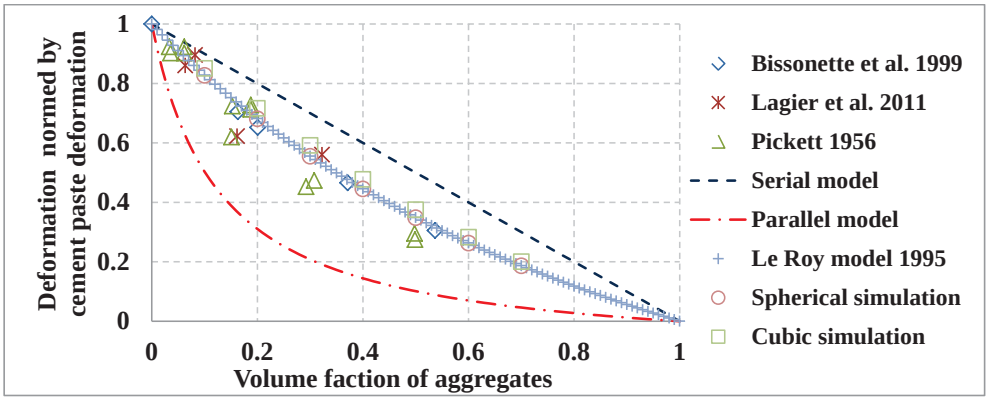

Figure 8 – Comparison between experimental, homogenization and simulation results. Impact of the aggregate volume fraction on drying shrinkage.

5. Conclusion

The results gathered so far highlight the significant effects of aggregate parameters on the delayed deformations and the evolution of mechanical properties.
The first results evidence several phenomenon :

- Aggregate size and volume fraction don't affect the mass loss
- Aggregate volume fraction has a significant impact on the delayed deformations. The more aggregates there are in the samples; the less it will be subjected to delayed shrinkage due to the substitution of the cement paste (responsible for the shrinkage) by rigid inclusions.
- Aggregate size also has an impact on the delayed formations. The samples with 10-12 mm aggregates tend to shrink less than the ones with 6-8 mm aggregates.
- Finally, the aggregate size seems to influence the damaging induced by drying, with leads to different behavior when assessing the mechanical performances. The samples with 10-12mm aggregates display a bigger loss of flexure resistance than the ones with 6-8mm aggregates, which could result from a more important internal cracking induced by drying.

The experimental study presented in this paper is to be enhanced with more results. Within the next months, they will be completed by mechanical tests: compressive tests, and the end of the flexural tests; by several tests to conclude on the evolution of the transport properties (after potential drying cracks): water porosity and chloride diffusion; and a visualisation and quantification of the cracking by tomography.
Besides, three other formulations are to be tested: cement paste, mortar and "real" concrete, which will allow us to conclude more precisely on the effect of aggregates in concrete, but also permit a more precised comparison between experimental and modelling results.

6. Acknowledgments

This research was achieved in the framework of the French research Project ANR MOSAIC. The authors would like to extend their appreciation and gratitude for the financial support provided by the French National Research Agency.

References

[1] Bisschop, J. and van Mier, J.G.M., Effect of aggregates on drying shrinkage microcracking in cement-based composites, Materials and Structures, Vol.30, September-October 2002, 453-461
[2] Bisschop, J. and van Mier, J.G.M., How to study drying shrinkage microcracking in cement-based materials using optical and scanning electron microscopy, Cement Concrete Res, 32 (2002), 279-287
[3] Bissonette, B., Pierre , P., Pigeon P., Influence of key parameters on drying shrinkage of cementitious materials, Cement Concrete Res, 32 (1999), 279-287
[4] Burlion, N., Yurtdas, I., Skoczylas F., Comportement mécanique et séchage de matériaux à matrice cimentaire, (In French), Rev Française Génie Civil, Vol.7(2) (2003), 145-165

[5] Burlion, N., Bourgeois F., Shao J.-F., Effects of desiccation on mechanical behaviour of concrete, Cement Concrete Compos, 27 (2005), 367-379
[6] De Sa, C., Etude hydro-mécanique et thermo-mécanique du béton (In French), PhD thesis, Ecole Normale Supérieure de Cachan, France (2007)
[7] De Sa, C., Benboudjema F., Thiery M., Sicard J., Analysis of microcraking induced by differential drying shrinkage, Cement Concrete Compos, 30 (2008), 947-956.
[8] Grassl, P., Wong, H.S., Buenfeld, N.R., Influence of aggregate size and volume fraction on shrinkage induced micro-cracking of concrete and mortar, Cement Concrete RES 40(1) (2010), 85-93
[9] Hearn, N., Effect of shrinkage and load-induced cracking on water permeability of concrete, ACI Mater , 96(2) (1999), 234-241
[10] Hill, R., Elastic properties of reinforced solids : some theorical principles, Mech. Phys. Solids, (1976) 773-782
[11] Lagier, F., Jourdain, X., De Sa, C., Benboudjema F., Colliat J.-B., Numerical strategies for prediction of drying cracks in heterogeneous materials: Comparison upon experimental results, Engineering Struct., 33(3) (2011), 920-931
[12] Le Roy, R., Déformations instantanées et différées des bétons à hautes performances (In French), PhD thesis, Ecole Nationale des Ponts et Chaussées, France (1995)
[13] Pickett, G., Effects of aggregates on shrinkage of concrete and a hypothesis concerning shrinkage, Proceedings, 1 (1956), 581-590
[14] Torrenti, J.-M., Comportement multiaxial du béton : aspects expérimentaux et modélisation (In French), PhD thesis, Ecole Nat Ponts et Chaussées, France (1987)
[15] Wong, H.S., Zobel, M., Buenfeld, N.R., Zimmerman R.W., Influence of interfacial transition zone and microcracking on the diffusivity, permeability and soptivity of cement-based materials after drying, Concrete Res, 61 (8) (2009), 571-589
[16] Commissariat à l'Energie Atomique CEA DEN/DM2S/SEMT, Cast3m finite element code, http://www-cast3m.cea.fr, 2005

International RILEM Conference on Materials, Systems and Structures in Civil Engineering
Conference segment on Service Life of Cement-Based Materials and Structures
22-24 August 2016, Technical University of Denmark, Lyngby, Denmark

STUDY ON THE EFFECTS OF DEFORMED STEEL FIBRES ON STRENGTHENING AND TOUGHENING OF ULTRA-HIGH PERFORMANCE CONCRETE

Gai-Fei Peng [(1)], Xu-Jing Niu [(1)], Yi-Lin Zhao [(1)], Yi-Gang Li [(1)]

(1) Faculty of Civil Engineering, Beijing Jiaotong University, China

Abstract
In order to investigate the effects of deformed steel fibres on strengthening and toughening of the characteristics of ultra-high performance concrete (UHPC), direct tensile loading and bending tests have been conducted on UHPC with different steel fibre geometries, dosages and distributions. Moreover, the pull-out channels and pull-out sections of fibres were observed by means of microscope. The results indicate that deformed steel fibres are very helpful to improve the tensile strength and fracture energy of UHPC. The higher the dosage of steel fibres, the better the effects of strengthening and toughening. Notably, the steel fibres orientated along the direction of tensile stress provide a better performance than the randomly-distributed steel fibres, with respect to tensile strength, post-cracking ductility and fracture energy of UHPC. Furthermore, compared with hooked steel fibres, the influence of crimped steel fibres on strengthening and toughening of UHPC are more efficient and the pull-out channels are more zigzag. Moreover, adding crimped steel fibres with higher strength is a promising approach to prepare a novel UHPC which will have high toughness, high durability and a long service life.

1. Introduction

As the most widely used structural material, concrete has been developed to meet constantly renewed requirements raised by construction of more and more structures including ultra-high-rise buildings and large span bridges, etc. Consequently, ultra-high performance concrete (UHPC) with ultra-high properties in terms of strength, durability [1], and fatigue resistance, has attracted more and more research attention in recent years. However, an obvious shortage of concrete with largely enhanced strength grade is brittleness, which is of great concern related to the structural safety.
Employing steel fibres is a routine approach for strengthening and toughening of UHPC. Many researches have been reported on this aspect. Yang et al [2] found that the toughness

and fracture energy of UHPC with steel fibres were one time and 34 times higher than that of plain concrete, respectively. Another research focused on the effect of fibre length by Yoo et al [3] found that flexural strength of UHPC increased gradually with the length of steel fibre but reached to an upper limit when the length increased to 19.5 mm. Similar researches have also been conducted on deformed steel fibres [4] with specific attention on its effect on strengthening and toughening of UHPC. Taher et al [5] revealed that hooked steel fibres increased tensile load and tensile energy of UHPC by 115 % and 95 % compared with that of straight fibres, respectively. Wille et al [6] indicated that direct tensile strength and ultimate tensile strain of concrete reinforced by crimped steel fibres were 1.6 and 3 times of that with straight steel fibres, respectively, when the volume dosage of fibre was 1.5 %. Tran et al [7] found that the tensile resistance of twisted steel fibre was the highest compared with that of the smooth fibres at static rate. At a research on the influence of hybrid steel fibre (long fibre + short fibre) on tensile performance and flexural toughness of UHPC, Park et al [8-9] found that short steel fibres assisted concrete in strain hardening behaviour and multiple cracking, while hybrid fibres were obviously beneficial to both strengthening and toughening, especially when long steel fibre was of screw type. Furthermore, when the dosage of long steel fibres was fixed, tensile properties and fracture toughness increased significantly with increasing dosage of short steel fibres.

Apart from dosage [10], geometry [11] or treatment [12-13] of steel fibres, distribution or orientated of steel fibres are also very important to affect the properties of concrete. Kang et al [14-15] investigated the effect of steel fibre orientated on the tensile and flexural behaviour of UHPC. Their results show that the orientated of steel fibres had little influence on the tensile behaviour of concrete before cracking, but affected that after cracking very significantly. The specimens with steel fibres orientated along the direction of tensile loading resulted in direct tensile strength 50 % higher than that with steel fibres randomly distributed. Meanwhile, the fibre orientated distribution also strongly impacted the UHPC deflection hardening behaviour in bending. In addition, Mu et al [16] has prepared concrete incorporating steel fibres orientated one dimensionally with an orientated efficiency factor over 0.90, by means of magnetic field control. They found that, the higher the orientated efficiency factor, the larger the enhancement in tensile strength of concrete.

To identify the effects of the geometry, dosage and distribution of steel fibre on mechanical properties of UHPC, an experimental research is presented in this paper, using deformed steel fibres (crimped) and commonly used hooked steel fibre to prepare UHPC, which was tested via direct tensile tests and bending tests.

2. Raw materials and test methods

2.1 Raw materials

Cement: ordinary Portland cement, strength grade 52.5 MPa (Chinese cement grading system). Silica fume (SF): specific surface area of 22205 m^2/kg and SiO_2 content of 90 %. Fine aggregate: manufactured sand, with the modulus of fineness of 2.94. A polyacrylate superplasticizer was used in the mix to maintain the slump of mixture around 180 ± 20 mm.

The physical properties of steel fibre diameter of crimped steel fibres (CS) was 0.8 mm, while the diameter of hooked steel fibres (HS) was 0.9 mm, as given in Table 1.

Table 1: Physical properties of used steel fibres

Fibre types	Geometry	Tensile strength (MPa)	Length (mm)	Diameter (mm)	Aspect ratio
CS	Crimped	1100	40	0.8	50
HS	Hooked	1100	35	0.9	38.9

2.2 Mix proportions

In order to investigate how deformed steel fibres can strengthen and toughen UHPC, the mix proportions of concrete were designed by changing the geometry, dosage and distribution of the steel fibres. The details of mix proportions are given in Table 2.

Table 2: Mix proportions of concrete (kg/m^3)

Type	W/B	Water	Cement	SF	Sand	Dosage of fibre	Arrangement of fibre
18Plain	0.18	162	810	90	620	0	No fiber
18CS-D30 or 18HS-D30	0.18	162	810	90	620	30	Randomly
18CS-O30 or 18HS-O30	0.18	162	810	90	620	30	Orientated [a] (l = 5 mm , c = 10 mm)
18CS-D60 or 18HS-D60	0.18	162	810	90	620	60	Randomly
18CS-O60 or 18HS-O60	0.18	162	810	90	620	60	Orientated [a] (l = 5 mm , c = 5 mm)

[a] Orientated means the steel fibres orientated along the direction of tensile stress, l for the line spacing of arrangement of steel fibres, c for the column spacing of arrangement of steel fibre.

2.3 Preparation of specimens

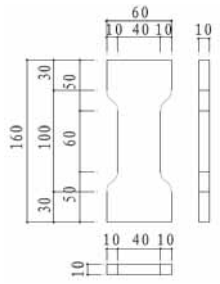

Figure 1: Specimen geometry in tensile test

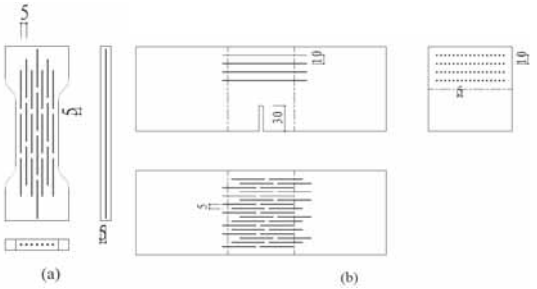

Figure 2: Orientated arrangement of steel fibres

During randomly distributed fibre concrete casting, the fine aggregate and 20 % of total water were mixed for the first 2 min. The cement and silica fume were added thereafter and mixed for about 6 min. Then the steel fibres were added gradually during mixing. Afterwards, the superplasticizer and remaining water were added and mixed for 3~5 min.

Compared with the situation presented, the casting process of concretes with orientated-arranged fibres was different. Firstly, half of a mould was filled by pouring the fresh cement mortar which mixed like randomly fibre concrete. Secondly, the steel fibres were orientated manually along the direction of tensile stress according to the Table 2, which was one layer for direct tensile specimens and four layers for three-point bending specimens (the distance on each layer was 10 mm and the cement mortar was poured after the complement of each layer). Finally, the remaining mould was filled with the cement mortar. With 60 kg/m^3 fibre dosage for example, Figure 2 (a) and (b) showed the orientated arrangement of fibres in direct tensile specimens and three-point bending specimens, respectively. After demoulding, all specimens were cured in water at 20 °C till 28 days.

2.4 Test methods

The Direct tensile test was conducted in a displacement controlled mode at a loading rate of 0.015 mm/min. And the fracture energy was determined with a loading rate of 0.05 mm/min according to a RILEM test method [17] which also specified the calculation procedure of fracture energy.

3. Results and Discussion

3.1 Direct tensile test

3.1.1 Dosage and geometry of steel fibres

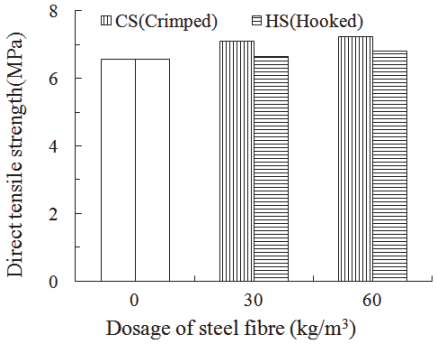

Figure 3: Direct tensile strength of UHPC at different dosages of steel fibre

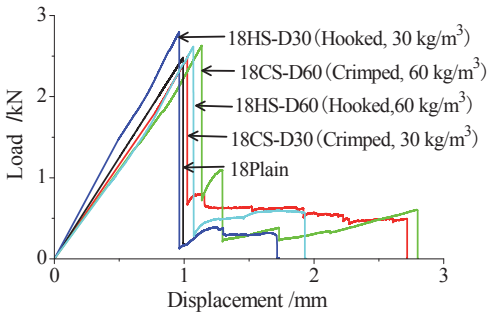

Figure 4: Tensile load-displacement curve of UHPC at different dosages of steel fibre

The effect of steel fibres on the direct tensile strength of UHPC with different fibre dosages and geometries is presented in Figure 3. Whatever crimped or hooked steel fibre, the direct tensile strength of UHPC was enhanced gradually with the increasing dosages of steel fibres.

However, specimens with crimped steel fibres showed obviously higher strength values compared to those with hooked steel fibres, at a given fibre dosage. Incorporating 30 kg/m^3 and 60 kg/m^3 steel fibres, the direct tensile strengths of UHPC with crimped steel fibres increased by 8.1 % and 10.2 %, while those with hooked steel fibres only increased by 1.06 % and 3.3 %, respectively, compared to the control UHPC without steel fibre.

The similar results have been found through tensile load-displacement curve of UHPC in different dosages and geometries of steel fibres in Figure 4. With steel fibre dosage increasing, UHPC became more ductile. A higher load-bearing capacity and longer ductility section were shown after reaching the peak load. Moreover, UHPC incorporating crimped steel fibre showed more significant effect on toughening compared to those with hooked steel fibre.

This may be attributed to the different bonding strength associated with steel fibre geometry, which is mainly provided by chemical bond, anchorage mechanical force and friction at fibre-matrix interface. It was suggested that crimped steel fibres provide better mechanical interlock compared with hooked steel fibres in the direct tensile test.

Therefore, incorporating higher strength crimped steel fibre is a promising method to design a novel UHPC characterized by ultra-high compressive strength and strain hardening behaviour [18] which manifests the improvement of toughness from initial cracking load to the peak load. The novel UHPC will have ultra-high durability similar to that of common UHPC [19]. Such novel UHPC will recover its original durability and have a long service life, as revealed by a research of Kunieda et al [20], which will be a new direction for the future research.

3.1.2 Distribution of steel fibres

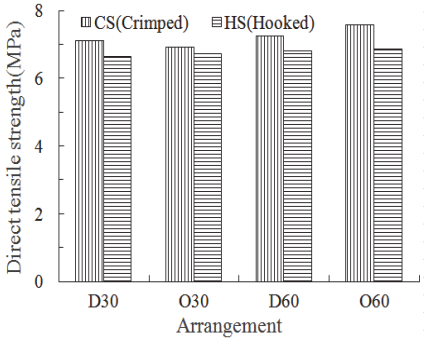

Figure 5: Direct tensile strengths of UHPC with different fibre arrangement

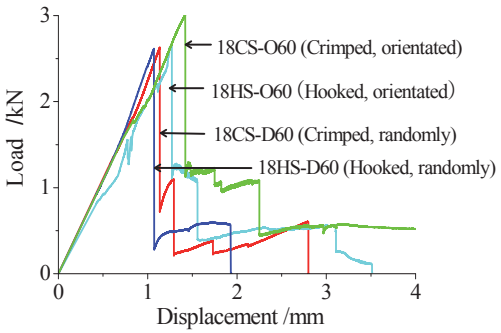

Figure 6: Tensile load-displacement curves of UHPC with different fibre arrangement

The bonding action of fibre-matrix related not only with the concrete matrix strength but also with the angle between steel fibres and the direction of tensile load, which can be confirmed by Figure 5 and 6. For instance, the tensile strength of UHPC incorporating 60 kg/m^3 orientated-arranged hooked steel fibres increased by 0.74 % compared to the specimens with

randomly-distributed fibres, and the post-cracking displacement of the former was 2.57 times that of the latter.

3.2 Bending test

3.2.1 Dosage and geometry of steel fibres

The load versus displacement curves and fracture energies are given in Figure 7 and Figure 8, respectively. As a whole, an addition of steel fibres had a profound effect on enhancing the deflection capacity and toughness. The post-peak part of the curves of steel fibre reinforced concrete became relatively gentler, and the post-cracking load-bearing properties increased with the steel fibre dosage.

In comparison to plain concrete (0.18Plain), the peak load, peak deflection and fracture energy of UHPC incorporating 30 kg/m^3 crimped steel fibres separately increased by 23.1 %, 44.1 % and 975.8 %, while for incorporating 60 kg/m^3 crimped steel fibres, the corresponding increments were 79.9 %, 179.4 % and 3216.9 %, respectively. This is mainly because that the bridging stress by steel fibres limits the crack propagation within the ligament of a beam.

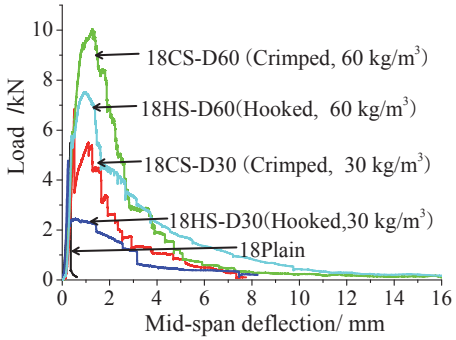

Figure 7: Load-deflection curves of UHPC at different dosages of steel fibres

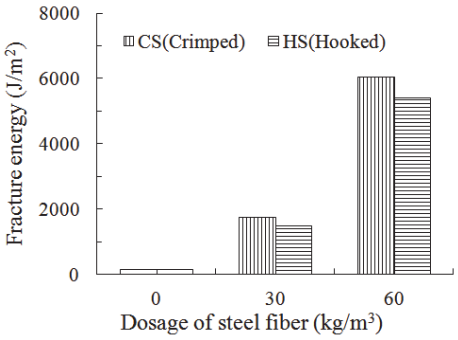

Figure 8: Fracture energies of UHPC at different dosages of steel fibres

Furthermore, under the same steel fibre dosage, the toughening effect of crimped steel fibres on UHPC was obviously superior to that of hooked steel fibres. For example, the peak load, peak deflection and fracture energy of UHPC incorporating 60 kg/m^3 crimped steel fibres was 1.2, 1.3 and 1.1 times of the UHPC incorporating hooked steel fibres at the same dosage.

3.2.2 Distribution of steel fibres

Figure 9 indicates that the fibre orientated-arranged along the direction of tensile stress is more efficient to improve fracture energy of concrete. For instance, the fracture energy of UHPC incorporating 60 kg/m^3 crimped steel fibres orientated arranged is 8.2 % more than that of UHPC with randomly arranged steel fibres.

An obvious advantage in toughening can be observed from Figure 10 for UHPC with the orientated-arranged steel fibres. The flexural load of 18CS-O60 at a deflection of 4 mm was found to be 3.86 kN, approximately 2.03 times higher than that of 18CS-D60. As a matter of

fact, the orientated arranged steel fibre along the direction of tensile stress can limit crack propagation, decrease the stress concentration on the crack tip.

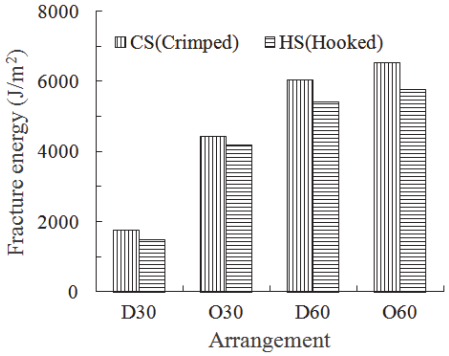

Figure 9: Fracture energy of UHPC with different fibre arrangement

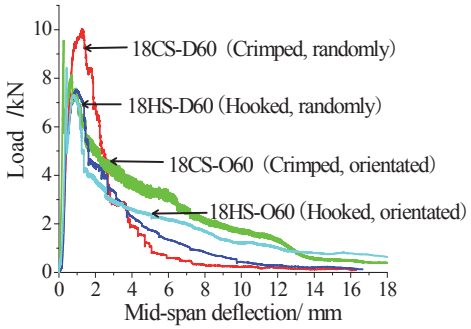

Figure 10: Load-deflection curves of UHPC with different fibre arrangement

It is necessary to point out that once matrix cracking occurred, the post-cracking load of concrete with steel fibres of the orientated arrangement would drop rapidly. The declining trend could be stopped until the bridging and anti-cracking effects of steel fibre worked.

3.3 Comparison of different loading modes

The relative increments of peak stress obtained from the two different loading models are given in Table 3. In 18CS-D60, the increment of peak load relative to 18Plain obtained from the three-point bending test was 79.9 %, which was more prominent than the relative increment (10.2 %) obtained from direct tensile test. The ability seems to be associated with the stress state of specimens in different loading modes.

Table 3: The strengthening effects of steel fibres on the peak stress of UHPC tested in two different loading modes

Types of steel fibres	Dosage (kg/m^3)	Relative increments of peak load (%)	
		Direct tensile test	Three-point bending test
18CS-D30	30	8.1	23.1
18CS-D60	60	10.2	79.9
18HS-D30	30	1.1	1.5
18HS-D60	60	3.3	34.9

During direct tensile test, the uniform tensile stress was obviously distributed throughout the whole section of a specimen. However, in the three-point bending test, there appeared strain gradient obviously due to the different stress state of specimens (the upper was compression area and the lower was tensional area). With the growing of macro-crack in the ligament of a beam, the tensile stress could be undertaken by two factors, i.e. the steel fibre across the

cracks and the compressive part of the beam over the neutral axis. Then the tensile stress on the steel fibre would be weakened to a certain extent, and the efficiency of steel fibre could be improved remarkably.

Microscope observation

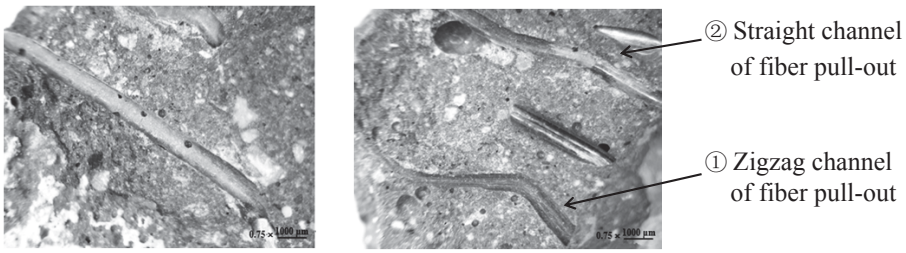

(a) Hooked steel fibre (b) Crimped steel fibre

Figure 11: Pull-out channels of steel fibres

In order to understand the different behaviour of steel fibres during tensile loading, the pull-out channels of steel fibres observed by means of microscope are illustrated in Figure 11. Compared with the relatively straight and smooth channel left by hooked steel fibre (see Figure 11(a)), the pull-out channels of crimped steel fibre were more curved (see Figure 11(b)) and apparently associated to its crimped shape. It also could be found from Figure 11(b) that the curved degree of channel ② as marked in this figure decreased evidently than that of channel ①. The more pronounced mechanical interlocking between crimped steel fibre and mortar matrix will enhance the interfacial bond in between, and further result in the gradually straightened part of steel fibre.

Besides, both of the two types of steel fibres demonstrated necking phenomenon during tension, owing to the yield behaviour of steel fibre (see Figure 12).

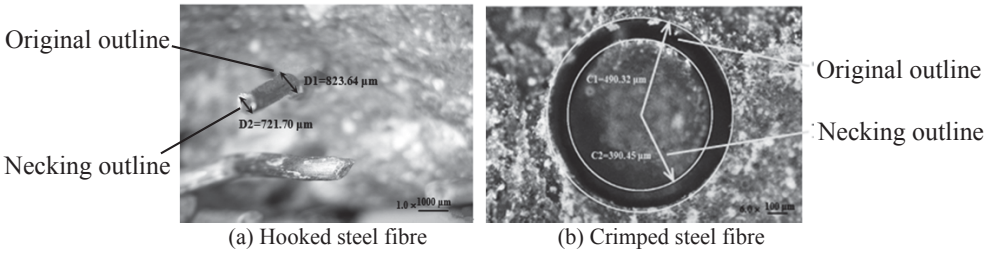

(a) Hooked steel fibre (b) Crimped steel fibre

Figure 12: A necking phenomenon of steel fibre

4. Conclusions

(1) Deformed steel fibres can greatly improve both the tensile behaviour and bending toughness of UHPC. The higher the dosage of steel fibres, the more pronounced the effect of

strengthening and toughening. Moreover, adding crimped steel fibres with higher strength is a promising approach to prepare a novel UHPC which have high durability and a long service life.

(2) Compared with hooked steel fibres, the influence of crimped steel fibre on strengthening and toughening of UHPC is more efficient, mainly due to a more pronounced mechanical interlocking between crimped steel fibre and mortar matrix, which can be confirmed by the more bent pull-out channels than those of the hooked steel fibres observed by means of microscope.

(3) The steel fibres orientated along the direction of tensile stress provide a better performance than the randomly-distributed steel fibres, with respect to tensile strength, post-cracking ductility, and fracture energy of UHPC.

(4) By comparison with between different loading modes, the enhancement effect of peak stress which obtained by three-point bending test seems to be higher than those of the direct tensile test.

Acknowledgements

The authors gratefully acknowledge the financial support of the National Science Foundation of China (Project No. 51278048).

References

[1] Cheyrezy, M., Maret, V., Frouin, L., Microstructural analysis of RPC (Reactive Powder Concrete), Cem Concr Res 25 (1995), 1491-1500.
[2] Yang, J.J., Liu, J.X., Han, J.Y., et al, Studies on mechanical property of high fluidity steel fibre reinforced ultra-high strength concrete, Journal of Building Materials, China 13 (2010), 1-6.
[3] Yoo, D.Y., Kang, S.T., Yoon, Y.S., Effect of fibre length and placement method on flexural behaviour, tension-softening curve, and fibre distribution characteristics of UHPFRC, Construction and Building Materials 64 (2014), 67-81.
[4] Wille, K., Tawil, S.El., Naaman, A.E., Properties of strain hardening ultra high performance fiber reinforced concrete (UHP-FRC) under direct tensile loading, Cement and Concrete Composites 48 (2014), 53-66.
[5] Taher, A.L., Sameera, H., William, H., et al, Effect of matrix strength on pullout behaviour of steel fibre reinforced very-high strength concrete composites, Construction and Building Materials 25 (2011), 39-46.
[6] Wille, K., Naaman, A.E., Sherif, E.T., et.al, Ultra-high performance concrete and fibre reinforced concrete: achieving strength and ductility without heat curing, Materials and Structures 45 (2012), 309-24.

[7] Tran, N.T., Trana, T.K., Kima, D.J., High rate response of ultra-high-performance fibre-reinforced concretes under direct tension, Cement and Concrete Research 69 (2015), 72-87.
[8] Park, S.H., Kim, D.J., Ryu, G.S., et al, Comparative flexural behaviour of hybrid ultra high performance fibre reinforced concrete with different macro fibre, Construction and Building Materials 25 (2011), 4144-4155.
[9] Park, S.H., Kim, D.J., Ryu, G.S., et al, Tensile behaviour of ultra high performance hybrid fibre reinforced concrete, Cement and Concrete Composites 34 (2012), 172-184.
[10] Güneyisi, E., Gesoglu, M., Özturan, T., et al, Fracture behavior and mechanical properties of concrete with artificial lightweight aggregate and steel fiber, Construction and Building Materials 84 (2015), 156-168.
[11] Soulioti, D.V., Barkoula, N.M., Paipetis, A., et al, Effects of fibre geometry and volume fraction on the flexural behaviour of steel-fibre reinforced concrete, Strain 47 (2011), e535-e541.
[12] Soulioti, D.V., Barkoula, N.M., Koutsianopoulos F., et al, The effect of fibre chemical treatment on the steel fibre/cementitious matrix interface, Construction and Building Materials 40 (2013), 77-83.
[13] Corinaldesi, V., Nardinocchi, A., Influence of type of fibers on the properties of high performance cement-based composites, Construction and Building Materials 107 (2016), 321-331.
[14] Kang, S.T., Kim, J.K., The relation between fibre orientated and tensile behaviour in an Ultra High Performance Fibre Reinforced Cementitious Composites (UHPFRCC), Cem and Con Res 41 (2011), 1001-1014.
[15] Kang, S.T., Kim, J.K., Investigation on the flexural behavior of UHPCC considering the effect of fiber orientated distribution, Construction and Building Materials 28 (2012), 57-65.
[16] Mu, R., Li, H., Wang, X.W., et al, Aligned steel fibre reinforced cement based composites(Ⅱ): Preparation and reinforcement of aligned steel fibres, Journal of Building Materials, China 18 (2015), 387-392.
[17] RILEM, FMC1, Determination of the fracture energy of mortar and concrete by means of three-point bend tests on notched beams, RILEM Technical Recommendations for the Testing and Use of Construction Materials, E and FN SPON, London (1994).
[18] Nehdi, M.L., Abbas, S., Soliman, A. M., Exploratory study of ultra-high performance fibre reinforced concrete tunnel lining segments with varying steel fibre lengths and dosages, Engineering Structures 101 (2015), 733-742.
[19] Abbas, S., Soliman A. M., Nehdi M.L., Exploring mechanical and durability properties of ultra-high performance concrete incorporating various steel fibre lengths and dosages, Construction and Building Materials 75 (2015), 429-441.
[20] Kunieda, M., Kang, C., Ueda, N., et al. Recovery of protective performance of cracked ultra high performance strain hardening cementitious composites (UHP-SHCC) due to autogenous healing, Journal of Advanced Concrete Technology 10 (2012), 313-322.

International RILEM Conference on Materials, Systems and Structures in Civil Engineering
Conference segment on Service Life of Cement-Based Materials and Structures
22-24 August 2016, Technical University of Denmark, Lyngby, Denmark

COUPLINGS BETWEEN CREEP AND DAMAGE: ROLE OF THE FRACTURE CRITERION

Cyrille Dunant [(1)], Adrien Hilaire [(2)]

(1) University of Cambridge United Kingdom
(2) Ecole polytechnique Federale de Lausanne, Switzerland

Abstract
Couplings between creep and damage have to be considered to study the serviceability of concrete structures. This problem is of fundamental importance for structures exposed to relatively high loads over long time scales, e. g. ASR loads. Numerical simulations are performed via the AMIE framework. An appropriate algorithm is proposed and implemented to consider creep-damage couplings. Three-points bending tests on concrete notched beams are modelled and analysed. This kind of structures exhibits a snap-back instability. It is highlighted that the post-peak softening response is dependent on the fracture criterion and on the rate of loading. An experimental campaign to distinguish between proposed criteria has been launched: beams are tested under different loading rates.

1. Introduction

Concrete is most frequently modelled as a quasi-brittle material [1]. Although the fracture energy as well as the limit stress and strains are commonly measured experimentally, the post-peak behaviour of the material is generally treated using any softening curve which corresponds to the right dissipation of energy, as a precise experimental characterisation is difficult. This approach is largely valid in the quasi-static case. Nonetheless, extending the behaviours developed for instantaneous response to creeping concrete which is necessary in long term degradation modelling presents some difficulties. This paper explores the implicit assumptions made when adapting a fracture criterion developed static cases to visco-elastic modelling.
Modelling the failure behaviour of concrete elements presents a number of numerical challenges for the results to be energetically correct. One of the most important ones is capturing the snap-back [2]: the brutal release of stored elastic energy, characterised by a negative slope in the global stress-strain curve describing the response of the structural element upon the formation of a critical crack. Models of this behaviour are of practical

importance when modelling the collapse of buildings, and are useful in research to identify the softening of material models by comparing simulations with experiments. In the case of a visco-elastic concrete model, the speed of loading will affect the amount of free energy available and the development of the post-peak.
Although creep is normally considered to act over months and years for engineering purposes [3, 4], concrete exhibits viscous behaviour under load from the first second [5]. Therefore, the speed of loading is an important experimental parameter which must be taken into account. In turn, it is necessary when calibrating a material model to be able to distinguish between the irreversible dissipation of elastic energy through the opening of cracks, and the reversible creep. It is therefore not possible to simply stagger the creep and damage steps as these two relaxation processes, damage and creep can be intimately coupled, and can occur over the same time scale. The numerical algorithm presented in this paper has already been used, in a simplified form, for the modelling of creep and the alkali-silica reaction [6]. To test the algorithm, we have extended commonly used material models.
A number of material models have been proposed to describe the softening behaviour of concrete in a continuum damage framework. These models all attempt to capture some essential features of the post-peak, whilst staying as simple as possible. Two models of particular importance due to their use in practice are the Mazars model [7] and the modified compression field theory (MCFT). The Mazars model is usually implemented as an isotropic continuum damage model, whereas the MCFT is more commonly a rotating crack model [8]. In this paper, we compare the snap-back behaviour implied by both these models. We study the size effect caused by changing the dimensions of the sample as well as the role of speed-of-loading in our finite element platform, AMIE [9, 10].
Both models can be expressed in local and non-local forms. We have chosen to use the same regularisation in both models to better highlight the role of the fracture criterion.

2. Methods and materials

A visco-elastic model for creeping concrete was established by fitting experimental data. For the purpose of implementation, the concrete visco-elastic behaviour is represented using a generalised Kelvin-Voigt model with five branches. The parameters for the creep model used are given in table 1. They were calibrated according to basic creep tests performed on a concrete with w/c = 0.45. The evolution of the creep strain is plotted on the figure 1.

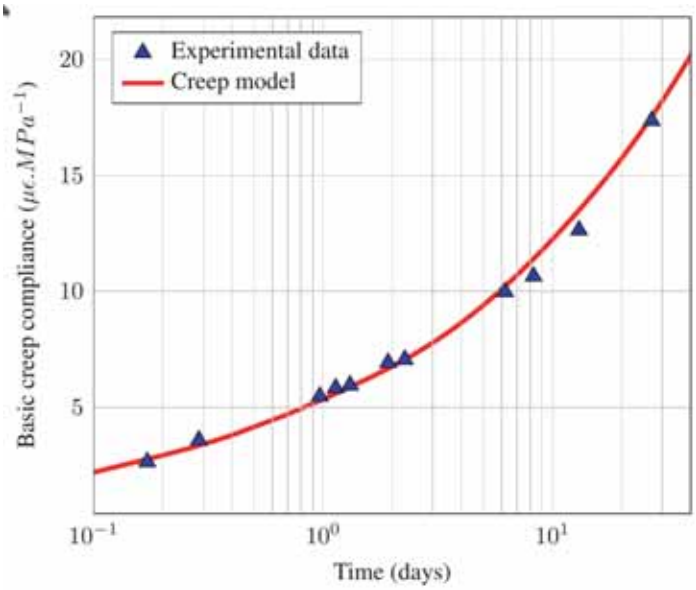

Figure 1: Creep compliance for the chosen visco-elastic model.

k_0 (GPa)	τ_0 (d)	k_1 (GPa)	τ_1 (d)	k_2 (GPa)	τ_2 (d)	k_3 (GPa)	τ_3 (d)
540	0.05	390	0.5	202	5	51	50

Table 1: Table for the generalised Kelvin-Voigt chain used.

The damage model chosen in all the simulation is isotropic scalar damage. The effective modulus of the material is computed as:

$$E = E_0(1 - d) \tag{1}$$

With d the damage E the modulus (viscous or otherwise) and the 0 indicating the initial value. This damage model is quite simple and may not be adequate for the representation of complex crack patterns. However, in this case, a single crack develops over the course of the experiment and does not close. Therefore this simple model suffices to capture all the important features of the simulation. The softening is applied on all the springs and dashpots of the rheological assembly. Two softening behaviour are tested, MCFT and Mazars. These are implemented as fracture criteria: they represent effectively the envelope of allowable combination of stresses and strain for the material. The damage variable is local in all simulations, unlike the criteria which are non-local.
In the following descriptions, the strain is smoothed over a characheristic distance d_{char}. This smoothed strain is used to compute the effective non-local strain in the expressions of the criteria. The choice of the characteristic distance what done following the works of Bazant ADD REF, who recommanded a value of 2-3 times the maximum diameter of aggregates, in

this case, d_{char} = 32mm. Of note, using the proposed approach it suffices that the criterion is non-local to obtain a non-local solution.

2.1 MCFT

For unreinforced concrete, ε_{ch} and ε_{te} describe strains over which the concrete ransitions to complete rupture, and ε^{crit} the critical tensile strain at cracking (f_c' in MPa). This relation is purely empirical but is commonly used in civil engineering applications.

$$\epsilon_1^{\text{crit}} = \frac{0.65|f_c'|^{0.33}}{E_0} \tag{2}$$

With E_0 the initial modulus We first define:

$$\phi_t^{\text{bare}} = \begin{cases} 1 & \text{if } \epsilon_1 < \epsilon_1^{\text{crit}} \\ \frac{1}{1+\sqrt{k(\epsilon_1-\epsilon_1^{\text{crit}})}} & \text{if } \epsilon_1^{\text{crit}} \leq \epsilon_1 < \epsilon_{ch} \\ \frac{1}{1+\sqrt{k(\epsilon_1-\epsilon_1^{\text{crit}})}} \frac{\epsilon_{te}-\epsilon_1}{\epsilon_{te}-\epsilon_{ch}} & \text{if } \epsilon_{ch} \leq \epsilon_1 < \epsilon_{te} \\ 0 & \text{otherwise} \end{cases} \tag{3}$$

In this expression, the coefficient k is chosen so that the integral under the stress- strain curve be equal to the dissipated fracture energy at failure, assumed to be G_f = 75 N/m. We then get the effective limit strain, with d_t the current damage for the tensile branch:

$$\epsilon_1^{\text{crit,eff}} = \phi_t^{\text{bare}} \frac{\sigma_1}{E_0(1-d_t)} \tag{4}$$

And the unreinforced concrete tensile criterion C_t^{bare} is

$$\mathcal{C}_t^{\text{bare}} = \begin{cases} 1 - \frac{\epsilon_1^{\text{crit,eff}}}{\epsilon_1} & \text{if } \epsilon_2 > \epsilon_1^{\text{crit,eff}} \\ -1 + \frac{\epsilon_1}{\epsilon_1^{\text{crit,eff}}} & \text{otherwise} \end{cases} \tag{5}$$

Table 2: Parameters for the MCFT simulation.

E	ν	f_c'	ϵ_2^{crit}	$\epsilon_{ch}^{\text{bare}}$	$\epsilon_{te}^{\text{bare}}$
37 GPa	0.2	37 MPa	0.0025	0.00694	0.00694×5

2.2 Mazars

The second fracture behaviour is the Mazars model, which was implemented in AMIE without modifications using non-local fields for its expression instead of local ones. The evolution of the damage variable is calculated according to the following relationships where the effective strain is introduced and ε_{crit} is the tensile strain threshold:

$$\tilde{\epsilon} = \sqrt{\langle\epsilon\rangle_+ : \langle\epsilon\rangle_+} \tag{6}$$

$$\begin{aligned} &\text{if } \tilde{\epsilon} > \epsilon_{crit} \text{ then } : \\ &\quad d = 1 - \frac{\epsilon_{crit}}{\tilde{\epsilon}} exp(-B_t(\tilde{\epsilon} - \epsilon_{crit})) \\ &\text{if } \tilde{\epsilon} \leq \epsilon_{crit} \text{ then } : \\ &\quad \dot{d} = 0 \end{aligned} \tag{7}$$

The damage parameters are given in the Tab. 3.

ϵ_{crit}	G_{ft}(J.m^{-2})
0.0001	10

Table 3: Damage parameters

3. Methods

Finite elements in space and time were proposed not long after the initial formulation of the method [11, 12]. Nonetheless, usage for the purpose of modelling visco-elastic solids is quite recent [13, 14, 15, 16]. In this framework, it is natural to model visco-elastic behaviours as assemblies of springs and dash-pots. The displacement field u and several internal displacement fields aj describe the state of the springs and dash-pots. and αj are the strains derived from these displacement fields. x is concatenation of the displacement field and the internal displacement fields: x = [u, . . . , aj , . . .]
A set of partial differential equations relating the stress σ to , the αj , and heir respective rates ˙ and α ˙ j is used to describe the rheological behaviour of the assembly. The elementary differential equations and their assembly is described in detail in [16]; this set of partial differential equations can always be expressed as a symmetric matrix [17], lending itself to efficient numerical solving.

3.1 Space-Time Discretisation

In the framework of space-time finite elements framework, the usual triangular shape functions

$$\{x,\ y,\ 1 - x - y\} \tag{8}$$

become

$$\left\{ \frac{x(1-t)}{2},\ \frac{y(1-t)}{2},\ \frac{(1-x-y)(1-t)}{2},\right.$$
$$\left. \frac{x(t-1)}{2},\ \frac{y(t-1)}{2},\ \frac{(1-x-y)(t-1)}{2} \right\} \quad (9)$$

Using this discretisation, one can write a system of linear equations in the form of:

$$[\mathbb{K}(d) + \mathbb{L}(d, \Delta t)]\, \mathbf{x}_F = \mathbf{f}_F(d) - \mathbb{L}(d, \Delta t)\, \mathbf{x}_S \quad (10)$$

With K the stiffness matrix, L the viscosity matrix, $\mathbf{x}_S$ and $\mathbf{x}_F$ the vectors of nodal displacements at t_S and t_F respectively, and $\mathbf{f}_F$ the nodal forces at t_F . The use of prismatic space-time elements ensures the following properties are true if the material properties are constant in time:

- **K** is independent of the time step.
- **L** is inversely proportional to the time step.

This formulation yields symmetric matrices, suitable for efficient solving using a conjugate gradient. This formulation behaves like a linear time integration scheme, but the cost of adapting the time step is considerably reduced. This is particularly important as the damage algorithm requires changing it at every iteration.

The damage is computed using a novel algorithm, which allows seamless integration with the visco-elastic response. The strong coupling between the visco-elastic response and the damage results from using this algorithm: no assumption of separation of time scales is required, and the impact of both dissipation mechanism is fully accounted for.

- A visco-elastic step is computed over δt.
- if an element is beyond its failure surface, the instant at which the failure surface was reached is computed,
- using the displacement at that instant as the initial condition, a new visco-elastic step is computed over the remainder of δt,
- the element having reached its surface has linearly growing damage. The rate of damage is $\alpha(1 - d_0)/\delta t$,
- The process is repeated until δt is reached.

This algorithm adapts the rate of damage to the minimum which can be sustained without going over the failure surface defined by the damage criterion. Determining the rate of damage is key to computing the coupled visco-elastic-damage response. As the minimum rate is also the one where the minimum amount of energy is dissipated, this is also likely the physical response [18]. A limitation to this approach is that a minimum rate of damage is imposed, chosen by giving an appropriate value to α. Although the minimum rate can be chosen freely to be as close to zero as possible, numerical efficacy imposes that it should not be chosen too low, otherwise many steps of acceleration will be required. Interestingly, the rate of damage not imposed arbitrarily — except for its lower bound — but emerges from the choice of fracture criterion. This numerical strategy is therefore suited to identify the implied visco-elastic coupling between damage and energy release when choosing the softening behaviour.

To capture the snap-back behaviour of the sample, every 10 damage steps of imposed displacement of the sample is scaled to find the value for which no damage should occur. Further loading then proceeds from that point. The rate of unloading using this strategy is then as high as necessary to find the equilibrium.
However, the rate of the subsequent loading is kept constant during each experiment. It is necessary to proceed this way as there may be no equilibrium solution if the rate of unloading is the same as the rate of loading. In general, we believe that this strategy allows capturing the snap back characteristic of the chosen rate of loading. Indeed, the viscous relaxation in the sample which happens in conjunction with damage always occurs from displacements imposed at the same rate.

3.2 Setup

A three-point bending setup as per the figure 2 was used. Two sample sizes were used to assess the importance of the size effect in the fracture behaviour ofconcrete sample. Three loading speeds, 1.44, 0.144 and 0.0144 mm/h were used to vary the free elastic energy stored in the sample at the onset of the fracture.

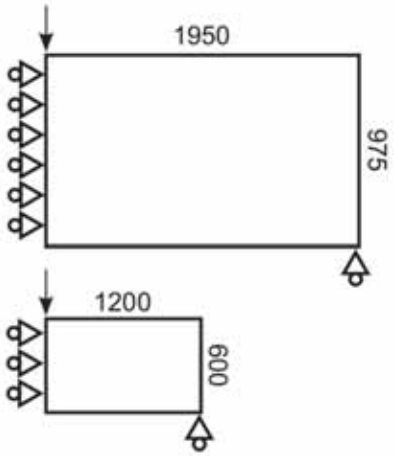

Figure 2: The numerical setup used for the simulation in this paper. The two samples are represented to size. Symmetry was modelled by imposing displacements along the vertical axis at the centreline

The damage was computed using the strategy delineated above. The snap-back was captured by finding the equilibrium imposed displacement every 10 damage steps. The average damage in the sample as well as the average strains and stresses were recorded. This allowed in post-processing to measure the energy stored in the sample, and relate it to the damage.
In this setup, a single crack evolves. Therefore, the amount of damage in the sample can be easily related to an apparent crack length, as the regularisation parameter is the same in all simulations.

4. Results and discussion

The simulations show that the snap-back is well captured by the algorithm (Figure 3). The smaller samples reach higher average stresses but lower strains. The peak stress goes down with the loading rate and the peak strain is slightly increased.
The two fracture behaviour both have the same energy dissipated under their stress-strain curves and are both implemented using the same regularisation parameters. Therefore, the differences observed in the relationship between energy release rate and visco-elastic behaviour are the result of the implied coupling between the damage behaviour and the viscous dissipation.
The Mazar criterion is perfectly continuous and smooth, whereas the MCFT is discontinuous, with a vertical slope at the onset of damage. The Mazar criterion also implies a thinner "tail" in the softening part of the damage curve. The simulations become very noisy when the sample is close to the breaking point. This is probably a numerical limitation due to the choice of discretisation. The rate of damage resulting from the propagation of a crack is probably better read before this point is reached.
We find that as expected, the elastic energy K_e stored in the sample reaches lower peak values as the loading rate diminishes. Using the non-viscous components of stress and strain:

$$K_e = 0.5\sigma : \epsilon \tag{11}$$

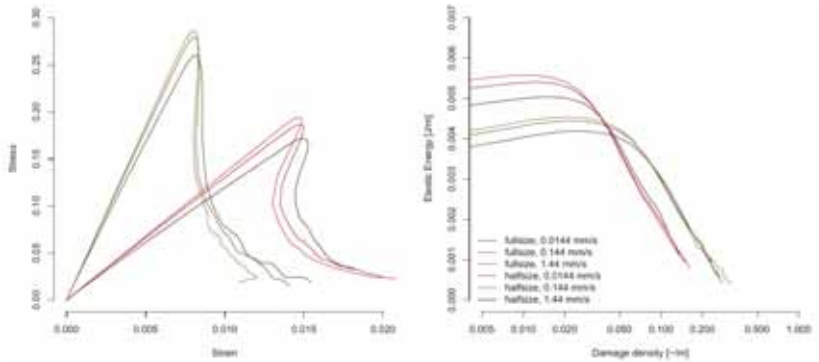

Figure 3: Snap-back behaviour of the samples as a function of the sample type and loading rate (left). Elastic energy stored in the sample as a function of the damage (renormalised by sample depth, right)

The rate of release of this energy as a function of the damage is independent of the initial value or of the dimension of the sample in the case of the Mazar criterion. It is not clear that this is the case for the MCFT, perhaps due to the discontinuity in the expression. This indicates that the constitutive equations, for a given choice of fracture criterion, imply a rate of release of energy with damage which is an intrinsic material property (Figure 4). This result is non-trivial as the material is visco-elastic and the fracture criterion only considers limit stress and strain states.

The scale effect, that is the apparent energy release rate as a function of the dimensions of the sample, an important consideration in fracture mechanics seems to depend on the choice of the fracture criterion and the loading rate. This indicates that for real materials, that is not well modelled by linear elastic fracture mechanics, but characterised by fracture process zones and a transition from continuum to discontinuum there may not be a universal scale effect rule.

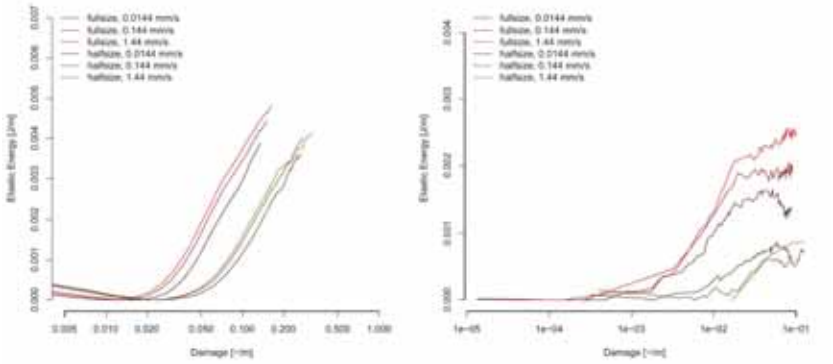

Figure 4: Elastic energy dissipated in the sample as a function of the damage renormalised by sample depth, using the Mazars criterion (left) and the MCFT (right)

5. Conclusion

We show in this paper that the choice of fracture criterion implies a particular coupling with the viscous response of the concrete. We have demonstrated a numerical strategy which allows exploring this link. The most important observation is that fracture criteria, even when empirically derived like the MCFT impose energy release rates. This indicates that it is possible to use empirical behaviours behave as though they had been formally derived from an energy potential.

In future works, the energy release rate imposed in phase field damage models should be related to the implied rate which can be measured using the method outlined here.

References

[1] CF Dunant and EC Bentz. Algorithmically imposed thermodynamic compliance for material models in mechanical simulations using the aim method. International Journal for Numerical Methods in Engineering, 2015.

[2] MA Crisfield. Snap-through and snap-back response in concrete structures and the dangers of under-integration. International Journal for Numerical Methods in Engineering, 22(3):751–767, 1986.

[3] NJ Gardner and MJ Lockman. Design provisions for drying shrinkage and creep of normal-strength concrete. Materials Journal, 98(2):159–167, 2001.

[4] A. Hilaire, F. Benboudjema, A. Darquennes, Y. Berthaud, and G. Nahas. Modeling basic creep in concrete at early-age under compressive and tensile loading. Nuclear Engineering and Design, 269:222–230, 2014.
[5] Matthieu Vandamme. The nanogranular origin of concrete creep: a nanoindentation investigation of microstructure and fundamental properties of calcium-silicate-hydrates. PhD thesis, Massachusetts Institute of Technology, 2008.
[6] A.B. Giorla, K.L. Scrivener, and C.F. Dunant. Influence of visco-elasticity on the stress development induced by alkali–silica reaction. Cement and Concrete Research, 70:1–8, 2015.
[7] Jacky Mazars. A description of micro-and macroscale damage of concrete structures. Engineering Fracture Mechanics, 25(5-6):729–737, 1986.
[8] Evan C Bentz, Frank J Vecchio, and Michael P Collins. Simplified modified compression field theory for calculating shear strength of reinforced concrete elements. ACI Structural Journal, 103(4):614, 2006.
[9] C.F. Dunant and K.L. Scrivener. Micro-mechanical modelling of alkali–silica-reaction-induced degradation using the amie framework. Cement and Concrete Research, 40(4):517–525, 2010.
[10] Cyrille F Dunant, St´ ephane PA Bordas, Pierre Kerfriden, Karen L Scrivener, and Timon Rabczuk. An algorithm to compute damage from load in composites. Frontiers of Architecture and Civil Engineering in China, 5(2):180–193, 2011.
[11] JH Argyris and DW Scharpf. Finite elements in time and space. Nuclear Engineering and Design, 10(4):456–464, 1969.
[12] I Fried, Marc A Cremer, and Patrick A McMurtry. Finite-element analysis of time-dependent phenomena. AIAA Journal, 7(6):1170–1173, 1969.
[13] A Idesman, R Niekamp, and E Stein. Finite elements in space and time for generalized viscoelastic maxwell model. Computational Mechanics, 27(1):49–60, 2001.
[14] C.I. Bajer and B. Dyniewicz. Virtual functions of the space–time finite element method in moving mass problems. Computers & Structures, 87(7):444–455, 2009.
[15] Serge Dumont and Franck Jourdan. A space-time finite element method for elastodynamics problems with a moving loading zone. In Proceedings of the Eleventh International Conference on Computational Structures Technology, 2012.
[16] A.B. Giorla, K.L. Scrivener, and C.F. Dunant. Finite elements in space and time for the analysis of generalised visco-elastic materials. International Journal for Numerical Methods in Engineering, 97(6):454–472, 2014.
[17] M.A. Biot. Theory of stress-strain relations in anisotropic viscoelasticity and relaxation phenomena. Journal of Applied Physics, 25(11):1385–1391, 1954
[18] G.A. Francfort and J-J. Marigo. Revisiting brittle fracture as an energy minimization problem. Journal of the Mechanics and Physics of Solids 46(8): 1319-1342,1998.

International RILEM Conference on Materials, Systems and Structures in Civil Engineering
Conference segment on Service Life of Cement-Based Materials and Structures
22-24 August 2016, Technical University of Denmark, Lyngby, Denmark

SERVICE LIFE PREDICTION OF A CEMENTITIOUS COATING SYSTEM BASED ON CHLORIDE-INDUCED CORROSION

Hua Dong [(1)], Guang Ye [(1)]

(1) Delft university of Technology, Delft, The Netherlands

Abstract
Cementitious materials are usually applied as an overlay to enhance the durability of concrete structures. This study takes into account the time dependent chloride binding isotherms of materials in the overlay system, and predicts the service life of reinforced concrete structures based on the chloride-induced corrosion. In order to realize a more realistic simulation, an interval of 25 years is specified to replace the overlay material on the concrete substrate. For comparison, simulation of chloride ingress into a single reinforced concrete substrate is conducted, on which the concrete cover is also renewed in the same time interval. The results show that a thin layer of cementitious overlay material with the thickness of no more than 10 mm can significantly improve the resistivity of concrete structures to chloride ingress. A cementitious overlay system with replacement of a thin overlay material in every 25 years has only a slight influence on the evolution of chloride profiles in concrete substrate, compared to an overlay system without replacement of overlay material. Furthermore, the efficiency of a thin overlay material on extending the service life of reinforced concrete structures is found to be comparable to the case that concrete cover is renewed periodically.

1. Introduction

In service, concrete structures may suffer from deteriorations in different forms, including shrinkage-induced cracking, carbonation and reinforcement corrosion due to chloride ingress. Cementitious material as an overlay [1, 2] is commonly used to protect the underlying concrete. The overlay is used as a physical barrier towards external ingressive sources, such as moisture, chloride and sulfate. As a protection method, the assessment of service life of overlay system is of great importance. With respect to chloride induced reinforcement corrosion, numerical solution is needed for the chloride transport process in a double layer system. Song et al. [3] applied a finite difference method to solve the diffusion equation,

taking into account the time dependent surface chloride ion concentration and the time span for the concrete cover replacement. However, chloride binding is also very important during chloride transport through cementitious materials. Chloride binding behavior of cementitious materials highly depends on their composition. Among the hydration products, the calcium silicate hydrate (C-S-H) phase and the monosulfate (AFm) phase, are best known to bind chloride ions, with the chemical binding from AFm compounds through chemical substitution, and the physical binding from C-S-H phase due to its high specific surface values [4]. Different chloride binding isotherms, including linear and non-linear isotherms, are studied by Perez et al. [5] to accentuate their significance in time of steel depassivation.

In this study, a cement paste with the thickness of 6 mm or 10 mm is applied as an overlay material. Time dependent chloride binding isotherm is taken into account for the simulation on chloride transport through the cementitious coating system. To mimic practical coating systems, coating material is replaced every 25 years in the simulation. As above-mentioned, in [3] a periodically replaced concrete cover has been a solution to keep chloride content under a safe level. In this study, concrete cover replacement on a single substrate is also simulated as a reference for comparison with coating systems.

2. Chloride diffusion

In saturated cement-based materials, diffusion is a process in which ions migrate from higher concentration area to lower concentration area with water as a media. The Fick's 2nd law is commonly used to describe this process.

$$\frac{\partial C_c}{\partial_t} = div(D_t grad C_c) \tag{1}$$

where C_c is the chloride content in concrete (kg in unit volume of cementitious material), D_t is the time dependent chloride diffusion coefficient (m^2/s), t is time (s).

In order to conserve the mass of chloride diffusing through the coating and the substrate, the chloride concentration C_f in the pore solution of each material is introduced, and linked to the chloride content C_c in the materials by total porosity $\emptyset_T$. With $C_c = \emptyset_T C_f$, a new form of Eq. (1) reads:

$$\frac{\partial \emptyset_T C_f}{\partial_t} = \frac{dC_f}{dC_t} div\left(D_t grad\left(\emptyset_T C_f\right)\right) \tag{2}$$

where C_t is the total chloride concentration with respect to the pore solution, in mole of chloride per liter of the pore solution. The term dC_f/dC_t accounts for chloride binding, and can be determined according to the binding isotherm.

3. Parameter determination

In Eq. (2), for either the coating or the substrate, total porosity $\emptyset_T$, chloride diffusion coefficient D_t and the term dC_f/dC_t are time dependent. Their values change with the proceeding hydration of cementitious materials. During the simulation, each of them needs to be determined with respect to time.

3.1 Diffusion coefficient

This study focuses on chloride transport through the saturated cementitious materials. A power function in terms of concrete age t, is usually adopted to account for the time dependent diffusion coefficient D(t) with the form: $D(t) = D_T(T/t)^n$. Where D_T is the chloride diffusion coefficient for concrete at age T (reference time), n is the exponential coefficient for D(t), which is also referred to as aging factor in DuraCrete [6]. In this study, n is specified as 0.37 for OPC concrete in tidal and splashed zone, according to DuraCrete. Since it is not rational to assume D(t) decreases infinitely with exposure time, the decreasing curve of D(t) is truncated at $t = 25$ years.

A concrete with a water to cement ratio of 0.5, and a volumetric cement content of 450 kg, is used as a substrate. The diffusion coefficient of concrete D_{sub} is highly dependent on its water to cement ratio. According to [7], the diffusion coefficient of concrete at 28 days follows the relation: $D_{sub-28} = 10^{-12.06+2.4w/c}$. For a concrete with a water to cement ratio of 0.5, D_{sub} is $1.38 \times 10^{-11}\ m^2/s$. A cement paste with a water to cement ratio of 0.35, and a volumetric cement content of 1498 kg, is used as a coating material in this study. The diffusion coefficient of coating material D_{co} is obtained from [8], with $D_{co-28} = 3.26 \times 10^{-12}\ m^2/s$.

3.2 Binding isotherm

In cement paste, C-S-H and monosulphate hydrate are believed to have significant chloride binding capacities. Hirao et al. [9] investigated chloride binding isotherms of these hydrates, and found that the chloride binding by monosulfate hydrates is attributed to the formation of Friedel's salt, while the chloride-binding of C-S-H is a physical process due to its high specific surface values. The chloride binding isotherm of AFm followed a Freundlich-type adsorption (Eq. (3)), while C-S-H followed a Langmuir-type adsorption (Eq. (4)):

$$C_{b-AFm} = 0.86{C_f}^{0.58} \tag{3}$$

$$C_{b-C-S-H} = 0.61 \times \frac{2.65C_f}{1 + 2.65C_f} \tag{4}$$

where C_{b-AFm} is bound chloride, in moles of chloride per mole of AFm, $C_{b-C-S-H}$ is bound chloride, in mili-moles of chloride per gram of C-S-H, and C_f is free chloride, in moles of free chloride per liter of the pore solution. To calculate the term dC_f/dC_t, it is necessary to use the same unit for free and bound concentrations. For this reason, the units are converted to moles of chloride per liter of the pore solution. Three parameters should be involved for the conversion, including the mass of monosulphate m_{AFm}, the mass of C-S-H

gel m_{C-S-H}, and total porosity $\emptyset_T$. The unit of m_{AFm} and m_{C-S-H} is in kilograms of the hydrates per cubic meter of the cementitious material. Determination of m_{C-S-H}, m_{AFm}, and $\emptyset_T$ will be discussed in the following part.

3.3 Determination of $\emptyset_T$, m_{C-S-H}, and m_{AFm}

For simplification, in concrete substrate, only pores of cement paste are taken into account in this study, despite pores in other forms may exist: e.g. pores in the interface transition zone between aggregates and cement paste. The total porosity $\emptyset_T$ of cement paste consists of capillary porosity $\emptyset_{cap}$ and gel porosity $\emptyset_{gp}$. Gel porosity is based on the amount of C-S-H gel m_{C-S-H} formed during hydration. The composition of cement is an important parameter to the hydration process. Generally, ordinary Portland cement consists of four clinkers, i.e., tricalcium silicate (alite: C_3S), dicalcium silicate (belite: C_2S), tricalcium aluminate (C_3A) and tetracalcium aluminoferrite (ferrite: C_4AF). In addition, gypsum ($C\underline{S}H_2$) is added as an inhibitor to prevent flash setting. In this study, Portland cement with a specific mineral composition is used. The mass composition of cement is as follows: *C_3S : C_2S : C_3A : C_4AF : Gypsum = 53.5% : 21% : 7.5% : 10% : 8%.*

3.3.1 Capillary porosity

The fresh cement paste consists of cement particles and water filled pores. Over hydration, water is gradually consumed for the reaction, and transferred to hydration products. The volume of initially water filled pores gets smaller and smaller due to the precipitation of hydration products. Capillary pore is the residual volume of unfilled space between cement particles. The capillary porosity depends on the degree of hydration of cement paste. Degree of hydration $\alpha(t)$ and capillary porosity $\emptyset_{cap}$, can be calculated according to a modified Power's model [10-12].

3.3.2 Amount of C-S-H gel and AFm

The mass fraction of C-S-H and AFm over hydration can be deduced from the chemical equilibrium of cement reactions. According to Taylor [13], the chemical reactions describe the hydration process of OPC, these reactions can be used to determine the mass stoichiometries of the reactants and products. During hydration, the reactions of four major phases develop differently, degree of reaction of the each phase can be approximated by Avrami equations [14].

3.3.3 Gel porosity

Distinct from capillary pores, the finest pores with the sizes ranging from approximately 10 nm to 0.5 nm are called gel pores [15]. Literally, gel pores are from the C-S-H gel phase, where low density C-S-H (LD C-S-H) and high density C-S-H (HD C-S-H) are distinguished. Apparently, pore structures of these two types of gels are different. It is believed that only some of the pores in LD C-S-H are accessible to nitrogen [16]. In this study, assumption is made that chloride ions can only enter the pores which nitrogen can enter. Consequently, gel porosity $\emptyset_{gp}$ refers to chloride accessible gel pores. Detailed information for determining gel porosity $\emptyset_{gp}$ can be found from [16].

4. Numerical model

In this study, a cement paste as a coating material is applied on concrete substrates. 1 dimensional (1D) case of chloride transport through a substrate or a coating system is simulated. The thickness of the substrate is 150 mm, on which a 6 mm or 10 mm-thick coating is applied. The top surface of the substrate or the coating system is exposed to a chloride environment (tidal and splashed zone), while the bottom surface is considered sealed. Steel reinforcements are placed in the substrate at a depth of 30 mm from the top surface. 4 scenarios are considered: 1. Chloride transport through a concrete substrate; 2.Chloride transport through a concrete substrate, but the 30 mm-thick concrete cover is renewed every 25 years; 3. Chloride transport through a coating system, a 6 mm or 10 mm-thick coating is applied on the substrate; 4. Chloride transport through a coating system as in scenario 3, but the coatings are renewed every 25 years. The 4 scenarios are also listed in Tab. 1.

Table 1 Scenarios in this study.

Scenario	**1**	**2**	**3**	**4**
Substrate	Yes	Yes	Yes	Yes
Coating (6 or 10 mm)			Yes	Yes
Cover replacement		Yes		
Coating replacement				Yes

All substrates are subjected to a mist curing for 7 days before the exposure to a chloride environment or the application of coatings. As regards the surface chloride content, it is conventionally expressed by its mass percentage to the cement paste. The surface chloride content is also found to be time dependent [17]. In this study, to avoid the complexity of surface chloride content, a constant chloride concentration of 0.5 mol/l is assumed and assigned on the exposing surface of all specimens from scenario 1-4. The total exposure time is 100 years. To facilitate the description of these series, abbreviations are adopted (see Tab. 2). For instance, “CS06Rep25Cov30” stands for a coating system consisting of a 6 mm-thick coating material and a concrete substrate, the thickness of concrete cover is 30 mm, and the coating is replaced every 25 years. “SubRep25Cov30” refers to a substrate with a 30 mm-thick concrete cover, and the concrete cover is replaced every 25 years.

5. Results and discussion

The commercial FEM software COMSOL Multiphysics is adopted to solve Eq. (2). Numerical analysis is performed on both concrete substrate and coating systems.

5.1 Substrate and coating system

Chloride profiles of a substrate concrete and a coating material, after 25-year and 100-year exposure in chloride environment, are shown in Fig. 1 (a). In this figure, Sub - 25y stands for a substrate exposed in chloride environment for 25 years, etc. A coating is found to effectively

retard the chloride ingress. There exists a steeper gradient of chloride concentration in the coating material than in the concrete substrate, because the coating has a lower chloride diffusivity, expected from a lower w/c of 0.35 compared to the one of the concrete substrate (w/c = 0.5).

Table 2 Abbreviations used for each scenario in this study.

	1	2	3	4
Substrate	Sub			
Cover thickness	Cov30			
Coating-substrate system[(a)]			CS06 CS10	
Substrate (cover replacement)		SubRep25		
Coating-substrate system[(a)] (Coating replacement)				CS06Rep25 CS10Rep25
Exposure time	100y			

(a): Coatings with the thickness of 6 mm or 10 mm are used.

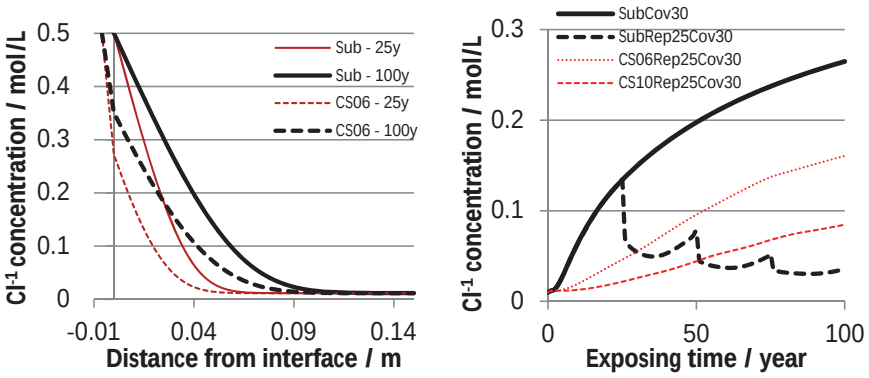

(a) (b)

Fig. 1 (a) Chloride profile in the substrate and the coating material. (b) Evolution of chloride concentration at the depth of 30 mm (location of reinforcement) in the substrate and the coating systems.

5.2 Concrete cover replaced every 25 years

In practice, the coating material is believed to require replacement in certain time period. Time period for replacement in this study is specified as 25 years. Reinforcement is placed at the depth of 30 mm under the surface of substrate. For reference, in a monolithic concrete substrate, a 30 mm-thick concrete cover is replaced every 25 years as well. The case of concrete cover replacement is studied first. At the depth of 30 mm (cover thickness), evolution of chloride concentration as function of exposing time is depicted in Fig. 1 (b). In this figure, 4 cases are concerned, including a concrete substrate with a 30 mm cover

(SubCov30), a concrete substrate with 30 mm-thick cover replaced every 25 years (SubRep25Cov30), and two coating systems, with a 6 mm-thick coating (CS06Rep25Cov30) and a 10 mm-thick coating (CS10Rep25Cov30), respectively. In the case of SubCov30, chloride concentration at the depth of reinforcement increases smoothly over time. However, with the cover replaced periodically after the first 25 years (SubRep25Cov30), a stepwise decrease of chloride concentration is observed at the depth of reinforcement. For the cases of two coating systems, i.e. CS06Rep25Cov30 and CS10Rep25Cov30, chloride concentrations at the depth of reinforcement are effectively reduced, compared to the case of SubCov30. It is clear that the thicker coating exhibits a higher efficiency in protecting the substrate from chloride ingress.

5.3 Coating replaced every 25 years

This part aims to study the influence of the coating and the coating replacement on chloride transport through a coating system, where 06 mm-thick and 10 mm-thick coatings are used, and replaced every 25 years. As a reference, coating systems without coating replacement are also investigated. Evolution of chloride concentration in a coating system with a 06 mm-thick coating is shown in Fig. 2 (a). Two locations, i.e., the interface between two materials and the depth of reinforcement are concerned. After the first 25 years in service, the coating material is replaced. Clear difference in chloride concentration can be found at the interfaces from coating systems with or without coating replacement. With coating replacement, chloride concentration at interface is even higher than the one without coating replacement. This is somehow counterintuitive, because a fresh coating is supposed to absorb chloride from the substrate. However, the effects from a new coating are two fold. On one hand, it absorbs chloride from the substrate. On the other hand, a higher diffusivity at early age allows a quicker chloride ingress from the exposing surface. These two processes impact each other and result in different situations. Fig. 2 (b) shows the evolution of chloride concentration in a coating system with a 10 mm-thick coating. In contrast to Fig. 2 (a), a lower chloride concentration at the interface of CS10Rep25Cov30 is observed, compared to the one of CS10Cov30. Nevertheless, chloride concentration at the depth of 30 mm is not affected when the coatings are replaced periodically, indicated both in Fig. 2 (a) and Fig. 2 (b); this is because that, the chloride concentration at deeper locations in concrete substrates is less influenced by the variation of chloride concentration at the surface of concrete surface, which can also be indicated from Fig. 1 (a).

5.4 Cover replacement versus coating replacement

Fig. 1 (b) shows the evolution of chloride concentration in different structures, including a concrete substrate, a substrate with cover replacement and two coating systems (06 mm-thick coating and 10mm-coating) with coating replacement. Comparisons are made to see the difference of initiation time of corrosion in each case. The initiation time refers to chloride based service life of structures in this study. It is worth noting that the thickness of concrete cover and critical chloride concentration are two of the main factors to determine the service life of reinforced concrete structures. The concrete cover thickness is specified as 30 mm in this study. However, the critical chloride concentration is dependent on many factors, e.g. type and surface pretreatment of reinforcement, binding behavior of cement-based matrix, etc. With the steel embedded in cement-based material (laboratory conditions), the published

critical free chloride concentration has a great range from 0.045 to 3.22 mol/l of pore solution [18]. Regarding this issue, different critical chloride concentrations, e.g. 0.1 or 0.15 moles of chloride in per liter of pore solution, are used to calculate the time when corrosion of reinforcement is initiated. The results are presented in Fig. 3. With a critical chloride concentration of 0.1 mol/l, the service life of Sub, SubRep25, CS06Rep25 and CS10 Rep25 are 17, 17, 53 and 100 years, respectively. Note that the critical chloride concentration for the initaition of reinforcement corrosion will also have an effect on the calculated results of chloride-based service life. It is obvious that a thicker coating will result in a slower progress of increasing chloride concentration on the surface of reinforcement. However, no general conclusion can be drawn on different methods in terms of cover replacement or coating replacement, because the comparison also depends on the critical chloride concentration. For example, given a critical chloride concentration of 0.15 mol/l, the service life of Sub, SubRep25, CS06Rep25 and CS10Rep25 are 31, 100, 89 and 100 years, respectively. In this case, CS06Rep25 has a shorter service life than SubRep25, while CS06Rep25 has a longer service life than SubRep25 when 0.1 mol/l is specified as a critical chloride concentration.

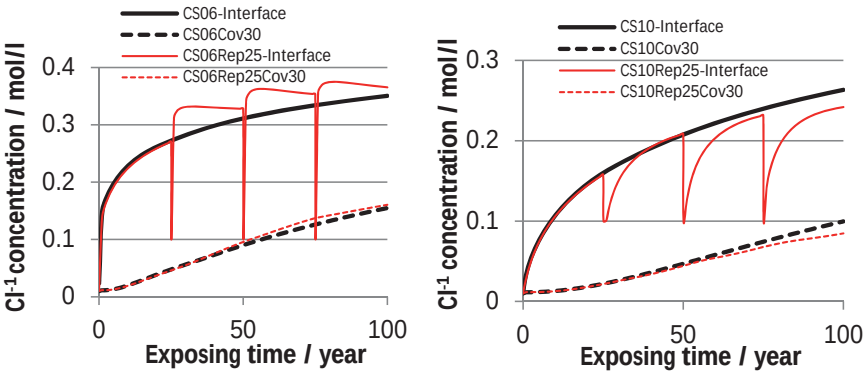

(a) 06 mm-thick coating (b) 10 mm-thick coating

Fig. 2 Chloride profile of coating systems with or without coating material replaced.

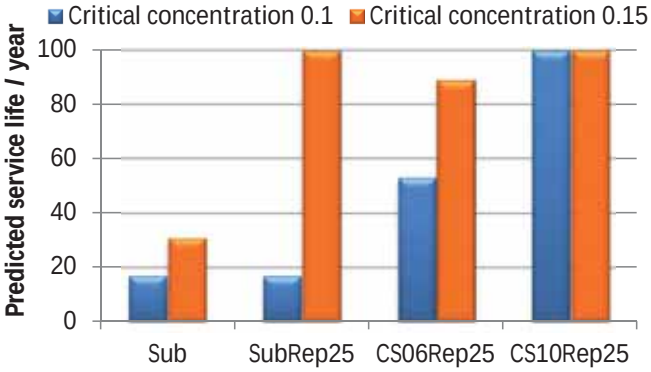

Fig. 3 Predicted service life of reinforced concrete structures.

Therefore, this simulation is essential to figure out the efficiency of each method (concrete cover replacement or application of coating materials), and to evaluate the extent of chloride-based service life of a reinforced concrete structure with application of coatings.

6. Conclusion

In this study, chloride transport through the concrete substrates and the coating systems is simulated, taking into account the chloride binding effect. Cover replacement and coating replacement in every 25 years are considered and compared to each other. Several conclusions can be drawn:

- Cementitious coatings with the thickness of 6 mm or 10 mm have a significant influence on chloride ingress into concrete structures. A steeper concentration gradient in coating materials is observed because the coating has a lower water to cement ratio than the substrate.
- In the case that the coating is replaced periodically, coating replacement results in different chloride concentrations at the interface between two materials. Evolution of chloride concentration at the interface is found to depend on the coating thickness. When a thin coating (e.g. 6 mm-thick) is replaced periodically, chloride concentration at the interface of a coating system can be even higher, compared to the case that the coating is not replaced in a coating system.
- Coating replacement has a minor influence on the chloride concentration at the location of reinforcement (30 mm from substrate surface in this study). It has to be pointed out that this influence will also depend on the coating thickness and the cover thickness, etc.
- Chloride transport through a substrate with the cover replaced every 25 years is also simulated. A stepwise reduction of chloride concentration at the location of reinforcement is observed. Concrete cover replacement in a single substrate is compared to coating replacement in coating systems, in terms of their influence on chloride concentration at the location of reinforcement. Service life prediction is conducted by specifying different critical chloride concentrations. The efficiency of cover replacement or coating replacement depends on many factors, e.g. cover thickness, coating thickness and composition of the coating, etc. Therefore, this simulation is essential to evaluate their efficiency, and instructive for practical issues, including the concrete cover replacement and the application of cementitious coatings.

Acknowledgements

The authors would like to acknowledge the financial support by the Dutch Technology Foundation (STW) for the project 10981-“Durable Repair and Radical Protection of Concrete Structures in View of Sustainable Construction”.

References

[1] Saricimen, H. et al, Evaluation of a surface coating in retarding reinforcement corrosion,

Constr Build Mater, 10 (1996), 507-513
[2] Al-Dulaijan, S. U. et al, Performance evaluation of cement-based surface coatings, ACI Special Publication, 193 (2000)
[3] Song, H. W. et al, Service life prediction of repaired concrete structures under chloride environment using finite difference method, Cem Concr Compos, 31 (2009), 120-127
[4] Florea, M. V. A. and Brouwers, H. J. H., Chloride binding related to hydration products Part I: Ordinary Portland Cement, Cem Concr Res, 42 (2012), 282-290
[5] Martin-Perez, B. et al, A study of the effect of chloride binding on service life predictions, Cem Concr Res, 30 (2000), 1215-1223
[6] EUB EuRam III, DuraCrete Final Technical Report, Probabilistic Performance Based Durability Design of Concrete Structures, Document BE95-1347/R17 May, (2000)
[7] Thomas, M. and Bentz, E., Life-365 manual, Released with program by Master Builders, (2000), 6-10
[8] Sun, G. W. et al, Relationship between chloride diffusivity and pore structure of hardened cement paste, J Zhejiang Univ Sci A, 12 (2011), 360-367.
[9] Hirao, H. et al, Chloride binding of cement estimated by binding isotherms of hydrates, J Adv Concr Technol, 3 (2005), 77-84
[10] Powers, T. C. and Brownyard, T. L., Studies of the physical properties of hardened portland cement paste, Portland Cement Association, Research Laboratories (1948)
[11] Snyder, K. A. and Bentz, D. P., Suspended hydration and loss of freezable water in cement pastes exposed to 90% relative humidity, Cem Concr Res, 34 (2004), 2045-2056
[12] Bentz, D. P., Influence of water-to-cement ratio on hydration kinetics: Simple models based on spatial considerations, Cem Concr Res, 36 (2006), 238-244
[13] Taylor, H. F., Cement chemistry, Thomas Telford (1997)
[14] Taylor, H. F., A method for predicting alkazi ion concentrations in cement pore solutions, Adv Cem Res, 1 (1987), 5-17
[15] Mindess, S. et al, Concrete, Prentice Hall, Englewood Cliffs, NJ, (1981), 481
[16] Tennis, P. D. and Jennings, H. M., A model for two types of calcium silicate hydrate in the microstructure of Portland cement pastes, Cem Concr Res, 30 (2000), 855-863
[17] Ann, K. Y. et al, The importance of chloride content at the concrete surface in assessing the time to corrosion of steel in concrete structures, Constr Build Mater, 23 (2009), 239-245
[18] Angst, U. et al, Critical chloride content in reinforced concrete — A review, Cem Concr Res, 39 (2009), 1122-1138

International RILEM Conference on Materials, Systems and Structures in Civil Engineering
Conference segment on Service Life of Cement-Based Materials and Structures
22-24 August 2016, Technical University of Denmark, Lyngby, Denmark

USABILITY OF BASALT FIBRES IN FIBRE REINFORCED CEMENTITIOUS COMPOSITES

Zehra Canan Girgin [(1)]

(1) Yildiz Technical University, Istanbul, Turkiye

Abstract

In this study, the flexural performance and usability of basalt fibres (BF), which has been recently introduced, in the fibre reinforced cementitious composites (BRC) are investigated incorporating mineral admixtures. Two types of sustainable puzzolanic admixtures were used, nano clay (NC) as a natural resource and granulated blast furnace slag (GGBS) as a byproduct. The experimentinal studies were carried out in 3,7,28,56,90 and 120-day curing periods and afterwards in harsh durability test conditions. All the tests were conducted compared with glass fibre (GF) reinforced cementitious composites (GRC). It is noticed that the matrix modification have positive effect on the flexural performance of BRC by puzzolanic reaction. The reduction trend in strains beyond 7 days in 100% cement ones is retarded to 28 and 56 days by enhancing matrix-fibre interface. In spite of the fact that the pull-out mechanism is improved during freeze-thaw cycles, BRC is still sensitive to heat-rain cycles. Meanwhile, there is no sign of alkaline attack on basalt fibre in SEM micrographs. Further research on BRC is necessary to satisfy the flexural performance in severe durability conditions.

1. Introduction

Basalt fibres were industrially produced in 1985 [1] from igneous rock. BF has 20-30% higher tensile strength, modulus of elasticity, fire resistance [2,3], and durability in alkaline conditions [4] compared with GF.
BF, which is a relatively new fibre type, is receiving increasing attention especially in fibre reinforced polymer composites (BFRP) [5]. Nowadays, a few studies are available on the utilization of basalt fibres in cementitious matrix. The effect of basalt fibres on the mechanical characteristics were investigated in geopolymer concretes (GPC) [6], fibre

reinforced concrete (BFRC) [7,8], textile reinforced mortar (TRM) [9], and high performance concrete (HPFRC) [10]. The research studies on BF indicated significant increase in fracture energy and flexural characteristics, but these studies are limited with only standard curing period. According to the author's knowledge, in the current literature, there is only one study [11] on the durability of BRC, or BFRC, whose long-term performance is revealed, e.g. heat-rain test. Further research efforts on BRC, or BFRC, incorporating mineral admixtures are necessary due to unsatisfactory long-term performance of BRC in 100% cement matrix.

Calcined clay, or namely metakaolin, is the hydrocalcination product of kaolin contained clays. Since the mid-1990s, the studies concentrated on this highly puzzolanic material whose usage in the range 5% to 15 % by weight significantly increases the mechanical performance and durability of concrete [12]. Nowadays, another economic and natural resource is available, nano-clay (NC). Recently, there are a few studies on NC usage in concrete. It is indicated that NC promotes the hydration process in the matrix and contribute to more compact concrete, e.g. 5% NC addition [13] provides improvement in freeze-thaw resistance and chloride diffusion coefficient.

Ground granulated blast furnace slag (GGBS), or shortly slag, is a byproduct obtained from blast furnaces. It is generally used in high ratios (50-80%) in cement e.g. CEM III/B, or replacing with cement in predetermined ratios. Slag provides significant reduction in hydration heat, corrosion, alkali silica reaction rate [14,15], and the enhancement in mechanical characteristics at later ages through more dense interface.

In this study, to investigate and improve the flexural strain capacity in durability tests as well as in standard curing conditions are addressed incorporating two types local and sustainable mineral admixtures mentioned above, nano-clay and slag. The flexural results are evaluated in figures, tables and SEM micrographs.

2. Experimental Procedure

2.1 Materials and mixture proportions

Typical design of fibre reinforced cement composite, e.g. GRC, consists of cement, sand, water, polymer, often supplementary cementitious materials, and dispersed chopped fibres. In this study, nano-clay and slag from the local producers were used as mineral admixtures to enhance matrix-fibre interface and flexural strain capacity of fibres. The physical and chemical compositions of the binding materials are presented in Table 1. The particle size distributions of cement, nano clay and slag are displayed in Fig. 1.

Table 1: Physical and chemical compositions of cement, nano clay and slag.

Binder materials	CaO	SiO_2	Al_2O_3	Fe_2O_3	MgO	Blaine fineness	Specific gravity
			%			cm^2/g	
Cement CEM II/B-L 42.5R	63.18	16.51	3.37	0.16	0.84	5840	3.0
Nano clay (NC)	24.19	35.62	11.11	0.29	0.22	9180	2.6
Slag (GGBS)	33.99	40.29	11.30	2.34	5.76	5350	2.9

Total six mixtures were designed with three types of cementitious matrices. Three mixtures were conducted with BF, and remaning three mixtures with GF (Table 2). The ratios of nano

clay (NC) and slag (S1, S2) to total binding materials are 15 %, 50% and 80% by weight, respectively. In the mixture, fine silica sand (1300 μm to 150 μm in diameter) as aggregate and acrylic copolymer (4% by weight with respect to binding materials) were used similar to common GRC applications. Water to binder ratio is 0.33 in all mixture designs. Polymer component in the mixtures provides internal curing by minimizing water demand.

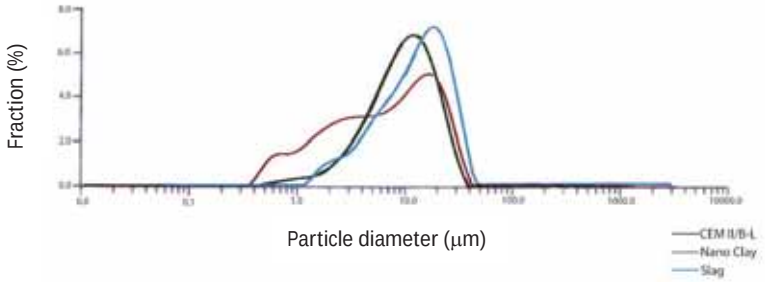

Figure 1: Particle size distribution of cement, nano-clay and slag.

Table 2: Mixture compositions.

Mix	Cement	Nano clay	Slag	Total binder	Silica sand	Polymer	Basalt fibre	Glass fibre
				kg/m^3				
NC	732	130			948.6			
S1	431		431	862	957.0	34.5	56	53.6
S2	172		690		940.7			

The main characteristics of BF and GF are given in Table 3. The volumetric fibre ratio (V_f) of basalt and glass fibres were chosen 2%, thus it is aimed to compare the experimental results with the previous study [11]. This ratio is also the upper limit for premix design of any fibre reinforced cementitious mix. Meanwhile, fibre ratios up to about 6 % via spray-up method are utilized in the industrial cladding applications.

Table 3: Properties of glass and basalt fibres.

Fibre type	Length (mm)	Dia. (μm)	Density (g/cm^3)	Elastic modulus (GPa)	Tensile strength (MPa)	Elong. (%)	Source
Glass	24	13-20	2.68	72	3500	4.5	CEMFIL®
Basalt	24	14-20	2.80	89	4840	3.15	Golden basalt®

2.2 Specimens preparation and testing

The experiments were carried out through the spray-up method to observe actual performance of BRC and GRC. There is no workability problem in this method. The spray gun chops the incoming continuous roving to fibres of a predetermined length. After completing the spray-up process to the mould, the roller is applied to compact the composite.

The fresh mixes were applied to 12 mm x 600 mm x 600mm-square sheet moulds and 50 mm-cubic moulds. All the specimens were demoulded 24 hours later. For all the mixture

designs, the sheets were categorized for the bending tests at the specific curing times as well as for the durability cycles.
Five cubes were poured for each curing time in all mixture series. 20 plates (11 x 50 x 270 mm) were cut from each sheet, total 18 sheets, for four-point bending tests in the curing periods of 3, 7, 28, 56, 90 and 120 days. 18 plates (11 x 60 x 250 mm) were cut from each sheet, total 10 sheets, for three-point bending tests regarding freeze-thaw tests. For heat-rain tests, total 24 sheets were preserved without cutting. All the specimens were placed in an environmental chamber at 35% relative humidity (RH) at 20±2°C until the day of testing. Polymer component allows to this internal curing regime, in addition, it is preferred for industrial applications.
Compressive and bending strength tests were carried out in accordance with EN 1170-4/5:1997, durability tests were executed according to EN 12467. Microstructural characteristics in some plates were examined by means of Zeiss EVO LS 10 type Scanning Electron Microscope (SEM), exactly to decide the fracture mechanism in BRC and GRC specimens.

2.2.1 Compressive strength tests
Compressive strength tests were carried out in the computer controlled Universal Testing Machine (TCS group) with 200 kN load cell at the load rate of 2400 N/s.
For nano-clay specimens (NC), the average strengths are 43.7 MPa (BF) and 37.8 MPa (GF) at 28 days. 15% nano-clay replacement enhanced the compressive strength in the level of 13% in BF-specimens compared with 100% cement one (38.5 MPa), and the strength enhancement in BF-cubes was not observed in GF-ones (37.6 MPa). This phenomenon may be related with the integrity fibre and matrix. Compressive strength increase in NC-series continued up to 56 days (52.0 MPa for BF, 45.17 MPa for GF), slightly drop is observed in the later curing periods. 7 to 28-day strength ratio is 0.8 and lower than 100% cement case (0.86-0.88) [11].
%50 slag replacement (S1) decreased 28-day average compressive strength 28% for BF and only 3% for GF. Increasing slag ratio (80%) gives rise to a greater reduction in the strengths, e.g. 52% for BF and 47% for GF in S2 series. In BF-S1 and BF-S2 series, the compressive strengths increased about 40% up to 90 days (34.3 MPa, 25.4 MPa). Slag replacements in GF-specimens did not significantly improve those strengths in later curing times after 28 days.

2.2.2 Bending tests
In the four-point bending tests, the span is 250 mm between roller supports. Following to 5 N preloading, the bending test is executed on a displacement controlled servo-hydraulic testing system with 500 Kgf load cell (Testometric Micro 350) at the load rate of 0.03±0.003 mm/s. Load and midspan deflection levels are recorded on a computerized data system and converted to stress-strain.
The typical stress-strain variation of BRC and GRC under flexure are given in Figure 2. Stresses and strains concerning the limit of proportionality (σ_{LOP} , ε_{LOP}) and the modulus of rupture (σ_{MOR} , ε_{MOR}), namely ultimate limits, (MOR) are displayed in this figure. A bilinear stress-strain variation is observed in BF-specimens similar to GF-specimens owing to strain hardening.

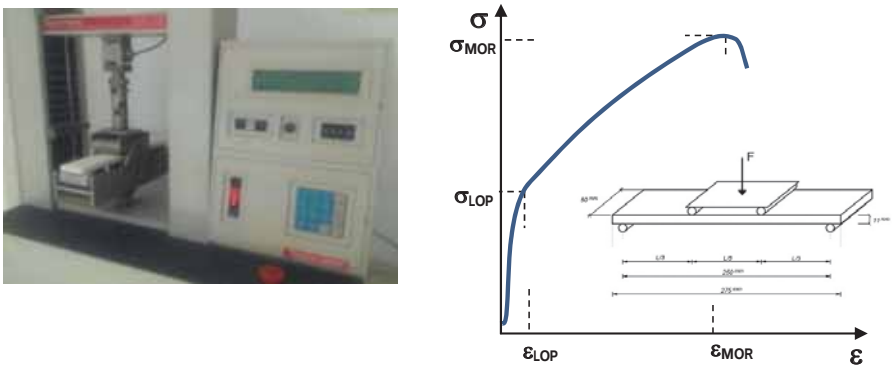

Figure 2: Bending test apparatus and typical stress-strain of preloaded BF-,GF-specimen [11].

Four-point bending tests were executed on at least ten BF- and GF-plate specimens from top and bottom surfaces. After discarding a few scattered data, the average ultimate strengths and strains (σ_{MOR} , ε_{MOR}) at 3,7, 28,56, 90 and 120 days are presented in Fig. 3. The coefficients of variation in stresses and strains are in the range 6-18%. The proportionality strengths and strains ($\sigma_{LOP,}$ ε_{LOP}) were not given for the sake of brevity. σ_{MOR} , ε_{MOR} values of this study are partially compared with 100% cement (control) ones of the previous study [11]. In that study, the experimental results until 28 days are available as the puzzolanic effect is not under consideration. The following evaluations can be made from all the experimental results.

Nano clay (15%)-specimens
In NC-specimens, 7-day flexural strength (13.08 MPa) of BF-specimens is lower only 5% than that of control ones (13.82 MPa), 28-day strengths (12.60 MPa) are 7% higher than those ones (11.82 MPa). 7-day strain (0.75%) of BF-specimens is 17% lower, 28-day strain (0.76%) is 9% higher than control specimens (0.88%, 0.64%). It is observed that NC addition eliminated the significant drop (38%) of strain capacity in control mixes from 7 days to 28 days. The reduction rate in strain capacity decreased and retarded with NC admixture in the later curing days.
The effect of NC-addition on flexural strengths is not significant in GF-specimens as much as BF-specimens. 7- and 28-day flexural strengths are 32% and 27% lower than GF-control specimens (13.66 MPa, 13.98 MPa. However, the positive effect of NC addition on strains is under consideration for GF-ones as well, e.g. 28-day strain (0.93%) is 19% is higher than the control specimen (0.78%) respectively. As a result, nano-clay has a substantial positive effect especially on strain capacities of both BF and GF fibre-matrix interface due to puzzolanic effect.

Slag (50%, 80%)-specimens
50% slag replacement (S1) leads the reduction of 43% and 22% in 7- and 28-day strengths of BF specimens compared with BF-control specimens. 80% slag replacement (S2) causes a very significant strength drop (40%, 53%) at 28 days compared with respectively BF-S1 and control specimens.

The drop trend in the strains begins from 28 days in BF-S1 and GF-S1 series, this trend was retarded to 56 days in S2 series. It is interesting that the strain capacities display similarities in GF-NC and –S2 series in 56 days and beyond it. Strain performances of GF-S1 and GF-S2 series are higher than BF-ones. The most positive effect of slag admixture is on the strains, the increase in flexural strengths is lower than NC-ones.

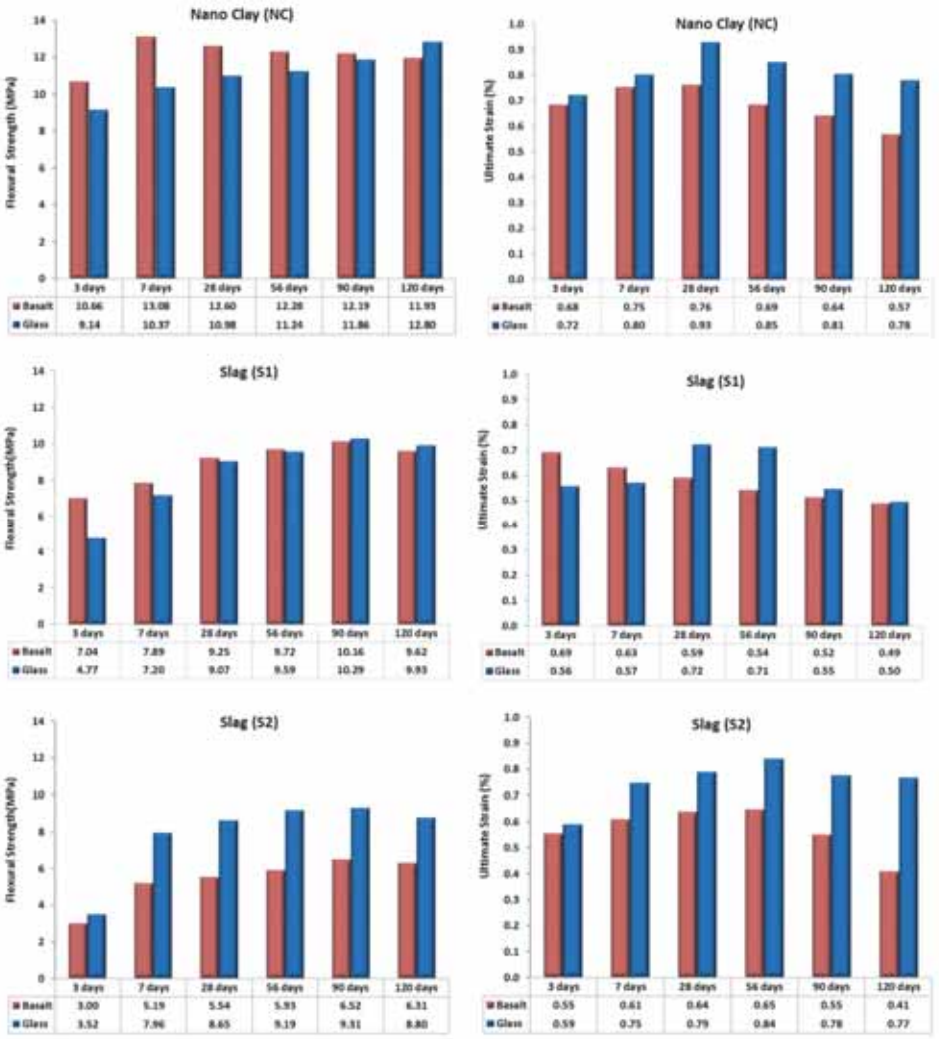

Figure 3: Variation in averaged ultimate flexural strengths and strains of basalt and glass fibres with curing time for the replacements of nano clay (15%), and slag (50%, 80%).

3. Durability Performance

Durability tests were conducted in a suitable stage after 28 days until 90 days by considering production process of the firm where the experiments were conducted. For this reason, the flexural tests for reference specimens were also carried out prior to starting heat-rain or freeze-thaw cycles.

3.1 Heat-rain test

Heat-rain test is an accelerated weathering test to observe visible problems (cracks, delamination etc.) in the sheets and to determine the variation in the flexural characteristics after harsh exposure cycles. The test is composed total 50 cycles, and each cycle continues 6 hours. In each cycle, the sheets are exposed to about 1 l/m^2/min. water spray for completely wetting face (2h 50 min±5 min) + radiant heating in 60±5°C (2h 50 min±5 min) steps with 10 min. intervals. After reference sheet tests, total six (3+3) BF and GF-sheets for each mineral additive were fixed at the vertical position in computer controlled test cabin. The relevant sheets were taken outside in 8th, 26th and the last 50th cycles. Herein, the findings from average values of flexural test results (Fig.4) are evaluated.

Although nano-clay and slag replacement in BF-specimens retard the strain drop especially in earlier cycles compared with 100% cement one [11], the performance in the later cycles is poor and quiet similar to control specimens. It seems that this severe exposure may lead to increase the pullout resistance and overbonding by ongoing hydration and calcium silicate hydrate (C-S-H) accumulation around basalt fibres. These conditions give rise to fast drops in the strains of BF-specimens during the ongoing cycles.

The reference strengths (10.73 MPa, 9.52 MPa, 8.81 MPa) of GF-specimens in NC, S1 and S2 series are significantly lower than control specimen (13.37 MPa). However, the drop rate in strengths under continuous cycles is lower than those ones, even an increment is available as from 8th cycles to be relevant with the adherence variation in the matrix-fibre interface. It is interesting that there is a noticable adherence-induced enhancement in strain capacity (up to about 1%) for 80% slag ratio (S2) as from the initial cycles.

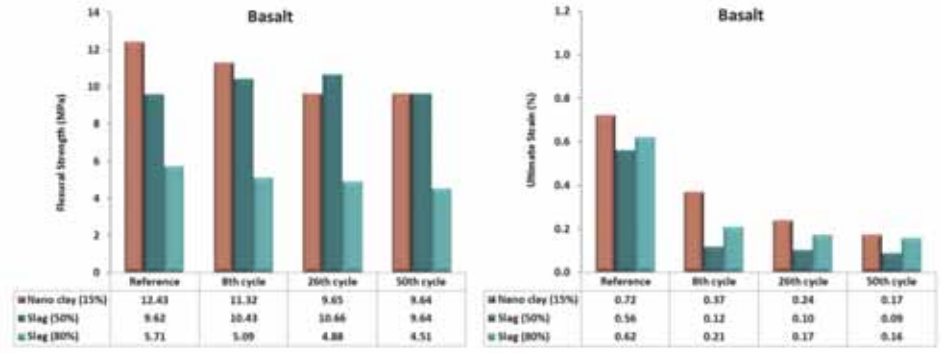

Figure 4: Variation in averaged ultimate flexural strengths and strains of basalt and glass fibres under heat-rain cycles.

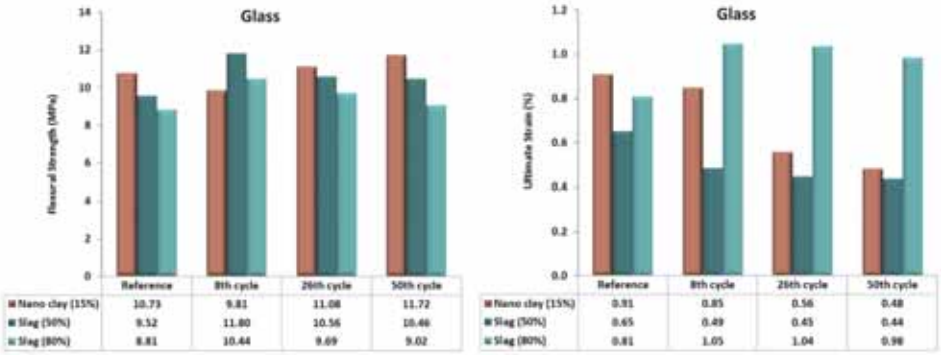

Figure 4: *continued*

3.2 Freeze-thaw test

In freeze-thaw test, each cycle continues 4 h to 6 h , max. 72 h interval between cycles which the plate specimens are stored in water at 20 °C. Ten plates for each series are exposed to total 100 cycles. In a cycle, first stage is to cool in the freezer down to (-20 ± 4) °C within 1 h to 2 h and holding at this temperature for a further 1 h; and the second stage is to heat in the water bath up to (20 ± 4) °C within 1 h to 2 h and hold at this temperature for a further 1 h. The relevant plates were taken outside in 25th and last 100th cycles. Herein, the findings from flexural test results (Fig.5) are evaluated.

There is a different trend for BF-specimens in freeze-thaw cycles compared with heat-rain cycles. Brittle fracture trend due to C-S-H accumulation around fibres disappears and more ductile behaviour is under consideration in BF-NC, S1 and S2 series. In first cycles, the strength enhancement may be observed.

It is noticed that the fibre-matrix integrity significantly degraded in GF-S2 series, thus, no value was displayed concerning 100th cycle of GF-S2 series. The possible reason may be weakening bond between the matrix and fibres due to freeze-thaw cycles and the disintegrity of the matrix incorporated with fibre debonding.

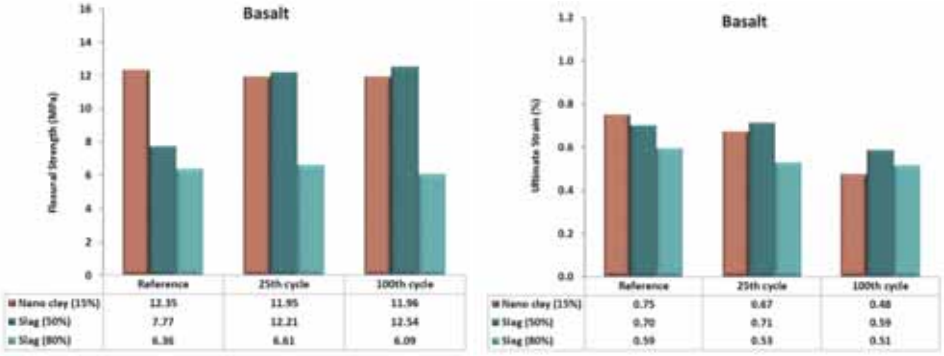

Figure 5: Averaged ultimate flexural strengths and strains of basalt and glass fibres under freeze-thaw cycles

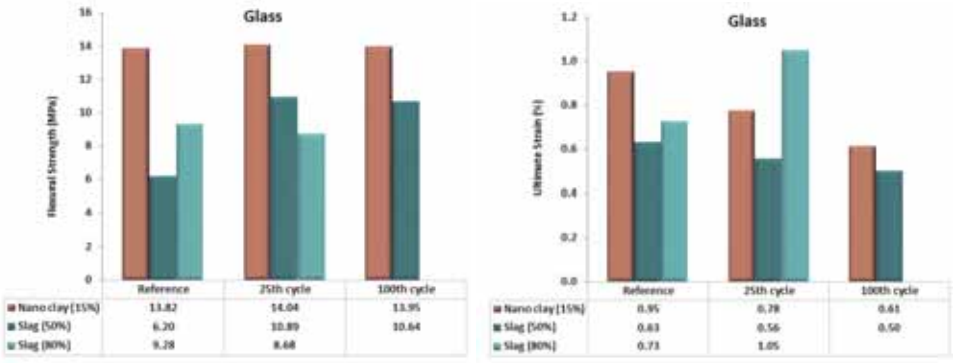

Figure 5: *continued*

4. Discussion of Test Results

The flexural performances are evaluated in this section by considering mineral admixture incorporation compared with control specimens. The cement matrix negatively influences the BF fibre-matrix interface after 7 days. Drop rate in averaged flexural strains is evident (28%) from 7 days to 28 days [11]. It can be seen in SEM images that the appearance of fibre is no-longer smooth, and the surface is filled with C-S-H more and more (Fig.6 a,b). Mineral admixture replacement retards the C-S-H deposits to 28 days and beyond it. In addition, the drop rate of strains in following curing times decreases as well. In all the experiments, both BF and GF presented high dimensional stability.

C-S-H densification accelerates in severe wetting-heating durability cycles (Fig.6 c,d) as a result of ongoing hydration in cement particles. Consequently, a sharp brittle failure mode is observed even after first cycles. None of BF-NC,S1,S2 series gives rise acceptable performance in heat-rain cycles possibly due to the humid/warm conditions supporting hydration process.

In BF-NC,S1, S2 series, it is interesting that remaining strain capacity after 100^{th} freeze-thaw cycles is in the range of 0.4-0.6%. Brittle behaviour of BF-specimens in the heat-rain cycles is not observed in freeze-thaw cycles (Fig.6 e,f). The structure of matrix and fibre ductility were improved with mineral admixtures.

It is interesting that debonding and degradation in matrix are monitored in GF-S2 series after freeze-thaw cycles, quite smooth surface of fibre and trace of debonding are observed in the SEM images (Fig.6 g,h). In heat-rain cycles, 20% increase in strain capacity is under consideration, however this enhancement may be a sign of partial debonding as well.

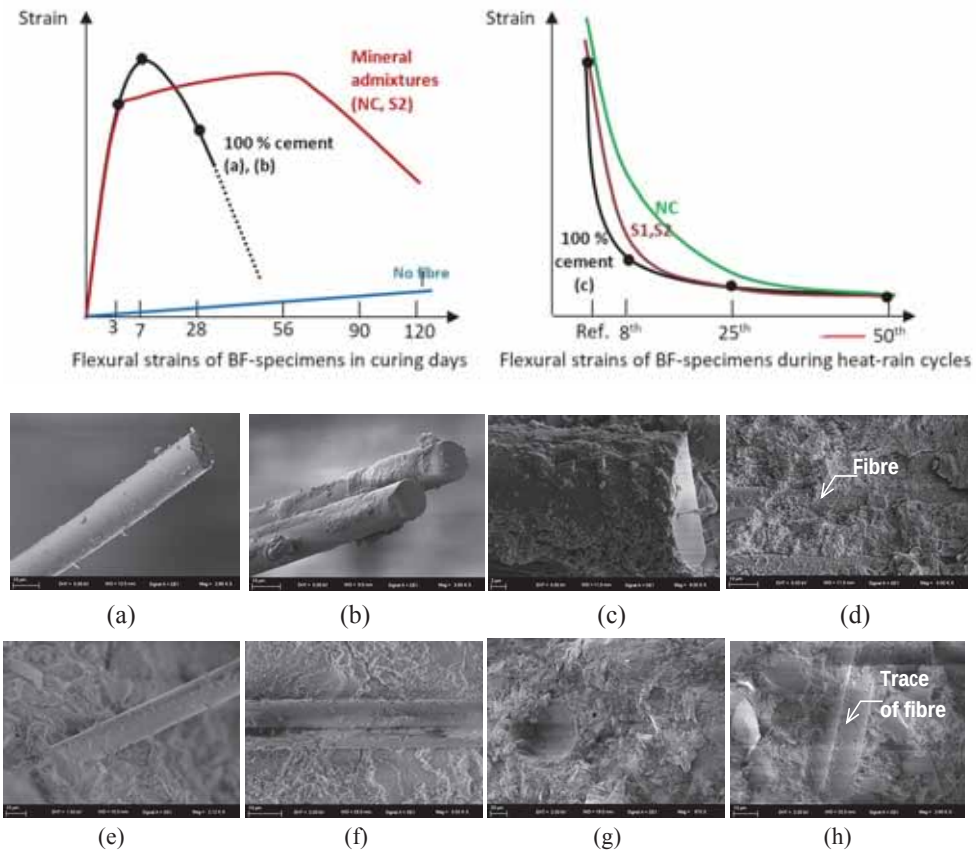

Figure 6 : Schematical strain comparisons of BF- cementitious composites under flexure test and SEM micrographs from (a) BF, 7 days, 100% cement; (b) BF, 28 days, 100% cement; (c),(d) BF after heat-rain 50th cycles, 100% cement; (e),(f) BF surface and cementitious matrix in BF-S1 after 100th freeze-thaw cycle; (g),(h) cementitious matrix and trace of fibre debonding in GF-S2 after 100th freeze-thaw cycle .

5. Conclusions

In this study, the variations of flexural capacities at 3,7,28,56,90 and 120 days as well as at durability conditions of basalt fibre cementitious composites are addressed. It is aimed to improve BF-matrix interface by mineral additives and to compare GF-ones. The findings from this study are given below:

- 100% cement use gives rise to significant reductions in flexural capacity after 7 days in BF-cementitious composites. Deposition of C-S-H and CH changes and densifies the fibre-matrix interface, and the failure mode leads to brittle behaviour due to overbonding. Any sign of

alkali attack due to CH or lamination due to C-S-H deposits are not observed on the surface of basalt fibres.

- By using sustainable natural or byproduct puzzolanic admixtures as from local sources, e.g nano clay and high-volume slag, strength and strain retention were provided up to 56 days, afterwards the drop trend especially in strains substantially slow down compared to 100% cement case. C-S-H accumulation on fibre surface induced embrittlement decreased significantly.
- 15% nano-clay use enhanced 28-day strength over 100% cement ones in BF-specimens, and decreased the strain reduction from 7 to 28 days. High slag ratios (50%, 80%) especially decreased the flexural strengths and strains of BF-ones higher than GF-ones. However the rate in strain reduction at the later curing periods decreased significantly.
- It is interesting that 80% slag ratio affected fibre-matrix bond mechanism in GF-ones, the fibre debonding accompanies to matrix degradation under freeze-thaw conditions. This situation is partially observed in heat-rain test.
- Further research is necessary to solve the brittleness of BF-cementitious composites during heat-rain test. Heating and wet conditions accelerate the hydration and lead brittle behaviour. Any degradation in matrix or debonding is not under consideration compared to GF-ones. New matrix modifications and maybe another surface treatment for basalt fibres may be experienced.
- The freeze-thaw resistance of BRC were enhanced through the mineral admixtures. Flexural strains in the range of 0.4-0.6% become possible. Thus, a step to toward ductile failure mode was succeeded. This research will proceed with further experiments on this subject.

Acknowledgement
The experiments in this study were carried out in Fibrobeton Inc. Material, employer and equipment support of those firm to this experimental research are greatly appreciated. I'm also thankful to MSc student Cihan Yolcu for his assistance to compiling of some data and to Dr.Ali Can Zaman for his attention in SEM micrographs.

References

[1] Morova, N. Investigation of usability of basalt fibres in hot mix asphalt concrete. Constr Build Mater 47 (2013), 175-180.
[2] Fiore V., Scalici T. and Bella G.D., Valenza, A A review on basalt fibre and its composites. Composites Part B: Eng 74 (2015),74-94.
[3] Sim, J., Park, C., Moon, D.Y. Characteristics of basalt fiber as a strengthening material for concrete structures. Composites Part B: Eng 36 (2005), 504–512.
[4] Lee, J.J., Song, J. and Kim, H. Chemical Stability of Basalt Fiber in Alkaline Solution. Fibres and Poly, 15(11) (2014), 2329-2334.
[5] Campione, G. et al. Behavior in compression of concrete cylinders externally wrapped with basalt fibres. Compos Part B, 69 (2015), 576–586.
[6] Dias, D.P. and Thaumaturgo, C. Fracture toughness of geopolymeric concretes reinforced with basalt fibres. Cem Concr Compos 27 (2005), 49–54.

[7] Kabay, N. Abrasion resistance and fracture energy of concretes with basalt fiber. Constr and Build Mater 50 (2014), 95–101.
[8] Jiang, C., Fan, K., Wu, F. and Chen, D. Experimental study on the mechanical properties and microstructure of chopped basalt fibre reinforced concrete. Mater and Design 58 (2014) 187-193.
[9] Larrinaga, P., Chastre, C., Biscaia, H.C. and San-José, J.T. Experimental and numerical modeling of basalt textile reinforced mortar behavior under uniaxial tensile stress. Mater and Design 55 (2014), 66-74.
[10] Ayub, T., Shafiq, N., and Nuruddin, M.F. Effect of chopped basalt fibers on the microstructure and the mechanical properties of high performance fiber reinforced concrete. Adv in Mater Sci and Eng, 14 (2014), 14 pages.
[11] Girgin, Z.C. and Tak, M. Usability of basalt fibres in fibre reinforced cement composites. Mater and Struc (online version in October 2015), printed version in August 2016.
[12] Bonakdar, A., Bakhshi, M. and Ghalibafian, M. Properties of high-performance concrete containing high reactivity metakaolin. American Concrete Institute, SP-228-21 (2005).
[13] Fan, Y., Zhang, S., Wang,Q, Shah, S.P Effects of nano-kaolinite clay on the freeze–thaw resistance of concrete. Cem & Conc Compos 62 (2015) 1–12.
[14] Polder, R.B., Nijland, T.G. and de Rooji, M.R. Slag cement concrete-the Dutch experience. Traffic Safety, Environment and Technology Department (2014).
[15] Fernando S. Fonseca, F.S., Watterson, S.M. and Siggard, K. Compressive and time-dependent strength of concrete masonry constructed with type M mortar and grouts containing high volume of fly ash and slag. ACI Mater J, 113(2) (2016), 185-195.

International RILEM Conference on Materials, Systems and Structures in Civil Engineering
Conference segment on Service Life of Cement-Based Materials and Structures
22-24 August 2016, Technical University of Denmark, Lyngby, Denmark

USE OF ULTRASONIC P- AND S-WAVES TRANSMISSION VELOCITY FOR THE EARLY AGE BEHAVIOUR OF ECO-CONCRETE

Jérôme Carette[(1)], Stéphanie Staquet[(1)]

(1) Laboratory of Civil Engineering, BATir department, Université Libre de Bruxelles (ULB), Belgium

Abstract
The well established ultrasonic pulse velocity method has been widely used in the past decades for monitoring the setting process, compressive strength and dynamic elastic properties of concrete. In this study, the simultaneous monitoring of P-wave and S-wave transmission velocity through cement-based materials samples allows a clear picture of their early age behaviour. It is observed that this method can be used to determine the initial and final setting times, as well as the early age compressive strength and tensile strength evolution. A novel methodology for the determination of the activation energy from such measurements is proposed. The results of a large experimental campaign are presented, discussing the effect of parameters such as w/c ratio, presence of various mineral additions in terms of nature and substitution rate, presence of aggregates, and temperature. It is shown that the combination of P-waves and S-waves transmission velocity provides a detailed picture of the setting process and hardening of all tested cement-based materials. It also provides an effective alternative to the isothermal calorimetry measurement for the determination of the apparent activation energy, applicable at the concrete scale.

1. Introduction

The ultrasonic pulse transmission velocity has been widely used in the past decades for many concrete applications. The measurement of the compression wave velocity is generally easy to implement, and can be performed in laboratory as well as in-situ conditions. It is very sensitive to the porosity of concrete, and therefore to its compressive strength [1,2], as well as to its elastic properties [3]. Also, such measurements can be performed in order to monitor the setting process of cement-based materials [4,5].
More recently, the combined measurement of compression wave (P-wave) and shear wave (S-wave) transmission velocity has enabled a more complete description of the setting, early age, hardening and hardened behaviour of concrete [6,7,8]. In particular, dynamic elastic

properties can be computed. In addition, the S-wave is more sensitive to the solid percolation during the setting process than the P-wave, allowing to define specific initial and final setting criteria for cement-based materials.
In this study, ultrasonic early age P-wave and S-wave transmission velocity measurements are performed on concrete containing various amounts and nature of supplementary cementitious materials (SCM), such as limestone filler and blast furnace slag. In parallel, measurements of compressive, tensile strength, and semi-adiabatic calorimetry are performed. On the basis of this large experimental campaign, the potential of the ultrasonic method (combined P-wave and S-wave velocities) for the determination of the early age properties of concrete is assessed. Relationships between the dynamic elastic modulus and the concrete final setting time, compressive strength and tensile strength are suggested. Tests performed at various temperatures allows an accurate computation of the apparent activation energy.

2. Experimental setup

2.1. Concrete mix designs

Five concrete compositions are tested, containing various amounts of blast furnace slag (BFS), limestone micro filler (LMF), gypsum and water. The granular skeleton remains constant through all compositions. First, a reference compositions (C-REF) contains only CEM I as binding material. The water to cement ratio (w/c) is fixed at 0.4. Then, compositions C-BFS and C-LMF contain respectively a 75% and 30% cement substitution rate by blast furnace slag and limestone filler. The gypsum content is adapted for each composition so that the total amount of sulphate in the binding phase is equivalent to the reference composition. A fourth composition C-ECO contains 25% of CEMI, 30% of LMF, and the remaining of BFS and gypsum. All four compositions previously described present the same w/c ratio. An additional composition C-WAT presents no SCM, but has an increased water content of 0.57. Additional information regarding these compositions can be found in [9].

Table 1. Concrete mix designs

[kg/m³]	C-REF	C-BFS	C-LMF	C-ECO	C-WAT
Aggregate 10/14	873	873	873	873	873
Aggregate 6/10	210	210	210	210	210
Sand 0/4	852.5	852.5	852.5	852.5	852.5
Cem I 52.5	432	104	285	103	349
Blast-furnace slag	0	291	0	164	0
Limestone filler	0	0	126	124	0
Gypsum	0	22	10	22	0
Water	172.8	166.8	168.6	165.2	199.1
w/c	0.40	0.40	0.40	0.40	0.57

2.2. Test setups

2.2.1. Ultrasonic measurements

The used ultrasonic device is a modified version of the FreshCon system [5]. It was specifically developed for the early age measurements of P-wave and S-wave transmission information. Ultrasonic pulses of 5 µs width at 800 V are used. The broadband transducers have a resonant frequency of 0.5 MHz. Two moulds are used corresponding to the two wave types. These two moulds can be used to perform simultaneous measurements on the same concrete batch. A thin layer of coupling agent is applied at the interface between the sensor and concrete. The distance between sensors is 47mm, which is significantly larger than the largest aggregate (14mm). The measurements are performed in a thermally regulated chamber, and the samples are prevented from drying by appropriate waterproof coating. Various studies performed at the BATir laboratory of civil engineering of Université Libre de Bruxelles with this device have already been published, and can be referred to for additional information [9, 10, 11]. Measurements are performed during 3 days. At 20°C, three samples from different batches are performed for each composition. The presented results are an average of these three tests. A discussion on the reproducibility of these measurements is made in [10]. When tests are performed at curing temperature different from 20°C, the whole testing device is placed inside a temperature-controlled chamber, in order to ensure a uniformity of temperature between the moulds, the sensors and the concrete. In this conditions, it is considered that the ultrasonic method can be applied to concrete between at temperatures of at least 10°C and 35°C. From these measurements, a dynamic elastic modulus (Ed) can be computed from equations 1 and 2.

$$\nu_d = \frac{V_p^2 - 2V_s^2}{2V_p^2 - 2V_s^2} \quad \text{Eq 1}$$

$$E_d = V_p^2 \rho \frac{(1+\nu_d)(1-2\nu_d)}{(1-\nu_d)} \quad \text{Eq 2}$$

2.2.2. Compressive strength measurements

Compressive strength is measured since the initial setting up to three days. Measurements are performed on 100x100x100mm cubes. Drying on the top surface is prevented by applying a waterproof film. For each composition, a thermocouple is placed in one of the samples for early age temperature measurement. The results are issued from at least three different batches of concrete.

2.2.3. Tensile strength measurements

Tensile strength is approximated from splitting tensile strength measurements since the initial setting up to three days. Measurements are performed on 110x220mm cylinders. Drying on the top surface is prevented by applying a waterproof film. For each composition, a thermocouple is placed in one of the samples for early age temperature measurement. The results are issued from at least three different batches of concrete.

2.2.4. Semi-adiabatic calorimetry

Semi adiabatic calorimetry is performed according to the test setup described in [12]. Tests were realized at various initial temperatures (10°C and 30°C) on concrete samples. Then, the superposition method was applied in order to obtain the apparent activation energy of all five

mixes. This parameter is supposed constant through the whole hydration process. These results were already presented elsewhere [9]. The respective activation energies were respectively 35.9 (C-REF), 51.1 (C-BFS), 39.1 (C-LMF), 49.7 (C-ECO), and 35.9 kJ/mol (C-WAT). In this study, all mention to the age of concrete actually refers to the equivalent age (t_e) considering the above values for the activation energy (E_a) in equation 3, where T refers to the concrete temperature, and T_{ref} is fixed at 293°K.

$$t_e = \sum_{0}^{t} e^{\frac{-E_a}{R}\left(\frac{1}{T}-\frac{1}{T_{ref}}\right)}.\Delta t \qquad \text{Eq 3}$$

3. Results and discussion

3.1. Setting time

The determination of the setting time of concrete with the ultrasonic P-wave and S-wave transmission velocity for these concrete compositions as already presented elsewhere [9], based on a method previously developed [10]. These studies are based on comparisons between the setting time obtained by standard ATSM C403 and the ultrasonic method for mortars, as well as with additional mechanical measurements for concrete samples (such as very early age elastic modulus and early strength gain). The initial setting time can be determined based on the time at which the S-wave velocity increases at its maximal rate. In the same way, the final setting time determination is based on the dynamic elastic modulus (E_d) as computed from P-wave and S-wave velocity. The final setting occurs at the time when the rate of increase of E_d versus time is maximal. This is verified for all compositions. The obtained final setting times are 4.1h for C-REF, 8.5h for C-BFS, 4.6h for C-LMF, 6.8h for C-ECO and 5.9h for C-WAT. This confirms that the ultrasonic method is very sensitive to the presence of various amount and nature of SCM and w/c ratio.

3.2. Compressive strength

The results of compressive strength during the first three days after hydration are shown for all compositions in Figure 1. These results of Figure 1a confirm the well known effects of the tested mix design parameters. In the presence of limestone filler, the initiation or strength is similar to C-REF, but tends to lower values due to the dilution effect. In the same way, a higher water content tends to decrease the early age compressive strength. Interestingly, C-WAT presents lower compressive strength than C-LMF for a higher CEM I content. In the presence of blast furnace slag, the strength starts to develop later than for the reference concrete, and it rises very slowly.

Figure 1b displays the relationship existing between the dynamic elastic modulus obtained from ultrasonic measurements and the compressive strength of concrete. It is observed that the nature has only a low effect on the relationship between both properties. However, it is expected that parameters such as aggregate content and nature affect this relationship. Indeed, for similarly shaped and sized aggregates of another nature, the elastic modulus might be more strongly affected than the compressive strength, the former being related to the respective elastic modulus of all the concrete components, and the latter being a more complex property which is mainly related to the porosity of the material. The relationship

between compressive strength and dynamic elastic modulus can be modelled by an exponential relationship such as $f_c=0.135\ e^{0.125\ Ed}$.

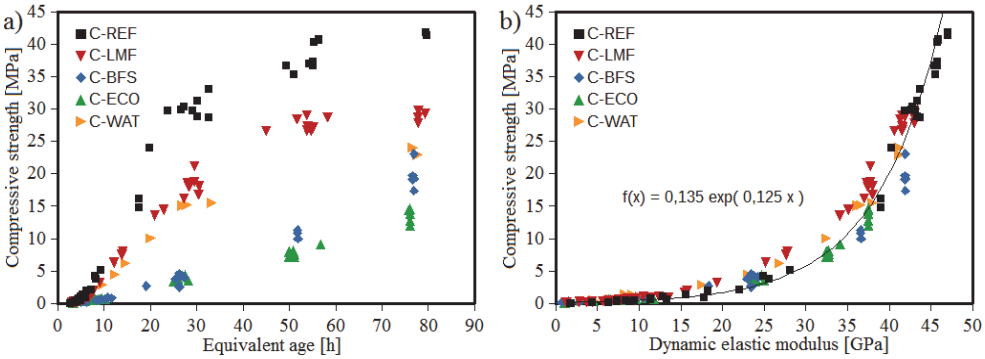

Figure 1. Compressive strength evolution as a function of equivalent age (a) and dynamic elastic modulus (b)

3.3. Tensile strength

The effect of mineral additions and water content on the tensile strength of concrete is mainly similar to what is observed for compressive strength. However, Figure 2a indicates that for tensile strength, C-WAT and C-LMF present similar values. In addition, C-ECO has a higher tensile strength than C-BFS, which was the opposite for compressive strength. This demonstrates that both properties are not governed by the same mechanisms, and that there exists no direct relationship between both. As a consequence, the relationship between tensile strength and dynamic elastic modulus shows a dependency to the nature of the binder as demonstrated in Figure 2b. However, as for compressive strength, this relationship can be modelled by an exponential relationship such as $f_t=0.017\ e^{0.114\ Ed}$. The lower accuracy of this model's prediction in comparison with compressive strength is attributed to the higher scattering of the splitting tensile strength test.

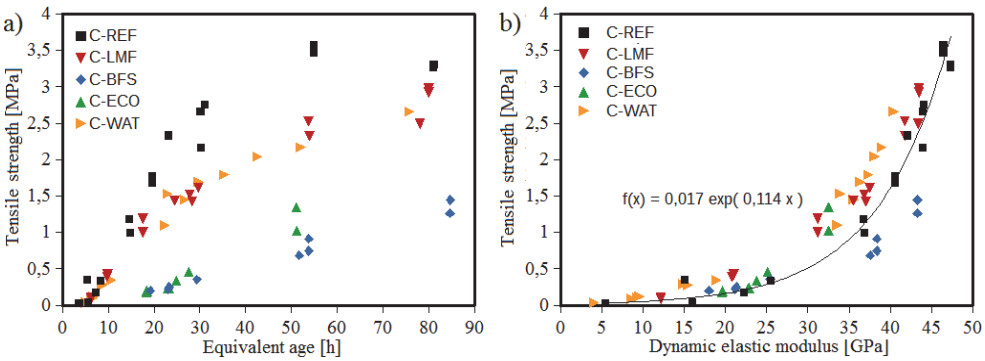

Figure 2. Tensile strength evolution as a function of equivalent age (a) and dynamic elastic modulus (b)

3.4. Activation energy

The apparent activation energy is determined through the well-established superposition method [13]. As presented before, this was previously made for semi-adiabatic measurements. In this study, ultrasonic tests are performed on all compositions except C-WAT. Indeed, it presents the same apparent activation energy than C-REF since both contain the same reactive compounds. Tests are performed at 10°C, 20°C, 30°C and 35°C. The results for one composition (C-ECO) are displayed in Figure 3a and 3b.

The apparent activation energies that can be computed from the superposition method for the dynamic elastic modulus are shown in table 2, along with the corresponding results from the semi-adiabatic calorimetry. The well known effect of blast furnace slag is observed, since every composition containing BFS shows an important increase of apparent activation energy, whatever the method used. In parallel, LMF seems to induce a slight increase in the early age apparent action energy. Finally, the combination of BFS and LMF presents apparent activation energy similar to that of cement with BFS only. These results also confirm that semi-adiabatic calorimetry (chemical measurement) and ultrasonic pulse velocity (mechanical measurement) both provide similar values for the apparent activation energy by the superposition method. The interest of using the ultrasonic method is that these tests can be easily performed on a small volume of concrete and that as such, the temperature in the sample remains approximately constant, in contrast with semi-adiabatic calorimetry, which only works as long as temperature variations in the sample are significant. It should be noticed that considering the scattering of the results, it is considered that both methods used for the determination of activation energies presented in table 2 yield equivalent results. This scattering is due to the variability of the calorimetry and ultrasonic methods, as well as to the chosen time scale during which the superposition method is applied.

Table 2. Activation energy obtained from chemical and mechanical measurements

[kJ/mol]	C-REF	C-BFS	C-LMF	C-ECO
Semi-adiabatic calorimetry	35.9	51.1	39.1	49.7
Ultrasonic measurements	38.3	48.9	41.6	48.3

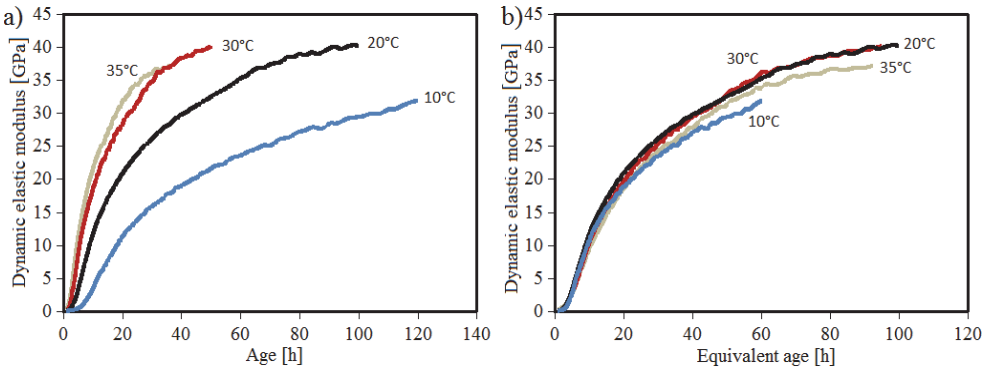

Figure 3. Dynamic elastic modulus evolution as a function of age (a) and equivalent age (b) for the C-ECO mix design at various curing temperature.

4. Conclusions and perspectives

A continuous non destructive alternative to classical measurements of the setting time, compressive strength, tensile strength and apparent activation energy is presented in this study. These properties were determined through the monitoring of P-wave and S-wave transmission velocity from the casting up to a few days of hydration. These results indicate that:

- The initial setting time can be determined from ultrasonic measurements as the time at which the S-wave velocity increases at its maximum rate.
- The final setting corresponds to the time at which the rate of increase of the dynamic elastic modulus is maximal.
- The compressive and tensile strengths can be correlated to the increase of dynamic elastic modulus through an exponential law. The parameters of this model should be calibrated for a given concrete, except for slight variations in the nature of the binder, which does not affect significantly these relationships.
- The apparent activation energy of concrete can be determined easily with the ultrasonic method.

References

[1] Keating, J.; Hannant, D. & Hibbert, A. Correlation between cube strength, ultrasonic pulse velocity and volume change for oil well cement slurries, Cement and Concrete Research, 1989, 19, 715 – 726
[2] Popovics, S.; Rose, J. L. & Popovics, J. S. The behaviour of ultrasonic pulses in concrete, Cement and Concrete Research , 1990, 20, 259 - 270
[3] Sayers, C. & Dahlin, A. Propagation of ultrasound through hydrating cement pastes at early times, Advanced Cement Based Materials, 1993, 1, 12 – 21
[4] Lee, H.; Lee, K.; Kim, Y.; Yim, H. & Bae, D. Ultrasonic in-situ monitoring of setting process of high-performance concrete Cement and Concrete Research, 2004, 34, 631 - 640
[5] Reinhardt, H. & Grosse, C. Continuous monitoring of setting and hardening of mortar and concrete Construction and Building Materials, 2004, 18, 145 – 154
[6] Boumiz, A.; Vernet, C. & Tenoudji, F. Mechanical properties of cement pastes and mortars at early ages: Evolution with time and degree of hydration, Advanced Cement Based Materials, 1996, 3, 94 – 106
[7] Krauss, M. & Hariri, K. Determination of initial degree of hydration for improvement of early-age properties of concrete using ultrasonic wave propagation Cement and Concrete Composites, 2006, 28, 299 – 306
[8] Zhu, J.; Kee, S.-H.; Han, D. & Tsai, Y.-T. Effects of air voids on ultrasonic wave propagation in early age cement pastes Cement and Concrete Research, 2011, 41, 872 – 881
[9] Carette J., Staquet S. Monitoring the setting process of eco-binders by ultrasonic P-wave and S-wave transmission velocity measurement: Mortar vs concrete, Construction and Building Materials, 2016, 110, 32-41

[10] Carette J., Staquet S. Monitoring the setting process of mortars by ultrasonic P and S-wave transmission velocity measurement, Construction and Building Materials, 2015, 94, 196-208

[11] Delsaute, B., Boulay, C., Granja, J., Carette, J., Azenha, M., Dumoulin, C., Karaiskos, G., Deraemaeker, A., & Staquet, S. Testing Concrete E-modulus at Very Early Ages Through Several Techniques: An Inter-laboratory Comparison, Strain, 2016, 52, 91-109

[12] C. Boulay, J.-L. Andre, J.-M. Torrenti, Draft operating protocol to determine the level of heat released during cement hydration on a concrete specimen placed in a quasi-adiabatic calorimeter designed for concretes (QAB), BLCPC, 278 (2010), pp. 37–42

[13] Broda, M.; Wirquin, E. & Duthoit, B. Conception of an isothermal calorimeter for concrete: Determination of the apparent activation energy, Materials and Structures, 2002, 35, 389-394

International RILEM Conference on Materials, Systems and Structures in Civil Engineering
Conference segment on Service Life of Cement-Based Materials and Structures
22-24 August 2016, Technical University of Denmark, Lyngby, Denmark

CONCRETE DRYING: EFFECTS OF BOUNDARY CONDITIONS AND SPECIMEN SHAPE

Jérôme Carette[(1,2)], Farid Benboudjema[(1)], Georges Nahas[(2)], Kamilia Abahri[(1)], Aveline Darquennes[(1)], Rachid Bennacer[(1)]

(1) LMT-Cachan / ENS Cachan / CNRS / Université Paris Saclay, Cachan, France
(2) IRSN, Fontenay-aux-Roses, FRANCE

Abstract
In the framework of the ODOBA project, representative structures in reinforced concrete are submitted to various types of durability distress, in order to have elements of knowledge on pathologies which could develop in the course of time. Among studied issues are the alkali-aggregate reaction (AAR) and the delayed ettringite formation (DEF), which appear after a large induction period, but develop then quickly, inducing irreversible structure damage. These issues are closely related to the water distribution and to the surrounding humidity. Controlling the processes of drying and wetting of concrete is of major importance in this regard. However, the mechanisms at their origin are currently not well established and modelled. This work is a preliminary study aiming at identifying the main mechanisms in play during drying-wetting cycles through a coupled experimental-numerical study of the humidity gradient inside concrete. In this paper, the drying of various concrete samples is cautiously studied through refined measurement of the mass loss and internal relative humidity distribution. Various sample sizes and shapes are tested. A simulation strategy is described, including the modelling of water vapour diffusion and liquid water permeation. The introduction of a boundary layer at the drying interface improves the mass variation prediction.

1. Introduction

In the framework of the pre-ODOBA ENSC/IRSN and ODOBA project of the IRSN (French Institut de Radioprotection et de Sûreté Nucléaire), representative structures of reinforced concrete will be built on the IRSN Cadarache nuclear research centre. In these structures will be developed pathologies of concrete such as swelling reactions (internal sulphate attack (ISA) and alkali-aggregate reaction (AAR)). The concrete used in the construction of these structures are chosen by equivalence to the concrete used in the studied nuclear facilities. These issues usually develop after a very long induction period (10 to 30 years). Unfortunately, after the onset of signs of swelling, development is very rapid with

consequences for the safety functions of these structures. These issues are highly dependent on the presence of water in the pore system of concrete. Therefore, control of the process of drying-wetting becomes an important parameter, which remains the object of scarce results in the literature. Indeed, there remain questions regarding the mechanisms involved. Thus, it is difficult to simulate the distribution of the water content in concrete models, which leads to difficulties in quantifying the deformation gradients due to the swelling reactions (ISA, AAR).
This work aims at identifying the main mechanisms in play during drying-wetting cycles through a coupled experimental-numerical study of the humidity gradient inside concrete. In this paper, the drying of various concrete samples is cautiously studied through refined measurement of the mass loss and internal relative humidity distribution. Various sample sizes and shapes are tested. A simulation strategy is described, including the modelling of water vapour diffusion and liquid water permeation [1, 2]. A limited amount of samples were tested in this study. In addition, many parameters of the model were determined by other authors on the same concrete. Therefore, this study must be considered as a preliminary methodology for the monitoring and simulating the drying of concrete rather. Additional ongoing tests will provide more information regarding further validation of the suggested model.

2. Experimental setup

2.1. Mix design

The tested concrete composition is referred to as B11 concrete. This concrete, which composition and major properties are shown in Table 1, is used because it is equivalent to the concrete actually used in French internal nuclear power plant vessels. In addition, it has been widely studied in previous studies [1] and its properties are therefore mostly known.

Table 1: (left) B11 mix design (right) B11 concrete main properties

	ρ [t/m^3]	**B11** [kg/m^3]	***w/c***	[-]	0.573
Cement (CEM II Airvault Calcia)	3.1	336	ρ	[t/m^3]	2.324
Sand (0/4)	2.572	740	**Slump**	[cm]	8-11
Aggregates (4/12,5)	2.57	303	**Porosity**	[-]	13.2-13.8
Aggregates (10/20)	2.57	752	f_c (28 days)	[MPa]	46.5
Water	1	193	f_t (28 days)	[MPa]	3.29
Superplasticizer (Plastiment HP)	$1.185\ 10^{-3}$	1.174	E (28 days)	[GPa]	31.34

2.2. Curing conditions

In order to submit all the concrete specimens to the same curing conditions (temperature T and relative humidity RH), à large storage bin was developed. The climatic chamber was

rejected for several reasons, the main one being the difficulty of limiting the forced convection on the faces subjected to drying, and of ensuring the uniformity of this phenomenon on all sides. The requirements of the storage bin are similar to those of a desiccator. It must be able to contain saline and be impermeable to air and moisture. In order to enable placing several temperature and relative humidity sensors inside the storage bin, sealing plugs were installed. The concrete samples were placed on a plastic honeycomb duckboard allowing maximized interaction between the salt solution and the ambient air. This setup is shown in Figure 1. The saturated salt solution was made using potassium carbonate in order to reach an ambient *RH* of close to 45%. The room temperature was controlled at 25°C.
The concrete samples were prevented from drying until the test started. The samples were submitted to drying more than two months after mixing. Due to the high *w/c* ratio of the B11 concrete, it can therefore be considered that the hydration reactions were completed, and that the auto-desiccation phenomenon could be neglected [3].

Figure 1: Experimental setup linked to the continuous measurement of *RH* and T sensors

2.3. Test setup

The experimental measurements consisted in mass loss measurements at regular intervals and in the continuous measurement of the internal relative humidity in concrete samples at various distances from the drying interface. Four sample geometries were considered:
- G1: 70x70x280mm prism, drying on the two opposite lateral faces,
- G2: 70x70x110mm prism, drying on the two opposite lateral faces,
- G3: 70x110mm cylinder, radial drying,
- G4: 70x70x110mm prism, drying on the four longitudinal faces.

For each of these geometries, the average drying radius (r_d) was computed as the ratio between the drying surface and the sample volume. This resulted in r_d of 0.14, 0.055, 0.0275 and 0.0175m for geometries G1, G2, G3 and G4 respectively.
The mass loss measurements were performed on 3 samples for G1, 2 samples for G2 and G3, and on 1 sample for G4. This study focuses on the first weeks after drying was initiated. The

relative humidity was measured at various distances from the drying interface on geometries G1, G2 and G3 according to the distribution shown in Figure 2.

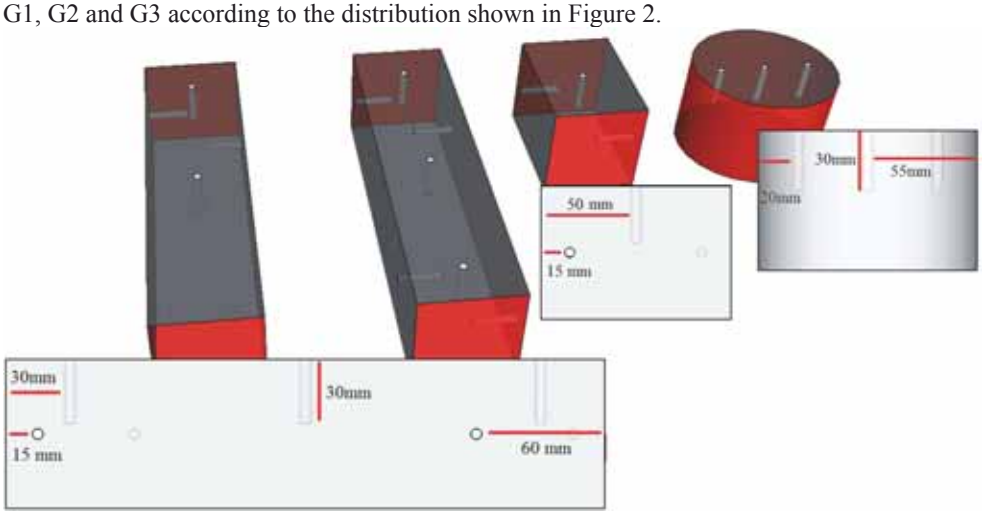

Figure 2: layout plan of *RH* sensors (sides submitted drying displayed in red)

3. Drying model

The drying model used in this study assumes that two mechanisms are at the origin of the water transport in the concrete: the diffusion of water vapour and the permeation of liquid water. If the concrete porous network is saturated, the latter mechanism is the predominant one, whereas for a low degree of saturation, the movement of water in the form of vapour diffusion cannot be neglected.

The liquid water flow can be expressed through Darcy's law, which relates the fluid mass flow through a medium to the pressure gradient of this fluid as expressed in the equation (1), where K_{eff} is the concrete effective permeability (s), p_c the capillary pressure (Pa), and J_l is the rate of liquid water flow (kg.m^{-2}.s^{-1}).

$$J_l = -K_{eff}\frac{\partial p_c}{\partial x} \quad (1)$$

According to the Kelvin equation, the relationship between the capillary forces and the relative humidity in concrete can be expressed as shown in equation 2, where M_w is the molecular mass of water (kg/mol), ρ_l is the liquid water density (kg/m^3), R is the gas constant (J.K^{-1}.mol^{-1}) and T is the temperature (K).

$$p_c = \frac{-\rho_l RT ln(hr)}{M_w} \quad (2)$$

In order to take into account the dependency of the water permeability to the degree of saturation, equation 3 can be used, where K_0 is the intrinsic water permeability of concrete in saturated conditions, μ_l is the water dynamic viscosity , and k_{rl} is the relative permeability. This latter term can be determined through the Mualem empirical relationship [4] shown in equation 4, where S_l is the saturation degree, p_{krl} is a fitting parameter. The relationship

between the degree of saturation and relative humidity is given by the van Genuchten equation [5] (equation 5), where a_{vg} and b_{vg} are two parameters that can be obtained by fitting experimental results of the desorption isotherm for the tested material.

$$K_{eff} = k_{rl}\frac{K_0}{\mu_l} \tag{3}$$

$$k_{rl} = {S_l}^{p_{krl}}\left(1-\left(1-{S_l}^{\frac{1}{a_{vg}}}\right)^{a_{vg}}\right)^2 \tag{4}$$

$$S_l = \left(1+\left(-b_{vg}ln(hr)\right)^{\frac{1}{1-a_{vg}}}\right)^{-a_{vg}} \tag{5}$$

Thus, equations 1-2 can be re-written as equation 6, while equations 3-5 allow to solve this equation for any given relative humidity.

$$J_l = -k_{rl}\frac{K_0\rho_l RT}{\mu_l M_w hr}\frac{\partial hr}{\partial x} \tag{6}$$

On the other hand, when the saturation degree decreases, pores are progressively not filled with water. This leaves space for a flow of water vapour (J_v, expressed in kg.m^{-2}.s^{-1}) due to the gradient of vapour pressure (p_v) between the inside of concrete and the ambient conditions according to Fick's law, as shown in equation 7.

$$J_v = -D_{eff}\frac{M_w}{RT}\frac{\partial p_v}{\partial x} \tag{7}$$

The effective diffusion coefficient in a porous medium (D_{eff}, expressed in m².s^{-1}) can be related to the degree of saturation, to the porosity (Φ) and to the diffusion coefficient of water in air (D_0) through the empirical Millington and Quirk relationship [6] expressed in equation 8. In equation 9, the relative humidity is related to the saturation vapour pressure p_{vs} and to the vapour pressure of water p_v.

$$D_{eff} = D_0.\Phi^{a_{mq}}.(1-S_l)^{b_{mq}} \tag{8}$$

$$hr = \frac{p_v}{p_{vs}} \tag{9}$$

The saturation vapour pressure is temperature dependent and can be determined by the Clausius-Clapeyron relationship (equation 10), where L_v is the heat of vaporisation of water (J/kg), T_0 is the reference temperature (273 K) and T is the air temperature (K). In the same way, the dependency of D_0 to temperature can be taken into consideration by equation 11.

$$P_{vs} = P_{atm}.e^{\frac{M_W.L_v}{R}\left(\frac{1}{T_0}-\frac{1}{T}\right)} \tag{10}$$

$$D_0 = 217.10^{-5}.\left(\frac{T}{T_0}\right)^{288} \tag{11}$$

From combining equations 6, 7 and 9, to the continuity equation, the equation that has to be solved for the moisture transport can be expressed as equation 12.

$$\Phi\frac{\partial S_l}{\partial hr}\frac{\partial hr}{\partial t} = \mathrm{div}\left[\left(K_{eff}\frac{\rho_l RT}{\mu_l M_v hr}+D_{eff}\frac{M_v P_v^{sat}}{\rho_l RT}\right)grad(hr)\right] \tag{12}$$

The modelling of drying requires the definition of adapted boundary conditions. Indeed, imposing the ambient relative humidity directly at the air-concrete interface is a possibility [1, 7]. However, such methodology does not take into account the presence of a boundary layer

of air at the air-concrete interface whose moisture content depends on the distance to the surface of concrete. This is important at the initiation of drying, because the high moisture content initially observed at the concrete surface gives rise to a boundary layer of air with high humidity at the air-concrete interface, which initially slows the drying kinetics. The thickness of this boundary layer strongly depends on the ambient conditions (air flow, temperature) and the material surface condition (surface roughness and moisture) [8]. Such boundary conditions can be more accurately represented by equation 13, in which J_{BC} represents the flow of water vapor at the air-concrete external interface, hr_s is the relative humidity at the interface and hr_e is the external air relative humidity. The value of h_{BC} is not well defined and can reach values from $1.x10^{-2}$ [8] to $8. x\ 10^{-7}$ [9] in natural conditions.

$$J_{BC} = -h_{BC}.(hr_s - hr_e) \tag{13}$$

4. Results and discussion

The ongoing tests related to the evolution of the humidity gradient measured by relative humidity sensors will not be presented in this section, which focuses on the mass loss. The results presented in Figure 3a indicate that when increasing the drying radius, the mass loss as a function of time is decreased. The curves representing the mass loss as a function of the square root of time (Figure 3b) present three successive stages. First, during the first hours after the drying starts, the mass loss increases with an accelerating rate. This stage, which is particularly marked in G4, lasts until approximately one day. Then, during the second stage, the mass loss increases as a linear function of the square root of time (which corresponds to the exact analytical simulation for semi-infinite media). This stage lasts longer as the drying radius increases. After more than one month, G1, which has the larger drying radius, still exhibits a linear evolution of the mass loss as a function of the square root of time. On the other hand, the second stage ends approximately after 3 days. Finally during the third stage, the mass loss increases with a decreasing rate. This stage occurs until the equilibrium between the concrete sample and the ambient air is reached, at which point no mass variations will be observed. These stages are described more thoroughly in following sections.

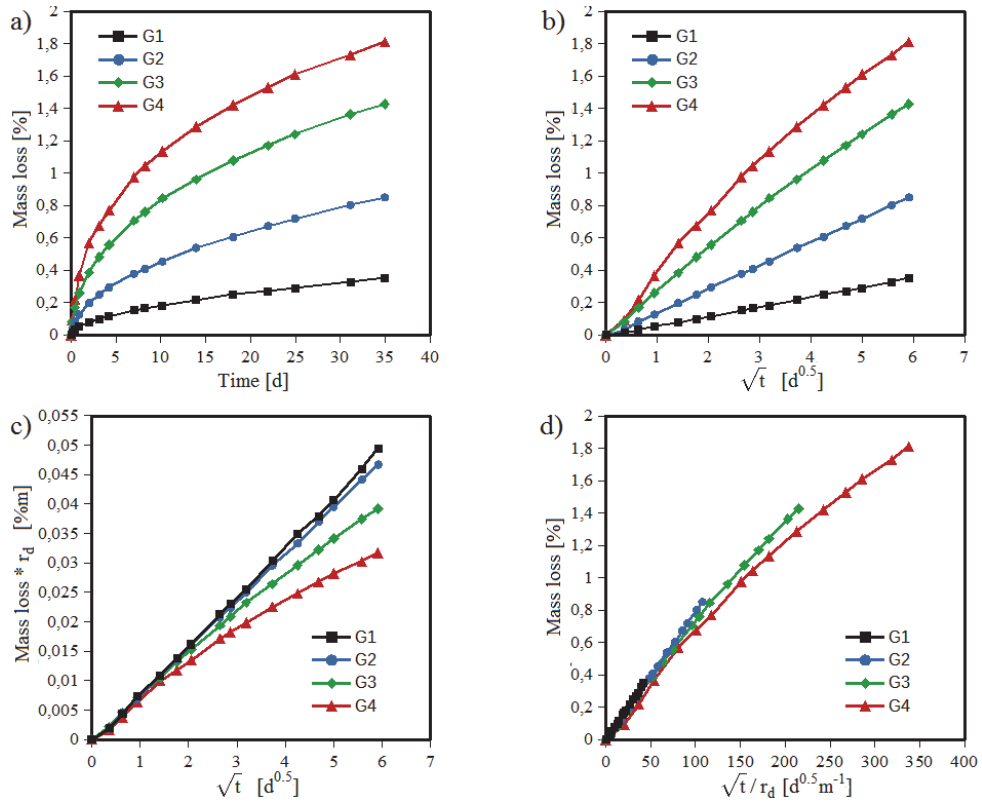

Figure 3: Various representations of the mass loss as a function of time and drying radius

4.1. Stage 1: initial drying and boundary layer

During the first hours and up to one day after the drying starts, the mass loss can be expressed as a non-linear function of the square root of time. This observation can be explained by the presence of a boundary layer of air at the concrete-air interface. Initially, all water extracted from the sample is present in the form of water vapour close to the concrete surface. This tends to increase the relative humidity of the ambient air, and therefore decrease the drying kinetics. Progressively, the water contained in the porosity in direct contact with the concrete surface evaporates. Due to the high diffusivity coefficient of water vapour in air in comparison with the concrete(equivalent) permeability and diffusivity, the relative humidity of the boundary layer decreases, until eventually reaching a value close to the actual ambient conditions.

In order to calibrate the value of parameter h_{CL}, preliminary tests are performed by measuring the relative humidity of the air against the drying surface through time. These measurements are shown in Figure 4a. Right after drying is initiated, the relative humidity at the surface is close to 80%. Then, progressively, it decreases until reaching a value of 55% at 5 days (120h). Initially, in order to correspond to these measurements, the best fit value of h_{BC} is situated

between 2.10^{-6} and 10^{-5}. However, progressively, the experimental dots tend to reach values closer to h_{BC} of 5.10^{-5}. One reason for this is that the exchange coefficient might change in time. This experiment indicates that as the saturation degree close to the surface decreases, the rate of exchange of water from the surface to the ambient air also decreases. Figure 4b shows the effect of changing h_{BC} on the mass loss during the first hours after drying. In the following simulations, a value $h_{BC}=10^{-5}$ is chosen.

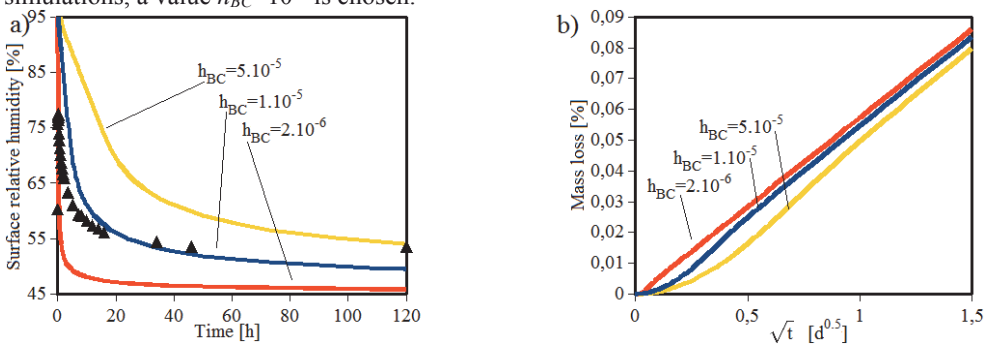

Figure 4: Effect of the exchange coefficient h_{BC} on the surface relative humidity, and comparison with experimental values (markers)

The results illustrated in Figure 5a show that the simulation strategy developed in section 3 allows representing the initial mass loss kinetics. The experiments are shown by dots, while the numerical simulations are represented by dashed lines. In these simulations, all parameters are kept constant, except for the geometry of the sample. The values of the parameters are all extracted from [1], except for the intrinsic permeability, which is fixed at $1.15x10^{-21}$. For G4, the value of the parameter h_{BC} is different than for other geometries. This is due to the specific drying surfaces of G4, one of which is the "top" side of the sample which was not in contact with the mould during setting and hardening.

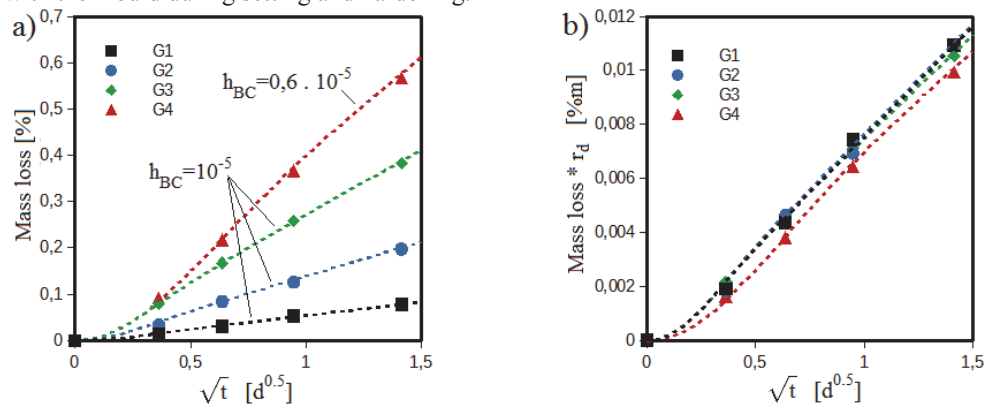

Figure 5: Initial mass loss during stage 1 (dots = experiments, dashed lines = simulations)

The surface roughness and porosity is therefore significantly different from all other surfaces, justifying a change in the exchange coefficient h_{BC}. In the same way, Figure 5b indicates that

except for G4, the sample size and shape effects on the initial mass loss can be accurately taken into consideration by multiplying the mass loss by the corresponding drying radius. However, this is only true if similar concrete and surface conditions are applied to all geometries.

4.2. Stage 2: main drying initiation

The second stage of drying consists in a linear increase of the mass loss as a function of the square root of time. The slope of this increase is related both to the concrete properties (porosity, permeability, diffusivity, …) and to the humidity gradient between the concrete and the ambient air. As for the first stage, the effect of the sample size and shape can be accurately taken into account by the drying radius. A higher drying radius induces a lower slope. By multiplying the drying radius by the slope of the mass loss curve during this second stage, all geometries present the same behaviour, as shown in Figure 4c and 4d. The end of this stage is not clearly defined, and probably occurs at a point where the effective permeability is significantly decreased in comparison with its initial value. This occurs when the overall humidity has significantly decreased in the whole sample, which could occur close to a specific mass loss. Further results should provide additional answers regarding this observation.

4.3. Stage 3: advanced drying and permeability decrease

As stated previously, the third stage consists in a significant decrease of the mass loss, resulting in a progressive decrease of the slope of the mass loss versus square root of time curve. At a given time, this phenomenon is more clearly observed in Figure 6a for geometries with lower drying radius. Indeed, G4 and G3 have already lost a significant amount of water, in contrast with G1 or G2.

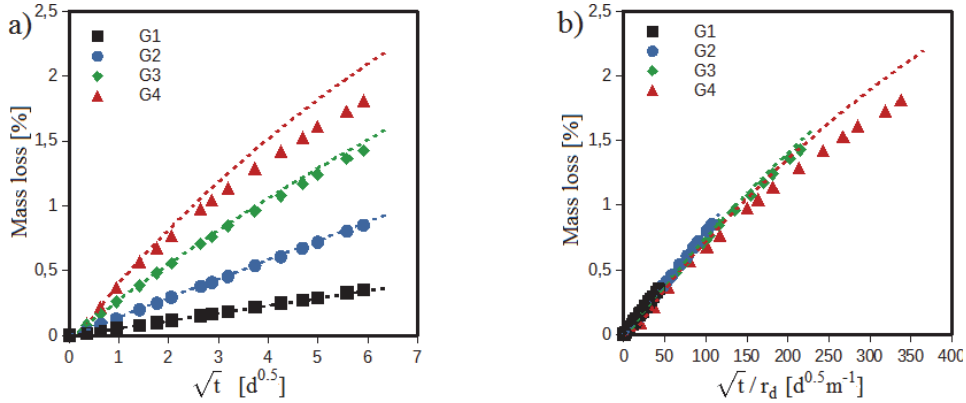

Figure 6: Whole mass loss curves (dots = experiments, dashed lines = simulations)

As for the first and second stage, the simulation captures this behaviour. However, as the mass loss increases, an overestimation of the simulation can be observed, especially when it overpasses 1%. This is due to the parameters expressed in equations 4, 5 and 8. These equations relate the relationship between saturation degree, relative humidity, and effective permeability and diffusivity. Indeed, all parameters from these equations were extracted from

another study [1]. Therefore, even if the same concrete was used, these equations should be adapted to this study. In particular, the decrease of effective permeability when decreasing the saturation degree should be more important. This point will be discussed further when longer term experiments have been performed on all sample sizes and shapes.

5. Conclusion and perspectives

Mass loss experiments on various specimen size and shape are performed. The model developed and used in [1] is improved by taking into account the boundary layer of air at the sample-air interface during drying. The curves of mass loss as a function the square root of time can be divided in three stages identified in this study: a non-linear acceleration initial stage, a linear drying initiation, and an advanced drying consisting in a decreased slope of the curve. These three stages can be accurately reproduced by the model, independently on the sample size and shape.
Further works are required in order to confirm the relevance of this model for longer term experiments, and for identifying mechanisms at the origin of the switch between the second stage and the thirst stage. Additional results regarding the relative humidity gradient inside the specimens will allow a mode complete description of these phenomena, as well as an improved strategy for identifying the parameters of the model. Finally, this validity of this model should be challenged with drying/wetting cycles experiments.

References

[1] Hilaire A., Etude des déformations différées des bétons en compression et en traction, du jeune au long terme : application aux enceintes de confinement, PhD Thesis, ENS Cachan, 2014
[2] Huang, Q.; Jiang, Z.; Gu, X.; Zhang, W. & Guo, B., Numerical simulation of moisture transport in concrete based on a pore size distribution model, Cem Conc Res , 2015, 67, 31-43
[3] Briffaut, M., Etude de la fissuration au jeune âge des structures massives en béton : influence de la vitesse de refroidissement, des reprises de bétonnage et des armatures, PhD Thesis, ENS Cachan, 2010
[4] Mualem, Y. (1976). A new model for predicting the hydraulic conductivity of unsaturated porous media. Water resources research, 12(3):513–522
[5] van Genuchten, M. A Closed-form Equation for Predicting the Hydraulic Conductivity of Unsaturated Soils. Soil Science Society of America Journal, 44(5):892–898, 1980
[6] Millington, R., Quirk, J. (1961). Permeability of porous solids. Transactions of the Faraday Society, 57:1200–1207
[7] Oxfall, M.; Johansson, P. & Hassanzadeh, M. Long-term hygrothermal performance of nuclear reactor concrete containments – Laboratory evaluations of measurement setup, in situ sampling, and moisture flux calculations, Cem and Conc Composites , 2016, 65, 128 – 138
[8] Zhang, J.; Wang, J. & Han, Y. Simulation of moisture field of concrete with pre-soaked lightweight aggregate addition, Construction and Building Materials , 2015, 96, 599 – 614
[9] Ožbolt, J.; Oršanić, F. & Balabanić, G. Modeling influence of hysteretic moisture behavior on distribution of chlorides in concrete, Cement and Concrete Composites , 2016, 67, 73 – 84

International RILEM Conference on Materials, Systems and Structures in Civil Engineering
Conference segment on Service Life of Cement-Based Materials and Structures
22-24 August 2016, Technical University of Denmark, Lyngby, Denmark

MITIGATION OF EARLY AGE SHRINKAGE OF UHPFRC BY USING SPENT EQUILIBRIUM CATALYST

Ana Mafalda Matos [(1)], Sandra Nunes [(1)], Carla Costa [(2)]

(1) CONSTRUCT-LABEST, Faculty of Engineering (FEUP), University of Porto, Portugal
(2) Department of Civil Engineering, High Institute of Engineering of Lisbon (ISEL), Portugal

Abstract
Strengthening of structural concrete elements with ultra-high performance fibre reinforced composites (UHPFRC) layers is being successfully performed in recent years. The main advantage of UHPFRC in this context is that it can play a double function (water tightness and strengthening), while enabling short-time interventions.
UHPFRC material exhibits remarkable mechanical properties namely, strain hardening in tension and extremely low water permeability. However, due to the very low water/binder ratio it is prone to autogenous shrinkage. The restraint provided by the substrate to the free shrinkage of the new layer generates built-in stresses which can impair its performance. As such, seeking strategies to reduce the autogenous shrinkage is an objective to pursue.
The spent equilibrium catalyst (ECat) is a waste generated by the oil refinery industry with very high pozzolanic activity and high specific surface (150 m^2/g) which promotes a significant water absorption (about 30%, by mass), thus has a great potential to work as an internal curing agent in UHPFRC. Within this scope, this paper describes research on the viability of using ECat to mitigate autogenous shrinkage of UHPFRC. Test results showed a significant reduction of autogenous shrinkage in UHPFRC mortars without fibres and 20% and 30% of sand replacement by ECat.

1. Introduction

Nowadays, performance assessment of concrete mixtures is not limited to workability and compressive strength testing. Due to the growing relevance of life cycle cost analysis, the durability issues are of primordial importance within the aim of evaluating the suitability of a concrete mixture or constituent [1].
Ultra-high performance fibre reinforced composites (UHPFRC) - which have been developed recently - exhibits remarkable mechanical properties (compressive strength >150 MPa and tensile strengths of 10-20 MPa), notably strain hardening in tension (3-10 ‰) and extremely

low water permeability. Strengthening of structural concrete elements with UHPFRC layers is being successfully performed in recent years. The main advantage of UHPFRC in this context is that it can play a double function (water tightness and strengthening), while enabling short-time interventions. However, due to its low water–binder ratio and high-fineness additives without any coarse aggregate it is prone to exhibit high autogenous shrinkage deformations.
When a layer of fresh mortar or concrete is applied over an existing concrete the restriction conferred by the substrate to the new layer deformation generates internal tensile stresses. The magnitude of these internal stresses, which can result in premature cracks, depends on the development of material properties during early ages, namely, the magnitude and evolution of shrinkage, tensile creep and the evolution of the young´s modulus of elasticity. If conventional concretes/mortars are used these internal tensions often lead to cracking, making the intervention ineffective. Since UHPFRC exhibits significant strain hardening behaviour in tension is more suitable for these applications because only very fine microcracks can occur, without compromising the impermeability of the material. Nevertheless, in zones with poor fibre distribution or orientation larger cracks might occur in the UHPFRC layer, impairing the long-term performance of UHPFRC. Thus, attempts have been made to mitigate the autogenous shrinkage of UHPFRC.
Both, external curing and internal curing are two potential approaches to pursue the aforementioned goal. However, it has been reported that external curing is not effective enough to mitigate the autogenous shrinkage of UHPFRC because its microstructure is so dense that the external water has difficulties to penetrate into the concrete [2], [3]. As such, internal curing seems to be a more effective method to mitigate the autogenous shrinkage for UHPFRC. Currently, superabsorbent polymers (SAP) are the most popular internal curing agents [4]-[6]. SAP possible disadvantages are that they may destabilize the air void system (leaving voids larger than 600 μm in concrete matrix [2], [7], [8]), retard the hydration reactions (increasing the setting time) and reduce the strength [3], [6], [8]-[10]. In addition, the number of practical applications is limited due to the high costs involved [11]. In an attempt to overcome these disadvantages, this work fosters the assessment of a waste generated by the oil refinery industry - namely, the spent equilibrium catalyst (ECat) - as internal curing agent.
The equilibrium catalyst is used in Fluid Catalytic Cracking (FCC) unit during the cracking process to convert heavy oils into more valuable gasoline and lighter products. Since, during the FCC process, the catalyst active sites are deactivated it undergoes rigorous thermal treatments. Nevertheless, after several regeneration cycles it loses its catalytic activity and has to be removed from the process giving rise to a waste [12] which is mainly disposal of in landfills. Every year the worldwide ECat supply is estimated at about 840,000 tonnes [13]. This amount of ECat can be easily used by incorporating in concrete, as the 2014 world cement production was 4.3 billion tonnes [14]. Chemically, the ECat is essentially an aluminosilicate which main active phase is Y-zeolite, a crystalline aluminossilicate with a structure consisting of tunnels and cages that leads to a high (internal and external) surface specfic area. The exact composition of these catalysts depends on the manufacturer and on the oil refining process that is going to be used.
Therefore, due to its aluminosilicate chemical composition, ECat has a potential pozzolanic activity confirmed in the bibliography [15]-[23], hence, is likely to be use as cement-based material additive. In this use, ECat may contributes to accelerate the hydration and the setting process [18] as well as to increase the compressive and flexural strengths [1], [15], [18], [20],

[24], [25]. In terms of durability, studies showed that ECat incorporation on cement-based materials enhances chloride and sulphate ingress resistance as well as reduces alkali-silica reaction occurring susceptibility [1], [21], [25]. Moreover, the high specific surface of the ECat with water affinity promotes a significant water absorption (about 30%, by mass), thus has a great potential to work as an internal curing agent in UHPFRC. Nevertheless, limited work has been carried out on the application of ECat in special types of concrete [15].
The present work aims to investigate the viability of using ECat to mitigate autogenous shrinkage of UHPFRC. However, this preliminary study was carried out on UHPFRC mixtures without fibres named as UHPC. For this purpose, it were studied two reference mixtures with and without silica fume incorporated in the binder as well as other four mixtures with partial replacement of sand with 10%, 20%, 30% and 40% by ECat. The workability, the setting time, the evolution of autogenous shrinkage deformations up to 7 days, and compressive strength (at 7 and 28 curing days) were assessed for all mixtures.

2. Experimental program and results

2.1 Materials and procedures

The materials used in this study were typical commercial Type I 42.5R Portland cement (specific gravity of 3.16 g/cm^3), ECat generated by Portuguese refinery company (specific gravity of 2.69 g/cm^3 and water absorption value of 28%, by mass), silica fume (specific gravity of 1.38 g/cm^3 and solid content 50%), limestone filler (specific gravity of 2.68 g/cm^3), siliceous sand (1 mm maximum aggregate size, specific gravity of 2.66 g/cm^3 and water absorption value of 0.02%). A polycarboxylate type superplasticizer (Sp) of specific gravity of 1.08 g/cm^3 and 40% solid content was also used. The high specific surface of the ECat (150 m^2/g) [25] promotes a significant water absorption which was taken into account in the total water added to the mixture. Furthermore, the mixing time at the beginning of the mixing procedure was extended in relation to what is typical to allow the ECat saturation. Particle size distribution of each material can be seen in Figure 1.
The UHPC mixtures produced were *i*) two references mixtures - REF, SF - which binders were, respectively, plain cement (c) and cement partially replaced with 10% by volume of silica fume (sf) and *ii*) four mixtures – SF+ECat10, SF+ECat20, SF+ECat30 and SF+ECat40 – that besides the blended binder (c+sf) incorporated ECat as partial sand replace varying, respectively, from 10 to 40% by volume, with an increment of 10%. Limestone filler (f) was added to all mixtures in order to complete the aggregates granulometric curve. The water to binder (cement + sf) volume ratio (Vw/Vb) was kept constant for all mixtures. The superplasticizer dosage was adjusted when needed. The mixture proportions are listed in Table 1.
Immediately after mixing, a Vicat mould [26] was filled with the mortar in order to determine final setting time and corrugated moulds were filled and placed in autogenous setup measurement. Mortar test using the flow cone (Dflow) with the same internal dimensions as the Japanese equipment, was carried out to characterize fresh state (see [27] for details on equipment and test procedures). Results of flow test and final setting time are presented in Table 1. Prismatic specimens (4x4x16cm^3) were produced to assess compressive strength at 7 and 28 days of concrete age. After demoulding the following day, test specimens were cured in water at 20 °C in a fog room until testing.

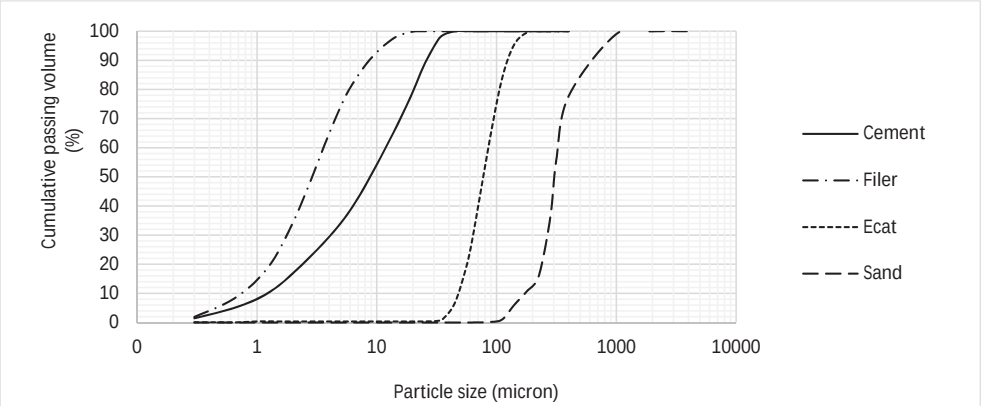

Figure 1 - Particle size distribution of materials used.

Table 1 - Mixture compositions of UHPC.

Constituents \ Mixture		**REF (kg/m^3)**	**SF (kg/m^3)**	**SF+ ECat10 (kg/m^3)**	**SF+ ECat20 (kg/m^3)**	**SF+ ECat30 (kg/m^3)**	**SF+ ECat40 (kg/m^3)**
Binder	Cement (c)	885.91	794.90	794.90	794.90	794.90	794.90
	Silica fume (sf)	-	79.49	79.49	79.49	79.49	79.49
Aggregates	Sand	1019.86	1019.86	917.88	815.89	713.90	611.92
	ECat	-	-	103.23	206.45	309.68	412.91
	Limestone Filler (f)	311.43	311.43	311.43	311.43	311.43	311.43
	Water	178.00	153.76	182.66	211.57	240.47	269.37
	Sp	22.00	13.75	13.75	13.75	17.90	24.74
Ratios	ECat/sand ratio (%)	0	0	10	20	30	40
	Vw/Vb ratio free	0.68	0.68	0.68	0.68	0.68	0.68
	w/c ratio	0.22	0.25	0.23	0.27	0.30	0.34
	Sp/(c+sf+f) ratio (%)	1.84	1.20	1.20	1.20	1.65	2.46
Fresh state properties	Dflow (mm)	280	275	307	290	289	289
	Final setting time (hh:mm)	02:55	02:40	02:20	02:00	01:40	01:50

2.2 Mechanical strength test

Compressive strength testing was undertaken at 7 and 28 curing days for all mixtures following the standard procedure in NP EN 196-1 [28]. Results are presented in Figure 2.

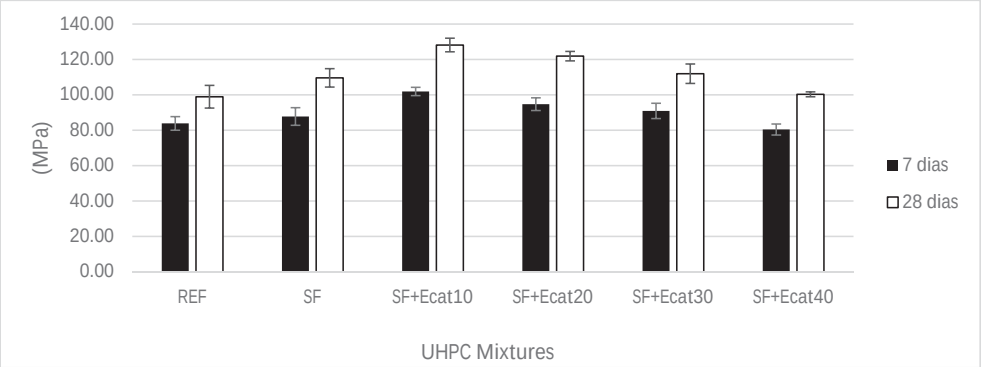

Figure 2 - Compressive strength results.

2.3 Autogenous shrinkage test

The autogenous shrinkage of UHPC mixtures was measured based on the ASTM C1698 [29], in which three sealed corrugated moulds of 440 mm length and 28.5 mm average diameter were filled for each mix composition. After filling the tubes, each specimen was measured and weighted, and kept inside a chamber with controlled temperature (23±1°C) (see Figure 3). Shrinkage deformations were recorded continuously using DC LVDT and a dataTaker DT500 acquisition system. According to this standard, the length change of samples should be evaluated starting at the time of final setting of the mixture. Final setting time test was carried out on the UHPC mixtures adapting the procedure of section 6.3 of standard EN 196-3 [26].
After 7 days, each specimen was weighted again and mass change was recorded in order to validate the test [29]. Figure 4 shows the development of autogenous shrinkage of REF and SF UHPC mixtures and Figure 5 presents autogenous shrinkage of mixtures incorporating different amounts of ECat. Each curve corresponds to an average of the length change of three specimens tested for each mixture. Table 2 presents the autogenous shrinkage results at 24 hours and at 7 days along with the corresponding the mass variation, as well as the corresponding predicted values according to Japan Society of Civil Engineers (JSCE) [30].

Figure 3 – Experimental setup for autogenous shrinkage testing.

Table 2 - Autogenous shrinkage (between brackets the standard deviation) and mass variation results at 7 days.

Mixture	**REF**	**SF**	**SF+ECat10**	**SF+ECat20**	**SF+ECat30**	**SF+ECat40**
Autogenous Shrinkage at 24h (μm/m)	873(±2%)	989(±3%)	843(±3%)	607(±8%)	664(±5%)	1201(±5%)
Autogenous Shrinkage at 7 days (μm/m)	959(±1%)	1118(±3%)	881(±3%)	687(±6%)	750(±6%)	1305(±5%)
Mass Variation (%)	-0.04	-0.17	0.01	0.00	0.00	0.00
JSCE autogenous shrinkage prediction (μm/m) at 7 days [30]				778		

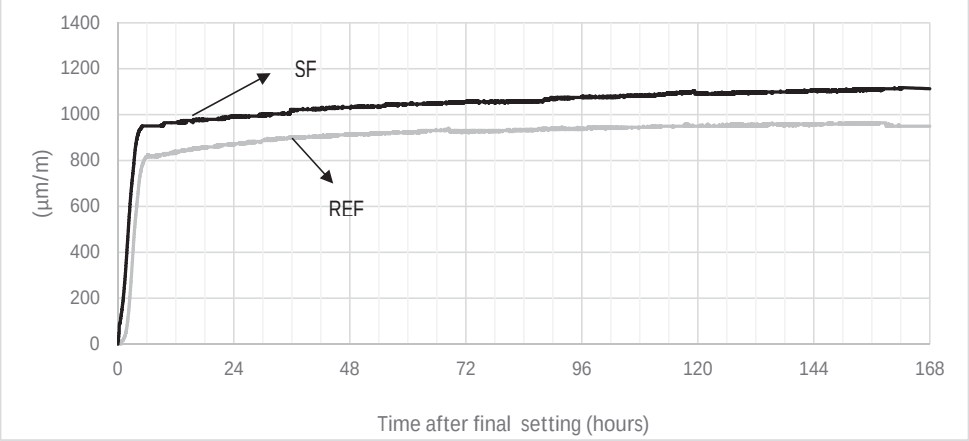

Figure 4 - Autogenous shrinkage of REF and SF mixtures.

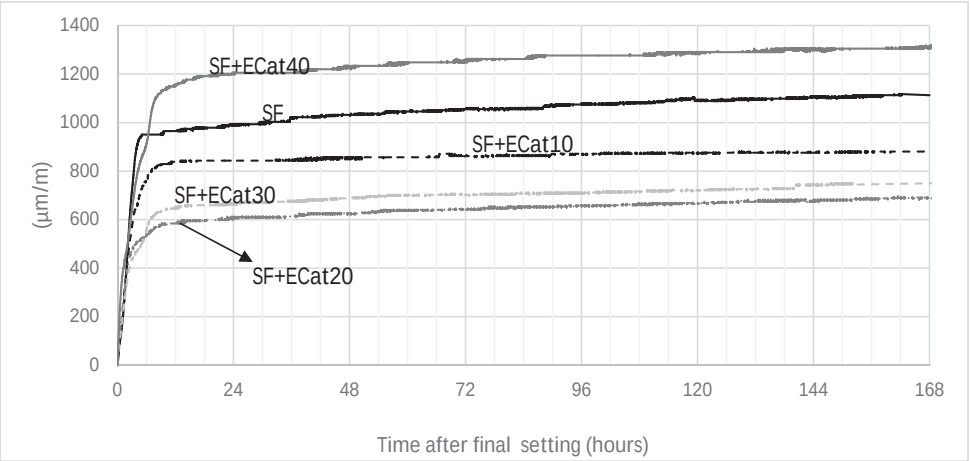

Figure 5 - Autogenous shrinkage of REF, SF and SF+ECat mixtures.

2.3 Discussion of results

Regarding fresh state of UHPC mixtures, ECat influenced the flow ability of mixtures (Table 1). Up to 20% replacement level of sand with ECat the effect on Dflow was negligible, however for higher amounts Dflow decreased substantially, needing extra superplasticizer dosage, corroborating the findings of previous studies [12], [22], [31], [32]. In general, the higher the sand replacement percentage by ECat, the shorter the setting times.

The results of the mechanical properties (Figure 2) show that on the 7-day curing the compressive strength of the SF mortar is already slightly higher than that of plain cement mortar (REF) and that this difference increased at 28-days curing. These compressive strength improvement, since early age, is attributed to the relevant pozzolanic reactivity of SF. Furthermore, mortars with partial sand replacement with ECat up to 30% also show a strength-enhanced slightly higher than those of the REF and SF mortars. These results are due to the fact that besides the binder, these mortars contain the ECat generated in the Portuguese refinery that also possess high early pozzolanic activity of [22], [23] which forms additional strength-providing reaction products, C-A/S-H, that promotes the mechanical properties improvement too. However, both at 7 and 28 curing days, mortars show an approximately linear decrease in the compressive strengths with the increase of the ECat incorporation level. This trend may be attributed to changes in the particle size distribution of the sand-ECat mixtures (Figure 1) that may lead to a decrease in their packing ability and, therefore, compromising the strength development. In fact, this phenomenon can also explain the need of extra superplasticizer in the mortars with higher level of sand replacement with ECat.

The autogenous shrinkage of all UHPC mixtures exhibited a strong increase during the first hours from the final setting, particularly in the first six hours, and then increased but with a lower rate (Figure 5). SF mixture presented a higher autogenous shrinkage than REF mixture, as expected. Previous studies showed that no Relative Humidity change was linked to the silica fume pozzolanic reaction during which CH-crystals were consumed and explained the additional shrinkage as chemical shrinkage that markedly increases autogenous shrinkage compared with mixtures with Portland cement only. The finer pore structure of the cement

paste due to silica fume addition increases self-desiccation and thus shrinkage [8], [33]-[35]. In terms of autogenous shrinkage prediction, the Japan Concrete Institute underestimated the autogenous shrinkage of both the Ref and SF mixtures, taking into account water/binder ratio and considering ordinary Portland cement as the binder.
When 20% and 30% of sand was replaced with ECat occurred a reduction of about 32% and 38%, respectively, in autogenous shrinkage of the mortars compared with that of SF mixture . Lower reductions were found for 10% of sand replacement by ECat (see Figure 5). But a strong increase of shrinkage deformations was observed for 40% sand replacement with ECat. This might be due to the strong reduction of aggregate, it means sand which was replaced by ECat, phase volume or increase of binder phase. This might be due to the strong reduction in the inert materials present in the aggregates and, concomitantly, to a significant increase in the reactive materials present both in the binder phase and the ECat incorporated as a surrogate for sand. In addition, one can expect that after a given replacement level the dispersion of ECat particles in the matrix becomes less uniform and its effect as internal water reservoirs to mitigate autogenous shrinkage is less efficient.

3. Conclusions

This paper studied the efficiency of ECat for mitigating the autogenous shrinkage of UHPC, when used as a partial surrogate for sand. The results revealed that ECat particles act as internal reservoirs in UHPC matrix, feeding the capillary pores or a source of curing water to the paste volume in its vicinity. Among the replacement levels studied, 20% and 30% sand replacement by ECat was found to perform better in terms of autogenous shrinkage reduction without impairing the workability, and even improving the compressive strength at both the 7 and 28 days. Thus, further improvements of UHPC mixtures can be envisaged by replacing, simultaneously, part of the binder (cement+SF) and part of the fine aggregate by ECat, without impairing other properties like workability, compressive strength and durability. It should be mentioned also that a decrease of shrinkage deformations is also expected after the inclusion of fibres. Finally, the incorporation of ECat in UHPFRC saves landfill usage, turning an otherwise polluting waste into a value-added by-product.

Acknowledgement

The first author wishes to thank the financial support of the Portuguese Foundation for Science and Technology (FCT) through the PhD scholarship PD/BD/113636/2015, attributed within the Doctoral Program in Eco-Efficient Construction and Rehabilitation (EcoCoRe). The authors are also grateful to Dr. Eng. Lino Maia and CONSTRUCT. Acknowledgements are also due to Secil, GALP and Sika for supplying, respectively, cement, ECat and admixtures.

References

[1] R. Neves, C. Vicente, A. Castela, and M. F. Montemor, “Durability performance of

concrete incorporating spent fluid cracking catalyst," *Cem. Concr. Compos.*, vol. 55, pp. 308–314, Jan. 2015.

[2] W. J. W. Dale P. Bentz, "Internal Curing: A 2010 State-of-theArt Review," USA, 2011.

[3] D. P. Bentz and O. M. Jensen, "Mitigation strategies for autogenous shrinkage cracking," *Cem. Concr. Compos.*, vol. 26, no. 6, pp. 677–685, Aug. 2004.

[4] O. M. Jensen and P. F. Hansen, "Water-entrained cement-based materials," *Cem. Concr. Res.*, vol. 32, no. 6, pp. 973–978, 2002.

[5] G. Ye, N. Van Tuan, and H. Huang, "Rice Hush Ash as smart material to mitigate autogenous shrinkage in high (ultra-high) performance concrete," in *Third International Conference on Sustainable Construction Materials and Technologies (SCMT2013), At Kyoto, Japan*, 2013.

[6] A. M. Soliman and M. L. Nehdi, "Effect of drying conditions on autogenous shrinkage in ultra-high performance concrete at early-age," *Mat. Str.*, vol. 44, pp. 879–899, 2011.

[7] K. Kovler and O. M. Jensen, "Report rep041 : Internal Curing of Concrete - State-of-the-Art" Report of RILEM Technical Committee 196-ICC, 2007.

[8] Viet-Thien-An Van, Christiane Rößler, Danh-Dai Bui, and Horst-Michael Ludwig, "Rice husk ash as both pozzolanic admixture and internal curing agent in ultra-high performance concrete," *Cem. Concr. Compos.*, vol. 53, pp. 270–278, 2014.

[9] D. P. Bentz, M. R. Geiker, and K. K. Hansen, "Shrinkage-reducing admixtures and early-age desiccation in cement pastes and mortars," *Cem. Concr. Res.*, vol. 31, no. 7, pp. 1075–1085, Jul. 2001.

[10] K. J. Folliard and N. S. Berke, "Properties of high-performance concrete containing shrinkage-reducing admixture," *Cem. Concr. Res.*, vol. 27, no. 9, pp. 1357–1364, 1997.

[11] H.X.D. Lee, H.S.Wong and N.R. Buenfeld, "Self-sealing of cracks in concrete using superabsorbent polymers," *Cem. Concr. Res.*, vol. 79, pp. 194–208, Oct. 2016.

[12] N. T. Castellanos and J. T. Agredo, "Using spent fluid catalytic cracking (FCC) catalyst as pozzolanic addition - a review," *Ing. E Inv.*, vol. 30, no. 2, pp. 35–42, 2010.

[13] F. Ferella, V. Innocenzi, and F. Maggiore, "Oil refining spent catalysts: A review of possible recycling technologies," *Res. Cons. Recycl.*, vol. 108, pp. 10–20, Mar. 2016.

[14] "Key facts & figures | CEMBUREAU." [Online]. Available: http://www.cembureau.be/about-cement/key-facts-figures. [Accessed: 31-Mar-2016].

[15] L. S. Martínez, "Nuevas aportaciones en el desarrollo de materiales cementantes con residuo de Catalizador de Craqueo Catalítico Usado (FCC)," UNIVERSIDAD POLITECNICA DE VALENCIA, 2007.

[16] Y.-S. Tseng, C.-L. Huang, and K.-C. Hsu, "The pozzolanic activity of a calcined waste FCC catalyst and its effect on the compressive strength of cementitious materials," *Cem. Concr. Res.*, vol. 35, no. 4, pp. 782–787, 2005.

[17] B. Pacewska, M. Bukowska, I. Wilińska, and M. Swat, "Modification of the properties of concrete by a new pozzolan - A waste catalyst from the catalytic process in a fluidized bed," *Cem. Concr. Res.*, vol. 32, pp. 145–152, 2002.

[18] B. Pacewska, I. Wilińska, M. Bukowska, and W. Nocuń-Wczelik, "Effect of waste aluminosilicate material on cement hydration and properties of cement mortars," *Cem. Concr. Res.*, vol. 32, no. 11, pp. 1823–1830, 2002.

[19] J. Payá, J. Monzó, M. V. Borrachero, and S. Velázquez, "Evaluation of the pozzolanic activity of fluid catalytic cracking catalyst residue (FC3R). Thermogravimetric analysis

studies on FC3R-Portland cement pastes," *Cem. Concr. Res.*, vol. 33, no. 4, pp. 603–609, 2003.

[20] Sammy Y. N. Chan and X. Ji, "Comparative study of the initial surface absorption and chloride diffusion of high performance zeolite, silica fume and PFA concretes," *Cem. Concr. Compos.*, vol. 21, no. 4, pp. 293–300, Aug. 1999.

[21] J. June, U. Politecnica, E. Zornoza, P. Garcés, M. V Borrachero, and J. Payá, "Durability Properties of Mortars Partially Substituted with Spent Catalytic Cracking Catalyst," 2010.

[22] C. Costa and P. Marques, "Low-Carbon Cement with Waste Oil-Cracking Catalyst Incorporation," *2012 IEEE-IAS/PCA 54th Cement Industry Technical Conference*. IEEE, San Antonio, USA.

[23] Pedro Raposeiro Da Silva and Carla Costa, "Fresh Properties and Compressive Strength of self-compacting concrete containing waste fluid catalytic cracking catalyst," in *7th RILEM International Conference on SelfCompacting Concrete and 1st RILEM International Conference on Rheology and Processing of Construction Materials*, 2013.

[24] N. Su, H.-Y. Fang, Z.-H. Chen, and F.-S. Liu, "Reuse of waste catalysts from petrochemical industries for cement substitution," *Cem. Concr. Res.*, vol. 30, no. 11, pp. 1773–1783, 2000.

[25] C. Costa, M. S. Ribeiro, and N. Brito, "Effect of Waste Oil-Cracking Catalyst Incorporation on Durability of Mortars," *Mater. Sci. Appl.*, vol. 5, no. November, pp. 905–914, 2014.

[26] IPQ, "NP EN 196-3. Methods of testing cement - Part 3: Determination of setting times and soundness." 2006.

[27] H. Okamura and M. Ouchi, "Self-Compacting Concrete," *J. Adv. Concr. Technol.*, vol. 1, no. 1, pp. 5–15, 2003.

[28] IPQ, "NP EN 196-1: 2006. Methods of testing cement Part 1: Determination of strength." IPQ, Lisbon, pp. 1–33, 2005.

[29] ASTM, "ASTM C 1698-09. Standard Test Method for Autogenous Strain of Cement Paste and Mortar," vol. i, no. C. pp. 1–8, 2013.

[30] Japan Society of Civil Engineers, "Recommendations for Design and Construction of High Performance Fiber Reinforced Cement Composites with Multiple Fine Cracks (HPFRCC)," Concr. Eng. Ser., vol. 82, p. Testing Method 6–10, 2008.

[31] K. C. Hsu, Y. S. Tseng, F. F. Ku, and N. Su, "Oil cracking waste catalyst as an active pozzolanic material for superplasticized mortars," *Cem. Concr. Res.*, vol. 31, no. 12, pp. 1815–1820, 2001.

[32] J. Payá, J. Monzó, and M. V. Borrachero, "Physical, chemical and mechanical properties of fluid catalytic cracking catalyst residue (FC3R) blended cements," *Cem. Concr. Res.*, vol. 31, pp. 57–61, 2001.

[33] K. Habel, "Structural behaviour of elements combining Ultra-High Performance Fibre Reinforced Concretes (UHPFRC) and Reinforced Concrete," 2004.

[34] P. F. Jensen, O.Mejlhede; Hansen, "Autogenous deformation and change of the relative humidity in silica fume-modified cement paste," *ACI Mater. J.*, vol. 93, pp. 539–543, 1996.

[35] P. K. Mehta and P. J. M. Monteiro, *Concrete: microstructure, properties, and materials*. 2006.

Author Index

Kamilia Abahri 385
Lucas Adelaide 95
Yilmaz Akkaya 453
Marcos G. Alberti 287
Hartmann Alberts 39
Ouali Amiri 221
Ali Amiri 493
Armen Amirkhanian 211
José J. Anaya 755
Sofia Aparicio 755
Paul Archbold 513
Miguel Azenha XIII 297 651
Jesus Miguel Bairan 145
Diana Bajare 435
Luis Baquerizo 463
Zeynep Basaran Bundur 493
Muhammed Basheer 307
Farid Benboudjema 59 325 675 715 725
Ahmed Zakarya Bendimerad 407
Rachid Bennacer 385
Shashank Bishnoi 573
Dubravka Bjegović 553
Edgar Bohner 165
Stéphanie Bonnet 533
Elia Boonen 735
Xavier Bourbon 95 425
Véronique Bouteiller 95
Rok Bregar 503
Matthieu Briffaut 125
Eric Brouard 483
Laurie Buffo-Lacarrière 425
Vesna Bulatović 523
Girts Bumanis 435
Paulo Cachim 195
Yin Cao 579 695
Jérôme Carette 377 385
Pietro Carrara 543
Thierry Chaussadent 95
Jiayi Chen 745
Özlem Cizer 317 573
Utkan Corbacioglu 453
Manuel Corbin 79
Pedro Costa 195
Carla Costa 395
Alex Coyle 211
Maria D. Crespo 145
Wilson Ricardo Leal Da Silva 463
Aveline Darquennes 325 385 725
Gheorghe-Alexandru David 503
Nele De Belie 177
José de Frutos 621
Laura De Lorenzis 543
Caroline De Sa 325
Geert De Schutter 203
Ákos Debreczeni 415
Arnaud Delaplace 483
Brice Delsaute 407
Fuat Demir 443
Dries Devisscher 177
Joris Dockx 317
Hua Dong 355
Wei Dong 685
Peter Dubruel 177
Cyrille Dunant 345
Youssef El Bitouri 425
Mats Emborg 609
Alejandro Enfedaque 287
Oskar Esping 155
Rui Faria 641
Emanuel Felisberto 641
Ignasi Fernandez Perez 231
Denise Ferreira 145
Miguel Ferreira 165
John Flattery 513
José Vicente Fuente 755
Ivan Gabrijel XIII 553 705
Erez Gal 789
Jaime C. Galvez 287
Peng Gao 789
Ricardo García-Rovés 621
Paolo Gardoni 631
Fabrice Gatuingt 675
Carlos Gil Berrocal 231
Zehra Canan Girgin 365
Margarita González 755
Jorge Gosalbez 755
Joan Govaerts 259
José Granja 297
Viktor Gribniak 279
Eugenijus Gudonis 279
Alex-Walter Gutsch 39
Karolina Hajkova 463
Petr Havlasek 463
Hans Hedlund 609
Peter Heinrich 249
Christian Hellmich 665
Wibke Hermerschmidt 39 715
Adrien Hilaire 345
Volker Hirthammer 115
Douglas Hooton 105
Liesbeth Horckmans 317
Muhammad Irfan-Ul-Hassan 665
Diederik Jacques 203 259
Michaela Jakubickova 735
Ronaldas Jakubovskis 279
Ole Mejlhede Jensen XIII XV
Shiju Joseph 573
Xavier Jourdain 675
Joachim Juhart 503
Mantas Juknys 279
Sakdirat Kaewunruen 135
Gintaris Kaklauskas 269 279
Zainab Kammouna 125
Terje Kanstad XIII 589
Gediminas Kastiukas 685
Said Kenai 777
Egemen Kesler 453
Vitaliy Kindrachuk 115
Gunrid Kjellmark 589
Anja Estensen Klausen 589
Agnieszka Knoppik-Wróbel 49
Eduardus Koenders 599
Pavel Krivenko 1 11
Markus Krüger 503
Josip Kujek 553
Markus Königsberger 665
Serhii Lakusta 11
Oles Lastivka 11
Martin Laube 39
Kefei Li 69

Quanwang Li 69
Ming Li 241
Yi-Gang Li 335
Juan Li 579
Anders Lindvall 155
Xian Liu 745
Olfa Loukil 95
Ahmed Loukili 407
Ivan Lukić 523
Karin Lundgren 231
Tang Luping 155 307
Ingemar Löfgren 155 231 609
Marie Malbois 325
Yann Malecot 125
Mirjana Malešev 523
Antonio Mari 145
Enrico Masoero 21
Benoit Masson 79
Ana Mafalda Matos 395
Thomas Matschei 463
W. John McCarter 307
Belkacem Menadi 777
Esperanza Menéndez 621
Arn Mignon 177
Shintaro Minoura 135
André Monteiro 195
Gábor Mucsi 415
Cecilie Myklebust Helle 29
Georges Nahas 385
Sreejith Nanukuttan 307 599 651
Phu Tho Nguyen 221
Xu-Jing Niu 335
Sandra Nunes 395
Ravi A. Patel 203 259
Gai-Fei Peng 335
Janez Perko 203 259
Frantisek Peterka 735
Bernhard Pichler 665
Christoph Pohl 115
Marc Quiertant 95
Miroslava Radeka 523
Vlastimir Radonjanin 523
Frédéric Raguenau 95
Regimantas Ramanauskas 269 279
Alex Remennikov 135
Encarnación Reyes 287
Desmond Robinson 599
Pierre Rossi 765
Emmanuel Rozière 407 651
Igor Rudenko 11
Sergio Ruiz 621
Samindi Samarakoon 29
Emre Sancak 443
Faez Sayahi 609
Tereza Sazavska 735
Dirk Schlicke XIII 49 249 563 651
Dalibor Sekulic 705
Alain Sellier 425
Tristan Senga Kiesse 533
Marijana Serdar 651
Mahmoud Shakouri 631
G Sherzer 789
Igor Shvab 21
Vit Smilauer 463
Ruben Snellings 317
Adrien Socie 325
Aleksandr Sokolov 279
François Soleilhet 675
Carlos Sousa 641
Radoslav Sovjak 473
Robert Spragg 211
Stéphanie Staquet 377 407 651
Jan Sælensminde 29
Tayfun Altuğ Söylev 187
Olli Saarela 165
Van Loc Ta 533
Jean-Louis Tailhan 765
Robert Teuber 39
Eckart Thoms 39
Qian Tian 241
Thomas Titscher 115
David Trejo 631
Laurent Trenty 95
Gregor Trtnik 651
Nguyen Viet Tue 563
Viktor Török 415
Neven Ukrainczyk 599
Jörg F. Unger 115
Koenraad Van Balen 317 573
Klaas Van Breugel 203
Céline Van Bunderen 317
Sandra Van Vlierberghe 177
Jos Vandekeybus 317
Lucie Vandewalle 317
Mariana Vasylchenko 725
Anne Ventura 533
Jolien Vermeulen 177
Clément Vert 483
Yujiang Wang 241
Ling Wang 579
Zhendi Wang 579
Ling Wang 695
Zhendi Wang 695
Tsutomu Watanabe 135
Jason Weiss 211
Walid Yahiaoui 777
Yan Yao 579 695
Guang Ye 203 355 745 789
T. Alper Yıkıcı 453
Dongdong Zhang 69
Yi-Lin Zhao 335
Xiangming Zhou 685
Semion Zhutovsky 105
Şükrü Özkan 443

Materials, Systems and Structures in Civil Engineering 2016

Service Life of Cement-Based Materials and Structures

Vol. 1

Edited by
Miguel Azenha, Ivan Gabrijel, Terje Kanstad, Dirk Schlicke and Ole Mejlhede Jensen

RILEM Proceedings PRO 109
ISBN Vol. 1: 978-2-35158-170-4
ISBN Vol. 2: 978-2-35158-171-1
ISBN Vol. 1&2: 978-2-35158-172-8
e-ISBN: 978-2-35158-173-5

This volume contains the proceedings of the MSSCE 2016 conference segment on "Service Life of Cement-Based Materials and Structures", which is organized by COST Action TU1404 (www.tu1404.eu). This COST Action is entitled: "Towards the next generation of standards for service life of cement-based materials and structures", dedicated to assist deepening knowledge regarding the service life behaviour of cement-based materials and structures. The main purpose of this Action is to bring together relevant stakeholders (experimental and numerical researchers, standardization offices, manufacturers, designers, contractors, owners and authorities) in order to reflect today's state of knowledge in new guidelines/recommendations, introduce new products and technologies to the market, and promote international and inter-speciality exchange of new information, creating avenues for new developments. The COST Action is basically divided in three main workgroups targeted to this purpose:

WG1 – Testing of cement-based materials and RRT$^+$

WG 2 – Modelling and benchmarking

WG 3 – Recommendations and products

Also, two important instruments of the Action are now under way: the Extended Round Robin Testing Program (RRT$^+$), and the numerical benchmarking. The RRT$^+$ is currently involving 43 laboratories.

The present conference segment deals with a wide breadth of topics related to the service life of concrete, comprising aspects related to the 3 Workgroups mentioned above. The conference segment is attended by 80 presenters from university, industry and practice representing more than 30 different countries. All contributions have been peer reviewed.

The event "Materials, Systems and Structures in Civil Engineering 2016", 15-29 August 2016, Lyngby, Denmark, is scientifically sponsored by RILEM. The event is hosted by the Department of Civil Engineering at the Technical University of Denmark and is financially sponsored by a number of independent foundations and organizations.

RILEM Publications S.a.r.l.
157 rue des Blains, F-92220 Bagneux - FRANCE
Tel: +33 1 45 36 10 20 Fax: +33 1 45 36 63 20
E-mail: dg@rilem.net